International Journal of Geophysics

Seismic Imaging

Guest Editors: Martin Tygel, Norm Bleistein, Yu Zhang, and Sergey Fomel

Seismic Imaging

International Journal of Geophysics

Seismic Imaging

Guest Editors: Martin Tygel, Norm Bleistein, Yu Zhang, and Sergey Fomel

Editorial Board

Contents

Hindawi Publishing Corporation
International Journal of Geophysics
Volume 2011, Article ID 815357, 2 pages
doi:10.1155/2011/815357

Editorial

Seismic Imaging

Martin Tygel,[1] Norm Bleistein,[2] Yu Zhang,[3] and Sergey Fomel[4]

[1] *Department of Applied Mathematics, State University of Campinas (UNICAMP), R. Sérgio Buarque de Holanda 651, 13083-859 Campinas, SP, Brazil*
[2] *Center for Wave Phenomena (CWP), Colorado School of Mines, Golden, CO 80401, USA*
[3] *Processing Imaging & Reservoir, CGGVeritas, Crompton Way, Manor Royal Estate, Crawley, West Sussex RH10 9QN, UK*
[4] *Bureau of Economic Geology, The University of Texas at Austin, University Station, Box X, Austin, TX 78759, USA*

Correspondence should be addressed to Martin Tygel, tygel@ime.unicamp.br

Received 7 December 2011; Accepted 7 December 2011

As organized and intelligible displays of data, seismic images constitute invaluable tools for gaining and conveying information on structural and material properties of the Earth. The present special issue on "*Seismic imaging*" aims to explore basic and/or applied aspects of seismic data that are relevant to meet today's challenges in subsurface imaging. It comprises 13 articles, covering a wide variety of state-of-the-art topics on seismology and seismics, on both theoretical, and practical issues.

H. Kern examines, in the form of a review, the interdependence of elastic wave propagation and physical and lithological parameters. For that aim, compressional (Vp), shear wave velocities (Vs) and velocity anisotropy of crustal rocks measured at conditions of greater depth are used to evaluate how elastic properties of rock materials are controlled by lithology at in situ pressures and temperatures. Laboratory seismic measurements and theoretical calculations are used to interpret a shallow seismic reflection line and a deep-crust refraction profile.

P. Singh and T. Davis investigate the detection of Morrow sandstones in connection to the exploration of new oil fields and the characterization of existing ones. Such sandstones are often very thin and laterally discontinuous. Full waveform modeling is performed to understand the Morrow sandstone signatures on compressional wave (P-wave), converted-wave (PS-wave), and pure shear wave (S-wave) gathers. Modeling tied with the field data demonstrates that S-waves are more robust than P-waves in detecting the Morrow sandstone reservoirs.

By means of a detailed study of P-wave arrival times of a significant number of local earthquakes, H. Li et al. obtain three-dimensional, high-resolution, P-wave velocity models under the Zipingpu reservoir in Longmenshan fault. The 3D velocity images at shallow depth show that the low-velocity regions have strong correlation with the surface trace of the reservoir. From the study, the infiltration depths directly from the Zipingpu reservoir, and also downwards along the Beichuan-Yingxiu, are quantitatively estimated.

In a review article, M. Kanao et al. analyze broadband seismic deployments carried out in the Lützow-Holm Bay region, East Antarctica. Recorded teleseismic and local events enable imaging the structure and dynamics of the crust and mantle of the terrain. By combining the active and passive source studies of the mantle structure, an evolution model for constructing the present mantle structure in the region is proposed.

X. Yu et al. present a new tomographic method that uses P arrival times to determine 3D crustal velocity structures, as well as hypocenter parameters of seismic events under the Beijing-Tianjin-Tangshan region. In the North China Basin, the depression and uplift areas are imaged as slow and fast velocities, respectively. A broad low-velocity anomaly exists in Tangshan and surrounding area from 20 km down to 30 km depth. The results suggest that the top boundary of low-velocity anomalies is at about 25.4 km depth. The event relocations inverted from double-difference tomography are clustered tightly along the Tangshan-Dacheng Fault and form three clusters on the vertical slice. The maximum focal depth after relocation is about 25 km in the Tangshan area.

Nowack assesses the potential of dynamically focused Gaussian beams for seismic imaging. Focused Gaussian beams away from the source and receiver plane allow the narrowest and planar portions of the beams to occur at the depth of a specific target structure. To provide additional control of the imaging process, dynamic focusing is investigated where all subsurface points are specified to have the same planar beam fronts. The approach is tested with a simple model of 5-point scatterers which are then imaged with the data, and then to the imaging of a single dynamically focused beam for one shot gather computed from the Sigsbee2A model.

W. Burnett and S. Fomel extend time-domain velocity continuation to the zero-offset 3D azimuthally anisotropic case. Velocity continuation describes how a seismic image changes given a change in migration velocity. This description turns out to be of a wave propagation process, in which images change along a velocity axis. In the anisotropic case, the velocity model is multiparameter, so that anisotropic image propagation is multidimensional. A three-parameter slowness model is considered which is related to azimuthal variations in velocity, as well as their principal directions. This information is useful for fracture and reservoir characterization from seismic data. Synthetic diffraction imaging examples are provided to illustrate the concept and potential applications of azimuthal velocity continuation and to analyze the impulse response of the 3D velocity continuation operator.

J. van der Neut et al. employ controlled-source seismic interferometry to redatum sources to downhole receiver locations without requiring a velocity model. Interferometry is generally based on a source integral over cross-correlation pairs of full, perturbed (time-gated), or decomposed wavefields. An overview is provided on the effects of ghosts, multiples, and spatial blurring that can occur for different types of interferometry. It is shown that replacing crosscorrelation by multidimensional deconvolution (MDD) can deghost, demultiple, and deblur retrieved data, but it leaves particular multiples in place. To remove all overburden-related effects, MDD of decomposed fields should be applied.

T. van Leeuwen et al. explore the use of stochastic optimization methods for seismic waveform inversion. The concept of stochasticity is introduced in waveform inversion problem in a rigorous way via a technique called randomized trace estimation. Theoretical results are reviewed that underlie the use of stochastic methods for waveform inversion. By means of illustrative numerical examples, it is found that it is possible to reproduce results that are qualitatively similar to the solution of the full problem with modest batch sizes. This may lead to an order of magnitude speedup for waveform inversion in practice.

T. Alkahlifah and P. Sava consider transversely isotropic (TI) models in which the tilt is constrained to be normal to the dip. Such consideration allows for simplifications in the imaging and velocity model building efforts as compared to a general transversely isotropic TI (TTI) model. Although this model cannot be represented physically in all situations, it handles arbitrary reflector orientations under the assumption of symmetry axis normal to the dip. Utilizing the reflection features of such a model, efficient downward continuation algorithms, as compared to the general TTI ones, can be constructed. These features enable a process in which one can extract velocity information by including tools that expose inaccuracies in the velocity model in the downward continuation process. The model is tested on synthetic data corresponding to a general TTI medium showing good results.

E. G. Asgedom et al. develop a higher-resolution method for the estimation of the three travel-time parameters that are used in the 2D zero-offset, Common-Reflection-Surface stack method. The underlying principle in this method is to replace the coherency measure performed using semblance with that of MUSIC (multiple signal classification) pseudospectrum that utilizes the eigenstructure of the data covariance matrix. The performance of the two parameter estimation techniques (i.e., semblance and MUSIC) is investigated using both synthetic seismic diffraction and reflection data corrupted with white Gaussian noise, as well as a multioffset ground penetrating radar (GPR) field data set. The estimated parameters employing MUSIC were shown to be superior of those from semblance.

Three-dimensional wave-equation migration techniques are still quite expensive because of the huge matrices that need to be inverted. J. C. Costa et al. compare the performance of splitting techniques for stable 3D Fourier finite-difference (FFD) migration techniques in terms of image quality and computational cost. The FFD methods are complex Padé FFD and FFD plus interpolation, and the compared splitting techniques are two- and four-way splitting. From numerical examples in homogeneous and inhomogeneous media, we conclude that, though theoretically less accurate, alternate four-way splitting yields results of comparable quality as full four-way splitting at the cost of two-way splitting.

Linearized multiparameter inversion is a model-driven variant of amplitude-versus-offset analysis, which seeks to separately account for the influences of several model parameters on the seismic response. R. Nammour and W. W. Symes suggest an approach based on the mathematical nature of the normal operator of linearized inversion, which is a scaling operator in phase space, and on a very old idea from linear algebra, namely, Cramer's rule for computing the inverse of a matrix. The approximate solution of the linearized multiparameter problem so produced involves no ray theory computations. It may be sufficiently accurate for some purposes; for others, it can serve as a preconditioner to enhance the convergence of standard iterative methods.

Martin Tygel
Norm Bleistein
Yu Zhang
Sergey Fomel

Hindawi Publishing Corporation
International Journal of Geophysics
Volume 2011, Article ID 216315, 13 pages
doi:10.1155/2011/216315

Research Article

Seismic Imaging and Seismicity Analysis in Beijing-Tianjin-Tangshan Region

Xiangwei Yu,[1] Wenbo Zhang,[1] and Yun-tai Chen[2]

[1] Key Laboratory of Computational Geodynamics, Chinese Academy of Sciences, Beijing 100049, China
[2] School of Earth and Space Sciences, Peking University, Beijing 100871, China

Correspondence should be addressed to Xiangwei Yu, yuxw@gucas.ac.cn

Received 13 December 2010; Revised 22 March 2011; Accepted 20 May 2011

Academic Editor: Yu Zhang

In this study a new tomographic method is applied to over 43,400 high-quality absolute direct P arrival times and 200,660 relative P arrival times to determine detailed 3D crustal velocity structures as well as the absolute and relative hypocenter parameters of 2809 seismic events under the Beijing-Tianjin-Tangshan region. The inferred velocity model of the upper crust correlates well with the surface geological and topographic features in the BTT region. In the North China Basin, the depression and uplift areas are imaged as slow and fast velocities, respectively. After relocation, the double-difference tomography method provides a sharp picture of the seismicity in the BTT region, which is concentrated along with the major faults. A broad low-velocity anomaly exists in Tangshan and surrounding area from 20 km down to 30 km depth. Our results suggest that the top boundary of low-velocity anomalies is at about 25.4 km depth. The event relocations inverted from double-difference tomography are clusted tightly along the Tangshan-Dacheng Fault and form three clusters on the vertical slice. The maximum focal depth after relocation is about 25 km depth in the Tangshan area.

1. Introduction

Beijing-Tianjin-Tangshan (BTT) region (114°E~120°E, 37.5°N~41.5°N) is situated in the northern part of North China. Figure 1 shows the major geological structure in the BTT region. This study region is under complex tectonic process with the Taihangshan uplift in the west, the Yanshan uplift in the northeast, and the North China Basin in the middle portion, which is a large continental basin and is characterized as an alternate uplift and depression zone [7, 8]. As shown in Figure 1, in the North China Basin and Taihangshan uplift, there are several active Cenozoic faults, such as Weixian-Yanqing Fault, Tongxian-Nanyuan Fault, Xiadian-Fengheying-Caojiawu Fault, and Tangshan-Dacheng Fault, that are oriented in NE-SW direction. There are also some active faults in NW-SE direction in the BTT region, such as Western Luanxian Fault, Laishui Fault, Ninghe Fault, and Nankou-Sanhe Fault.

The BTT region is a very active area with high seismicity. In this region, earthquakes are concentrated in four seismic zones: Zhangjiakou-Bohai seismic zone, Tangshan-Hejian-Cixian seismic zone, Sanhe-Linshou seismic zone, and Huailai-Weixian seismic zone. The Zhangjiakou-Bohai seismic zone in NW-SE direction is most active with a majority of large earthquakes in the BTT region. The other three seismic zones are parallel to each other in the NE-SW direction. Historically, strong earthquakes occurred frequently in this region. So far, more than 100 earthquakes with magnitude equal to and larger than 5.0 have occurred there since 780 BC. Thirty-four of them are with magnitudes larger than 6.0 and seven with magnitudes larger than 7.0. The great Tangshan earthquake ($M_S = 7.8$) in 1976 is one of the most destructive earthquakes in history, which totally destroyed Tangshan city and caused a casualty of ~240,000. Therefore, a detailed investigation of the crustal structure and seismicity of the BTT region is very important not only for the understanding of physics of continental earthquakes but also for the assessment and mitigation of seismic hazard.

A lot of studies have been performed in the past three decades to invert for the three-dimensional (3D) seismic velocity structure of the crust and upper mantle beneath this region using arrival times from local and/or teleseismic events [2, 9–15] as well as the seismicity in this region [16–24]. However, the spatial resolution and the accuracy of event

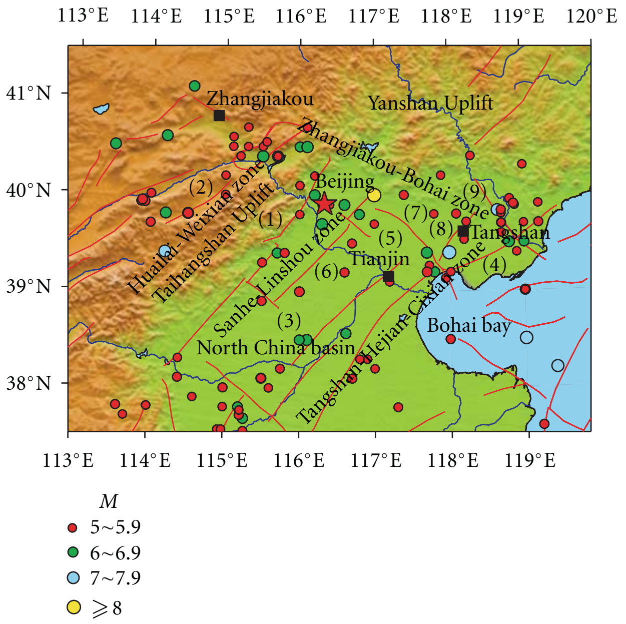

Figure 1: Geological setting and historical earthquakes in the BTT region. Colorful circles show the earthquakes with magnitudes (M) equal to or greater than 5.0 that occurred in the BTT region since 780 BC. Black squares denote major cities. Red star shows the capital of China. Thick curved lines show major active faults: (1) Tongxian-Nanyuan Fault; (2) Weixian-Yanqing Fault; (3) Laishui Fault; (4) Changli-Ninghe Fault; (5) Nankou-Sanhe Fault; (6) Xiadian-Fengheying-Caojiawu Fault; (7) Ninghe Fault; (8) Tangshan-Dacheng Fault; (9) Western Luanxian Fault.

location are limited by using only the absolute arrival times. To improve the resolution of regional tomography, some seismic tomographic techniques have been developed, such as double-difference tomography (tomoDD) [6], which uses both absolute and relative arrival time data to determine a 3D velocity structure jointly with the absolute and relative event location. Furthermore, most of the previous efforts have focused on the crustal and mantle structure [2, 9–15] whereas little effort has been devoted to the study of relationship between seismicity of small earthquakes and velocity anomaly. Where is the location of top boundary of low velocity beneath Tangshan area? What is the deepest focal depth of the relocated earthquakes inverted by tomography? What is the main dynamic source for the great Tangshan earthquake? The detailed structure of hypocentral area is still unclear beneath the Tangshan area. Determining a high-resolution 3D velocity model of the crust and upper mantle beneath this region is the key for answering these questions. The tomoDD imaging has the potential to bring substantial insight into them by using both absolute and relative arrival time data.

In this study, we apply the tomoDD method to combine absolute and relative arrival time data to invert for the detailed 3D crustal P wave velocity structure jointly with absolute and relative event locations in the BTT region. Our results will shed new light on the relationship between relocated seismicity and the 3D velocity structure.

2. Data and Method

Both absolute and relative arrival times are used in this study. We carefully select the data such that each event has at least 6 recordings (8 in the Tangshan area). The resulting data include over 43,400 high-quality absolute direct P arrival times and 200,660 relative P arrival times from 3,983 earthquakes recorded by one or more of the 112 stations of the North China Telemetry Seismic Network (NCTSN) and the Capital Digital Seismic Network (CDSN) from 1993 to 2004 in the BTT region (Figure 2). The accuracy of the first P arrival time picking is estimated to be 0.2~0.3 s. The focal depth varies from ground surface down to about 30 km depth. The ray path coverage is generally good except Bohai Bay where no seismic station is present (Figure 3).

The tomoDD, developed by Zhang and Thurber [6], is used in this study to determine a 3D velocity structure jointly with the absolute and relative event location, which is based on the hypoDD of Waldhauser and Ellsworth [5] and also uses both absolute and relative arrival time data. With standard tomography, event locations will be somewhat scattered due to imprecise picks and origin-time errors. The tomoDD method uses the differential arrival times which are free from origin-time errors, and thus it removes some fuzziness from the velocity model.

Our starting 1D model is inferred from a minimum 1D velocity model [2] for the crust (0~25 km depth) and from deep seismic soundings [25, 26] for the deeper crust and upper mantle (25~40 km depth) (Figure 4). A 3D regular grid is used in this study [27]. The velocity values are interpolated by using a trilinear interpolation method. The model has been parameterized into an optimal grid spacing of 50 km laterally and 5 km vertically after a number of resolution tests for different grid spacing. Distance weighting is used in this study to control the maximum separation between event pairs. For closer event pairs a larger weight is applied. Considering the trade-off between the roughness and the stabilization of the model, we choose the model using smoothing weight of 5 as the preferred model. Velocity structure and hypocentral parameters of the local earthquakes are all taken to be unknown parameters in the inversion. A detailed description of the method is given by Zhang and Thurber [6].

3. Seismic Tomography

Local (regional) earthquake tomography (LET) plays an important role in studying the velocity structure of the Earth's interior, which has become a relatively routine application for use in seismically active regions covered by one or more dense seismic network.

We conduct many inversions using different values of damping parameter for the variance of the velocity perturbations and root-mean-square (rms) travel time residuals. We find that the best value of the damping parameter is 150. In order to confirm the main features of our tomographic image, we conduct a resolution test to assess the adequacy of the ray coverage and to evaluate the resolution [28, 29]. An initial checkerboard velocity model is created by assigning

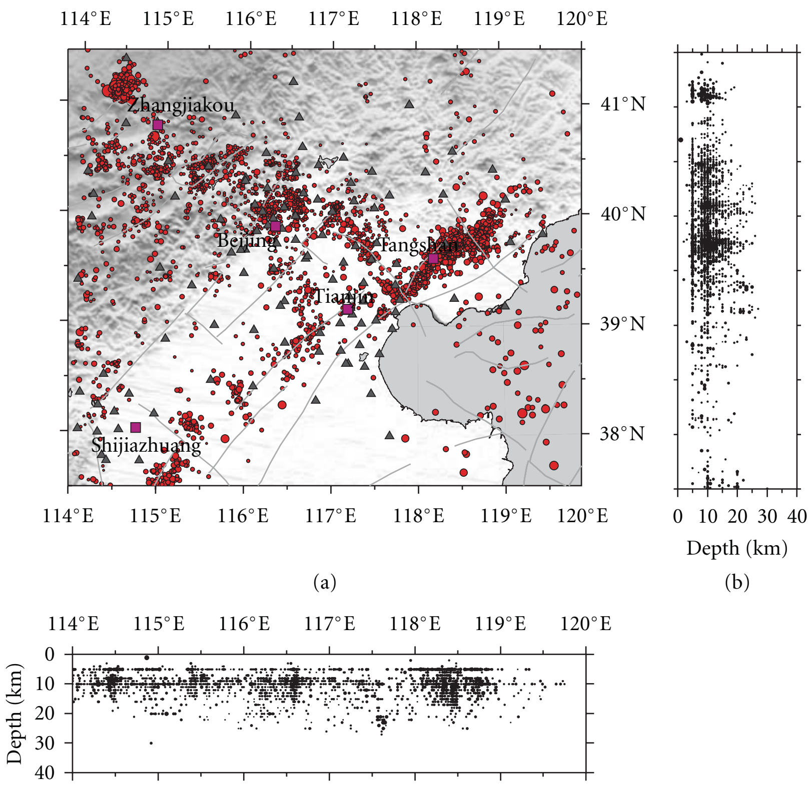

(a)

(b)

(c)

Figure 2: Distribution of seismic stations and earthquake hypocenters used in this study. (a) shows distribution of earthquake epicenters (circles) and seismic stations (triangles). Squares show the major cities. Thick lines denote active faults; (b) and (c) show the cross sectional view of focal depth along latitude and longitude profiles, respectively.

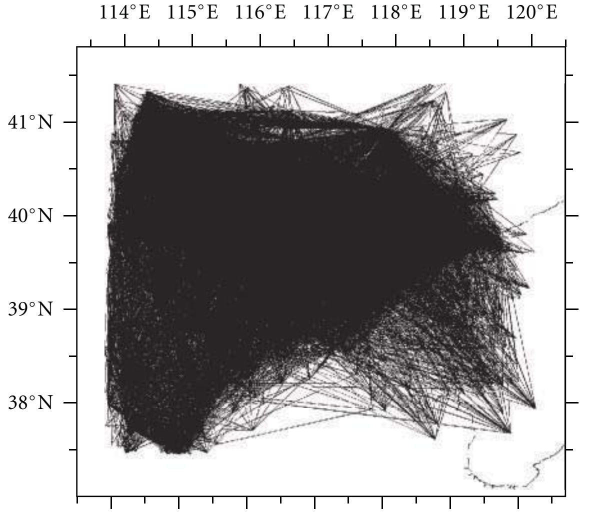

Figure 3: Distribution of P wave ray paths used in this study in map view.

alternately positive and negative velocity anomalies (3%) to the 3D grid nodes in the model space. Synthetic travel times are calculated for the checkerboard model using the real event and receiver locations. A random noise with zero mean and standard deviation of 0.1 s is added to the synthetic data. The resolution is considered to be good for regions where the checkerboard image is well recovered. Figure 5 shows the result. The checkerboard pattern is recovered for almost the entire study region except for Bohai Bay and the edge of the BTT region (Figures 5(a)–5(f)). Areas with low resolution are excluded from the resulting tomographic images (Figure 6). The best resolution is in the depth range of 5–20 km (Figures 5(a)–5(d)), where the amplitude of velocity anomalies is well recovered across the whole region. The resolution is reduced below 30 km depth. But the checkerboard positive and negative patterns are basically recovered.

In order to show more clearly the continuous variations of velocity anomalies in the depth direction, our resulting tomographic images are presented in Figure 6. In general, the results reveal strong lateral heterogeneities in both of the crust and uppermost mantle. It is noted that the media beneath the Tangshan area are very different from adjacent areas throughout the crust and upper mantle. In the shallow depth (Figures 6(a) and 6(b)), the inversion results are consistent with the local geological settings and follow the trend of active faults in the BTT region. The tomographic images illustrate that the low P velocity (low-V) anomalies exist beneath depressions and basins (such as the North China Basin) and high P velocity (high-V) anomalies exist

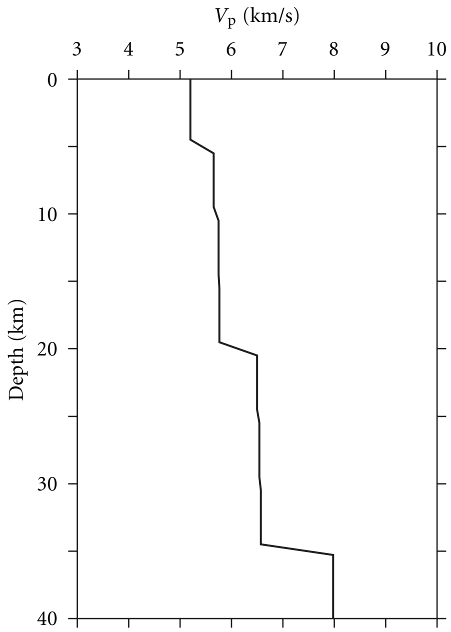

Figure 4: The starting 1D model used for the tomoDD in this study.

beneath mountains and uplifts (such as Yanshan uplift and Taihangshan uplift), which is consistent with the previous standard tomographic studies [2, 9–15]. But our model has sharper velocity contrasts near the boundary between low-*V* and high-*V* anomalies than previous tomography models do. Although the Tangshan area is located in the North China Basin, it is an uplifted block beside the Zhangjiakou-Bohai seismic zone [21]; hence, it shows up as high-*V* anomaly. At the 35 km depth, our present result has revealed that a broad and prominent low-*V* anomaly exists beneath the Taihangshan uplift area and the Tangshan area, and high-*V* anomaly exists beneath the Yanshan uplift and the North China Basin. These results are consistent with the P_n tomographic results [15, 30, 31].

Several cross-sections along the different longitudes (115.5°E, 116.5°E, 117.5°E, and 118.5°E) and latitudes (40.5°N, 39.8°N, and 39.0°N) are presented in Figure 7. At shallow depth (5∼10 km), the boundary between the low-*V* anomaly and high-*V* anomaly is well consistent with the boundary between mountain/uplift and plain/basin, such as the 39.5°N area at the 115.5°E profile (Figure 5(a)) and 118.0°E area at the 39.8°N profile (Figure 7(b)). Our tomoDD model shows a high-*V* anomaly of ∼90 km length at 10∼20 km depth under the Beijing, Tianjin, and the Tangshan area at the profile of 116.5°E, 117.5°E, and 118.5°E (Figure 5(a)). A prominent broad low-*V* anomaly is discovered from 20 km to 30 km both beneath Yanshan uplift, the North China Basin area at the profile of 115.5°E (Figure 5(a)), and beneath the Tangshan area at the profile of 118.5°E (Figure 5(a)). At the profile of 39.8°N (Figure 5(b)), the P velocity is high beneath the east of the Tangshan area, where there is uplift block near the Zhangjiakou-Bohai seismic zone. Moreover, it can also be found that a broad high-*V* anomaly beneath the Taihangshan uplift extends toward the east and down to ∼20 km depth beneath the Beijing area.

4. Relationship between Seismicity and Tomography Image in the BTT Region

An advantage of the tomoDD is that it determines the 3D velocity model as well as the absolute and relative event location compared with standard tomography. We analyzed 3,983 earthquakes with magnitudes from *M* 1.0 to 6.2 recorded by 112 stations. An event will be excluded from the inversion if it cannot be connected to any other events, and as a result only 2,809 hypocentral parameters of both absolute and relative locations are given by the tomoDD. The weighted rms travel-time residuals decrease from 1.2 s to 0.3 s. Figure 2 shows the catalog locations, which are scattered along major active fault zone both in horizontal direction and depth direction due to imprecise picks, origin-time errors, and simple 1D velocity model. After relocation, the tomoDD method provides a sharp picture of the seismicity in the BTT region, which is concentrated along with the major faults in a shape of alignment (Figure 8).

To illuminate the relationship between seismicity and velocity anomaly, we present our tomographic images together with hypocentral locations of both relocated earthquakes within 5 km off each layer depth and historic earthquakes ($M \geq 6.0$) that occurred in the BTT region (Figure 9). Although we do not know the accurate focal depths of the historic earthquakes, the statistic analysis of focal depth after the tomoDD relocation [32] suggests that most of earthquakes that occurred in the middle and lower crust under the BTT region and the North China are mainly clustered at 1∼24 km depth. In the tomographic image of 10 km and 15 km depth (Figure 9), both the relocated earthquakes and historic earthquakes have a similar feature, that is, most of the earthquakes are located in the conjunctional areas of low-*V* and high-*V* anomalies. They are slightly closer to the high-*V* anomaly areas. The epicentral location of the 1976 Tangshan earthquake, the 1976 Luanxian earthquake, and the 1679 Sanhe earthquake is in the transitional area closer to the high-*V* anomalies. It is notable that the distribution of relocated small earthquakes is consistent with the trend of high-*V* anomalies under the Beijing-Tangshan area. Maybe it suggests that the conjunctional zones of low-*V* and high-*V* anomalies represent weak sections of the seismogenic crust. The tectonic stresses are prone to being accumulated in the "brittle" high-*V* anomalies area, and hence the earthquake ruptures happened closer to the high-*V* anomalies zones. The locations of earthquakes, especially destructive earthquakes, are not random and are related closely to their deep structure of crust and upper mantle.

Figure 10(a) shows a cross-section along profile AA′ (Figure 10(c)) passing through the Tangshan-Hejian-Cixian seismic zone. A prominent high-*V* anomaly zone about 100 km in length is visible from 10 km down to 20 km depth along the Tangshan-Tianjin area, while a broad low-*V* anomaly exists in Tangshan and the north of the Tangshan area from 20 km down to 30 km, which is in agreement with the tomographic results of Huang and Zhao [15] using

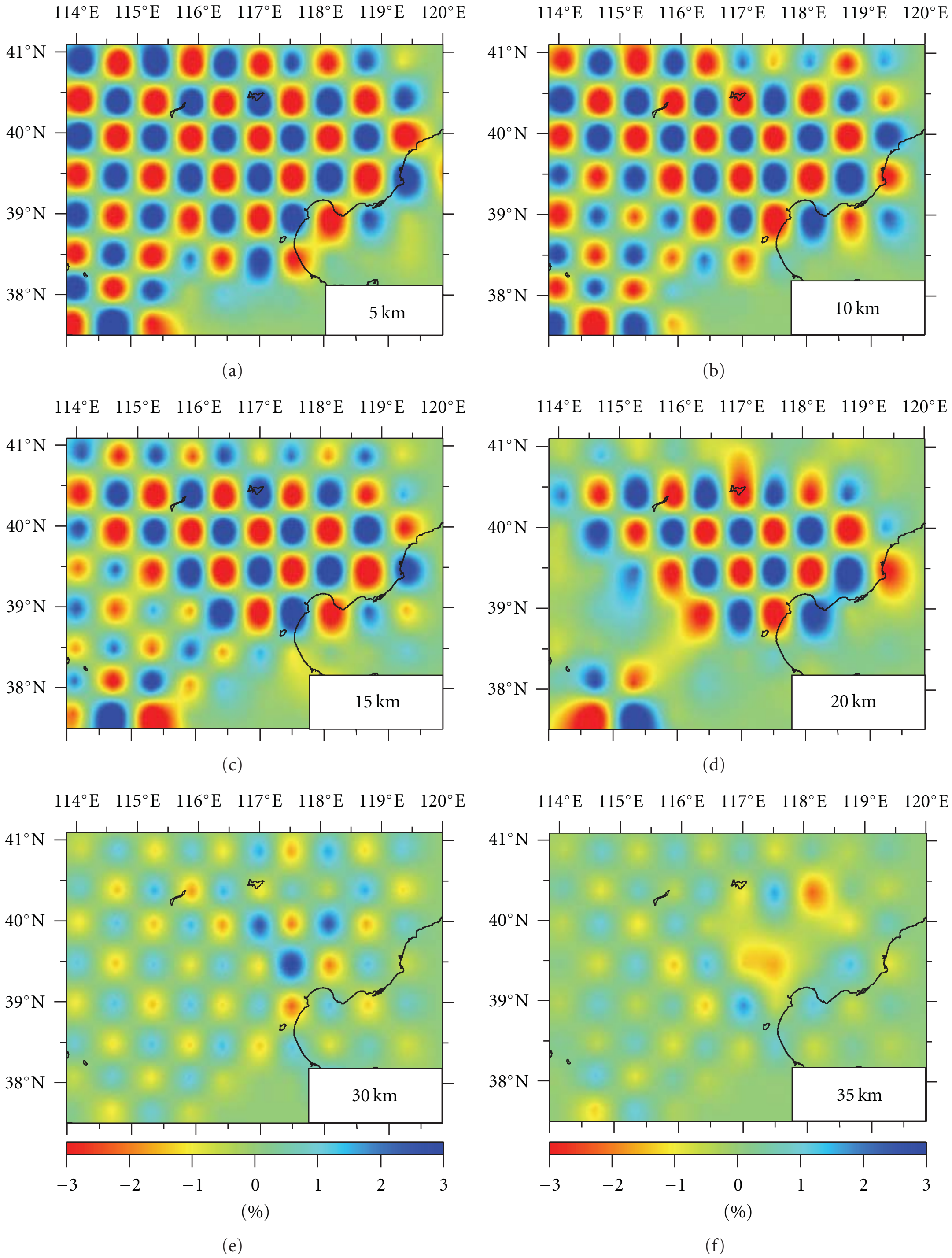

FIGURE 5: Results of checkerboard resolution test. The depth of the layer is shown on the right bottom of each map. The velocity perturbation scale (in %) is shown at the bottom.

local crustal earthquakes, controlled seismic explosions, and quarry blasts. Due to the differential arrival time data used to improve the precision of event location in the tomoDD, we obtained similar tomographic image only with local earthquakes. In the upper crust, the cross-sectional images show that discontinuous low-*V* anomalies exist under the Tangshan-Hejian-Cixian seismic zone, while, in the middle and lower crust, the low-*V* anomalies change to high-*V* anomalies. Under the Tangshan area, the maximum focal depth locates at the boundary of low-*V* anomaly in the middle and lower crust.

Figure 10(b) shows a cross-section along profile BB′ passing through the Zhangiakou-Bohai seismic zone. Under the Tangshan area, our result displays a transitional zone of

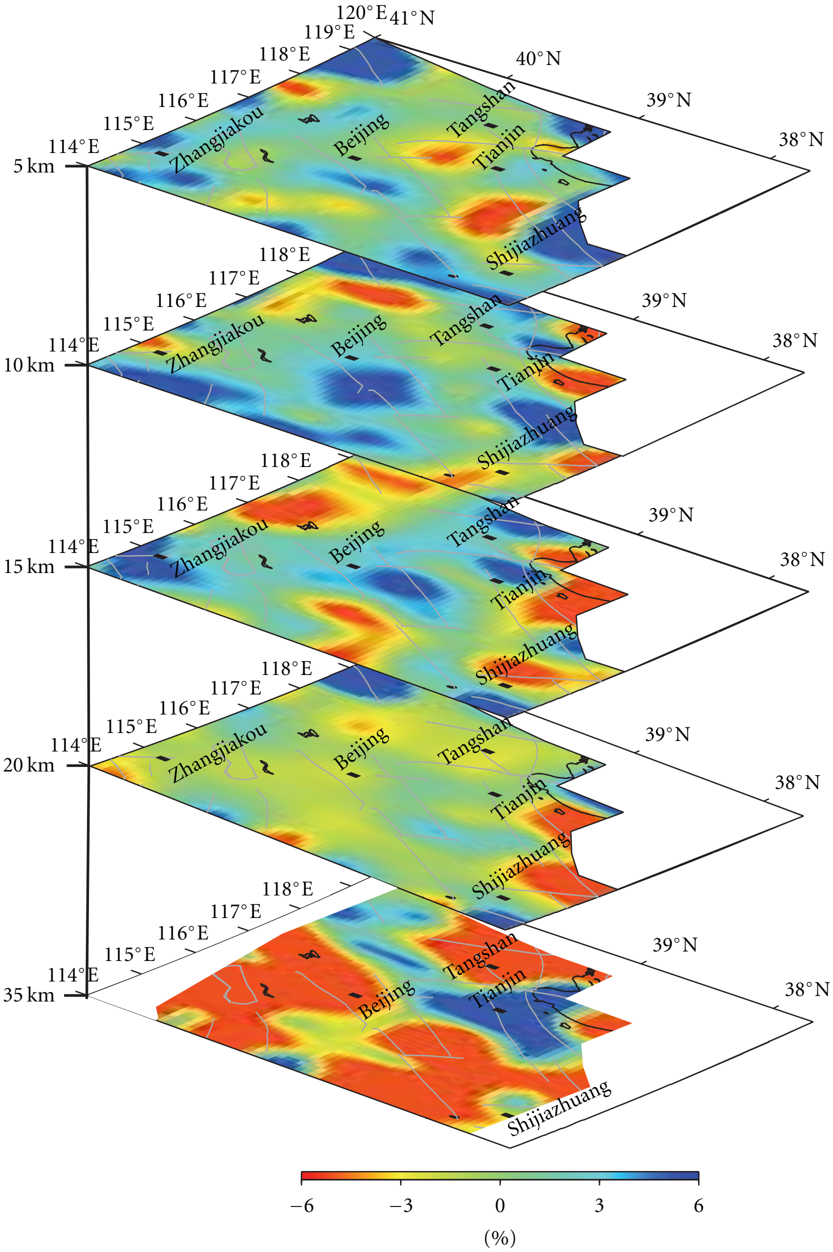

Figure 6: P wave velocity perturbation (in %) from the 1D velocity model as shown in **Figure 4** at each depth slice. Red and blue colors denote slow and fast velocity anomalies, respectively. The velocity perturbation scale is shown at the bottom.

low-V anomaly in the northwest and high-V anomaly in the southeast in the upper crust, while a very prominent low-V anomaly exists in the middle and lower crust (20~30 km depth). The focal depth of relocated earthquakes that occurred in the Tangshan area is distributed in the transitional zones of low-V anomaly and high-V anomaly. In the Zhangjiakou area, the northwest of profile BB′, the deepest focal depth of relocated earthquakes with magnitude $M_L \geq 4.0$ is about 15 km, which occurred on the margin of high-V anomalies.

The Tangshan area, in the about 160 km southeast of Beijing, has the highest level of seismicity in BTT region. In this area numerous small earthquakes have occurred frequently since the great Tangshan earthquake in 1976. During 1993~2004, 118 earthquakes with $M_L \geq 3.0$ occurred in the area, 17 of them were larger than M_L4.0, such as the earthquake with M_L5.9 on 6 October 1995 and M_L5.0 on 20 January 2004 in the northeast of Tangshan.

Figure 11 shows the epicenters of earthquakes before (open circles) and after relocation (solid circles) using the tomoDD in the Tangshan area. Compared with the catalog locations, which are scattered along the fault zone, relocated hypocenters appear more clustered in the NE-SW direction along Tangshan-Dacheng fault. **Figure 11** shows three clusters in different colors: the Tangshan cluster oriented in the NE-SW direction (grey solid circles), the Luanxian cluster

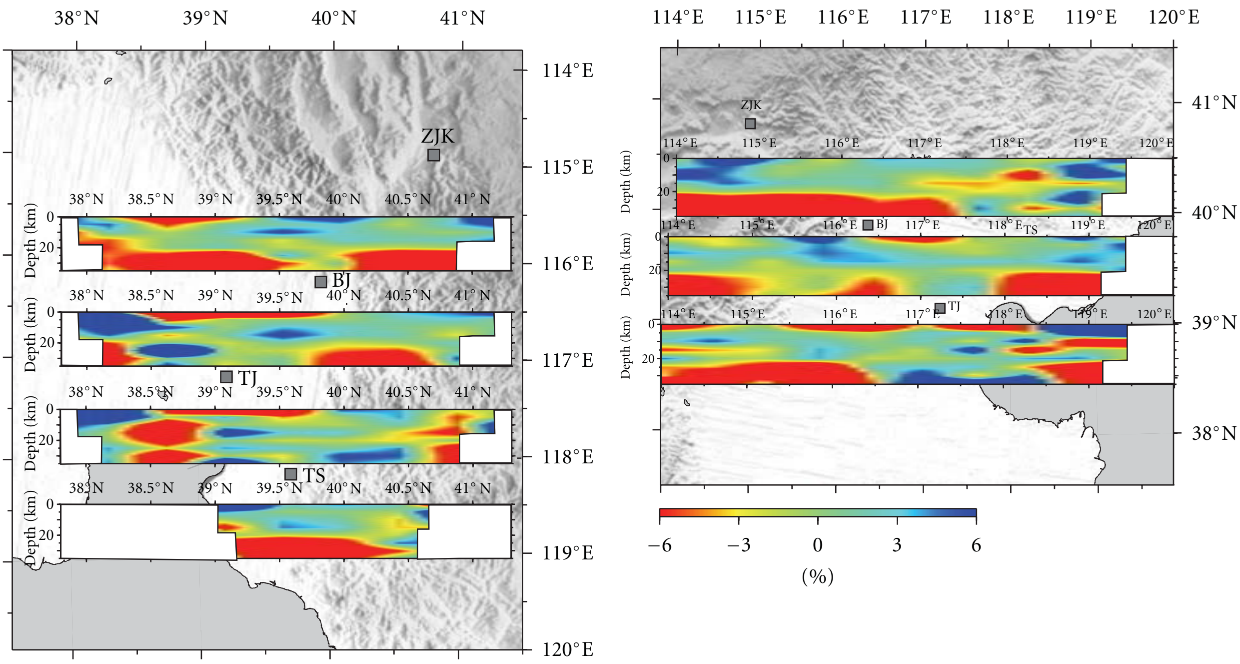

(a)

(b)

Figure 7: Vertical cross-sections of P wave velocity perturbation at each longitude (115.5°E, 116.5°E, 117.5°E, and 118.5°E) (a) and each latitude (40.5°N, 39.8°N, and 39.0°N) (b). Red and blue colors denote slow and fast-velocity anomalies, respectively. The velocity perturbation scale (in %) is shown at the bottom. BJ: Beijing; TJ: Tianjin; TS: Tangshan; ZJK: Zhangjiakou; SJZ: Shijiazhuang.

oriented nearly in the E-W direction (green solid circles), and the Qian'an cluster oriented in the NE-SW direction (blue solid circles).

In the cross-section along profile TT′ (Figure 12), the distribution of hypocenters displays a big difference between the catalog location, which is layered and scattered without clear cluster characteristic (Figure 12(a)), and the relocated location with the tomoDD, which is clustered clearly as cluster A, cluster B, and cluster C (Figure 12(b)). The Tangshan cluster (Figures 11 and 12(b), grey solid circles) becomes two clusters in depth: cluster A and cluster B. In addition, an earthquake (M_L5.9) without depth parameter before relocation is relocated in cluster A with focal depth 6.3 km.

In the cross-section along profile MN, perpendicular to TT′, the distribution of hypocenters before and after relocation using the tomoDD is also very different (Figure 13). Most of the tomoDD locations are centralized on a narrow zone within 10 km off the profile TT′ (Figure 13(b)). The earthquake relocation with $M_L \geq 4.0$ (Figure 13(b), stars) shows a near-vertical plane between 5 km and 15 km and a slight west dip between 15 km and 25 km, which is in agreement with the results of deep seismic soundings (DSSs) [33]. This indicates that the Tangshan fault is near-vertical in the shallow depth and west dip in the depth of about 22 km.

For comparison, we also relocate the events by using the DD location method, and extract the hypocenter parameters of earthquakes that occurred in the Tangshan area from previous results of the two standard tomography methods [2, 4]. The same minimum 1D velocity model [2] is used for both standard tomography and tomoDD as the initial model, which is also used for DD event location.

Figure 14 shows the event locations along profile TT′ in the Tangshan area inferred from different methods. Figure 14(a) shows the catalog locations by NCTSN. Figures 14(b) and 11(c) show the event relocations [2, 4] by the two standard tomography methods by Thurber [1] and Zhao et al. [3], respectively, where only the absolute arrival times were used for the inversion. The event locations are still scattered, similar to the catalog locations (Figure 14(a)).

Figures 14(d) and 11(e) show the event relocations by the DD location method [5] and the tomoDD method [6], respectively. In the DD location method, the weighted rms residuals decrease from 1.0 s to 0.6 s, while, in the tomoDD method, the weighted rms residuals decrease from 1.2 s to 0.3 s. After the relocation, both the DD methods provide similar features, three typical clusters under the Tangshan area. Although most of the relative event locations from the two DD methods are quite similar, there are some differences between them in detail. First, it can be noted that the absolute event locations with $M_L \geq 4.0$ are different between the two methods. The focal depth of earthquakes with $M_L \geq 4.0$ varies from 0 km to 20 km in the DD location method. In the tomoDD method, however, it varies from 5 km to 20 km. Second, in the tomoDD, earthquake relocations with $M_L \geq 4.0$ show a near-vertical plane between 5 km and 15 km and a slight west dip between 15 km and 25 km, which is in agreement with the results of deep seismic soundings

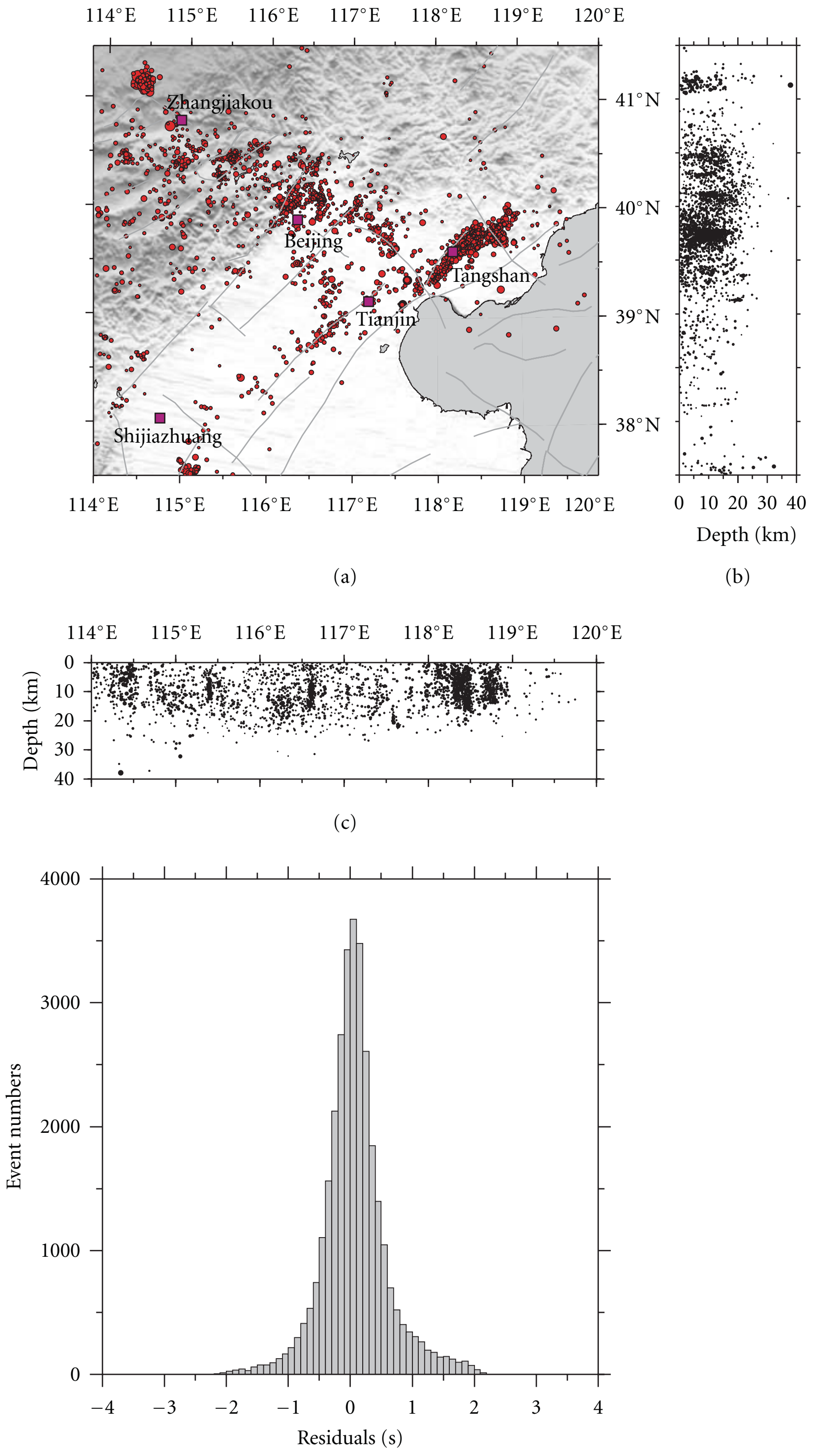

(a) (b)

(c)

(d)

Figure 8: Earthquake hypocenters relocated in this study. (a) shows distribution of relocated earthquake epicenters (circles); squares show the major cities. Thick lines denote active faults; (b) and (c) show the cross-sectional view of focal depth along latitude and longitude profiles, respectively; (d) denotes histogram of P wave absolute travel-time residuals after relocation using tomoDD method.

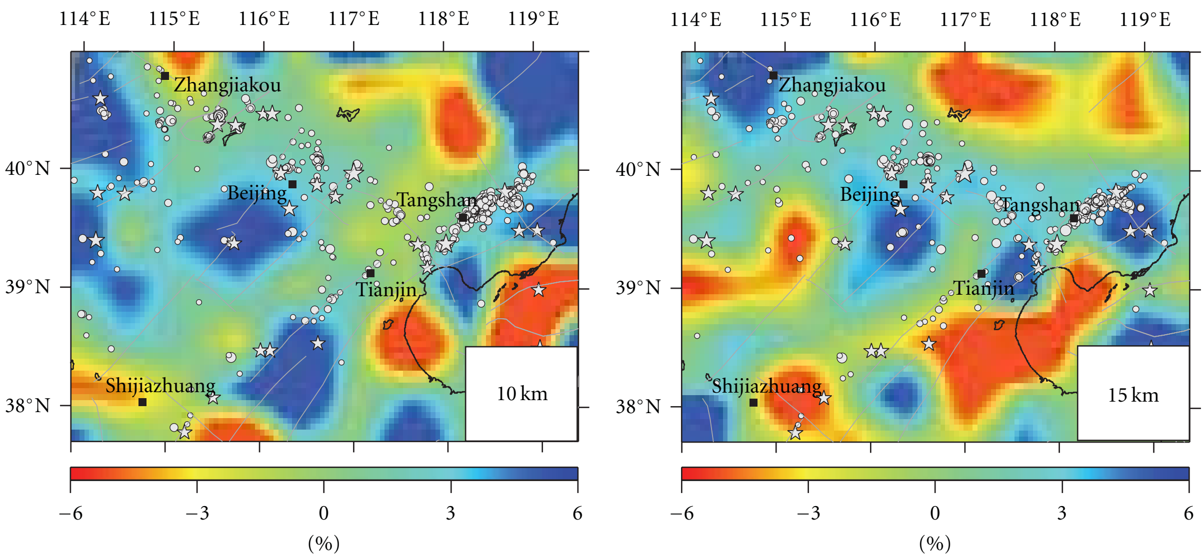

(a)

(b)

Figure 9: (a) and (b) show the map view of P wave velocity perturbations (in %) and distribution of relocated earthquake hypocenters at 10 km and 15 km, respectively. The white circles denote small earthquakes within 5 km off the different layer depth. The white stars show historic earthquake hypocenters ($M \geq 6.0$). Red and blue colors denote slow- and fast-velocity anomalies, respectively. The velocity perturbation scale (in %) is shown at the bottom.

(DSS) [33], while no such dipping is observed in the DD location method.

Figure 15 shows the velocity perturbations, resulting from the tomoDD, along the vertical cross-section of profile TT′ passing through the Tangshan area and the seismicity in this area. Only earthquakes that occurred within 0.25° off profile TT′ are chosen to project on the vertical slice. It can be clearly seen that all of the three clusters (Figure 12(b)) are relocated in the conjunctional area of low-V and high-V anomalies, slightly closer to the high-V anomaly zones. Only a few earthquakes have ever occurred within the low-V anomalies. The maximum focal depth (about 25.4 km) locates in the uppermost boundary of low-V anomaly from 20 km to 30 km under the Tangshan area. Our results suggest that the top boundary of low-V anomalies is at about 25.4 km depth in the Tangshan area, which is different from results obtained by previous standard tomography studies [15]. This indicates that the top boundary of low-V anomalies is at 20 km depth in the Tangshan area, which is consistent with the maximum of focal depth of relocation by the tomoDD.

Our tomographic results show an evident low-velocity anomaly in the lower crust beneath the BTT region (Figures 6, 7, 10(a), and 10(b)), specially beneath the Tangshan area. The results of S structure by using receiver function method [34] showed that there exist obvious heterogeneous low-V media in the upper mantle and middle crust and the crust-mantle boundary had an obvious uplift beneath the Tangshan area. Thus the existence of prominent low-V anomalies in the lower crust may suggest that there is probably massive intrusion derived from the upper mantle beneath the Tangshan area. Our tomographic results of the crust and upper mantle support such a conclusion. The main dynamic source for the Tangshan earthquake is the vertical movement of the upper mantle, which leads to material and energy exchange between the crust and upper mantle [34]. The long-term influence of the upwelling of mantle materials on the seismogenic layer would change the stress distribution and compositional evolution of fault zones, and the stresses are easier to concentrate on the high-V media, which would lead to the mechanical failure and the earthquake occurrence.

5. Conclusions

The tomoDD method is efficient in relocating a large number of earthquakes accurately and in characterizing the local velocity structure with high resolution. With this approach a high-resolution tomography model of crust and upper mantle under the BTT region has been obtained by using both absolute and relative arrival times of local earthquakes recorded by NCTSN or DCSN. Simultaneously, our results provide accurate hypocentral parameters of both absolute and relative event locations in the BTT region. The velocity images of the upper crust correlate well with the surface geological and topographic features. In the North China Basin, the depression and uplift areas are imaged as slow and fast velocities, respectively. A broad low-V anomaly exists in Tangshan and the north of the Tangshan area from 20 km down to 30 km depth, which suggests that there is probably massive intrusion derived from the upper mantle beneath the Tangshan area. Our results suggest that the top boundary of low-V anomalies is at about 25.4 km depth in the Tangshan area.

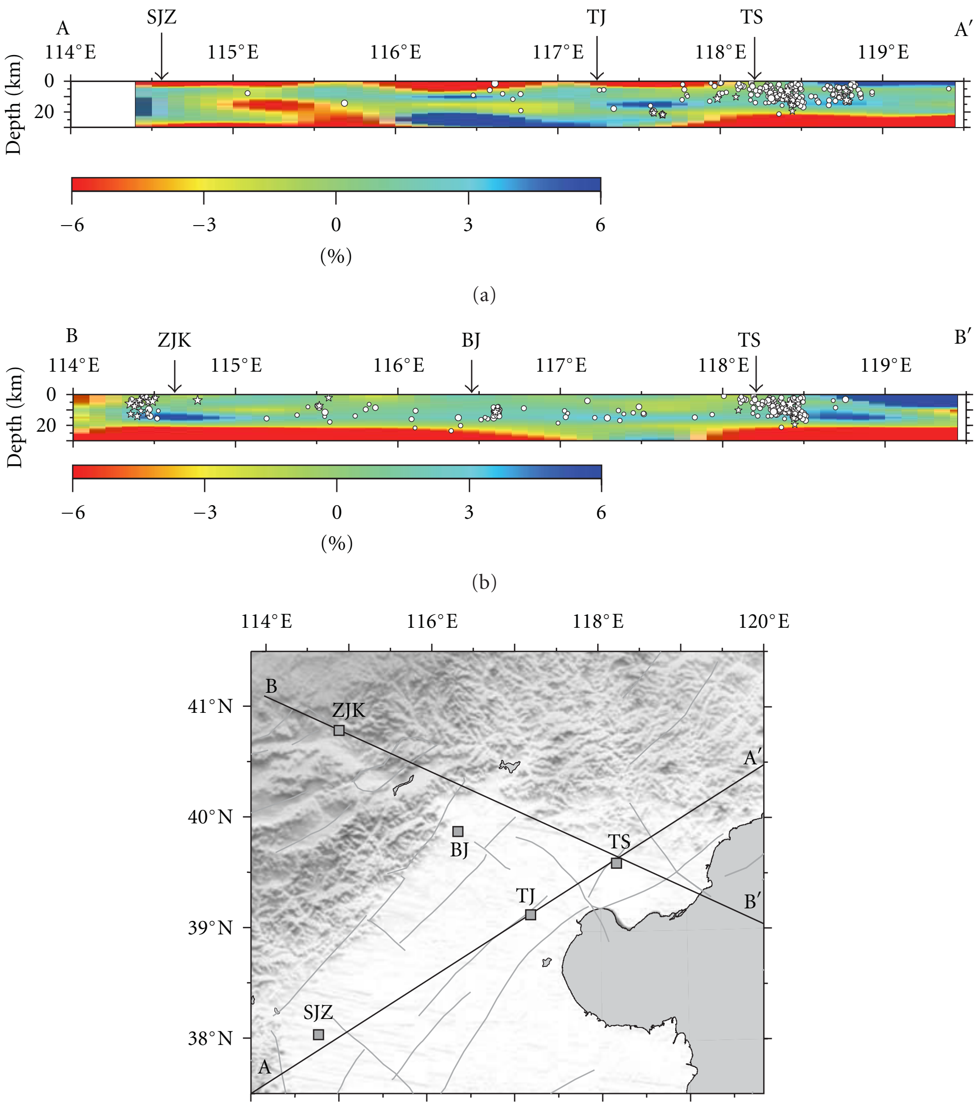

(a)

(b)

(c)

FIGURE 10: (a) and (b) show the vertical cross-sections of P wave tomographic image along the profiles. White stars and circles denote the earthquakes of $M_L \geq 4.0$ and $M_L < 4.0$, respectively, which occurred within 0.25° off the profile. Red and blue colors denote slow- and fast-velocity anomalies, respectively. No vertical exaggeration. (c) shows the location of profiles. BJ: Beijing; TJ: Tianjin; TS: Tangshan; ZJK: Zhangjiakou; SJZ: Shijiazhuang.

After relocation, the tomoDD method provides a sharp picture of the seismicity in the BTT region, which is concentrated along with the major faults in a shape of alignment. The seismicity of both the relocated earthquake hypocenters and the historic earthquakes shows that majority of the hypocenters are located in the conjunctional areas of low and high P wave velocity anomalies. And they are slightly closer to the high P wave velocity abnormal areas. Only a few earthquakes have epicenters in either high or low P wave velocity areas. It might suggest that the conjunctional zones of low-V and high-V anomalies represent weak sections of the seismogenic crust. The tectonic stresses are prone to being accumulated in the "brittle" high-V anomalies area and hence the earthquake ruptures happened closer to the high-V anomalies zones.

The surface event relocations in the Tangshan area are centered along the Tangshan-Dacheng fault. In the vertical slice along profile TT′, all the earthquakes are clustered in three clusters as shown in Figure 9(b), two clusters lie beneath the Tangshan-Ninghe fault, and another one lies beneath the Luanxian area. The maximum of focal depth of relocated earthquakes is 25 km, where there is the top boundary of low-V anomalies beneath the Tangshan area.

Acknowledgments

The authors thank Dr. Haijiang Zhang for providing his tomoDD code and thoughtful discussions. This work was supported by a grant from the National Natural Science Foundations of China (40404002) to X. Yu as well as a

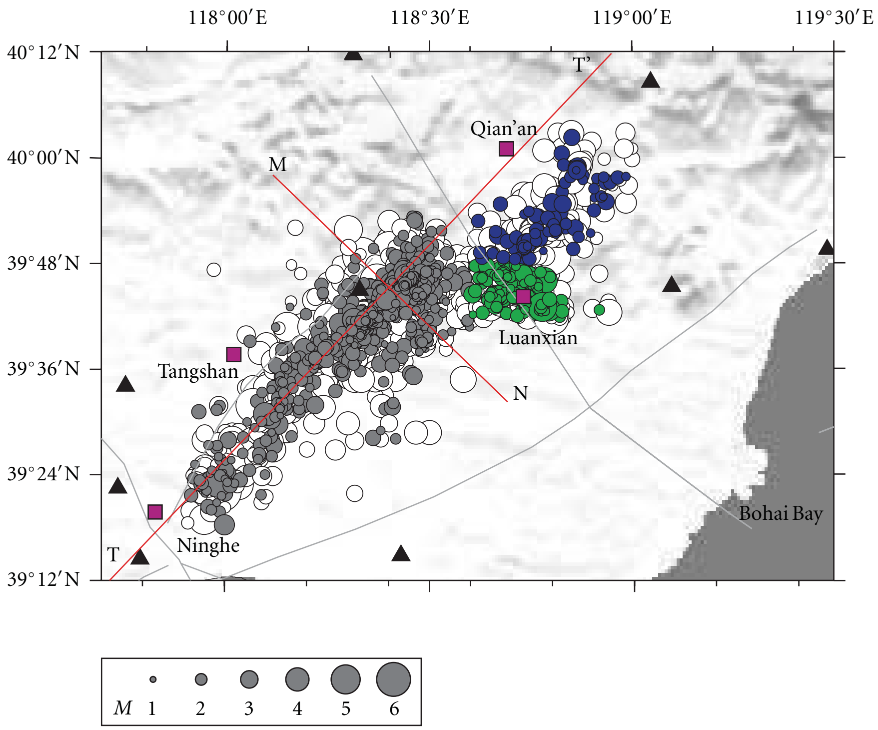

Figure 11: Epicentral distribution of earthquakes before (open circles) and after (solid circles) relocation using the tomoDD in the Tangshan area.

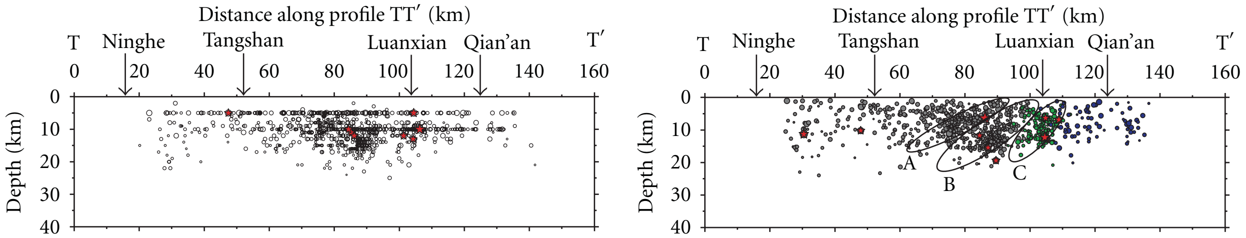

(a)

(b)

Figure 12: Cross-section along profile TT′ of focal depth before (a) and after (b) relocation using tomoDD in the Tangshan area. Stars and circles show the earthquakes of $M_L \geq 4.0$ and $M_L < 4.0$, respectively. The epicentral locations of earthquakes with different colors in Figure 12(b) are the same as in Figure 11.

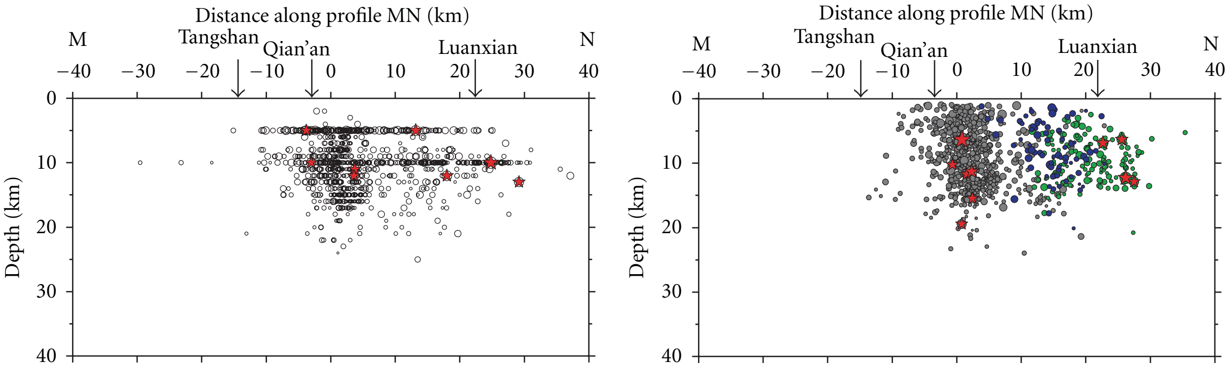

(a)

(b)

Figure 13: Cross-section along profile MN of focal depth before (a) and after (b) relocation using tomoDD in the Tangshan area. Origin of coordinates is set at the intersection point of MN and TT′. Other symbols are the same as in Figure 12.

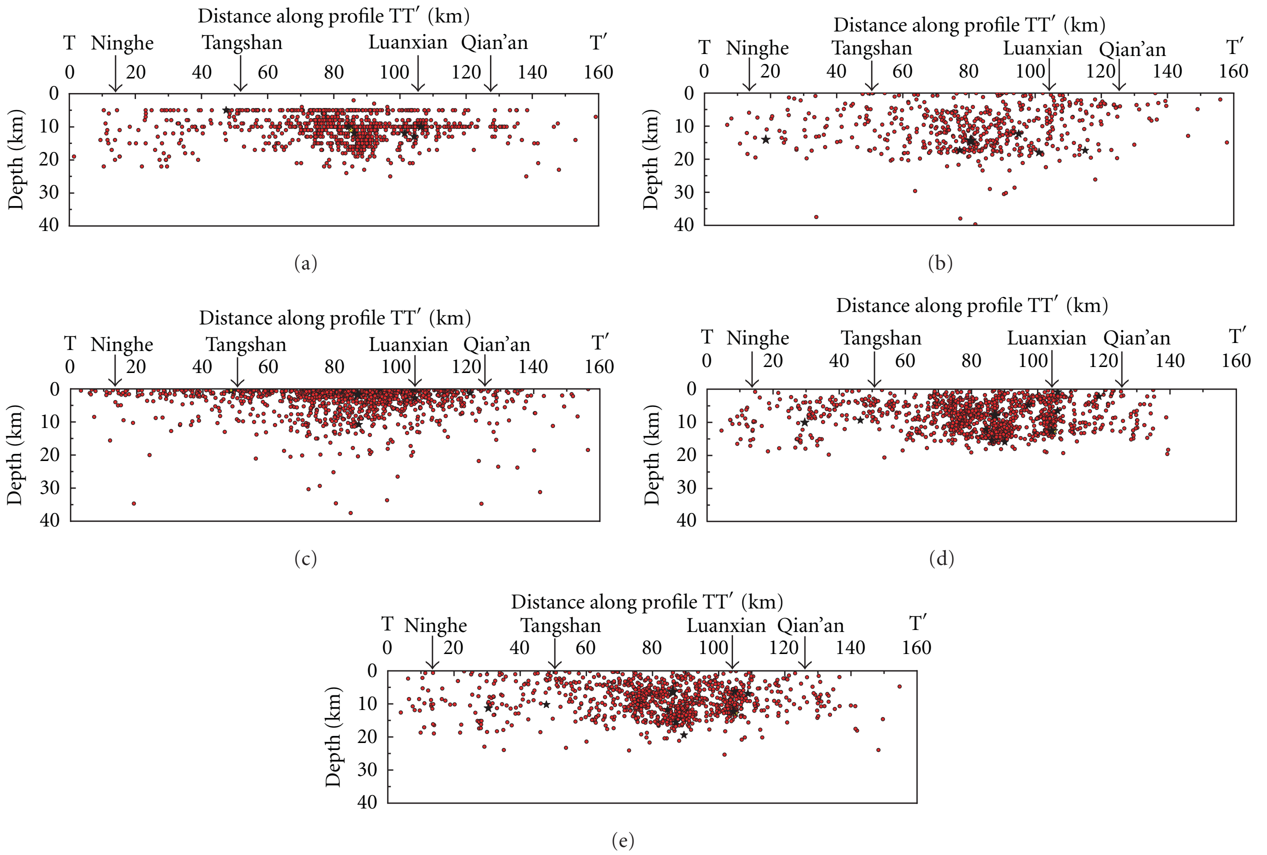

(a)

(b)

(c)

(d)

(e)

FIGURE 14: Cross-section of focal depth along the profile TT′ by various methods in the Tangshan area. Stars and circles show the earthquakes of $M_L \geq 4.0$ and $M_L < 4.0$, respectively. (a) Distribution of focal depth by Capital Digital Seismic Network and North China Telemetry Seismic Network; (b) distribution of focal depth using local tomography with Thurber [1] method [2]; (c) distribution of focal depth using seismic tomography with Zhao et al. [3] method [4]; (d) distribution of focal depth using DD location method [5]; (e) distribution of focal depth using tomoDD method [6].

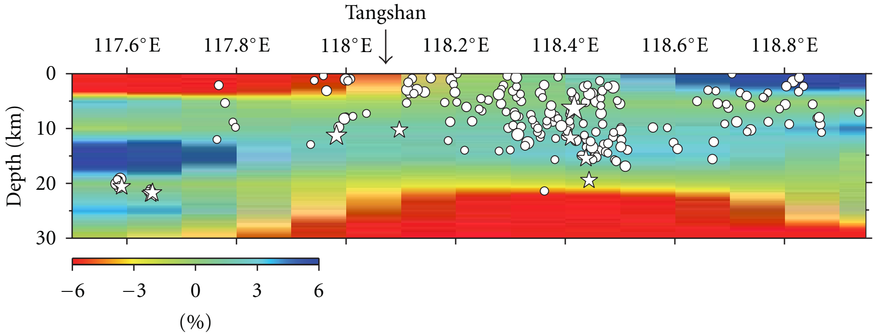

FIGURE 15: Vertical cross-section of P wave tomographic image along profile TT′ in Tangshan area. White stars and circles denote the earthquakes of $M_L \geq 4.0$ and $M_L < 4.0$, respectively, the occurred within 0.25° off the profile. Red and blue colors denote slow and fast velocity anomalies, respectively. No vertical exaggeration. The location of profile TT′ is shown in Figure 11.

grant from the National Natural Science Foundations of China (90715019) to W. Zhang and by the Special Research Project in Earthquake Science, CEA, to Y.-T. Chen (no. 200808068). The figures were made by using GMT [35]. They also thank the editor (Professor Y. Zhang) and four anonymous referees for their constructive comments and suggestions which improved the paper.

References

[1] C. H. Thurber, "Earthquake locations and three-dimensional crustal structure in the Coyote Lake area, central California," *Journal of Geophysical Research*, vol. 88, no. 10, pp. 8226–8236, 1983.

[2] X. Yu, Y. T. Chen, and P. D. Wang, "Three-dimensional P wave velocity structure in Beijing-Tianjin-Tangshan area," *Acta*

Seismologica Sinica, vol. 25, no. 1, pp. 1–14, 2003 (Chinese), (with English abstract).

[3] D. Zhao, A. Hasegawa, and S. Horiuchi, "Tomographic imaging of P and S wave velocity structure beneath northeastern Japan," *Journal of Geophysical Research*, vol. 97, no. 13, pp. 19909–19928, 1992.

[4] X. W. Yu, *Theory of Regional Seismic Tomography and Applications in Northern China*, Ph.D. thesis, Institute of Geophysics, CSB, Beijing, China, 2003, (in Chinese with English abstract).

[5] F. Waldhauser and W. L. Ellsworth, "A Double-difference earthquake location algorithm: method and application to the Northern Hayward fault, California," *Bulletin of the Seismological Society of America*, vol. 90, no. 6, pp. 1353–1368, 2000.

[6] H. J. Zhang and C. H. Thurber, "Double-difference tomography: the method and its application to the Hayward fault, California," *Bulletin of the Seismological Society of America*, vol. 93, no. 5, pp. 1875–1889, 2003.

[7] H. Ye, K. Sheldlock, and S. Hellinger, "The North China basin: an example of a Cenozoic rifted intraplate basin," *Tectonics*, vol. 4, no. 2, pp. 153–169, 1985.

[8] H. Ye, B. Zhang, and F. Mao, "The Cenozoic tectonic evolution of the Great North China: two types of rifting and crustal necking in the Great North China and their tectonic implications," *Tectonophysics*, vol. 133, no. 3-4, pp. 217–227, 1987.

[9] A. S. Jin, F. T. Liu, and Y. Z. Sun, "Three-dimensional P velocity structure of the crust and upper mantle under the Beijing region," *Chinese Journal of Geophysics*, vol. 23, no. 2, pp. 172–182, 1980 (Chinese), (with English abstract).

[10] F. T. Liu, K. X. Qu, and H. Wu, "Seismic tomography of North China region," *Chinese Journal of Geophysics*, vol. 29, no. 5, pp. 442–449, 1986 (Chinese), (with English abstract).

[11] K. M. Shedlock and S. W. Roceker, "Elastic wave velocity structure under the crust and upper mantle beneath the North China," *Journal of Geophysical Research*, vol. 92, pp. 9327–9350, 1987.

[12] L. P. Zhu, R. S. Zeng, and F. T. Liu, "3-D P wave velocity structure under the Beijing network area," *Chinese Journal of Geophysics*, vol. 33, no. 3, pp. 267–277, 1990 (Chinese), (with English abstract).

[13] R. M. Sun and F. T. Liu, "Crust structure and strong earthquake in Beijing, Tianjin, Tangshan area: I. P wave velocity structure," *Chinese Journal of Geophysics*, vol. 38, no. 5, pp. 599–607, 1995 (Chinese), (with English abstract).

[14] Z. F. Ding, *Regional Seismic Tomography: Theory and Applications*, Ph.D. thesis, Institute of Geophysics, CSB, Beijing, China, 1999, (in Chinese with English abstract).

[15] J. L. Huang and D. P. Zhao, "Crustal heterogeneity and seismotectonics of the region around Beijing, China," *Tectonophysics*, vol. 385, no. 1–4, pp. 159–180, 2004.

[16] Y. T. Chen, L. R. Huang, and B. H. Lin, "A dislocation model of the Tangshan earthquake of 1976 from inversion of geodetic data," *Chinese Journal of Geophysics*, vol. 22, no. 3, pp. 201–217, 1979 (Chinese), (with English abstract).

[17] R. S. Zeng, H. H. Lu, and Z. F. Ding, "Seismic refraction and reflection profilings across Tangshan epicentral region and their implication to seismogenic processes," *Chinese Journal of Geophysics*, vol. 31, no. 4, pp. 383–397, 1988 (Chinese), (with English abstract).

[18] W. X. Gao and J. Ma, Eds., *Seismo-Geological Background and Earthquake Hazard in Beijing Area*, Seismological Press, Beijing, China, 1993, (in Chinese).

[19] S. Y. Wang, Z. H. Xu, and Y. X. Yu, "Relocation of micro earthquakes in Beijing and its neighbouring areas and its tectonic implication," *Earthquake Research in China*, vol. 11, no. 3, pp. 257–269, 1994 (Chinese), (with English abstract).

[20] S. Y. Wang, Z. H. Xu, and Y. X. Yu, "Relocation of micro earthquakes in northwestern Beijing," *Acta Seismological Sinica*, vol. 7, no. 1, pp. 33–41, 1995 (Chinese), (with English abstract).

[21] C. F. Xu, "The cause of formation of the upper mantle and crust high conductive layers in Chinese mainland and the study of Tangshan earthquake," *Earth Science Frontiers*, vol. 10, supplement, pp. 102–111, 2003 (Chinese), (with English abstract).

[22] L. Bai, T. Z. Zhang, and H. Z. Zhang, "Multiplet relative location approach and wave correlation rectify and application," *Acta Seismological Sinica*, vol. 16, no. 6, pp. 606–615, 2003 (Chinese), (with English abstract).

[23] A. L. Zhu, X. W. Xu, and P. Hu, "Relocation of small earthquakes in Beijing area and its implication to seismotectonics," *Geological Review*, vol. 51, no. 3, pp. 268–274, 2005 (Chinese), (with English abstract).

[24] Z. H. Qiu, J. Ma, and G. X. Liu, "Discovery of the great fault of the Tangshan earthquake," *Seismology and Geology*, vol. 27, no. 4, pp. 669–677, 2005 (Chinese), (with English abstract).

[25] China Seismological Bureau, *Findings of Exploring the Crust and Upper Mantle Structure of China*, Seismological Press, Beijing, China, 1986, (in Chinese with English abstract).

[26] S. L. Li, X. K. Zhang, and Z. L. Song, "Three-dimensional crustal structure of the capital area obtained by a joint inversion of deep seismic sounding data from multiple profiles," *Chinese Journal of Geophysics*, vol. 44, no. 3, pp. 360–368, 2001 (Chinese), (with English abstract).

[27] J. Um and C. H. Thurber, "Fast algorithm for two-point seismic ray tracing," *Bulletin of the Seismological Society of America*, vol. 77, no. 3, pp. 972–986, 1987.

[28] E. Humphreys and R. Clayton, "Adaptation of back projection tomography to seismic travel time problems," *Journal of Geophysical Research*, vol. 93, no. 2, pp. 1073–1085, 1988.

[29] H. Inoue, Y. Fukao, and K. Tanabe, "Whole mantle P wave travel time tomography," *Physics of the Earth and Planetary Interiors*, vol. 59, no. 4, pp. 294–328, 1990.

[30] S. Y. Wang, Z. H. Xu, and S. P. Pei, "Velocity structure of the uppermost mantle beneath North China from Pn tomography and its implications," *Science in China*, vol. 46, supplement, pp. 130–140, 2003 (Chinese), (with English abstract).

[31] S. P. Pei, J. M. Zhao, Y. S. Sun et al., "Upper mantle seismic velocities and anisotropy in China determined through Pn and Sn tomography," *Journal of Geophysical Research B*, vol. 112, no. 5, Article ID B05312, 2007.

[32] X. W. Yu, H. Zhang, and Y. T. Chen, "Analysis of relocated earthquakes in North China region," *Journal of Geodesy and Geodynamics*, vol. 30, no. 2, pp. 29–33, 2010 (Chinese), (with English abstract).

[33] X. K. Zhang, Z. P. Zhu, and C. K. Zhang, "Crust and upper mantle structure of the Zhangjiakou-Bohai Sea seismic zone," *Active Fault Research*, vol. 6, no. 1, pp. 1–16, 1998 (Chinese), (with English abstract).

[34] Q. Y. Liu, J. Wang, and J. H. Chen, "Seismogenie tectonic environment of 1976 great Tangshan earthquake: results given by dense seismic array observations," *Earth Science Frontiers*, vol. 14, no. 6, pp. 205–213, 2007 (Chinese), (with English abstract).

[35] P. Wessel and W. Smith, "New version of the generic mapping tools (GMT) version 3.0 released," *EOS Transactions American Geophysical Union*, vol. 76, p. 329, 1995.

Hindawi Publishing Corporation
International Journal of Geophysics
Volume 2011, Article ID 272646, 15 pages
doi:10.1155/2011/272646

Review Article

Broadband Seismic Deployments for Imaging the Upper Mantle Structure in the Lützow-Holm Bay Region, East Antarctica

Masaki Kanao,[1] Yusuke Usui,[2] Tomofumi Inoue,[2] and Akira Yamada[2]

[1] *National Institute of Polar Research, Research Organization of Information and Systems, 10-3 Midori-cho, Tachikawa-shi, Tokyo 190-8518, Japan*
[2] *Geodynamics Research Center, Ehime University, Bunkyo-cho 2-5, Matsuyama, Ehime 790-8577, Japan*

Correspondence should be addressed to Masaki Kanao, kanao@nipr.ac.jp

Received 16 January 2011; Revised 14 May 2011; Accepted 31 May 2011

Academic Editor: Martin Tygel

Broadband seismic deployments have been carried out in the Lützow-Holm Bay region (LHB), Dronning Maud Land, East Antarctica. The recorded teleseismic and local events are of sufficient quality to image the structure and dynamics of the crust and mantle of the terrain. Passive seismic studies by receiver functions and shear wave splitting suggest a heterogeneous upper mantle. Depth variations in topography for upper mantle discontinuities were derived from long period receiver function, indicating a shallow depth discontinuity at 660 km beneath the continental area of LHB. These results provide evidence of paleo upwelling of the mantle plume associated with Gondwana break-up. SKS splitting analysis anticipated a relationship between "fossil" anisotropy in lithospheric mantle and past tectonics. Moreover, active source surveys (DSSs) imaged lithospheric mantle reflections involving regional tectonic stress during Pan-African and succeeding extension regime at the break-up. By combining the active and passive source studies of the mantle structure, we propose an evolution model of LHB for constructing the present mantle structure.

1. Introduction

Deployments of broadband seismic arrays on the Antarctic continent have often been the ambitious dreams of dedicated Earth scientists. Existing seismic stations belonging to the Federation Digital Seismographic Network (FDSN) allow resolution of the structure beneath the Antarctic continent at a horizontal scale of 1000 km, which is sufficient to detect fundamental differences in the lithosphere beneath East and West Antarctica, but not to clearly define the structure within each sector. In addition, seismicity around the Antarctic region is limited by sparse station distribution, and the detection level for earthquakes remains inadequate for full evaluation of tectonic activity [2]. A strategy of attaining a sufficient density of seismic stations on the Antarctic continent will allow for optimal ray path coverage across Antarctica and improvement of seismic tomography resolution [3–5].

Polar field deployments have been carried out in the past decades around several regions withinin the continental margins of Antarctica [6–9] including the "TransAntarctic Mountain SEISmic experiment (TAMSEIS; [10, 11])." Discussions at the working group of the Antarctic Neotectonics program (ANTEC) under the Science Committee on Antarctic Research (SCAR) (Siena, Italy, 2001) and the workshop on the "Structure and Evolution of the Antarctic Plate (SEAP)" (Boulder, Colorado, 2003) have led to Antarctic seismic array deployments. The principle ideas of the Antarctic arrays were derived from components of the "Regional Leapfrogging Arrays (RLA)" and the "Program Oriented Experiments (POE)".

The resultant seismic stations in Antarctica were installed as a part of several international programs initiated during the International Polar Year (IPY 2007-2008; http://classic.ipy.org/; Figure 1). Followed by the successful TAMSEIS deployment held in 2000–2002, several big geoscience projects were contacted regarding a collaborative effort to reach the interior of the Antarctic continent and surrounding region. The "Antarctica's GAmburtsev Province (AGAP; http://www.ldeo.columbia.edu/~mstuding/AGAP/)", the "GAmburtsev Mountain SEISmic experiment (GAMSEIS; http://epsc.wustl.edu/seismology/GAMSEIS/, [12, 13])" under AGAP, as well as the "Polar Earth Observing Network (POLENET; http://www.polenet.org/)" were major contrib-

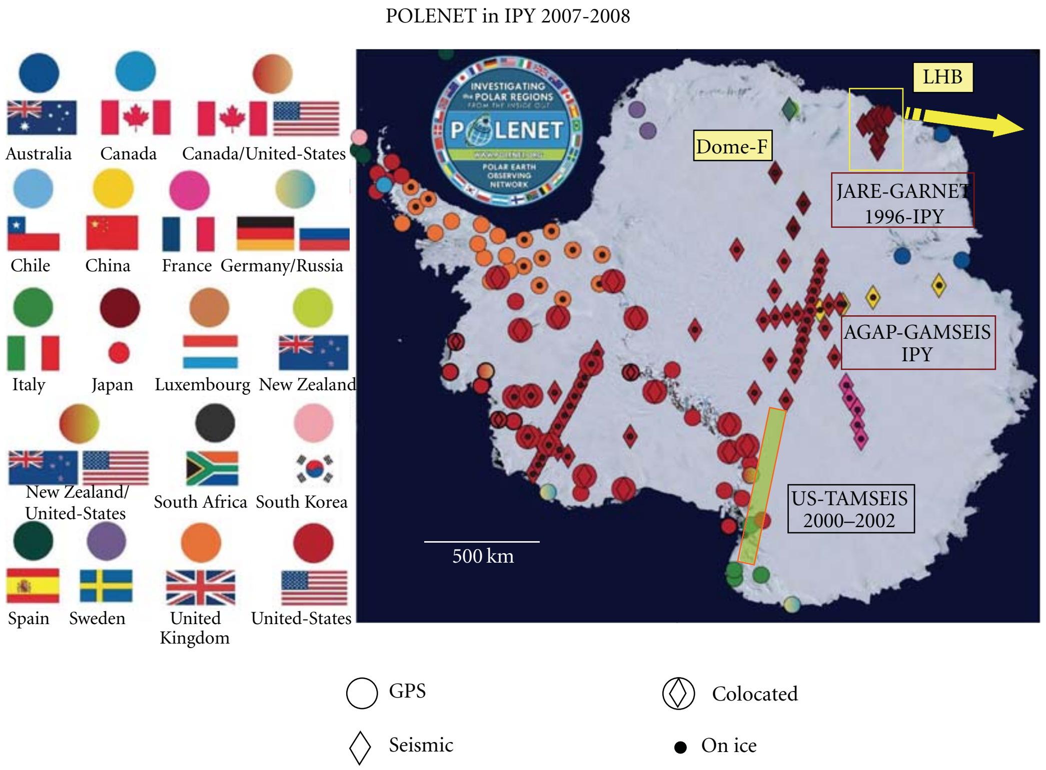

Figure 1: Distribution map of seismic and the other geophysical stations planned for deployed during IPY 2007-2008. The GARNET-JARE project regions are shown, as well as those of AGAP/GAMSEIS and TAMSEIS. All stations in Antarctica contribute to the POLENET program in the bipolar region. The LHB map is extended in Figure 2.

utors in establishing a geophysical network inside the Antarctic continent during the IPY.

Similar to other regions in Antarctica, monitoring observations have been conducted in the last decade by the Japanese Antarctic Research Expedition (JARE) around the Lützow-Holm Bay region (hereafter LHB), Dronning Maud Land (Figure 1). The obtained seismic data are utilized to clarify the heterogeneous structure of the Earth, particularly around the Antarctic region. Seismic deployments can efficiently study the crust and upper mantle, as well as the Earth's deep interior, including features such as the Core-Mantle-Boundary (CMB) and the lowermost mantle layer (D″ zone) [14, 15]. The broadband arrays in LHB make a significant contribution not only to the permanent global network of FDSN, but also to such projects as the Global Alliance of Regional Networks (GARNET), RLA, POE, POLENET, and IPY.

In this paper, data from broadband seismological studies are reviewed in order to provide clear images of the upper mantle structure and dynamics beneath LHB. By combining the passive and active source results, a regional evolution model of LHB is presented to explain the formation of the present mantle structure. Regional tectonic history such as the Pan-African orogenic event, together with the break-up process of Gondwana supercontinent in mid-Mesozoic age, could be the plausible cause of present upper mantle structure. The multidisciplinary seismic investigations reviewed in this paper supply fruitful information for understanding the regional tectonic evolution of this area.

2. Broadband Deployments in LHB

Broadband seismic deployments in LHB have been carried out since 1996 until present, including deployment during IPY 2007-2008 as one of the major contributions to GARNET. The stations were established on the outcrops and ice sheet around the continental margins of LHB (Figure 2). Seismic array response functions were calculated in dominant frequency of 0.03 Hz and 0.1 Hz for receiver space distribution of all the GARNET stations (Figure 3). It is expected that both the short period body waves and long period surface waves are detected and space resolution from the analyses by using the detected waveform data could evaluate the area. Except for power supply failure of some stations during winter seasons, observations have been conducted fairly well and a significant number of events were recorded of global earthquakes, local earthquakes, as well as ice-related events within close proximity to the stations (Figure 4). During the IPY period, a total number of seven stations (TOT, LNG, SKV, SKL, S16, RDV, and BTN) were continuously operated. The last three stations (S16, RDV, and BTN) were started simultaneously at the beginning of the IPY.

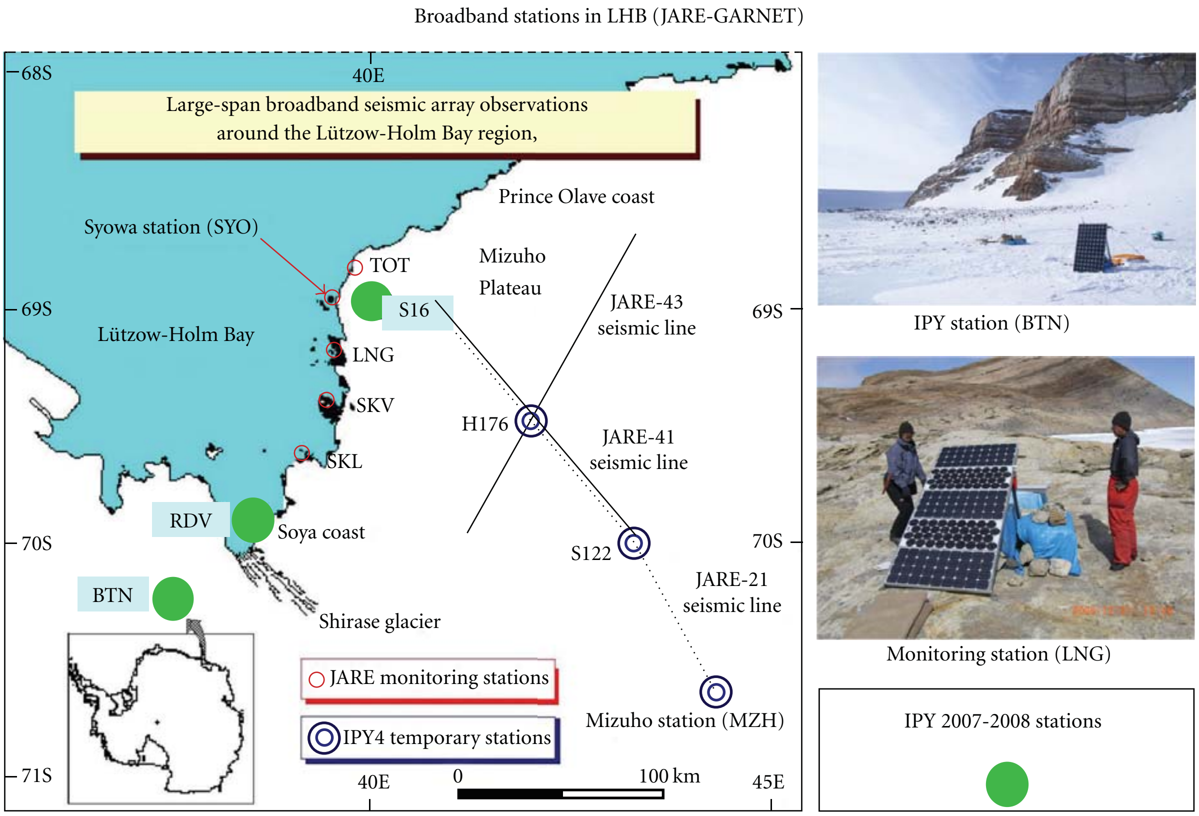

Figure 2: Broadband seismic stations in LHB including IPY period. Monitoring stations (red open circles), IPY stations (green solid circles), and future planned stations (blue double-open circles) are indicated, respectively.

The observation systems consisted of a portable broadband seismometer and a data-recorder (type LS8000-WD, -XT by Hakusan Co.), combined with lead-acid and solar batteries. The CMG-40T portable seismometers (Guralp System LTD.) were used with a three-component velocity-response (flat frequency response for velocity in 0.05–10 Hz). The velocity signal was digitized at a sampling frequency of 10–100 Hz with a dynamic range of 90 dB (16 bits), and stored in a hard-disk (2 GB) or compact flash (CF) card (10 GB). Total solar panel power was 250–270 W with 12 V DC output, and the capacity of the lead batteries was more than 500 Ah for each station. The systems operated continuously except in very dark and cold periods during Antarctic winters. Details of the observation systems in the first few years were described in [19, 20]. More detailed information for the GARNET stations in LHB and operational details are available from the website of the National Institute of Polar Research (NIPR) (http://polaris.nipr.ac.jp/~pseis/garnet/).

The GARNET data are initially stored and accessible to cooperative researchers through the data library server of NIPR (POLARIS; http://polaris.nipr.ac.jp/~pseis/garnet/). After a defined period, the data are made available to world data centers of seismology, such as Incorporated Research Institute of Seismology/Data Management System (IRIS/DMS). The global data centers provide data to seismologists studying the polar regions, the Standing Committee on Antarctic Data Management (SCADM) under the Scientific Committee on Antarctic Research (SCAR), as well as the Antarctic Master Directory (AMD) in the Global Change Master Directory (GCMD) of NASA.

During the IPY, broadband seismic deployments in LHB were conducted under the endorsed JARE project. By combining with the other big IPY projects such as the AGAP/GAMSEIS [13], moreover, the deployments in LHB could provide constraints on the origin of the Gamburtsev Subglacial Mountains in terms of understanding the broader structure of Antarctic Pre-Cambrian craton and the subglacial environment. Detection of seismic signals from basal sliding of the ice sheet and ice streams [10, 21] would be expected from the future study, as well as the detection of outburst floods from subglacial lakes.

3. Seismic Velocity Discontinuities

Interesting seismic evidence related to the structure and dynamics of LHB was obtained in the last decade by JARE geoscientific activities. The recorded teleseismic data in LHB are of sufficient quality for usage of various analyses to clarify the heterogeneous features of the Antarctic lithosphere-asthenosphere system, as well as deep interiors [5, 14, 15, 22–24]. In recent years, moreover, glacial-related seismic events were detected by the LHB array stations [25, 26]. Seismic signals involving ice-related phenomena, also known as “ice-quakes (ice-shocks)”, have been associated with

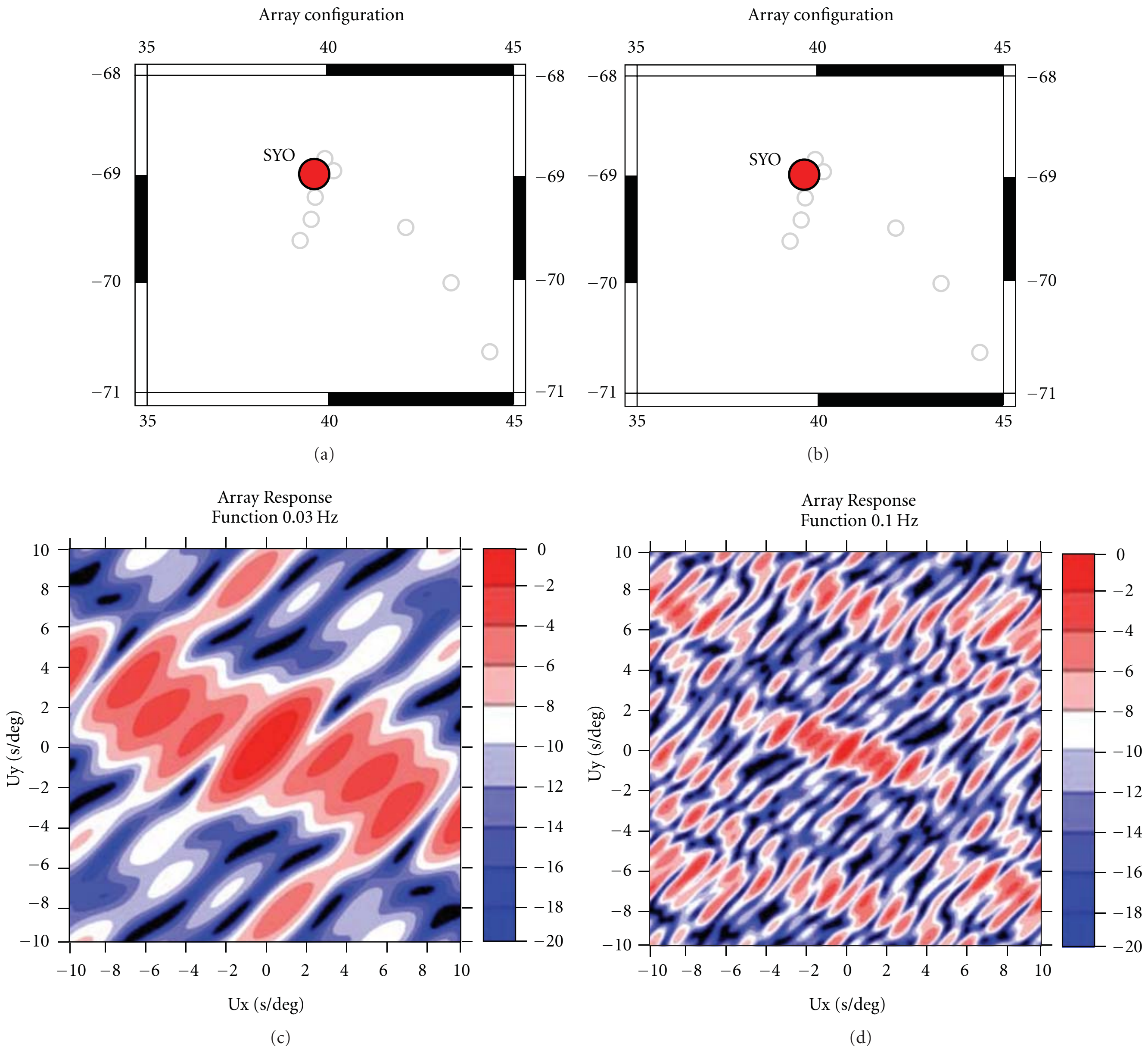

(a) (b) (c) (d)

Figure 3: Simulated seismic array response functions in dominant frequency of 0.03 Hz and 0.1 Hz for receiver distribution for all GARNET stations as shown in Figure 2.

glacially related mass movements of ice-sheets, sea-ice, tide-cracks and icebergs in the polar areas [10, 25]. Despite the development of local networks in the last two decades, we can hardly distinguish a difference between waveforms by local tectonic earthquakes and those of ice-related phenomena (e.g., the unknown X-phases reported by [26]). The ice-related signals can provide unique information for local impact on Antarctic region involving global climate change.

The recorded waveforms are of sufficient quality to analyze the crust-upper mantle structure and tectonic evolution of the region. Passive seismic source studies of receiver functions, shear wave splitting, and surface wave tomography were carried out by using the data recorded from systems located on outcrops in LHB. Shear wave velocity models were inverted by fitting synthetic receiver functions to the observed data in short-period ranges. The obtained model investigated from azimuthal variations of the receiver functions represents a slightly dipping crust-mantle boundary toward the coast [27]. Moreover, a gradual thickened structure of the crust in LHB was identified from the north toward the south [28]. Variations in crustal thickness along the coast may reflect the tectonic history, with increasing metamorphic grade in crystalline crust towards the south in LHB [29].

The long period receiver functions reveal depth variations in seismic discontinuities of the upper mantle (for 410 km and 660 km) beneath the LHB [1]. Long period receiver functions (after 0.2 Hz low-pass filter) were

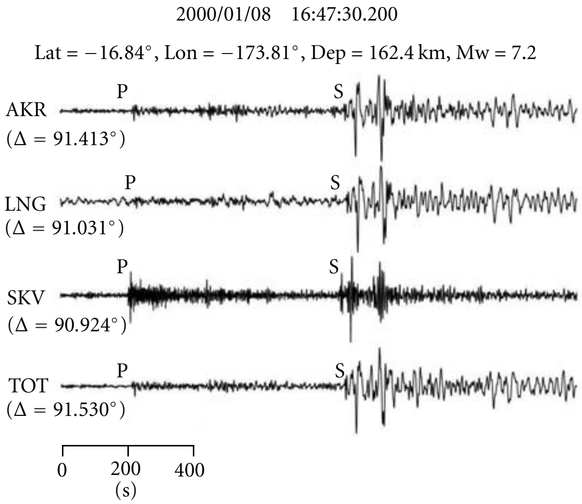

Figure 4: Example of the teleseismic waveforms (Fiji Island region) recorded at the GARNET stations deployed at LHB.

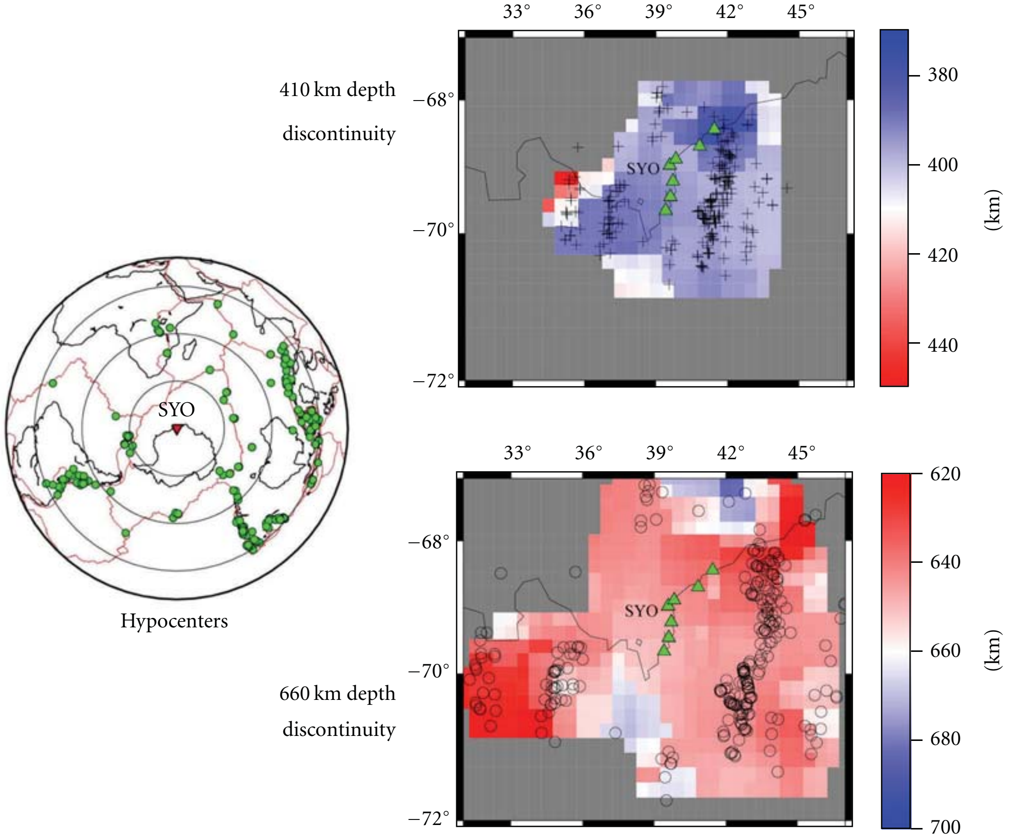

Figure 5: (left) Distribution of hypocenters of teleseismic events used for long-period receiver function analysis (solid circles) and SYO stations (solid triangles). (right) Distribution of P-S conversion depth points for 410 km (upper, crosses) and 660 km discontinuity (lower, open circles), respectively. Location of the conversion depth points was obtained by combining GARNET station positions in LHB and hypocenters of the utilized teleseismic events. Topographic depth variations of the upper mantle discontinuities are presented by the color contours (modified after Kanao et al. 2007 [1]).

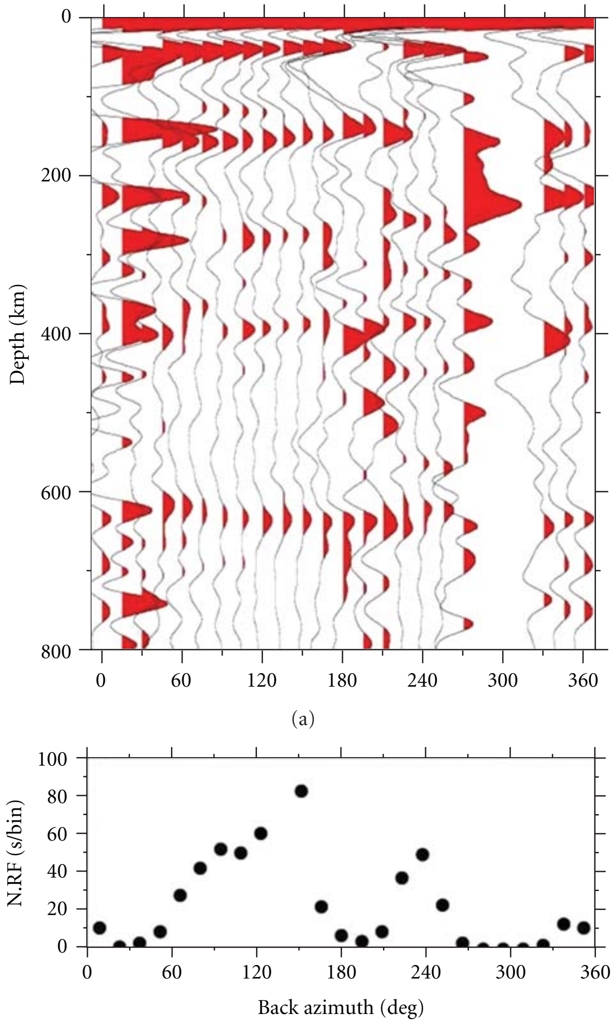

(a)

(b)

Figure 6: (a) Back azimuth distribution for the depth converted receiver functions in the upper mantle compiled for all the GARNET stations. The number of receiver functions for each 15 azimuth range is shown in (b). The back azimuths are represented from Syowa Station (SYO) against the depth conversion points calculated for all the hypocenter-station pairs.

generated using 62 teleseismic events recorded by the local broadband arrays (Figure 5, left). Variations in depth distribution of P-S conversion points were identified particularly about the 660 km discontinuity (Figure 5, right). Shallow depths in topography for the 660 km discontinuity were found beneath the continental ice sheet area, that is, SE part from the GARNET stations along the coast. The evidence might reflect the paleo upwelling of the mantle plume associated with supercontinent break-up in Mid-Mesozoic age.

Back azimuth distribution for depth-converted receiver functions was compiled for all the GARNET stations (Figure 6). The back azimuths were defined as directions of depth conversion points calculated for all the hypocenter-station pairs from Syowa Station (SYO) as a center. Back azimuth distribution for the depth variations in the upper mantle discontinuities was compiled for all stations (Figure 7). The color contours in Figure 6 indicate the smoothed amplitudes of the receiver functions. The heterogeneities were observed in both 410 and 660 km discontinuities in both azimuth ranges of 20–50° and 200–260°. The two back azimuth groups are almost parallel with the coast and may indicate the relationship with the break-up process of Gondwana. The evidence of break-up supported by other studies from teleseismic shear wave anisotropy and reflection imaging by active sources is shown in the succeeding chapter.

4. Upper Mantle Anisotropy

Seismic wave anisotropy provides information on recent and/or fossil mantle flows reflecting tectonic evolution of the study region. The seismic anisotropy in the upper mantle of LHB was derived from SKS splitting analysis for teleseismic events recorded on the GARNET stations (Figure 8; [16]). Averaged delay times of SKS wave splitting for all analyzed stations were obtained as 1.3 s, which were almost equal to the global average. A two-layer model was assumed to model the upper mantle anisotropy; the upper layer is generally considered to correspond to the “lithosphere” and the lower layer to the “asthenosphere”. For six stations in LHB, we can recognize the azimuthal variation of the splitting parameters (Figure 9).

The fast polarization directions of SKS waves were compared with the directions of Absolute Plate Motion (APM), which reflects recent mantle flow [30]. The directions of APM around LHB are about N145°E, and the velocity is about 1.1 cm/yr based on the HS3-NUVEL1 model [31] (Figure 10). Since the fast polarization directions of the lower layer were generally parallel to the directions of APM, it was considered that the lower layer anisotropy reflected asthenospheric anomalies due to the horizontal mantle flow along the APM.

In contrast, the fast polarization directions of the upper layers never coincide with the APM direction (the difference is up to 100°). We offer an idea that the anisotropic structure could be involved with past tectonic events and the origin of anisotropy is “frozen” in the lithosphere. Gondwana assembly in Early Paleozoic was one of the major events in LHB [32]. The LHB experienced regional high-grade metamorphism during the Pan-African orogeny [33]. The metamorphic grade increases progressively from north to south along the coast and the maximum thermal axis lies in the southernmost part of LHB [34].

A “fossil” anisotropy in the lithospheric mantle can be estimated as caused by the past regional tectonics. The majority of the fast polarization directions in the upper layer, corresponding to the “lithosphere”, were orientated in an NE-SW direction (Figure 10). This is consistent with the direction of the paleo compression stress during the Pan-African age and the conversion stage between East and West Gondwana supraterrains. We proposed that the mantle anisotropy was created by lithological orientation of mantle minerals during the amalgamation process of Gondwana, rather than in current asthenospheric flow parallel to APM.

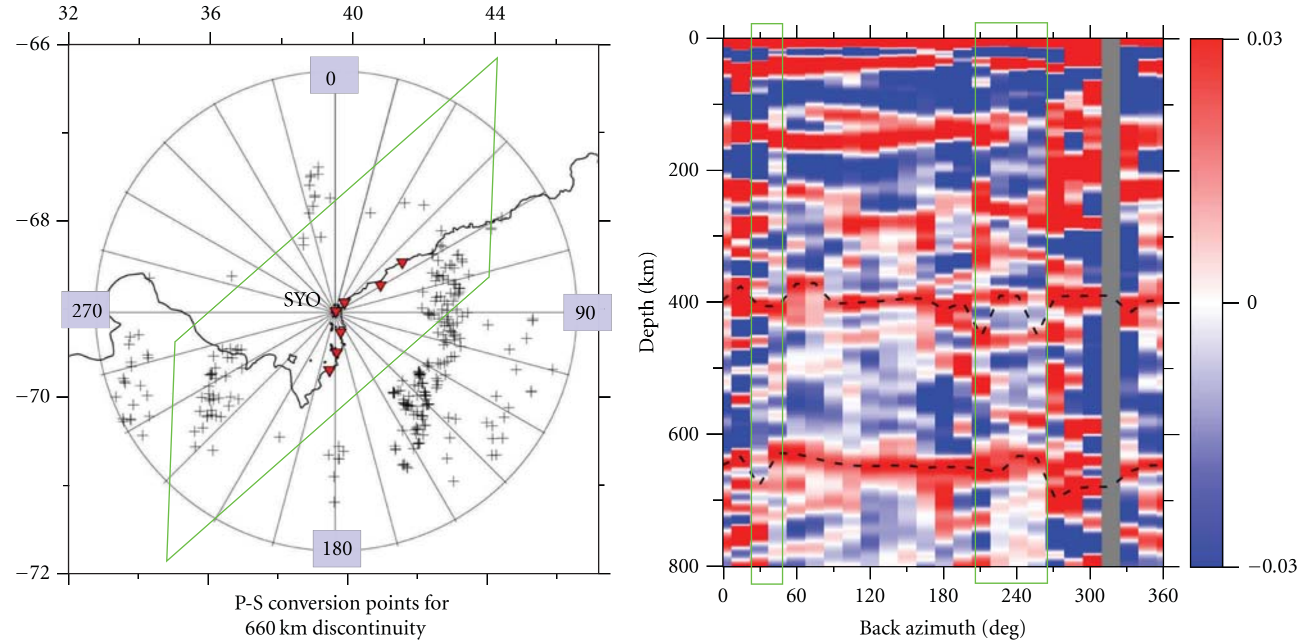

(a)

(b)

Figure 7: (a) Back azimuth distribution for depth variation in upper mantle discontinuities by receiver function analyses for all GARNET stations. Color images represent the smoothed amplitudes of the receiver functions shown in Figure 6. Two dashed lines are traced for the maximum amplitudes of both 410 km and 660 km depth discontinuities. The two back azimuth groups for strong depth variations in upper mantle discontinuities are circled by the light green open squares. (b) Location of the strong heterogeneous azimuths in LHB. The area for strong depth variations in upper mantle discontinuities is represented by the light green open squares, which are almost parallel with the coastal line. Symbolic notation for the P-S conversion points at the mantle discontinuities are the same as in Figure 5.

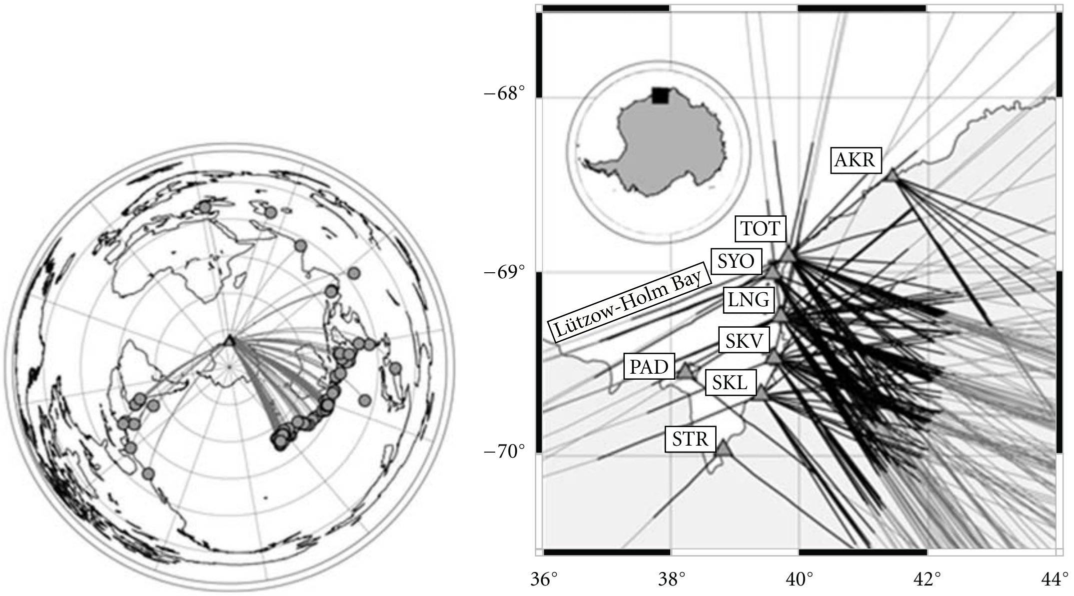

(a)

(b)

Figure 8: (upper) The global distribution of teleseismic events (solid circles) and used stations in LHB for SKS analysis (triangles). Gray lines are the ray paths from the sources. (lower) Map of the study area in LHB showing the seismic stations (triangles). Gray lines indicate SKS wave paths, and black lines indicate wave paths above 410 km depth. All the figures are after Usui et al. [16].

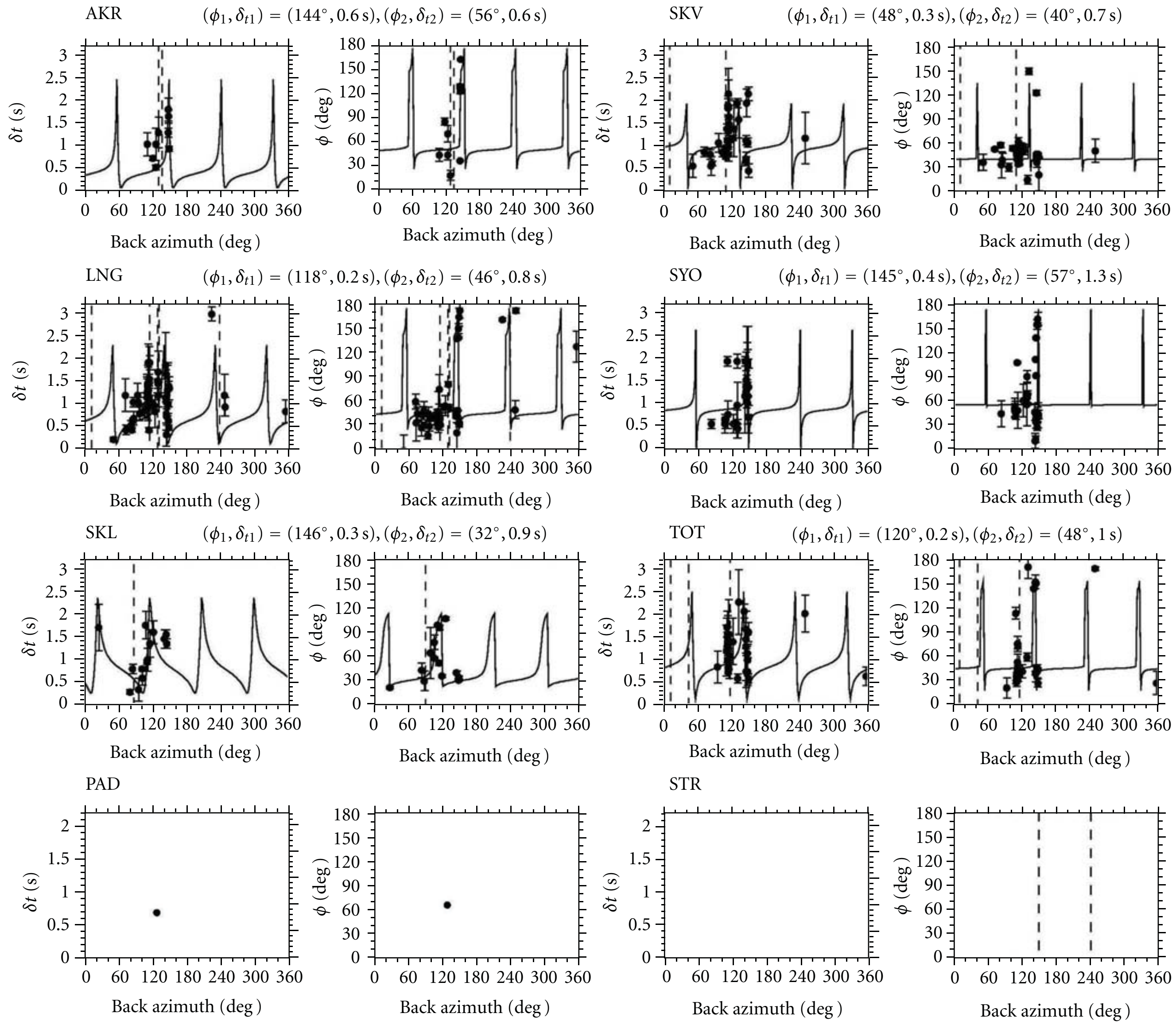

FIGURE 9: Splitting parameters of ϕ and δt plotted as a function of back azimuth. Vertical dashed lines are the direction of null measurements. At stations for AKR, LNG, SKL, SKV, SYO, and TOT, the azimuthal variations of apparent splitting parameters are modeled by a two-layer case of anisotropy. The parameter pair (ϕ_1, δt_1) describes the lower layer anisotropy and (ϕ_2, δt_2) corresponds to the upper layer. All the figures are after Usui et al. [16].

5. Seismic Reflection Imaging

Besides the broadband passive studies, deep crust and upper mantle in LHB were investigated by active source studies (the Deep Seismic Surveys; DSS) by JARE [35–37] (Figure 11). DSS was conducted on the continental ice sheet of LHB in austral summers in 2000 and 2002 as one of the "Structure and Evolution of the East Antarctic Lithosphere (SEAL)" program. The deployments required significant logistical efforts, including the explosion of large dynamite shots along the seismic profiles on the ice sheet plateau in LHB.

Sophisticated DSS processing demonstrated pronounced reflection images of the crust-upper mantle boundary (Moho discontinuity) and of the lithospheric mantle structure [17, 38]. A laminated layering around the crust-mantle boundary was well imaged using coherency enhancement processing after the Normal Move Out (NMO) corrections applied to far-offset data of the SEAL-2000, -2002 profiles. For the SEAL-2000 profile, the single coverage CDP section with only far offset shots was shown in the upper part of Figure 12(a) and the single coverage CDP only with nearer traces could be identified in the lower part. Figure 12(b) shows a single-fold CDP section using only far offset shots for the SEAL-2002 profile (upper), and the CDP stack section with offsets less than 120 km is depicted for the same profile (lower), respectively.

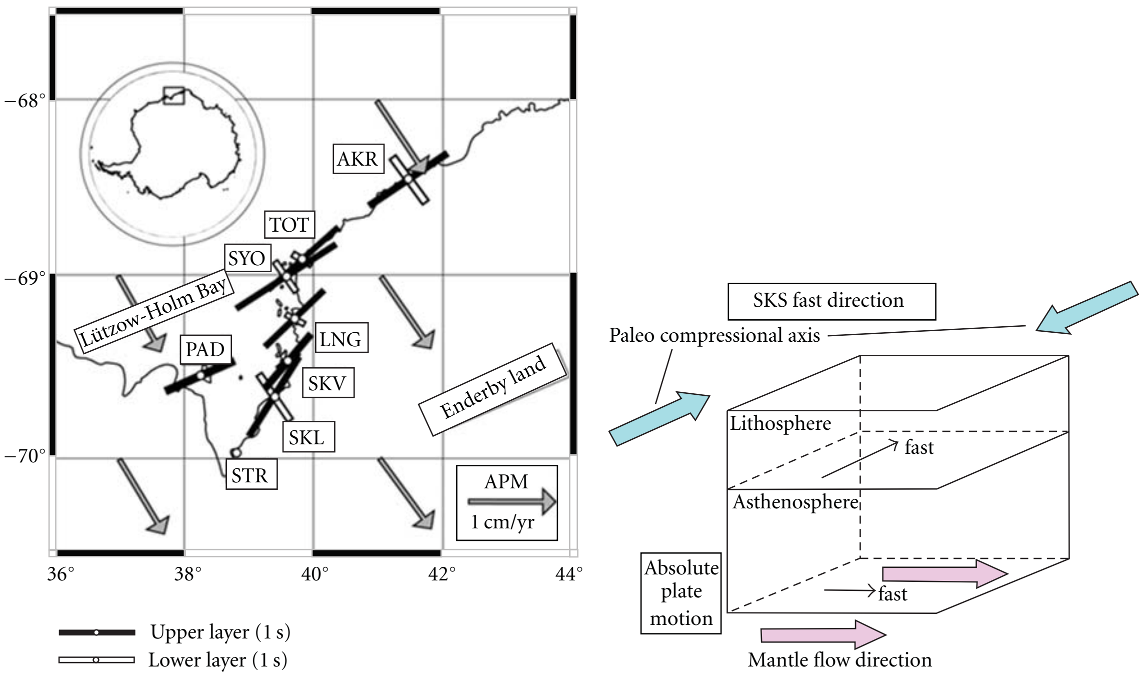

(a)

(b)

Figure 10: (a) Schematic illustration of the two-layered model for obtaining anisotropy. (b) Upper mantle anisotropy in LHB derived from SKS splitting (after Usui et al. 2007 [16]). At stations AKR, LNG, SKL, SYO, and TOT, the lower layer anisotropy was suspected to be caused by recent asthenospheric flow. For almost all other stations, the direction of the upper layer anisotropy (corresponds to the "lithosphere") was parallel to NE-SW convergence during the Pan-African age.

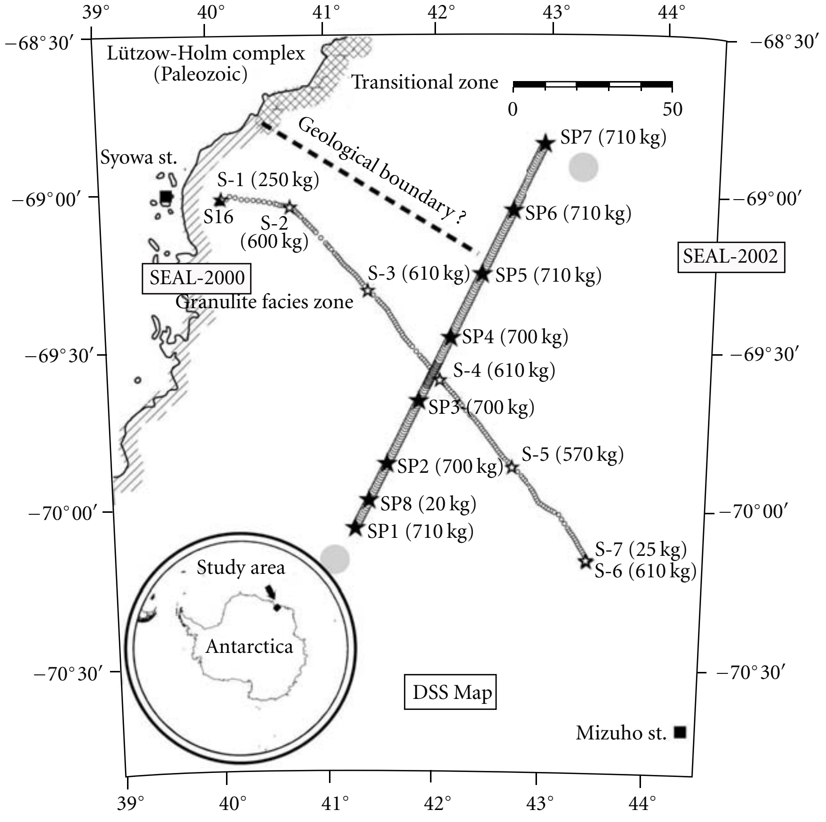

Figure 11: Map showing the location of DSS in LHB (after Kanao et al. 2010 [17]). Solid and open stars indicate the shot locations in SEAL-2002 and -2000, respectively. Large and small circles represent the geophone stations on ice sheet for both the DSS operations. The size of each shot given is weight of dynamite used.

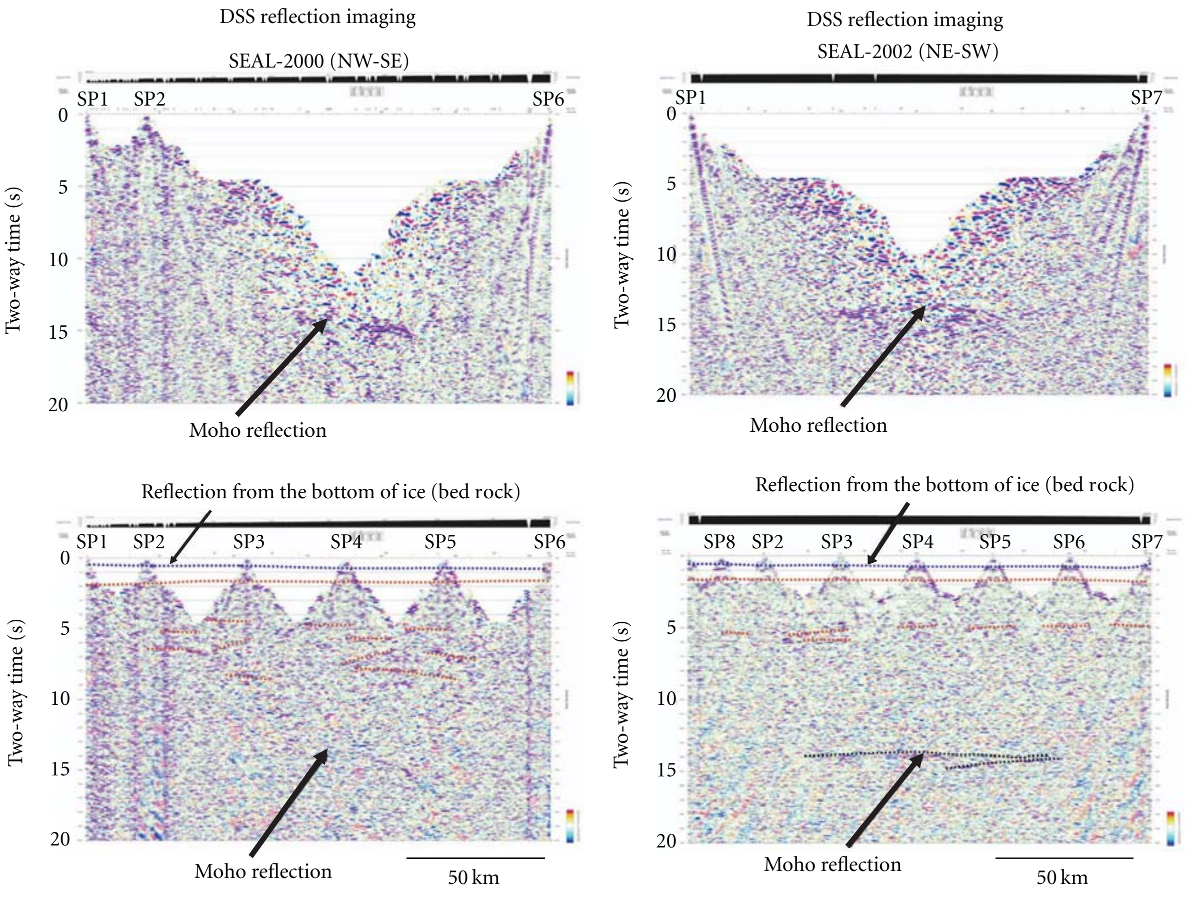

(a) (b)

Figure 12: (a) (upper) Single-fold CDP section showing far offset shots for SP 1, SP 2, and SP 6 of the SEAL-2000 profile. The Moho reflections are indicated by black solid arrow. (lower) CDP stack section offset linked to near traces for the SEAL-2000 profile. Several reflections in the crust and the Moho are identified by red broken lines and black solid arrows, respectively. In addition, reflections from the bottom of the ice sheet are traced by the light-blue broken line. All the figures are after Kanao et al. [17]. (b) (upper) Single-fold CDP section showing far offset shots for SP 1 and SP 7 of the SEAL-2002 profile. The Moho reflections are indicated by black solid arrows. (lower) CDP stack section with offset limited to traces within 120 km for the SEAL-2002 profile. Several reflections in the crust and the Moho are identified by red- and black-colored broken lines. In addition, reflections from the bottom of the ice sheet are traced by the light-blue broken line. All the figures are after Kanao et al. [17].

Laminated layers of the lower crust in LHB, moreover, were numerically modeled by comparing synthetic receiver functions with those of observed waveforms in short period bands (0.1–1.0 Hz) [39]. The repetitive crust-mantle transition zone imaged by the SEAL-2002 profile suggests the presence of compression stress in an NE-SW orientation during the Pan-African age, in the last formation stage of a broad mobile belt between East and West Gondwana terrains. Successive break-up processes of Gondwana in the mid-Mesozoic could account for the formation of the stretched reflection structure around the Moho discontinuity as imaged on the SEAL-2000 profile (Figure 12(a)).

These seismic reflections were considered to represent multigenetic origins, including igneous intrusions, lithologic and metamorphic layering, mylonite zones, shear zones, seismic anisotropy, or fluid layers [40, 41]. Though the cause of reflectivity may have a multigenetic origin, we suggest that metamorphic layering could be the principal cause in the case of LHB. A strong reflectivity in the deeper crust-upper mantle can be expected to result from layered sequences of mafic and felsic rocks [42]. In addition, such a reflectivity can be created where mafic rocks are interlayered with upper amphibolite and lower granulite facies metapelites [43].

In any continental terrains on Earth, the primary causes for reflectivity might be enhanced by ductile stretching during a late tectonic extensional process [44]. In particular, the reflecting layers near the Moho were predominantly found in crustally thinned tectonic areas. Accordingly, the reflectivity in the lower crust and lithospheric mantle beneath LHB might have been enhanced under extensional conditions caused by the last breakup of the Gondwana supercontinent.

6. Discussion

In this section, a regional evolution model of LHB is presented to explain the formation process of the present structure as reviewed in the previous sections. A summary of evolution history, including major tectonic events in LHB, is demonstrated in Figure 14.

Geological studies by JARE revealed the regional metamorphism of LHB during the Pan-African orogeny [33]. Metamorphic grade increases progressively from amphibolite facies in the NE to granulite facies in the SW of LHB. The maximum thermal axis runs through the southern LHB with an NNW-SSE striking direction [29]. From geological evidence, the LHB terrain experienced deformation *r* compression stress-oriented perpendicular to the thermal axis, almost parallel to the coast, during the last stage of the deformation process of a mobile belt located between the East- and West-Gondwana [32]. The high-amplitude magnetic anomalies occurring in LHB compared to those in the surrounding terrains ([45]; Figure 13) indicate the LHB may be located in one of the major suture zones of the Pan-African mobile belt. This has been pointed out in recent studies in East Africa and in East Antarctica. These major suture zones appear to continue from LHB to the Shackleton Range of West Antarctica [32, 46].

The lower crust and upper mantle beneath LHB were characterized to have lateral and vertical variations as shown in seismological studies reviewed in this paper. The gently inland dipping Moho discontinuity (38–42 km) beneath the SEAL-2000 profile was inverted by travel-time analysis from refraction and wide-angle reflection surveys [18]. The present structure is attributed to hold the past regional tectonics, particularly metamorphic and orogenic activities in Pan-African age. Inferred thrust duplicated (similar to the wedge shaped) lower crust-upper mantle transition structures interpreted on the SEAL-2002 profile (Figure 12(b), [17]) also imply a compressive stress regime along the profile oriented in an NE-SW direction during the Pan-African. Through consideration with geophysical and lithologic information, LHB is considered to be formed under convergence, perpendicular to the thermal axis, during the collision between supraterrains of Gondwana during the last stage of supercontinent formation [39, 47]. If LHB underwent NE-SW compression, related paleo-mantle flow along this direction could produce the seismic anisotropy associated with the thermal axis of progressive metamorphism. Since the direction of paleo-compression is consistent with the resultant fast polarization by SKS splitting [16], anisotropy in the upper layer in Figure 9 can be explained by "lithospheric" deformation during the formation of LHB at Pan-African.

During the break-up between Antarctica and Australia-India at ~150 Ma [48], the LHB experienced extensional stress, which caused thinning at the continental margins of East Antarctica. The flat lying reflectors above the crust-mantle boundary recognized in the SEAL-2000 profile (Figure 12(a)) suggest the presence of an extensional stress regime in the NW-SE direction resulting from break-up. The seismic reflective layers at the crust-mantle boundary and lithospheric mantle may have been enhanced by extensional conditions during the final stages of break-up. The Lattice Preferred Orientation (LPO) induced mechanical anisotropy developed along the direction of preexisting lithospheric structure during continental rifting [49]. The origin of anisotropy beneath Western Dronning Maud Land was pointed out as the ancient lithospheric structure modified by rifting processes during break-up [50]. As the spreading direction off the Enderby Land was NW-SE initial stage of break-up [51], a strike of the rift was generally parallel to the continental margin of LHB. The fast polarization directions of the upper layer ("lithosphere") in SKS analysis were roughly parallel to the continental margin. Therefore, it is plausible that break-up affected the formation of anisotropy in the lithosphere. The preexisting lithospheric structure might also influence the formation of anisotropy in succeeding break-up processes.

Finally, besides the studies for the crust and upper mantle, the recorded teleseismic waveforms have advantages to investigate the deep Earth's interiors such as the lower mantle, D′′ zones [15], Core-Mantle-Boundary (CMB), and the Inner Core [14, 52]. The GARNET data in LHB can be utilized to study the deep Earth interior of the southern high latitudes. Further, these data can be combined with data from other projects in the region, such as AGAP/GAMSEIS and projects from collaborating nations in Antarctica. The broadband deployments in LHB offer effective contributions to GARNET, international Antarctic Array program, FDSN, POLENET, and the broader goals of the IPY and beyond.

7. Conclusions

Broadband seismic deployments around the Pan-African terrain of LHB, East Antarctica, provided clear images of characteristic structure of the upper mantle. Passive source studies using teleseismic events such as receiver functions and shear wave splitting demonstrated heterogeneous structure along the coast in the region. Depth variations of the upper mantle discontinuities (410 km and 660 km) were derived from long-period receiver functions recorded at LHB array stations. Shallow depths in topography of the upper mantle discontinuity particularly about 660 km depths were cleared beneath the continental ice sheet area where SE apart from the stations. These results may reflect paleo upwelling of the mantle plume associated with Gondwana break-up.

Lithospheric mantle anisotropy derived by SKS splitting anticipated relationship between "fossil" anisotropy and past tectonics. Fast polarization directions, mainly in NE-SW, were consistent with paleo compression during the Pan-African. The origin of mantle anisotropy might be caused chiefly by LPO involving supercontinent assembly, rather than present asthenospheric flow parallel with Absolute Plate Motion. In addition, multidisciplinary lithospheric mantle images were combined by both active and passive sources conducted at LHB. DSS was carried out on the continental ice-sheet in 2000 and 2002 and provided clear information on the crust-mantle boundary, together with inner crustal and lithospheric mantle reflections. After processing of NMO

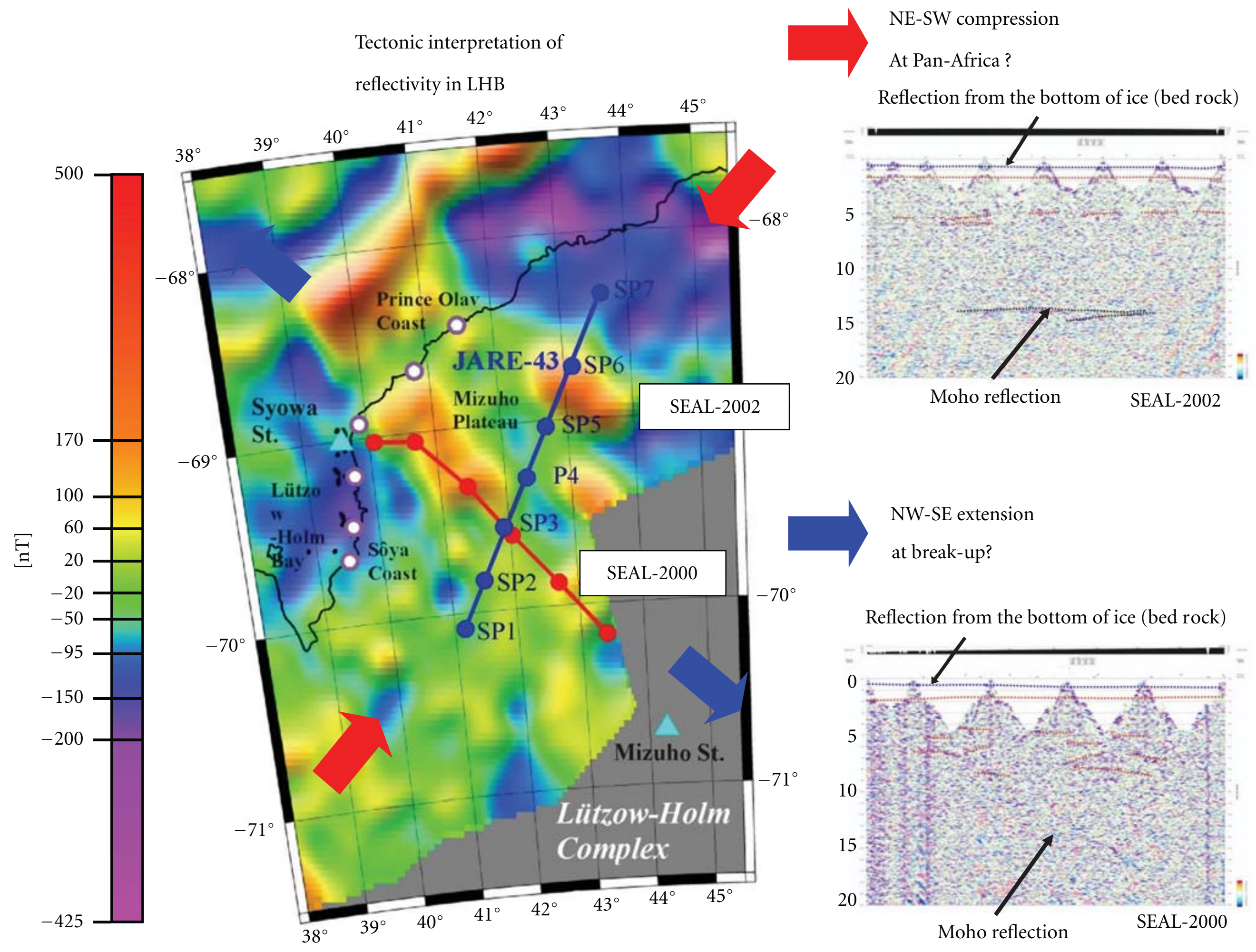

FIGURE 13: Aeromagnetic anomalies (by Golynsky et al., 1996 [18]) around LHB with GARNET stations and DSS profiles (modified after Kanao et al., 2010 [17]). Tectonic interpretation is illustrated with associated interpretations of reflection cross sections by DSS.

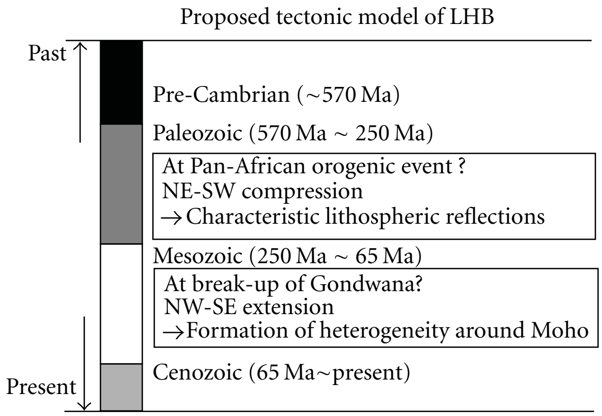
Proposed tectonic model of LHB

Past

Pre-Cambrian (~570 Ma)

Paleozoic (570 Ma ~ 250 Ma)

At Pan-African orogenic event ?
NE-SW compression
→Characteristic lithospheric reflections

Mesozoic (250 Ma ~ 65 Ma)

At break-up of Gondwana?
NW-SE extension
→Formation of heterogeneity around Moho

Cenozoic (65 Ma~present)

Present

FIGURE 14: Summary of tectonic history proposed by seismological studies in LHB. Pan-African orogeny and Mid-Mesozoic break-up could be the major two events affecting the formation of the present upper mantle structure.

corrections and CDP stacking, the DSS extracted lithospheric images imply tectonic influence of compressive stress during the Pan-African.

The broadband deployments in LHB, accordingly, could give rise to an effective contribution to regional and global seismic networks, international Antarctic Array programs, together with POLENET during IPY.

Acknowledgments

The authors would like to express their special appreciation to the participants of the JARE members for their great efforts to carry out the seismic array deployments around the LHB. The authors would like to express sincere thanks to Professors. K. Kaminuma, K. Shibuya, Y. Nogi, K. Doi, Y. Aoyama and the all staff of NIPR for their useful discussion about seismic deployments and upper mantle studies. They would like to thank the collaborators in the IPY projects for AGAP/GAMSEIS (Professor D. Wiens of Washington University, Professor A. Nyblade of Penn. State University, and others) and POLENET (Professor T. Wilson of the Ohio State University, Dr. S. Konfal, and others). They appreciate so much S. Konfal and T.Wilson for checking the paper and giving useful comments. The authors would like to express their sincere thankfulness for Professor J. Gamble of the Department of Geology, National University of Ireland, Professor A. K. Cooper of the Department of Geological and Environmental Sciences, Stanford University, and two anonymous referees of the special issue on "*Seismic Imaging*" in International Journal of Geophysics for their sincere and useful comments.

References

[1] M. Kanao, Y. Usui, T. Inoue et al., "Broadband seismic array deployments and Lithospheric structure around the Lützow-Holm Bay region, East Antarctica," in *Antarctica: A Keystone in a Changing World. U. S. Geological Survey and The National Academies*, A. K. Cooper, P. Barrett, H. Stagg et al., Eds., 2007, USGS OF-2007-1047, Extended Abstract 145.

[2] A. M. Reading, "Antarctic seismicity and neotectonics," in *Antarctica at the Close of a Millennium*, J. A. Gamble, Ed., vol. 35 of *The Royal Society of New Zealand Bulletin*, pp. 479–484, Wellington, 2002.

[3] G. Roult, D. Rouland, and J. P. Montagner, "Antarctica II: upper-mantle structure from velocities and anisotropy," *Physics of the Earth and Planetary Interiors*, vol. 84, no. 1-4, pp. 33–57, 1994.

[4] M. H. Ritzwoller, N. M. Shapiro, A. L. Levshin, and G. M. Leahy, "Crustal and upper mantle structure beneath Antarctica and surrounding oceans," *Journal of Geophysical Research B*, vol. 106, no. 12, pp. 30645–30670, 2001.

[5] R. Kobayashi and D. Zhao, "Rayleigh-wave group velocity distribution in the Antarctic region," *Physics of the Earth and Planetary Interiors*, vol. 141, no. 3, pp. 167–181, 2004.

[6] S. Bannister and B. L. N. Kennett, "Seismic activity in the Transantarctic Mountains - Results from a broadband array deployment," *Terra Antarctica*, vol. 9, no. 1, pp. 41–46, 2002.

[7] C. Müller and A. Eckstaller, "Local seismicity detected by the Neumayer seismological network, Dronning Maud Land, Antarctica: tectonic earthquakes and ice-related seismic phenomena," in *Proceedings of the 9th International Symposium on Antarctic Earth Sciences*, Potsdam, Germany, 2003, Programme and Abstracts 236.

[8] A. M. Reading, "The SSCUA broadband seismic development, East Antarctica," in *Proceedings of the 9th International Symposium on Antarctic Earth Sciences*, 2003, Programme and Abstracts 270.

[9] D. Robertson, D. A. Wiens, and P. J. Shore, "Seismicity and tectonics of the South Shetland Islands and Bransfield Strait from the SEPA broadband seismograph deployment," in *Antarctica at the Close of a Millennium*, J. A. Gamble et al., Ed., vol. 35, pp. 549–554, The Royal Society of New Zealand Bulletin, Wellington, New Zealand, 2002.

[10] D. A. Wiens, S. Anandakrishnan, A. A. Nyblade et al., "Remote detection and monitoring of glacial slip from Whillans Ice Streeam using seismic rayleigh waves recorded by the TAMSEIS array," *Eos, Transactions, American Geophysical Union,*, vol. 87, no. 52, 2006.

[11] J. F. Lawrence, D. A. Wiens, A. A. Nyblade, S. Anandakrishan, P. J. Shore, and D. Voigt, "Upper mantle thermal variations beneath the Transantarctic Mountains inferred from teleseismic S-wave attenuation," *Geophysical Research Letters*, vol. 33, no. 3, Article ID L03303, 2006.

[12] D. A. Wiens, "Broadband Seismology in Antarctica: recent progress and plans for the international polar year," in *Proceedings of the International Symposium Asian Collaboration in International Polar Year National Committee*, pp. 21–24, Tokyo, Japan, March 2007.

[13] S. E. Hansen, A. A. Nyblade, D. S. Heeszel, D. A. Wiens, P. Shore, and M. Kanao, "Crustal structure of the Gamburtsev Mountains, East Antarctica, from S-wave receiver functions and Rayleigh wave phase velocities," *Earth and Planetary Science Letters*, vol. 300, no. 3-4, pp. 395–401, 2010.

[14] T. Isse and I. Nakanishi, "Inner-core anisotropy beneath Australia and differential rotation," *Geophysical Journal International*, vol. 151, no. 1, pp. 255–263, 2002.

[15] Y. Usui, Y. Hiramatsu, M. Furumoto, and M. Kanao, "Evidence of seismic anisotropy and a lower temperature condition in the D″ layer beneath Pacific Antarctic Ridge in the Antarctic Ocean," *Physics of the Earth and Planetary Interiors*, vol. 167, no. 3-4, pp. 205–216, 2008.

[16] Y. Usui, M. Kanao, and A. Kubo, "Upper mantle anisotropy from teleseismic SKS splitting beneath Lützow-Holm Bay region, East Antarctica," in *Antarctica: A Keystone in a Changing World. U. S. Geological Survey and The National Academies*, A. K. Cooper, P. Barrett, H. Stagg et al., Eds., 2007, SGS OF-2007-1047, Short Research Paper 013.

[17] M. Kanao, A. Fujiwara, H. Miyamachi et al., "Reflection imaging of the crust and the lithospheric mantle in the Lützow-Holm complex, Eastern Dronning Maud Land, Antarctica, derived from the SEAL transects," *Tectonophysics*, vol. 508, no. 1–4, pp. 73–84, 2011.

[18] A. V. Golynsky, V. N. Masolov, Y. Nogi et al., "Magnetic anomalies of Precambrian terrains of the East Antarctic shield coastal region (20E-50E)," *Polar Geoscience*, vol. 9, pp. 24–39, 1996.

[19] H. Negishi and M. Kanao, "Field seismic observations by portable broadband seismometers in the Lutzow-Holm Bay Region, East Antarctica," *Antarctic Record*, vol. 42, no. 2, pp. 179–189, 1998.

[20] M. Kanao and T. Higashi, "Geophysical research from field observations by the Earth Science Division in the 38th

Japanese Antarctic Research Expedition (1996–1998)," *Antarctic Record*, vol. 43, no. 3, pp. 375–405, 1999.

[21] J. P. Winberry, "Stick-slip motion of antarctic ice streams: observations from the meter scale and the hundred-kilometer scale," in *Proceedings of the International Workshop on Geophysics of Interior Antarctica*, p. 20, Beijing, China, October 2010

[22] K. Kuge and Y. Fukao, "High-velocity lid of East Antarctica: evidence of a depleted continental lithosphere," *Journal of Geophysical Research B*, vol. 110, no. 6, pp. 1–15, 2005.

[23] K. Nawa, N. Suda, K. Satake et al., "Loading and gravitational effects of the 2004 Indian Ocean tsunami at Syowa Station, Antarctica," *Bulletin of the Seismological Society of America*, vol. 97, no. 1, pp. S271–S278, 2007.

[24] Y. Usui, Y. Hiramatsu, M. Furumoto, and M. Kanao, "Thick and anisotropic D′′ layer beneath Antarctic Ocean," *Geophysical Research Letters*, vol. 32, no. 13, pp. 1–4, 2005.

[25] M. Kanao and K. Kaminuma, "Seismic activity associated with surface environmental changes of the Earth system, around Syowa Station, East Antarctica," in *Antarctica: Contributions to Global Earth Sciences*, D. K. Futterer, D. Damaske, and G. Kleinschmidt, Eds., pp. 361–368, Springer, Berlin, Germany, 2006.

[26] A. Yamada, M. Kanao, and M. Yamashita, "Features of seismic waves recorded by seismic exploration in 2002: responses from valley structure of the bedrock beneath Mizuho Plateau," *Polar Geoscience*, vol. 17, pp. 139–155, 2004.

[27] M. Kanao, "Variations in the crustal structure of the Lützow-Holm Bay region, East Antarctica using shear wave velocity," *Tectonophysics*, vol. 270, no. 1-2, pp. 43–72, 1997.

[28] M. Kanao, A. Kubo, T. Shibutani et al., "Crustal structure around the Antarctic margin by teleseismic receiver function analyses," in *Antarctica at the Close of a Millennium*, J. A. Gamble, D. N. B. Skinner, and S. Henrys, Eds., vol. 35, pp. 485–491, Royal Society of New Zealand Bulletin, 2002.

[29] Y. Hiroi, K. Shiraishi, and Y. Motoyoshi, "Late Proterozoic paired metamorphic complexes in East Antarctica, with special reference to the tectonic significance of ultramafic rocks," in *Geological Evolution of Antarctica*, M. R. A. Thomson, J. A. Crame, and J. W. Thomson, Eds., pp. 83–87, 1991.

[30] L. P. Vinnik, L. I. Makeyeva, A. Milev, and A. Y. Usenko, "Global patterns of azimuthal anisotropy and deformations in the continental mantle," *Geophysical Journal International*, vol. 111, no. 3, pp. 433–447, 1992.

[31] A. E. Gripp and R. G. Gordon, "Young tracks of hotspots and current plate velocities," *Geophysical Journal International*, vol. 150, no. 2, pp. 321–361, 2002.

[32] I. C. W. Fitzsimons, "Grenville-age basement provinces in East Antarctica: evidence for three separate collisional orogens," *Geology*, vol. 28, no. 10, pp. 879–882, 2000.

[33] K. Shiraishi, D. J. Ellis, Y. Hiroi, C. M. Fanning, Y. Motoyoshi, and Y. Nakai, "Cambrian orogenic belt in East Antarctica and Sri Lanka: implications for Gondwana assembly," *Journal of Geology*, vol. 102, no. 1, pp. 47–65, 1994.

[34] Y. Motoyoshi, S. Matsubara, and H. Matsueda, "P-T evolution of the granulite facies rocks of the Lützow-Holm Bay region, East Antarctica, Evolution of Metamorphic Belts," in *Geological Society Special Publication*, J. S. Daly et al., Ed., vol. 43, pp. 325–329, 1989.

[35] H. Miyamachi, H. Murakami, T. Tsutsui et al., "A seismic refraction experiment in 2000 on the Mizuho Plateau, East Antarctica (JARE-41)—outline of observation," *Antarctic Record*, vol. 45, pp. 101–147, 2001 (Japanese).

[36] H. Miyamachi, S. Toda, T. Matsushima et al., "A seismic refraction and wide-angle reflection exploration in 2002 on the Mizuho Plateau, East Antarctica—outline of observations (JARE-43)," *Antarctic Record*, vol. 47, pp. 32–71, 2003 (Japanese).

[37] M. Kanao, M. Ishikawa, M. Yamashita, K. Kaminuma, and L. D. Brown, "Structure and evolution of the East Antarctic lithosphere: tectonic implications for the development and dispersal of Gondwana," *Gondwana Research*, vol. 7, no. 1, pp. 31–41, 2004.

[38] M. Yamashita, H. Miyamachi, M. Kanao et al., "Deep Reflection Imaging beneath the Mizuho Plateau, East Antarctica, by SEAL-2002 Seismic experiment," in *Antarctica: Contributions to Global Earth Sciences*, D. K. Futterer, D. Damaske, G. Kleinschmidt et al., Eds., pp. 147–154, Springer, Berlin, Germany, 2006.

[39] M. Kanao and M. Ishikawa, "Origins of the lower crustal reflectivity in the Lützow-Holm Complex, Enderby Land, East Antarctica," *Earth, Planets and Space*, vol. 56, no. 2, pp. 151–162, 2004.

[40] R. D. Hyndman and P. M. Shearer, "Water in the lower continental crust: modelling magnetotelluric and seismic reflection results," *Geophysical Journal International*, vol. 98, no. 2, pp. 343–365, 1989.

[41] S. B. Smithson and R. A. Johnson, "Crustal structure of the western U. S. based on reflection seismology: geophysical framework of the continental United States," *Geological Society Special Publication*, vol. 172, pp. 577–612, 1989.

[42] J. A. Goff, K. Holliger, and A. Levander, "Modal fields: a new method for characterization of random seismic velocity heterogeneity," *Geophysical Research Letters*, vol. 21, no. 6, pp. 493–496, 1994.

[43] L. Burlini and D. M. Fountain, "Seismic anisotropy of metapelites from the Ivrea-Verbano zone and Serie dei Laghi (northern Italy)," *Physics of the Earth and Planetary Interiors*, vol. 78, no. 3-4, pp. 301–317, 1993.

[44] M. Warner, "Basalts, water, or shear zones in the lower continental crust?" *Tectonophysics*, vol. 173, no. 1–4, pp. 163–174, 1990.

[45] L. A. Lawver and C. R. Scotese, "A revised reconstruction of Gondwanaland," in *Gondwana Six: Structure, Tectonics and Geophysics*, G. D. McKenzie, Ed., pp. 17–23, 1987.

[46] K. Yoshii, K. Ito, H. Miyamachi, and M. Kanao, "Crustal structure derived from refractions and wide-angle reflections in the Mizuho Plateau, East Antarctica," *Polar Geoscience*, vol. 17, pp. 112–138, 2004.

[47] M. Ishikawa and M. Kanao, "Structure and collision tectonics of Pan-African orogenic belt—scientific significance of the geotransect for a supercontinent: gondwanaland," *Bulletin of Earthquake Research Institute, University of Tokyo*, vol. 77, pp. 287–302, 2002 (Japanese).

[48] D. L. Anderson, "Superplumes or supercontinents?" *Geology*, vol. 22, no. 1, pp. 39–42, 1994.

[49] A. Tommasi and A. Vauchez, "Continental rifting parallel to ancient collisional belts: an effect of the mechanical anisotropy of the lithospheric mantle," *Earth and Planetary Science Letters*, vol. 185, no. 1-2, pp. 199–210, 2001.

[50] C. Müller, "Upper mantle seismic anisotropy beneath Antarctica and the Scotia Sea region," *Geophysical Journal International*, vol. 147, no. 1, pp. 105–122, 2001.

[51] Y. Nogi, N. Seama, N. Isezaki et al., "Magnetic anomaly lineations and fracture zones deduced from vector magnetic

anomalies in the West Enderby Basin, in Weddell Sea Tectonics and Gondwana Break-up," in *Geological Society Special Publication*, B. C. Storey, E. C. King, and R. A. Livermore, Eds., vol. 108, pp. 265–273, 1996.

[52] X. Song and P. G. Richards, "Seismological evidence for differential rotation of the earth's inner core," *Nature*, vol. 382, no. 6588, pp. 221–224, 1996.

Hindawi Publishing Corporation
International Journal of Geophysics
Volume 2011, Article ID 780291, 12 pages
doi:10.1155/2011/780291

Research Article

Multiparameter Inversion: Cramer's Rule for Pseudodifferential Operators

Rami Nammour and William W. Symes

Department of Computational and Applied Mathematics, Rice University, 6100 Main Street, Houston, TX 77005, USA

Correspondence should be addressed to William W. Symes, symes@caam.rice.edu

Received 16 January 2011; Accepted 31 May 2011

Academic Editor: Sergey Fomel

Linearized multiparameter inversion is a model-driven variant of amplitude-versus-offset analysis, which seeks to separately account for the influences of several model parameters on the seismic response. Previous approaches to this class of problems have included geometric optics-based (Kirchhoff, GRT) inversion and iterative methods suitable for large linear systems. In this paper, we suggest an approach based on the mathematical nature of the normal operator of linearized inversion—it is a scaling operator in phase space—and on a very old idea from linear algebra, namely, Cramer's rule for computing the inverse of a matrix. The approximate solution of the linearized multiparameter problem so produced involves no ray theory computations. It may be sufficiently accurate for some purposes; for others, it can serve as a preconditioner to enhance the convergence of standard iterative methods.

1. Introduction

The linearized inverse problem in reflection seismology aims at recovering model perturbations from data perturbations, assuming known reference or background model. Both reference model and model perturbations consist of material parameter fields (functions of position x) that characterize wave propagation. As the background model is considered known, we will suppress it from the notation and use the word "model" and the symbol m and similar symbols to refer to model perturbations. The linearized scattering operator F maps a model perturbation m to the corresponding perturbation Fm of the predicted data.

With these conventions, the inverse problem may be stated as follows: given observed data d, find a model perturbation m so that

$$Fm \approx d. \tag{1}$$

Interpreting (1) in a least squares sense yields the *normal equations*

$$F^*Fm = F^*d. \tag{2}$$

F^* is the adjoint (transpose) of F: it is a migration operator (to be precise, the result of reverse time migration, properly construed). The migration operator maps the data space to model space. We will refer to the migration output $m_{\text{mig}} = F^*d$ as the migrated image, acknowledging its typical role in seismic processing. $N := F^*F$ is the normal operator, or Hessian (we will use these terms interchangeably).

An example of this setup is linear acoustics; we will treat this example explicitly in this paper. The model m consists of the velocity and density (or impedance and density, or any other equivalent combination) perturbation fields $m = (\delta v, \delta\rho)$, for instance. The forward map samples the solution of the linearized (Born approximation) acoustic wave equation for a source (right-hand side) indexed by source position, at receiver positions, possibly with additional filtering to emulate antenna patterns induced by source and receiver arrays.

In simulating seismic data generation with models such as linear acoustics, waves typically propagate over hundreds of wavelengths, and model fields must resolve features on the wavelength scale. The normal equations thus represent millions, or billions, of equations in the same number of unknowns, ruling out the possibility of solving them by means of direct matrix methods such as Gaussian elimination. This paper presumes that the computations implementing the application of the normal operator are carried out by "wave equation" methods, that is, finite difference or finite element simulation. Thus each application is an expensive, large-scale computational procedure, a fact which places practical limits on the number of steps taken in an iterative scheme to solve the normal equations (2). For example, Krylov subspace methods (such as the conjugate gradient method) require at least one application of the normal operator per iteration.

We present an efficient method to approximate the solution of the normal equations that requires a few applications of the normal operator (one for one-parameter inversion, two for two-parameter inversion, and six for three-parameter inversion). This method leverages the properties of the normal operator: under some conditions (background model parameter fields slowly varying on the wavelength scale, diving wave energy eliminated from data, data polarized by propagating phases), it is a special type of matrix-valued spatially varying filter [1–9]. This particular type of spatially varying filter, called a *pseudodifferential operator* in the mathematical literature [10], preserves the discontinuities (events) in the model m to which it is applied while effecting a dip- and frequency-dependent scaling of the amplitudes. Its application also mixes events when several model parameters (density, p- and s-wave velocities, etc.) are present: thus a density event will show up in the velocity component of acoustic migration output, and viceversa, for example.

In this work, we shall show how to separate the events corresponding to various model parameters by means of several applications of the normal operator to permuted image vectors, so that the result differs from an inversion of the data by an overall spatially dependent filter, common to all components. We have previously solved the problem of estimating and correcting for such a filter [11, 12]: it is the same problem as occurs in the solution of a single-parameter linearized inverse problem. Combining the two techniques, we recover an accurate approximate inversion for all parameters, within constraints which we shall illustrate.

We review our approach to single-parameter inversion (based on constant density acoustic modeling, for instance) in Appendix B. It belongs to the genre of *scaling methods* [13–16], which approximate the Hessian or its inverse by estimating a filter of some sort from a single application of the normal operator to a migrated image or some other test image. In previous work on single-parameter inversion, the second author pointed out that the pseudodifferential nature of the Hessian makes possible, a very simple, and accurate approximation, provided that the reflectivity dip is unique at every imaging location [16]. Our approach to single-parameter inversion without assuming uniqueness of dip (Appendix B) carries this idea further; it is similar to that described by Guilton [15], but with different constraints on filter structure motivated by the theory of the pseudodifferential normal operator cited above. The core of our method is the Pseudodifferential Operator Algorithm [17], an efficient algorithm for application of filters of the required type, which we review in Appendix A. Several other authors have explored similar pseudodifferential scaling methods based on other fast application algorithms [18, 19].

Note that data-adaptive scaling methods such as those cited in the previous paragraph differ in an essential way from scaling by an approximate diagonal of the Hessian [20, 21]. As noted by Rickett [14], a dip-independent scaling cannot well approximate an inverse Hessian in general, as the appropriate amplitude correction (from migrated image to inversion) depends on dip. On the other hand, these methods also differ from the so-called Kirchhoff or Generalized Radon Transform or Ray-Born inversion (e.g., [22–25]): both are asymptotic and approximate (either implicitly or explicitly) the normal operator as a pseudodifferential operator, but Generalized Radon Transform inversion involves explicit geometric optics computations, while scaling methods do not. Migration deconvolution methods [26] also approximate the Hessian, or its inverse, but differ from scaling methods in a similar way: migration deconvolution filters are constructed from approximate (layered) Green's function computations, rather than by data-adaptive fitting of an *a priori* limited filter class. Several authors have explored construction of localized filter representation of the Hessian or inverse Hessian using a more general class of Green's functions [27, 28]; again, scaling methods do not require precomputation of a Green's function database.

It has long been recognized that the offset (or scattering angle) dependence of a reflection event encodes material parameter changes across a reflector. Approximations to this relation motivated by the analysis of reflection and transmission in layered media (the Zoeppritz equations and linearization thereof, [29, 30]) lead to amplitude-versus-offset ("AVO") analysis techniques [31]. Linearized inversion for one or more material parameters might be viewed as a quantitative counterpart, that is, as AVO inversion, and attacked via iterative linear system solvers [32–34]. Herrmann [18] uses a single-parameter inversion approach resembling ours to precondition iterative inversion for faster convergence; we envision a similar use of our techniques. Note that migration deconvolution has also been used as an aid to quantitative AVO [35]. As already mentioned, migration deconvolution relies on layered modeling to obtain approximate Green's functions. Pseudodifferential scaling is limited in other ways but does not require modeled wave dynamics used to construct the approximate Hessian to be close to those of layered media (and does not require the construction of Green's functions).

Several studies have analyzed the conditioning, or error propagation properties, of multiparameter inversion [34, 36–38]. We will not discuss this important issue except in that characteristic conditioning behavior will be evident in our examples: for linearized acoustic inversion from surface data, velocity or impedance perturbations are considerably better resolved than are density perturbations.

We have used only synthetic data in the work reported here and rather simple synthetic data at that. In fact, the very few published examples of inversion (in the sense of noise-level data fit) of exploration-scale data [39–41], strongly suggest that the success of linearized multiparameter inversion is sensitive to other aspects of the inverse problem: source pulse and radiation pattern estimation, background field approximation, modeling the physics accurately (including elasticity, attenuation, etc.), and to very careful data preprocessing. In this work, we chose to avoid these issues and focus only on the mathematical/computational issue of multiparameter inversion, given model-consistent data.

2. Theory and Methods

Recall that the aim of this paper is to solve the normal equations

$$Nm = m_{\text{mig}} = F^* d \tag{3}$$

for a model vector $m = (m_1, \ldots, m_n)$ consisting of n component material parameter perturbation fields m_i. The migration output m_{mig} is a vector of the same type as the model, that is, an n-vector of components, which we shall call images, as they typically contain visual evidence of reflectors.

Since both input and output of the normal operator consist of n-vectors of material parameter fields, it is natural to represent N as an $n \times n$ block matrix of operators N_{ij} mapping material parameter fields of type i to those of type j. Since material parameter fields are positive, it is possible to use relative perturbations to parametrize the model (thus, $\delta\rho/\rho$ for instance), in which, case N and its blocks N_{ij} are nondimensional. We chose not to nondimensionalize the problem as the techniques to be described below automatically produce results with appropriate units.

The Hessian may be treated as a matrix of spatially varying filters. The filter coefficient A_{ij} defining the (i, j) component filter N_{ij} depends on both the spatial position x and the wavevector k,

$$N_{ij} m_j(\mathrm{x}) = \int A_{ij}(\mathrm{x}, k) \widehat{m_j}(k) e^{i\mathrm{x}\cdot\mathrm{k}}\, d\mathrm{k}, \tag{4}$$

in which $\widehat{m_j}$ denotes the spatial Fourier transform of the jth model component m_j. Denote by $N = \mathrm{op}(A)$ the operator defined by the matrix $A = (A_{ij})$ of filter coefficients via (4).

Under certain conditions, the normal operator is a matrix of spatially varying filters of a special type, known as pseudodifferential, to be described below. By Beylkin [1] and Rakesh [2] established the first results of this type, which were systematically extended by Nolan and Symes [4], Ten Kroode et al. [6], De Hoop and Bleistein [5], Stolk [42], Stolk and De Hoop [43] and others. We summarize the theory as follows: the Hessian is well approximated by a pseudodifferential operator provided

(i) the material parameters in the background model vary smoothly on the scale of a wavelength (since the theory is asymptotic in frequency, the technical assumption is that they are smooth, that is, infinitely differentiable, but the practical meaning is as stated here);

(ii) diving wave energy is not present in the data or has been muted or dip-filtered out;

(iii) the data has been polarized into propagating phase components.

These conditions are likely to be essential: either major reflectors in the background model or nonpolarized multiphase data lead to Hessians which produce nonphysical reflector images at some distance from their sources, hence cannot be well-approximated by their near-diagonal behavior. Since pseudodifferential operators are nearly local, in a sense to be made precise below, Hessians producing major reflector shifts cannot be approximated by them. For that matter, no near-diagonal approximation to the Hessian could be accurate in such cases, so these same limitations would seem to apply to all scaling methods.

Pseudodifferential operators are distinguished from other types of spatially varying filters by strong constraints on the filter coefficients A_{ij}, which must exhibit polynomial-like growth in the wavenumber $k = \sqrt{\mathrm{k} \cdot \mathrm{k}}$, as $k \to \infty$. more precisely, require that a real μ exist so that the mixed partial derivative of order $\alpha = \alpha_1 + \alpha_2 + \alpha_3$ grows like $k^{\mu-\alpha}$ as $k \to \infty$:

$$\left| \frac{\partial^\alpha}{\partial k_1^{\alpha_1} \partial k_2^{\alpha_2} \partial k_3^{\alpha_3}} A_{ij}(\mathrm{x}, \mathrm{k}) \right| \leq \text{const.} \times k^{\mu-\alpha}. \tag{5}$$

That is, A_{ij} grows like k^μ for large k, and every mixed partial derivative in k decreases the order of growth by the order of the derivative. It is also required that spatial derivatives do not increase the order of growth of the coefficient—we will not write down precisely how this additional constraint is imposed, referring the interested reader to Taylor [10] for a more complete account.

Condition (5) also describes the growth behavior of polynomials in k, which are the filter coefficients of differential operators. Other functions of k, for instance k itself, also satisfy these conditions, so the type of filter described by (5) is more general than differential operators. These considerations led to the name “pseudodifferential operator” being applied to this type of filter. In fact, it is possible to approximate any pseudodifferential operator arbitrarily well by the composition of a differential operator and a power of the Laplacian (i.e., a filter of the form k^μ). In this sense, pseudodifferential operators are nearly local, that is, diagonal.

By convention, filter coefficients obeying the growth rules described here are called *symbols*, and we shall use this terminology as well to distinguish these special filter coefficients from the Fourier representation of general filters. The number μ figuring in the constraint (5) is the *order* of the operator; it determines the extent to which application of the operator changes the growth (or decay) rate for in the Fourier domain, for large wavenumber. Note that order is inclusive, rather than precise: if an operator is of order μ, it is of order ν for any $\nu \geq \mu$. However, order does differentiate pseudodifferential operators by the size of their effect on oscillatory data, just as is the case for differential operators. The work cited at the beginning of this section shows how the order of the Hessian depends on the dimension of the model and the source-receiver geometry. For example, for constant density acoustics in 2D, the order is 1; for 3D and a full range (i.e., π) of azimuths, the order is 2.

Equation (5) is a very strict constraint on the structure of the pseudodifferential class of spatially varying filters, so it should not be a surprise that the behavior of such filters is also highly constrained. Very important in the sequel are the composition properties: if A is a ($n \times n$ matrix) pseudodifferential operator of order μ, B is another of order ν, then

(1) the product (in other words, composition) AB is again a pseudodifferential operator of order $\mu + \nu$, and the symbol of the product differs from the product of the symbols by a symbol of order $\mu + \nu - 1$;

(2) consequently, if $n = 1$ (scalar operators), then the commutator $AB - BA$ is of order $\mu + \nu - 1$.

That is, *to leading order in wavenumber, the product of pseudodifferential operators is simply obtained by multiplying their symbols, and scalar operators commute*. These properties single out pseudodifferential operators amongst general spatially varying filters. Proofs of these and other facts about pseudodifferential operators may be found in Taylor [10], for example.

The theory cited above also showed that the normal operator is "partly invertible", that is, at each point in the subsurface, the Hessian scales spatial Fourier components with a certain range of dips by a *positive* multiple of k^{μ}. It follows from point (2) above that an operator whose symbol is the reciprocal of that of the normal operator for this range of dips, and simply set to zero with suitable tapering outside this range will function as an approximate inverse Hessian. This construction gives an approximate inversion for the single-parameter inverse Hessian (e.g., for constant-density acoustics), illustrates the utility of these very special filters, and is explained briefly in Appendix B, and in more detail in [11, 12].

Multiparameter scattering results in a matrix Hessian, mixing influences between various parameters. In some cases, the Hessian is a matrix of pseudodifferential operators. For example, the Hessian for acoustic scattering or for polarized elastic scattering (P-P, S-S) has this property. Acoustic scattering has only one (p-wave) phase, so it has this property [44], as does elastic scattering with suitably polarized data [43]. The close relation between the matrix $A = (A_{ij})$ of symbols and the normal operator N which it defines again allows us to calculate an approximate inverse via symbol computations.

To this end, recall the definition of the *adjugate*, or classical adjoint, of an $n \times n$ matrix A, denoted by Adj(A): it is the transpose of the matrix of cofactors of A. Explicitly,

$$\mathrm{Adj}(A)_{ij} = (-1)^{i+j} \det M_{ji} \tag{6}$$

in which the $(n-1) \times (n-1)$ minor M_{ij} is obtained from A by dropping the ith row and jth column. The ji cofactor is the number on the right-hand side of (6). In our case, the transpose of the cofactor matrix may be ignored, as the matrix A and thus its adjugate are symmetric (since the Hessian N is symmetric).

The significance of the adjugate is this: when the matrix A is invertible, then the adjugate is proportional to the inverse,

$$A^{-1} := \frac{1}{\det(A)} \mathrm{Adj}(A). \tag{7}$$

This relation is *Cramer's rule* and is the critical observation leading to our approximation method. Note that

$$\mathrm{Adj}(A)A = A\mathrm{Adj}(A) = \det(A)I, \tag{8}$$

where I is the identity matrix. If we define the adjugate of N to be $\mathrm{Adj}(N) = \mathrm{op}(\mathrm{Adj}(A))$ (i.e., the matrix pseudodifferential operator with symbol matrix Adj(A)), with slight abuse of notation, then the multiplicative order properties of pseudodifferential operators described above imply that

$$\mathrm{Adj}(N)N \approx N\mathrm{Adj}(N) \approx \det(N)I. \tag{9}$$

The equation above features another abuse of notation, with $\det(N) := \mathrm{op}(\det(A))$. The power of (8) is revealed when applied to (3)

$$\mathrm{Adj}(N)m_{\mathrm{mig}} = \mathrm{Adj}(N)Nm \approx \det(N)m. \tag{10}$$

Equation (10) reduces the inversion of N to two steps: (i) application of Adj(N), followed by (ii) inversion of the scalar operator det(N), after the application of the adjugate.

Note also that while m_{mig} may be dimensionally heterogeneous, $\mathrm{Adj}(N)m_{\mathrm{mig}}$ has redimensionalized all components so that their units all bear the same relation to the units of the components of m. Inversion of det(N) removes this common unit factor and correctly dimensionalizes the model estimate.

For inversion of det(N), we resort to a method similar to the one we previously developed for $n = 1$ (reviewed in Appendix B). First apply the normal operator again to the left-hand side of (10), to form

$$\begin{aligned} N\mathrm{Adj}(N)m_{\mathrm{mig}} &= N\det(N)m \approx \det(N)Nm \\ &= \det(N)m_{\mathrm{mig}}. \end{aligned} \tag{11}$$

Here, we have used the fact that scalar pseudodifferential operators approximately commute with matrices of pseudodifferential operators to commute N and det(N).

Equation (11) shows how to find a pseudodifferential approximate inverse c to $\det N$, by minimizing an objective function, all parts of which are readily computable

$$\left\| m_{\mathrm{mig}} - cN\mathrm{Adj}(N)m_{\mathrm{mig}} \right\|^2, \tag{12}$$

over a suitable class of pseudodifferential operators c. From (9), a solution c will approximately invert det(N) and is scalar, since det(N) is. Since c removes from the left-hand side of (10) a scalar filter, it plays a similar role to the scaling factors encountered in the various scaling methods mentioned in the introduction, so we will also refer to c as a scaling factor, although it is a pseudodifferential operator.

The reader will recall that N is only partially invertible for a range of model wavevectors k, the symbol determinant det(A) is asymptotic to a positive multiple of $k^{n\mu}$ and to a lower power outside of this "illuminated" cone of model wavenumbers. The method explained in Appendix B constructs c as an approximation to the reciprocal of the symbol of det(N) in the illuminated wavenumber cone, tapered to zero outside of this cone.

The algorithm explained in Appendix B is iterative and requires at least one application of the trial scaling factor c at each iteration. An efficient method for numerical application of pseudodifferential operators is therefore required; we use an algorithm introduced by Bao and Symes [17], which we review in Appendix A.

Having constructed c, we approximate the solution of normal equations by

$$m_{\text{inv}} = c\,\text{Adj}(N)\,m_{\text{mig}}. \tag{13}$$

Equations (12) and (13) show that computation of the adjugate action is key to this approach, so we examine it more carefully. We will address the two parameter cases ($n = 2$) explicitly, both for inspiration and because it is this case for which we present examples in the next section. Writing

$$N = \begin{pmatrix} N_{11} & N_{12} \\ N_{12} & N_{22} \end{pmatrix}, \tag{14}$$

Adj(N) is

$$\begin{gathered} \text{Adj}(N) = \begin{pmatrix} N_{22} & -N_{12} \\ -N_{12} & N_{11} \end{pmatrix}, \\ \text{Adj}(N)m = \begin{pmatrix} N_{22}m_1 & -N_{12}m_2 \\ -N_{12}m_1 & +N_{11}m_2 \end{pmatrix}. \end{gathered} \tag{15}$$

It appears to be necessary to compute the various components of N separately: for example, if the underlying theory is acoustic scattering, then N_{22} might represent input and output density perturbations, and so on, so that each N_{ij} would appear to require a complete modeling/migration cycle.

In fact, it is possible to compute Adj(N)m using *only* applications of N, thus both reducing the cost of the application and eliminating the need to write special component-to-component migration codes. In the 2 × 2 case, only one application of N is required! In fact,

$$\text{Adj}(N) = J^T N J, \tag{16}$$

here, J is the so-called symplectic matrix,

$$J = \begin{pmatrix} 0 & -I \\ I & 0 \end{pmatrix}, \quad \text{so } J\begin{pmatrix} m_1 \\ m_2 \end{pmatrix} = \begin{pmatrix} -m_2 \\ m_1 \end{pmatrix}. \tag{17}$$

Note that units are implicitly changed (as they are in the application of the adjugate operator) and that in practice it is presumed that the discrete representations of the two parameters are the same, so that, for example, density can be swapped for velocity and vice versa.

Equation (16) implies that the application of the adjugate on the migrated image requires one application of N, rather than the four that a naive implementation would suggest. Thus, approximating the inverse for $n = 2$ requires two applications of the normal operator, plus a small amount of additional data manipulation.

The situation is more complicated for $n = 3$, but a similar result holds: it is possible to compute the application of the adjugate using five applications of the normal operator, a considerable improvement over the twenty-four that the naive algorithm based on the definition (6) would appear to require; note that separate application of every component N_{ij} by wave-equation methods is just as expensive as application of the entire operator N. See Nammour [38] for details. We conjecture that a similar drastic reduction is possible for general n.

As a final note, we can show explicitly for $n = 2$ the sense in which equation (9) is an approximation, while equation (8) is exact. Denoting the commutator of two operators by $[a, b] = ab - ba$,

$$\begin{aligned} \text{Adj}(N)N &= \left(N_{22}N_{11} - N_{12}^2\right)\begin{pmatrix} 1 & 0 \\ 0 & 1 \end{pmatrix} \\ &\quad + \begin{pmatrix} 0 & [N_{22}, N_{12}] \\ [N_{11}, N_{12}] & [N_{11}, N_{22}] \end{pmatrix} \\ &= \det(N)I + \begin{pmatrix} 0 & [N_{22}, N_{12}] \\ [N_{11}, N_{12}] & [N_{11}, N_{22}] \end{pmatrix}. \end{aligned} \tag{18}$$

The theory of pseudodifferential operators shows that the commutator of two pseudodifferential operators is of lower order than their composition, that is, relatively negligible for highly oscillatory input fields. Using ≈ to mean "differs by a lower order error",

$$\text{Adj}(N)N \approx N\,\text{Adj}(N) \approx \det(N). \tag{19}$$

3. Numerical Examples: Layered Variable Density Acoustics

As a first application to the two parameter inversion, we construct a variable density acoustics model perturbation consisting of a thin oscillatory velocity layer and a thin oscillatory density layer in a different place (see Figures 1 and 2). The background model is homogeneous with $vp = 2\,\text{km/s}$ and $dn = 2000\,\text{kg/m}^3$. The two thin layers are treated as perturbations.

We simulated reflection data for this model using the IWAVE software developed by The Rice Inversion project in linearized (Born) modeling mode [45]. The model extends around 1.7 km in depth and 6.5 km horizontally. One source is put in the middle, and receivers are laid out to created an offset ranging [−2.7 km, 2.7 km], spaced 20 m apart and 40 m below the (absorbing) surface. The isotropic point source wavelet was a 2.5–5–15–20 Hz trapezoidal zero-phase bandpass filter. 3 seconds of data were recorded at 151 receiver positions. The boundary conditions were absorbing on all sides of the domain, in particular, free surface effects were not modeled. Since the model is layered, only a single source gather need be modeled.

All (reverse-time) migrations were also carried out with IWAVE [46]. The output is a layered model (i.e., two depth traces, one for each velocity and density perturbations), which we shall display as layered fields.

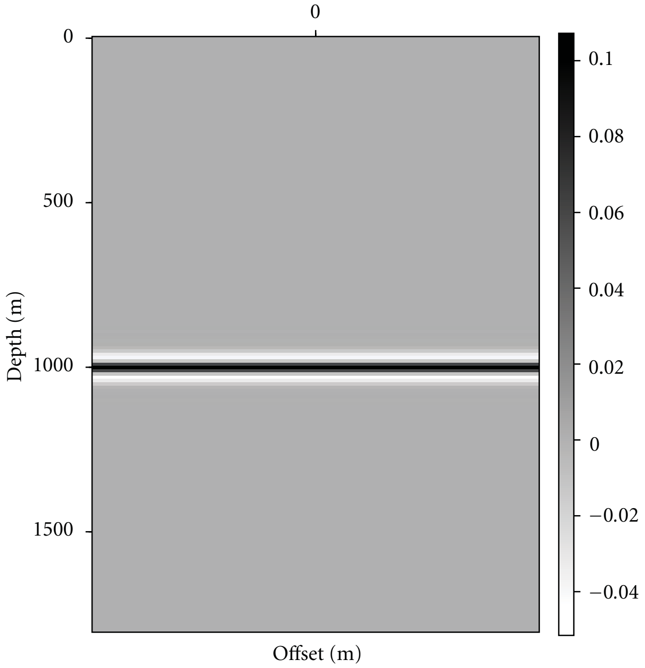

Figure 1: vp, velocity perturbation.

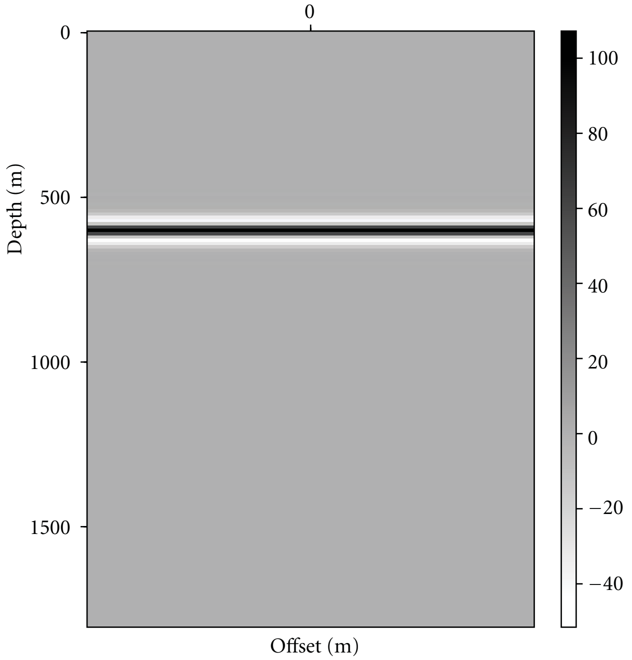

Figure 2: dn, density perturbation.

Migrating the Born data shows how migration mixes the effects of the two models in the two components of the migrated images (Figure 3). We shall refer to the migrated images as m_{mig_1} and m_{mig_2} to remain consistent with our notation where the vector of migrated images is m_{mig}. This example, albeit simple, stresses a new challenge of multiparameter inversion. For one parameter inversion, the events in the migrated image corresponded to events in the true model. In multiparameter inversion, events in the migrated images may correspond to an event in one or more of the components of the model. It is virtually impossible to tell that these migrated images correspond to a model with separate events for velocity and density without successful inversion.

Applying the scheme outlined above, we form

$$J^T N J m_{\mathrm{mig}} \approx \det(N)\ m. \tag{20}$$

The result is shown in Figure 4 and shows how one application of the normal operator effectively separated the contributions of the velocity and density events. It remains to effect an amplitude correction by approximating an inverse to $\det(N)$. For this end, we are required to form $N \det(N) m \approx \det(N) m_{\mathrm{mig}}$, shown in Figure 5.

The final step corrects the amplitudes of $\det(N)m$ by undoing the effect of $\det(N)$, which yields an approximate inverse. This final step complements the separation we obtained earlier with an amplitude correction Figure 6 shows that the approximate inverse compares favorably with true model. An interesting observation on this result is the fact that the velocity model is better recovered than the density model: traces of the velocity event in the density model are more apparent than those of the density event in the velocity model. This observation is in accordance with the theoretical fact that the recovery of velocity in variable density acoustics is better conditioned than the recovery of density. The inversion is successful in that the inverted model succeeds in fitting 70% of the target data (see Figure 7).

4. Discussion and Conclusion

We have presented a method to approximate the solution of the multiparameter linearized inverse problem an extension of Cramer's rule for matrices of pseudodifferential operators. The method consists of two steps:

(1) reducing the multiparameter problem to a one parameter problem, which yields an amplitude scaling of the solution;

(2) correcting the amplitudes of the result from the previous step to approximate the solution.

The application of the work flow to a layered variable density acoustics example shows how the effects of different material parameters, indistinguishable in the migrated images, are separated in the first step. The amplitude correction step successfully yields an approximate solution to the linearized inverse problem.

The work flow presented above applies without modification to any model. Results of application to models more complex than the layered model described above will be presented elsewhere. We point out that other aspects of the physics of seismic data generation will need to be accommodated if this (or any other) algorithm is to extract accurate results from field data. For example, as shown already by Minkoff and Symes [39], even when the Born approximation is adequate, the radiation pattern of the source has a first-order effect on the variation of amplitude

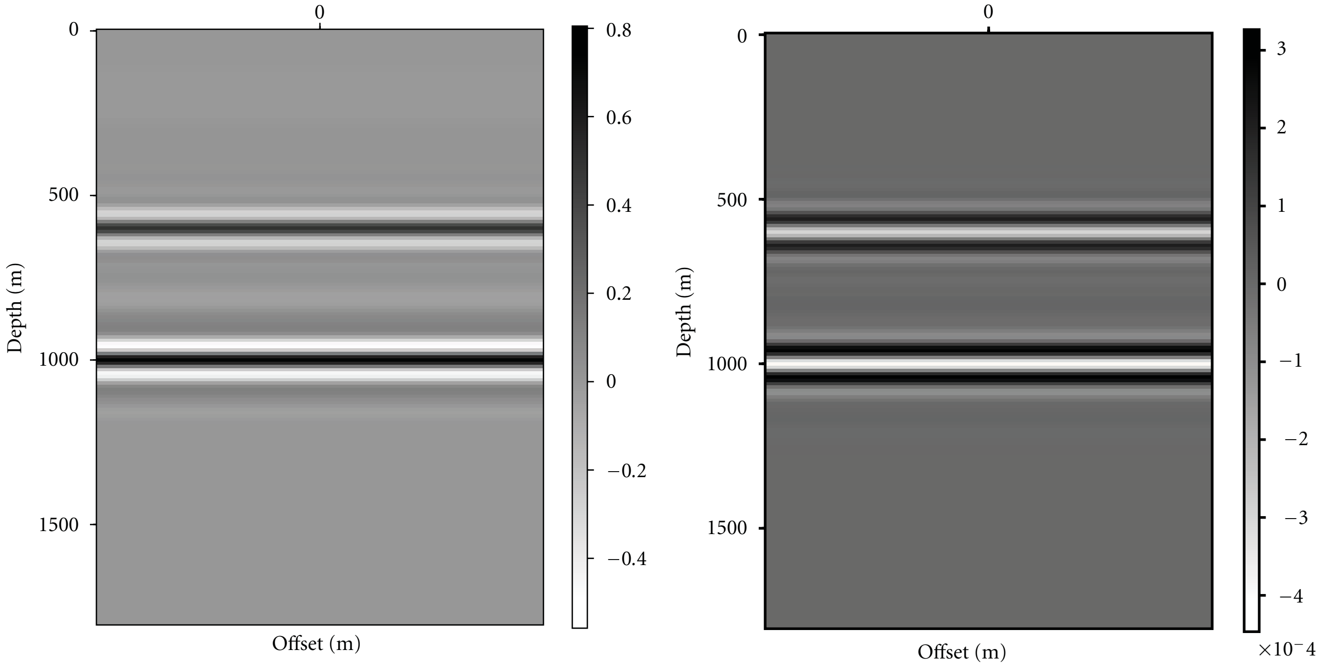

(a) m_{mig_1}, velocity component of the migrated image

(b) m_{mig_2}, density component of the migrated image

Figure 3: Migrated images mixing the contributions from density and velocity, and effecting a phase space scaling.

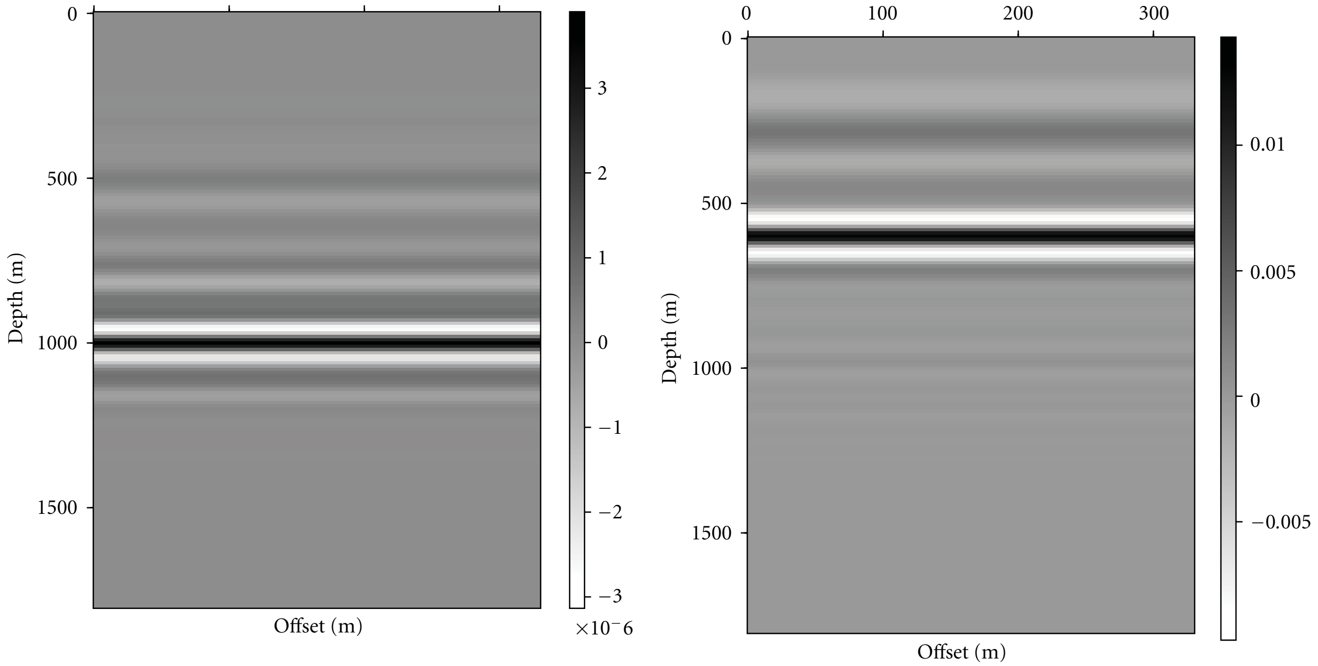

(a) $(J^T N J m_{\mathrm{mig}})_1 \approx \det(N) m_1$

(b) $(J^T N J m_{\mathrm{mig}})_2 \approx \det(N) m_2$

Figure 4: The application of the adjugate separates the velocity and density contributions. This result is a phase space scaling of the true model.

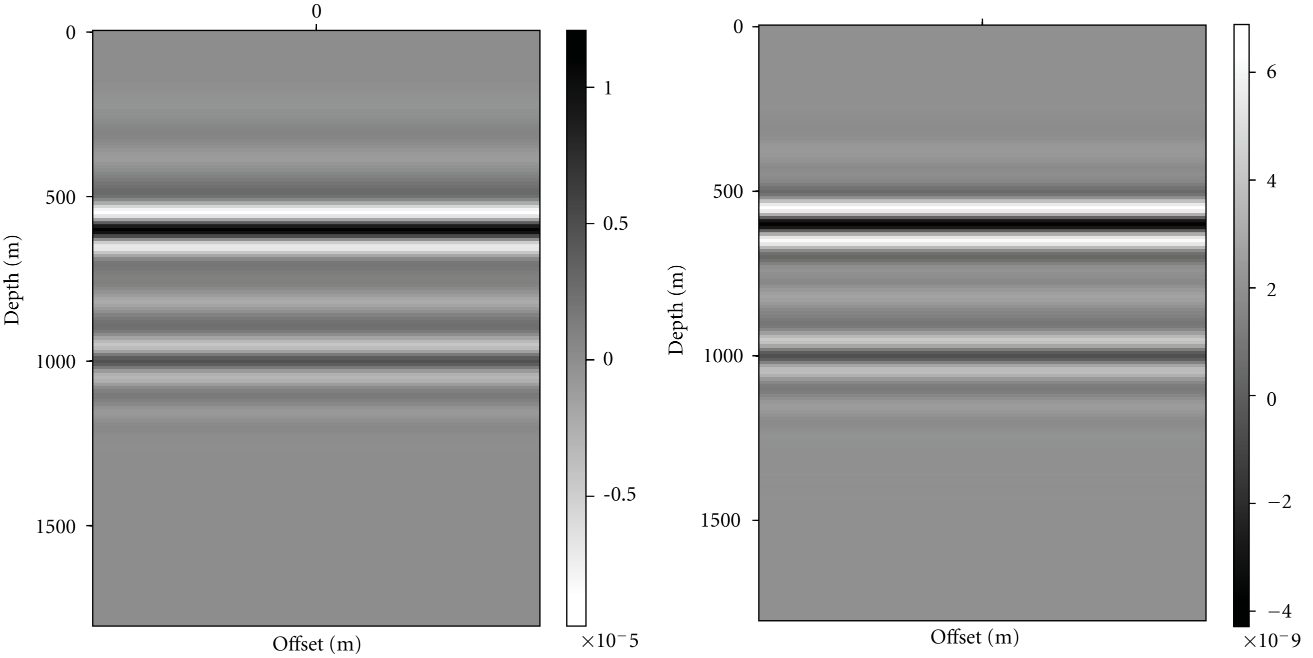

(a) $\det(N)m_{\mathrm{mig}_1}$ (b) $\det(N)m_{\mathrm{mig}_2}$

Figure 5: Scaling of the migrated images by $\det(N)$, used to undo the determinant.

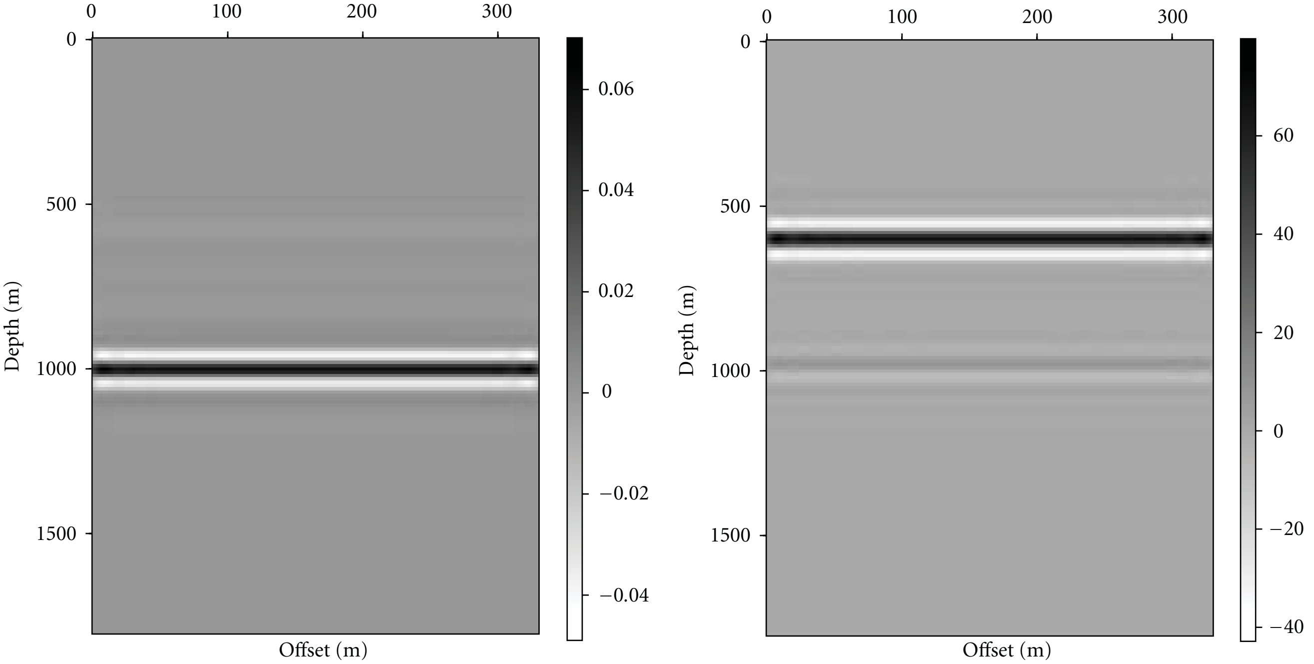

(a) $\mathrm{inv}_{\mathrm{vp}}$ (b) $\mathrm{inv}_{\mathrm{dn}}$

Figure 6: The approximate inverse. The contributions from velocity and density are separated, and the amplitudes are corrected.

with angle and must therefore be included in the parameters to be estimated.

We have extended the Pseudodifferential Operator Algorithm (Appendix A) to three spatial dimensions (3D) which allows approximate inversion of 3D models. The symbol is represented by a truncated spherical harmonics expansion. The formulation of the method in this case remains intact, though the cost of modeling and migration increases. This extension of the method is described in detail, and examples are given in Nammour [38].

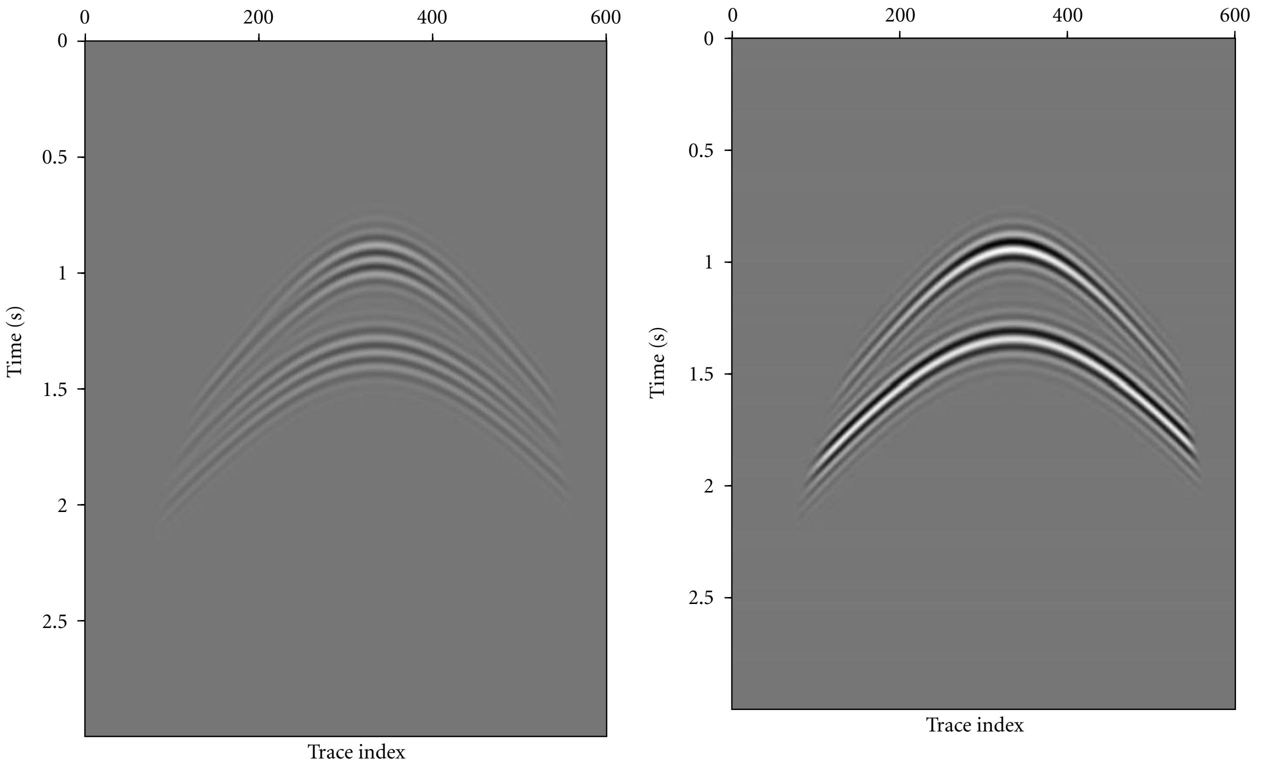

(a) Data misfit

(b) Target Data

Figure 7: Data misfit versus target data. The inverted model fits 70% of the data.

The explicit derivation analogous to $n = 2$ for more parameters (namely $n = 3$) is similar to the one presented here but requires tedious algebraic manipulations. The case $n = 3$ becomes relevant in the linearized inverse problem for linear elasticity, for example. Six applications of the normal operator are required to approximate the solution of the linearized inverse problem. See Nammour [38] for a detailed discussion.

We end by reminding the reader that the approach to approximate inversion pursued here relies on the validity of the pseudodifferential characterization of the Hessian. As mentioned in the theory section, two of the three conditions (background model smooth on the wavelength scale, polarized data) are essential for *any* near-diagonal Hessian approximation, adaptive or not, to be effective. These limitations seem likely to be acceptable in some exploration settings, for example, inversion of marine data for supersalt sediment properties with soft sea floor, but may seriously obstruct this type of technique in other settings.

Appendices

A. The Pseudodifferential Operator Algorithm

Bao and Symes [17] presents an algorithm to numerically apply pseudodifferential operators, which we use to represent the scaling factor c in (12). We will discuss this algorithm in this section as it is central to the feasibility of the method presented here.

This discussion is restricted to 2D, so we may write $\mathbf{x} = (x, z)$. Recall that a pseudodifferential operator is characterized by its symbol and defined by

$$Q_m u(x,z) = \iint q_m(x,z,k_x,k_z)\hat{u}(k_x,k_z)e^{i(xk_x+zk_z)}dk_x\,dk_z, \tag{A.1}$$

where $q_m(x,z,k_x,k_z)$ is the principal symbol, homogeneous of degree m, and $\hat{u} = \mathcal{F}[u]$ is the Fourier transform of u.

Thus, writing $k_x = \omega\cos\theta$, $k_z = \omega\sin\theta$ and using the homogeneity of q_m, we have

$$q_m(x,z,k_x,k_z) = \omega^m\tilde{q}_m(x,z,\theta). \tag{A.2}$$

Notice that $\tilde{q}_m(x,z,\theta) = q_m(x,z,\cos\theta,\sin\theta)$ is periodic and smooth in θ, and hence it admits a rapidly converging Fourier expansion. We thus truncate the Fourier series, approximating the symbol by its first $K+1$ Fourier modes,

$$\tilde{q}_m(x,z,\theta) \approx \sum_{l=-K/2}^{l=K/2} c_l(x,z)e^{il\theta} = \sum_{l=-K/2}^{l=K/2} \omega^{-l}c_l(x,z)(k_x+ik_z)^l. \tag{A.3}$$

Plugging (A.3) into (A.1), we obtain

$$Q_m u(x,z) \approx \sum_{l=-K/2}^{l=K/2} c_l(x,z)\mathcal{F}^{-1}\Big[\omega^{m-l}(k_x+ik_z)^l\hat{u}(k_x,k_z)\Big]. \tag{A.4}$$

Fourier transform theory identifies ω^{m-l} as the symbol of $(-\nabla)^{(m-l)/2}$, and k_x and k_z are, respectively, the symbols of $D_x = -i\partial_x$ and $D_z = -i\partial_z$.

Sampling the field $u(x,z)$ and the symbol $\widetilde{q}_m(x,z,\theta)$,

$$\begin{gathered} U_{ij} = u(x_0 + (i-1)\Delta x, z_0 + (j-1)\Delta z), \\ Q_{ijk} = \widetilde{q}_m(x_0 + (i-1)\Delta x, z_0 + (j-1)\Delta z, k\Delta\theta), \\ i = 1,\dots,M, \quad j = 1,\dots,N, \quad k = -\frac{K}{2},\dots,\frac{K}{2}. \end{gathered} \tag{A.5}$$

Choosing $\Delta k_x = 1/(M-1)\Delta x$ and $\Delta k_z = 1/(N-1)\Delta z$ yields the unaliased discretizations of the symbols of the square root of the negative Laplacian, D_x and D_z

$$\begin{gathered} \Omega_{\text{pr}} = 2\pi\sqrt{(p\Delta k_x)^2 + (r\Delta k_z)^2}, \\ X_{\text{pr}} = 2\pi p\Delta k_x, \\ Z_{\text{pr}} = 2\pi r\Delta k_z, \\ p = -\frac{M}{2},\dots,\frac{M}{2}, \quad r = -\frac{N}{2},\dots,\frac{N}{2}. \end{gathered} \tag{A.6}$$

Equation (A.4) suggests the following algorithm to estimate $Q_m u$ [17]. All Fourier transforms refer to a discrete Fourier transform.

```
(1) Compute $\hat{U}_{\text{pr}} = \mathcal{F}[U_{ij}]$.
(2) For each $i \in [1,M]$ and $j \in [1,N]$, compute $\hat{Q}_{ij} = \{\hat{Q}_{ijl}\}_{l=-K/2}^{K/2}$ the discrete Fourier transform of $Q_{ij} = \{Q_{ijk}\}_{k=-K/2}^{K/2}$.
(3) Initialize $(QU)_{ij} = 0$, for $i \in [1,M]$, $j \in [1,N]$, For $l = -K/2 : K/2$
        (a) compute $\{R_{ij}^l\}_{i=1,j=1}^{M,N} = \mathcal{F}^{-1}[\Omega_{\text{pr}}^{m-l}(X_{\text{pr}} + iZ_{\text{pr}})^l \hat{U}_{\text{pr}}]$ for $p = -M/2,\dots,M/2$ and $r = -N/2,\dots,N/2$,
        (b) accumulate$(QU)_{ij} = (QU)_{ij} + \hat{Q}_{ijl}R_{ij}^l$
    End
```

A straightforward discretization of (A.1) has a computational complexity of $O(N^4\log(N))$. The algorithm described above uses FFT (Fast Fourier Transform) and thus exhibits a complexity of $O(KN^2(\log(N)+\log(K)))$. The appeal of this approach is that K is independent of N. In fact, applications to reflection seismology require that the symbol be smooth and slowly varying in θ, thus, may be captured accurately by a modest number of Fourier modes or, more explicitly, a small K.

The dependence on dip is captured in the angle variable θ, and the method allows us to capture multiple dip events by increasing $K > 1$.

B. The One-Parameter Case

In this appendix, we review the method developed in [11, 12] to construct an approximate inverse Hessian in the one-parameter case. The aim is to solve

$$Nm = m_{\text{mig}}, \tag{B.1}$$

where $m_{\text{mig}} = F^*d \in \text{Range}(N)$. We seek a pseudo differential scaling factor and formulate its recovery as an optimization problem. Given the migrated image m_{mig} and the remigrated image Nm_{mig},

$$c = \operatorname*{argmin}_{c\in\Psi\text{DO}} \left\| m_{\text{mig}} - cNm_{\text{mig}} \right\|^2. \tag{B.2}$$

The scaling factor c is chosen from a class of pseudodifferential operators represented numerically using the PsiDO algorithm (Appendix A). In this setting, the scaling factor approximates the action of the inverse of the normal operator on the migrated image m_{mig}. More specifically,

$$\begin{aligned} m &= N^{-1}m_{\text{mig}} \approx N^{-1}c\, Nm_{\text{mig}} \approx cN^{-1}Nm_{\text{mig}} \\ &= c\, m_{\text{mig}} := m_{\text{inv}}. \end{aligned} \tag{B.3}$$

The first of these equations expresses the true solution m, the second approximate equality follows from because pseudodifferential operators approximately commute. Defining $m_{\text{inv}} := cm_{\text{mig}}$ thus yields an approximation to the true model m. Equation (B.3) shows that the scaling factor approximates the action of the inverse on the normal operator on the migrated image, and it is only in that sense that c approximates N^{-1}.

The scaling factor c is represented explicitly by the PsiDO algorithm,

$$\begin{aligned} &cNm_{\text{mig}}(x,z) \\ &\quad \approx \sum_{l=-K/2}^{l=K/2} c_l(x,z)\mathcal{F}^{-1}\left[\omega^{m-l}(k_x + ik_z)^l \widehat{Nm_{\text{mig}}}(k_x,k_z)\right]. \end{aligned} \tag{B.4}$$

We enforce the continuity of $c_l(x,z)$ using a parsimonious basis technique. Let $\{\psi_j(x,z)\}_{j=1}^J$be a set of smooth shape functions (cubic b-splines, for example). Write

$$c_l(x,z) = \sum_{j=1}^{J} c_l^j \psi_j(x,z), \tag{B.5}$$

and plug into the objective function,

$$\begin{aligned} J &= \left\| m_{\text{mig}} - cNm_{\text{mig}} \right\|^2 \\ &= \sum_{x_i,z_k} \left| m_{\text{mig}}(x_i,z_k) - \left(cNm_{\text{mig}}\right)(x_i,z_k) \right|^2. \end{aligned} \tag{B.6}$$

We have denoted by J the objective function in (B.2), and used the fact that the images m_{mig} and Nm_{mig} are discretized on a grid $\{x_i\}_{i=1}^N$, $\{z_k\}_{k=1}^M$ to write out the norm explicitly.

We use limited memory BFGS (lBFGS) to minimize the objective function (B.2), which requires the gradient to be supplied by the user. The gradient is easily derived as

$$\begin{aligned}\frac{\partial J}{\partial c_j^l} = 2\sum_{x_i,z_k}\Big\{&\Big(m_{\mathrm{mig}}(x_i,z_k) - \Big(cNm_{\mathrm{mig}}\Big)(x_i,z_k)\Big)\psi_j(x_i,z_k)\\ &\times\Big(\mathcal{F}^{-1}\Big[\omega^{m-l}(k_x+ik_z)^l\widehat{Nm_{\mathrm{mig}}}(k_x,k_z)\Big]\Big)\\ &\times\ (x_i,z_k)\Big\}.\end{aligned} \tag{B.7}$$

We have also explored enforcing the positivity of the scaling factor explicitly and other symmetries of the problem, which yields to slightly different representations of the scaling factor c and in turn different objective function gradient. For more details on this point and a discussion about the ability of the method to resolve multiple dip events please consult [12].

Acknowledgments

This work was supported in part by the National Science Foundation under grant DMS 0620821, and by the sponsors of The Rice Inversion Project. The authors are grateful to an anonymous reviewer and to Guest Editor Sergey Fomel for thoughtful critiques.

References

[1] G. Beylkin, "Imaging of discontinuities in the inverse scattering problem by inversion of a causal generalized Radon transform," *Journal of Mathematical Physics*, vol. 26, no. 1, pp. 99–108, 1985.

[2] Rakesh, "A linearized inverse problem for the wave equation," *Communications on Partial Differential Equations*, vol. 13, pp. 573–601, 1988.

[3] G. Beylkin and R. Burridge, "Linearized inverse scattering problems in acoustics and elasticity," *Wave Motion*, vol. 12, no. 1, pp. 15–52, 1990.

[4] C. J. Nolan and W. W. Symes, "Global solution of a linearized inverse problem for the wave equation," *Communications in Partial Differential Equations*, vol. 22, no. 5-6, pp. 919–952, 1997.

[5] M. V. de Hoop and N. Bleistein, "Generalized Radon transform inversions for reflectivity in anisotropic elastic media," *Inverse Problems*, vol. 13, no. 3, pp. 669–690, 1997.

[6] A. P. E. Ten Kroode, D. J. Smit, and A. R. Verdel, "A microlocal analysis of migration," *Wave Motion*, vol. 28, no. 2, pp. 149–172, 1998.

[7] R. Burridge, M. V. de Hoop, D. Miller, and C. Spencer, "Multiparameter inversion in anisotropic elastic media," *Geophysical Journal International*, vol. 134, no. 3, pp. 757–777, 1998.

[8] C. C. Stolk, *On the modeling and inversion of seismic data*, Ph.D. thesis, Universiteit Utrecht, 2000.

[9] S.-K. Foss, B. Ursin, and M. V. de Hoop, "Depth-consistent P- and S-wave velocity reflection tomography using PP and PS seismic data," in *Proceedings of the 53rd SEG Annual International Meeting*, Expanded Abstracts, pp. 2363–2367, Society of Exploration Geophysicists, 2004.

[10] M. Taylor, *Pseudodifferential Operators*, Princeton University Press, 1981.

[11] R. Nammour and W. Symes, "Approximate constant density acoustic inverse scattering using dip-dependent scaling," in *Proceedings of the 80th SEG Annual International Meeting*, Expanded Abstracts SI 3.6, Society of Exploration Geophysicists, 2009.

[12] R. Nammour, "Approximate inverse scattering using pseudodifferential scaling," Tech. Rep. 09-09, Department of Computational and Applied Mathematics, Rice University, Houston, Tex, USA, 2009.

[13] J. F. Claerbout and D. Nichols, "Spectral preconditioning," Tech. Rep. 82, Stanford Exploration Project, Stanford University, Stanford, Calif, USA, 1994.

[14] J. E. Rickett, "Illumination-based normalization for wave-equation depth migration," *Geophysics*, vol. 68, no. 4, pp. 1371–1379, 2003.

[15] A. Guitton, "Amplitude and kinematic corrections of migrated images for nonunitary imaging operators," *Geophysics*, vol. 69, no. 4, pp. 1017–1024, 2004.

[16] W. W. Symes, "Approximate linearized inversion by optimal scaling of prestack depth migration," *Geophysics*, vol. 73, no. 2, pp. R23–R35, 2008.

[17] G. Bao and W. W. Symes, "Computation of pseudo-differential operators," *SIAM Journal on Scientific Computing*, vol. 17, no. 2, pp. 416–429, 1996.

[18] F. J. Herrmann, P. Moghaddam, and C. C. Stolk, "Sparsity- and continuity-promoting seismic image recovery with curvelet frames," *Applied and Computational Harmonic Analysis*, vol. 24, no. 2, pp. 150–173, 2008.

[19] L. Demanet, P. Létourneau, N. Boumal, H. Calandra, J. Chiu, and S. Snelson, "Matrix probing: a randomized preconditioner for the wave-equation Hessian ," 2011, http://math.mit.edu/icg/papers/matrix-probing-seismic.pdf.

[20] C. Shin, S. Jang, and D.-J. Min, "Improved amplitude preservation for prestack depth migration by inverse scattering theory," *Geophysical Prospecting*, vol. 49, no. 5, pp. 592–606, 2001.

[21] U. Jang, D. J. Min, and C. Shin, "Comparison of scaling methods for waveform inversion," *Geophysical Prospecting*, vol. 57, no. 1, pp. 49–59, 2009.

[22] M. F. Sullivan and J. K. Cohen, "Prestack kirchhoff inversion of common-offset data," *Geophysics*, vol. 52, no. 6, pp. 745–754, 1987.

[23] N. Bleistein, "On the imaging of reflectors in the earth," *Geophysics*, vol. 52, no. 7, pp. 931–942, 1987.

[24] M. S. Operto, S. Xu, and G. Lambare, "Can we quantitatively image complex structures with rays?" *Geophysics*, vol. 65, no. 4, pp. 1223–1238, 2000.

[25] S.-K. Foss, M. V. de Hoop, and B. Ursin, "Linearized 2.5-dimensional parameter imaging inversion in anisotropic ela-stic media," *Geophysical Journal International*, vol. 161, no. 3, pp. 722–738, 2005.

[26] J. Yu, J. Hu, G. T. Schuster, and R. Estill, "Prestack migration deconvolution," *Geophysics*, vol. 71, no. 2, pp. S53–S62, 2006.

[27] G. Chavent and R.-E. Plessix, "An optimal true-amplitude least-squares prestack depth-migration operator," *Geophysics*, vol. 64, no. 2, pp. 508–515, 1999.

[28] A. A. Valenciano, B. Biondi, and A. Guitton, "Target-oriented wave-equation inversion," *Geophysics*, vol. 71, no. 4, pp. A35–A38, 2006.

[29] K. Aki and P. Richards, *Quantitative Seismology: Theory and Methods*, Freeman, 1980.

[30] R. T. Shuey, "Simplification of the zoeppritz equations," *Geophysics*, vol. 50, no. 4, pp. 609–614, 1985.

[31] F. Hilterman, *Seismic Amplitude Interpretation*, Society of Exploration Geophysicists, 2001.

[32] O. Gauthier, A. Tarantola, and J. Virieux, “Two-dimensional nonlinear inversion of seismic waveforms: numerical results,” *Geophysics*, vol. 51, no. 7, pp. 1387–1403, 1986.

[33] A. Bourgeois, B. F. Jiang, and P. Lailly, “Linearized inversion: a significant step beyond pre-stack migration,” *Geophysical Journal International*, vol. 99, no. 2, pp. 435–445, 1989.

[34] S. Jin, R. Madariaga, J. Virieux, and G. Lambare, “Two-dimensional asymptotic interative elastic inversion,” *Geophysical Journal International*, vol. 108, no. 2, pp. 575–588, 1992.

[35] J. Yu, J. Hu, and M. V. de Hoop, “Prestack migration deconvolution+AVO inversion,” in *Proceedings of the 73rd SEG Annual International Meeting*, Expanded Abstracts, pp. 1051–1054, Society of Exploration Geophysicists, 2003.

[36] F. Santosa and W. W. Symes, “High-frequency perturbational analysis of the surface point-source response of a layered fluid,” *Journal of Computational Physics*, vol. 74, no. 2, pp. 318–381, 1988.

[37] G. J. M. Lörtzer and A. J. Berkhout, “Linear avo inversion of multicomponent seismic data,” vol. 8, pp. 967–972, 1989, SEG Technical Program Expanded Abstracts.

[38] R. Nammour, “Approximate multi-parameter inverse scattering using pseudodifferential scaling,” Tech. Rep. 11-05, Department of Computational and Applied Mathematics, Rice University, Houston, Tex, USA, 2011.

[39] S. E. Minkoff and W. W. Symes, “Full waveform inversion of marine reflection data in the plane-wave domain,” *Geophysics*, vol. 62, no. 2, pp. 540–553, 1997.

[40] M. Charara, C. Barnes, and A. Tarantola, “Constrained waveform inversionof seismic well data,” in *Inverse Methods*, B. Jacobsen, K. Mosegaard, and P. Sibani, Eds., vol. 63 of *Lecture Notes in Earth Sciences*, pp. 98–112, Springer, Heidelberg, Germany, 1996.

[41] M. Charara and C. Barnes, “Nonlinear inversion of seismic waveforms: a NorthSea offset VSP example,” in *Proceedings of the 81st Annual International Meeting of Expanded Abstracts*, pp. 3966–3970, Society of Exploration Geophysicists, 2010.

[42] C. C. Stolk, “Microlocal analysis of a seismic linearized inverse problem,” *Wave Motion*, vol. 32, no. 3, pp. 267–290, 2000.

[43] C. C. Stolk and M. V. de Hoop, “Microlocal analysis of seismic inverse scattering in anisotropic elastic media,” *Communications on Pure and Applied Mathematics*, vol. 55, no. 3, pp. 261–301, 2002.

[44] W. Symes, “Mathematics of reflection seismology,” 1998, http://www.trip.caam.rice.edu .

[45] D. Sun and W. W. Symes, “IWAVE implementation of Born simulation,” Tech. Rep. 10-05, Department of Computational and Applied Mathematics, Rice University, Houston, Tex, USA, 2010.

[46] D. Sun and W. W. Symes, “IWAVE implementation of adjoint state method,” Tech. Rep. 10-06, Department of Computational and Applied Mathematics, Rice University, Houston, Tex, USA, 2010.

Hindawi Publishing Corporation
International Journal of Geophysics
Volume 2011, Article ID 714781, 12 pages
doi:10.1155/2011/714781

Research Article

A Comparison of Splitting Techniques for 3D Complex Padé Fourier Finite Difference Migration

Jessé C. Costa,[1,2] Débora Mondini,[3] Jörg Schleicher,[2,3] and Amélia Novais[2,3]

[1] *Faculty of Geophysics, Federal University of Pará, 66075-110 Belém, PA, Brazil*
[2] *DMA/IMECC, University of Campinas, 13083-859 Campinas, SP, Brazil*
[3] *National Institute of Petroleum Geophysics (INCT-GP), Brazil*

Correspondence should be addressed to Jörg Schleicher, js@ime.unicamp.br

Received 24 January 2011; Accepted 9 May 2011

Academic Editor: Yu Zhang

Three-dimensional wave-equation migration techniques are still quite expensive because of the huge matrices that need to be inverted. Several techniques have been proposed to reduce this cost by splitting the full 3D problem into a sequence of 2D problems. We compare the performance of splitting techniques for stable 3D Fourier finite-difference (FFD) migration techniques in terms of image quality and computational cost. The FFD methods are complex Padé FFD and FFD plus interpolation, and the compared splitting techniques are two- and four-way splitting as well as alternating four-way splitting, that is, splitting into the coordinate directions at one depth and the diagonal directions at the next depth level. From numerical examples in homogeneous and inhomogeneous media, we conclude that, though theoretically less accurate, alternate four-way splitting yields results of comparable quality as full four-way splitting at the cost of two-way splitting.

1. Introduction

Because of its superiority in areas of complex geology, wave-equation migration is substituting Kirchhoff migration in practice. However, while Kirchhoff migration counts on more than 30 years of technological development, wave-equation migration methods still need to be improved in various aspects. One of these aspects is the efficient implementation of three-dimensional wave-equation migration.

The application of a three-dimensional wave-equation migration technique adds the problem of computational cost to those of stability and precision of the chosen migration algorithm. To speed up migration techniques like finite-difference (FD) [1] or Fourier finite-difference (FFD) migration [2], a technique known as splitting is frequently used. In this context, splitting means the separation of a single-step 3D migration into two 2D passes within planes parallel to the horizontal coordinate axes, usually the inline and crossline directions [3].

When the splitting is applied to the implicit FD migration operator in such a way that the resulting equations are solved alternatingly in the inline and crossline directions, the resulting FD scheme is known as an alternating-direction-implicit (ADI) scheme. This procedure has the drawback of being incorrect for strongly dipping reflectors, resulting in large positioning errors for this type of reflectors when the dip direction is away from the coordinate directions and thus outside the migration planes. This imprecision leads to numerical anisotropy, that is, a migration operator that acts quite differently in different directions.

To improve this behaviour while retaining the advantages of a rather low computation cost, different procedures have been proposed over the years. Ristow ([4], see also [5]) proposed to perform, in addition to the 2D migration in the coordinate planes, also 2D migrations in the diagonal directions between the coordinate axes. Kitchenside [6] used phase-shift migration plus an additional FD propagation step of the residual field to reduce the splitting error. Graves and Clayton [7] proposed the implementation of a phase-correction operator using FD and incorporating a damping function to guarantee the stability of the 3D FD migration scheme.

Inverting the idea of Kitchenside [6], who propagated the field using phase shift and the residual using FD, Li [8] proposed to use conventional FD migration plus a residual field correction by phase shift to improve the migrated image quality. Without any need to modify the conventional 3D FD migration, the Li correction adds a phase-shift filter at certain steps of the downward extrapolation. This technique corrects not only for the splitting error but also for the positioning error of steeply dipping reflectors.

Collino and Joly [9] solved a family of new 3D one-way wave equations by the ADI method. These equations significantly reduce the numerical anisotropy, but are approximately four times as expensive as conventional two-way splitting. Wang [10] developed an alternative method to improve the precision of the FD solution of the one-way wave equation. To guarantee stability and efficiency, he keeps the implicit FD scheme and the alternation of directions, but interpolates between the ADI solution and the wavefield before each step of extrapolation. He calls the resulting method ADI plus interpolation (ADIPI). As a drawback, this ADIPI can produce instabilities in the presence of strong lateral velocity variations.

Zhou and McMechan [11] proposed a 45° one-way wave equation that can be expressed as a system of differential equations of first and second order [12] and factored into a product of two one-dimensional terms corresponding to the lateral directions [7, 13]. A big asset of the method is that the conventional FD extrapolation can be used with very little modification. In this way, the efficiency of conventional splitting is preserved, without adding the necessity of any error compensation. However, the method is also instable for strong lateral velocity contrasts and needs rather heavy model smoothing.

Biondi [14] showed that FFD migration is more precise than other methods that use implicit finite differences like pseudoscreen propagators [15] and high-angle screen propagators [16]. Given that the computational complexity of all three methods is approximately the same, FFD migration is more attractive than the others. Unfortunately, when conventional FFD migration is applied in the presence of strong velocity contrasts, it can generate numerical instabilities, too.

To overcome the problem of instabilities in models with strong lateral velocity contrasts, Biondi [14] presented a correction to the FFD method that avoids stability problems. To derive it, he adapted a theory of Godfrey et al. [17] and Brown [18], which improves the stability of the 45° equation. The corrected FFD method is unconditionally stable for arbitrary velocity variations, as much in the velocity model as in the reference velocity. Particularly, and differently from conventional FFD migration, it is unconditionally stable even if the reference velocity is smaller than the model velocity. This new property allows for the application of the interpolation technique, conventionally used to improve phase-shift and split-step migration [19] but impossible in FFD migration, because it needs propagation with a larger and a smaller reference velocity. The resulting migration technique is called FFD plus interpolation, or shortly FFDPI.

Another computationally less expensive method to stabilize FFD migration in the presence of strong lateral velocity contrasts was proposed by Amazonas et al. [20]. It substitutes the real Padé approximation [21] used in the derivation of FFD migration [2] by its complex version [22]. In this way, the incorrect treatment of near horizontal and slightly evanescent waves of the real Páde approximation is improved, leading to a more stable FFD algorithm, shortly referred to as complex Padé FFD (CPFFD) migration.

In this work, we study possibilities of efficiently implementing these stable FFD migration techniques in 3D. We implemented and compared splitting techniques for FFDPI [14] and CPFFD [20] migration. Our numerical tests indicate that a very robust, highly efficient, and satisfactorily accurate method is alternate four-way splitting, that is, splitting into the coordinate directions at one extrapolation step and into the diagonal directions at the next step.

2. Theoretical Background

2.1. The One-Way Wave Equation. The one-way wave equation [23] can be derived starting from the scalar wave equation, which for a homogeneous medium is given by

$$\frac{\partial^2 p(\mathbf{x},t)}{\partial z^2}+\frac{\partial^2 p(\mathbf{x},t)}{\partial x^2}+\frac{\partial^2 p(\mathbf{x},t)}{\partial y^2}-\frac{1}{c^2}\frac{\partial^2 p(\mathbf{x},t)}{\partial t^2}=0, \quad (1)$$

where $p(\mathbf{x},t)$ is the scalar wavefield and $c = c(\mathbf{x})$ is the spatially varying wave velocity. For moderately varying media, where velocity derivatives can be neglected, Fourier transform in time and horizontal coordinates x and y allows to represent (1) as

$$\begin{aligned}&\frac{\partial^2 P\left(k_x,k_y,z,\omega\right)}{\partial z^2}-\frac{(-i\omega)^2}{c^2}\left(1-\frac{c^2}{\omega^2}\left(k_x^2+k_y^2\right)\right)\\&\quad\times P\left(k_x,k_y,z,\omega\right)=0.\end{aligned} \quad (2)$$

Equation (2) can be factorized into

$$\begin{aligned}&\left[\frac{\partial}{\partial z}-\frac{(-i\omega)}{c}\sqrt{1-\frac{c^2}{\omega^2}\left(k_x^2+k_y^2\right)}\right]\\&\quad\times\left[\frac{\partial}{\partial z}+\frac{(-i\omega)}{c}\sqrt{1-\frac{c^2}{\omega^2}\left(k_x^2+k_y^2\right)}\right]\\&\quad\times P\left(k_x,k_y,z,\omega\right)=0.\end{aligned} \quad (3)$$

The two differential operators in (3) represent, when taken alone, one-way wave equations that describe up- and downgoing waves. For migration, the one-way wave equation of interest is the one describing downgoing waves, that is,

$$\frac{\partial P\left(k_x,k_y,z,\omega\right)}{\partial z}=\frac{(-i\omega)}{c}\sqrt{1-\frac{c^2}{\omega^2}\left(k_x^2+k_y^2\right)}P\left(k_x,k_y,z,,\omega\right). \quad (4)$$

Inverse Fourier transform in the horizontal wavenumbers k_x and k_y yields then formally

$$\frac{\partial P(\mathbf{x},\omega)}{\partial z}=\frac{(-i\omega)}{c(\mathbf{x})}\sqrt{1+\frac{c^2(\mathbf{x})}{\omega^2}\left(\frac{\partial^2}{\partial x^2}+\frac{\partial^2}{\partial y^2}\right)}P(\mathbf{x},\omega). \quad (5)$$

The actual restrictions that apply to (5) in inhomogeneous media are much less severe than the above derivation indicates. Of course, for the formal representation (5) to make practical sense, the square root of the differential operator needs to be approximated in terms of numerically executable operations.

2.2. Expansion of the Square Root. A well-used possibility for the approximation of the square root in the one-way wave equation (5) in terms of numerically executable operations is an expansion into a Padé series [21]:

$$\sqrt{1+Z} \approx 1 + \sum_{n=1}^{N} \frac{a_n Z}{1 + b_n Z}, \tag{6}$$

where the Padé coefficients are

$$a_n = \frac{2}{2N+1} \sin^2\left(\frac{n\pi}{2N+1}\right), \qquad b_n = \cos^2\left(\frac{n\pi}{2N+1}\right). \tag{7}$$

This approximation is used in most practical FD migration schemes. Depending on the number N of terms used in the expansion, it gives rise to the so-called 15°, 45°, or 60° migrations.

However, when the interest is on accurate imaging up to very high propagation angles, approximation (6) has a drawback, because its validity is limited to $Z > -1$. For $Z < -1$, the approximation breaks down abruptly, because the left side of (6) is imaginary, while its right side remains real. Thus, for propagation angles close to 90°, where the argument Z of (6) becomes close to -1, (6) becomes invalid, which causes instabilities when using the real approximation (6) for migration in models with strong lateral velocity contrasts.

To overcome this problem, Milinazzo et al. [22] proposed to rotate the branch cut of the complex plane before application of the Padé approximation. Denoting the rotation angle by α, the representation of the square root is

$$\sqrt{1+Z} = e^{i\alpha/2}\sqrt{(1+Z)e^{-i\alpha}} = e^{i\alpha/2}\sqrt{1 + [(1+Z)e^{-i\alpha} - 1]}, \tag{8}$$

which, after expansion into a Padé series according to (6), yields

$$\sqrt{1+Z} = C_0 + \sum_{n=1}^{N} \frac{A_n Z}{1 + B_n Z}, \tag{9}$$

where the complex Padé coefficients are given by

$$A_n \equiv \frac{a_n e^{-i\alpha/2}}{\left[1 + b_n\left(e^{-i\alpha} - 1\right)\right]^2}, \qquad B_n \equiv \frac{b_n e^{-i\alpha}}{1 + b_n\left(e^{-i\alpha} - 1\right)}, \tag{10}$$

$$C_0 \equiv e^{i\alpha/2}\left\{1 + \sum_{n=1}^{N} \frac{a_n\left(e^{-i\alpha} - 1\right)}{\left[1 + b_n\left(e^{-i\alpha} - 1\right)\right]}\right\}. \tag{11}$$

Note that, in (11), C_0 is an approximation to one. This approximation gets better the more terms N are used in the sum. However, for a finite number of terms N, this approximation is always imperfect. Therefore, it is more practical to directly use $C_0 = 1$. We will use this value for C_0 in the following derivations.

2.3. Fourier Finite Difference Migration. The complex Padé approximation (9) allows more stable implementations of not only FD but also FFD migration [20]. The derivation of 3D complex Padé FFD (CPFFD) migration is very similar to the original derivation of Ristow and Rühl [2]. It starts from the difference between the square root of (5) and a corresponding one where the velocity has been replaced by a constant reference velocity c_r, namely,

$$\begin{aligned} &\frac{i\omega}{c(\mathbf{x})}\sqrt{1 + \left(\frac{c(\mathbf{x})}{\omega}\right)^2\left(\frac{\partial^2}{\partial x^2} + \frac{\partial^2}{\partial y^2}\right)} \\ &\quad - \frac{i\omega}{c_r}\sqrt{1 + \left(\frac{c_r}{\omega}\right)^2\left(\frac{\partial^2}{\partial x^2} + \frac{\partial^2}{\partial y^2}\right)}. \end{aligned} \tag{12}$$

Expanding both square roots in (12) in complex Padé series according to (9), we find

$$\begin{aligned} &ik_0\left\{p\sqrt{1+X^2} - \sqrt{1+p^2X^2}\right\} \\ &\quad \approx ik_0\left\{p\left[1 + \sum_{n=1}^{N}\frac{A_nX^2}{1+B_nX^2}\right] - \left[1 + \sum_{n=1}^{N}\frac{A_np^2X^2}{1+B_np^2X^2}\right]\right\}, \end{aligned} \tag{13}$$

where we have used the notations

$$k_0 \equiv \frac{\omega}{c_r}, \qquad p \equiv \frac{c_r}{c(\mathbf{x})}, \qquad X^2 \equiv \left(\frac{c(\mathbf{x})}{\omega}\right)^2\left(\frac{\partial^2}{\partial x^2} + \frac{\partial^2}{\partial y^2}\right). \tag{14}$$

Joining the two series into one, expanding the fractions into Taylor series, and grouping the terms of equal power leads to

$$\begin{aligned} &ik_0\left\{p\sqrt{1+X^2} - \sqrt{1+p^2X^2}\right\} \\ &\approx ik_0\left\{p - 1 + \left[\sum_{n=1}^{N} A_n p(1-p)X^2\left(1 - B_n\frac{(1-p^3)}{1-p}X^2\right.\right.\right. \\ &\qquad \left.\left.\left. + B_n^2\frac{(1-p^5)}{1-p}X^4 - B_n^3\frac{(1-p^7)}{1-p}X^6 + \cdots\right)\right]\right\}. \end{aligned} \tag{15}$$

Since

$$\frac{1-p^{n+1}}{1-p} = 1 + p + p^2 + \cdots + p^n, \tag{16}$$

this expression is, up to second order, equivalent to a Taylor series expansion of a Padé expression of the form

$$\begin{aligned} &ik_0\left\{p\sqrt{1+X^2} - \sqrt{1+p^2X^2}\right\} \\ &\quad \approx ik_0\left\{(p-1) + \sum_{n=1}^{N}\frac{A_np(1-p)X^2}{1+\sigma B_nX^2}\right\}, \end{aligned} \tag{17}$$

where $\sigma = 1 + p + p^2$.

Using this approximation, the one-way wave equation (5) can be represented as

$$\frac{dP}{dz} = \left\{ -ik_0\sqrt{1+p^2X^2} - ik_0\left[(p-1) + \sum_{n=1}^{N}\frac{A_n p(1-p)X^2}{1+B_n\sigma X^2}\right]\right\}P, \tag{18}$$

which is the complex Padé equivalent to standard FFD migration [2].

As seen above, the theoretical value of σ obtained from this expansion is $\sigma = 1 + p + p^2$. However, 2D numerical experiments of Amazonas et al. [20] indicate that other expressions for σ can produce better results. For small contrasts, they suggest $\sigma = 3p$ and, for high fidelity up to high propagation angles, they propose $\sigma = 1 + p^3$.

2.4. Implementation. To solve (18), we separate it into a set of differential equations. The first two terms provide the equations

$$\begin{aligned}\frac{dP}{dz} &= -ik_0\sqrt{1+p^2X^2}P,\\ \frac{dP}{dz} &= -ik_0(p-1)P,\end{aligned} \tag{19}$$

the analytic solutions of which are

$$\begin{aligned}P(x,z+\Delta z,\omega) &= e^{-ik_0\sqrt{1+p^2X^2}\Delta z}P(x,z,\omega),\\ P(x,z+\Delta z,\omega) &= e^{-ik_0\Delta z(p-1)}P(x,z,\omega).\end{aligned} \tag{20}$$

The remaining terms of (18) from the Padé series are represented by differential equations:

$$\frac{dP}{dz} = -ik_0\frac{A_n p(1-p)X^2}{1+B_n\sigma X^2}P, \quad (n = 1,\ldots,N). \tag{21}$$

Discretizing these differential equations using a Crank-Nicolson FD scheme, we obtain

$$\frac{P^{j+1}-P^j}{\Delta z} = -ik_0\frac{A_n p(1-p)X^2}{1+B_n\sigma X^2}\frac{P^{j+1}+P^j}{2}, \tag{22}$$

where $P^j = P(\mathbf{r}, z_j, \omega)$. Equation (22) means that the following implicit equation needs to be solved:

$$\begin{aligned}&\left\{1+\left[B_n\sigma + i\frac{k_0\Delta z}{2}A_n p(1-p)\right]X^2\right\}P^{j+1}\\ &\quad= \left\{1+\left[B_n\sigma - i\frac{k_0\Delta z}{2}A_n p(1-p)\right]X^2\right\}P^j.\end{aligned} \tag{23}$$

We still need to discretize of the derivatives in the horizontal coordinates, that is, replace the differential operator X^2 by its difference operator

$$X^2 \approx \mathbf{X}^2 = \frac{c^2(x_k,y_l,z_j)}{\omega^2}\left(\frac{\mathbf{D}_x^2}{\Delta x^2}+\frac{\mathbf{D}_y^2}{\Delta y^2}\right), \tag{24}$$

where the matrices $\mathbf{D}_x^2$ and $\mathbf{D}_y^2$ represent difference operators for the second derivatives in x and y. For simplicity, we choose second-order difference operators, that is,

$$\begin{aligned}\mathbf{D}_x^2P_{k,l}^j &= P_{k+1,l}^j - 2P_{k,l}^j + P_{k-1,l}^j,\\ \mathbf{D}_y^2P_{k,l}^j &= P_{k,l+1}^j - 2P_{k,l}^j + P_{k,l-1}^j,\end{aligned} \tag{25}$$

for $k = 1,\ldots,n_x$ and $l = 1,\ldots,n_y$ with n_x and n_y denoting the number of grid points in the x and y directions. The resulting difference equation equivalent to differential equation (21) reads

$$\left[\mathbf{I}+\mathbf{C}_n\left(\frac{\mathbf{D}_x^2}{\Delta x^2}+\frac{\mathbf{D}_y^2}{\Delta y^2}\right)\right]\mathbf{P}^{j+1} = \left[\mathbf{I}+\mathbf{C}_n^*\left(\frac{\mathbf{D}_x^2}{\Delta x^2}+\frac{\mathbf{D}_y^2}{\Delta y^2}\right)\right]\mathbf{P}^j, \tag{26}$$

where $\mathbf{I}$ is the identity matrix and $\mathbf{P}^j$ is the matrix formed by the elements $P_{k,l}^j$ at a fixed depth level z_j. Moreover, $\mathbf{C}_n$ is the complex matrix with elements

$$(\mathbf{C}_n)_{k,l} = \frac{c^2}{\omega^2}\left[B_n\sigma + i\frac{k_0\Delta z}{2}A_n p(1-p)\right], \tag{27}$$

with $c = c(x_k,y_l,z_j)$, $\sigma = \sigma(x_k,y_l,z_j)$, and $p = p(x_k,y_l,z_j)$, and $\mathbf{C}_n^*$ denotes the matrix obtained when replacing i by $-i$ in (27).

2.5. Two-Way Splitting. In the technique called two-way splitting, also known as alternating-directions-implicit (ADI) method [13, 24, 25], one substitutes (26) by its approximate factorized form

$$\begin{aligned}&\left(\mathbf{I}+\mathbf{C}_n\frac{\mathbf{D}_x^2}{\Delta x^2}\right)\left(\mathbf{I}+\mathbf{C}_n\frac{\mathbf{D}_y^2}{\Delta y^2}\right)\mathbf{P}^{j+1}\\ &\quad= \left(\mathbf{I}+\mathbf{C}_n^*\frac{\mathbf{D}_x^2}{\Delta x^2}\right)\left(\mathbf{I}+\mathbf{C}_n^*\frac{\mathbf{D}_y^2}{\Delta y^2}\right)\mathbf{P}^j.\end{aligned} \tag{28}$$

This equation has the advantage of being solvable in two 2D steps. Under the assumption that the inverse operator in y, $(\mathbf{I}+\mathbf{C}_n\mathbf{D}_y^2/\Delta y^2)^{-1}$, commutes with both operators in x, equation (28) can be rewritten as

$$\left(\mathbf{I}+\mathbf{C}_n\frac{\mathbf{D}_x^2}{\Delta x^2}\right)\mathbf{P}^{j+1} = \left(\mathbf{I}+\mathbf{C}_n^*\frac{\mathbf{D}_x^2}{\Delta x^2}\right)\widetilde{\mathbf{P}}^j, \tag{29}$$

where the intermediate value $\widetilde{\mathbf{P}}^j$, defined as

$$\widetilde{\mathbf{P}}^j = \left(\mathbf{I}+\mathbf{C}_n\frac{\mathbf{D}_y^2}{\Delta y^2}\right)^{-1}\left(\mathbf{I}+\mathbf{C}_n^*\frac{\mathbf{D}_y^2}{\Delta y^2}\right)\mathbf{P}^j \quad , \tag{30}$$

can be found solving the system

$$\left(\mathbf{I}+\mathbf{C}_n\frac{\mathbf{D}_y^2}{\Delta y^2}\right)\widetilde{\mathbf{P}}^j = \left(\mathbf{I}+\mathbf{C}_n^*\frac{\mathbf{D}_y^2}{\Delta y^2}\right)\mathbf{P}^j. \tag{31}$$

The advantage of splitting is in the computational cost. While the numerical solution of (26) requires the solution of a

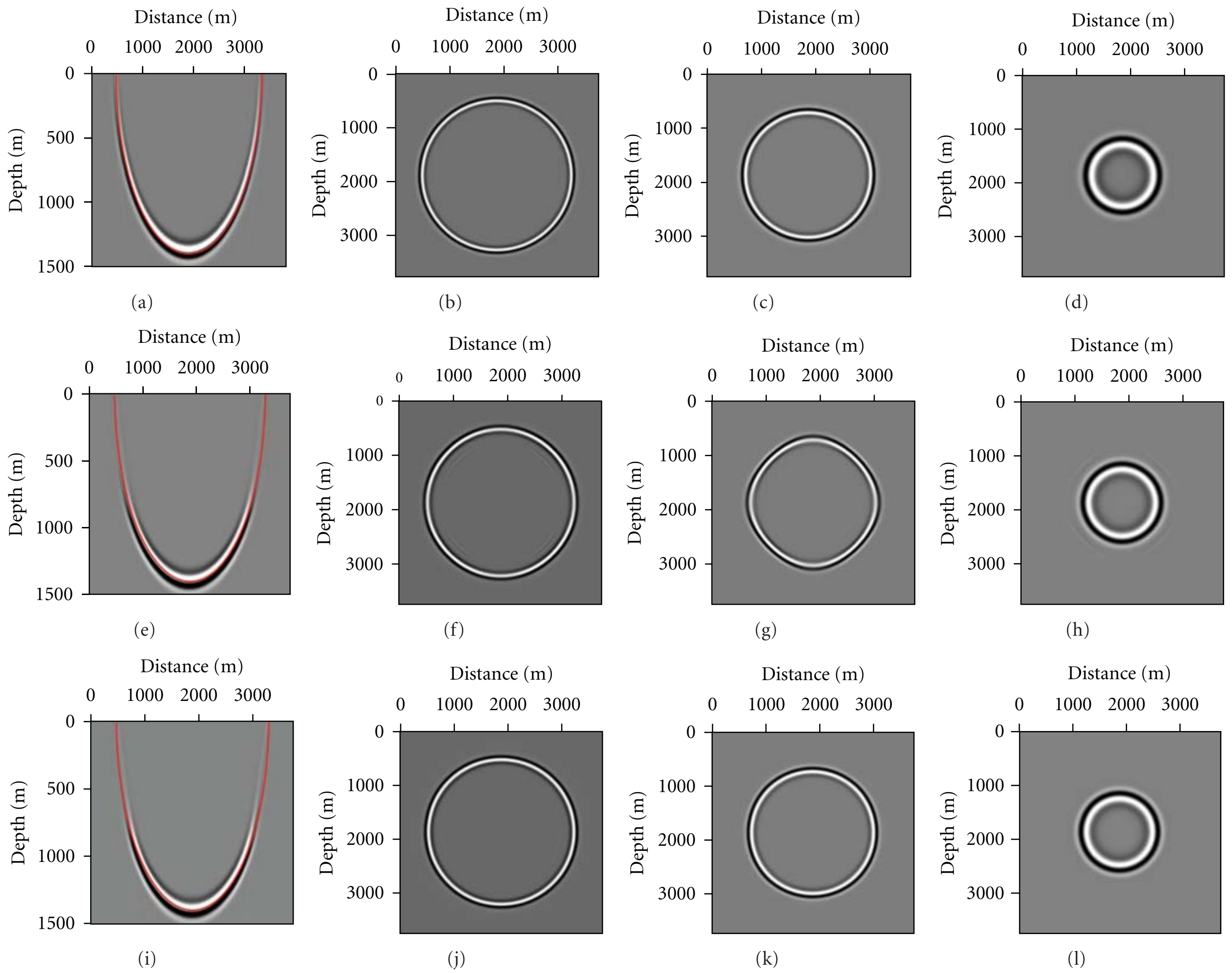

Figure 1: Migration impulse responses. (a)–(d): reference result by phase-shift migration using the true medium velocity. (e)–(h): FFD migration using conventional two-way splitting; $p = 0.75$. (i)–(l): FFD migration using conventional four-way splitting; $p = 0.75$. From left to right: central vertical cut in the x-z plane and horizontal cuts at 150 m, 750 m, and 1250 m depth.

system of size $n_x \times n_y$, the cascaded solution of (31) and (29) demands only the solution of n_x systems of size n_y, followed by n_y systems of size n_x. Since all these systems are tridiagonal, there are very efficient ways to solve them, which makes the splitting technique orders of magnitude faster than the solution of the original 3D system.

On the other hand, this procedure also has disadvantages. The biggest one is the introduction of numerical anisotropy into the propagation of the wavefield, because the numerical error increases with the azimuth between the propagation direction and the coordinate directions. This degrades the migrated image, introducing errors in the positioning of steeply dipping reflectors.

2.6. Splitting in More Directions. To overcome the problems with numerical anisotropy, Ristow and Rühl [5] proposed to generalize the technique to splitting into more than two directions. The idea is to approximate the 3D square-root operator by a sequence of 2D operators in different directions. In practice, most uses rely on three, four, or six directions to avoid symmetry problems. The unknown coefficients of these 2D operators are obtained from Taylor series expansions or by optimization techniques.

The multiway splitting form of the 2D Padé operators is given by the complex Padé expansion of the square-root operator in (5) for multiple directions:

$$\sqrt{1+\frac{c^2(\mathbf{x})}{\omega^2}\left(\frac{\partial^2}{\partial x^2}+\frac{\partial^2}{\partial y^2}\right)} \approx 1+\frac{2}{K}\sum_{j=1}^{K}\sum_{n=1}^{N}\frac{\alpha_n w_j^2}{1+\beta_n w_j^2}, \quad (32)$$

where K is the number of directions. Moreover, w_j are the derivative operators in the splitting directions, that is, $w_j = \cos\phi_j u + \sin\phi_j v$, with $\phi_j = (j-1)\Delta\phi$ (for $j = 1, 2, \ldots, K$, and $\Delta\phi = 2\pi/K$) being the azimuth of the rotated direction.

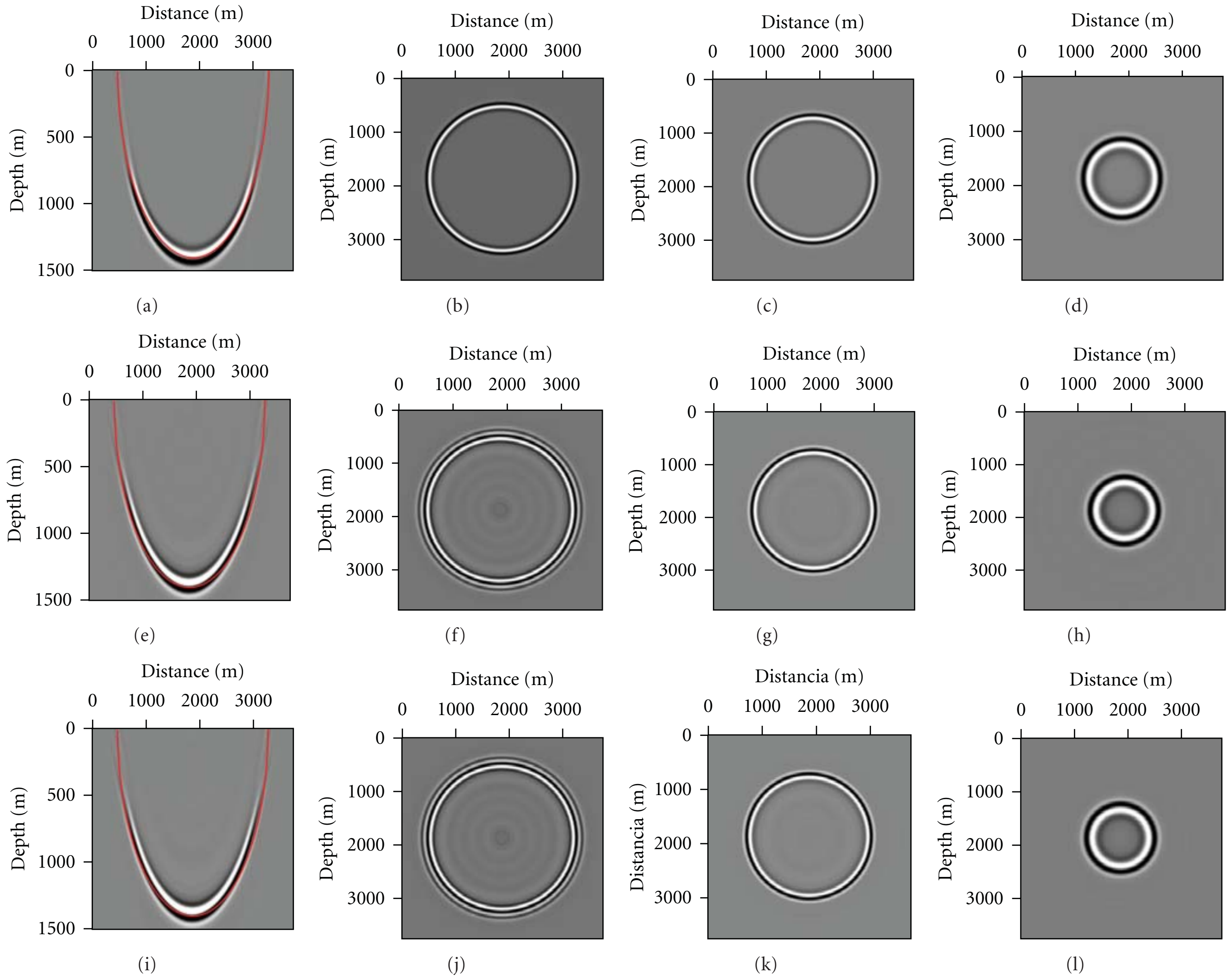

Figure 2: Migration impulse responses. (a)–(d): FFD migration using alternating four-way splitting; $p = 0.75$. (e)–(h): FFDPI migration using conventional two-way splitting, with interpolation between $p = 0.9$ and $p = 1.1$. (i)–(l): FFDPI migration using alternating four-way splitting, with interpolation between $p = 0.9$ and $p = 1.1$. From left to right: central vertical cut in the x-z plane and horizontal cuts at 150 m, 750 m, and 1250 m depth.

There are two ways of obtaining the unknown coefficients α_n and β_n in (32). One way is, as detailed above for the full 3D case, by Taylor series expansion of the fractions and comparison of the result with the direct Taylor series expansion of the square root. Alternatively, in practice, most often optimization techniques are employed to find optimum coefficients that minimize the numerical anisotropy for a certain range of medium velocities and a given reference velocity within the range of interest of propagation angles.

In conventional implementations of multiway splitting, operators (32) are applied in sequence at one single depth level before proceeding to the next one. In this paper, we apply the differential operators w_1 and w_3 for $\phi_1 = 0°$ and $\phi_3 = 90°$, that is, the derivatives in the x and y directions, at one depth level, and leave the application of the operators w_2 and w_4 for $\phi_2 = 45°$ and $\phi_4 = 135°$, that is, the derivatives in the diagonal directions, to the next depth level. In this way, we simulate four-way splitting, but with practically the same cost as conventional two-way splitting.

2.7. Stable FFD Migration and FFDPI Migration.

We compare our results of CPFFD migration to another stable FFD migration technique, FFDPI migration [14]. It is based on a correction to the FFD method that avoids stability problems. To derive it, Biondi [14] starts from the real version of (18). In our notation, he rewrites the last part of the operator inside the summation as

$$\frac{a_n p(1-p)X^2}{1+b_n\sigma X^2} = \frac{a_n p(1-p)}{b_n\sigma}\,\frac{b_n\sigma X^2}{1+b_n\sigma X^2}. \tag{33}$$

This representation of the operator corresponds to the differential equations

$$\frac{dP}{dz} = -ik_0\frac{a_n p(1-p)}{b_n\sigma}\,\frac{b_n\sigma X^2}{1+b_n\sigma X^2}P, \quad (n = 1,\ldots,N). \tag{34}$$

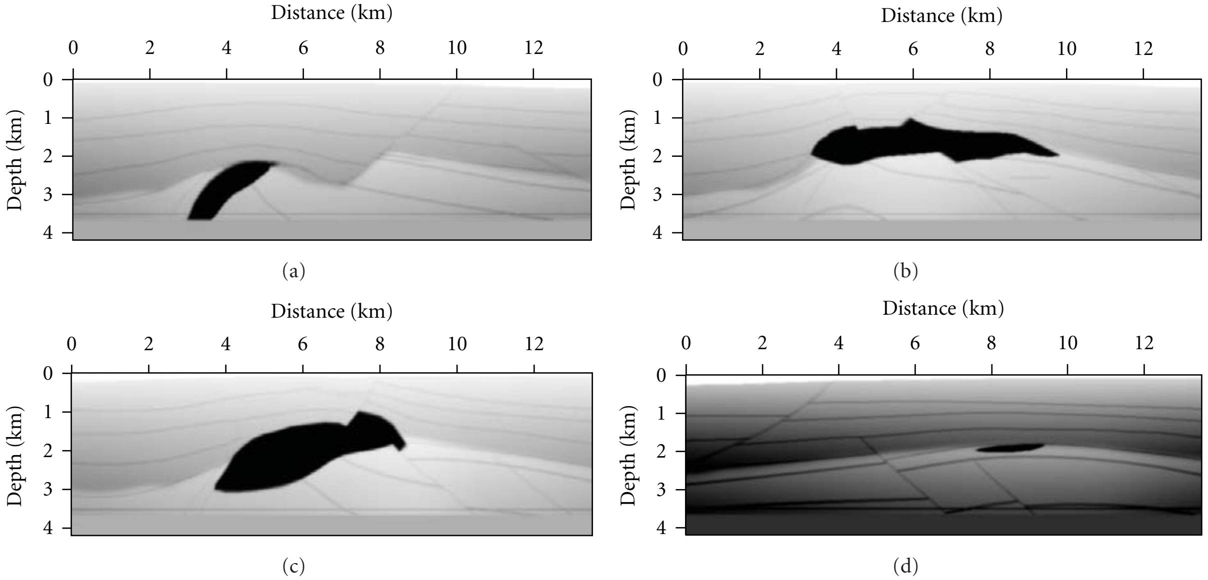

Figure 3: EAGE/SEG salt model. Representation by 4 vertical cuts at $x = 4.14$ km (a), $x = 6.80$ km (b), $y = 4.14$ km (c), and $y = 10.22$ km (d).

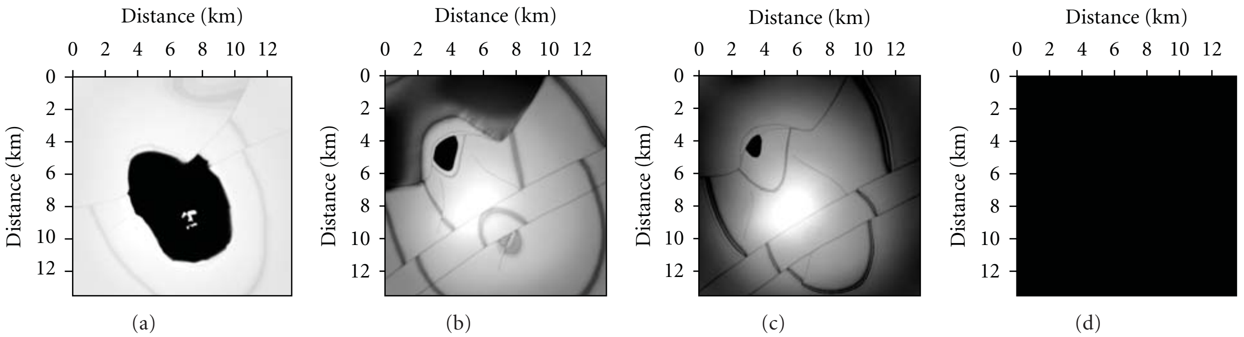

Figure 4: EAGE/SEG salt model. Representation by 4 horizontal cuts at $z = 1.7$ km, $z = 2.9$ km, $z = 3.5$ km, and $z = 4.1$ km (from (a) to (d)).

This form of the differential equation can be implemented in a stable way by the realization of the product σX^2 as a symmetrical matrix product $\mathbf{\Sigma}^T\mathbf{X}^2\mathbf{\Sigma}$, where $\mathbf{\Sigma}$ is a diagonal matrix containing the values of the square root of σ. The remaining factor $a_n p(1-p)/b_n\sigma$ can also be represented as a product with a diagonal matrix.

In 3D, after two-way splitting, the resulting difference equation is approximated by the system

$$\begin{gathered}\left[\mathbf{I}+\mathbf{C}_x\mathbf{\Sigma}_x^T\mathbf{D}_x^2\mathbf{\Sigma}_x\right]\mathbf{P}^{j+1} = \left[\mathbf{I}+\mathbf{C}_x^*\mathbf{\Sigma}_x^T\mathbf{D}_x^2\mathbf{\Sigma}_x\right]\widetilde{\mathbf{P}}^j, \\ \left[\mathbf{I}+\mathbf{C}_y\mathbf{\Sigma}_y^T\mathbf{D}_y^2\mathbf{\Sigma}_y\right]\widetilde{\mathbf{P}}^j = \left[\mathbf{I}+\mathbf{C}_y^*\mathbf{\Sigma}_y^T\mathbf{D}_y^2\mathbf{\Sigma}_y\right]\mathbf{P}^j,\end{gathered} \tag{35}$$

where $\mathbf{\Sigma}_x$ and $\mathbf{\Sigma}_y$ are diagonal matrices with elements

$$\begin{gathered}(\mathbf{\Sigma}_x)_{km} = \frac{c\left(x_k, y_l, z_j\right)}{\omega\Delta x}\sqrt{b_n\sigma\left(x_k, y_l, z_j\right)}\delta_{km}, \\ \left(\mathbf{\Sigma}_y\right)_{lm} = \frac{c\left(x_k, y_l, z_j\right)}{\omega\Delta y}\sqrt{b_n\sigma\left(x_k, y_l, z_j\right)}\delta_{lm}.\end{gathered} \tag{36}$$

Moreover, matrices $\mathbf{C}_x$ and $\mathbf{C}_y$ are given by

$$\mathbf{C}_x = \mathbf{I} + i\frac{k_0\Delta z}{2}\varepsilon\mathbf{\Delta}_x, \qquad \mathbf{C}_y = \mathbf{I} + i\frac{k_0\Delta z}{2}\varepsilon\mathbf{\Delta}_y, \tag{37}$$

where $\mathbf{\Delta}_x$ and $\mathbf{\Delta}_y$ are diagonal matrices with elements

$$\begin{gathered}(\mathbf{\Delta}_x)_{km} = \frac{a_n}{b_n}\frac{p\left(x_k, y_l, z_j\right)\left|1-p\left(x_k, y_l, z_j\right)\right|}{\sigma\left(x_k, y_l, z_j\right)}\delta_{km}, \\ \left(\mathbf{\Delta}_y\right)_{lm} = \frac{a_n}{b_n}\frac{p\left(x_k, y_l, z_j\right)\left|1-p\left(x_k, y_l, z_j\right)\right|}{\sigma\left(x_k, y_l, z_j\right)}\delta_{lm}\end{gathered} \tag{38}$$

and ε is given by

$$\varepsilon = \operatorname{sgn}(1-p) = \begin{cases} 1, & \text{if } c_r < c(\mathbf{x}), \\ -1, & \text{if } c_r > c(\mathbf{x}). \end{cases} \tag{39}$$

According to Biondi [14], for the equivalence between the original differential equation and its stable discretization to be guaranteed, it is essential that ε is constant on the depth level z_j under consideration, that is, that the reference velocity is larger or smaller than all model velocities at the current depth level.

Biondi [14] proves that this implementational correction stabilizes FFD migration, even in the presence of strong lateral velocity contrasts and for reference velocities larger than the medium velocity. In this way, this version of the FFD method possesses the necessary characteristics to be utilized as the main part of a precise and efficient high-angle wave-equation migration method. To attain a desired precision, one can interpolate between wavefields obtained for a sufficiently dense set of reference velocities. Theoretically, this allows to obtain arbitrary precision by increasing the number of reference velocities. The structure of this FFDPI method is similar to PSPI [19] and to the extended split-step method [26].

3. Numerical Experiments

3.1. Tests in a Homogeneous Medium. To study the numerical anisotropy of FFD migration operators after splitting, we calculated impulse responses for zero-offset migration in a homogeneous medium with velocity 2.5 km/s. The source pulse was a Ricker wavelet with central frequency 25 Hz, with its center positioned at an arrival time of 1.12 s. The migration grid was $\Delta x = \Delta y = 12.5$ m, and $\Delta z = 10$ m. All our examples used a complex Padé implementation of FFD migration with 3 terms in the series.

The top part of Figures 1(a)–1(d) show one vertical and three horizontal cuts through the reference impulse response, obtained with phase-shift migration using the true medium velocity. The amplitude decay at high propagation angles is caused by the source implementation, which did not use the amplitude correction of Wapenaar [27]. The red line in Figure 1(a) indicates the true theoretical position of the event, given by the half circle $z = \sqrt{(ct_e)^2 - (x - x_s)^2}$, where t_e is the observation time of the event in the data, here 0.56 s, and x_s is the source position, here the centre of the image, that is, $x_s = 1850$ m. The noncircular appearance of this line is due to the overstretched vertical axis. For a better comparison, we will present all other impulse responses below in the same way.

Figures 1(e)–1(h) show the corresponding four cuts of the impulse response of complex Padé FFD migration using conventional two-way splitting. Here, the value of the reference velocity was chosen as $c_r = 1875$ m/s, that is, $p = c_r/c(\mathbf{x}) = 0.75$. We observe the well-preserved circular shape of the impulse response in the deepest horizontal cut (Figure 1(i)), that is, for propagation directions close to the vertical axis. However, the shallow and, principally, medium horizontal cuts reveal a visible deformation, indicating the loss of quality for higher propagation angles. Also note the amplitude loss in the directions of the coordinate axes that are visible in the shallow and medium horizontal cuts. In the vertical cut (1(a)), only a slight deformation from circular shape is visible, which is due to the cut being within the coordinate plane, where the errors are the smallest. The amplitude loss for high propagation angles reflects the quality of the three-term Padé approximation. Note that the observed behaviour will be emphasized in media with strong lateral variations, where much smaller values of p will occur.

Figures 1(i)–1(l) show the impulse response of FFD migration using conventional four-way splitting. The circular shape of the impulse response has been nicely recovered by the application of the two additional differential operators in the diagonal directions. Also, the amplitude loss in the coordinate directions is no longer visible. Note that this image has about twice the computational cost of the one in the center.

Figures 2(a)–2(d) show the impulse response of CPFFD migration using alternating four-way splitting, that is, two-way splitting in the coordinate directions at one depth level and in the diagonal directions at the next depth level. It is hard to spot any difference to the result of complete four-way splitting (Figures 1(i)–1(l)). The circular format of the operator is almost perfect, and even the slight amplitude loss along the coordinate axes is as well recovered as by complete four-way splitting. Note that this image has about the same computational cost as the one obtained with conventional two-way splitting (Figures 1(e)–1(h)).

Figures 2(e)–2(h) shows the impulse response of FFDPI migration using conventional two-way splitting, with interpolation between wavefields obtained for $p = 0.9$ and $p = 1.1$. We chose these values to reflect the fact that, for FFDPI, generally reference velocities closer to the medium velocity are available for interpolation. We observe a good preservation of the circular shape, particularly in the horizontal cuts. In the vertical cut, we note that the wavefront lags slightly behind the true position, starting already at rather low propagation angles of about 35°. The amplitude decay for high propagation angles is reduced as compared to FFD, probably because the reference velocities are closer to the medium velocity than in the previous examples. Finally, the shallowest cut exhibits some numerical dispersion, causing a distorted pulse shape.

Figures 2(i)–2(l) show the impulse response of FFDPI migration using alternating four-way splitting, with interpolation between wavefields obtained for $p = 0.9$ and $p = 1.1$. Almost no improvement over the conventional two-way splitting result (center) is visible.

3.2. Tests in an Inhomogeneous Medium. For a more realistic test of the different splitting techniques for FFD migration, we calculated zero-offset impulse responses for the EAGE/SEG salt model. Here, we used a seismic pulse in the centre of the model, described by a Ricker wavelet with central frequency of 15 Hz, dislocated by $t_e = 2.2$ s, and a migration grid with $\Delta x = \Delta y = \Delta z = 20$ m. To avoid spurious events from the spike reflectors, we regularized the model using a 7 × 7 median filter. This is necessary because the EAGE/SEG salt model uses artificially high velocity values to define the reflectors.

We represent the results by vertical cuts parallel to the y-z plane at $x = 4.14$ km and $x = 6.80$ km and parallel to

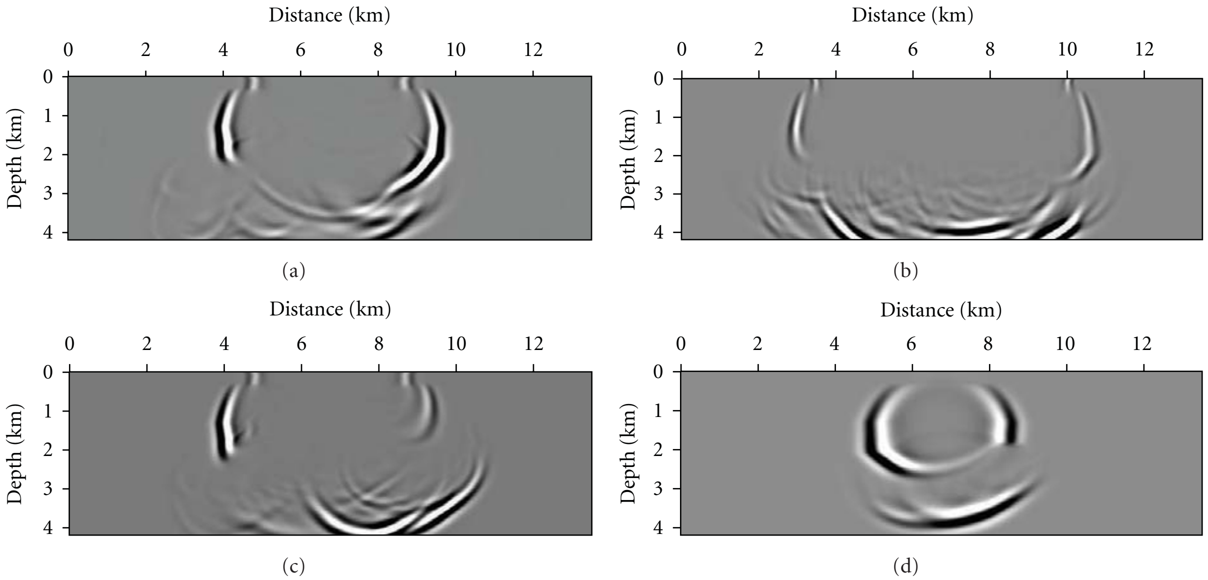

Figure 5: Impulse response of FFD migration with two-way splitting. Vertical cuts as in Figure 3.

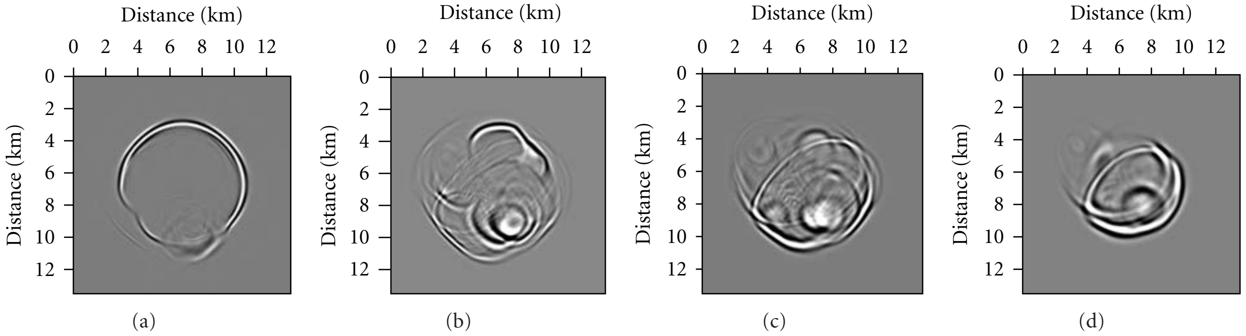

Figure 6: Impulse response of FFD migration with two-way splitting. Horizontal cuts as in Figure 4.

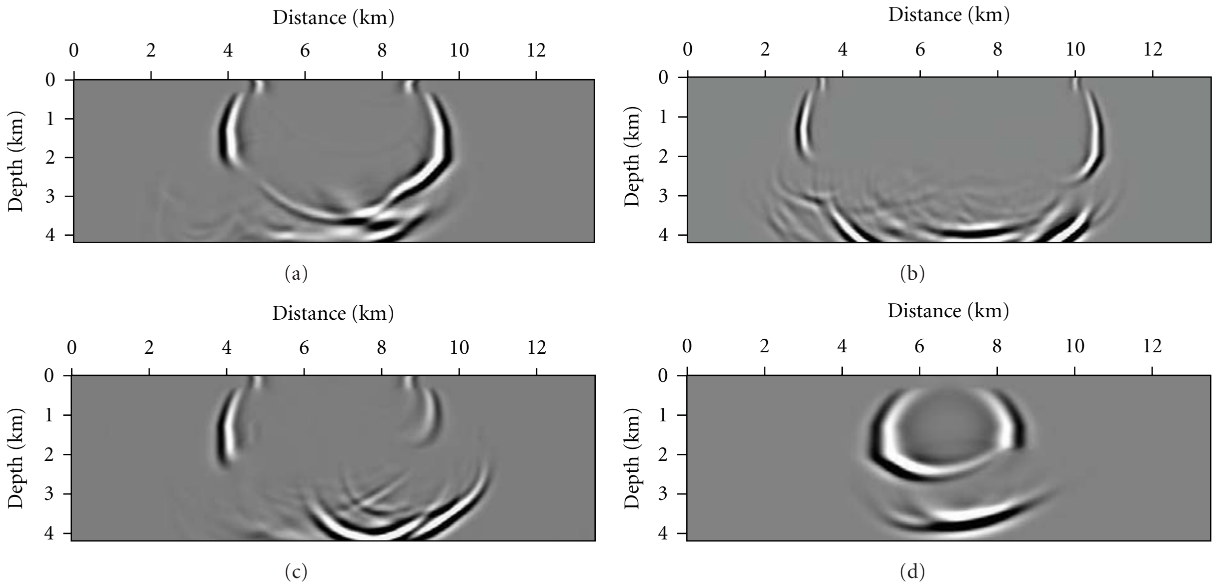

Figure 7: Impulse response of FFD migration with alternating four-way splitting. Vertical cuts as in Figure 3.

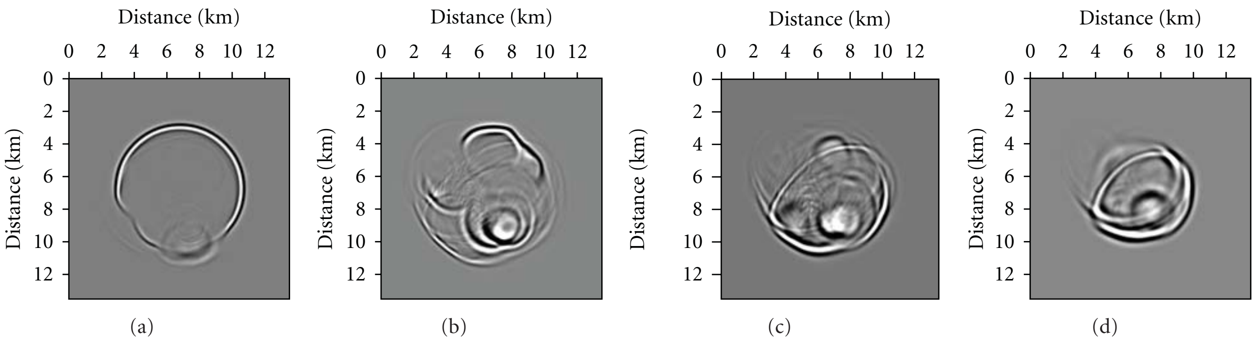

Figure 8: Impulse response of FFD migration with alternating four-way splitting. Horizontal cuts as in Figure 4.

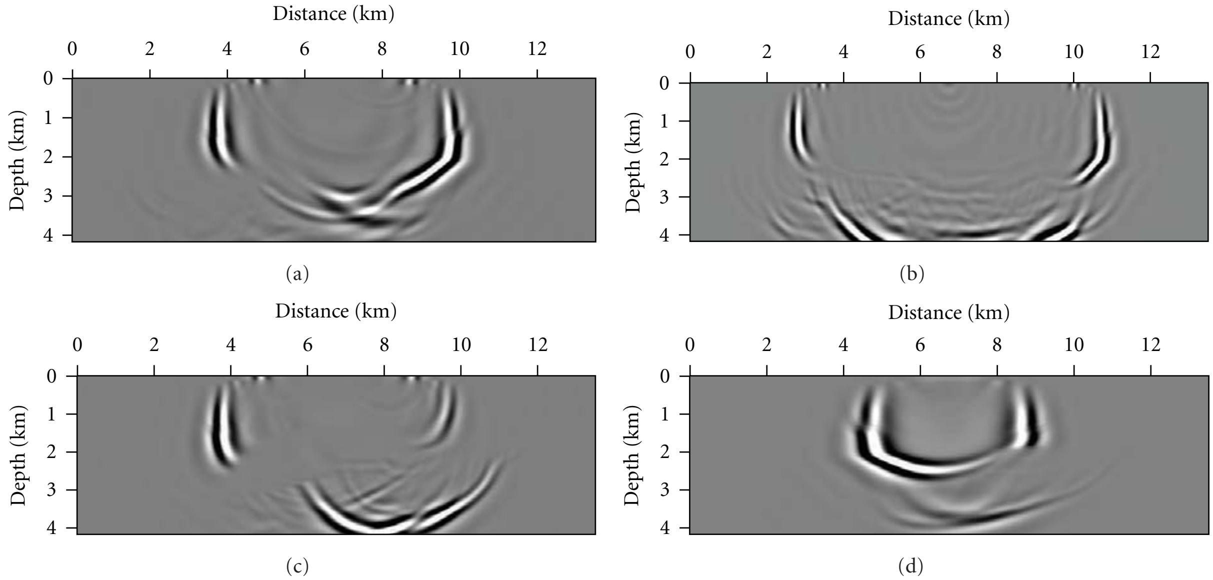

Figure 9: Impulse response of FFDPI migration with two-way splitting using 10 reference velocities. Vertical cuts as in Figure 3.

the x-z plane at $y = 4.14$ km and $y = 10.22$ km, as well as horizontal cuts at depths $z = 1.7$ m, $z = 2.9$ km, $z = 3.5$ km, and $z = 4.1$ km. Figures 3 and 4 show these cuts through the EAGE/SEG salt model after filtering.

Figures 5 and 6 show the corresponding cuts through the impulse response of FFD migration with two-way splitting and Figures 7 and 8 those of FFD migration with alternating four-way splitting. The differences between these sets of figures are due to numerical anisotropy, which is not always easy to see at this scale. The most visible difference is the one between Figures 6(a) and 8(a). The circular shape of three quarters of the wavefront is well preserved in Figure 8, while visibly distorted in Figure 6. Similar distortions are present in the other figure parts. Some events, particularly in the diagonal directions, are slightly more advanced in Figures 7 and 8 than in Figures 5 and 6. Also, some amplitude differences are visible. We refrain from presenting the results of complete four-way splitting, because they look virtually identical to those in Figures 7 and 8.

For comparison, Figures 9 and 10 show the impulse response of FFDPI migration with two-way splitting. Since the theory of Biondi [14] is only formulated for a single term of the Padé series, so is our implementation. Because of the strong dependence of FFDPI on reference velocities not too far from the true model velocity, this numerical experiment needed 10 reference velocities. For being a very robust method, the impulse response is not subject to any instabilities, even with the reference velocities being still a bit far from the medium velocities. This remains true even for less reference velocities, though the image quality degrades considerably. Because of the need for a rather large number of reference velocities, FFDPI is a rather expensive method. In our implementation, it used about three times the computational time of alternating four-way FFD.

Even for this experiment with 10 reference velocities, we still see some effects of numerical dispersion in Figures 9 and 10. Also, the results still exhibit quite visible differences to Figures 7 and 8. Since we have at this time no 3D reverse-time migration available, it is hard to tell which results are better positioned. Visual inspection and comparison to results of FD migration (not shown here) make us believe that the FFD results are more reliable than the FFDPI results with 10 reference velocities. More accurate results can be obtained by further increasing the number of reference velocities.

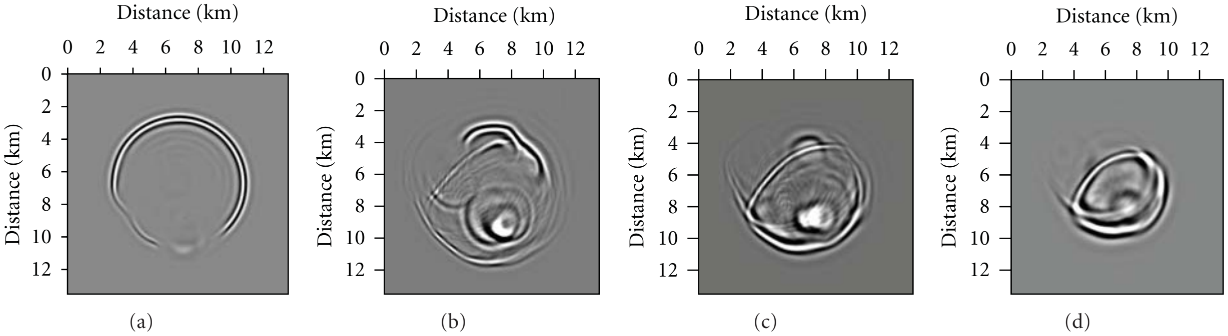

FIGURE 10: Impulse response of FFDPI migration with two-way splitting using 10 reference velocities. Horizontal cuts as in Figure 4.

4. Conclusions

In this paper, we have implemented 3D versions of complex Padé FFD (CPFFD) and FFD plus interpolation (FFDPI), which have proven to be more stable in the presence of strong lateral velocity contrasts than other FFD migration implementations. For CPFFD migration, we have compared the effects of different ways of directional splitting and compared its results to those of FFDPI migration. Alternating four-way splitting, that is, applying the differential operators in the coordinate directions at one depth level and in the diagonal directions at the next depth level, proved to be an improvement over conventional two-way splitting at almost no extra cost. Although this procedure is theoretically less accurate than complete four-way splitting, that is, all four directions applied at all depth levels, our numerical results were of comparable quality. Extensions of the alternating splitting technique can be thought of like eight-way splitting where the remaining directions are covered two by two in the next two depth steps.

From our numerical tests with splitting the CPFFD and FFDPI migration operators, we conclude that FFDPI migration is the most robust of the tested methods. Even implemented only using two-way splitting, it did show only a fair amount of numerical dispersion, but no visible numerical anisotropy. However, for practical use, FFDPI is a rather expensive method because it needs a large number of reference velocities to function with acceptable precision. Thus, for a more economic migration with acceptable image quality, alternating four-way splitting in FFD migration is an interesting alternative.

One minor problem of multiway splitting should be mentioned. The differential operator in the diagonal directions can cause aliasing effects because of the fact that the grid spacing in this direction is by a factor of $\sqrt{2}$ larger than in the coordinate directions. Off-diagonal directions may complicate things further, because they require resampling.

Acknowledgments

This work was kindly supported by the Brazilian agencies CAPES, FINEP, and CNPq, as well as Petrobras and the sponsors of the *Wave Inversion Technology (WIT) Consortium*.

References

[1] J. F. Claerbout, “Toward a unified theory of reflector mapping,” *Geophysics*, vol. 36, no. 3, pp. 467–481, 1971.

[2] D. Ristow and T. Rühl, “Fourier finite-difference migration,” *Geophysics*, vol. 59, no. 12, pp. 1882–1893, 1994.

[3] D. L. Brown, “Applications of operator separation in reflection seismology,” *Geophysics*, vol. 48, no. 3, pp. 288–294, 1983.

[4] D. Ristow, *3-D downward extrapolation of seismic data in particular by finite difference method*, Ph.D. thesis, University of Utrecht, Utrecht, The Netherlands, 1980.

[5] D. Ristow and T. Rühl, “3-D implicit finite-difference migration by multiway splitting,” *Geophysics*, vol. 62, no. 2, pp. 554–567, 1997.

[6] P. Kitchenside, “Steep dip 3-D migration: some issues and examples,” in *Proceedings of the 58th Annual International Meeting Society of Exploration Geophysicists*, pp. 976–978, 1988, Expanded Abstracts.

[7] R. W. Graves and R. W. Clayton, “Modeling acoustic waves with paraxial extrapolators,” *Geophysics*, vol. 55, no. 3, pp. 306–319, 1990.

[8] Z. Li, “Compensating finite-difference errors in 3-D migration and modeling,” *Geophysics*, vol. 56, no. 10, pp. 1650–1660, 1991.

[9] F. Collino and P. Joly, “Splitting of operators, alternate directions and paraxial approximation of the 3D wave equation,” *SIAM Journal on Scientific Computing*, vol. 16, no. 5, pp. 1019–1048, 1995.

[10] Y. Wang, “ADI plus interpolation: accurate finite-difference solution to 3D paraxial wave equation,” *Geophysical Prospecting*, vol. 49, no. 5, pp. 547–556, 2001.

[11] H. Zhou and G. A. McMechan, “One-pass 3-D seismic extrapolation with the 45° wave equation,” *Geophysics*, vol. 62, no. 6, pp. 1817–1824, 1997.

[12] G. Q. Zhang, S. L. Zhang, Y. X. Wang, and C. Y. Liu, “A new algorithm for finite-difference migration of steep dips,” *Geophysics*, vol. 53, no. 2, pp. 167–175, 1988.

[13] A. R. Mitchell and D. F. Griffiths, *The Finite Difference Method in Partial Differential Equations*, Wiley, 1980.

[14] B. Biondi, “Stable wide-angle Fourier finite-difference downward extrapolation of 3-D wavefields,” *Geophysics*, vol. 67, no. 3, pp. 872–882, 2002.

[15] S. Jin, R. S. Wu, and C. Peng, “Seismic depthmigration with pseudo-screen propagator,” *Computational Geosciencies*, vol. 3, no. 3-4, pp. 321–335, 1999.

[16] X. R. Xie and R. S. Wu, “Improve the wide angle accuracy of screen method under large contrast,” in *Proceedings of*

the 68th Annual International Meeting Society of Exploration Geophysicists, pp. 1811–1814, Institute of Tectonics, University of California, Santa Cruz , Calif, USA, 1998.

[17] R. J. Godfrey, F. Muir, and J. F. Claerbout, “Stable extrapolation,” Stanford Exploration Project Report SEP-16:83–87, 1979.

[18] D. Brown, “Muir’s rules for matrices: another look at stability,” Stanford Exploration Project Report SEP-20:125–142, 1979.

[19] J. Gazdag and P. Sguazzero, “Interval velocity analysis by wave extrapolation,” *Geophysical Prospecting*, vol. 32, no. 3, pp. 454–479, 1984.

[20] D. Amazonas, J. Costa, J. Schleicher, and R. Pestana, “Wide angle FD and FFD migration using complex padé approximations,” *Geophysics*, vol. 72, supplement 6, pp. S215–S220, 2007.

[21] A. Bamberger, B. Engquist, L. Halpern, and P. Joly, “Higher order paraxial wave equation approximations in heterogeneous media,” *Journal of Applied Mathematics*, vol. 48, pp. 129–154, 1988.

[22] F. A. Milinazzo, C. A. Zala, and G. H. Brooke, “Rational square-root approximations for parabolic equation algorithms,” *Journal of the Acoustical Society of America*, vol. 101, no. 2, pp. 760–766, 1997.

[23] M. A. Leontovich and V. A. Fock, “Solution of the problem of propagation of electromagnetic waves along the earth’s surface by the method of parabolic equation,” *Journal of Experimental and Theoretical Physics*, vol. 16, pp. 557–573, 1946.

[24] E. L. Wachspress and G. J. Harbetler, “An alternating-direction-implicit iteration technique,” *SIAM Journal*, vol. 8, pp. 403–424, 1960.

[25] J. Douglas, “Alternating direction methods for three space variables,” *Numerische Mathematik*, vol. 4, no. 1, pp. 41–63, 1962.

[26] W. Kessinger, “Extended split-step Fourier migration,” in *Proceedings of the 62nd Annual International Meeting Society of Exploration Geophysicists*, pp. 917–920, 1992, Expanded Abstracts.

[27] C. P. A. Wapenaar, “Representation of seismic sources in the one-way wave equations,” *Geophysics*, vol. 55, no. 6, pp. 786–790, 1990.

Hindawi Publishing Corporation
International Journal of Geophysics
Volume 2011, Article ID 819831, 10 pages
doi:10.1155/2011/819831

Research Article

Higher-Resolution Determination of Zero-Offset Common-Reflection-Surface Stack Parameters

Endrias G. Asgedom,[1, 2] Leiv J. Gelius,[1, 2] and Martin Tygel[3]

[1] *Department of Geosciences, University of Oslo, 0316 Oslo, Norway*
[2] *Department of Informatics, Centre for Imaging, University of Oslo, 0316 Oslo, Norway*
[3] *Department of Applied Mathematics, State University of Campinas, Campinas 1083-859 SP, Brazil*

Correspondence should be addressed to Leiv J. Gelius, l.j.gelius@geo.uio.no

Received 14 January 2011; Accepted 26 April 2011

Academic Editor: Sergey Fomel

We developed a higher resolution method for the estimation of the three travel-time parameters that are used in the 2D zero-offset, Common-Reflection-Surface stack method. The underlying principle in this method is to replace the coherency measure performed using semblance with that of MUSIC (multiple signal classification) pseudospectrum that utilizes the *eigenstructure* of the data covariance matrix. The performance of the two parameter estimation techniques (i.e., semblance and MUSIC) was investigated using both synthetic seismic diffraction and reflection data corrupted with white Gaussian noise, as well as a multioffset ground penetrating radar (GPR) field data set. The estimated parameters employing MUSIC were shown to be superior of those from semblance.

1. Introduction

Many important tasks in seismic processing and imaging require the estimation of travel-time parameters. Such parameters include, among others, *velocities* (e.g., for stacking and time-migration purposes), travel-time slopes and curvatures (e.g., for slant, common-reflection-surface (CRS), multifocus (MF) stacks) and event picking for tomographical methods. As shared with many other areas of activity, a basic feature of seismic signals (referred to as *events*) is that they exhibit some sort of *coherent* or *aligned* energy. More specifically, seismic events (e.g., reflections or diffractions) align themselves along curves or surfaces (referred to as *moveouts*) within the data. The basic strategy for signal detection and information extraction is to express these moveouts as a function of a few, meaningful parameters and to estimate such parameters so as the moveout optimally approximates the events. In general, the search for parameters, sometimes referred to as *wavefront shaping parameters*, carry key information about the geological structure under investigation.

To assess how well a moveout, defined by some trial parameters, approximates a target signal, a number of quantifiers (or *coherence measures*) has been proposed. General discussions on coherency measures applied to seismic data can be found in the pioneering papers of [1–3] with a clear emphasis on the second-order coherence measure *semblance*. Semblance quantifies the likelihood between the trial moveout and the target event by stacking the data along that moveout and measuring the energy of the output.

Adopting the notation as in [4], for a given sample, k, at a given (reference) trace, the so-called *semblance coefficient*, or simply *semblance*, S_c, can be mathematically written in the form

$$S_c = \frac{\sum_{j=k-N/2}^{j=k+N/2} \left| \sum_{i=1}^{M} x(j,i) \right|^2}{M \sum_{j=k-N/2}^{j=k+N/2} \sum_{i=1}^{M} \left| x(j,i) \right|^2}. \quad (1)$$

Here, the semblance coefficient is computed for N samples taken from M traces in a window centered about the trajectory defined by the moveout equation generated by the trial travel-time parameters (cf. Figure 1). In the following, the given sample, k, and reference trace, as well as the number of samples, N, and number of traces, M, will be fixed throughout. As a consequence, we do not need to incorporate them into the semblance notation, which will be simply written as S_c. To construct the window in Figure 1, proper interpolation is performed to select the appropriate samples. In the language of electrical engineers, the above-described windowing process *steers* the stacking along the trial moveout.

Semblance can be described in terms of the covariance matrix of the data. Following, for example, [5], within the selected time window along the chosen trial moveout, semblance can be written in the form

$$S_c = \frac{\mathbf{u}^T \mathbf{R} \mathbf{u}}{M \operatorname{tr}(\mathbf{R})}, \tag{2}$$

where $\mathbf{u}$ is a column vector of ones, which can be referred to as the *unitary steering* vector, and $\mathbf{R}$ is the covariance of the data. Assuming that the different sources can be described by a zero-mean stochastic process, the data covariance matrix is given as

$$\mathbf{R} = E\left\{\mathbf{D}\mathbf{D}^H\right\}, \tag{3}$$

where $\mathbf{D} = (d_{ij})$ is the data matrix, in which d_{ij} is the recorded data at the ith trace and jth sample. As in usual notation, $E\{\}$ and tr() represent the expected value and matrix trace, respectively. Moreover, superscripts T and H represent transpose and conjugate transpose, respectively. As pointed out by [2], Equation (2) provides the interpretation that semblance can be regarded, within the selected time window, as a normalized output/input energy ratio. The denominator, $\operatorname{tr}(\mathbf{R})$, is the normalization used by semblance in order to generate a maximum peak of unity at the "correct" moveout parameters (namely, the ones for which we have the optimal stack).

Even though semblance is a good measure of coherency, it can in many times provide insufficient resolution for the parameter estimation. That is the case, in particular, for interfering events. There is, thus, a motivation to look for alternatives to overcome these difficulties. Attempts have been made to further improve semblance by using only those parts of the data with higher resolving power [6] and also by introducing weights in the standard semblance formulation [7]. Statistical approaches have also been introduced to increase the resolution of the velocity analysis [8]. In this paper, an alternative to semblance-like techniques will be investigated.

As recognized in sonar and radar applications, methods exploiting the properties of the eigenstructure (namely, eigenvalues and eigenvectors) of the data covariance matrix can lead to far better resolution results than semblance [4, 9, 10]. The basic idea of the eigenstructure approach is to decompose the data covariance matrix into two orthogonal subspaces. The first is the *signal* subspace, which is generated by the eigenvectors associated to high eigenvalues. The second is the *noise* subspace, generated by the small or zero eigenvalues. In this paper, we use the eigenstructure method called *multiple signal classification (MUSIC)*, introduced by [9]. MUSIC exploits the fact that the "correct" moveout, represented as a steering vector, must lie in the signal subspace and, therefore, is orthogonal to the noise subspace eigenvectors. As a consequence, the *projection* of the steering vector onto the noise subspace provides a nearly vanishing value. The inverse of such a projection (namely, the sum of the dot products of the steering vector with the noise eigenvectors) should peak when the steering vector represents a correct moveout.

This work can be seen as a followup of [10], in which the application of MUSIC to single-parameter velocity analysis and slant stacks is described. Here, we extend the application of MUSIC to common-reflection-surface (CRS) multi-parameter estimation. Besides the theoretical exposition of the technique, applications to first synthetic examples, consisting of dipping planar reflectors and point diffractors, are provided. Comparisons of the obtained results and conventional semblance confirm, at least for these initial examples, the expected far better resolution of MUSIC. To further support this conclusion a real multioffset GPR data set was also analysed. It was demonstrated that MUSIC, unlike semblance, was able to better resolve interfering events.

2. Classical Music: Narrowband and Uncorrelated Signals

In its original or classical form [9], MUSIC considers an array of N_r receivers recording W incoming reflected or diffracted signals, in an arbitrary background medium. In time domain, the data recorded by the ith receiver can be modeled as

$$d_i(t) = \sum_{w=1}^{W} s_w\left(t - \tau_{i,w}^{\theta}\right) + n_i(t), \quad (i = 1, 2, \ldots, N_r), \tag{4}$$

where $s_w(t)$ is the source pulse associated with event w, and $n_i(t)$ is the additive random noise at the ith receiver. Finally, $\tau_{i,w}^{\theta}$ is the travel-time (or time delay) of the wth incoming signal (or event) arriving at the ith receiver. The superscript, θ, indicates that the moveouts depend on a set of one or more parameters, here denoted, by a so-called *parameter vector*, $\boldsymbol{\theta}$. The most popular trial-moveout example is the normal-moveout (NMO), applied for velocity analysis in the common-midpoint (CMP) configuration. In the 2D situation, the single parameter to be estimated is the NMO-velocity. An example of multiparameter moveout is the general hyperbolic moveout used by the common-reflection-surface (CRS) stacking method. As previously indicated, application of MUSIC to velocity analysis has been described by [10]. Here, we extend the analysis to CRS parameter estimation in 2D data. In this situation, three parameters are to be estimated. In order not to disturb the main flow, the description of the generalized hyperbolic or, more simply, the CRS travel-times, $\tau_{i,w}$, is postponed to the appendix.

2.1. Narrowband Signals. For narrowband signals $s_w(t)$, the travel-times can be expressed as exponential phase shifts

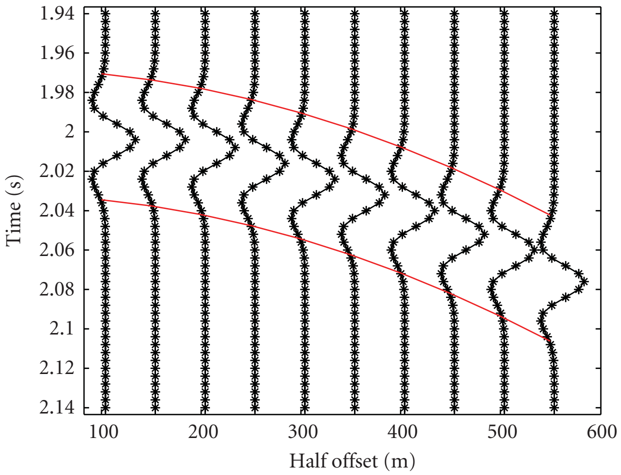

Figure 1: Time window used to compute semblance. The two red lines show the travel-time trajectories bounding the window used to select the data.

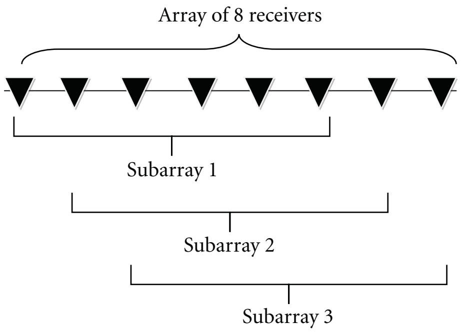

Figure 2: Concept of spatial smoothing.

around the center angular frequency ω. For notation simplicity, that fixed frequency will be omitted. As a consequence, the data model in (4) can be recast as

$$d_i(t) = \sum_{w=1}^{W} s_w(t) \exp\left(-i\omega\tau_{i,w}^{\theta}\right) + n_i(t). \tag{5}$$

After time discretization, the above equation can be recast in matrix form as

$$\mathbf{D} = \mathbf{A}(\boldsymbol{\theta})\mathbf{S} + \mathbf{N}, \tag{6}$$

where $\mathbf{D} = (d_{ij}) = (d_i(t_j))$ and $\mathbf{N} = (n_{ij}) = (n_i(t_j))$ are, respectively, the $N_r \times N_t$ *data* and *additive noise* matrices, and $\mathbf{S} = (s_{wj}) = (s_w(t_j))$ is the $W \times N_t$ *source* matrix. Finally,

$$\mathbf{A}(\boldsymbol{\theta}) = \left(\mathbf{a}_1(\boldsymbol{\theta}), \ldots, \mathbf{a}_w(\boldsymbol{\theta}), \ldots, \mathbf{a}_W(\boldsymbol{\theta})\right) \tag{7}$$

is the $N_r \times W$ *array response matrix* containing all the *steering vectors*

$$\mathbf{a}_w(\boldsymbol{\theta}) = \begin{bmatrix} \exp\left(-i\omega\tau_{1,w}^{\theta}\right) \\ \exp\left(-i\omega\tau_{2,w}^{\theta}\right) \\ \vdots \\ \exp\left(-i\omega\tau_{N_r,w}^{\theta}\right) \end{bmatrix}. \tag{8}$$

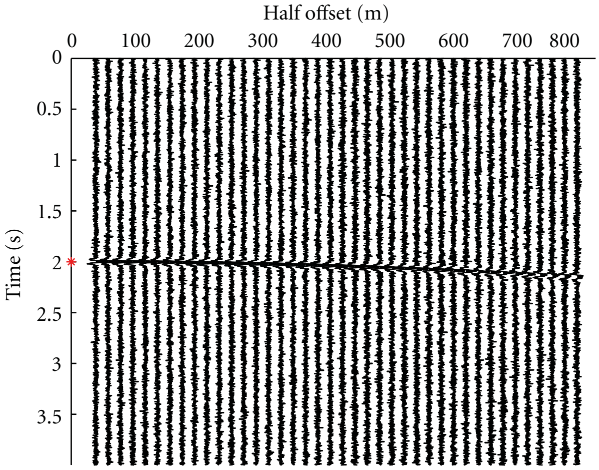

Figure 3: Synthetic CMP data used for comparison of MUSIC with semblance. A point diffractor and a dipping reflector ($\beta = 20^0$) with the same $\tau_0 = 2$ sec is used to generate the data. Note that the two events are very close to each other and it is difficult to distinguish them.

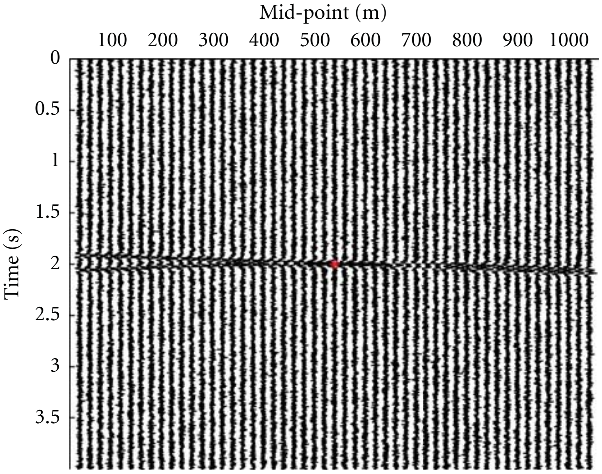

Figure 4: Synthetic ZO section used for comparison of MUSIC with semblance. A point diffractor and a dipping reflector ($\beta = 20^0$) is used to generate the data. The red dot ($x_0 = 540$ m and $\tau_0 = 2$ sec) shows the location where we performed the parameter search.

MUSIC utilizes the eigenstructure of the data covariance matrix defined by (3). Substituting (6) into (3) and assuming uncorrelated noise with variance of σ_n^2, the covariance matrix can be recast as

$$\begin{aligned} \mathbf{R} &= \mathbf{A}(\boldsymbol{\theta})\left[E\left\{\mathbf{S}\mathbf{S}^H\right\}\right]\mathbf{A}(\boldsymbol{\theta})^H + E\left\{\mathbf{N}\mathbf{N}^H\right\} \\ &= \mathbf{A}(\boldsymbol{\theta})\mathbf{R}_s\mathbf{A}(\boldsymbol{\theta})^H + \sigma_n^2\mathbf{I}, \end{aligned} \tag{9}$$

where $\mathbf{R}_s$ and $\mathbf{I}$ are, respectively, the source covariance and identity matrices. The MUSIC algorithm performs an eigendecomposition of this covariance matrix

$$\mathbf{R}\mathbf{U} = \boldsymbol{\Lambda}\mathbf{U}, \tag{10}$$

where $\boldsymbol{\Lambda} = \operatorname{diag}(\lambda_1, \lambda_2, \ldots, \lambda_{N_r})$ contains the eigenvalues satisfying $\lambda_1 \geq \lambda_2 \geq \cdots \geq \lambda_{N_r}$, and $\mathbf{U} = [\mathbf{u}_1, \mathbf{u}_2, \ldots, \mathbf{u}_{N_r}]$

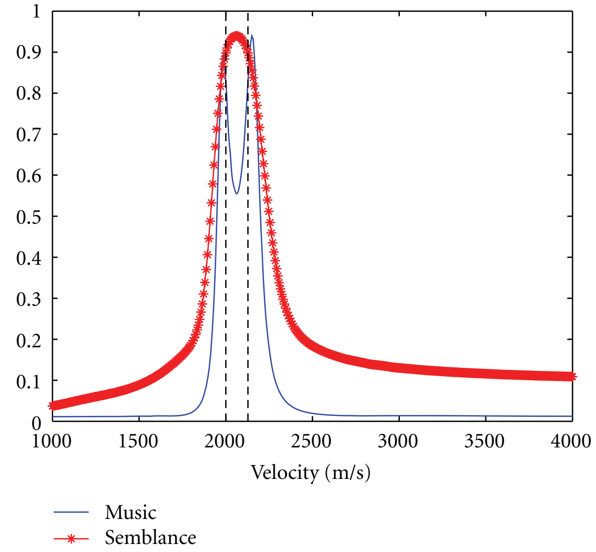

FIGURE 5: Spectrum of parameter C using both MUSIC and semblance (point diffractor and a dipping reflector $\beta = 20^0$). The black dotted lines show the correct location of the parameters C_{diff} and C_{dip}. We see that only MUSIC was able to resolve the two parameters.

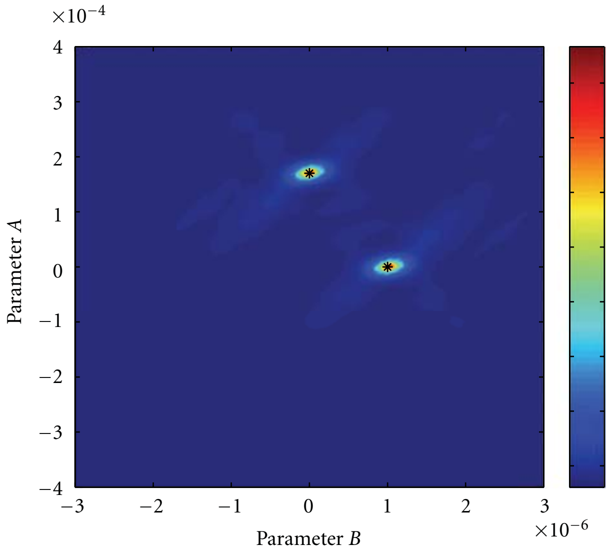

FIGURE 6: Uncorrelated sources: Determination of parameters A and B based on MUSIC for a diffractor and a dipping reflector $\beta = 20^0$. The black stars show the correct parameter locations.

is the matrix that consists of the corresponding (column) orthonormal eigenvectors of $\mathbf{R}$. The unitary matrix of eigenvectors $\mathbf{U}$ can be decomposed further as $\mathbf{U} = [\mathbf{U}_s\ \mathbf{U}_n]$, where the columns of $\mathbf{U}_s$ comprise the eigenvectors corresponding to the largest eigenvalues of $\mathbf{R}$ (the signal subspace), and with $\mathbf{U}_n$ containing the remaining (noise) eigenvectors.

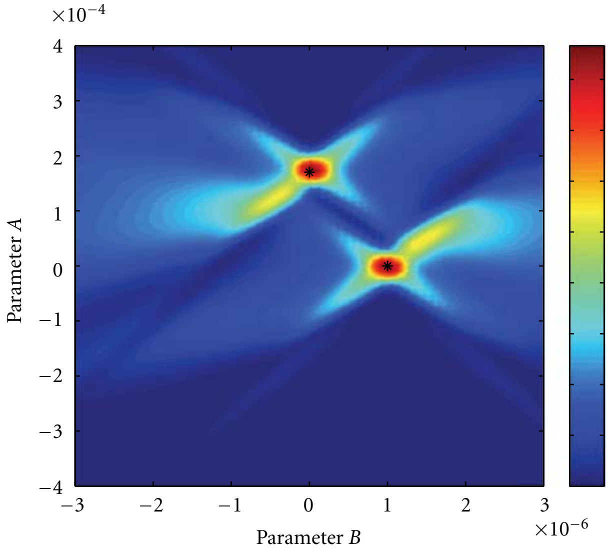

FIGURE 7: Uncorrelated sources: Determination of parameters A and B based on semblance for a diffractor and a dipping reflector $\beta = 20^0$. The black stars show the correct parameter locations.

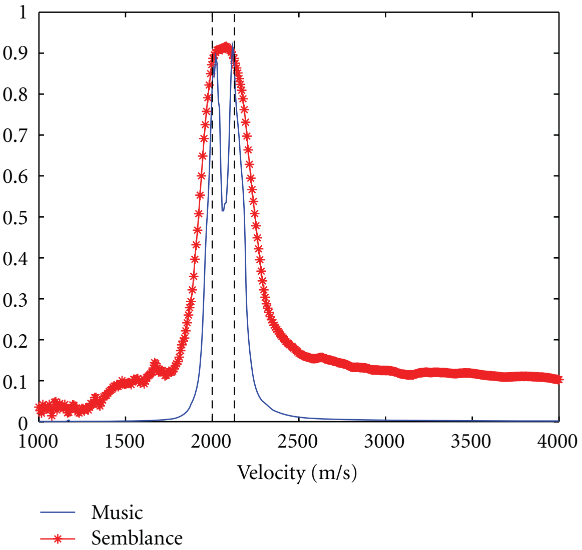

FIGURE 8: Parameter C determined using both MUSIC and semblance (point diffractor and a dipping reflector $\beta = 20^0$). The black dotted lines show the correct parameter locations.

2.2. Uncorrelated Signals. For MUSIC to be applicable in our parameter search problem, the different source pulses, $s_w(t)$, should be uncorrelated resulting in a covariance matrix $\mathbf{R}_s$ having full rank equal to the number of events W recorded at the receivers. If the M source vectors are linearly independent, then the matrix $\mathbf{R}_s$ is positive definite which results in $\mathbf{A}(\boldsymbol{\theta})\mathbf{R}_s\mathbf{A}(\boldsymbol{\theta})^H$ to be a positive semidefinite matrix with its rank spanning the steering vectors corresponding to the appropriate parameters we are searching. With the above condition satisfied and since the noise subspace is orthogonal to the signal subspace, the MUSIC *pseudospectrum*, $\mathbf{P}_{\text{MU}}(\boldsymbol{\theta})$, is given by

$$\mathbf{P}_{\text{MU}}(\boldsymbol{\theta}) = \frac{\mathbf{a}(\boldsymbol{\theta})\mathbf{a}(\boldsymbol{\theta})^H}{\mathbf{a}(\boldsymbol{\theta})\mathbf{P}_n\mathbf{a}(\boldsymbol{\theta})^H}, \tag{11}$$

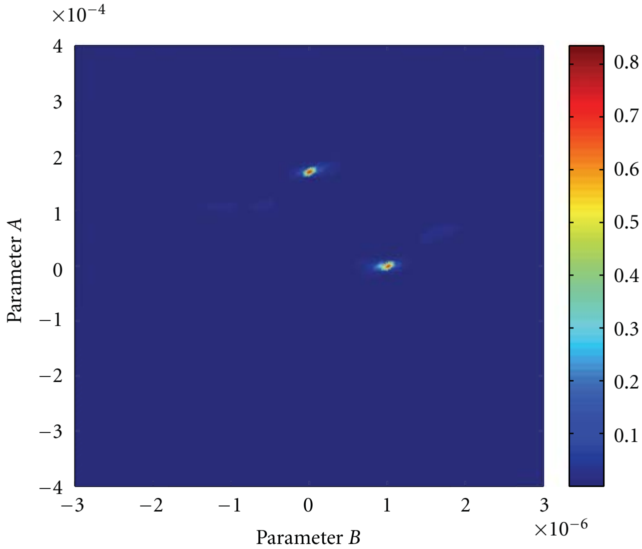

Figure 9: Correlated sources: Determination of parameters A and B based on MUSIC for a diffractor and a dipping reflector $\beta = 20^0$. The black stars show the correct parameter locations.

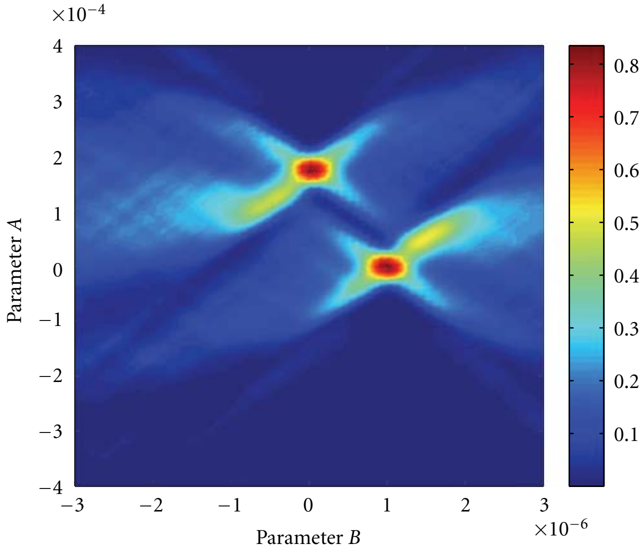

Figure 10: Correlated sources: Determination of parameters A and B based on semblance for a diffractor and a dipping reflector $\beta = 20^0$. The black stars show the correct parameter locations.

where $\mathbf{a}(\boldsymbol{\theta})$ is the test steering vector and $\mathbf{P}_n$ is the noise subspace projection matrix given by $\mathbf{P}_n = \mathbf{U}_n\mathbf{U}_n^H$. Since the steering vectors $\mathbf{a}(\boldsymbol{\theta})$ are orthogonal to the eigenvectors spanning the noise subspace $\mathbf{u}_n$, it follows that the parameter estimates will occur at those parameter values for which we have

$$\mathbf{a}(\boldsymbol{\theta})\mathbf{P}_n\mathbf{a}(\boldsymbol{\theta})^H \approx 0. \tag{12}$$

This corresponds to large peaks in the MUSIC pseudospectrum as given by (11).

2.3. Wideband Uncorrelated Signals. As indicated above, the MUSIC algorithm was originally developed for narrowband and uncorrelated signal applications. If the condition of uncorrelated signals is maintained, an alternative to this situation is to decompose a wideband data into narrowband data components and then treat each narrowband separately [10]. The MUSIC pseudospectrum at the center angular frequency ω_i of the ith narrowband now takes the form

$$\mathbf{P}_{MU}(\boldsymbol{\theta};\omega_i) = \frac{\mathbf{a}(\boldsymbol{\theta};\omega_i)\mathbf{a}(\boldsymbol{\theta};\omega_i)^H}{\mathbf{a}(\boldsymbol{\theta};\omega_i)\mathbf{P}_n(\omega_i)\mathbf{a}(\boldsymbol{\theta};\omega_i)^H}, \tag{13}$$

where $\mathbf{a}(\boldsymbol{\theta};\omega_i)$ and $\mathbf{P}_n(\omega_i)$ are respectively the test steering vector and the noise subspace projection matrix at the ith center angular frequency ω_i. The strategy followed in this work is to Fourier transform the test data and select a narrowband close to the center frequency of the source pulse as input to MUSIC.

3. Seismic Music: Wideband and Correlated Signals

Seismic signals are highly correlated and require a special modification to be used by the original MUSIC algorithm. The consequence of having correlated sources is that there will be a rank deficiency in the source covariance matrix $\mathbf{R}_s$ that will result in a mix of signal and noise subspaces. As a result, the MUSIC algorithm will loose its power to peak at the "right" parameters.

In order to handle correlated sources, spatial smoothing over the covariance matrix, can be employed [10]. The idea is to subdivide the array of N_r sensors into K identical overlapping subarrays of $N_r - K + 1$ receivers (cf. Figure 2) and then compute the covariance for all the subarrays and average the result. If the covariance matrix for subarray k is $\mathbf{R}_k$, the spatially smoothed covariance is given by

$$\mathbf{R}_K = \frac{1}{K}\sum_{k=1}^{K}\mathbf{R}_k. \tag{14}$$

To be able to implement spatial smoothing within seismics, one has to taper the data within a window following the event(s) (cf. Figure 1). The purpose of this tapering is to make the delay times of the event linear (which is the basic requirement behind spatial smoothing) [10].

The other advantage of performing the analysis in a given window is to make the steering vectors, required for generating the MUSIC pseudospectrum, to be frequency independent. This allows us to handle wideband seismic data. This process of windowing the event can also be interpreted as steering of the correlation matrix before eigendecomposition and using unity steering vectors for generating the MUSIC pseudospectrum [4].

Ideally, when the window is "perfectly" matching the event, which will be the case of an optimal choice of the moveout parameters, the signal would be flattened and all traces will nearly have the same moveout. As a consequence, the steering vectors used in (11) will be simply replaced by a vector of ones making them frequency independent. In

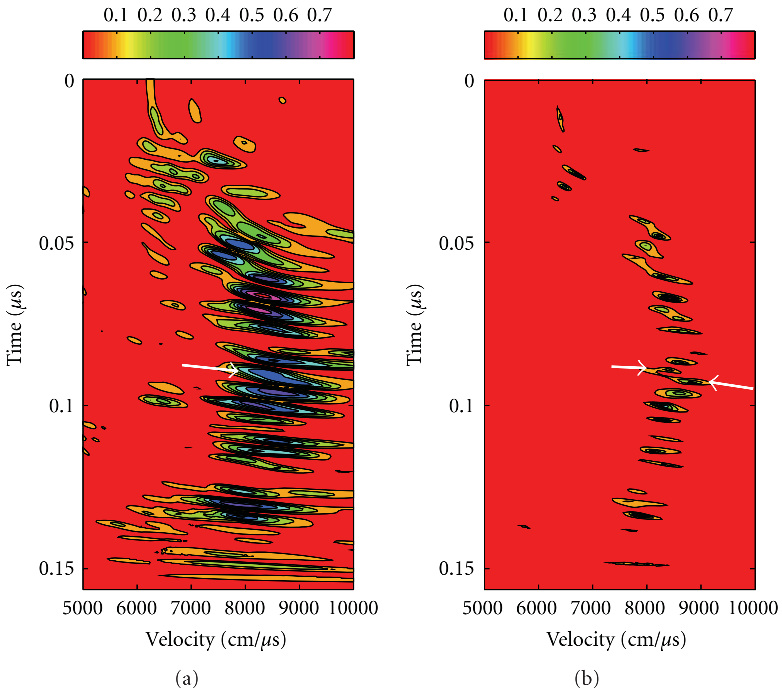

Figure 11: Velocity spectra obtained employing, respectively, semblance (a) and SB-MUSIC (b). The white arrows indicate the apparent single event associated with semblance and the corresponding two events computed from SB-MUSIC.

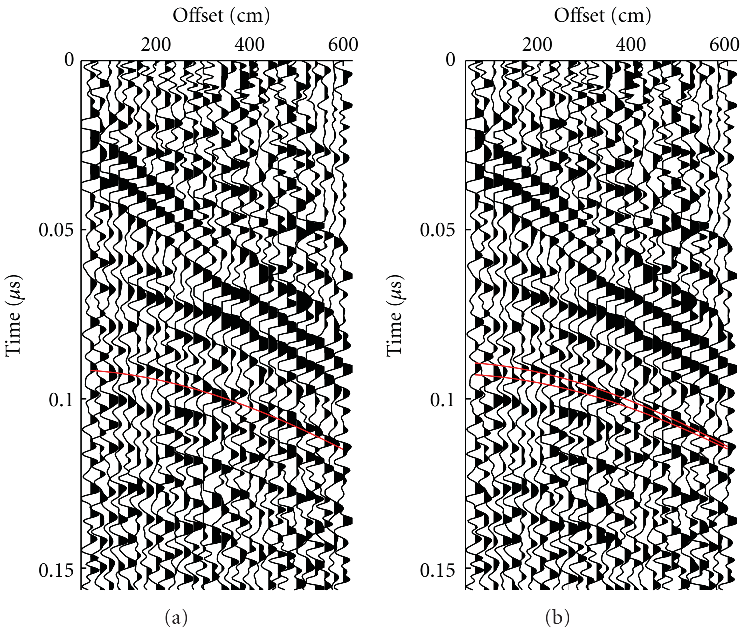

Figure 12: CMP gather superimposed the hyperbolic moveouts (red curves) for the interfering events based on semblance (a) and SB-MUSIC (b).

this situation, the MUSIC pseudospectrum generates a peak resulting in the identification of the optimal estimates of the parameters.

In practice, the windows are constructed by moveouts, defined by trial parameters. Peaking of the corresponding MUSIC pseudospectra identifies, thus, the "correct" parameters. Following this approach, [4] has shown that MUSIC can be applied for the single-parameter case of velocity analysis. The objective was, thus, to obtain a high-resolution velocity spectrum. In this work, we extend that strategy to the CRS

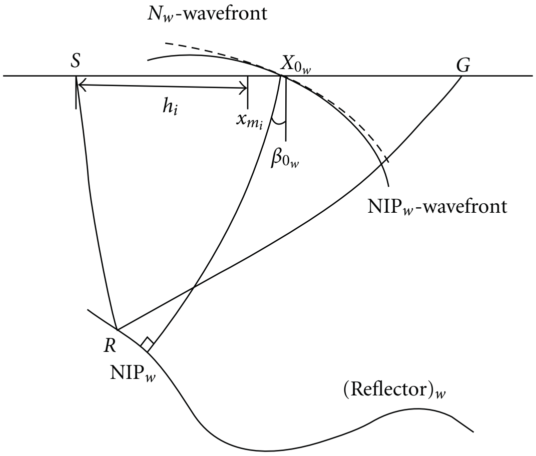

Figure 13: CRS parameters for a given source-receiver pair around a central ray at x_{0_w}.

multi-parameter estimating problem. In other words, our objective is to obtain high-resolution estimates of the CRS parameters, which are three in the present 2D situation.

4. Numerical Examples

In this section, we compare MUSIC and semblance for travel-time parameter estimation in the situations of classical MUSIC (narrowband uncorrelated signals) and seismic MUSIC (wideband correlated signals). For a simple model of a point diffractor and a dipping reflector with a homogeneous overburden, we analyzed the cases: (a) CMP configuration, which requires the determination of a single parameter, C of CRS travel-time (cf. (A.1)) and (b) ZO configuration, which requires the determination of two parameters, namely, parameters A and B of the CRS travel-time (cf. (A.1)). The two events (diffraction and reflection) were chosen to be almost undistinguishable. All the test parameter points with RMS velocities within [1000 : 4000] m/s (step size 7.5 m/s) were tested for parameter C and points within $[-4\times10^{-4} : 4\times10^{-4}]$ (step size 1×10^{-5}) for parameter A and points within $[-3\times10^{-6} : 3\times10^{-6}]$ (step size 1×10^{-7}) for parameter B. As seen below, in all situations, MUSIC performed much better then semblance.

4.1. Classical Music. To illustrate the application of MUSIC for narrowband uncorrelated signals, we considered a point diffractor and a dipping reflector illuminated under a CMP configuration. For a given CMP gather, the data consists of (compare with (5))

$$d_i(t) = s_{\text{diff}}(t)\exp(-i\omega\tau_{\text{diff}}) + s_{\text{dip}}(t)\exp\left(-i\omega\tau_{\text{dip}}\right) + n_i(t), \tag{15}$$

where s_{diff} and s_{dip} are the sources and τ_{diff} and τ_{dip} are the travel-times for the diffractor and dipping reflector events, respectively. Moreover, $n_i(t)$ is the additive noise. The travel-times for these two events are described by the ordinary NMO equations

$$\tau^2_{\text{diff}}(h) = \tau_0^2 + C_{\text{diff}}h^2, \qquad \tau^2_{\text{dip}}(h) = \tau_0^2 + C_{\text{dip}}h^2, \tag{16}$$

where the velocity coefficients for the diffractor, C_{diff}, and dipping reflector, C_{dip}, are given by

$$C_{\text{diff}} = \frac{4}{v^2_{\text{RMS}}}, \qquad C_{\text{dip}} = \frac{4\cos^2\beta}{v^2_{\text{RMS}}}. \tag{17}$$

Here, v_{RMS} and β represent the root mean square (RMS) velocity and the dip angle, respectively.

The sources, $s_{\text{diff}}(t)$ and $s_{\text{dip}}(t)$ are produced by a single narrowband source, $s(t)$, modified by two realizations of a random phase perturbation, $\phi_{\text{diff}}(\omega)$ and $\phi_{\text{dip}}(\omega)$, so as to produce uncorrelated sources. In frequency domain, this process is generally described as

$$\begin{aligned} s_{\text{diff}}(\omega) &= s(\omega)\exp\left[i\phi_{\text{diff}}(\omega)\right], \\ s_{\text{dip}}(\omega) &= s(\omega)\exp\left[i\phi_{\text{dip}}(\omega)\right]. \end{aligned} \tag{18}$$

A synthetic CMP gather was generated employing (15), (16), and (18) together with a Ricker zero-phase wavelet with a center frequency of 20 Hz (cf. Figure 3). The fold was 40 representing a half-offset range from 40 m to 820 m. The data was sampled with 2 ms and white Gaussian noise with a variance of 10% of the maximum trace amplitude was added. The parameter estimation process was benchmarked using the classical semblance analysis of [2].

The output from MUSIC (cf. (13)) is shown in Figure 5 together with the result obtained using semblance. For both cases we used, a window size of 11 samples and in addition for MUSIC we considered two signal subspaces and the rest as noise subspaces. As a result, MUSIC is seen to outperform semblance and resolve the two parameters well. It is well known that the values output from MUSIC are arbitrary. To avoid this phenomenon, we have introduced a *semblance balancing*. This technique is discussed in detail in connection with the real-data example presented below.

To perform a two-parameter test, we have now simulated a zero-offset (ZO) section for the same previous point diffractor and dipping reflector (cf. Figure 4). The corresponding two ZO travel-times for diffraction and reflection are now given by

$$\begin{aligned} \left[\tau_{\text{diff}}(x_m)\right]^2 &= \tau_0^2 + B_{\text{diff}}(x_m - x_0)^2, \\ \left[\tau_{\text{dip}}(x_m)\right]^2 &= \tau_0 + A_{\text{dip}}[(x_m - x_0)]^2, \end{aligned} \tag{19}$$

with $B_{\text{diff}} = C_{\text{diff}}$ and $A_{\text{dip}} = 1.71\times10^{-4}$ (corresponding to a dip of 20^0 and a homogeneous medium with constant velocity 2000 m/s). As seen from the Appendix, the above equations represent the generalized hyperbolic (CRS) travel-time of equation (A.1), in which the conditions

$$B_{\text{diff}} = C_{\text{diff}}, \qquad B_{\text{dip}} = 0, \tag{20}$$

have been implemented. As indicated in the Appendix, the far-left equation above represents the diffraction condition. The far-right equation is due to the fact that in this considered experiment, the N-wave is planar.

Based on (19), using the previous uncorrelated sources (18), synthetic ZO data were computed for midpoints between 40 m and 1040 m. The results from the two-parameter search (A and B) are shown for, respectively, MUSIC (cf. Figure 6) and semblance (cf. Figure 7). MUSIC gives well-resolved results, as opposed to the semblance, where the estimated parameters are more inaccurate.

4.2. Seismic Music. To examine the performance of MUSIC compared to semblance in case of wideband correlated signals, we generated synthetic data based on the travel-time (16) for a CMP gather and (19) for a ZO section. The parameter search was performed within a time window of 25 time samples with the ZO travel-time being the middle sample and following a hyperbolic delay trajectory defined by the travel-times. For the computation of the MUSIC pseudospectrum, the samples within the hyperbolic window were used to form the data covariance matrix and the associated eigendecomposition. In order to reduce the correlated source effect we performed spatial smoothing of the covariance matrix using 31 subarrays each consisting of 10 receivers for the CMP data and 37 subarrays each consisting of 15 receivers for the ZO data.

The results of the parameter search is shown in Figure 8 for the CMP data (i.e., determination of parameter C) and Figures 9 and 10 for the ZO section (i.e., determination of parameters A and B). It is apparent that both semblance and MUSIC can resolve parameters A and B, but MUSIC shows a higher resolution in general. Moreover, for parameter C only MUSIC is able to resolve the two events.

4.3. Real Data Example Using GPR Data. The first step of the CRS analysis determining the C parameter can be regarded as a CMP-based velocity analysis. As indicated by our previous synthetic data example, MUSIC was seen to have a better potential than semblance for resolving interfering events (cf. Figures 5 and 8). We will now investigate whether that feature is confirmed in real data. Prior to our analysis, however, the following normalization issue has to be considered. As opposed to semblance, which produces normalized values between 0 and 1, MUSIC, despite its high-resolution capability, yields arbitrary amplitude values. Such behavior makes the simple replacement of semblance with MUSIC as a coherency measure, for example, in standard velocity analysis, not adequate.

In order to condition MUSIC to be a normalized quantity, we introduce a scaled version of it, denoted by *semblance-balanced* MUSIC or, more simply, SB-MUSIC. In the framework of velocity analysis, SB-MUSIC is defined as follows: for a given CMP location, as well as a selection of N zero-offset time samples, t_i and M trial stacking velocities, V_j, we let m_{ij} and s_{ij} represent the coherency values obtained from MUSIC and semblance, respectively. In other words, (m_{ij}) and (s_{ij}) represent $N \times M$ velocity spectra associated with MUSIC and semblance coherency measures. Denoted by $\widehat{m}_{ij}$, SB-MUSIC is given by

$$\widehat{m}_{ij} = \frac{A_{s,i}}{A_{m,i}} m_{ij}, \tag{21}$$

where

$$A_{s,i} = \sqrt{\sum_{k=1}^{M} s_{ik}^2}, \qquad A_{m,i} = \sqrt{\sum_{k=1}^{M} m_{ik}^2}. \tag{22}$$

Application of the above conditioning makes sure that those amplitude anomalies inherent to the original MUSIC velocity spectrum are *balanced* according to the energy level of semblance.

A real multioffset GPR data set was used to test out the feasibility of this approach. For an in depth description and discussion of these data, the readers are referred to [11]. Figure 11 shows an example of a typical velocity spectrum obtained from the GPR data using both semblance and SB-MUSIC. In these computations, we used a window size of eleven samples for both semblance and MUSIC. In addition, we performed spatial smoothing of subarray size 15 from a fold of 28 to ensure that MUSIC handles the correlated GPR signals properly. Figure 11 clearly demonstrates that interfering events are much better resolved in the SB-MUSIC spectrum (Figure 11(b)) than in its corresponding semblance spectrum (Figure 11(a)). In particular, as indicated by white arrows, it can be seen how two interfering events are unresolved by semblance (Figure 11(a)) and well resolved by SB-MUSIC (Figure 11(b)). To further validate the previous observation, the hyperbolic moveout curves corresponding to those two events were superimposed to the corresponding CMP-gather (cf. Figure 12(b)). These curves seem to correlate well with two interfering events. As a reference, the result obtained using semblance is also included (cf. Figure 12(a)). It can be regarded as a fit based on a mix between the two interfering events.

5. Conclusions

In this paper, we discussed the CRS travel-time parameters estimation problem in seismic signal processing. The conventional semblance algorithm was found to generate lower-resolution estimates of the parameters. For the purpose of obtaining higher-resolution parameter estimates, we replaced semblance with MUSIC algorithm. Such procedure allowed us to estimate the parameters within a resolution limit that is significantly better. This work can be seen as a followup of previous applications of MUSIC to single-parameter velocity analysis and slant stacks. Now, MUSIC has been extended to Common-Reflection-Surface (CRS) multiparameter estimation. Applications of the technique to first synthetic examples, consisting of dipping planar reflectors and point diffractors, and comparison to semblance, confirm, at least for these initial situations, the expected far better resolution of MUSIC. To further support this analysis, CMP velocity analysis has been applied to a real multioffset GPR data set. In this situation, better results were obtained upon the introduction of a scaled version of MUSIC, denoted semblance-balanced MUSIC. The new algorithm was seen to outperform semblance in resolving interfering events.

Appendix

General Hyperbolic Moveout

The CRS method uses the so-called generalized hyperbolic (normal) moveout, which is the natural generalization of the NMO, valid for CMP gathers, to CRS supergathers, in which source-receiver pairs are arbitrarily located around the (reference) central point, usually taken as a CMP. In 2D, the generalized hyperbolic moveout depends on three parameters, as opposed to conventional NMO, which depends on a single parameter (NMO velocity).

Mathematically, the generalized hyperbolic moveout, $\tau_{i,w}$, associated with the event, w, measured at receiver i, is specified by the zero-offset (ZO) travel-time, τ_{0_w}, and (reference) trace location, x_{0_w}, and given by (see Figure 13)

$$\left[\tau^{\theta}_{i,w}(x_{m_i},h_i)\right]^2 = \left[\tau_{0_w} + A_w(x_{m_i}-x_{0_w})\right]^2 + B_w(x_{m_i}-x_{0_w})^2 + C_w \mathrm{h}_i^2, \tag{A.1}$$

where x_{m_i} is the midpoint coordinate and h_i is the half-offset coordinate for the ith receiver. Here,

$$\boldsymbol{\theta} = \{\mathrm{A}_w, \mathrm{B}_w, \mathrm{C}_w\} \tag{A.2}$$

is the CRS parameter vector, with three parameters, A_w, B_w and C_w, to be estimated from the data. It is instructive to recall that these parameters are related to the angle and curvature quantities as follows [12]:

$$A_w = \frac{2\sin\beta_{0_w}}{v_{0_w}}, \qquad B_w = \frac{2\tau_{0_w}\cos^2\beta_{0_w}}{v_{0_w}} K_{N_w}, \qquad C_w = \frac{2\tau_{0_w}\cos^2\beta_{0_w}}{v_{0_w}} K_{\mathrm{NIP}_w}, \tag{A.3}$$

where K_{N_w} and K_{NIP_w} are the curvatures of respectively the normal (N) and normal-incident-point (NIP) wavefronts, β_{0_w} is the emergence angle and v_{0_w} is the medium velocity. All these quantities are evaluated at the central point, x_{0_w}. Still considering the CRS parameters, we make the following observations

(a) In the CMP configuration of source-receiver pairs symmetrically located with respect to the central point, namely, $x_{m_i} = x_{0_w}$, we have

$$\left[\tau^{\theta}_{i,w}(h_i)\right]^2 = \tau^2_{0_w} + C_w h_i^2, \tag{A.4}$$

with the CMP, single parameter vector $\boldsymbol{\theta} = \{C_w\}$. Moreover, we have the relation

$$C_w = \frac{4}{v^2_{\mathrm{NMO}}}, \tag{A.5}$$

with C_w given by the lower-most (A.3).

(b) In case the recorded data stems from a diffraction, the condition $B_w = C_w$ holds. This is because as the reflector shrinks to a point, the N-wave turns out to be identical to the NIP-wave [13]. As a consequence, the hyperbolic moveout of diffraction (or *diffraction travel-time*), reduces to

$$\left[\tau^{\theta}_{i,w}(x_{m_i},h_i)\right]^2 = \left[\tau_{0_w} + A_w(x_{m_i}-x_{0_w})\right]^2 + B_w\left[(x_{m_i}-x_{0_w})^2 + h_i^2\right], \tag{A.6}$$

with the diffraction, two-parameter vector $\boldsymbol{\theta} = \{A_w, B_w\}$.

Acknowledgments

The authors would like to thank Dr. Hervé Perroud for providing the GPR dataset. E. Asgedom has been funded by a PhD grant from the University of Oslo and the Norwegian Science Foundation. This work has been carried out partly while he was visiting State University of Campinas. M. Tygel acknowledges support of the Brazilian Council of Scientific and Technological Development (CNPq) and the sponsors of the Wave Inversion Technology (WIT) Consortium.

References

[1] T. Taner and F. Koehler, "Velocity spectra—digital computer derivation and applications of velocity functions," *Geophysics*, vol. 34, no. 6, pp. 859–881, 1969.

[2] N. Neidell and M. Taner, "Semblance and other coherency measures for multichannel data," *Geophysics*, vol. 36, pp. 482–497, 1971.

[3] B. Gelchinsky, E. Landa, and V. Shtivelman, "Algorithms of phase and group correlation," *Geophysics*, vol. 50, no. 4, pp. 596–608, 1985.

[4] R. L. Kirlin, "The relationship between semblance and eigenstructure velocity estimators," *Geophysics*, vol. 57, no. 8, pp. 1027–1033, 1992.

[5] W. Du and R. L. Kirlin, "Discrimination power enhancement via high resolution velocity estimators," in *Proceedings of the IEEE Acoustics, Speech, and Signal Processing*, vol. 4, pp. 13–16, Minneapolis, Minn, USA, 1993.

[6] K. Larner and V. Celis, "Selective-correlation velocity analysis," *Geophysics*, vol. 72, no. 2, pp. U11–U19, 2007.

[7] S. Luo and D. Hale, "Velocity analysis using weighted semblance," *SEG Expanded Abstracts*, pp. 4093–4097, 2010.

[8] M. Sacchi, "A bootstrap procedure for high-resolution velocity analysis," *Geophysics*, vol. 63, no. 5, pp. 1716–1725, 1998.

[9] R. O. Schmidt, "Multiple emitter location and signal parameter estimation," *IEEE Transactions on Antennas and Propagation*, vol. 34, no. 3, pp. 276–280, 1986.

[10] B. Biondi and C. Kostov, "High-resolution velocity spectra using eigenstructure methods," *Geophysics*, vol. 54, no. 7, pp. 832–842, 1989.

[11] H. Perroud and M. Tygel, "Velocity estimation by the common-reflection-surface (CRS) method: using ground-penetrating radar data," *Geophysics*, vol. 70, no. 6, pp. B43–B52, 2005.

[12] R. Jäger, J. Mann, G. Höcht, and P. Hubral, "Common-reflection-surface stack: image and attributes," *Geophysics*, vol. 66, no. 1, pp. 97–109, 2001.

[13] Y. Zhang, S. Bergler, and P. Hubral, "Common-reflection-surface (CRS) stack for common offset," *Geophysical Prospecting*, vol. 49, no. 6, pp. 709–718, 2001.

Hindawi Publishing Corporation
International Journal of Geophysics
Volume 2011, Article ID 530106, 5 pages
doi:10.1155/2011/530106

Research Article

Migration Using a Transversely Isotropic Medium with Symmetry Normal to the Reflector Dip

Tariq Alkhalifah[1] and Paul Sava[2]

[1] *King Abdullah University of Science and Technology, Thuwal, Saudi Arabia*
[2] *Center for Wave Phenomena, Colorado School of Mines, Golden, CO 80401, USA*

Correspondence should be addressed to Tariq Alkhalifah, tariq.alkhalifah@kaust.edu.sa

Received 14 December 2010; Accepted 10 March 2011

Academic Editor: Martin Tygel

A transversely isotropic (TI) model in which the tilt is constrained to be normal to the dip (DTI model) allows for simplifications in the imaging and velocity model building efforts as compared to a general TI (TTI) model. Although this model cannot be represented physically in all situations, for example, in the case of conflicting dips, it handles arbitrary reflector orientations under the assumption of symmetry axis normal to the dip. Using this assumption, we obtain efficient downward continuation algorithms compared to the general TTI ones, by utilizing the reflection features of such a model. Phase-shift migration can be easily extended to approximately handle lateral inhomogeneity using, for example, the split-step approach. This is possible because, unlike the general TTI case, the DTI model reduces to VTI for zero dip. These features enable a process in which we can extract velocity information by including tools that expose inaccuracies in the velocity model in the downward continuation process. We test this model on synthetic data corresponding to a general TTI medium and show its resilience.

1. Introduction

Migration velocity analysis (MVA), despite the many developments in recent years, is still a challenging process especially in complex media. MVA is even more of a challenge in anisotropic media in which the medium is described by several parameters, all of which can change as a function of position. Anisotropy introduces flexibility to the model to better simulate the Earth subsurface, but it also introduces a null space to the parameter estimation process or MVA. As a result, we need to use anisotropy to allow for more freedom up to the point where data seize to influence the model, or even part of it. This anisotropy null-space tradeoff has recently guided us to using a transversely isotropic (TI) medium with a tilted axis of symmetry (TTI). To avoid the null space, such tilt is assumed to be in the direction of the dip [1, 2]. In fact, Audebert et al. [2] referred to this medium as structurally conformed transversely isotropic (STI), in which parameter description becomes simpler by fixing the symmetry axis to be normal to the structure. In their formulation, the symmetry axis field is measured from the image (a representation of the structure) and used along with regular TTI equations to implement migration and velocity analysis.

In transversely isotropic with vertical symmetry axis (VTI) media, the acoustic problem can be described by three parameters [3]: the velocity in the symmetry direction, the normal-moveout (NMO) velocity measured with respect to the symmetry direction (related to the second derivative of the phase velocity with respect to phase angle at the symmetry direction), and an anisotropy parameter that relates the NMO velocity to the velocity in the direction normal to the symmetry axis, usually labeled η. For TI media with a tilt in the axis of symmetry, two angles, that describe the tilt in 3D, are also needed to fully characterize acoustic wave propagation.

Alkhalifah and Sava [4] introduce the concept of using the assumption that symmetry axis is normal to the reflector dip as a constrain to develop simplified and explicit representations for moveout in extended images, for angle gather mapping, and for migration. They refer to the model as dip-constrained TI (DTI). In this paper, we use the explicit formulations provided by the DTI model to perform downward continuation and discuss its potential for TTI parameter estimation. In this context, many of the familiar tools developed for the isotropic case apply with little or no modifications. We utilize this to build a framework for imaging and velocity model building for DTI models and illustrate the method with synthetic data.

2. Downward Continuation

Downward continuation, with the double-square equation in the DTI framework, utilizes the equal incidence and reflection angles imposed by the constraint. As shown by Alkhalifah and Sava [4], the downward continuation process includes two steps: determining the offset wavenumber corresponding to a particular reflection angle and then using the offset wavenumber to determine the required phase shift based on the double-square-root (DSR) equation. The two steps are given by explicit equations that can be implemented using the algorithm suggested by Alkhalifah and Sava [4].

Considering that angle gather extraction is a localized process relying on the plane wave behavior around the scattering point, it is applicable, within the limits of high frequencies compared to medium variations, to complex media. To allow the DSR-based downward continuation to honor lateral inhomogeneity at least approximately, we can utilize the phase-shift-plus-interpolation concept [5]. In this case, we downward continue multiple times for various symmetry-direction anisotropy parameters and then interpolate the wavefields using the lateral velocity information in space. However, the split-step approach of Stoffa et al. [6] lends itself better to this approach as we maintain reflection angle information in the space domain needed for a good zero-dip velocity, $v(x, y, z)$, correction.

Wavefield reconstruction for multioffset migration based on the one-way wave equation under the survey-sinking framework [7] is implemented by recursive phase shift of prestack wavefields

$$u_{z+\Delta z}(\mathbf{m},\mathbf{h}) = e^{-ik_z\Delta z} u_z(\mathbf{m},\mathbf{h}), \tag{1}$$

followed by extraction of the image at time $t = 0$. Here, $\mathbf{m}$ and $\mathbf{h}$ represent the midpoint and half offset coordinates. In (1), $u_z(\mathbf{m},\mathbf{h})$ represents the acoustic wavefield for a given frequency ω at all midpoint positions $\mathbf{m}$ and half offsets $\mathbf{h}$ at depth z, and $u_{z+\Delta z}(\mathbf{m},\mathbf{h})$ represents the same wavefield extrapolated to depth $z + \Delta z$. The phase shift in laterally homogeneous media is given by the depth wavenumber k_z which is defined by the DSR formula. In the case of the 2D DTI model, the dispersion relation is given by the following formula [4]:

$$\begin{aligned} k_z &= k_{zs} + k_{zr} \\ &= \sqrt{\frac{\omega^2}{v_p^2(\theta)} - (k_m - k_h)^2} + \sqrt{\frac{\omega^2}{v_p^2(\theta)} - (k_m + k_h)^2}, \end{aligned} \tag{2}$$

where ω is the angular frequency, k_m is the midpoint wavenumber, v_p is the phase velocity as a function of the reflection angle (half of the scattering angle for DTI), θ, and k_{zs} and k_{zr} are the source and receiver vertical wavenumbers, respectively. The offset wavenumber, k_h, is evaluated using the following formula:

$$k_h^2(\theta) = \left(\frac{2\omega\sin\theta}{v_p(\theta)}\right)^2 - k_m^2\tan^2\theta. \tag{3}$$

To implement such a phase shift downward continuation, we loop, per depth step, over ω, k_m, and most importantly θ. The phase velocity used in (2) can be regarded as a reference velocity in laterally inhomogeneous media corresponding to anisotropy parameters, for example, from the center of the model. For a split-step implementation, we apply a space domain correction corresponding to zero dip. Thus, the phase correction in the space domain has the following form:

$$k_{zc} = 2\sqrt{\frac{\omega^2}{v_p^2(x,\theta)} - k_h^2} - 2\sqrt{\frac{\omega^2}{v_p^2(\theta)} - k_h^2}, \tag{4}$$

where $v_p(x,\theta)$ is the laterally varying phase velocity corresponding to anisotropic parameters at their space location. The offset wave number is given now by a simpler equation

$$k_h(x,\theta) = \frac{2\omega\sin\theta}{v_p(x,\theta)}. \tag{5}$$

For completeness, the laterally varying phase velocity for TI media is given as

$$\begin{aligned} v_p^2(x,\theta) &= \frac{1}{2}\left(a\sin^2\theta + b\cos^2\theta\right) \\ &\quad + \frac{1}{4}\sqrt{4a^2\sin^4\theta + 2ab\sin^2(2\theta) + 4b^2\cos^4\theta}, \end{aligned} \tag{6}$$

where $a = v^2(x)(1+2\eta(x))$, $b = v_T^2(x)$, v_T is the velocity in the symmetry direction, v is the NMO velocity with respect to the symmetry axis, and η is the anisotropy parameter relating the NMO velocity to the velocity normal to the symmetry axis. The angle θ in (6) is measured from the symmetry axis. Here, we are relying on the zero dip for the lateral correction, though the model is DTI, which implies a VTI model for this dip.

3. Velocity Analysis

Having an analytical representation for the migration operator allows us to develop migration analysis tools. The dependency of the migration operator on medium parameters is at the heart of such developments. Using the Sava and Vlad [8] approach to develop the velocity analysis operator in 3D, we can assume the separation of the extrapolation slowness $s(\mathbf{m}) = 1/v_p^2(\theta)$ into a background component $s_0(\mathbf{m})$ and an unknown perturbation component $\Delta s(\mathbf{m})$. Then, we can construct a wavefield perturbation $\Delta u(\mathbf{m},\mathbf{h})$ at depth z and frequency ω related linearly to the slowness perturbation $\Delta s(\mathbf{m})$. Linearizing the depth wavenumber given by the DSR equation (2) relative to the background slowness $s_0(\mathbf{m})$, we obtain

$$k_z \approx k_{z0} + \left.\frac{dk_{zs}}{ds}\right|_{s_0}\Delta s(\mathbf{m}-\mathbf{h}) + \left.\frac{dk_{zr}}{ds}\right|_{s_0}\Delta s(\mathbf{m}+\mathbf{h}), \tag{7}$$

where the depth wavenumber in the background medium is

$$k_{z0} = \sqrt{[\omega s_0(\mathbf{m}-\mathbf{h})]^2 - \left|\frac{\mathbf{k_x}-\mathbf{k_h}}{2}\right|^2} + \sqrt{[\omega s_0(\mathbf{m}+\mathbf{h})]^2 - \left|\frac{\mathbf{k_x}+\mathbf{k_h}}{2}\right|^2}, \tag{8}$$

and $\mathbf{k_x}$ and $\mathbf{k_h}$ are the wavenumber vectors for the midpoint and half offset, respectively, in 3D. Here, $s_0(x,\theta)$ represents the spatially variable *background* slowness at depth level z. Using the wavenumber linearization given by (7), we can reconstruct the acoustic wavefields in the background model using a phase-shift operation

$$u_{z+\Delta z}(\mathbf{m},\mathbf{h}) = e^{-ik_{z0}\Delta z}u_z(\mathbf{m},\mathbf{h}). \tag{9}$$

We can represent wavefield extrapolation using a generic solution to the one-way wave equation. This indicates that the wavefield $u_{z+\Delta z}(\mathbf{m},\mathbf{h})$ is reconstructed from the wavefield $u_z(\mathbf{m},\mathbf{h})$ using the background slowness $s_0(\mathbf{m})$. This operation is repeated independently for all frequencies ω.

However, our desire is to relate the wavefield perturbation directly to medium perturbation, not just the phase velocity. For the DTI model, $s(\mathbf{m})$ is dependent on the TI model parameters, which for the acoustic case are v_T, v, and η. Thus, (7) becomes

$$\begin{aligned} k_z \approx k_{z0} &+ \frac{dk_{zs}}{ds}\frac{\partial s}{\partial v_T}\bigg|_{s_0}\Delta v_T(\mathbf{m}-\mathbf{h}) \\ &+ \frac{dk_{zs}}{ds}\frac{\partial s}{\partial v}\bigg|_{s_0}\Delta v(\mathbf{m}-\mathbf{h}) \\ &+ \frac{dk_{zs}}{ds}\frac{\partial s}{\partial \eta}\bigg|_{s_0}\Delta \eta(\mathbf{m}-\mathbf{h}) \\ &+ \frac{dk_{zr}}{ds}\frac{\partial s}{\partial v_T}\bigg|_{s_0}\Delta v_T(\mathbf{m}+\mathbf{h}) \\ &+ \frac{dk_{zr}}{ds}\frac{\partial s}{\partial v}\bigg|_{s_0}\Delta v(\mathbf{m}+\mathbf{h}) \\ &+ \frac{dk_{zr}}{ds}\frac{\partial s}{\partial \eta}\bigg|_{s_0}\Delta \eta(\mathbf{m}+\mathbf{h}), \end{aligned} \tag{10}$$

where $s(\mathbf{m}) = 1/v_p^2(\theta)$ is given by (6), and thus, the partial derivatives in (10) can be obtained analytically. We can focus on perturbation in one parameter (i.e, η) and thus end up with a one-to-one linearized relation between the image field and that parameter. For a detailed implementation of such an approach, we refer to [8].

4. Dip-Constrained TTI: Not a Physical Model

One question that arises is how does the DTI constraint be imposed on a model? Specifically, what happens when we have conflicting dips? For the equations developed here and especially those of Alkhalifah and Sava [4], based on a plane wave representation, the DTI constraint is explicitly handled in the formulations. This implies that even for conflicting dips at some position in space, the symmetry axis is always normal to the reflector dip, as if the dips were handled in separate planes. This can not be represented in the physical space, and thus, it is a process. If conflicting dips exist, then the dip that physically adheres to the constraint is handled properly. Figure 1 shows the BP anisotropic model with arrows pointing to conflicting dips. However, the axis of symmetry is single valued, and thus, the DTI model handles the reflections that adhere to this assumption. Nevertheless, conflicting dips are truly conflicting (cross at a point) if the true velocity is used in imaging. Otherwise, their conflict is in an inaccurate position and thus do not reflect the physical behavior of the reflectors.

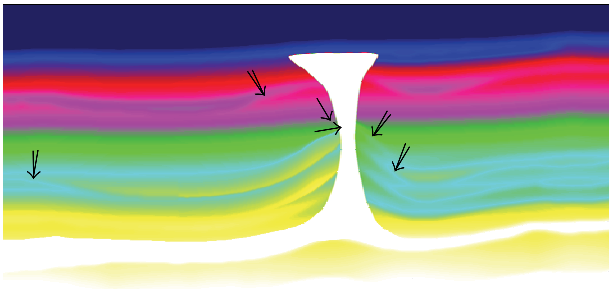

Figure 1: Part of BP anisotropic velocity model that contains a salt body. The abrupt change in velocity magnitude can be interpreted as reflections, and the arrows point to examples of the possible directions of TI symmetry tilt to accommodate a DTI model.

Thus, in the BP model shown in Figure 1, we typically use the reflections that underlay the sediments, especially those near the salt flanks, to constrain the velocity model. These sediments are assumed to be TI with the symmetry axis normal to the layering. In this case, the simplified DTI model can accurately image those sediments at a reduced effort and cost. The effort is typically spent in generating velocity models that include an additional file containing the symmetry axis direction, which is not required in the DTI model. In addition, the cost of using DTI equations is far less than TTI ones, even less than using VTI equations.

5. The Impulse Response

The response of imaging to a dataset that includes pulses reveals some of the features of the operator involved in the imaging process. Here, our input data to the migration includes five pulses at times 0.6, 1.2, 1.8, 2.4, and 3 seconds at zero offset under the common midpoint (CMP) location of 4 km. The medium is vertically inhomogeneous with velocity increasing linearly with depth and $\eta = 0.2$. Figure 2 shows the migration (response) in the prestack domain with coordinates of distance, depth, and angle gather. The three sections here and throughout represent slices in the prestack cube with the black lines representing the location of these slices relative to each other. As a result, the section on the right is simply the angle gather at location 4 km.

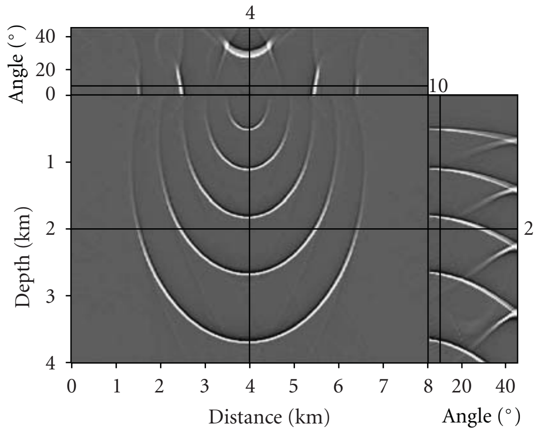

FIGURE 2: The impulse response for the prestack DTI phase-shift migration of 5 pulses at zero offset in a vertically inhomogeneous DTI model with $v(z) = 1.5 + 0.6z$ km/s and $\eta = 0.2$ and $\delta = 0$. The three sections represent slices in the prestack cube with the black lines representing the location of these slices relative to each other. As a result, the section on the right is simply the angle gather at distance 4 km.

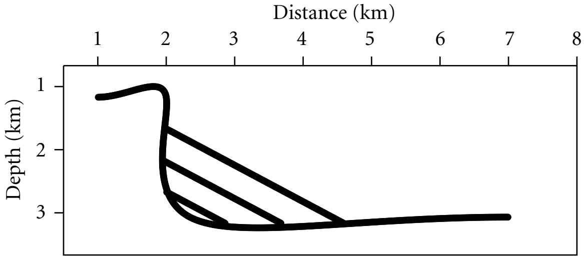

FIGURE 3: A reflector model depicting a salt flank with three parallel reflectors laying alongside the flank. The angle of symmetry is normal to the three reflectors at 30 degrees from the vertical.

As expected, the response is symmetric despite the DTI nature of the medium. Unlike the TTI case, where the symmetry axis is set to a direction, the symmetry axis here is set to be normal to the reflector, and since the response includes all dips, it will also includes all possible symmetry directions. The angle gather behavior of the impulse response completes the saddle shape of the 3D operator.

6. Synthetic Example

In the following example, we use for simplicity a vertically inhomogeneous model, although nothing in the development of processes for DTI requires that. We consider the reflector model in Figure 3, which is made up of a salt-flank-like reflector in addition to three parallel reflectors depicting sediments laid over the salt flank. The TTI in this model has a symmetry axis normal to the three reflectors at 30° angle from vertical. This model allows us to test the DTI concept for these three reflectors by analyzing the angle gather at 2.5 km location. It also allows us to observe the errors for reflectors that do not adhere to the constraint, like the salt flank and semihorizontal reflector. For a velocity of 1.5 km/s at the surface and increasing at a gradient of $0.6\,\mathrm{s}^{-1}$, and $\eta = 0.2$, we generate the prestack synthetic dataset shown in Figure 4. We use Kirchhoff modeling to obtain the synthetic data [9], and despite that the bottom reflector is semihorizontal, the clear influence of the tilt in the symmetry axis resulted in a dipping appearance on the synthetic section.

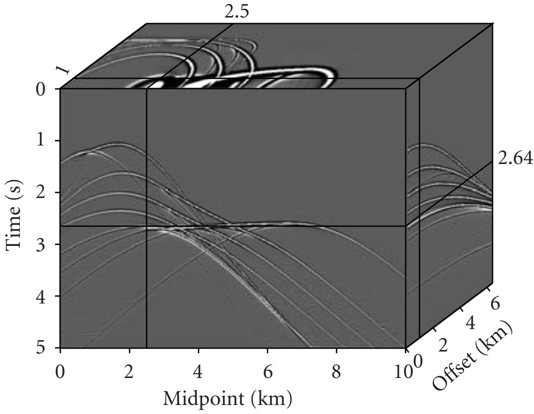

FIGURE 4: Prestack synthetic data generated using Kirchhoff modeling for the TTI model in Figure 3 with velocity (NMO and along the tilt) equals 2 km/s and $\eta = 0.2$.

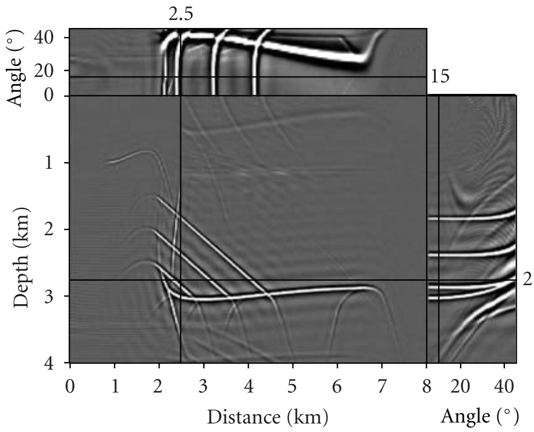

FIGURE 5: Migrated section after an isotropic migration with velocity of 2 km/s of the TTI syntheticdata in Figure 4. The angle gathers obtained using an isotropic mapping at 2.5 km location are displayed on the right, and the top section shows a depth slice as a function of angle gather at depth 2 km.

Conventional phase shift downward continuation requires that no lateral velocity variation be present. Since the synthetic model has no lateral velocity variation, we use the phase-shift approach to migrate the data. However, prior to applying the zero-lag imaging condition, we map the offset wavenumbers to angle and, thus, obtain angle gathers. Figure 5 shows the isotropically migrated section at near zero angle. It also shows on the right hand side the angle gather for isotropic angle decomposition. Clearly, the angle gather includes residuals resulting from ignoring anisotropy. They include predominantly nonhyperbolic errors associated

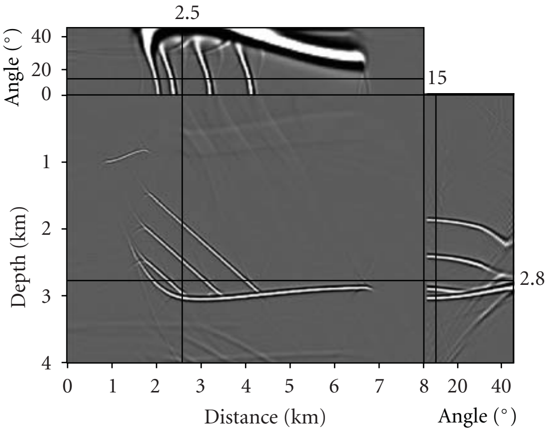

Figure 6: Migrated section after a VTI migration with velocity of 2 km/s and $\eta = 0.2$ of the TTI synthetic data in Figure 4. Again, the angle gathers obtained using an isotropic mapping at 8 km location are displayed on the right, and the top section shows a depth slice as a function of angle gather at depth 2 km.

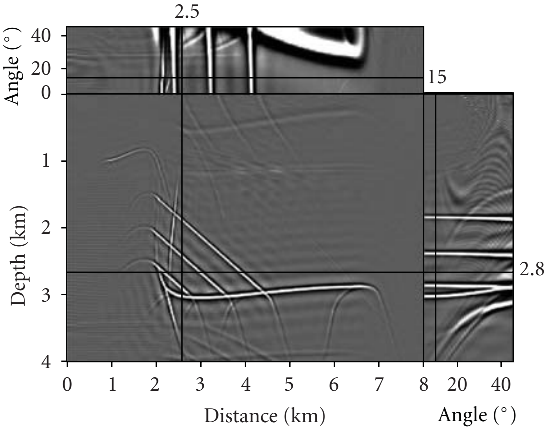

Figure 7: Migrated section after DTI-based migration with velocity of 2 km/s and $\eta = 0.2$ of the TTI synthetic data in Figure 4. The angle gathers obtained, now, using the VTI mapping at 2.5 km location are displayed on the right. The top section shows a depth slice as a function of angle gather at depth 2 km.

with anisotropy with some second-order errors associated with the dip [3]. The top plot in Figure 5 is a 2 km depth slice section and includes some residual error information spanning other angle gathers.

If we downward continue using a VTI phase-shift migration followed by an anisotropic angle gather mapping [10], we obtain the image shown in Figure 6. Both the image and the angle gathers reflect the inaccuracy of the VTI imaging for this TTI model. However, the residual moveout in the angle gathers is less than those for the isotropic case. On the other hand, the phase shift migration under the DTI assumption results in the image and angle gather shown in Figure 7. While the reflections and diffractions associated with angle not normal to the axis of symmetry show clear errors, the three parallel reflections show accurate placement and no residuals in the angle gather. This implies that the parameters used (velocity and η) are accurate within the DTI model that was appropriate to these reflections.

This synthetic test shows an example of the usefulness of the DTI model for analysis of key reflections. Usually, for migration velocity analysis purposes, the symmetry axis is set to be normal to the reflector dip for the reflections used in the analysis, and this is the case even for isotropic layers, which is a special case of DTI where η and δ equal zero.

7. Conclusions

Constraining the symmetry axis of a transversely isotropic medium to be normal to the reflector dip (DTI) allows for explicit formulation of plane waves around the scattering point. These formulations form the basis for angle decomposition and simplified downward continuation. As a result, DTI is a convenient model for anisotropy parameter estimation in media in which such models are applicable. This model also allows us to use the general TTI assumption in a simplified form that better fits the information embedded in the recorded data. A simple synthetic example demonstrated the potential features of this model.

Acknowledgment

The authors thank KAUST and the Center of Wave Phenomena at Colorado School of Mines for their support.

References

[1] T. Alkhalifah and J. Bednar, “Building a 3-D anisotropic model: its implications to traveltime calculation and velocity analysis,” in *Proceedings of the 70th Annual International Meeting, Society of Exploration Geophysicists*, pp. 965–968, 2000.

[2] F. S. Audebert, V. Dirks, and A. Pettenati, “TTI anisotropic depth migration: what tilt estimate should we use?” *SEG Technical Program Expanded Abstracts*, vol. 25, no. 1, pp. 2382–2386, 2006.

[3] T. Alkhalifah and I. Tsvankin, “Velocity analysis for transversely isotropic media,” *Geophysics*, vol. 60, no. 5, pp. 1550–1566, 1995.

[4] T. Alkhalifah and P. Sava, “A transversely isotropic medium with a tilted symmetry axis normal to the reflector,” *Geophysics*, vol. 75, pp. A19–A24, 2010.

[5] J. Gazdag and P. Sguazzero, “Migration of seismic data by phase-shift plus interpolation,” *Geophysics*, vol. 49, no. 2, pp. 124–131, 1984.

[6] P. L. Stoffa, J. T. Fokkema, R. M. de Luna Freire, and W. P. Kessinger, “Split-step Fourier migration,” *Geophysics*, vol. 55, no. 4, pp. 410–421, 1990.

[7] J. F. Claerbout, *Imaging the Earth’s Interior*, Blackwell Scientific Publications, Oxford, UK, 1985.

[8] P. Sava and I. Vlad, “Numeric implementation of wave-equation migration velocity analysis operators,” *Geophysics*, vol. 73, no. 5, pp. VE145–VE159, 2008.

[9] T. Alkhalifah, “Efficient synthetic-seismogram generation in transversely isotropic, inhomogeneous media,” *Geophysics*, vol. 60, no. 4, pp. 1139–1150, 1995.

[10] T. Alkhalifah and S. Fomel, “Angle gathers in wave-equation imaging for vti media,” *SEG Technical Program Expanded Abstracts*, vol. 28, pp. 2899–2903, 2009.

Hindawi Publishing Corporation
International Journal of Geophysics
Volume 2011, Article ID 689041, 18 pages
doi:10.1155/2011/689041

Research Article

Seismic Waveform Inversion by Stochastic Optimization

Tristan van Leeuwen, Aleksandr Y. Aravkin, and Felix J. Herrmann

Department of Earth and Ocean Sciences, University of British Columbia, Vancouver, BC, Canada V6T 1Z4

Correspondence should be addressed to Tristan van Leeuwen, tleeuwen@eos.ubc.ca

Received 15 December 2010; Accepted 31 March 2011

Academic Editor: Sergey Fomel

We explore the use of stochastic optimization methods for seismic waveform inversion. The basic principle of such methods is to randomly draw a batch of realizations of a given misfit function and goes back to the 1950s. The ultimate goal of such an approach is to dramatically reduce the computational cost involved in evaluating the misfit. Following earlier work, we introduce the stochasticity in waveform inversion problem in a rigorous way via a technique called *randomized trace estimation*. We then review theoretical results that underlie recent developments in the use of stochastic methods for waveform inversion. We present numerical experiments to illustrate the behavior of different types of stochastic optimization methods and investigate the sensitivity to the batch size and the noise level in the data. We find that it is possible to reproduce results that are qualitatively similar to the solution of the full problem with modest batch sizes, even on noisy data. Each iteration of the corresponding stochastic methods requires an order of magnitude fewer PDE solves than a comparable deterministic method applied to the full problem, which may lead to an order of magnitude speedup for waveform inversion in practice.

1. Introduction

The use of simultaneous source data in seismic imaging has a long history. So far, simultaneous sources have been used to increase the efficiency of data acquisition [1, 2], migration [3, 4], and simulation [5–7]. Recently, the use of simultaneous source encoding has found its way into waveform inversion. Two key factors play a role in this development: (i) in 3D, one is forced to use modeling engines whose cost is proportional to the number of shots (as opposed to 2D frequency-domain methods where one can reuse the LU factorization to cheaply model any number of shots) and (ii) the curse of dimensionality: the number of shots and the number of gridpoints grows by an order of magnitude.

The basic idea of replacing single-shot data by randomly combined "super shots" is intuitively pleasing and has lead to several algorithms [8–11]. All of these aim at reducing the computational costs of full waveform inversion by reducing the number of PDE solves (i.e., the number of simulations). This reduction comes at the cost of introducing random crosstalk between the shots into the problem. It was observed by Krebs et al. [8] that it is beneficial to recombine the shots at every iteration to suppress the random crosstalk and that the approach might be more sensitive to noise in the data. In this paper, we follow Haber et al. [12] and introduce randomized source encoding through a technique called *randomized trace estimation* [13, 14]. The goal of this technique is to estimate the trace of a matrix efficiently by sampling its action on a small number of randomly chosen vectors. The traditional least-squares optimization problem can now be recast as a *stochastic* optimization problem. Theoretical developments in this area go back to 1950s, and we review them in this paper. In particular, we discuss two distinct approaches to stochastic optimization. The *stochastic approximation* (SA) approach consists of a family of algorithms that use a different randomization in each iteration. This idea justifies a key part of the approach described in Krebs et al. [8]. Notably, the idea of averaging the updates over the past is important in this context to suppress the random crosstalk; lack of averaging over the past likely explains the noise sensitivity reported by Krebs et al. [8]. The theory we treat here concerns only first-order optimization methods, though there has been a recent effort to extend similar ideas to methods that exploit curvature information [15].

Another approach, called the *sample average approximation* (SAA), replaces the stochastic optimization problem by an ensemble average over a set of randomizations. The ensemble size should be big enough to suppress the crosstalk. The resulting problem may be treated as a deterministic optimization problem; in particular, one may use any optimization method to solve it.

Most theoretical results in SA and SAA assume that the objective function is convex, which is not the case for seismic waveform inversion. However, in practice one starts from a "reasonable" initial model, and we may be able to converge to the closest local minimum. One would expect SA and SAA to be applicable in the same framework. Understanding the theory behind SA and SAA is then very useful in algorithm design, even though the theoretical guarantees derived under the convexity assumption need not apply.

As mentioned before, the gain in computational efficiency comes at the cost of introducing random crosstalk between the shots into the problem. Also, the influence of noise in the data may be amplified by randomly combining shots. We can reduce the influence of these two types of noise by increasing the batch size, recombining the shots at every iteration, and averaging over past iterations. We present a detailed numerical study to investigate how these different techniques affect the recovery.

The paper is organized as follows. First, we introduce randomized trace estimation in order to cast the canonical waveform inversion problem as a stochastic optimization problem. We describe briefly how SA and SAA can be applied to solve the waveform inversion problem. In Section 3, we review relevant theory for these approaches from the field of stochastic optimization. The corresponding algorithms are presented in Section 4. Numerical results on a subset of the Marmousi model are presented in Section 5 to illustrate the characteristics of the different stochastic optimization approaches. Finally, we discuss the results and present the conclusions.

2. Waveform Inversion and Trace Estimation

The canonical waveform inversion problem is to find the medium parameters for which the modeled data matches the recorded data in a least-squares sense [16]. We consider the simplest case of constant-density acoustics and model the data in the frequency domain by solving

$$H[m]u = q, \tag{1}$$

where $H[m]$ is the discretized Helmholtz operator $[\omega^2 m + \nabla^2]$ for the squared slowness m (with appropriate boundary conditions), u is the discretized wavefield, and q is the discretized source function; both are column vectors. The data are then given by sampling the wavefield at the receiver locations: $d = Pu$. Note that all the quantities are monochromatic. We hide the dependence on frequency for notational simplicity.

We denote the corresponding optimization problem as

$$\min_m \phi(m, Q, D) = \sum_\omega \left\| PH[m]^{-1}Q - D \right\|_F^2, \tag{2}$$

where $D = [d_1, d_2, \dots, d_N]$ is a frequency slice of the recorded data, and $Q = [q_1, q_2, \dots, q_N]$ are the corresponding source functions. Note that the dependence of H on ω has been suppressed. $\|\cdot\|_F$ denotes the Frobenius norm, which is defined as $\|A\|_F = \sqrt{\operatorname{trace}(A^T A)}$ (here $\cdot^T$ denotes the complex-conjugate transpose. We will use the same notation for the transpose in case the quantity is real). Note that we assume a fixed-spread acquisition where each receiver sees all the sources.

In practice, H^{-1} is never computed explicitly but involves either an LU decomposition (cf., [17–19]) or an iterative solution strategy (cf., [20, 21]). In the worst case, the matrix has to be inverted separately for each frequency and source position. For 3D full waveform inversion, both the costs for inverting the matrix *and* the number of sources increase by an order of magnitude. Recently, several authors have proposed to reduce the computational cost by randomly combining sources [8–12].

We follow Haber et al. [12] and introduce this encoding in a rigorous manner by using a technique called *randomized trace estimation*. This technique was introduced by Hutchinson [13] as a technique to efficiently estimate the trace of an implicit matrix. Some recent developments and error estimates can be found in Avron and Toledo [14].

This technique is based on the identity

$$\operatorname{trace}\left(A^T A\right) = \mathrm{E}_w\left(w^T A^T A w\right) = \lim_{K \to \infty} \frac{1}{K} \sum_{k=1}^{K} w_k^T A^T A w_k, \tag{3}$$

where E_w denotes the expectation over w. The random vectors w are chosen such that $\mathrm{E}_w(ww^T) = I$ (the identity matrix). The identity can be derived easily by using the cyclic permutation rule for the trace (i.e., $\operatorname{trace}(ABC) = \operatorname{trace}(CAB)$), the linearity of the expectation, and the aforementioned property of w. At the end of the section, we discuss different choices of the random vectors w. First, we discuss how randomized trace estimation affects the waveform inversion problem.

Using the definition of $\|A\|_F$, we have

$$\phi(m, Q, D) = \mathrm{E}_w \phi(m, Qw, Dw). \tag{4}$$

This reformulation of (2) is a *stochastic* optimization problem. We now briefly outline approaches to solve such optimization problems.

2.1. Sample Average Approximation.

A natural approach to take is to replace the expectation over w by an ensemble average

$$\phi_K(m) = \frac{1}{K} \sum_{k=1}^{K} \phi(m, Qw_k, Dw_k). \tag{5}$$

This is often referred to in the literature as the sample average approximation (SAA). The random crosstalk can be controlled by picking a "large enough" batch size. As long as the required batch size is smaller than the actual number of sources, we reduce the computational complexity.

For a fixed m, it is known that the error $|\phi - \phi_K|$ is of order $1/\sqrt{K}$ (cf., [14]). However, it is not the value of the misfit that we are trying to approximate, but the minimizer.

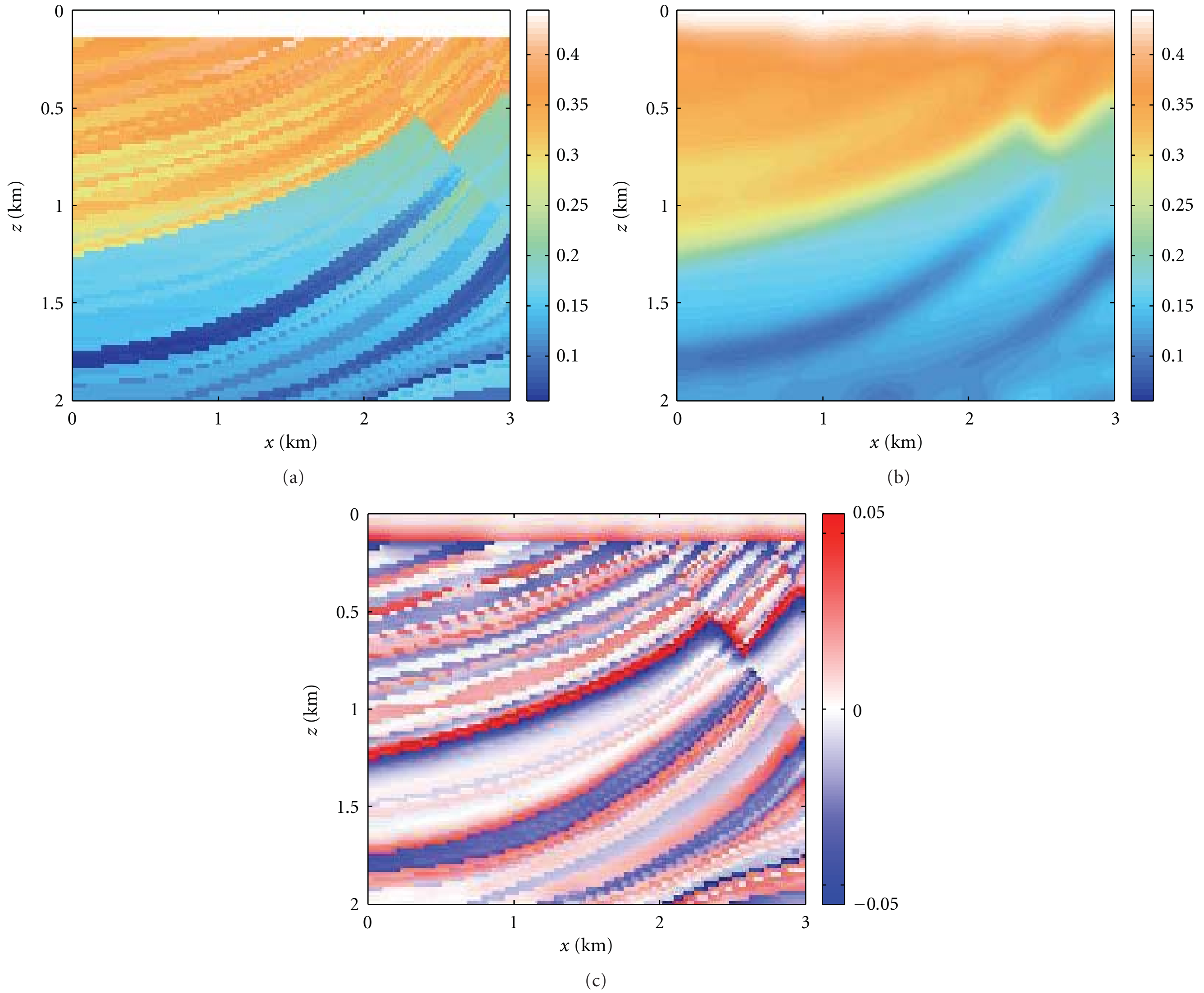

(a)

(b)

(c)

FIGURE 1: True (a) and initial (b) squared-slowness models (s^2/km^2) and the true reflectivity.

Unfortunately, the difference between the minimizers of ϕ and ϕ_K is not readily analyzed. Instead, we perform a small numerical experiment to get some idea of the performance of the SAA approach for waveform inversion.

We investigate the misfit along the direction of the negative gradient g_k (defined below)

$$f_K(\alpha) = \phi_K(m - \alpha g_K). \qquad (6)$$

The data are generated for the model depicted in Figure 1(a), for 61 colocated, equidistributed sources and receivers along a straight line at 10 m depth and 7 randomly chosen frequencies between 5 and 30 Hz. The source signature is a Ricker wavelet with a peak frequency of 10 Hz. We use a 9-point discretization of the Helmholtz operator with absorbing boundary conditions and solve the system via an (sparse) LU decomposition (cf., [22]). We note that this setup is quite efficient already since the LU decomposition can be reused for each source. Reduction of the number of sources becomes of paramount importance in 3D where one is forced to use iterative methods whose costs grow linearly with the number of sources. The search direction g_K is the gradient of ϕ_K evaluated at the initial model m_0, depicted in Figure 1(b). The gradient is computed in the usual way via the adjoint-state method (cf., [23]). The full gradient as well as the gradients for $K = 1, 5, 10$ are depicted in Figure 2. The error between the full and approximated gradient, caused by the crosstalk, is depicted in Figure 3. As expected, the error decays as $1/\sqrt{K}$. The misfit as a function of α for various K, as well as the full misfit (no randomization), is depicted in Figure 4. This shows that the minimizer of ϕ_K is reasonably close to the minimizer of the full misfit ϕ, even for a relatively small batch size K.

2.2. Stochastic Approximation.

A second alternative is to apply specialized stochastic optimization methods to problem (4) directly. This is often referred to as the stochastic

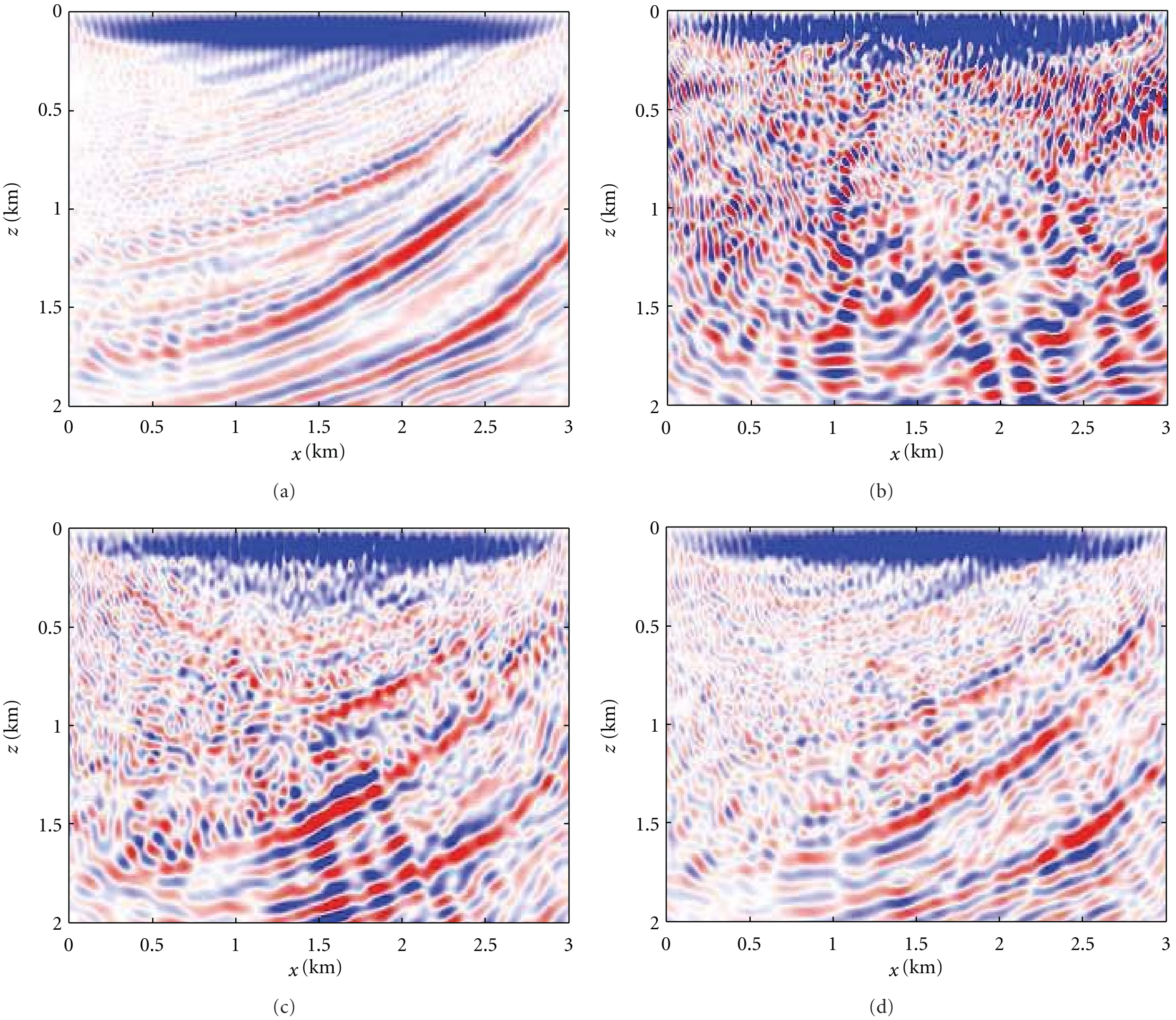

(a) (b) (c) (d)

Figure 2: The full gradient is depicted in (a). The approximate gradients for various K are depicted in (b) $K = 1$, (c) $K = 5$, and (d) $K = 10$. For a relatively small batch size, the approximate gradients already show the main features.

approximation (SA). The main idea of such algorithms is to pick a new random realization in each iteration and possibly average over past iterations to suppress the resulting stochasticity. In the context of the full waveform inversion problem, this gives an iterative algorithm of the form

$$m^{\nu+1} = m^{\nu} - \gamma_{\nu} \nabla \phi_{K,\nu}(m^{\nu}), \tag{7}$$

where batch size K can be as small as 1, $\{\gamma_{\nu}\}$ represent step sizes taken by the algorithm, and the notation $\phi_{K,\nu}$ emphasizes that a new randomization is used at every iteration ν (in contrast with the SAA approach).

We discuss theoretical performance results and describe SAA and SA in more detail in the next section.

2.3. Accuracy and Efficiency of Randomized Trace Estimation.

Efficient calculation of the trace of a positive semidefinite matrix lies at the heart of our approach. Factors that determine the performance of this estimation include the random process for the *i.i.d.* w's, the size of the source ensemble K, and the properties of the matrix. Hutchinson's approximation [13], which is based on w's drawn from a Rademacher distribution (i.e., random ±1), attains the smallest variance for the estimate of the trace. The variance can be used to bound the error via confidence intervals. However, the variance is not the *only* measure of the error. In particular, Avron and Toledo [14] derive bounds on the batch size in terms of ϵ and δ, defined as follows. A randomized-trace estimator $T_K = K^{-1}\sum w_i^T B w_i$ is an (ϵ, δ)-approximation of $T = \mathrm{trace}(B)$ if

$$\Pr\left(\frac{|T_K - T|}{|T|} \leq \epsilon\right) \geq 1 - \delta. \tag{8}$$

The expressions for the minimum batch size K for which the relative error is smaller than ϵ with probability δ are listed in Table 1 (adapted from Avron and Toledo [14]). Smaller ϵ's

TABLE 1: Summary of bounds, adapted from Avron and Toledo [14].

Estimator	Distribution of w	Variance of one sample	Bound on K for (ϵ, δ) bound
Hutchinson			
$H_K = (1/K)\sum_{j=1}^{K} w_j^{\top} A w_j$	$\Pr(w_j = \pm 1) = 1/2$	$2(\|A\|_F^2 - \sum_{i=1}^{N} A_{ii}^2)$	$6\epsilon^{-2}\ln(2\,\mathrm{rank}(A)/\delta)$
Gaussian			
$G_K = (1/K)\sum_{j=1}^{K} w_j^{\top} A w_j$	$w_j \in N(0,1)$	$2\|A\|_F^2$	$20\epsilon^{-2}\ln(2/\delta)$
Phase encoded			
$L_K = (N/K)\sum_{j=1}^{K} w_j^{T} \mathcal{F} A \mathcal{F}^{T} w_j$	w_j drawn uniformly from $\{e_1, \ldots, e_N\}$	n/a	$2\epsilon^{-2}\ln(4n^2/\delta)\ln(4/\delta)$

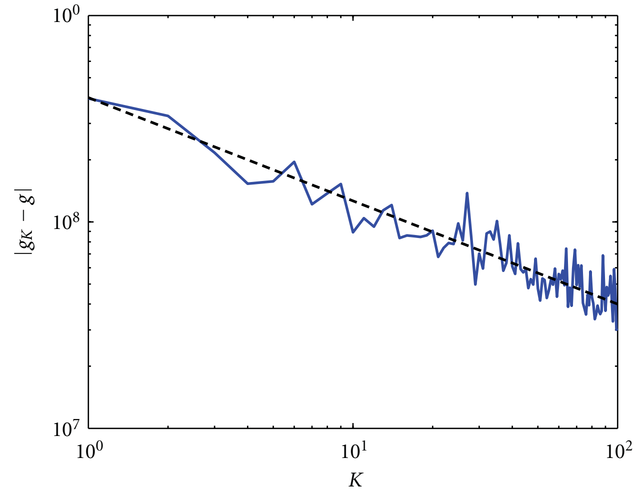

FIGURE 3: Error in the gradient as a function of the batch size K. As expected, the error goes down as $1/\sqrt{K}$ (dashed line).

TABLE 2: This table shows the theoretical lower bounds (see Table 1) on the batch size K for $\delta = 10^{-1}$ for the matrix shown in Figure 5.

	$\epsilon = 10^{-1}$	$\epsilon = 10^{-2}$	$\epsilon = 10^{-3}$
Gauss	$6 \cdot 10^3$	$6 \cdot 10^5$	$6 \cdot 10^7$
Hutchinson	$4 \cdot 10^3$	$4 \cdot 10^5$	$4 \cdot 10^7$
Phase	$9 \cdot 10^3$	$9 \cdot 10^5$	$9 \cdot 10^7$

and δ's lead to larger K, which in turn leads to more accurate trace estimates with increased probability.

Of course, these bounds depend on the choice of the probability distribution of the *i.i.d.* w's and the matrix B. Aside from obtaining the lowest value for K, simplicity of computational implementation is also a consideration. In Table 1, we summarize the performance of four different choices for the w's, namely,

(1) the Rademacher distribution, that is, $\Pr(w[i] = \pm 1) = 1/2$, ($w[i]$ denotes the ith element in the vector w) yielding $\mathrm{E}\{w[i]\} = 0$ and $\mathrm{E}\{w[i]^2\} = 1$ for $i = 1 \cdots N$. Aside from the fact that this estimator H_K (see Table 1) leads to minimum variance, the advantage of this choice is that it leads to a fast implementation with a small memory imprint. The disadvantage of this method is that the lower bound depends on the rank of A and requires larger K compared to w's defined by the Gaussian (see Table 1);

(2) the standard normal distribution, that is, $w[i] \in N(0,1)$ for $i = 1 \cdots N$. While the variance for this estimator G_K (see Table 1) is larger than the variance for H_k, the lower bound for K does not depend on the size or the rank of A and is the smallest of all four methods. This suggests that we can use a fixed value of K for arbitrarily large matrices. However, this method is known to converge slower than Hutchinson's for matrices A that have significant energy in the off-diagonals. This choice also requires a more complex implementation with a larger memory imprint;

(3) the fast phase-encoded method where w's selected uniformly from the canonical basis, that is, from $\{e_1, \ldots, e_N\}$. this estimator

$$L_K = \frac{N}{K}\sum_{j=1}^{K} w_j^{T} \mathcal{F} A \mathcal{F}^{T} w_j, \tag{9}$$

where $\mathcal{F}$ is a unitary (i.e, $\mathcal{F}^{T} = \mathcal{F}^{-1}$) random mixing matrix. The idea is to mix the matrix B such that its diagonal entries are evenly distributed. This is important since the unit vectors only sample the diagonal of the matrix. The flatter the distribution of the diagonal elements, the faster the convergence (if all the diagonal elements were to be the same, we need only one sample to compute the trace exactly).

The lower bounds summarized in Table 1 tell us that Gaussian w's theoretically require the smallest K and hence the fewest PDE solves. However, this result comes at the expense of more complex arithmetic, which can be a practical consideration [8]. Aside from the lowest bound, the estimator based on Gaussian w's has the additional advantage that the bound on K does not depend on the size or rank of the matrix B. Hutchinson's method, on the other hand, depends logarithmically on the rank of B but has the reported advantage that it performs well for near diagonal matrices [14]. This has important implications for our application because our matrix B is typically full rank and can be considered nearly diagonal only when our optimization procedure is close to convergence. At the beginning of the optimization, we can expect the residual to be large and a B that is not necessarily diagonal dominant.

We conduct the following stylized experiment to illustrate the quality of the different trace estimators. We solve the discretized Helmholtz equation at 5 Hz for a realistic acoustic model with 301 colocated sources and receivers located at 10 m depth. We compute matrix $B = A^{T}A$ for a residue A given by the difference between simulation results for the hard and smooth models shown in Figure 1. As expected, the resulting matrix B, shown in Figure 5, contains

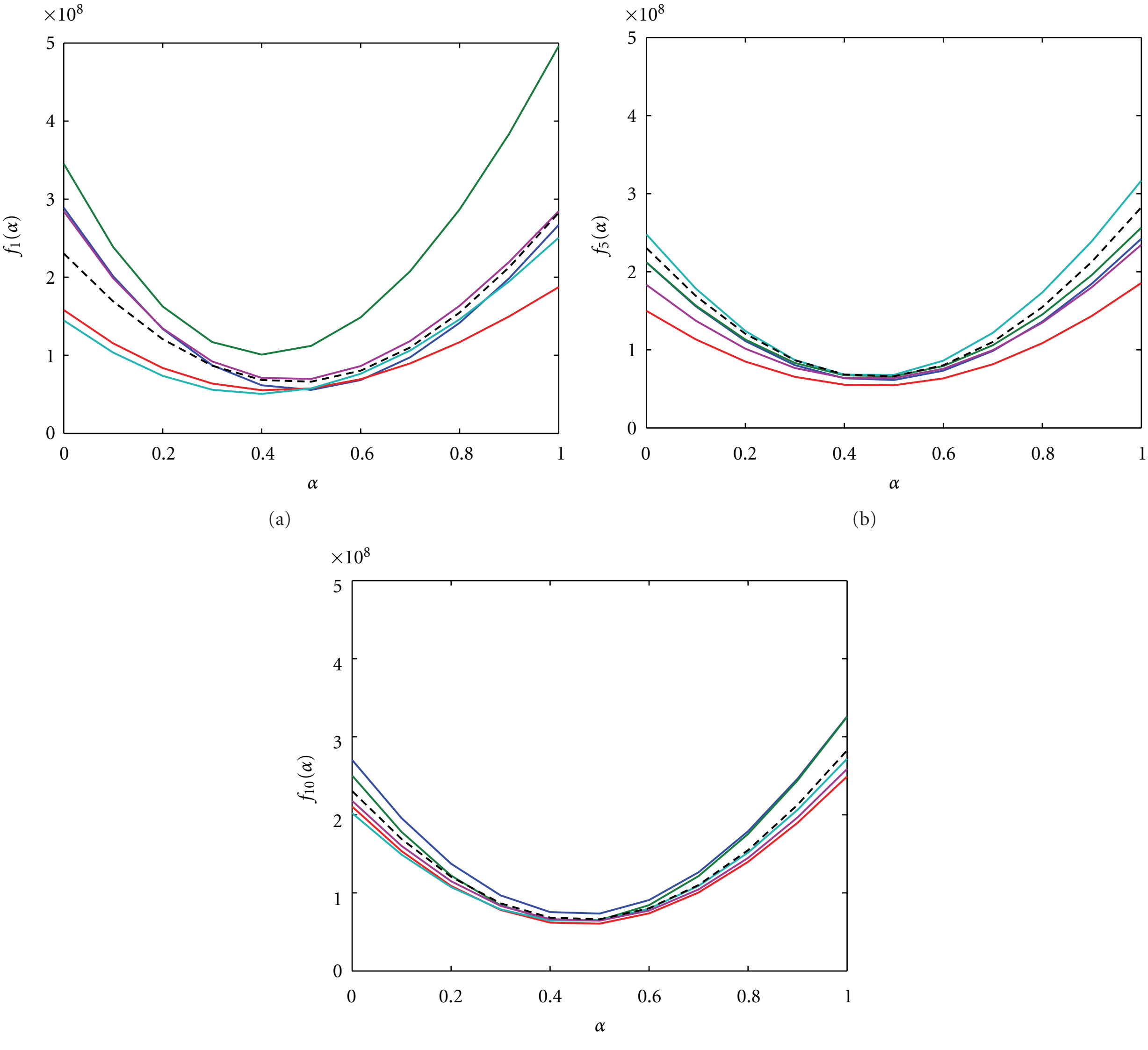

(a)

(b)

(c)

Figure 4: Behavior of misfit for various K. Shown are five different stochastic realizations and the true misfit (dashed line) for (a) $K = 1$, (b) $K = 5$, and (c) $K = 10$. The stochastic misfits approximate the true misfit fairly well for relatively small batch sizes.

significant off-diagonal energy. For the phase-encoded part of the experiment, we use a random mixing matrix based on the DFT, as suggested by Romberg [24]. Such mixing matrices are also commonly found in compressive sensing applications [7, 24–26].

We evaluated the different trace estimators 1000 times for batch sizes ranging from $K = 1 \cdots 1000$. The probability for the error level ϵ is estimated by counting the number of times we were able to achieve that error level for each K. The results for the different trace estimators and error levels are summarized in Figure 6. For this particular example, we see little difference in performance between the different estimators. The corresponding *theoretical* bounds on the batch size, as given by Table 1, are listed in Table 2. Clearly, these bounds are overly pessimistic in this case. In our experiments, we observed that we get similar reconstruction behavior if we use a finer source/receiver sampling. This suggests that the gain in efficiency will increase with the data size, since we can use larger batch sizes for a fixed downsampling ratio. We also noticed, in this particular example, little or no change in behavior if we change the frequency.

3. Optimization

3.1. Sample Average Approximation. The sample average approximation (SAA) is used to solve the following class of stochastic optimization problems:

$$\min_{x\in X}\{f(x) = \mathrm{E}_w\{F(x,w)\}\}, \tag{10}$$

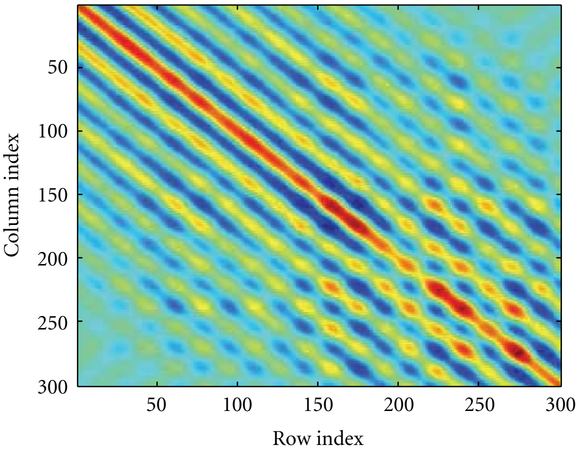

Figure 5: Residual matrix $A = S^T S$, where S is the data residual corresponding to the smooth model depicted in Figure 1(a) at 5 Hz.

where $X \subset \mathbb{R}^n$ is the set of admissible models (assumed to be a compact convex set, for example, box constraints $x_{\min} \leq x \leq x_{\max}$), w is a random vector with distribution supported on $W \subset \mathbb{R}^d$, $F : X \times W \rightarrow \mathbb{R}$, and the function $f(x)$ is convex [27]. The last important assumption is the law of large numbers (LLN), that is, $\widehat{f}_K(x) \rightarrow f(x)$ with probability 1 as $K \rightarrow \infty$. These assumptions are required for most of the known theoretical results about convergence of SAA methods. The convexity assumption and LLN assumption can be relaxed in the case when $F(\cdot, w)$ is continuous on X for almost every $w \in W$ and $F(x, w)$ is dominated by an integrable function $G(w)$, so that $|f(x)| \leq \mathrm{E}_w\{G(w)\}$ for every $x \in X$ [28]. Given an optimization problem of type (10), the SAA approach [27] is to generate a random sample $w_1, \ldots, w_K$ and solve the approximate (or sample average) problem

$$\min_{x \in X} \left\{ \widehat{f}_K(x) = \frac{1}{K} \sum_{j=1}^{K} F\left(x, w_j\right) \right\}. \tag{11}$$

When these assumptions are satisfied, the optimal value of (11) converges to the optimal value of the full problem (10) with probability 1. Moreover, under more technical assumptions on the distribution of the random variable w, conservative bounds have been derived on the batch size K necessary to obtain a particular accuracy level ϵ [29, equation (22)]. These bounds do not require the convexity assumptions but instead require assumptions on local behavior of $F(\cdot, w)$. It is worth underscoring that "accuracy" here of solution $\overline{x}$ with respect to the optimal solution x^* is defined with respect to the function value difference $f(x) - f(x^*)$, rather than in terms of $\|x - x^*\|$ or other measure in the space of model parameters. From a practical point of view, the SAA approach is appealing because it allows flexibility in the choice of algorithm for the solution of (11). This works on two levels. First, if a faster algorithm becomes available for the solution of (11), it can immediately impact (10). Second, having fixed a large $\overline{K}$ and $\widehat{f}_{\overline{K}}$ to obtain reasonable accuracy in the solution of (10), one is free to approximately solve a sequence of smaller problems ($K_i \ll \overline{K}$) with warm starts on the way to solving $\widehat{f}_{\overline{K}}$ [12]. In other words, SAA theory guarantees the existence of a K large enough for which the approximate problem is close to the full problem; however, the algorithm for solving the approximate problem (11) is left completely to the practitioner and in particular may require the evaluation of very few samples at early iterations.

3.2. Stochastic Approximation. Stochastic approximation (SA) methods go back to Robbins and Monro [30], who considered the root-finding problem

$$g(x) = g_0, \tag{12}$$

in the case where $g(x)$ cannot be evaluated directly. Rather, one has access to a function $G(x, w)$ for which $\mathrm{E}_w\{G(x, w)\} = g(x)$. The approach can be translated to optimization problems of the form

$$\min f(x) \tag{13}$$

by considering g to be the gradient of f and setting $g_0 = 0$. Again, we cannot evaluate $f(x)$ directly, but we have access to $F(x, w)$ for which $\mathrm{E}_w\{F(x, w)\} = f(x)$. More generally, for problems of type (10), Bertsekas and Tsitsiklis [31] and Bertsekas and Tsitsiklis [32] consider iterative algorithms of the form

$$x^{\nu+1} = x^{\nu} - \gamma_{\nu} s^{\nu}, \tag{14}$$

where γ_ν are a sequence of step sizes determined a priori that satisfy certain properties, and s^ν can be thought of as noisy unbiased estimates of the gradient (i.e., $\mathrm{E}_w s^\nu = \nabla f(x^\nu)$). Note that right away we are forced into an algorithmic framework, which never appears in the SAA discussion. The positive step sizes γ_ν are chosen to satisfy

$$\sum_{\nu=0}^{\infty} \gamma_\nu = \infty, \qquad \sum_{\nu=0}^{\infty} \gamma_\nu^2 < \infty. \tag{15}$$

The main idea is that the step sizes go to zero, but not too fast. A commonly used example of such a sequence of step sizes is

$$\gamma_\nu \propto \frac{1}{\nu}. \tag{16}$$

The main result of Bertsekas and Tsitsiklis [31] is that if ∇f satisfies the Lipshitz condition with constant L

$$\|\nabla f(x) - \nabla f(y)\| \leq L\|x - y\|, \tag{17}$$

that is, the changes in the gradient are bounded in norm by changes in the parameter space, and if the directions s^ν on average point "close to" the gradient and are not too noisy, then the sequence $f(x^\nu)$ converges, and every limit point $\overline{x}$ of $\{x^\nu\}$ is a stationary point of f (i.e., $\nabla f(\overline{x}) = 0$). Under stronger assumptions that the level sets of f are bounded and the minimum is unique, this guarantees that the algorithms described above will find it. A similar family of algorithms

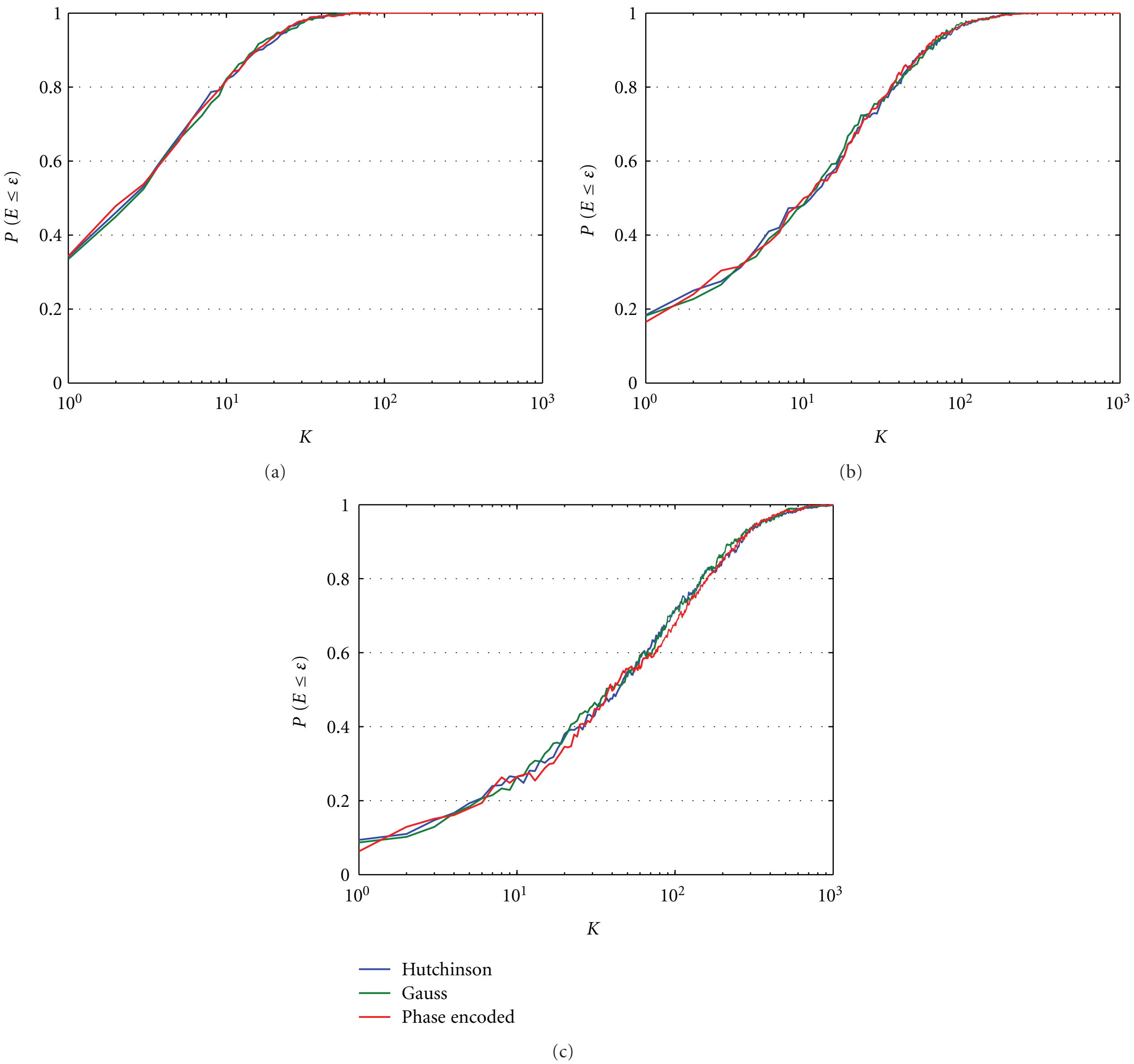

(a) (b) (c)

Figure 6: Reconstruction as a function of K for various methods and error levels: (a) $\epsilon = 10^{-1}$, (b) $\epsilon = 10^{-2}$, and (c) $\epsilon = 10^{-3}$.

was studied by Polyak and Juditsky [33], who considered larger step sizes γ_ν but included averaging model estimates into their algorithm. In the context discussed above, the step size rule 10 is replaced by

$$\frac{\gamma_\nu - \gamma_{\nu+1}}{\gamma_\nu} = o(\gamma_\nu). \tag{18}$$

A particular example of such a sequence cited by the paper is

$$\gamma_\nu \propto \nu^{-\beta}, \qquad 0 < \beta < 1. \tag{19}$$

The iterative scheme is then given by

$$\begin{aligned} x^{\nu+1} &= x^\nu - \gamma_\nu s^\nu, \\ \overline{x}^\nu &= \frac{1}{\nu}\sum_{i=0}^{\nu-1} x^i. \end{aligned} \tag{20}$$

Under assumptions similar in spirit to the ones in Bertsekas and Tsitsiklis [31], there is a result for the convergence of the iterates x^ν to the true estimate x^*, namely, $\overline{x}^\nu \rightarrow x^*$ almost surely and

$$\sqrt{\nu}(\overline{x}^\nu - x^*) \longrightarrow_D \mathbf{N}(0, V), \tag{21}$$

where the convergence is in distribution, and the matrix V is in some sense optimal and is related to the Hessian of f at the solution x^*. A more recent report [34] also considers averaging of model iterates in the context of optimizing (not necessarily smooth) convex functions of the form

$$f(x) = \mathrm{E}_w\{F(x, w)\} \tag{22}$$

over a convex set X. When f is smooth, this situation reduces to the previous discussion. Nesterov and Vial [34] choose

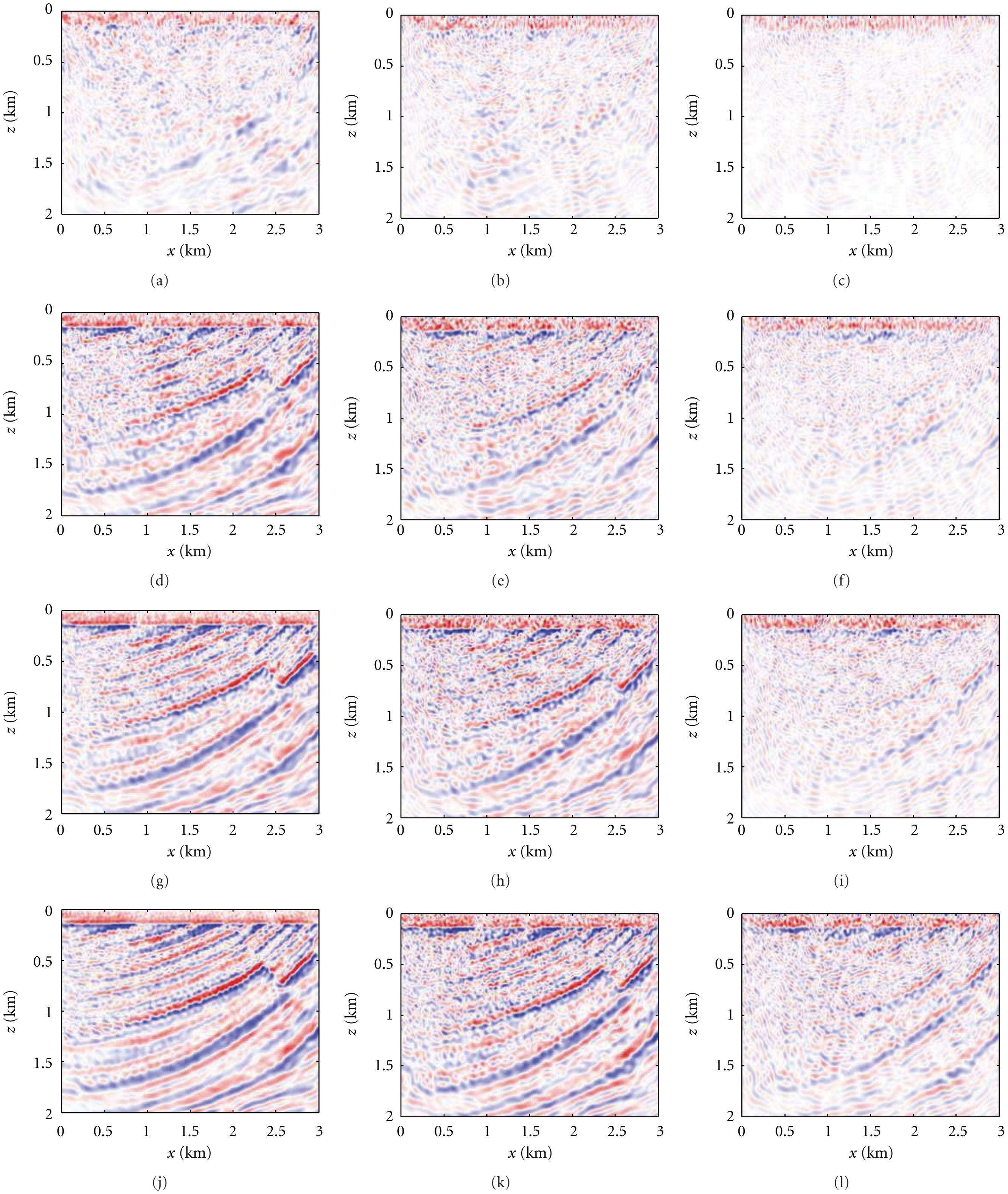

Figure 7: Inversion result for the SAA approach with various batch sizes and noise levels. The rows represent different batch sizes $K = 1, 5, 10, 20$, while the columns represent different noise levels: no noise, SNR = 20 dB, and SNR = 10 dB. The reconstruction with $K = 20$ for noiseless data (j) is qualitatively comparable to the full reconstruction. The quality deteriorates quickly for small batch sizes and noisy data.

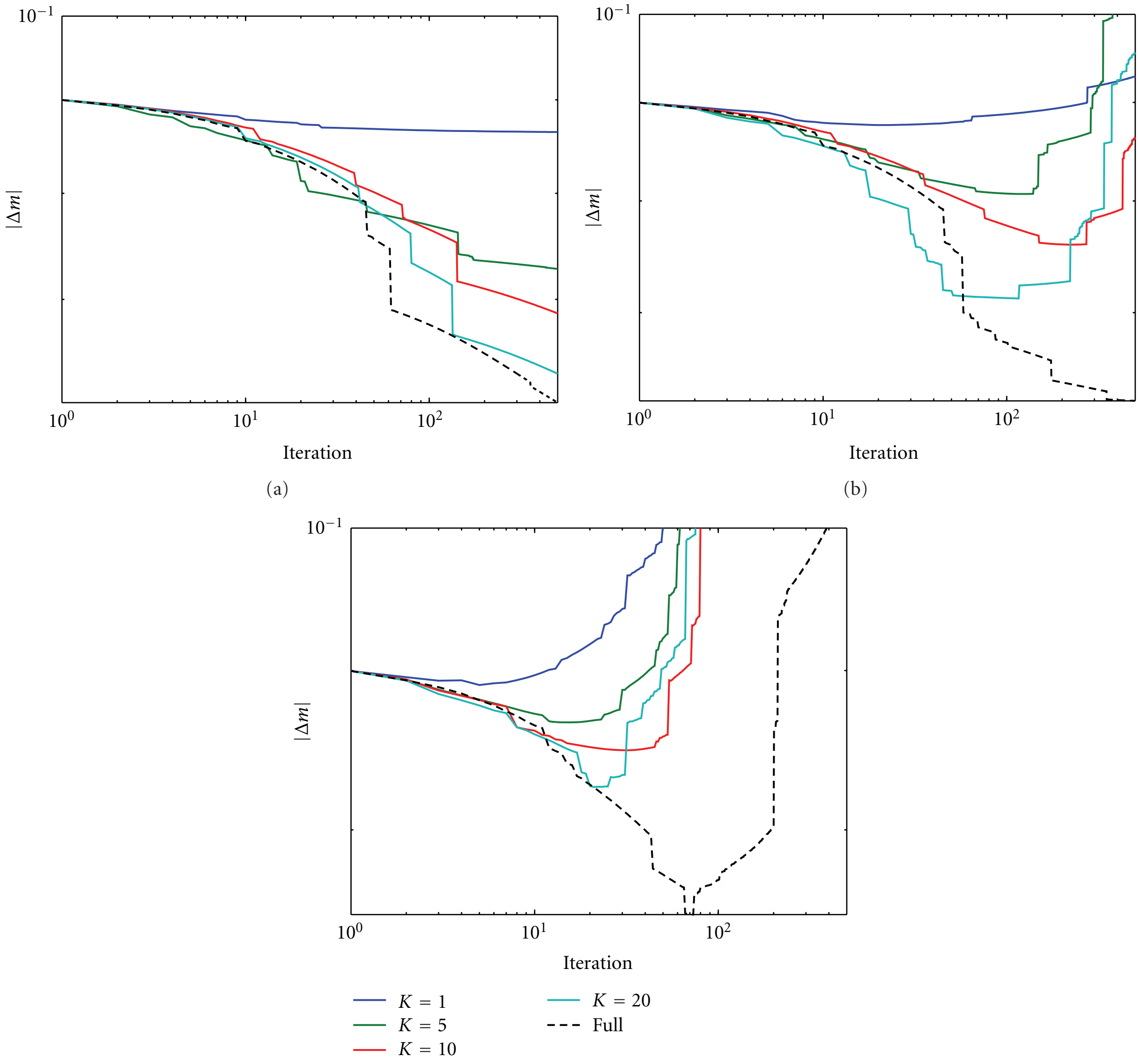

(a)

(b)

(c)

FIGURE 8: Error between the inverted and true model for the SAA approach with various batch sizes and the full problem, (a) without noise, (b) with noise (SNR = 20 dB), and (c) with noise (SNR = 10 dB). On noiseless data, we achieve a qualitatively comparable result with $K = 20$, as can be seen from (a). For noisy data, however, the largest batch size is not enough to prevent overfitting.

a finite sequence of N step sizes a prior and consider the error in the expected value function

$$\mathrm{E}_{\overline{x}^{\nu}}\{f(\overline{x}^{\nu})\} - f(x^{*}) \tag{23}$$

after N iterations. This is similar to the SAA analysis but is much easier to interpret, because now the desired accuracy in the objective value directly translates to the number of iterations of a particular algorithm

$$\begin{aligned} x^{\nu+1} &= \pi_X(x^{\nu} - \gamma_{\nu} s^{\nu}), \\ \overline{x} &= \frac{\sum_{\nu=0}^{N-1} \gamma_{\nu} x^{\nu}}{\sum_{\nu=0}^{N-1} \gamma_{\nu}}, \end{aligned} \tag{24}$$

where π_X is projection onto the convex set of admissible models X. Unfortunately, the error is $O(L^2(\sum \gamma_{\nu}^2/\sum \gamma_{\nu}) + R^2(1/\sum \gamma_{\nu}))$, where R is the diameter of the set X (related to the bounds on x from our earlier example) and L is a uniform bound on $\|\nabla f\|$, and so the estimate may be overly conservative. If all the γ_{ν} are chosen to be uniform, the optimal size is $\gamma = R/L\sqrt{N}$, and then the result is simply

$$\mathrm{E}_{\overline{x}^{\nu}}\{f(\overline{x}^{\nu})\} - f(x^{*}) \le \frac{LR}{\sqrt{N}}. \tag{25}$$

For a recent survey of stochastic optimization and new robust SA methods, please see Nemirovski et al. [27].

Note that the error rate in the objective values is $O(1/\sqrt{N})$, where the constant depends in a straightforward way

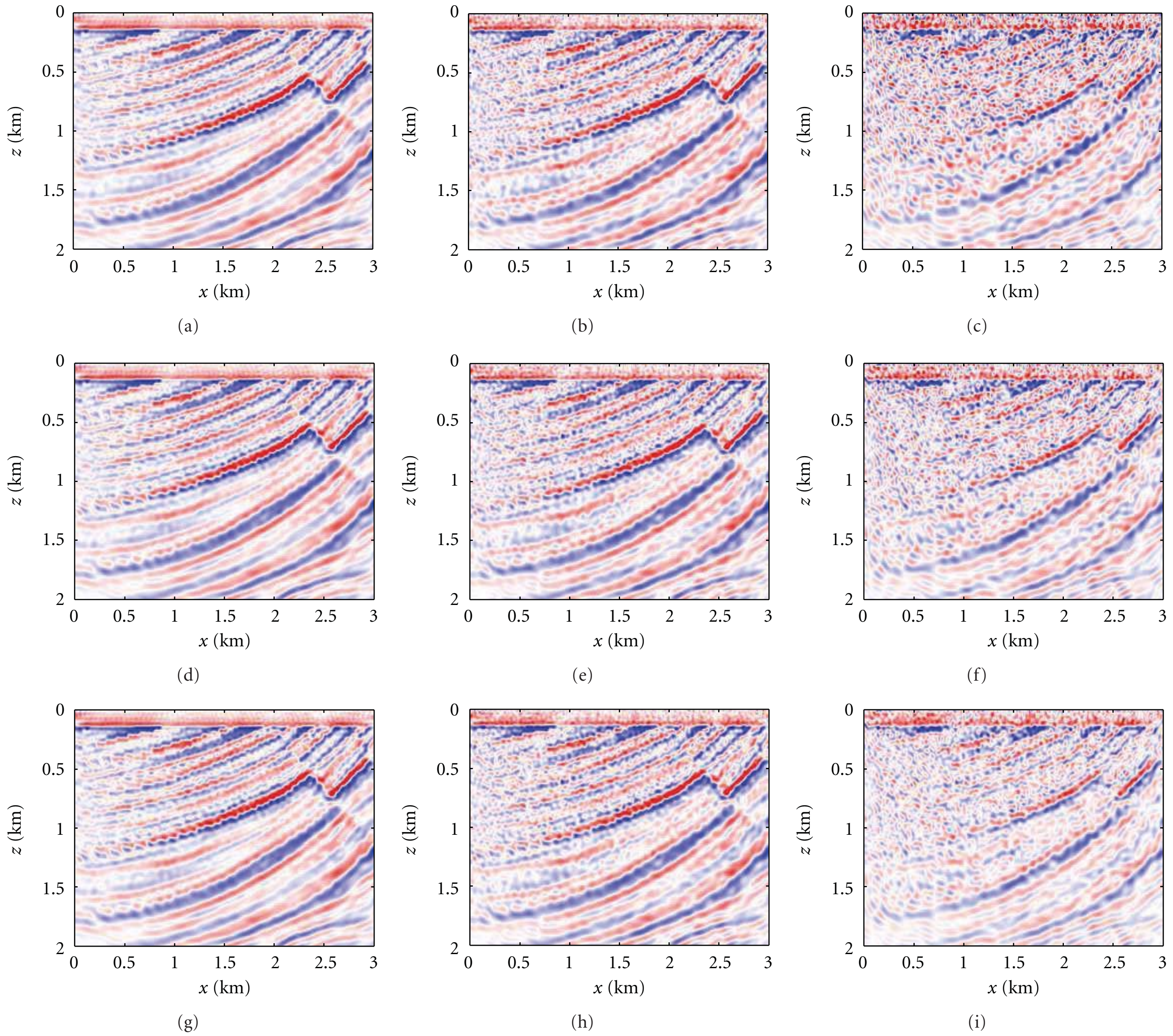

(a) (b) (c) (d) (e) (f) (g) (h) (i)

Figure 9: Inversion result for the SA approach without averaging for various batch sizes and noise levels. The rows represent different batch sizes $K = 1, 5, 10$, while the columns represent different noise levels: no noise, SNR = 20 dB, and SNR = 10 dB. We obtain good results with $K = 1$, and the quality does not improve dramatically for larger batch sizes, except for the highest noise level.

on the size of the set X and the behavior of $\|\nabla f\|$. Compare this to the $O(1/\sqrt{K})$ error bound for the SAA approach. In contrast to the SAA, the SA approach translates directly into a particular algorithm. This makes it easier to implement for full waveform inversion, but also leaves less freedom for algorithm design than in SAA, where any algorithm can be used to solve the deterministic ensemble average problem.

4. Algorithms

To test the performance of the SAA approach, we chose to use a steepest descent method with an Armijo line search (cf., [35]). Although one could in principle use a second-order method (such as L-BFGS), we chose to use a first-order method to allow for better comparison to the SA results. The pseudocode is presented in Algorithm 1.

The SA methods are closely related to the steepest descent method. The main difference is that for each iteration a new random realization is drawn from a prescribed distribution and that the result is averaged over past iterations. We chose to implement a few modifications to the standard SA algorithms. First, we use an Armijo line search to determine the step size instead of using a prescribed sequence such as that discussed in the previous section. This assures some descent at each iteration with respect to the current realization of ϕ_K, and we found that this greatly improved the convergence. Second, we allow for averaging over the past n iterations instead of the full history. This prevents

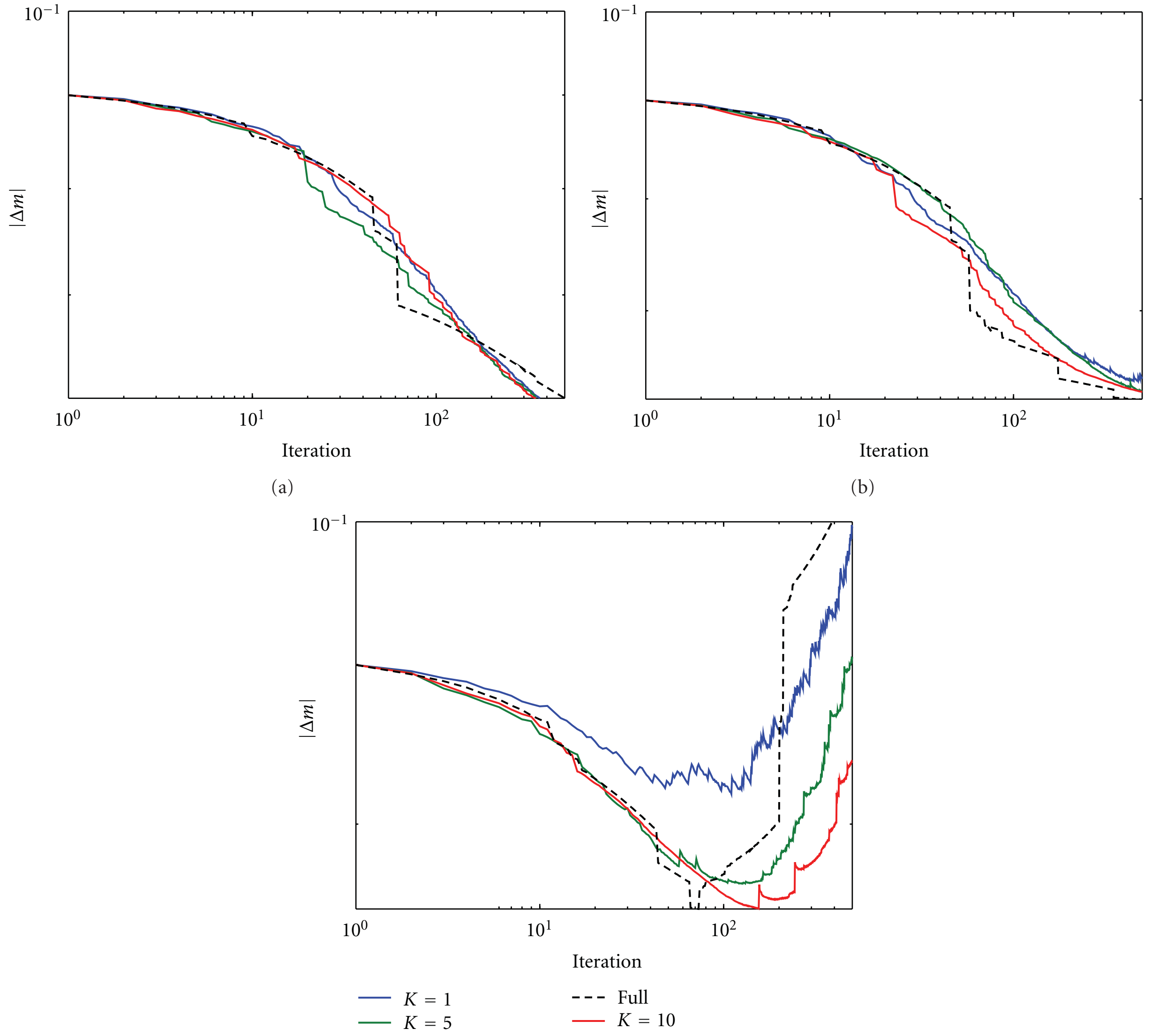

(a) (b) (c)

Figure 10: Error between the inverted and true model for the SA approach without averaging for various batch sizes and the full problem, (a) without noise, (b) with noise (SNR = 20 dB), and (c) with noise (SNR = 10 dB). We get qualitatively similar results, compared to the full inversion, with $K = 1$ for noiseless data and data with 10 dB of noise. For very noisy data (20 dB), we need a larger batch size. Although the SA approach requires roughly the same number of iterations as the full inversion, the iterations are much cheaper. For $K = 1$, we model the data for only one simultaneous source per iteration, compared to 61 for the full inversion.

the method from stalling. The pseudo-code is presented in Algorithm 2.

5. Results

For the numerical experiments, we use the true and initial squared-slowness models depicted in Figure 1. The data are generated for 61 equispaced, colocated sources and receivers at 10 m depth and 7 randomly chosen (but fixed) frequencies between 5 and 30 Hz. The latter strategy is inspired by results from compressive sensing (cf., [7, 36, 37]). The basic idea is to turn aliases that are introduced by sub-Nyquist sampling into random noise.

The Helmholtz operator is discretized on a grid with 10 m spacing, using a 9-point finite difference stencil and absorbing boundary conditions. The point sources are represented as narrow Gaussians. As a source signature, we use a Ricker wavelet with a peak frequency of 10 Hz. The noise is Gaussian with a prescribed SNR.

We run each of the optimization methods for 500 iterations and compare the performance for various batch sizes and noise levels to the result of steepest descent on the full problem. Remember that by using small batch sizes, the iterations are very cheap, so we can afford to do more. The random vectors are drawn from a Gaussian distribution with zero mean and unit variance. We chose to use the Gaussian

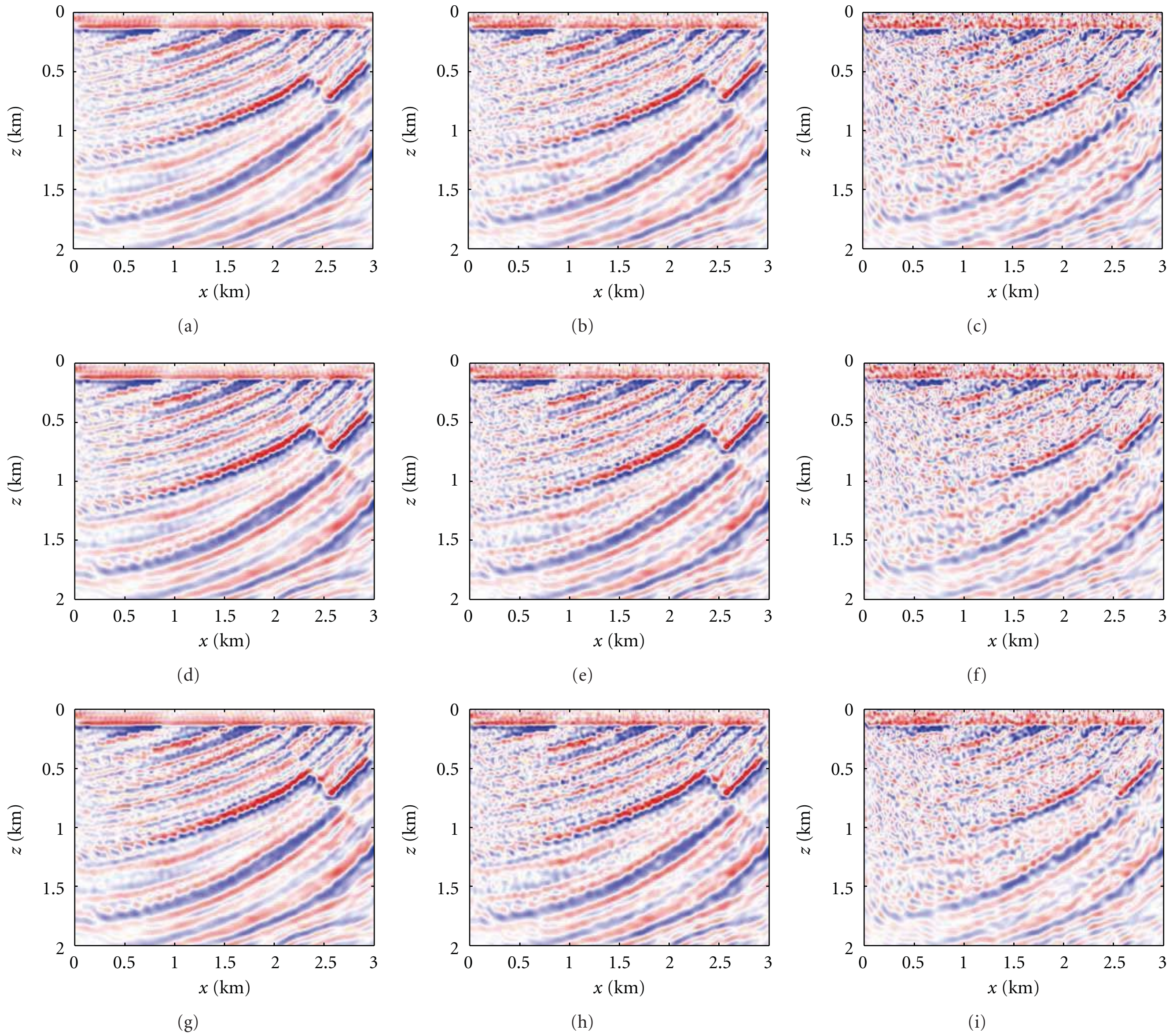

(a) (b) (c)

(d) (e) (f)

(g) (h) (i)

Figure 11: Inversion result for the SA approach with limited averaging ($n = 10$) for various batch sizes and noise levels. The rows represent different batch sizes $K = 1,\ 5,\ 10$, while the columns represent different noise levels: no noise, SNR = 20 dB, and SNR = 10 dB. We obtain good results with $K = 1$, and the quality does not improve dramatically for larger batch sizes, except for the highest noise level.

because the theoretical bounds on K do not depend on properties of the residual matrix. Although the matrix will change constantly during the optimization, we can at least expect a uniform quality of the approximation.

In a realistic application, one might want to add a regularization term. In particular, this would prevent the overfitting that we observe in the noisy case. Note that limiting the amount of iterations also serves as a form of regularization [38].

5.1. Sample Average Approximation. We choose a set of K Gaussian random vectors with zero mean and unit variance and run the steepest descent algorithm presented previously on the resulting deterministic optimization problem. The results after 500 iterations on data without noise are shown in the first column of Figure 7. The error between the recovered and true model is shown in Figure 8(a). As reference, the error between the true and recovered model for the inversion with *all* the sequential sources is also shown. As expected, the recovery is better for larger batch sizes. The recovered models for data with noise are shown in the second column (SNR = 20 dB) and third (SNR = 10 dB) columns of Figure 7. The corresponding recovery error is shown in Figures 8(b) and 8(c), respectively. It shows that the SAA approach starts overfitting in an earlier stage than the full inversion. Also, we are not able to reach the same model error as the full inversion.

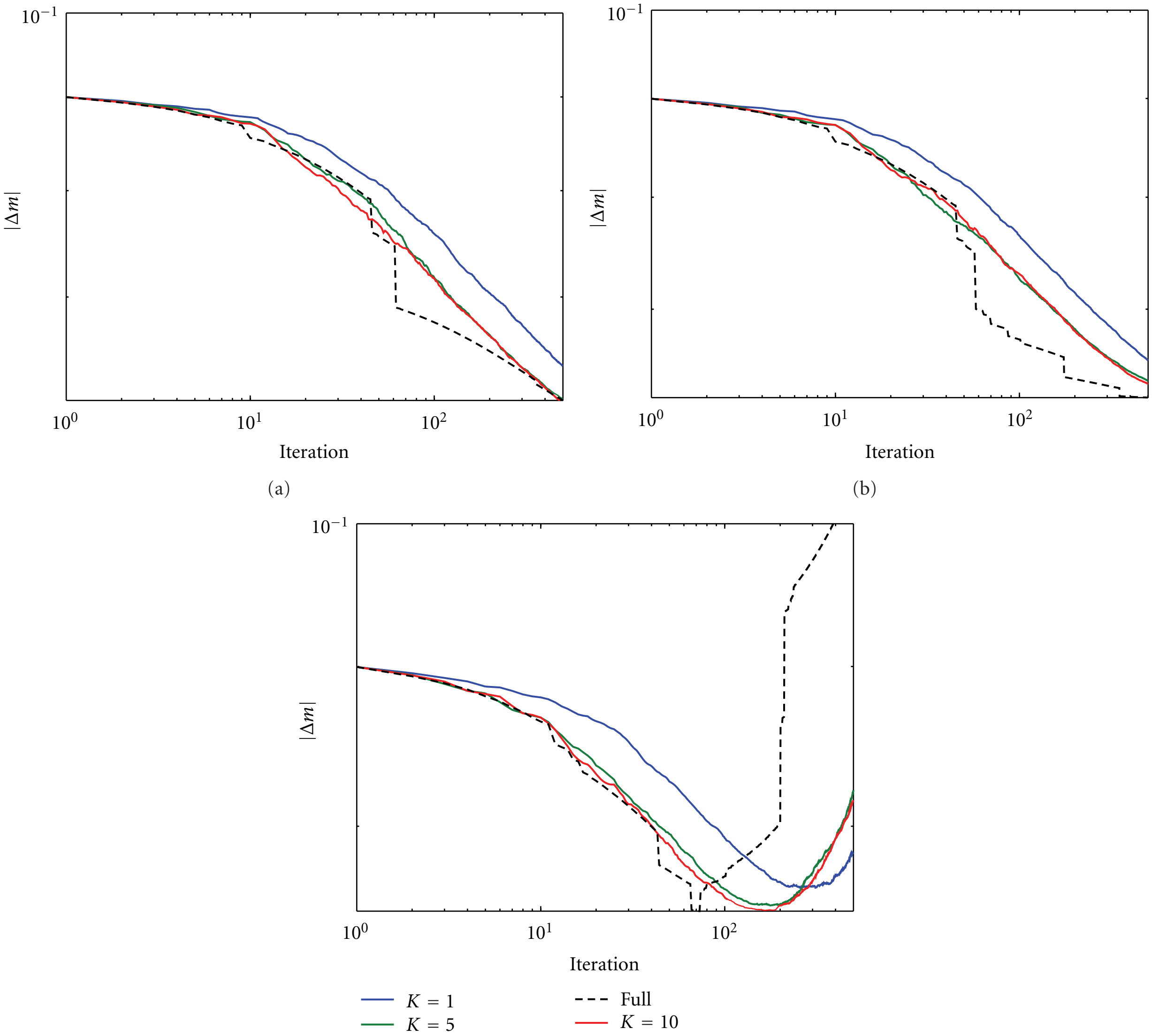

(a)

(b)

(c)

Figure 12: Error between the inverted and true model for the SA approach with limited averaging for various batch sizes and the full problem, (a) without noise, (b) with noise (SNR = 20 dB), and (c) with noise (SNR = 10 dB). The convergence is smoother than that of SA without averaging, especially when the data is very noisy (10 dB). The averaging seems to slow down the convergence slightly, however, and we need a batch size $K = 5$ for the best results.

5.2. Stochastic Approximation. We run the stochastic descent algorithm for varying batch sizes ($K = 1, 5, 10$) and history sizes ($n = 0, 10, 500$).

The results obtained without averaging are shown in Figure 9. The columns represent different batch sizes, while the rows represent different noise levels. The recovery errors for the different batch sizes and noise levels are shown in Figure 10. In the noiseless case, we are able to achieve the same recovery error as the full inversion with only one simultaneous source. When noise is present in the data, one simultaneous source is not enough, however. Still, we can achieve the same recovery error as the full problem with only 10 simultaneous sources. This yields an order of magnitude improvement in our computation, since the *total* number of iterations needed by the stochastic method to achieve a given level of accuracy is roughly the same as required by a deterministic first-order method used on the full system, but *each* stochastic iteration requires ten times fewer PDE solves than a deterministic iteration on the full system.

Results obtained with averaging over the past 10 iterations are shown in Figure 11. The rows represent different batch sizes, while the columns represent different noise levels. The corresponding recovery errors are shown in Figure 12. It shows that averaging helps to overcome some of the noise sensitivity, and we are now able to achieve a good reconstruction with only 5 simultaneous sources. Also, the averaging damps the irregularity of the convergence somewhat.

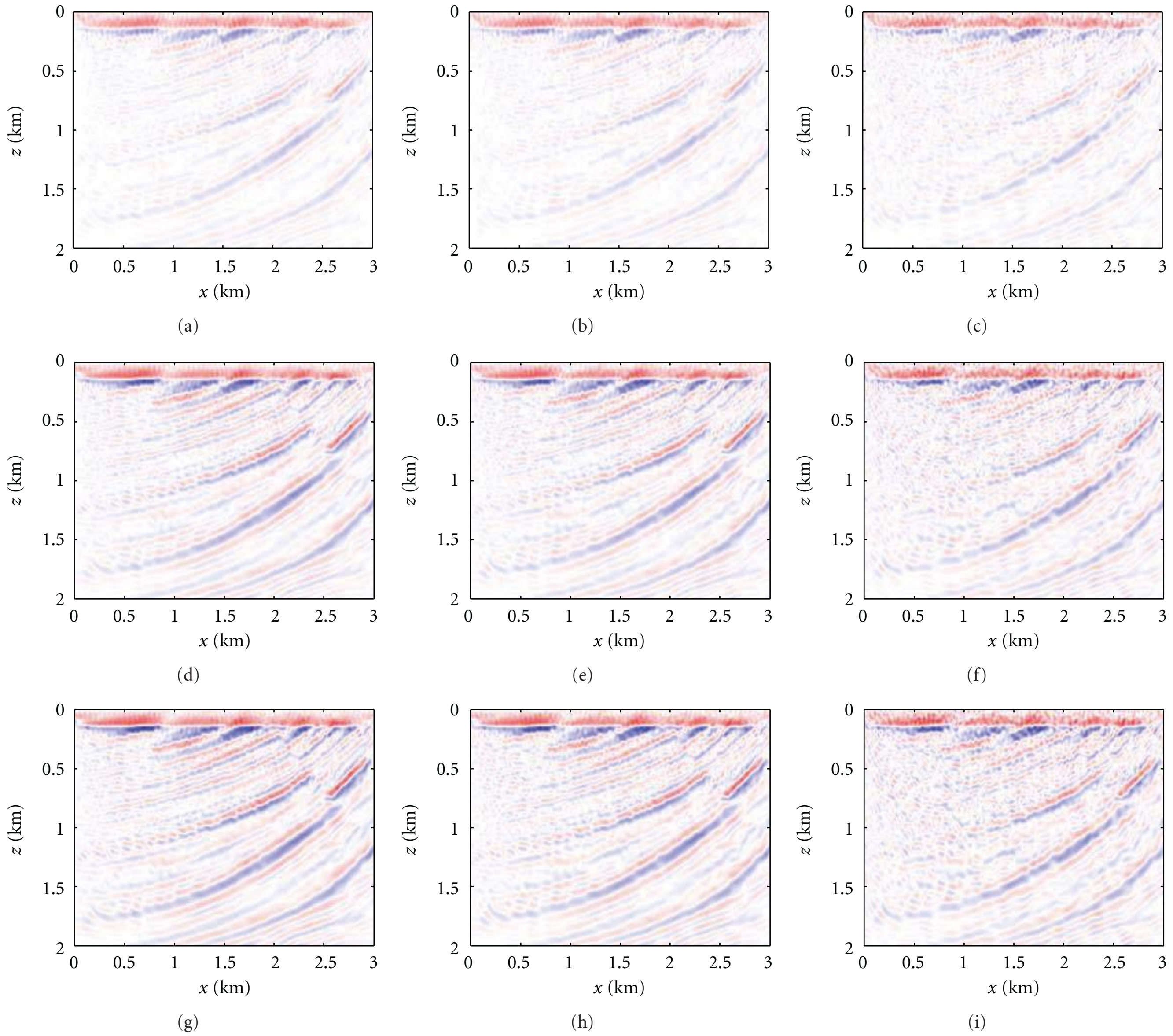

(a) (b) (c)

(d) (e) (f)

(g) (h) (i)

Figure 13: Inversion result for the SA approach with full averaging ($n = 500$) for various batch sizes and noise levels. The rows represent different batch sizes $K = 1,\ 5,\ 10$, while the columns represent different noise levels: no noise, SNR = 20 dB, and SNR = 10 dB. Averaging over the full past dramatically deteriorates the reconstruction.

```
While not converged do
    $s \leftarrow -\nabla\phi[m_i]/\|\nabla\phi[m_i]\|_2$
    find $\lambda$ s.t. $\phi[m_i + \lambda s] \leq \phi[m_i] + c\lambda\nabla\phi[m_i]^T s$
    $m_{i+1} \leftarrow m_i + \lambda s$
    $i \leftarrow i + 1$
end while
```

Algorithm 1: Steepest descent.

```
While not converged do
    draw $w$ from a pre-scribed distribution
    $s \leftarrow -\nabla\phi[m_i, w]/\|\nabla\phi[m_i, w]\|_2$
    find $\lambda$ s.t. $\phi[m_i + \lambda s, w] \leq \phi[m_i, w] + c\lambda\nabla\phi[m_i, w]^T s$
    $m_{i+1} \leftarrow (1/(n+1))(\sum_{i-n}^{i} m_i + \lambda s)$
    $i \leftarrow i + 1$
end while
```

Algorithm 2: Stochastic descent.

Finally, we show the result obtained by averaging over the full history in Figure 13. The corresponding recovery error is shown in Figure 14. It shows that too much averaging slows down the convergence.

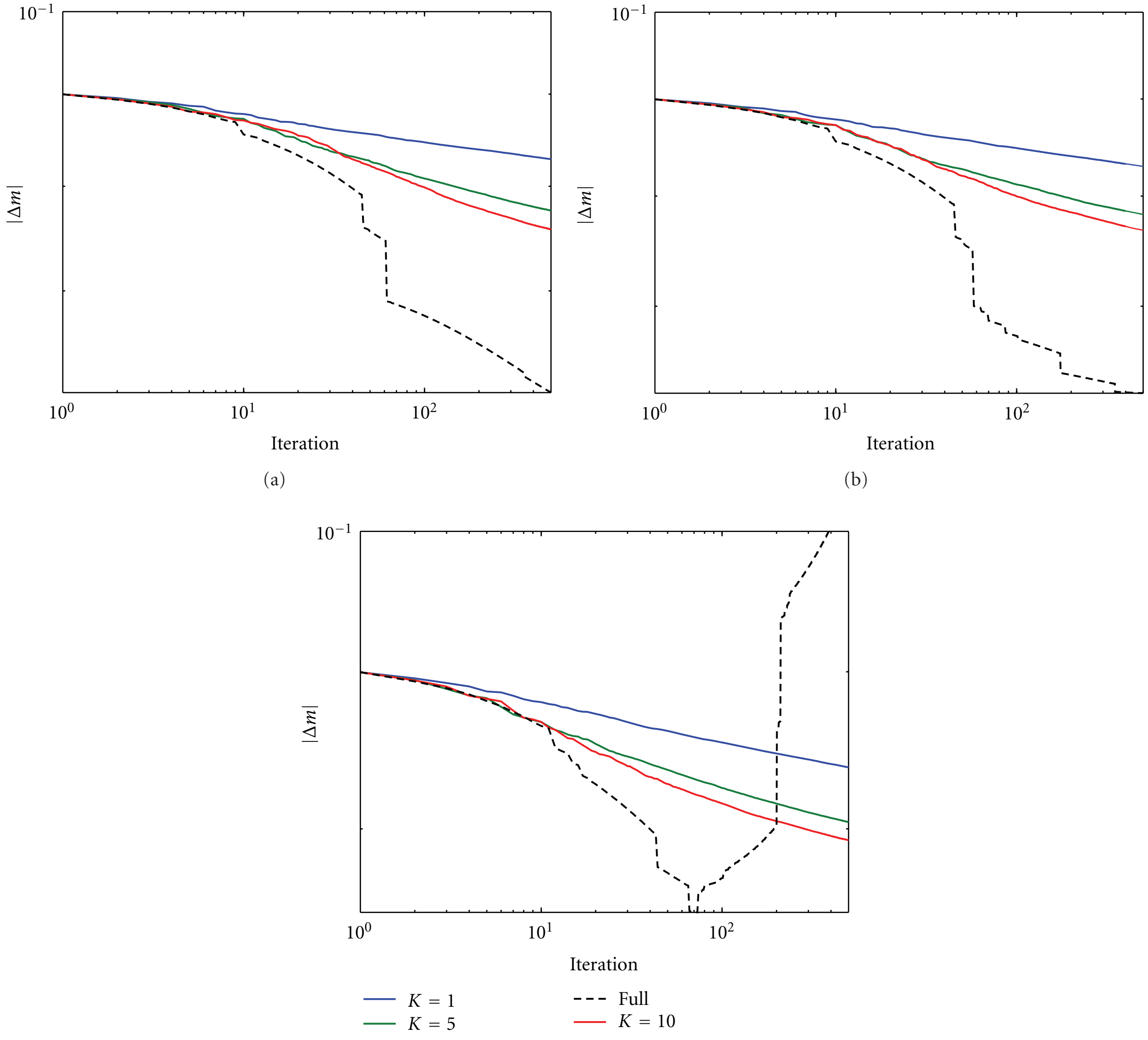

(a)

(b)

(c)

Figure 14: Error between the inverted and true model for the SA approach with full averaging for various batch sizes and the full problem, (a) without noise, (b) with noise (SNR = 20 dB), and (c) with noise (SNR = 10 dB). Averaging over the full past slows down the convergence dramatically.

6. Conclusions and Discussion

Following Haber et al. [39], we reduce the dimensionality of full waveform inversion via *randomized trace estimation*. This reduction comes at the cost of introducing random crosstalk between the sources into the updates. The resulting optimization problem can be treated as a *stochastic optimization problem*. Theory for such methods goes back to the 1950s and justifies the approach presented by Krebs et al. [8]. In particular, we use theoretical results by Avron and Toledo [14] on randomized trace estimation to get bounds for the batch size needed to approximate the misfit to a given accuracy level with a given probability. Numerical tests show, however, that these bounds may be overly pessimistic and that we get reasonable approximations for modest batch sizes.

Theory from the field of stochastic optimization suggests several approaches to tackle the optimization problem and reduce the influence of the crosstalk introduced by the randomization. The first approach, the *sample average approximation*, dictates the use of a fixed set of random sources and relies solely on increasing the batch size to get rid of the crosstalk. The *stochastic approximation*, on the other hand, dictates that we redraw the randomization each iteration and average over the past in order to suppress the stochasticity of the gradients.

We note that, as opposed to *randomized* dimensionality reduction, several authors have proposed methods for *deterministic* dimensionality reduction [39, 40]. These techniques are related to optimal experimental design and try to determine the source combination that somehow optimally illuminates the target. It is not quite clear how such methods compare to the randomized approach discussed here. It is clear, however, that by using random superpositions we have access to powerful results from the field of compressive sensing to further improve the reconstruction. Li and Herrmann [11] use sparse recovery techniques instead of Monte Carlo sampling to get rid of the crosstalk.

In our experiments, we were able to obtain results that are comparable to the full optimization with a small fraction of the number of sources. In the noiseless case, we needed only *one* simultaneous source for the SA approach. Even with noisy data, *five* simultaneous sources proved sufficient. This is a very promising result, since using five simultaneous sources for the SA method means that every iteration requires 20 times fewer PDE solves, which directly translates to a 20x computational speedup compared to a first-order deterministic method. The key point is that both SA and the full deterministic approach require roughly the same number of iterations to achieve the same accuracy.

Averaging over a limited number of past iterations improved the results for a fixed batch size and allows for the use of fewer simultaneous sources. However, too much averaging slows down the convergence.

The results of the SA approach, where a new realization of the random vectors is drawn at every iteration, are superior to the SAA results, where the random vectors are fixed. However, one could use a more sophisticated (possibly black box) optimization method for the SAA approach to get a similar result with fewer iterations. The tradeoff between using a smaller batch size and first-order methods (i.e., more iterations) versus using a larger batch size and second-order methods (i.e., less iterations) needs to be investigated further. Random superposition of shots only makes sense if those shots are sampled by the same receivers. In particular, this hampers straightforward application to marine seismic data. One way to get around this is to partition the data into blocks that are fully sampled. However, this would not give the same amount of reduction in the number of shots because only shots that are relatively close to each other can be combined without losing too much data.

The type of encoding used will most likely affect the behavior of both SA and SAA methods. It remains to be investigated which encoding is most suitable for waveform inversion.

Acknowledgments

The authors thank Eldad Haber and Mark Schmidt for insightful discussions on trace estimation and stochastic optimization. This work was in part financially supported by the Natural Sciences and Engineering Research Council of Canada Discovery Grant (no. 22R81254) and the Collaborative Research and Development Grant DNOISE II (no. 375142-08). This research was carried out as part of the SINBAD II project with support from the following organizations: BG Group, BP, Chevron, ConocoPhillips, Petrobras, Total SA, and WesternGeco.

References

[1] C. J. Beasley, R. E. Chambers, and Z. Jiang, "A new look at simultaneous sources," *SEG Technical Program Expanded Abstracts*, vol. 17, pp. 133–135, 1998.

[2] A. J. G. Berkhout, "Changing the mindset in seismic data acquisition," *The Leading Edge*, vol. 27, no. 7, pp. 924–938, 2008.

[3] L. A. Romero, D. C. Ghiglia, C. C. Ober, and S. A. Morton, "Phase encoding of shot records in prestack migration," *Geophysics*, vol. 65, no. 2, pp. 426–436, 2000.

[4] W. Dai, C. Boonyasiriwat, and G. T. Schuster, "3D multisource least-squares reverse time migration," *SEG Technical Program Expanded Abstracts*, vol. 29, pp. 3120–3124, 2010.

[5] L. Ikelle, "Coding and decoding: seismic data modeling, acquisition and processing," *SEG Technical Program Expanded Abstracts*, vol. 26, no. 1, pp. 66–70, 2007.

[6] N. Neelamani, C. Krohn, J. Krebs, M. Deffenbaugh, and J. Romberg, "Efficient seismic forward modeling using simultaneous random sources and sparsity," in *Proceedings of the 78th Annual Meeting SEG International Exposition*, 2008.

[7] F. J. Herrmann, Y. A. Erlangga, and T. Lin, "Compressive simultaneous full-waveform simulation," *Geophysics*, vol. 74, no. 4, pp. A35–A40, 2009.

[8] J. R. Krebs, J. E. Anderson, D. Hinkley et al., "Fast fullwavefield seismic inversion using encoded sources," *Geophysics*, vol. 74, no. 6, pp. WCC177–WCC188, 2009.

[9] P. P. Moghaddam and F. J. Herrmann, "Randomized fullwaveform inversion: a dimensionality-reduction approach," *SEG Technical Program Expanded Abstracts*, vol. 29, pp. 977–982, 2010.

[10] C. Boonyasiriwat and G. T. Schuster, "3D multisource fullwaveform inversion using dynamic random phase encoding," *SEG Technical Program Expanded Abstracts*, vol. 29, pp. 1044–1049, 2010.

[11] X. Li and F. J. Herrmann, "Full-waveform inversion from compressively recovered model updates," *SEG Expanded Abstracts*, vol. 29, pp. 1029–1033, 2010.

[12] E. Haber, M. Chung, and F. J. Herrmann, "An effective method for parameter estimation with PDE constraints with multiple right hand sides," Technical Report 4, UBC-Earth and Ocean Sciences Department, Vancouver, British Columbia, Canada, 2010.

[13] M. Hutchinson, "A stochastic estimator of the trace of the influence matrix for lapla-cian smoothing splines," *Communications in Statistics—Simulation and Computation*, vol. 18, pp. 1059–1067, 1989.

[14] H. Avron and S. Toledo, "Randomized algorithms for estimating the trace of an implicit symmetric positive semi-definite matrix," *Journal of the ACM*. In press.

[15] R. Byrd, G. Chin, W. Neveitt, and J. Nocedal, "On the use of stochastic hessian in-formation in unconstrained optimization," Technical report, Optimization Center, North-Western University, 2010.

[16] A. Tarantola, "Inversion of seismic reflection data in the acoustic approximation," *Geophysics*, vol. 49, no. 8, pp. 1259–1266, 1984.

[17] K. J. Marfurt, “Accuracy of finite-difference and finite-element modeling of the scalar and elastic wave equations,” *Geophysics*, vol. 49, no. 5, pp. 533–549, 1984.

[18] R. G. Pratt, “Seismic waveform inversion in the frequency domain, part 1: theory and verification in a physical scale model,” *Geophysics*, vol. 64, no. 3, pp. 888–901, 1999.

[19] S. Operto, J. Virieux, P. Amestoy, L. Giraud, and J. Y. L’Excellent, “3D frequency-domain finite-difference modeling of acoustic wave propagation using a massively parallel direct solver: a feasibility study,” *SEG Technical Program Expanded Abstracts*, vol. 25, no. 1, pp. 2265–2269, 2006.

[20] Y. A. Erlangga, C. W. Oosterlee, and C. Vuik, “A novel multigrid based preconditioner for heterogeneous Helmholtz problems,” *SIAM Journal of Scientific Computing*, vol. 27, no. 4, pp. 1471–1492, 2006.

[21] C. D. Riyanti, Y. Erlangga, R. E. Plessix, W. Mulder, C. Vuik, and C. Oosterlee, “A new iterative solver for the time-harmonic wave equation,” *Geophysics*, vol. 71, no. 5, pp. E57–E63, 2006.

[22] Y. Saad, *Iterative Methods for Sparse Linear Systems*, PWS, 1996.

[23] R. E. Plessix, “A review of the adjoint-state method for computing the gradient of a functional with geophysical applications,” *Geophysical Journal International*, vol. 167, no. 2, pp. 495–503, 2006.

[24] J. Romberg, “Compressive sensing by random convolution,” *SIAM Journal on Imaging Sciences*, vol. 2, no. 4, pp. 1098–1128, 2009.

[25] E. Candès, J. Romberg, and T. Tao, “Stable signal recovery from incomplete and inaccurate measurements,” *Communications on Pure and Applied Mathematics*, vol. 59, no. 8, pp. 1207–1223, 2006.

[26] D. L. Donoho, “Compressed sensing,” *IEEE Transactions on Information Theory*, vol. 52, no. 4, pp. 1289–1306, 2006.

[27] A. Nemirovski, A. Juditsky, G. Lan, and A. Shapiro, “Robust stochastic approximation approach to stochastic programming,” *SIAM Journal on Optimization*, vol. 19, no. 4, pp. 1574–1609, 2008.

[28] A. Shapiro, “Monte carlo sampling methods,” in *Stochastic Programming*, vol. 10 of *Handbooks in Operation Research and Management Science*, North-Holland, 2003.

[29] A. Shapiro, “On complexity of stochastic programming problems,” in *Continuous Optimization: Current Trends and Application*, Springer, New York, NY, USA, 2005.

[30] H. Robbins and S. Monro, “Robust stochastic approximation approach to stochastic programming,” *Annals of Mathematical Statistics*, vol. 22, pp. 400–407, 1951.

[31] D. P. Bertsekas and J. Tsitsiklis, *Neuro-Dynamic Programming*, Athena Scientific, Belmont, Mass, USA, 1st edition, 1996.

[32] D. P. Bertsekas and J. N. Tsitsiklis, “Gradient convergence in gradient methods with errors,” *SIAM Journal on Optimization*, vol. 10, no. 3, pp. 627–642, 2000.

[33] B. T. Polyak and A. B. Juditsky, “Acceleration of stochastic approximation by averaging,” *SIAM Journal on Control and Optimization*, vol. 30, no. 4, pp. 838–855, 1992.

[34] Y. Nesterov and J. P. Vial, “Confidence level solutions for stochastic programming,” Tech. Rep. 2000013, Universit catholique de Louvain, Center for Opera-tions Research and Econometrics (CORE), 2000.

[35] J. Nocedal and S. Wright, *Numerical Optimization*, Springer Series in Operations Research, Springer, 1999.

[36] G. Hennenfent and F. J. Herrmann, “Simply denoise: wavefield reconstruction via jittered undersampling,” *Geophysics*, vol. 73, no. 3, pp. V19–V28, 2008.

[37] T. T. Y. Lin and F. J. Herrmann, “Compressed wavefield extrapolation,” *Geophysics*, vol. 72, no. 5, pp. SM77–SM93, 2007.

[38] P. C. Hansen, *Rank-Deficient and Discrete Ill-Posed Problems: Numerical Aspects of Linear Inversion*, Society for Industrial Mathematics, Philadelphia, Pa, USA, 1998.

[39] E. Haber, L. Horesh, and L. Tenorio, “Numerical methods for the design of large-scale nonlinear discrete ill-posed inverse problems,” *Inverse Problems*, vol. 26, no. 2, Article ID 025002, 2010.

[40] W. Symes, “Source synthesis for waveform inversion,” *SEG Expanded Abstracts*, vol. 29, pp. 1018–1022, 2010.

Hindawi Publishing Corporation
International Journal of Geophysics
Volume 2011, Article ID 407673, 6 pages
doi:10.1155/2011/407673

Research Article

Seismic Structure of Local Crustal Earthquakes beneath the Zipingpu Reservoir of Longmenshan Fault Zone

Haiou Li,[1] Xiwei Xu,[1] Wentao Ma,[1] Ronghua Xie,[2] Jingli Yuan,[1] and Changpeng Xu[1]

[1] *Institute of Geology, China Earthquake Administration, Beijing 100029, China*
[2] *Institute of Reservoir Earthquake, Earthquake Administration of Sichuan Province, Chengdu 610041, China*

Correspondence should be addressed to Haiou Li, li_hai_ou@126.com

Received 15 January 2011; Revised 7 April 2011; Accepted 21 April 2011

Academic Editor: Martin Tygel

Three-dimensional P wave velocity models under the Zipingpu reservoir in Longmenshan fault zone are obtained with a resolution of 2 km in the horizontal direction and 1 km in depth. We used a total of 8589 P wave arrival times from 1014 local earthquakes recorded by both the Zipingpu reservoir network and temporary stations deployed in the area. The 3-D velocity images at shallow depth show the low-velocity regions have strong correlation with the surface trace of the Zipingpu reservoir. According to the extension of those low-velocity regions, the infiltration depth directly from the Zipingpu reservoir itself is limited to 3.5 km depth, while the infiltration depth downwards along the Beichuan-Yingxiu fault in the study area is about 5.5 km depth. Results show the low-velocity region in the east part of the study area is related to the Proterozoic sedimentary rocks. The Guanxian-Anxian fault is well delineated by obvious velocity contrast and may mark the border between the Tibetan Plateau in the west and the Sichuan basin in the east.

1. Introduction

The 12 May Wenchuan earthquake occurred beneath the Longmenshan thrust belt and was the most destructive earthquake in China in the last 30 years. Due to the 10 km distance of the Wenchuan epicenter to the Zipingpu reservoir and abnormal seismicity increases around the Zipingpu reservoir, the possibility that the Wenchuan earthquake was a reservoir-induced earthquake is obviously an important issue and has become a debating issue [1–3]. Most recent publications [4–8] give possible scenarios obtained from the calculation of the Coulomb stress change under a set of assumptions. However, those results are critically dependent on assumptions such as diffusivity and the fault plane orientation. Ge et al. presented that the Zipingpu reservoir potentially hastened the occurrence of the Wenchuan earthquake by tens to hundreds of years [4]. Zhou et al. [7] repeated Ge et al.'s work and found that an improper dip angle parameter might lead to a wrong conclusion. Their modeling results based on the 2-D model and 3-D model with proper fault parameters show the Coulomb stress changes alone neither were large enough nor had the correct orientation to affect the occurrence of the Wenchuan earthquake.

During recent years, different seismic studies have been performed to explore the relationship between the crustal velocity structure and the occurrence of the Wenchuan earthquake [9, 10] or aftershocks of the Wenchuan earthquake [11, 12]. However, the large distance between stations in Zipingpu reservoir has hindered the achievement of enough resolution of the seismic images to correlate the velocity anomalies with geological structures and possible connections between velocity structure and abnormal seismicity increases since the filling of the Zipingpu reservoir. In this paper, the results of a seismic tomography study are shown based on local earthquakes near the Zipingpu reservoir. The resolution obtained is higher than in previous studies. The seismic images are compared with the geological setting and the submerged region of the Zipingpu reservoir.

2. Geological Setting

The Zipingpu reservoir lies in the Longmenshan fault zone which is characterized by a NE strike and composed of

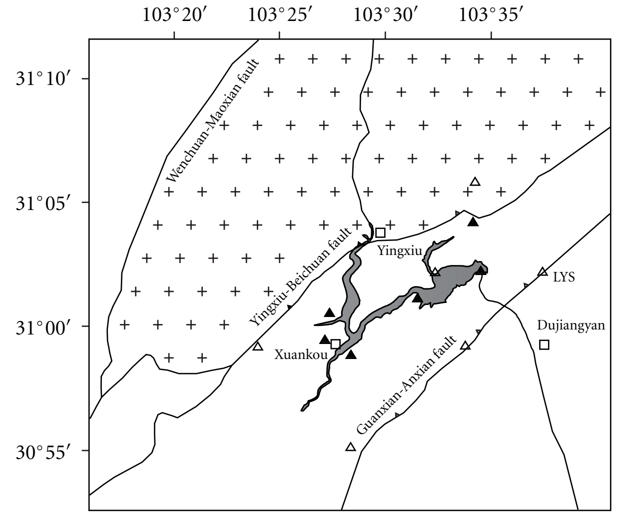

Figure 1: Geological sketch map of the study area. The areas filled with plus symbols are igneous rocks of the Pengguan massif, and the other areas are sedimentary rocks. Black open triangles are seismic stations of the Zipingpu reservoir network. Black closed triangles are the temporary seismic stations. Bold lines denote the faults. Fine lines denote the river. Gray region represents the Zipingpu reservoir. Squares represent the county. LYS represents the name of the station.

three major faults: the Wenchuan-Maoxian fault in the northwest, the Beichuan-Yingxiu fault in the central, and the Guanxian-Anxian fault in the southeast (Figure 1). Analyses of field measurements of surface ruptures and coseismic deformations suggest that the Beichuan-Yingxiu part of the Longmenshan fault zone close to the Zipingpu reservoir is a northeast-striking northwest-dipping thrust with small right-lateral strike-slip component [13, 14]. The outcrops between the Wenchuan-Maoxian and Beichuan-Yingxiu faults in the study area are Proterozoic igneous Pengguan massif composed of diorites and granites and the other areas are mainly covered by Proterozoic sedimentary rocks which are older towards the Pengguan massif.

3. Data and Methods

3.1. Aftershock Observations. To investigate the seismic structures around the submerged region of the Zipingpu reservoir, we refined the reservoir monitoring network which includes seven stations around the Zipingpu reservoir (1 destroyed by the Wenchuan earthquake) with 6 temporary seismic stations at the beginning of the year of 2009. The seismicity in the studied area is characterized by abnormal increases since the filling of Zipingpu reservoir, especially after the occurrence of the Wenchuan earthquake. Most of earthquakes recorded by above 12 stations have low magnitude ($M < 3$). An et al. [10], using digital data recorded by 26 seismic stations, show the results of P-velocity model around the main shock epicenter region. They did not emphasize their focus on the Zipingpu reservoir during their study or previous studies. In this paper, we have more appropriate station distribution around the Zipingpu reservoir.

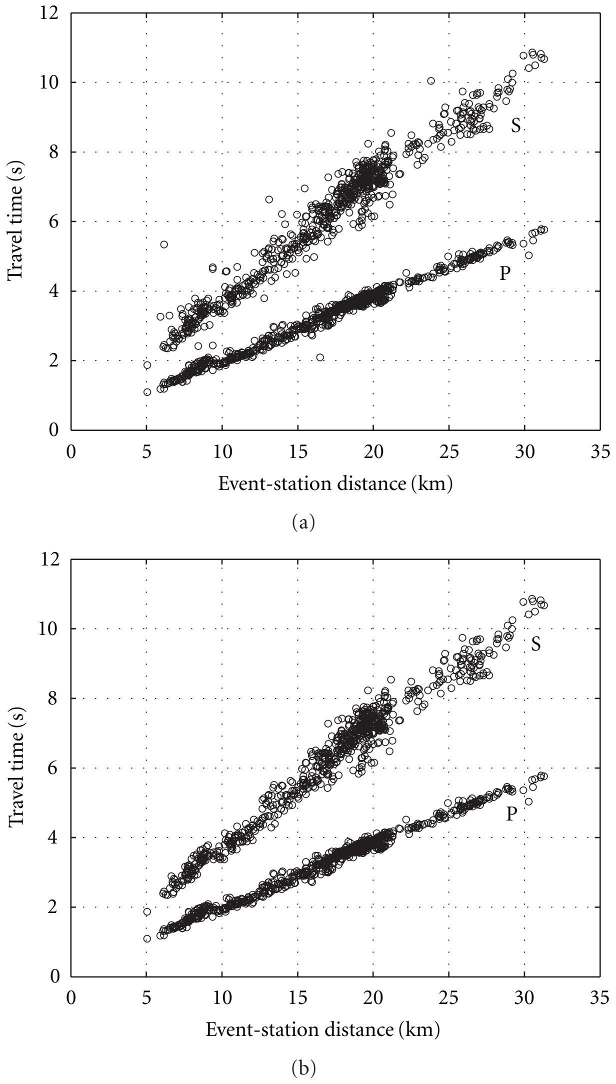

(a)

(b)

Figure 2: Travel time variations of the station LYS with change of the event-station distances before (a) and after (b) removal of abnormal travel times.

3.2. Data Selection. We have used P wave arrival times from digital data recorded in 2009 by our temporary 6 seismic stations and the Zipingpu reservoir seismic network which belongs to reservoir institute of Sichuan Earthquake Administration. Figure 1 shows the distribution of seismic stations used in this study. We have selected the local earthquakes which have been recorded at least five stations and whose standard errors of epicenters are not further than 8 km. This procedure helps in the relocating of local earthquakes. Figure 2 shows the P wave and S wave travel time with epicentral distance at station LYS, before and after removal of outliers. After removal of any arrival time that is far away from the distribution trend with the event-station distances, the local earthquakes were relocated using

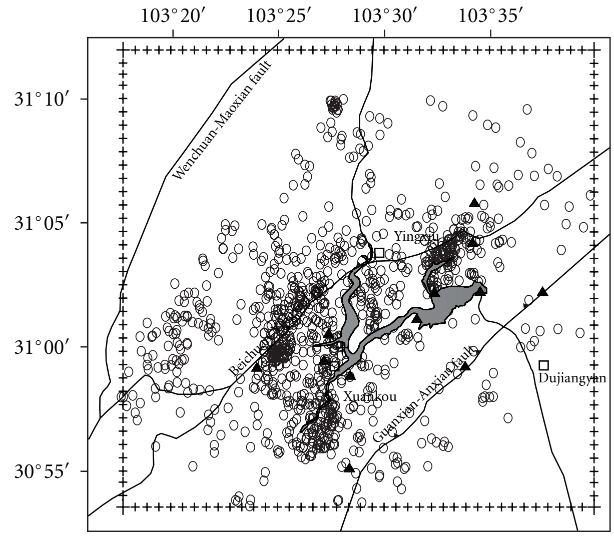

Figure 3: Distribution of the local earthquakes used in the present study. Ellipses denote earthquake epicenters given by the double-difference relocation. Solid triangles are all stations (temporary + permanent) used in the relocation and tomography inversion. The plus symbols present the area of the tomography grids and that of velocity inversion as shown in Figure 5. The others are the same as in Figure 1.

Zhang and Thurber's [15] program which can produce not only the relative relocations but also absolute relocations. We treat all the events as one cluster. Because travel time tomography was done in this method, relocations are more reliable than those obtained just from relative relocation algorithm. The tomography grids were arranged at intervals of 10 km and 3 km in horizontal and vertical directions separately. Careful tomography results were obtained by Hole and Zelt's tomography method [16]. Finally, we selected a total of 1014 from 1085 local earthquakes, with 8589 P wave travel time observations. The average differences between initial and relocated hypocenters are 100 m, 91 m, and 198 m in horizontal and vertical directions. Due to topography and station elevations, the parameter of air depth is set as −1 km. So, the depth of the selected earthquakes ranges from −0.8 km to 10.5 km. The distribution of the relocation in horizontal profile is shown in Figure 3, where the ellipses denote the hypocenter of earthquakes given by double-difference tomography program.

3.3. Methodology and Resolution. The tomography method of Hole and Zelt [16] was used to determine the 3-D P wave velocity structure. This method introduces special headwave operators to better deal with the presence of strong velocity contrast and permits placing the shots at free location of the velocity model. Twelve seismic stations were set as the shots and local earthquakes as the receivers in order to simplify the input files.

The area selected for the tomographic study is located between 30°55′ N and 31°10′ N and from 103°20′ E to 103°38′ E, comprising 36 km (latitude) × 32 km (longitude). We set up a 3-D grid in this study with a grid spacing of 1 km in the horizontal and vertical directions. Lateral and vertical model smoothing as regularization was introduced to result in a more physically reasonable structure model. After removal of outliers, the average RMS of travel time residuals is 0.67 s for the reference 1-D model, and it is reduced to 0.25 s for the tomography model after the fourth iteration. We applied a checkerboard resolution test to examine the resolution scale of the present data set. We assigned positive and negative velocity anomalies of 3% to the reference model. The synthetic data was calculated by 3-D finite-difference forward modeling. Random noise was not added to the synthetic data. The inverted model of the checkerboard tests retrieved checkers with a size of 2 km in lateral directions beneath the submerged region of the Zipingpu reservoir (Figure 4).

4. Results and Discussion

The P wave velocities from the seismic tomography are displayed at different depths (Figure 5). The most robust features imaged at shallow depths are the several pronounced low-velocity regions at the background of the velocity larger than 6 km/s. We can see that low-velocity regions in the central of the study area were placed close to the surface trace of the Zipingpu reservoir, and those low-velocity regions extend downwards and vanish at 3.5 km depth. The obvious features at the depth of 3.5 km are two low-velocity regions trending NE-SW which correspond to the Beichuan-Yingxiu strike-slip thrust fault and the Guanxian-Anxian fault.

It is widely recognized that low-velocity regions are a feature of some old or active strike-slip zones [17]. Especially for the place where there is a significant fracturing with contained fluids, the fault zone will exhibit low velocity [18, 19]. Hence, these features of the low-velocity distribution can be related with the infiltration water of the Zipingpu reservoir. From 5.5 km depth downwards, the low-velocity region indicating the range of infiltration water along the Beichuan-Yingxiu strike-slip thrust fault vanished. It is worth noting that the zone of high pore pressure is not the same as the zone of water infiltration. Due to probable existence of high pore pressure deeper, caused by the reservoir loading, we are not sure whether the impoundment of the Zipingpu reservoir triggers the main shock of 2008 or not. If the Zipingpu reservoir triggered the 2008 main shock, the epicenter of it should be located on the Beichuan-Yingxiu fault which is the main passage of leakage or pressure transmission deduced from the low-velocity regions.

As shown in Figure 5, with increasing depth, the range of the high velocity part indicating the Pengguan massif [10] gradually diminishes, and the range of the relative low velocity in the east of the study area broadens westwards. Those results support the recognitions that the Longmenshan fault thrusts eastwards to the Sichuan basin. The distribution of the low velocity means that the Guanxian-Anxian fault marks the border between the Tibetan Plateau in the west and the Sichuan basin in the east even though the surface rupture of this fault lies in the Sichuan basin.

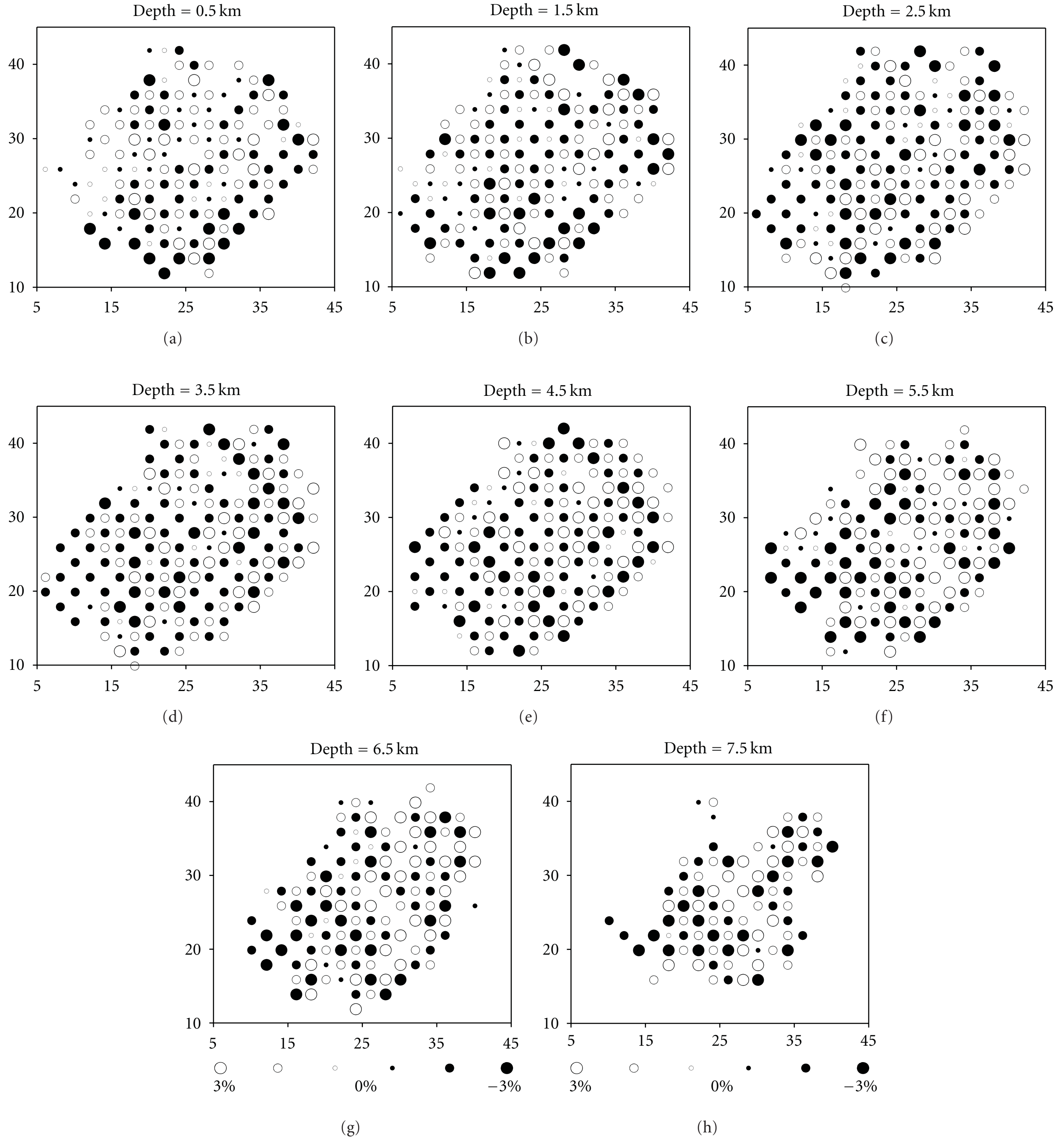

(a) (b) (c) (d) (e) (f) (g) (h)

Figure 4: Results of checkerboard resolution test. Open and closed circles denote slow and fast velocities, respectively. The depth of each layer is shown at the upper part of the map. The grid spacing is 2 km in the horizontal direction and 1 km in depth. The perturbation scale is shown on the right. The coordinates are in km.

5. Summary and Conclusions

Through the use of digital data from more appropriate station distribution around the Zipingpu reservoir, seismic images are obtained with high resolution. Results not only confirmed previous sharp velocity changes at both sides of the fault and higher velocity of the Pengguan massif, but also found the correlation between low velocity and possible infiltration zone of the Zipingpu water reservoir. Velocity distribution provided a sign of water diffusion, but

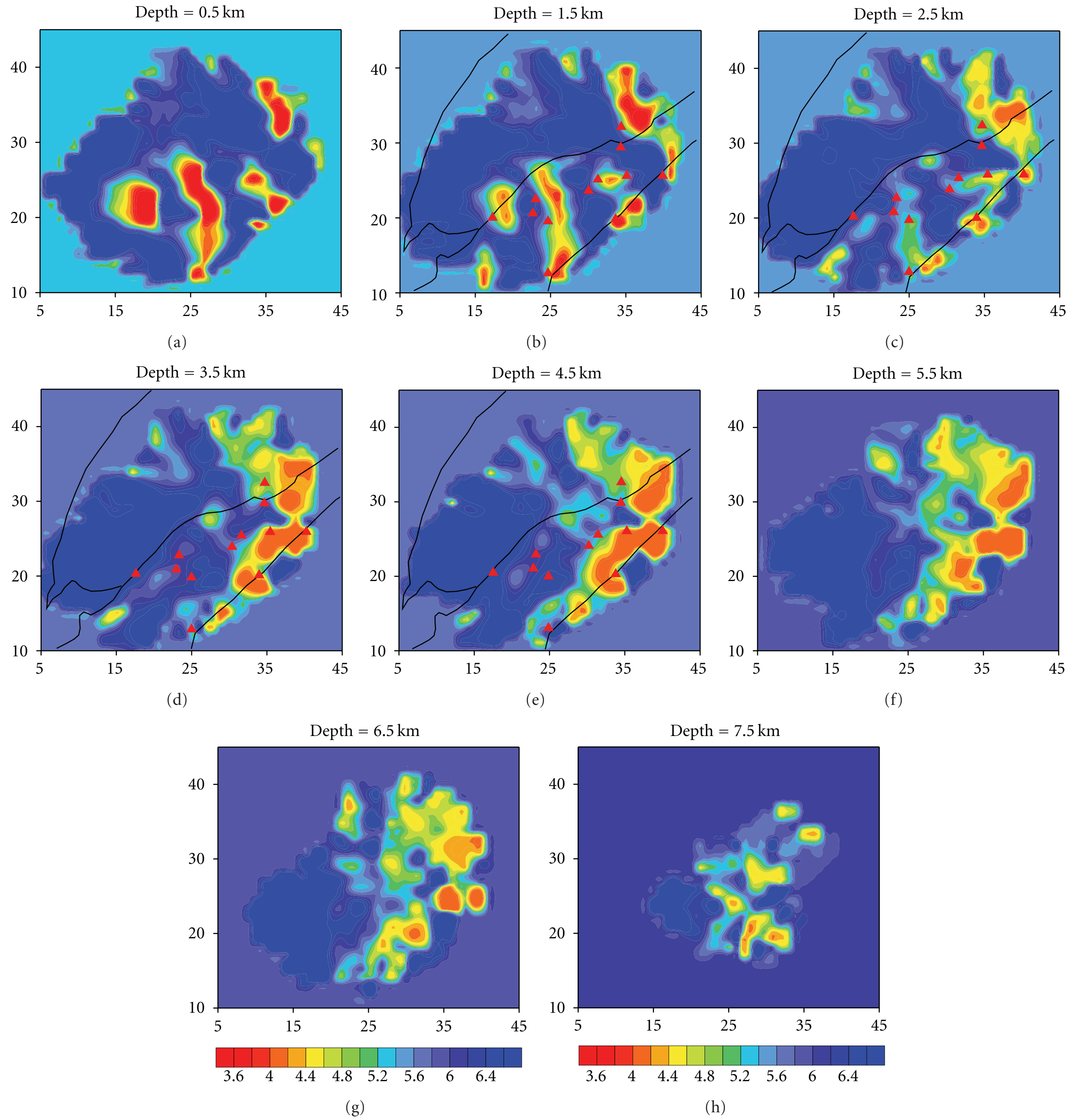

(a) (b) (c)

(d) (e) (f)

(g) (h)

Figure 5: P wave velocity models at different depth. The depth of each layer is shown at the upper part of the map. Red triangles represent the stations. The P wave velocity scale is shown on the bottom. Color scale is absolute P wave velocity (km/s). Background velocity near the edges denotes the initial 1-D velocity model. The coordinates are in km.

the conclusions from the results may need to be examined thoroughly in the future by other observable geophysical properties, such as electric and magnetic properties.

The principal findings of this study are as follows.

(1) The low-velocity regions placed close to the surface trace of the Zipingpu reservoir are correlated with the submerged region of the Zipingpu reservoir. Those low-velocity regions under the Zipingpu reservoir extend downwards and vanish at 3.5 km depth, which means that water possibly infiltrates downwards to this depth.

(2) At 3.5 km depth, two pronounced NE-SW trending low-velocity regions can be associated with the Beichuan-Yingxiu fault and the Guanxian-Anxian

fault. The low-velocity region along the Beichuan-Yingxiu fault can be traced up to 2.5 km depth, where it is connected with the other low-velocity regions below the western branch of the Zipingpu reservoir. At 5.5 km depth, the low-velocity region along the Beichuan-Yingxiu fault fades. So, possible downwards infiltration depth along the Beichuan-Yingxiu fault in the study area is deduced at about 5.5 km depth.

(3) The Guanxian-Anxian fault is well delineated by obvious velocity contrast. The distribution of the low velocity in the east of the study area indicates that the Guanxian-Anxian fault marks the border between the Tibetan Plateau in the west and the Sichuan basin in the east.

Acknowledgments

This work has been supported by the Key Project of Chinese National Science and Technology (Grant 2008BAC38b0401) and the Basic Research Foundation of the Institute of Geology, CEA (Grant DF-IGCEA060828). Finally, the authors are grateful to two reviewers and the editors for their constructive reviews.

References

[1] Y. Chen, "Did the reservoir impoundment trigger the Wenchuan earthquake?" *Science in China, Series D*, vol. 52, no. 4, pp. 431–433, 2009.

[2] R. A. Kerr and R. Stone, "Two years later, new rumblings over origins of Sichuan Quake," *Science*, vol. 327, no. 5970, p. 1184, 2010.

[3] R. A. Kerr and R. Stone, "A human trigger for the great quake of Sichuan?" *Science*, vol. 323, no. 5912, p. 322, 2009.

[4] S. Ge, M. Liu, N. Lu, J. W. Godt, and G. Luo, "Did the Zipingpu reservoir trigger the 2008 Wenchuan earthquake?" *Geophysical Research Letters*, vol. 36, no. 20, Article ID L20315, 2009.

[5] K. Deng, S.-Y. Zhou, R. Wang, R. Robinson, C.-P. Zhao, and W.-Z. Cheng, "Evidence that the 2008 M_w 7.9 Wenchuan earthquake could not have been induced by the Zipingpu reservoir," *Bulletin of the Seismological Society of America*, vol. 100, no. 5B, pp. 2805–2814, 2010.

[6] K. Gahalaut and V. K. Gahalaut, "Effect of the Zipingpu reservoir impoundment on the occurrence of the 2008 Wenchuan earthquake and local seismicity," *Geophysical Journal International*, vol. 183, no. 1, pp. 277–285, 2010.

[7] S.-Y. Zhou, K. Deng, C.-P. Zhao, and W.-Z Cheng, "Discussion on 'Was the 2008 Wenchuan earthquake triggered by Zipingpu reservoir?'," *Earthquake Science*, vol. 23, no. 6, pp. 577–581, 2010.

[8] X.-L. Lei, "Possible roles of the Zipingpu reservoir in triggering the 2008 Wenchuan earthquake," *Journal of Asian Earth Sciences*, vol. 40, no. 4, pp. 844–854, 2011.

[9] Q.-S. Li, R. Gao, H.-Y. Wang et al., "Deep background of Wenchuan earthquake and the upper crust structure beneath the Longmen Shan and adjacent areas," *Acta Geological Sinica*, vol. 83, no. 4, pp. 733–739, 2009.

[10] M.-J. An, F. Mei, S.-W. Dong et al., "Seismogenic structure around the epicenter of the May 12, 2008 Wenchuan earthquake from micro-seismic tomography," *Acta Geological Sinica*, vol. 83, no. 4, pp. 724–732, 2009.

[11] J. P. Wu, Y. Huang, T. Z. Zhang, Y.-H. Ming, and L.-H. Fang, "Aftershock distribution of the Ms 8.0 Wenchuan earthquake and three dimensional P wave velocity structure in and around source region," *Chinese Journal of Geophysics*, vol. 52, no. 2, pp. 320–328, 2009 (Chinese).

[12] Y. Xu, R.-Q. Huang, Z.-W. Li, Y. Xu, J.-S. Liu, and J. H. Liu, "S-wave velocity structure of the Longmen Shan and Wenchuan earthquake area," *Chinese Journal of Geophysics*, vol. 52, no. 2, pp. 329–338, 2009 (Chinese).

[13] G.-H. Chen, X.-W. Xu, R.-Z. Zheng et al., "Quantitative analysis of the co-seismic surface rupture of the 2008 Wenchuan earthquake, Sichuan, China along the Beichuan-Yingxiu fault," *Seismology and Geology*, vol. 30, no. 3, pp. 723–737, 2008 (Chinese).

[14] X.-W. Xu, X.-Z Wen, G.-H. Yu et al., "Coseismic reverse- and oblique-slip surface faulting generated by 2008 Mw 7.9 Wenchuan earthquake, China," *Geology*, vol. 37, no. 6, pp. 515–518, 2009.

[15] H.-J Zhang and C. H. Thurber, "Double-difference tomography: the method and its application to the Hayward fault, California," *Bulletin of the Seismological Society of America*, vol. 93, no. 5, pp. 1875–1889, 2003.

[16] J. A. Hole and B. C. Zelt, "3-D finite-difference reflection travel times," *Geophysical Journal International*, vol. 121, no. 2, pp. 427–434, 1995.

[17] T. A. Stern and J. H. McBride, "Seismic exploration of continental strike-slip zones," *Tectonophysics*, vol. 286, no. 1–4, pp. 63–78, 1998.

[18] D. Eberhart-Phillips, B. D. Rodriguez, and W. J. Lutter, "Surface seismic and electrical methods to detect fluids related to faulting," *Journal of Geophysical Research*, vol. 100, no. B7, pp. 12919–12936, 1995.

[19] I. Serrano, D.-P. Zhao, J. Morales, and F. Torcal, "Seismic tomography from local crustal earthquakes beneath eastern Rif Mountains of Morocco," *Tectonophysics*, vol. 367, no. 3-4, pp. 187–201, 2003.

Hindawi Publishing Corporation
International Journal of Geophysics
Volume 2011, Article ID 870819, 28 pages
doi:10.1155/2011/870819

Research Article

Deghosting, Demultiple, and Deblurring in Controlled-Source Seismic Interferometry

Joost van der Neut,[1] Maria Tatanova,[2] Jan Thorbecke,[1] Evert Slob,[1] and Kees Wapenaar[1]

[1] *Department of Geotechnology, Faculty of Civil Engineering and Geosciences, Delft University of Technology, Stevingweg 1, 2628 CN, Delft, The Netherlands*
[2] *Earth's Physics Department, Saint Petersburg State University, Ulyanovskaya Street 1, Saint Petersburg 198504, Russia*

Correspondence should be addressed to Joost van der Neut, j.r.vanderneut@tudelft.nl

Received 21 September 2010; Accepted 29 March 2011

Academic Editor: Sergey Fomel

With controlled-source seismic interferometry we aim to redatum sources to downhole receiver locations without requiring a velocity model. Interferometry is generally based on a source integral over cross-correlation (CC) pairs of full, perturbed (time-gated), or decomposed wavefields. We provide an overview of ghosts, multiples, and spatial blurring effects that can occur for different types of interferometry. We show that replacing cross-correlation by multidimensional deconvolution (MDD) can deghost, demultiple, and deblur retrieved data. We derive and analyze MDD for perturbed and decomposed wavefields. An interferometric point spread function (PSF) is introduced that can be obtained directly from downhole data. Ghosts, multiples, and blurring effects that may populate the retrieved gathers can be locally diagnosed with the PSF. MDD of perturbed fields can remove ghosts and deblur retrieved data, but it leaves particular multiples in place. To remove all overburden-related effects, MDD of decomposed fields should be applied.

1. Introduction

Seismic interferometry is an effective tool to redatum sources to receiver locations, without the need of a velocity model. Recently, we have seen an increase of various applications; see Curtis et al. [1] and Wapenaar et al. [2]. In this paper we restrict ourselves to controlled-source interferometry for data-driven redatuming. In a recent publication of Schuster [3], numerous applications in this field can be found. Among them is the well-known virtual-source method of Bakulin and Calvert [4].

Traditionally, the theory of interferometry has been derived from a reciprocity theorem of the correlation type or from time-reversal arguments [5, 6]. A few special applications are based on wavefield convolutions [7, 8]. For controlled-source applications, the theory is generally applied with one-sided illumination, meaning that sources are located at the earth's surface only and are not—as often assumed in theory—enclosing a volume. Moreover, interactions with the free surface and intrinsic losses are generally not taken into account. Because of these factors, spurious events can enter the retrieved gathers [9] and true amplitudes are generally not preserved [10].

To mitigate some of these artifacts, several methods have been proposed. In perturbation-based interferometry [11], incident and scattered wavefields are separated prior to cross-correlation. In the virtual source method [4, 12], a similar separation is achieved by time-gating the direct arrival prior to cross-correlation. Mehta et al. [13] showed that separation of up- and downgoing waves with multicomponent sensors can yield even further improvements. Vasconcelos et al. [14] demonstrate a variety of these methods in complex synthetic subsalt environments.

A different group of methods is based on deconvolution instead of cross-correlation (CC). Replacing cross-correlation by deconvolution can remove undesired multiples from the overburden [15], a concept that has also been referred to as Noah deconvolution [16] or Einstein deconvolution [17, 18]. An additional advantage of deconvolution is that the source wavelet is deconvolved before stacking, which can be beneficial if the source has a complicated signature [19, 20]. Various authors have suggested to redatum data by summing over single-station deconvolution traces [4, 21]. However, to retrieve an exact Green's function by deconvolution in 3D heterogeneous media, single-station deconvolution should be replaced by multidimensional deconvolution (MDD), as shown by Wapenaar et al. [22]. MDD is based on the inversion of a forward problem that is generally derived for decomposed wavefields. The method has a lot in common with Betti deconvolution, as implemented by Amundsen et al. [23] and Holvik and Amundsen [24] to remove free-surface multiples from ocean bottom cable (OBC) data. For various applications of MDD, see Wapenaar et al. [22]. Van der Neut et al. [25] showed that MDD can correct for attenuation and improve interferometric imaging below complex overburden. Minato et al. [26] applied MDD to virtual cross-well data. MDD can also be applied to ground penetrating radar [27], controlled-source electromagnetic exploration [28, 29], and lithospheric-scale imaging [30].

A typical application of controlled-source seismic interferometry is to redatum sources to a downhole receiver array below a complex overburden. Bakulin and Calvert [4] were pioneering in this field using the so-called virtual source method. A typical configuration is shown in Figure 1(a). Sources are situated at the earth's surface locations $\mathbf{x}_S$. Receivers are located at $\mathbf{x}_A$ and $\mathbf{x}_B$ in a well that can be horizontal, deviated, or vertical. The aim is to transform the data obtained with the configuration shown in Figure 1(a) into virtual data as if there was a source at $\mathbf{x}_A$ and a receiver at $\mathbf{x}_B$ (Figure 1(b)). Like Bakulin and Calvert [4], we will do so without requiring a velocity model, thus bypassing all complexities of the overburden. Schuster's group considered a range of other configurations [3], one of them being shown in Figure 1(c). Here the aim is to create a virtual source at location $\mathbf{x}_A$ by exploiting scattered or dived waves that illuminate the target (e.g., a salt flank) under angles that are unseen in conventional processing (Figure 1(d)); see Xiao et al. [31], Hornby and Yu [32], Lu et al. [33] and Ferrandis et al. [34] for applications. Another application is virtual cross-well acquisition, where $\mathbf{x}_A$ and $\mathbf{x}_B$ are located in separate wells that can be vertical [26, 35, 36], horizontal [37], or deviated; see Figures 1(e) and 1(f). Many of the formulations that appear in this paper require spatial integrals not only over source locations but also over receiver locations. For a 3D heterogeneous medium, this means that 2D arrays of both sources and receivers should be deployed. Since we assume the presence of downhole receivers, this is generally not feasible. That is why we restrict ourselves to wave propagation in a 2D plane, ignoring out-of-plane reflections.

In this paper we distinguish between ghosts and multiples. With ghosts we refer to spurious events that populate our retrieved gathers, because initial assumptions were not properly fulfilled. With multiples we refer to physical events stemming from multiple reflections. Blurring effects can occur if illumination conditions are imperfect. We analyze the ghosts and multiples that can occur in interferometry by CC of full, perturbed, and decomposed fields. Next we introduce MDD of perturbed and decomposed fields, which can be applied with single-component sensors. We analyze to what extent these methods can be used to remove ghosts, multiples, and blurring artifacts on single- and multicomponent data.

2. Cross-Correlation of Full Fields

Various authors have shown that cross-correlation of wavefields at two receivers followed by summation over a closed boundary of sources can provide a Green's function as if there was a virtual source at one of the receiver locations and a receiver at the other. In Figure 2 we give a more schematic illustration of the problem formulated in Figure 1(a). The aim is to redatum the source locations $\mathbf{x}_S$ to a receiver location $\mathbf{x}_A$ "below" the overburden but "above" the target of imaging, without requiring a velocity model of the medium. Note that the terminology of "below" and "above" can be interchanged with "left" and "right" for the situation of salt flank imaging (Figure 1(c)) or the virtual cross-well (Figure 1(e)).

To retrieve an exact Green's function, both monopole and dipole sources are required along the closed boundary spanned by $\partial\mathbb{S}$ and $\partial\mathbb{O}$. The medium should be free of intrinsic losses inside $\mathbb{V}$. Under these conditions, the following representation can be derived for Green's function retrieval [38]:

$$\begin{aligned} &\left|\hat{S}(\omega)\right|^2\left[\hat{G}(\mathbf{x}_B,\mathbf{x}_A,\omega)+\hat{G}^*(\mathbf{x}_A,\mathbf{x}_B,\omega)\right] \\ &\quad = \hat{I}^S(\mathbf{x}_B,\mathbf{x}_A,\omega)+\hat{I}^O(\mathbf{x}_B,\mathbf{x}_A,\omega). \end{aligned} \tag{1}$$

On the left hand side we find the Green's function $\hat{G}(\mathbf{x}_B,\mathbf{x}_A,\omega)$ as if there was an injection rate point source at $\mathbf{x}_A$ and a receiver for acoustic pressure at $\mathbf{x}_B$. It is given in the frequency domain, indicated by the hat and angular frequency ω. We also find its acausal counterpart $\hat{G}^*(\mathbf{x}_A,\mathbf{x}_B,\omega)$, where superscript $*$ denotes complex conjugation. Note that the retrieved response is bandlimited by $|\hat{S}(\omega)|^2$, where $\hat{S}(\omega)$ is the spectrum of the source wavelet. On the right-hand side, we find two integrals: $\hat{I}^S$ and $\hat{I}^O$. $\hat{I}^S$ is referred to as the "known integral," obtained by cross-correlations of wavefields from existing source locations $\mathbf{x}_S$ at $\partial\mathbb{S}$. $\hat{I}^O$ is the "missing integral," obtained by cross-correlation of wavefields from nonexisting source locations $\mathbf{x}_O$ at $\partial\mathbb{O}$. Even though the source locations $\mathbf{x}_O$ are not present in a realistic survey, we keep $\hat{I}^O$ in the representation, allowing us to quantify its contribution.

First, let us consider the known integral $\hat{I}^S$, as derived by Wapenaar and Fokkema [38]:

$$\begin{aligned} &\hat{I}^S(\mathbf{x}_B,\mathbf{x}_A,\omega) \\ &\quad = -\int_{\partial\mathbb{S}}\frac{1}{j\omega\rho(\mathbf{x}_S)} \\ &\qquad \times\Big[\{\mathbf{n}_S\cdot\nabla_S\hat{p}(\mathbf{x}_B,\mathbf{x}_S,\omega)\}\{\hat{p}(\mathbf{x}_A,\mathbf{x}_S,\omega)\}^* \\ &\qquad\quad -\{\hat{p}(\mathbf{x}_B,\mathbf{x}_S,\omega)\}\{\mathbf{n}_S\cdot\nabla_S\hat{p}(\mathbf{x}_A,\mathbf{x}_S,\omega)\}^*\Big]d\mathbf{x}_S. \end{aligned} \tag{2}$$

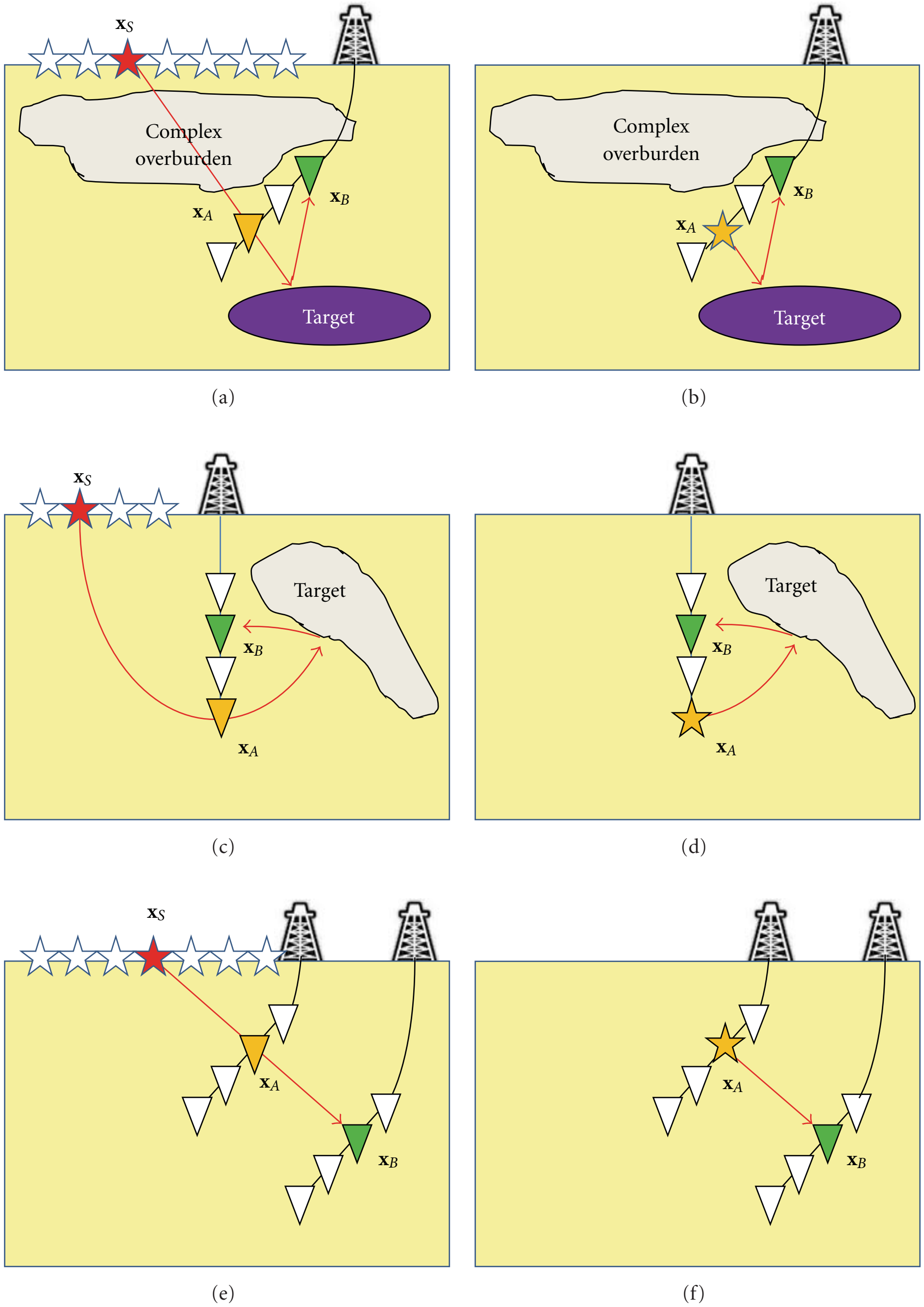

(a) (b)

(c) (d)

(e) (f)

Figure 1: Typical redatuming problems: (a) input data for redatuming through complex overburden; (b) output data after redatuming through complex overburden (with some types of interferometry, the overburden is replaced by a homogeneous halfspace); (c) input data for flank imaging; (d) output data for flank imaging after redatuming; (e) input data for virtual cross-well; (f) output data after virtual cross-well; $\mathbf{x}_S$ denote the source locations, $\mathbf{x}_A$ denote the receiver locations that are turned into virtual sources, and $\mathbf{x}_B$ denote other receiver locations.

Here $\hat{p}(\mathbf{x}_A, \mathbf{x}_S, \omega)$ represents the pressure recording at $\mathbf{x}_A$ due to a monopole source at $\mathbf{x}_S$. These recordings are assumed to be Green's functions (or impulse responses) $\hat{G}(\mathbf{x}_A, \mathbf{x}_S, \omega)$ convolved with source wavelet $\hat{S}(\omega)$. Normal vector $\mathbf{n}_S$ points perpendicular (outward) to the source array $\partial\mathbb{S}$. Further, $\nabla_S = (\partial/\partial x_{1,S}, \partial/\partial x_{2,S}, \partial/\partial x_{3,S})^T$, where $\mathbf{x}_S = (x_{1,S}, x_{2,S}, x_{3,S})^T$ and superscript T denotes the transposed. Hence, $\mathbf{n}_S \cdot \nabla_S \hat{p}(\mathbf{x}_A, \mathbf{x}_S, \omega)$ is interpreted as the response at $\mathbf{x}_A$ due to a dipole source at $\mathbf{x}_S$. $\rho(\mathbf{x}_S)$ is the mass density at the source array.

The representation of missing integral $\hat{I}^O$ is very similar. In this case responses of nonexisting source locations $\mathbf{x}_O$

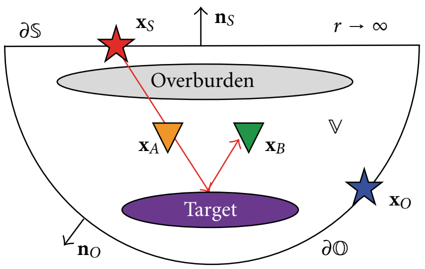

Figure 2: Configuration for controlled-source interferometry by cross-correlation of full fields; volume $\mathbb{V}$ is enclosed by the source array $\partial\mathbb{S}$ and an additional half sphere $\partial\mathbb{O}$ whose radius $r \to \infty$; $\mathbf{x}_S$ denotes a source location at $\partial\mathbb{S}$ and $\mathbf{n}_S$ is the unit normal vector of this surface; $\mathbf{x}_O$ denotes a source at $\partial\mathbb{O}$ and $\mathbf{n}_O$ is the unit normal vector of this surface; heterogeneities between sources and receivers are referred to as "overburden," whereas heterogeneities below the receivers are referred to as "target."

needs to be cross-correlated and $\mathbf{n}_S$ needs to be replaced by the normal vector $\mathbf{n}_O$ along $\partial\mathbb{O}$, yielding

$$\begin{aligned}\hat{I}^O&(\mathbf{x}_B,\mathbf{x}_A,\omega)\\ &= -\int_{\partial O}\frac{1}{j\omega\rho(\mathbf{x}_O)}\\ &\quad\times\Big[\{\mathbf{n}_O\cdot\nabla_O\hat{p}(\mathbf{x}_B,\mathbf{x}_O,\omega)\}\{\hat{p}(\mathbf{x}_A,\mathbf{x}_O,\omega)\}^*\\ &\quad\quad-\{\hat{p}(\mathbf{x}_B,\mathbf{x}_O,\omega)\}\{\mathbf{n}_O\cdot\nabla_O\hat{p}(\mathbf{x}_A,\mathbf{x}_O,\omega)\}^*\Big]d\mathbf{x}_O,\end{aligned}\tag{3}$$

where ∇_O is the spatial gradient at source location $\mathbf{x}_O$. Before addressing the implications of not evaluating integral $\hat{I}^O$, we focus our attention on $\hat{I}^S$. Evaluation in its present form would require both monopole and dipole sources at $\partial\mathbb{S}$. In practice, interferometry is generally applied with monopole sources only. To overcome this limitation, one often introduces a so-called far-field approximation [3, 38]. This approximation can only be made if the direction of wave propagation with respect to the source array is known. Therefore, we separate ingoing and outgoing wavefields with respect to the volume $\mathbb{V}$. We introduce $\hat{p}^{\text{in}}(\mathbf{x}_A,\mathbf{x}_S,\omega)$ and $\hat{p}^{\text{out}}(\mathbf{x}_A,\mathbf{x}_S,\omega)$, where superscripts in and out denote ingoing and outgoing fields at $\mathbf{x}_S$. We substitute $\hat{p} = \hat{p}^{\text{out}} + \hat{p}^{\text{in}}$ into (2). It can be shown that the cross-correlations of ingoing and outgoing waves cancel and that the remaining terms can be merged [38], such that

$$\begin{aligned}\hat{I}^S&(\mathbf{x}_B,\mathbf{x}_A,\omega)\\ &= \int_{\partial S}\frac{2}{j\omega\rho(\mathbf{x}_S)}\\ &\quad\times\Big[\big\{\hat{p}^{\text{in}}(\mathbf{x}_B,\mathbf{x}_S,\omega)\big\}\big\{\mathbf{n}_s\cdot\nabla_S\hat{p}^{\text{in}}(\mathbf{x}_A,\mathbf{x}_S,\omega)\big\}^*\\ &\quad\quad+\{\hat{p}^{\text{out}}(\mathbf{x}_B,\mathbf{x}_S,\omega)\}\{\mathbf{n}_s\cdot\nabla_S\hat{p}^{\text{out}}(\mathbf{x}_A,\mathbf{x}_S,\omega)\}^*\Big]d\mathbf{x}_S.\end{aligned}\tag{4}$$

Next, the far-field high-frequency approximation can be introduced. It is assumed that the medium is smooth in a small region around $\partial\mathbb{S}$. We find for ingoing constituents that $\mathbf{n}_S\cdot\nabla_S\hat{p}^{\text{in}} \approx -(j\omega/c(\mathbf{x}_S))\cos(\phi)\hat{p}^{\text{in}}$, where $c(\mathbf{x}_S)$ is the acoustic wave velocity along the source array and ϕ is the incidence angle of the dominant wavefield with respect to $\mathbf{n}_S$ [38]. Similarly, we find for outgoing constituents that $\mathbf{n}_S\cdot\nabla_S\hat{p}^{\text{out}} \approx +(j\omega/c(\mathbf{x}_S))\cos(\phi)\hat{p}^{\text{out}}$. We assume that ϕ is close to zero such that $\cos(\phi) \approx 1$. Substituting these approximations into (4) yields

$$\begin{aligned}\hat{I}^S&(\mathbf{x}_B,\mathbf{x}_A,\omega)\\ &\approx \int_{\partial S}\frac{2}{\rho(\mathbf{x}_S)c(\mathbf{x}_S)}\Big[\big\{\hat{p}^{\text{in}}(\mathbf{x}_B,\mathbf{x}_S,\omega)\big\}\big\{\hat{p}^{\text{in}}(\mathbf{x}_A,\mathbf{x}_S,\omega)\big\}^*\\ &\quad\quad-\{\hat{p}^{\text{out}}(\mathbf{x}_B,\mathbf{x}_S,\omega)\}\{\hat{p}^{\text{out}}(\mathbf{x}_A,\mathbf{x}_S,\omega)\}^*\Big]d\mathbf{x}_S.\end{aligned}\tag{5}$$

Before proceeding, it is helpful to provide a similar analysis for the missing integral $\hat{I}^O$. We assume that both density and wave velocity are constant at $r \to \infty$, such that all wavefields that would be recorded at receivers due to missing source locations $\mathbf{x}_O$ are ingoing at $\partial\mathbb{O}$ (such that $\hat{p} = \hat{p}^{\text{in}}$ and $\hat{p}^{\text{out}} = 0$). Given these considerations, it can be shown that both terms in the integrand of (3) give equal contributions to the stationary points, and therefore this equation can be rewritten as

$$\begin{aligned}\hat{I}^O&(\mathbf{x}_B,\mathbf{x}_A,\omega)\\ &= \int_{\partial O}\frac{2}{j\omega\rho(\mathbf{x}_O)}\{\hat{p}(\mathbf{x}_B,\mathbf{x}_O,\omega)\}\{\mathbf{n}_O\cdot\nabla_O\hat{p}(\mathbf{x}_A,\mathbf{x}_O,\omega)\}^*d\mathbf{x}_O.\end{aligned}\tag{6}$$

We can further simplify this equation by substituting the far-field approximation for ingoing fields $\mathbf{n}_O\cdot\nabla_O\hat{p} \approx -(j\omega/c(\mathbf{x}_O))\hat{p}$, yielding

$$\begin{aligned}\hat{I}^O&(\mathbf{x}_B,\mathbf{x}_A,\omega)\\ &\approx \int_{\partial O}\frac{2}{\rho(\mathbf{x}_O)c(\mathbf{x}_O)}\{\hat{p}(\mathbf{x}_B,\mathbf{x}_O,\omega)\}\{\hat{p}(\mathbf{x}_A,\mathbf{x}_O,\omega)\}^*d\mathbf{x}_O.\end{aligned}\tag{7}$$

So far we have shown that a Green's function can be retrieved by evaluation of integrals $\hat{I}^S$ and $\hat{I}^O$. In practice, we are generally not that fortunate. First, we miss the source locations $\mathbf{x}_O$ to compute $\hat{I}^O$. Second, we cannot discriminate between ingoing and outgoing wavefields to evaluate $\hat{I}^S$. Instead, we cross-correlate the full fields as emitted by the sources and integrate over $\partial\mathbb{S}$. We refer to the obtained function as the correlation function $\hat{C}$:

$$\begin{aligned}\hat{C}&(\mathbf{x}_B,\mathbf{x}_A,\omega)\\ &= \int_{\partial S}\frac{2W(\mathbf{x}_S)}{\rho(\mathbf{x}_S)c(\mathbf{x}_S)}\{\hat{p}(\mathbf{x}_B,\mathbf{x}_S,\omega)\}\{\hat{p}(\mathbf{x}_A,\mathbf{x}_S,\omega)\}^*d\mathbf{x}_S.\end{aligned}\tag{8}$$

We assume that the density and wave velocity are known at the source array. In most applications of interferometry, however, they are assumed constant and not evaluated inside the integrand. We have introduced an additional weighting factor $W(\mathbf{x}_S)$ that can be used to rebalance the sources before integration or to taper the edges of a finite source array in practical applications [39]. We can also define a weighting function that takes the wave propagation angle into account, reducing the artifacts introduced by the far-field approximation, where we neglected a $\cos\phi$-term. Sometimes we can approximate the incidence angle $\phi(\mathbf{x}_A, \mathbf{x}_S)$ of the dominant contribution of the incident wavefield $\hat{p}(\mathbf{x}_A, \mathbf{x}_S, \omega)$, for instance by ray tracing. In such cases, it can be beneficial to replace weighting factor $W(\mathbf{x}_S)$ with $W(\mathbf{x}_A, \mathbf{x}_S) = \cos\phi(\mathbf{x}_A, \mathbf{x}_S)$ to improve the retrieved amplitude variations with angle; see Schuster [3] for examples.

The fields in (8) consist of both ingoing and outgoing constituents at $\partial\mathbb{S}$. We substitute $\hat{p} = \hat{p}^{\text{out}} + \hat{p}^{\text{in}}$ into (8) and rewrite the result as

$$\begin{aligned}
&\hat{C}(\mathbf{x}_B, \mathbf{x}_A, \omega) \\
&\quad = \int_{\partial S} \frac{2W(\mathbf{x}_S)}{\rho(\mathbf{x}_S)c(\mathbf{x}_S)} \Big[\big\{\hat{p}^{\text{in}}(\mathbf{x}_B, \mathbf{x}_S, \omega)\big\} \big\{\hat{p}^{\text{in}}(\mathbf{x}_A, \mathbf{x}_S, \omega)\big\}^* \\
&\qquad\qquad - \{\hat{p}^{\text{out}}(\mathbf{x}_B, \mathbf{x}_S, \omega)\} \{\hat{p}^{\text{out}}(\mathbf{x}_A, \mathbf{x}_S, \omega)\}^* \Big] d\mathbf{x}_S \\
&\qquad + \int_{\partial S} \frac{2W(\mathbf{x}_S)}{\rho(\mathbf{x}_S)c(\mathbf{x}_S)} \Big[\{\hat{p}(\mathbf{x}_B, \mathbf{x}_S, \omega)\} \{\hat{p}^{\text{out}}(\mathbf{x}_A, \mathbf{x}_S, \omega)\}^* \\
&\qquad\qquad + \{\hat{p}^{\text{out}}(\mathbf{x}_B, \mathbf{x}_S, \omega)\} \{\hat{p}(\mathbf{x}_A, \mathbf{x}_S, \omega)\}^* \Big] d\mathbf{x}_S.
\end{aligned} \tag{9}$$

Note that the first integral at the right-hand side is identical to the desired integral in (5). The second integral is undesired and referred to as ghost $\hat{g}^S$:

$$\begin{aligned}
&\hat{g}^S(\mathbf{x}_B, \mathbf{x}_A, \omega) \\
&\quad = \int_{\partial S} \frac{2W(\mathbf{x}_S)}{\rho(\mathbf{x}_S)c(\mathbf{x}_S)} \Big[\{\hat{p}(\mathbf{x}_B, \mathbf{x}_S, \omega)\} \{\hat{p}^{\text{out}}(\mathbf{x}_A, \mathbf{x}_S, \omega)\}^* \\
&\qquad\qquad + \{\hat{p}^{\text{out}}(\mathbf{x}_B, \mathbf{x}_S, \omega)\} \{\hat{p}(\mathbf{x}_A, \mathbf{x}_S, \omega)\}^* \Big] d\mathbf{x}_S.
\end{aligned} \tag{10}$$

In a similar fashion we identify a second ghost, due to the missing source locations $\mathbf{x}_O$. This is done by redefining the integral $\hat{I}^O$ in (7) as

$$\begin{aligned}
&\hat{g}^O(\mathbf{x}_B, \mathbf{x}_A, \omega) \\
&\quad = -\int_{\partial O} \frac{2}{\rho(\mathbf{x}_O)c(\mathbf{x}_O)} \{\hat{p}(\mathbf{x}_B, \mathbf{x}_O, \omega)\} \{\hat{p}(\mathbf{x}_A, \mathbf{x}_O, \omega)\}^* d\mathbf{x}_O.
\end{aligned} \tag{11}$$

Next, we substitute (11), (7), (5), (1) and (10) into (9) and rewrite the result as

$$\begin{aligned}
\hat{C}(\mathbf{x}_B, \mathbf{x}_A, \omega) \approx{}& \big|\hat{S}(\omega)\big|^2 \Big[\hat{G}(\mathbf{x}_B, \mathbf{x}_A, \omega) + \hat{G}^*(\mathbf{x}_A, \mathbf{x}_B, \omega)\Big] \\
&+ \hat{g}^S(\mathbf{x}_B, \mathbf{x}_A, \omega) + \hat{g}^O(\mathbf{x}_B, \mathbf{x}_A, \omega).
\end{aligned} \tag{12}$$

Equation (12) is useful for identifying ghosts in interferometry by CC of full fields. We have shown that implementation of the correlation function (8) yields a bandlimited version of the desired Green's function $\hat{G}(\mathbf{x}_B, \mathbf{x}_A, \omega)$ and its acausal counterpart $\hat{G}^*(\mathbf{x}_A, \mathbf{x}_B, \omega)$ plus two additional ghost terms. The first ghost $\hat{g}^S$ is described by (10), which is due to the presence of any undesired reflectors above the source array $\partial\mathbb{S}$. Note that in typical controlled source applications, the free surface acts as such a reflector, scattering waves back into the volume $\mathbb{V}$, such that $\hat{p}^{\text{out}} \neq 0$. Consequently, spurious events can be expected to populate retrieved gathers due to free surface interactions if free surface ghosts and multiples are not eliminated prior to applying interferometry. Similar artifacts have also been found in passive seismic interferometry; see Draganov et al. [40]. The second ghost $\hat{g}^O$, described by (11), stems from the missing integral at $\partial\mathbb{O}$. For convolution-based reciprocity theorems, one often applies Sommerfeld's radiation condition [41] to show that boundary integrals over convolution products vanish when $r \to \infty$. However: these conditions do not apply for integrals of cross-correlation products like the one in (11). The integrand in (11) decays with order $\mathcal{O}(r^{-2})$, whereas the integration surface $\partial\mathbb{O}$ grows with order $\mathcal{O}(r^2)$, which is insufficient to cancel the integral. However, Wapenaar [42] showed that if sufficient scattering takes place in the volume $\mathbb{V}$, the decay of the integrand is stronger than $\mathcal{O}(r^{-2})$ and the integral can indeed be neglected. This condition has been referred to as the antiradiation condition [3]. Not obeying this condition can lead not only to incorrect amplitudes but also to the emergence of spurious events in the retrieved data [9].

To illustrate the ghosts in interferometry by CC of full fields, we define four synthetic 1D models in Figure 3. For simplicity, the velocity is kept constant at 2000 m/s with density contrasts introduced. In each model the aim is to generate a (zero-offset) response as if there was a virtual source at receiver location $\mathbf{x}_A$ (green star) and a receiver at the same location $\mathbf{x}_B = \mathbf{x}_A$. The real source is always located at the earth's surface location $\mathbf{x}_S$ and additional sources $\mathbf{x}_O$ are introduced to evaluate ghost g^O. Location $\mathbf{x}_E$ will play a role only later in this paper.

In the previous example, the ghost terms $g^S + g^O$ did not give a significant contribution outside $t = 0$ s. This is not the case for model B (Figure 3(b)), which is the same as model A, except for two additional contrasts at 500 m and 700 m depth. The reference response reveals not only the desired reflection at $t = 0.4$ s but also the reflections of the overburden at $t = 0.1$ s and $t = 0.3$ s and their multiples; see Figure 5(a). The ghosts $g^S + g^O$ and the correlation function C are shown in Figures 5(b) and 5(c), respectively. Since no reflectors are present above the source, $g^S = 0$. However, the second ghost g^O does give a significant contribution. The events at $t = 0.1$ s and $t = 0.3$ s appear with opposite polarity (Figure 5(b)) compared to the reference response (Figure 5(a)). Therefore, these events have incorrect amplitudes in the correlation function and are hardly visible (Figure 5(c)). More importantly, there is a ghost at $t = 0.2$ s (Figure 5(c)) that is not visible in the reference response

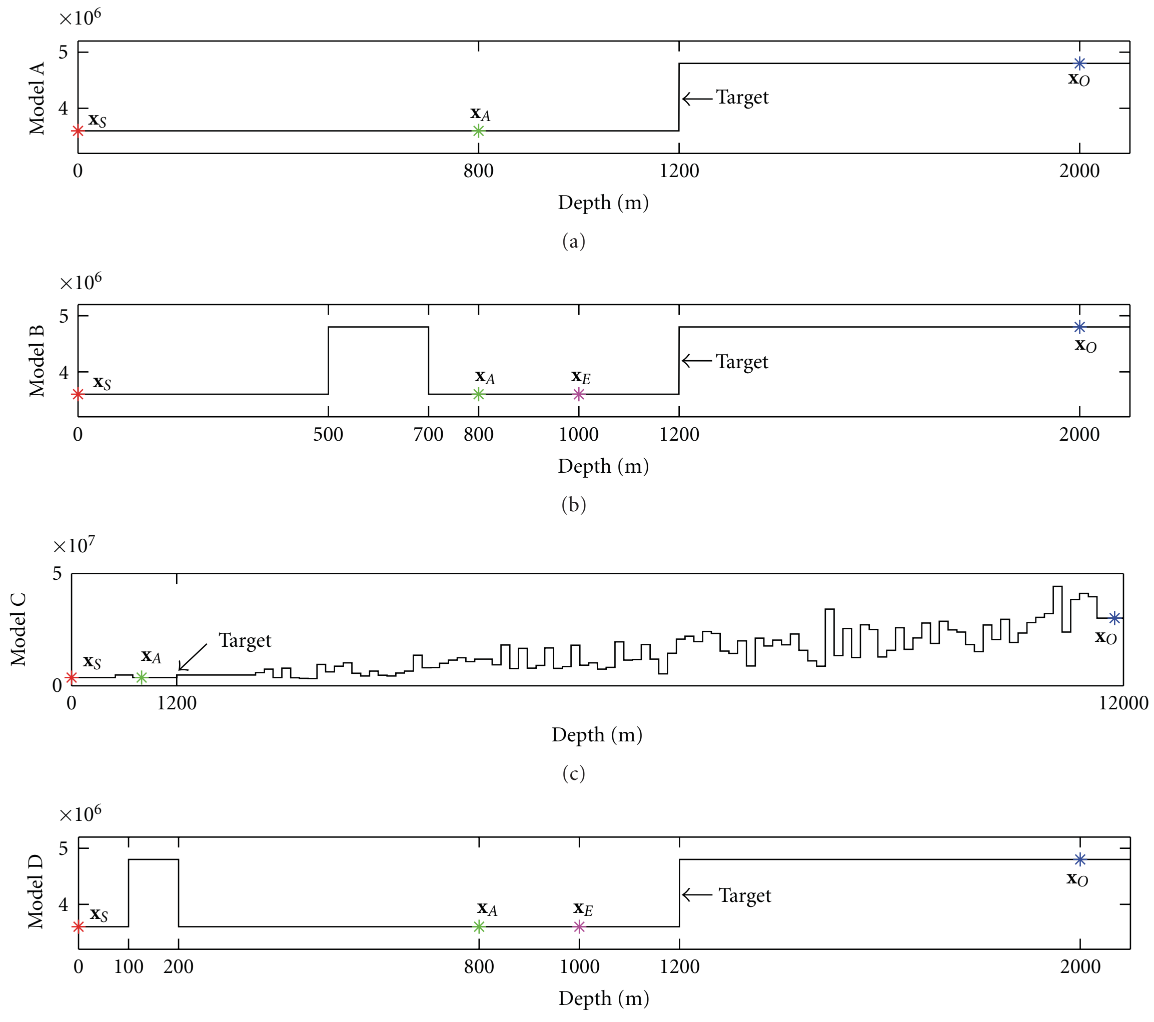

(a)

(b)

(c)

(d)

Figure 3: Impedance (in kg $\cdot$ m^{-2} $\cdot$ s^{-1}) versus depth (in m) for synthetic models A–D. The red star corresponds to source location $\mathbf{x}_S$, the green star to receiver/virtual source location $\mathbf{x}_A = \mathbf{x}_B$, the blue star to nonexisting source location $\mathbf{x}_O$, and the magenta star to nonexisting source location $\mathbf{x}_E$; models A–C have no free surface incorporated; model D has a free surface at 0 m depth.

(Figure 5(a)). This ghost originates from an internal multiple between the contrasts at 500 m and 700 m. Finally we note that the multiples at $t = 0.5$ s and $t = 0.7$ s also appear as ghost terms, with different amplitudes and polarities than the reference response. Therefore these responses are retrieved with incorrect amplitudes (Figure 5(c)). For practical applications this can be seen as advantageous, since these multiple reflections are generally not desired for further processing.

It has been demonstrated by Wapenaar [42] that ghost g^O vanishes if sufficient scattering occurs below the receiver array. To demonstrate this effect, we introduce model C, being similar to model B except for a series of additional random contrasts deeper in the subsurface superimposed by a trend of acoustic impedance increases with depth, see Figure 3(c) (note the differently scaled axes in Figures 3(b) and 3(c)). All contrasts lay sufficiently deep, such that the reference response is no different from that of model B within the display window. The ghosts $g^S + g^O$ and the correlation function C are shown in Figures 6(b) and 6(c), respectively. Indeed, the contributions of ghost g^O are minor and randomly distributed (Figure 6(b)). It can be shown analytically that placing infinitely many contrasts even completely eliminates g^O. Note that the reference response (Figure 6(a)) and the correlation function (Figure 6(c)) agree relatively well. The so-called antiradiation condition has thus been successful in eliminating the effects of one-sided illumination. Reflections of the target ($t = 0.4$ s) and overburden ($t = 0.1$ s and $t = 0.3$ s), including their multiples ($t = 0.5$ s and $t = 0.7$ s), have all been retrieved with true amplitudes. Note that recording times need to be sufficiently long for the antiradiation condition to hold [42]. In this example, the total recording time is 32 s. Moreover, it should be mentioned that the antiradiation condition can

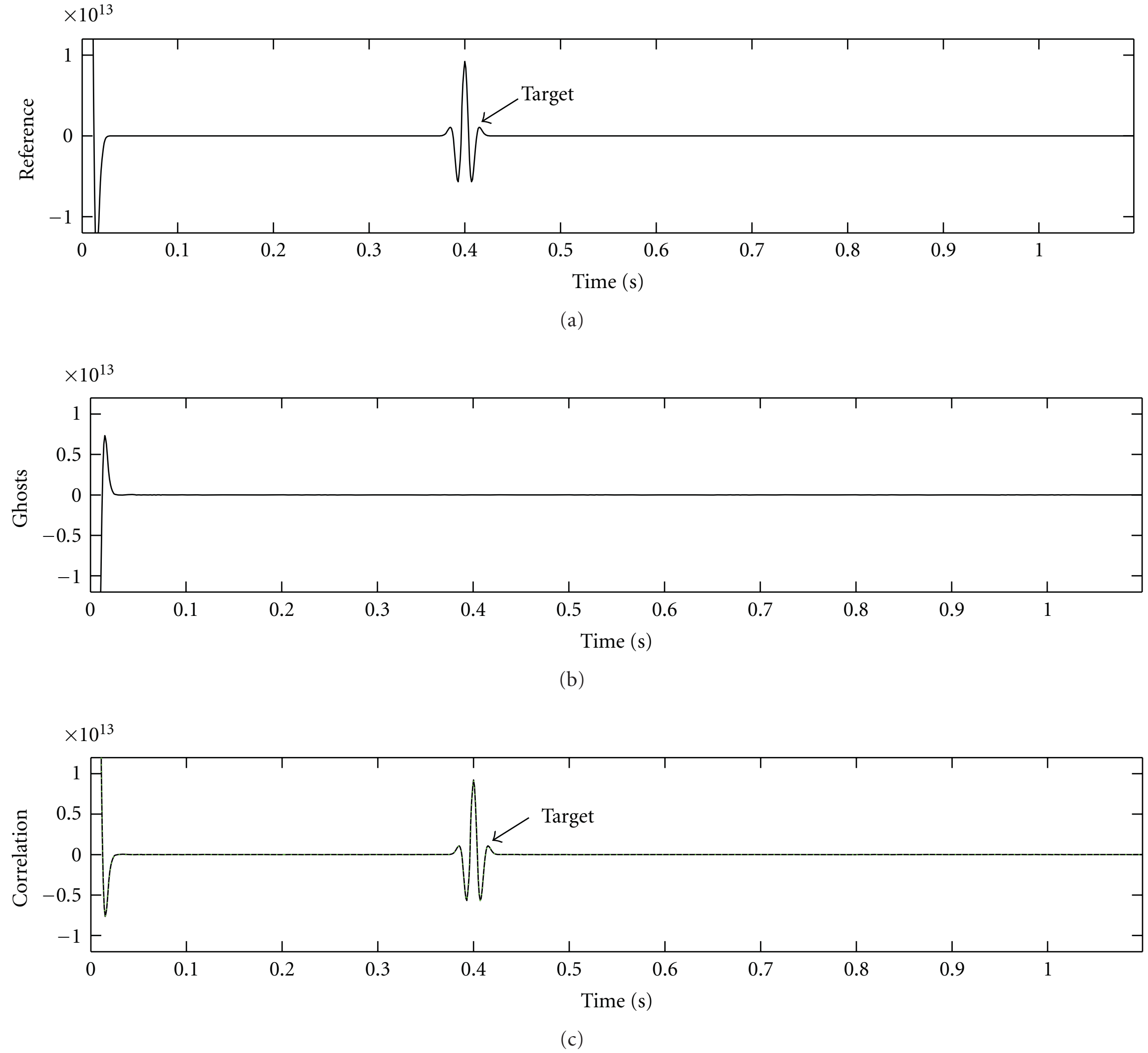

Figure 4: Cross-correlation of full fields for model A: (a) reference response by placing an active source at the virtual source location $\mathbf{x}_A$; (b) computed ghost terms $g^S + g^O$; (c) causal part of the correlation function C (black) and the sum of reference response + ghosts (dashed green).

not eliminate the effects of reflectors placed outside the volume $\mathbb{V}$, as $g^S \neq 0$ for such scenario.

In model D we demonstrate the effect of free surface interactions, by placing a free surface at 0 m and two contrasts at 100 m and 200 m depth, see Figure 3(d). As a result, the reference response does not only contain the desired reflection at $t = 0.4$ s but also the primaries of the overburden contrasts at $t = 0.6$ s and $t = 0.7$ s, the free surface reflection at $t = 0.8$ s; and free-surface multiples at $t = 0.9$ s and $t = 1.0$ s; see Figure 7(a). Ghosts $g^S + g^O$ and correlation function C are shown in Figures 7(b) and 7(c), respectively. We see strong spurious events at $t = 0.1$ s and $t = 0.2$ s in the retrieved response (and a weaker event at $t = 0.3$ s), stemming from interactions of the first reflectors with the free surface. We also observe that the reflections at $t = 0.6$ s and $t = 0.7$ s, their multiples, and the free surface reflection at $t = 0.8$ s are hardly retrieved due to the missing source at $\mathbf{x}_O$.

3. Cross-Correlation of Perturbed Fields

In many cases our aim is not to retrieve a full Green's function but to retrieve only a part of it. For controlled-source applications, for instance, a full Green's function would contain not only reflections from the target area but also reflections from the overburden. In practice we often wish to eliminate the latter by restricting a virtual source to radiate downwards only. In the virtual source method [4, 12], this is effectively achieved by time-gating the first arrival prior to cross-correlation. In perturbation-based methodology [11, 14], a similar discrimination is made between the incident field and the scattered field. These fields are usually obtained by time-gating the full fields.

In Figure 8 we show a typical configuration for interferometry by CC of perturbed wavefields. Note the similarities with Figure 2. The only difference is that boundary $\partial\mathbb{O}$ has been replaced with a boundary $\partial\mathbb{E}$, located between the

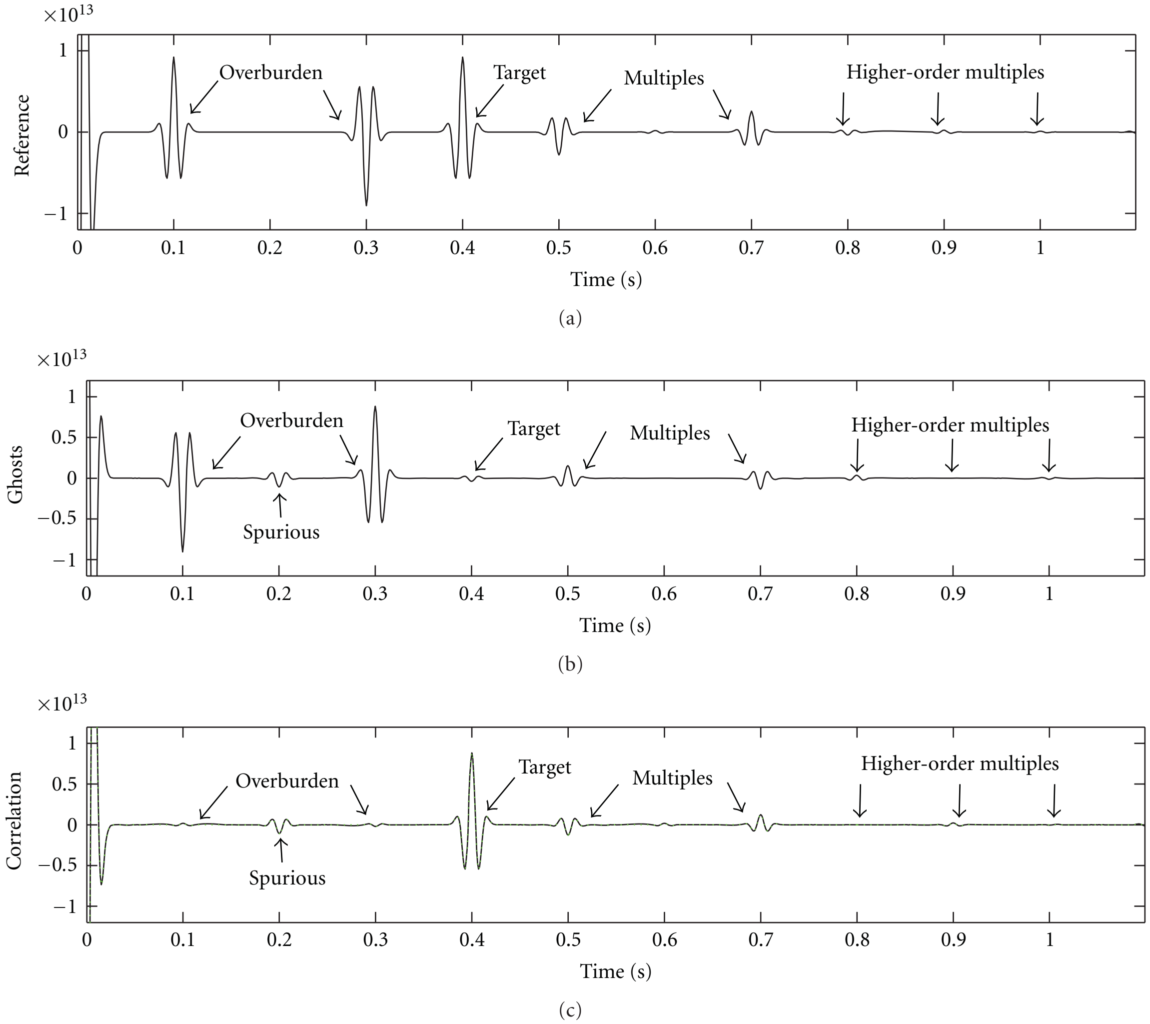

FIGURE 5: Cross-correlation of full fields for model B: (a) reference response by placing an active source at the virtual source location $\mathbf{x}_A$; (b) computed ghost terms $g^S + g^O$; (c) causal part of the correlation function C (black) and the sum of reference response + ghosts (dashed green).

overburden and the target area. Volume $\mathbb{V}$ is now enclosed by $\partial\mathbb{S}$ and $\partial\mathbb{E}$. We define a reference state by density $\rho_0(\mathbf{x})$ and velocity $c_0(\mathbf{x})$. In this reference state all heterogeneities outside volume $\mathbb{V}$ (namely the target) have been removed. These heterogeneities are referred to as the perturbations in density $\Delta\rho(\mathbf{x})$ and velocity $\Delta c(\mathbf{x})$, where $\rho(\mathbf{x}) = \rho_0(\mathbf{x})+\Delta\rho(\mathbf{x})$ and $c(\mathbf{x}) = c_0(\mathbf{x}) + \Delta c(\mathbf{x})$ represent the density and velocity of the true physical medium. Fields that propagate in the reference state are referred to as incident fields $\hat{p}_{\text{inc}}$. Fields that propagate in the physical medium can now be expressed as a superposition of the incident field and the so-called scattered field $\hat{p}_{\text{sc}}$, that is $\hat{p} = \hat{p}_{\text{inc}}+\hat{p}_{\text{sc}}$. Vasconcelos et al. [11] have derived a representation for Green's function retrieval of the scattered field between virtual source $\mathbf{x}_A$ and receiver $\mathbf{x}_B$ from cross-correlations of the scattered field at $\mathbf{x}_B$ and the incident field at $\mathbf{x}_A$:

$$\left|\hat{S}(\omega)\right|^2 \hat{G}_{\text{sc}}(\mathbf{x}_B,\mathbf{x}_A,\omega) = \hat{I}^S_{\text{ptb}}(\mathbf{x}_B,\mathbf{x}_A,\omega) + \hat{I}^E_{\text{ptb}}(\mathbf{x}_B,\mathbf{x}_A,\omega), \tag{13}$$

where subscript ptb stands for "perturbed." On the left-hand side we find the desired scattered Green's function, imprinted by the squared amplitude spectrum of the source wavelet. Note that no acausal Green's function is retrieved. On the right-hand side we find integral $\hat{I}^S_{\text{ptb}}$, stemming from the cross-correlations of incident and scattered fields from the actual sources at $\partial\mathbb{S}$:

$$\begin{aligned}\hat{I}^S_{\text{ptb}}&(\mathbf{x}_B,\mathbf{x}_A,\omega)\\ &= -\int_{\partial S} \frac{1}{j\omega\rho(\mathbf{x}_S)}\\ &\quad\times\Big[\{\mathbf{n}_S\cdot\nabla_S\hat{p}_{\text{sc}}(\mathbf{x}_B,\mathbf{x}_S,\omega)\}\{\hat{p}_{\text{inc}}(\mathbf{x}_A,\mathbf{x}_S,\omega)\}^*\\ &\quad-\{\hat{p}_{\text{sc}}(\mathbf{x}_B,\mathbf{x}_S,\omega)\}\{\mathbf{n}_S\cdot\nabla_S\hat{p}_{\text{inc}}(\mathbf{x}_A,\mathbf{x}_S,\omega)\}^*\Big]d\mathbf{x}_S.\end{aligned} \tag{14}$$

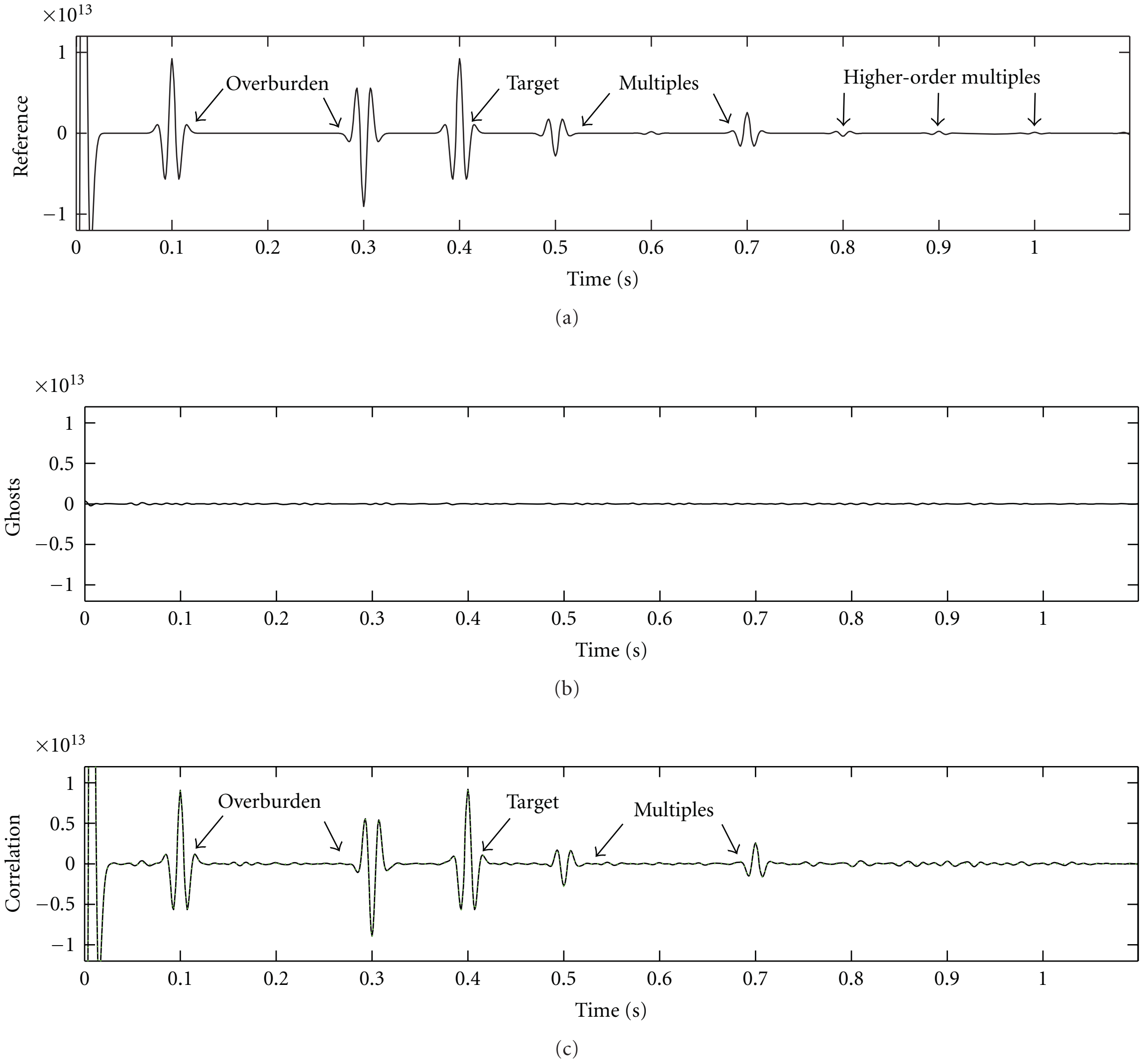

(a)

(b)

(c)

Figure 6: Cross-correlation of full fields for model C: (a) reference response by placing an active source at the virtual source location $\mathbf{x}_A$; (b) computed ghost terms $g^S + g^O$; (c) causal part of the correlation function C (black) and the sum of reference response + ghosts (dashed green).

The second integral, $\hat{I}^E_{\mathrm{ptb}}$, stems from similar cross-correlations of nonexisting sources $\mathbf{x}_E$ at $\partial\mathbb{E}$:

$$\begin{aligned}\hat{I}^E_{\mathrm{ptb}}&(\mathbf{x}_B,\mathbf{x}_A,\omega)\\ &= -\int_{\partial E}\frac{1}{j\omega\rho(\mathbf{x}_E)}\\ &\quad\times\Big[\{\mathbf{n}_E\cdot\nabla_E\hat{p}_{\mathrm{sc}}(\mathbf{x}_B,\mathbf{x}_E,\omega)\}\{\hat{p}_{\mathrm{inc}}(\mathbf{x}_A,\mathbf{x}_E,\omega)\}^*\\ &\qquad-\{\hat{p}_{\mathrm{sc}}(\mathbf{x}_B,\mathbf{x}_E,\omega)\}\{\mathbf{n}_E\cdot\nabla_E\hat{p}_{\mathrm{inc}}(\mathbf{x}_A,\mathbf{x}_E,\omega)\}^*\Big]d\mathbf{x}_E,\end{aligned} \tag{15}$$

where ∇_E is the spatial gradient at $\mathbf{x}_E$, $\mathbf{n}_E$ is the outward-pointing unit normal vector to $\partial\mathbb{E}$, and ρ_E is the density along this surface. We write the wavefields in (14) in terms of ingoing and outgoing constituents at $\partial\mathbb{S}$. It can be shown that the cross-correlations between ingoing and outgoing wavefields cancel each other and the remaining terms can be merged [11], such that

$$\begin{aligned}\hat{I}^S_{\mathrm{ptb}}&(\mathbf{x}_B,\mathbf{x}_A,\omega)\\ &= \int_{\partial S}\frac{2}{j\omega\rho(\mathbf{x}_S)}\\ &\quad\times\Big[\Big\{\hat{p}^{\mathrm{in}}_{\mathrm{sc}}(\mathbf{x}_B,\mathbf{x}_S,\omega)\Big\}\Big\{\mathbf{n}_S\cdot\nabla_S\hat{p}^{\mathrm{in}}_{\mathrm{inc}}(\mathbf{x}_A,\mathbf{x}_S,\omega)\Big\}^*\\ &\qquad+\{\hat{p}^{\mathrm{out}}_{\mathrm{sc}}(\mathbf{x}_B,\mathbf{x}_S,\omega)\}\{\mathbf{n}_S\cdot\nabla_S\hat{p}^{\mathrm{out}}_{\mathrm{inc}}(\mathbf{x}_A,\mathbf{x}_S,\omega)\}^*\Big]d\mathbf{x}_S.\end{aligned} \tag{16}$$

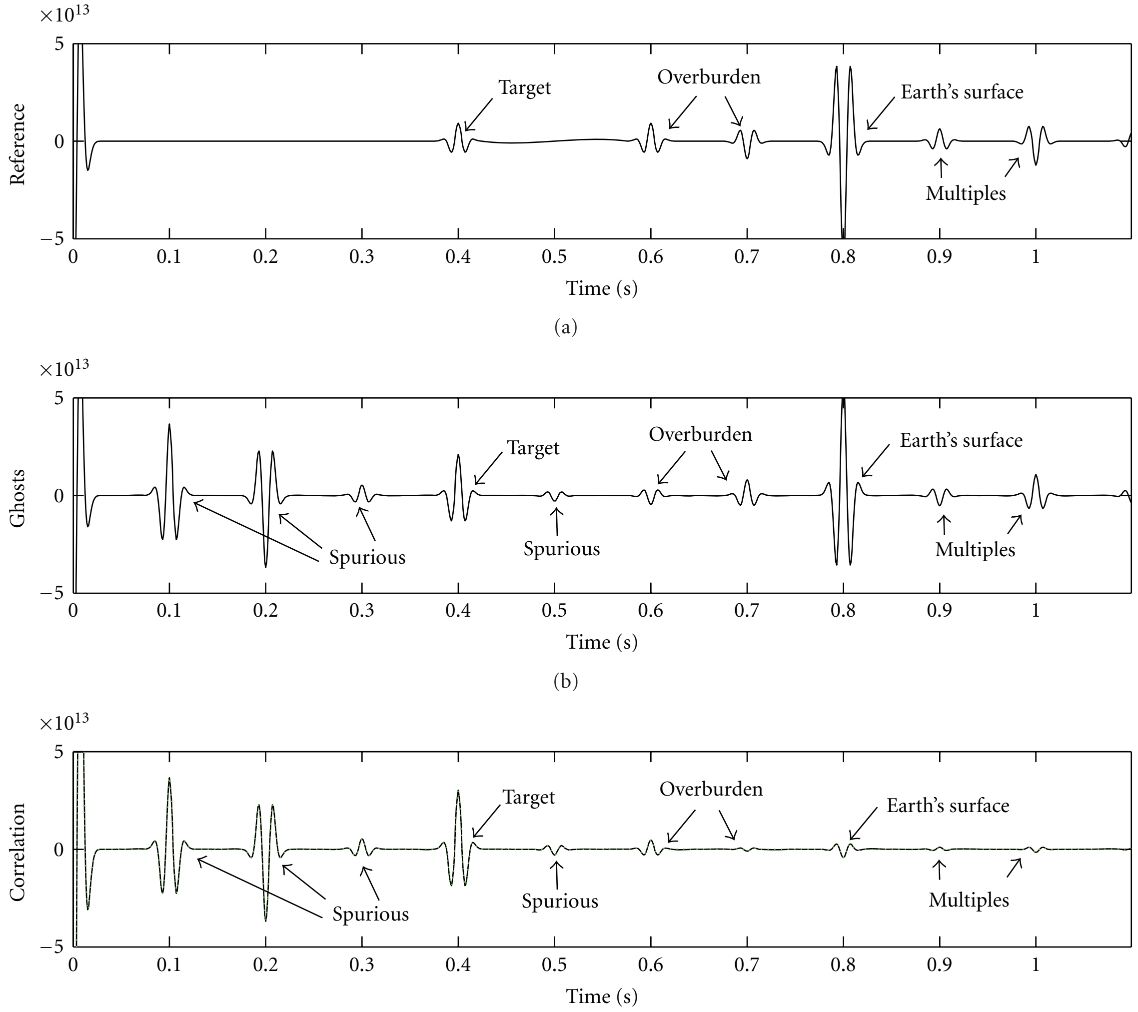

(a)

(b)

(c)

FIGURE 7: Cross-correlation of full fields for model D: (a) reference response by placing an active source at the virtual source location $\mathbf{x}_A$; (b) computed ghost terms $g^S + g^O$; (c) causal part of the correlation function C (black) and the sum of reference response + ghosts (dashed green).

Assuming that the relevant wavefields propagate near normal incidence, we can substitute far-field approximations $\mathbf{n}_S \cdot \nabla_S \hat{p}^{\text{out}}_{\text{inc}} \approx +(j\omega/c(\mathbf{x}_S))\hat{p}^{\text{out}}_{\text{inc}}$ and $\mathbf{n}_S \cdot \nabla_S \hat{p}^{\text{in}}_{\text{inc}} \approx -(j\omega/c(\mathbf{x}_S))\hat{p}^{\text{in}}_{\text{inc}}$ into (16), yielding

$$\begin{aligned}
&\hat{I}^S_{\text{ptb}}(\mathbf{x}_B, \mathbf{x}_A, \omega) \\
&\quad\approx \int_{\partial S} \frac{2}{\rho(\mathbf{x}_S)c(\mathbf{x}_S)} \Big[\Big\{ \hat{p}^{\text{in}}_{\text{sc}}(\mathbf{x}_B, \mathbf{x}_S, \omega) \Big\} \Big\{ \hat{p}^{\text{in}}_{\text{inc}}(\mathbf{x}_A, \mathbf{x}_S, \omega) \Big\}^* \\
&\qquad\qquad - \{ \hat{p}^{\text{out}}_{\text{sc}}(\mathbf{x}_B, \mathbf{x}_S, \omega) \} \{ \hat{p}^{\text{out}}_{\text{inc}}(\mathbf{x}_A, \mathbf{x}_S, \omega) \}^* \Big] d\mathbf{x}_S.
\end{aligned} \tag{17}$$

For integral $\hat{I}^E_{\text{ptb}}$ the situation is slightly different. Since we have chosen the reference state to have no heterogeneities below $\partial\mathbb{E}$, all wavefields arriving at the receivers are ingoing at $\partial\mathbb{E}$ (such that $\hat{p}_{\text{inc}} = \hat{p}^{\text{in}}_{\text{inc}}$ and $\hat{p}^{\text{out}}_{\text{inc}} = 0$). Cross-correlations between ingoing and outgoing fields cancel and the remaining terms can be merged [11], such that

$$\begin{aligned}
&\hat{I}^E_{\text{ptb}}(\mathbf{x}_B, \mathbf{x}_A, \omega) \\
&\quad= \int_{\partial E} \frac{2}{j\omega\rho(\mathbf{x}_E)} \\
&\qquad\times \Big[\Big\{ \hat{p}^{\text{in}}_{\text{sc}}(\mathbf{x}_B, \mathbf{x}_E, \omega) \Big\} \{ \mathbf{n}_E \cdot \nabla_E \hat{p}_{\text{inc}}(\mathbf{x}_A, \mathbf{x}_E, \omega) \}^* \Big] d\mathbf{x}_E.
\end{aligned} \tag{18}$$

The spatial derivative can be approximated with far-field approximation $\mathbf{n}_E \cdot \nabla_E \hat{p}_{\text{inc}} \approx -(j\omega/c(\mathbf{x}_E))\hat{p}_{\text{inc}}$, such that

$$\begin{aligned}
&\hat{I}^E_{\text{ptb}}(\mathbf{x}_B, \mathbf{x}_A, \omega) \\
&\quad\approx \int_{\partial E} \frac{2}{\rho(\mathbf{x}_E)c(\mathbf{x}_E)} \Big[\Big\{ \hat{p}^{\text{in}}_{\text{sc}}(\mathbf{x}_B, \mathbf{x}_E, \omega) \Big\} \{ \hat{p}_{\text{inc}}(\mathbf{x}_A, \mathbf{x}_E, \omega) \}^* \Big] d\mathbf{x}_E.
\end{aligned} \tag{19}$$

Note that evaluation of (17) still requires separation of ingoing and outgoing waves. In practice, we generally cross-correlate complete scattered and incident fields at the receivers to obtain the correlation function of perturbed wave fields $\widehat{C}_{\text{ptb}}$:

$$\widehat{C}_{\text{ptb}}(\mathbf{x}_B, \mathbf{x}_A, \omega) = \int_{\partial S} \frac{2W(\mathbf{x}_S)}{\rho(\mathbf{x}_S)c(\mathbf{x}_S)} \{\widehat{p}_{\text{sc}}(\mathbf{x}_B, \mathbf{x}_S, \omega)\} \{\widehat{p}_{\text{inc}}(\mathbf{x}_A, \mathbf{x}_S, \omega)\}^* \, d\mathbf{x}_S. \tag{20}$$

To evaluate the consequence of this choice, we separate the scattered and incident wavefields in up- and downgoing constituents according to $\widehat{p}_{\text{inc}} = \widehat{p}_{\text{inc}}^{\text{in}} + \widehat{p}_{\text{inc}}^{\text{out}}$ and $\widehat{p}_{\text{sc}} = \widehat{p}_{\text{sc}}^{\text{in}} + \widehat{p}_{\text{sc}}^{\text{out}}$ and substitute these representations into (20). The result can be written as

$$\begin{aligned} \widehat{C}_{\text{ptb}}(\mathbf{x}_B, \mathbf{x}_A, \omega) &= \int_{\partial S} \frac{2W(\mathbf{x}_S)}{\rho(\mathbf{x}_S)c(\mathbf{x}_S)} \Big[\Big\{ \widehat{p}_{\text{sc}}^{\text{in}}(\mathbf{x}_B, \mathbf{x}_S, \omega) \Big\} \Big\{ \widehat{p}_{\text{inc}}^{\text{in}}(\mathbf{x}_A, \mathbf{x}_S, \omega) \Big\}^* \\ &\qquad - \{\widehat{p}_{\text{sc}}^{\text{out}}(\mathbf{x}_B, \mathbf{x}_S, \omega)\} \{\widehat{p}_{\text{inc}}^{\text{out}}(\mathbf{x}_A, \mathbf{x}_S, \omega)\}^* \Big] d\mathbf{x}_S \\ &\quad + \int_{\partial S} \frac{2W(\mathbf{x}_S)}{\rho(\mathbf{x}_S)c(\mathbf{x}_S)} \big[\{\widehat{p}_{\text{sc}}(\mathbf{x}_B, \mathbf{x}_S, \omega)\} \{\widehat{p}_{\text{inc}}^{\text{out}}(\mathbf{x}_A, \mathbf{x}_S, \omega)\}^* \\ &\qquad + \{\widehat{p}_{\text{sc}}^{\text{out}}(\mathbf{x}_B, \mathbf{x}_S, \omega)\} \{\widehat{p}_{\text{inc}}(\mathbf{x}_A, \mathbf{x}_S, \omega)\}^* \big] d\mathbf{x}_S. \end{aligned} \tag{21}$$

The first integral in (21) can be identified as the desired integral $\widehat{I}_{\text{ptb}}^{S}$ (see (17)). The second integral is a ghost term that we redefine as

$$\begin{aligned} \widehat{g}_{\text{ptb}}^{S}(\mathbf{x}_B, \mathbf{x}_A, \omega) &= \int_{\partial S} \frac{2W(\mathbf{x}_S)}{\rho(\mathbf{x}_S)c(\mathbf{x}_S)} \big[\{\widehat{p}_{\text{sc}}(\mathbf{x}_B, \mathbf{x}_S, \omega)\} \{\widehat{p}_{\text{inc}}^{\text{out}}(\mathbf{x}_A, \mathbf{x}_S, \omega)\}^* \\ &\qquad + \{\widehat{p}_{\text{sc}}^{\text{out}}(\mathbf{x}_B, \mathbf{x}_S, \omega)\} \{\widehat{p}_{\text{inc}}(\mathbf{x}_A, \mathbf{x}_S, \omega)\}^* \big] d\mathbf{x}_S. \end{aligned} \tag{22}$$

The missing sources at $\mathbf{x}_E$ make up for a second ghost term that we define by rewriting the integral in (19) in the following way:

$$\widehat{g}_{\text{ptb}}^{E}(\mathbf{x}_B, \mathbf{x}_A, \omega) = - \int_{\partial E} \frac{2}{\rho(\mathbf{x}_E)c(\mathbf{x}_E)} \Big[\Big\{ \widehat{p}_{\text{sc}}^{\text{in}}(\mathbf{x}_B, \mathbf{x}_E, \omega) \Big\} \Big\{ \widehat{p}_{\text{inc}}(\mathbf{x}_A, \mathbf{x}_E, \omega) \Big\}^* \Big] d\mathbf{x}_E. \tag{23}$$

Now, by substituting (23), (19), (17), (13), and (20) into (21) we arrive at

$$\begin{aligned} \widehat{C}_{\text{ptb}}(\mathbf{x}_B, \mathbf{x}_A, \omega) &\approx \left| \widehat{S}(\omega) \right|^2 \widehat{G}_{\text{sc}}(\mathbf{x}_B, \mathbf{x}_A, \omega) \\ &\qquad + \widehat{g}_{\text{ptb}}^{S}(\mathbf{x}_B, \mathbf{x}_A, \omega) + \widehat{g}_{\text{ptb}}^{E}(\mathbf{x}_B, \mathbf{x}_A, \omega). \end{aligned} \tag{24}$$

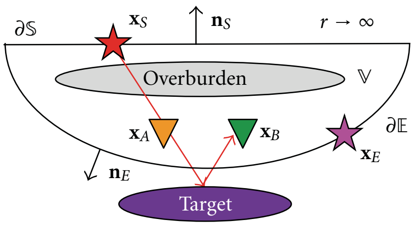

FIGURE 8: Configuration for controlled-source interferometry by cross-correlation of perturbed fields; volume $\mathbb{V}$ is enclosed by the source boundary $\partial\mathbb{S}$ and an additional boundary $\partial\mathbb{E}$ between overburden and target; $\mathbf{x}_S$ denotes a source location at $\partial\mathbb{S}$ and $\mathbf{n}_S$ is the unit normal vector of this surface; $\mathbf{x}_E$ denotes an additional source location at $\partial\mathbb{E}$ and $\mathbf{n}_E$ is the unit normal vector of this surface; heterogeneities between sources and receivers are referred to as "overburden," whereas heterogeneities below the receivers are referred to as "target."

Equation (24) is useful for identifying ghosts in interferometry by CC of perturbed fields. Computation of C_{ptb} (see (20)) yields a scaled bandlimited version of the desired scattered Green's function plus two ghost terms g_{ptb}^{S} and g_{ptb}^{E}. The first ghost g_{ptb}^{S} stems from reflectors outside the integration volume and behaves very similar to the ghost g^S that we found for CC of full fields. The second ghost g_{ptb}^{E} is relatively small. It consists of ingoing waves at $\mathbf{x}_E$ that have scattered in the target area before arriving at the receivers. However, to reach the target area, these waves should have also scattered in the overburden. This means that such fields have at least scattered twice. It is reasoned by Vasconcelos et al. [11] that such contributions can generally be neglected.

To illustrate the effectiveness of cross-correlation of perturbed fields we apply this methodology to model B (Figure 3(b)), with the additional source $\mathbf{x}_E$ located at 1000 m depth (instead of the source at $\mathbf{x}_O$). Incident fields are computed in a reference medium with all heterogeneities below $\mathbf{x}_E$ removed. Scattered fields are computed by subtraction of these incident fields from full fields. We generate the reference response by placing an active source at $\mathbf{x}_A$ and computing the scattered response at the same receiver; see Figure 9(a). We can clearly see not only the desired reflector at $t = 0.4$ s but also the multiple reflections from the overburden at $t = 0.5$ s and $t = 0.7$ s as well as higher-order multiples. In Figures 9(b) and 9(c) we show the ghosts $g_{\text{ptb}}^{S} + g_{\text{ptb}}^{E}$ and the correlation function C_{ptb}. Note which the spurious event at $t = 0.2$ s, that was visible in Figure 5(c), is significantly weakened and hardly visible. The multiples at $t = 0.5$ s and $t = 0.7$ s have smaller amplitudes in the correlation function (Figure 9(c)) than in the reference response (Figure 9(a)). This is a consequence of not having the source at $\mathbf{x}_E$.

In Figure 4(a) we computed the desired reference response with wavelet $|\widehat{S}(\omega)|^2$ for model A (Figure 3(a)) by placing an actual source at the virtual source location $\mathbf{x}_A$. We can clearly see the direct arrival at $t = 0$ s and an event at $t = 0.4$ s. The latter event is our target reflection, relating to the impedance contrast at 1200 m depth. Since no free

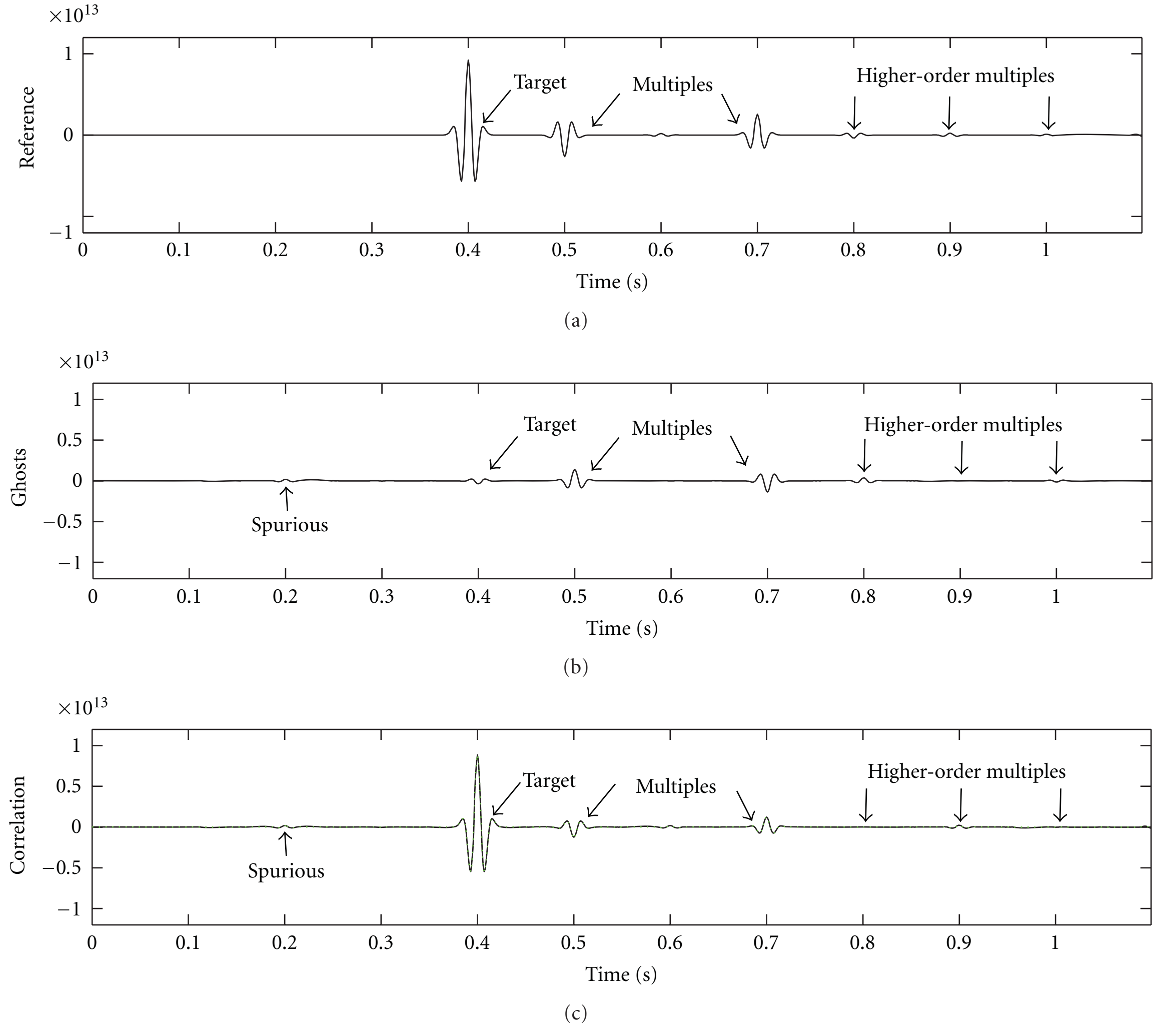

FIGURE 9: Cross-correlation of perturbed fields for model B: (a) reference response by placing an active source at the virtual source location $\mathbf{x}_A$; (b) computed ghost terms $g^S_{\text{ptb}} + g^E_{\text{ptb}}$; (c) correlation function C_{ptb} (black) and the sum of reference response + ghosts (dashed green).

surface is incorporated, no heterogeneities exist above the true source location $\mathbf{x}_S$, and hence all wavefields that arrive at $\mathbf{x}_A$ are ingoing at $\mathbf{x}_S$, such that $g^S = 0$ (10). We computed the second ghost g^O, using the additional source $\mathbf{x}_O$ below all medium heterogeneities. Since no reflection from this source is registered at $\mathbf{x}_A$, the only contribution to g^O stems from correlations of the direct field, mapping at $t = 0$ s in this zero-offset case. In Figure 4(b) we show the ghosts $g^S + g^O$. Note that indeed no other contribution is found outside $t = 0$ s. Therefore the correlation function C (8) is very similar to the true reflection response, except around $t = 0$ s. In Figure 4(c) we show C (black) and the sum of reference response and ghosts (dashed green), matching well.

To show that CC of perturbed fields does not offer a solution for reflectors above the source array, we apply the methodology to model D (Figure 3(d)) as well. In Figure 10(a) we show the reference response. We observe the target event at $t = 0.4$ s and a multiple at $t = 1.0$ s. Ghosts $g^S_{\text{ptb}} + g^E_{\text{ptb}}$ and C_{ptb} are shown in Figures 10(b) and 10(c), respectively. Note that we can still observe several spurious events and the undesired overburden reflections.

4. Cross-Correlation of Decomposed Fields

Another way to eliminate ghosts in interferometry is to separate up- and downgoing waves prior to cross-correlation, as proposed by Mehta et al. [13]. If receivers are installed in horizontal wells, decomposition can be implemented by combining pressure and particle velocity recordings along the receiver array [43, 44]. If wave propagation is close to normal incidence, these methods can be approximated by a weighted summation of pressure and particle velocity at a single receiver [13, 36, 45]. If receivers are installed in vertical wells, decomposition can be implemented by FK-filtering or taking vertical derivatives along the borehole [46]. Note that similar decomposition schemes can be applied for salt flank imaging in vertical wells (Figures 1(c) and 1(d)), where up- and downgoing have to be replaced by left and right going.

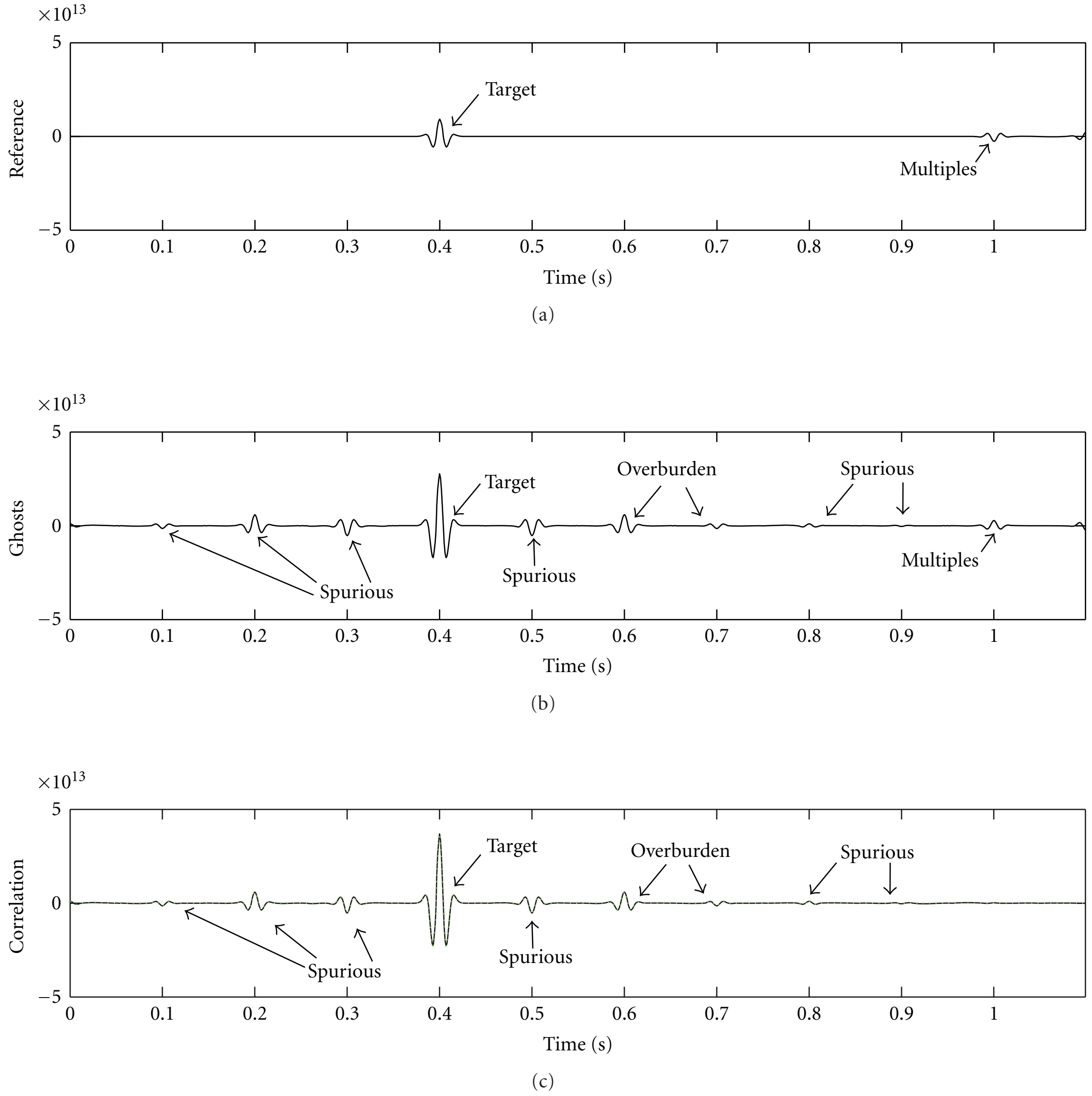

(a)

(b)

(c)

Figure 10: Cross-correlation of perturbed fields for model D: (a) reference response by placing an active source at the virtual source location $\mathbf{x}_A$; (b) computed ghost terms $g^S_{\text{ptb}} + g^E_{\text{ptb}}$; (c) correlation function C_{ptb} (black) and the sum of reference response + ghosts (dashed green).

We use the same configuration as in Figure 2. We define $\hat{p}^+(\mathbf{x}_A, \mathbf{x}_S, \omega)$ and $\hat{p}^-(\mathbf{x}_B, \mathbf{x}_S, \omega)$ as the downgoing and upgoing fields at receivers $\mathbf{x}_A$ and $\mathbf{x}_B$, respectively. Instead of evaluating the correlation function of full fields (see (8)), we define $\hat{C}_{\text{dcp}}$ as the correlation function between $\hat{p}^+$ and $\hat{p}^-$; that is

$$\hat{C}_{\text{dcp}}(\mathbf{x}_B, \mathbf{x}_A, \omega) = \int_{\partial S} \frac{2W(\mathbf{x}_S)}{\rho(\mathbf{x}_S)c(\mathbf{x}_S)} \hat{p}^-(\mathbf{x}_B, \mathbf{x}_S, \omega)\{\hat{p}^+(\mathbf{x}_A, \mathbf{x}_S, \omega)\}^* d\mathbf{x}_S, \tag{25}$$

where subscript dcp denotes "decomposed." As a consequence of this choice, we will reconstruct a Green's function $\hat{G}^{-,+}(\mathbf{x}_B, \mathbf{x}_A, \omega)$ as if there was a downgoing field emitted at $\mathbf{x}_A$ and an upgoing field registered at $\mathbf{x}_B$ plus an acausal Green's function $\{\hat{G}^{+,-}(\mathbf{x}_A, \mathbf{x}_B, \omega)\}^*$ as if there was an upgoing field emitted at $\mathbf{x}_B$ and a downgoing field registered at $\mathbf{x}_A$ [25]. We can find a representation for this case by rewriting (12) in terms of up- and downgoing constituents and removing all but those that are downgoing at $\mathbf{x}_A$ and upgoing at $\mathbf{x}_B$; that is

$$\begin{aligned}\hat{C}_{\text{dcp}}(\mathbf{x}_B, \mathbf{x}_A, \omega) &\approx \left|\hat{S}(\omega)\right|^2 \left[\hat{G}^{-,+}(\mathbf{x}_B, \mathbf{x}_A, \omega) + \left\{\hat{G}^{+,-}(\mathbf{x}_A, \mathbf{x}_B, \omega)\right\}^*\right] \\ &\quad + \hat{g}^S_{\text{dcp}}(\mathbf{x}_B, \mathbf{x}_A, \omega) + \hat{g}^O_{\text{dcp}}(\mathbf{x}_B, \mathbf{x}_A, \omega),\end{aligned} \tag{26}$$

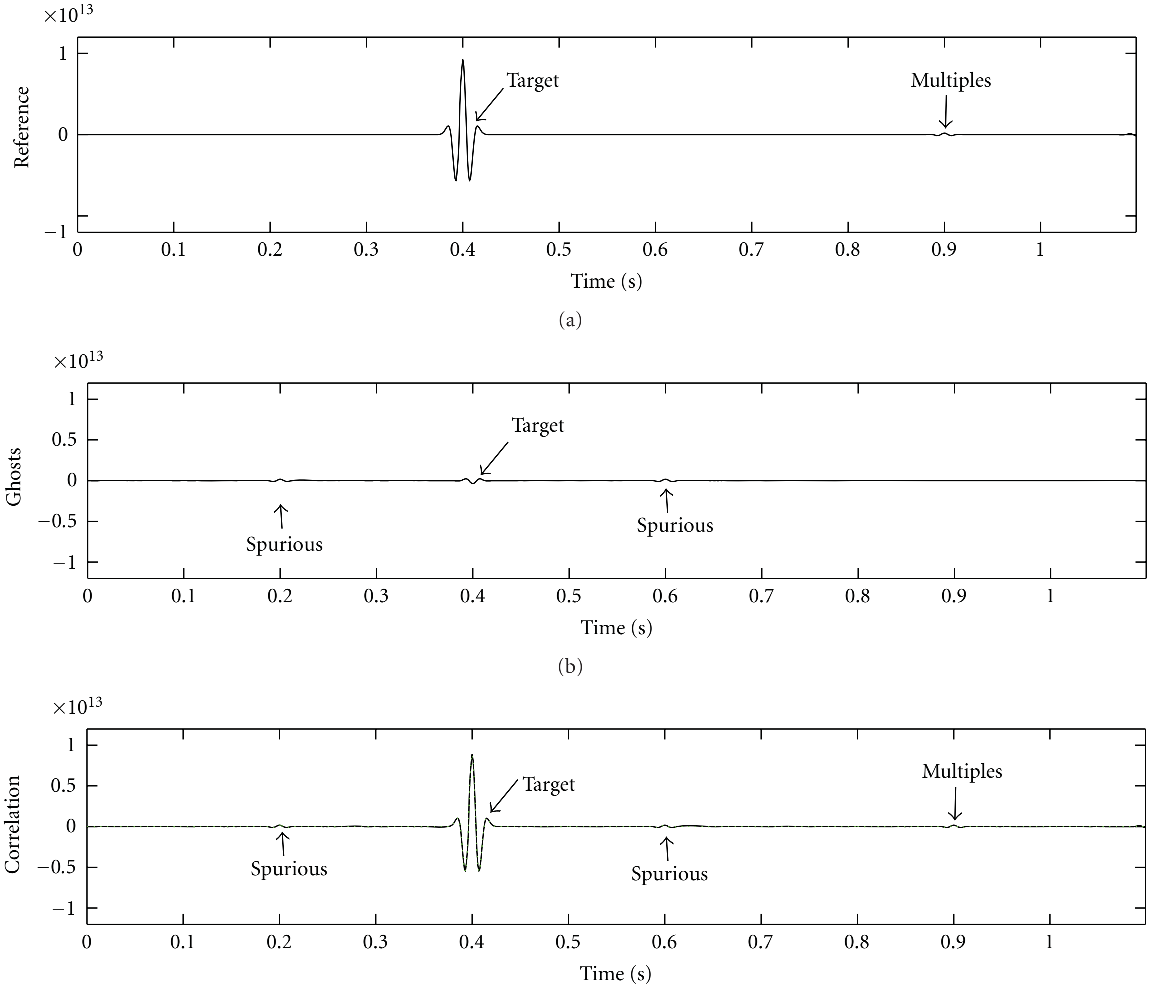

(a)

(b)

(c)

Figure 11: Cross-correlation of decomposed fields for model B: (a) reference response by placing an active source at the virtual source location $\mathbf{x}_A$; (b) computed ghost terms $g^S_{\rm dcp} + g^O_{\rm dcp}$; (c) correlation function $C_{\rm dcp}$ (black) and the sum of reference response + ghosts (dashed green).

where the decomposed ghosts are given by

$$\begin{aligned}
&\hat{g}^S_{\rm dcp}(\mathbf{x}_B,\mathbf{x}_A,\omega)\\
&\quad= \int_{\partial S} \frac{2W(\mathbf{x}_S)}{\rho(\mathbf{x}_S)c(\mathbf{x}_S)}\Big[\{\hat{p}^-(\mathbf{x}_B,\mathbf{x}_S,\omega)\}\{\hat{p}^{+,\rm out}(\mathbf{x}_A,\mathbf{x}_S,\omega)\}^*\\
&\qquad\qquad + \{\hat{p}^{-,\rm out}(\mathbf{x}_B,\mathbf{x}_S,\omega)\}\{\hat{p}^+(\mathbf{x}_A,\mathbf{x}_S,\omega)\}^*\Big]d\mathbf{x}_S,\\
&\hat{g}^O_{\rm dcp}(\mathbf{x}_B,\mathbf{x}_A,\omega)\\
&\quad= -\int_{\partial O} \frac{2}{\rho(\mathbf{x}_O)c(\mathbf{x}_O)}\{\hat{p}^-(\mathbf{x}_B,\mathbf{x}_O,\omega)\}\{\hat{p}^+(\mathbf{x}_A,\mathbf{x}_O,\omega)\}^*\,d\mathbf{x}_O.
\end{aligned}\tag{27}$$

Here $\hat{p}^{+,\rm out}(\mathbf{x}_A,\mathbf{x}_S,\omega)$ refers to the field that is outgoing at source $\mathbf{x}_S$ and downgoing at receiver $\mathbf{x}_A$. $\hat{p}^{-,\rm out}(\mathbf{x}_B,\mathbf{x}_S,\omega)$ refers to the field that is outgoing at source $\mathbf{x}_S$ and upgoing at receiver $\mathbf{x}_B$.

Equation (26) is useful for identifying ghosts in interferometry by CC of decomposed fields. It shows that cross-correlation of up- and downgoing constituents (25) yields as a causal part the desired Green's function $G^{-,+}(\mathbf{x}_B,\mathbf{x}_A,t)$ plus two additional ghost terms $g^S_{\rm dcp}$ and $g^O_{\rm dcp}$. Note that the acausal part can be used to generate virtual sources that radiate upwards, as demonstrated by van der Neut et al. [25].

To illustrate the consequence of decomposition, we demonstrate (25) on model B (Figure 3(b)). The reference response consists of a single reflection at $t = 0.4$ s and a weak multiple at $t = 0.9$ s; see Figure 11(a). The ghosts $g^S_{\rm dcp}+g^O_{\rm dcp}$ and correlation function $C_{\rm dcp}$ are shown in Figures 11(b) and 11(c), respectively. Note that the ghosts are close to zero, meaning that the reflection response is almost perfectly reconstructed, apart from two weak spurious events at $t = 0.2$ s and $t = 0.6$ s. Compared to interferometry by cross-correlation of perturbed fields (Figure 9(c)), the multiples at $t = 0.5$ s and $t = 0.7$ s have been effectively removed.

Wavefield decomposition does still not offer a solution for free-surface-related artifacts. To illustrate this, we apply the method to model D (Figure 3(d)). In Figure 12(a) we show the reference response, containing only the

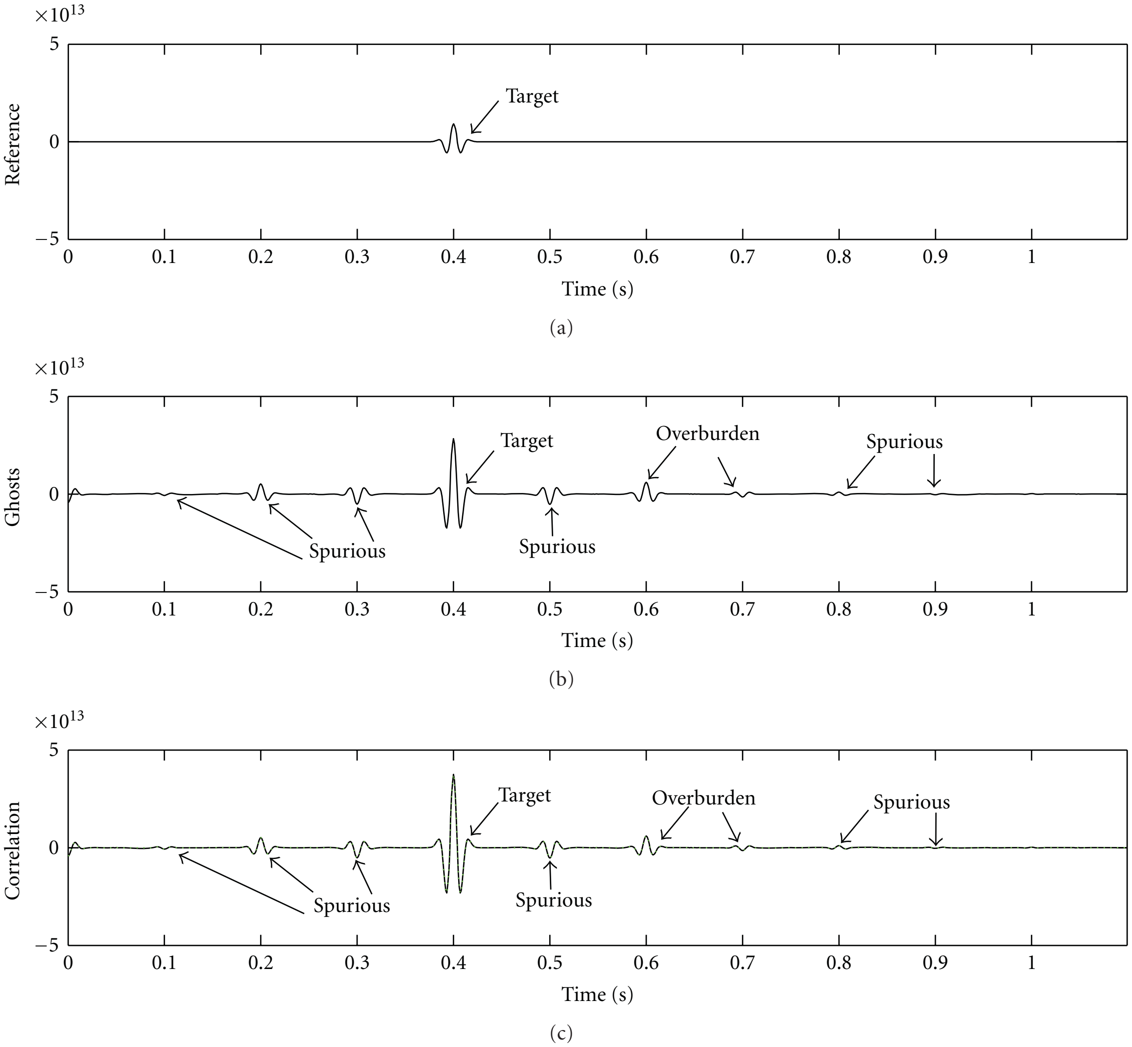

FIGURE 12: Cross-correlation of decomposed fields for model D: (a) reference response by placing an active source at the virtual source location $\mathbf{x}_A$; (b) computed ghost terms $g^S_{\text{dcp}} + g^O_{\text{dcp}}$; (c) correlation function C_{dcp} (black) and the sum of reference response + ghosts (dashed green).

desired reflection at $t = 0.4$ s. Ghosts $g^S_{\text{dcp}} + g^O_{\text{dcp}}$ and the retrieved correlation function C_{dcp} are shown in Figures 12(b) and 12(c), respectively. Note that artifacts are almost similar to those of perturbation-based interferometry (Figure 10(c)).

5. Multidimensional Deconvolution of Perturbed Fields

Another strategy to eliminate ghosts in interferometry is to replace cross-correlation by deconvolution or, more exact, multidimensional deconvolution (MDD) [22]. In MDD, a Green's function is retrieved by solving an inverse problem. This inverse problem is generally derived for decomposed wavefields and requires the installation of multicomponent receivers or two parallel receiver arrays close to each other. Before addressing MDD of decomposed fields, we present an alternative approach for perturbed fields, which can be applied with single-component sensors and time-gating.

To derive MDD for perturbed fields, we define a new volume $\mathbb{V}$, bounded by free surface $\partial\mathbb{F}$ and receiver array $\partial\mathbb{A}$, see Figure 13. We define a reference medium, which is similar to the physical medium within the integration volume, but homogeneous below $\partial\mathbb{A}$. All heterogeneities in the physical medium outside $\mathbb{V}$ are referred to as perturbations. Subscript inc indicates those fields that propagate in the reference medium. Subscript sc is used for scattered fields, where $\hat{p} = \hat{p}_{\text{inc}} + \hat{p}_{\text{sc}}$ denotes the full field in the physical medium. Vasconcelos et al. [11] derived a convolution-based representation for the scattered field with a source at $\mathbf{x}_S$ and a receiver at $\mathbf{x}_B$, where $\mathbf{x}_S$ is inside volume $\mathbb{V}$ and $\mathbf{x}_B$ is outside this volume, that is

$$\hat{p}_{\text{sc}}(\mathbf{x}_B, \mathbf{x}_S, \omega) = \hat{J}^A_{\text{ptb}}(\mathbf{x}_B, \mathbf{x}_S, \omega) + \hat{J}^F_{\text{ptb}}(\mathbf{x}_B, \mathbf{x}_S, \omega). \tag{28}$$

On the right-hand side we find two integrals. $\hat{J}^{A}_{\mathrm{ptb}}$ involves integration over the receiver array $\partial\mathbb{A}$:

$$\hat{J}^{A}_{\mathrm{ptb}}(\mathbf{x}_B,\mathbf{x}_S,\omega) = \int_{\partial A}\frac{1}{j\omega\rho(\mathbf{x}_A)} \times\Big[\Big\{\mathbf{n}_A\cdot\nabla_A\hat{G}_{\mathrm{sc}}(\mathbf{x}_B,\mathbf{x}_A,\omega)\Big\}\{\hat{p}_{\mathrm{inc}}(\mathbf{x}_A,\mathbf{x}_S,\omega)\} -\Big\{\hat{G}_{\mathrm{sc}}(\mathbf{x}_B,\mathbf{x}_A,\omega)\Big\}\{\mathbf{n}_A\cdot\nabla_A\hat{p}_{\mathrm{inc}}(\mathbf{x}_A,\mathbf{x}_S,\omega)\}\Big]d\mathbf{x}_A. \tag{29}$$

∇_A is the spatial gradient at receiver location $\mathbf{x}_A$ and $\mathbf{n}_A$ is the outward-pointing unit normal vector of $\partial\mathbb{A}$. Integral $\hat{J}^{F}_{\mathrm{ptb}}$ is a similar integral over $\partial\mathbb{F}$, which vanishes since all pressure recordings are zero at this interface. We rewrite the wavefield $\hat{p}$ at $\partial\mathbb{A}$ in terms of ingoing components $\hat{p}^{\mathrm{in}}$ and outgoing components $\hat{p}^{\mathrm{out}}$. Similarly, $\hat{G}_{\mathrm{sc}} = \hat{G}^{\mathrm{out}}_{\mathrm{sc}} + \hat{G}^{\mathrm{in}}_{\mathrm{sc}}$. Since the reference medium is homogeneous outside $\mathbb{V}$, $\hat{p}_{\mathrm{inc}}$ is purely outgoing at $\mathbf{x}_A$ (so $\hat{p}_{\mathrm{inc}} = \hat{p}^{\mathrm{out}}_{\mathrm{inc}}$ and $\hat{p}^{\mathrm{in}}_{\mathrm{inc}} = 0$). It can be shown that the convolutions between ingoing fields at the virtual source $\mathbf{x}_A$ and outgoing fields $\hat{p}_{\mathrm{inc}}(\mathbf{x}_A,\mathbf{x}_S,\omega)$ cancel and that the remaining terms can be merged [22]. Consequently, (28) and (29) can be rewritten as

$$\hat{p}_{\mathrm{sc}}(\mathbf{x}_B,\mathbf{x}_S,\omega) = \int_{\partial A}\hat{G}_{\mathrm{ptb}}(\mathbf{x}_B,\mathbf{x}_A,\omega)\hat{p}_{\mathrm{inc}}(\mathbf{x}_A,\mathbf{x}_S,\omega)d\mathbf{x}_A, \tag{30}$$

where we have introduced

$$\hat{G}_{\mathrm{ptb}}(\mathbf{x}_B,\mathbf{x}_A,\omega) = \frac{2}{j\omega\rho(\mathbf{x}_A)}\mathbf{n}_A\cdot\nabla_A\hat{G}^{\mathrm{out}}_{\mathrm{sc}}(\mathbf{x}_B,\mathbf{x}_A,\omega). \tag{31}$$

Equation (31) represents the exact scaled dipole Green's function that can be solved by inversion of (30). Since an exact solution of (30) is generally not feasible, we apply least-squares inversion. We show in Appendix A that finding a least-squares solution of this problem is equivalent to solving the so-called normal equation, which is obtained by correlating both sides of (30) with $\hat{G}_{\mathrm{inc}}(\mathbf{x}'_A,\mathbf{x}_S,\omega)$ and summing over $\mathbf{x}_S$ (where $\mathbf{x}'_A$ is at $\partial\mathbb{A}$). Hence

$$\hat{C}_{\mathrm{ptb}}(\mathbf{x}_B,\mathbf{x}'_A,\omega) = \int_{\partial A}\hat{G}_{\mathrm{ptb}}(\mathbf{x}_B,\mathbf{x}_A,\omega)\hat{\Gamma}_{\mathrm{ptb}}(\mathbf{x}_A,\mathbf{x}'_A,\omega)d\mathbf{x}_A. \tag{32}$$

On the left-hand side of (32) we have the correlation function of the incident field at $\mathbf{x}'_A$ and the scattered field at $\mathbf{x}_B$:

$$\hat{C}_{\mathrm{ptb}}(\mathbf{x}_B,\mathbf{x}'_A,\omega) = \sum_i W(\mathbf{x}_S)\hat{p}_{\mathrm{sc}}\left(\mathbf{x}_B,\mathbf{x}^{(i)}_S,\omega\right)\left\{\hat{p}_{\mathrm{inc}}\left(\mathbf{x}'_A,\mathbf{x}^{(i)}_S,\omega\right)\right\}^*, \tag{33}$$

Note that (33) is identical to a discrete scaled representation of (20), if the medium parameters are constant at $\partial\mathbb{S}$ and $\mathbf{x}'_A$ is replaced by $\mathbf{x}_A$. On the right-hand side of (32) we have the so-called point-spread-function (PSF) for perturbed fields, defined as

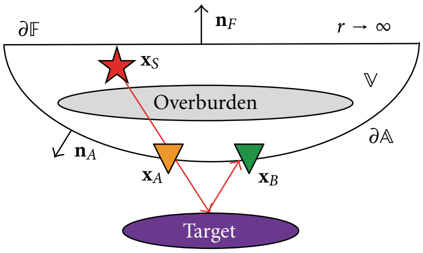

Figure 13: Configuration for controlled-source interferometry by multidimensional deconvolution of perturbed fields; integration volume $\mathbb{V}$ is enclosed by the free surface $\partial\mathbb{F}$ and receiver array $\partial\mathbb{A}$; $\mathbf{x}_S$ denotes a source location; $\mathbf{x}_A$ and $\mathbf{x}_B$ denote receiver locations at $\partial\mathbb{A}$ and $\mathbf{n}_A$ is the unit normal vector of the receiver array; $\mathbf{n}_F$ is the unit normal vector of the free surface; heterogeneities between sources and receivers are referred to as "overburden," whereas heterogeneities below the receivers are referred to as "target."

$$\hat{\Gamma}_{\mathrm{ptb}}(\mathbf{x}_A,\mathbf{x}'_A,\omega) = \sum_i W\left(\mathbf{x}^{(i)}_S\right)\hat{p}_{\mathrm{inc}}\left(\mathbf{x}_A,\mathbf{x}^{(i)}_S,\omega\right)\left\{\hat{p}_{\mathrm{inc}}\left(\mathbf{x}'_A,\mathbf{x}^{(i)}_S,\omega\right)\right\}^*. \tag{34}$$

In both expressions, $W(\mathbf{x}_S)$ is an optional source-dependent weighting function. If sufficient source and receiver locations are present, a multidimensional inverse $\hat{\Gamma}^{\mathrm{inv}}_{\mathrm{ptb}}$ of the PSF can be introduced, according to

$$\int_{\partial A}\hat{\Gamma}_{\mathrm{ptb}}(\mathbf{x}_A,\mathbf{x}'_A,\omega)\hat{\Gamma}^{\mathrm{inv}}_{\mathrm{ptb}}(\mathbf{x}'_A,\mathbf{x}''_A,\omega)d\mathbf{x}'_A = \delta(\mathbf{x}_A-\mathbf{x}''_A). \tag{35}$$

where $\mathbf{x}''_A$ is at $\partial\mathbb{A}$. The desired dipole response can now be found by filtering the correlation function with $\hat{\Gamma}^{\mathrm{inv}}$, according to

$$\hat{G}_{\mathrm{ptb}}(\mathbf{x}_B,\mathbf{x}''_A,\omega) = \int_{\partial A}\hat{C}_{\mathrm{ptb}}(\mathbf{x}_B,\mathbf{x}'_A,\omega)\hat{\Gamma}^{\mathrm{inv}}_{\mathrm{ptb}}(\mathbf{x}'_A,\mathbf{x}''_A,\omega)d\mathbf{x}'_A, \tag{36}$$

Implementation of (36) is referred to as MDD of perturbed fields. This method allows us to deghost and deblur the correlation function of perturbed fields. We retrieve a Green's function of an outward-radiating virtual source. However, this retrieved Green's function lives in the physical medium and multiples from the overburden can still populate the retrieved gathers.

We apply MDD of perturbed fields to model B (Figure 3(b)). The result is shown in Figure 14(a) (black) and compared with the reference response G_{ptb} (dashed green). Note that the MDD response is similar to the correlation function C_{ptb} (Figure 9(c)), apart from a very weak spurious event at $t = 0.2$ s, a scaling factor and subtle amplitude variations. We discussed that C_{ptb} can be interpreted as the desired response G_{ptb}, convolved with the PSF (see (32)). In Figure 14(b) we show that the PSF

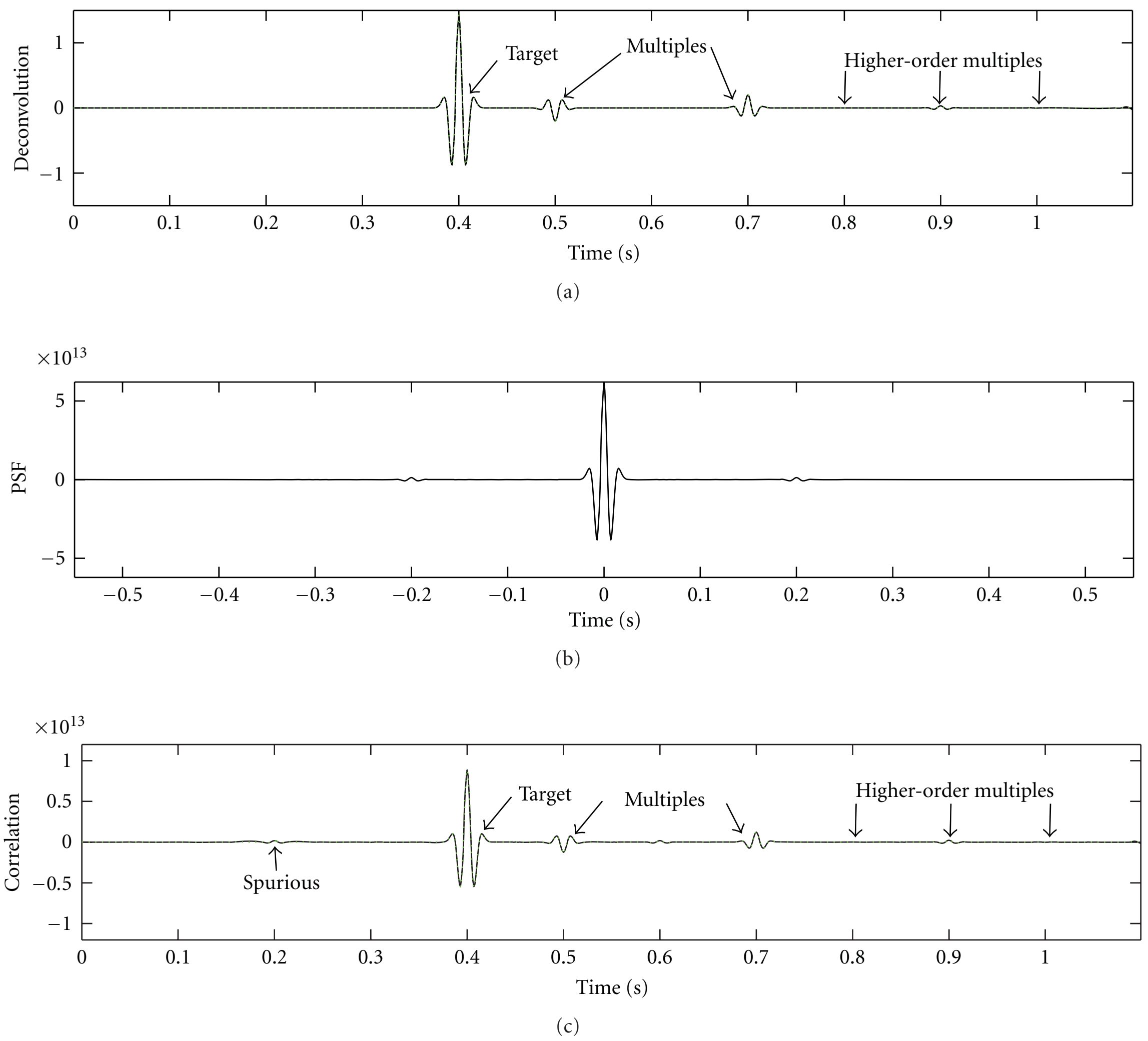

Figure 14: Deconvolution of perturbed fields for model B: (a) retrieved Green's function (black) and the reference response (dashed green); (b) point spread function Γ_{ptb}; (c) convolution of the reflection response with the PSF (black) and correlation function C_{ptb} (dashed green).

is close to a scaled band-limited delta function, with two additional weak events observed at $t = \pm 0.2$ s. If we convolve the reference response with the PSF, we find indeed the correlation function, see Figure 14(c). From the simple structure of the PSF, it could have been directly concluded that G_{ptb} and C_{ptb} are indeed very similar apart from a scaling factor.

This is not the case for model D (Figure 3(d)). The response of MDD of perturbed fields (black) is compared with the reference response G_{ptb} (dashed green) in Figure 15(a). Compared to the correlation function C_{ptb} (Figure 10(c)), the MDD response is very simple, containing only the target reflection at $t = 0.4$ s and a multiple at $t = 1.0$ s. The strong disagreement of the MDD result and the correlation function is reflected by the PSF; see Figure 15(b). In Figure 15(c) we show that convolution of the PSF and reference response yields indeed the correlation function C_{ptb}.

6. Multidimensional Deconvolution of Decomposed Fields

The response retrieved by MDD of perturbed fields can still contain undesired reflections from the overburden. If ingoing and outgoing waves are separated at the receiver level prior to MDD, also these multiples can be removed [22]. For this purpose we redefine our volume once more, see Figure 16. Instead of enclosing the volume above the receivers, we now define $\mathbb{V}$ as the volume enclosed by receiver array $\partial\mathbb{A}$ and a halfsphere $\partial\mathbb{O}$ below the receivers with radius $r \rightarrow \infty$. We define a reference state, in which all heterogeneities above $\partial\mathbb{A}$ are removed. Fields that propagate in this reference state are indicated with a bar; that is $\hat{\bar{G}}$. We formulate a convolution based representation for the field of source $\mathbf{x}_S$ at receiver $\mathbf{x}_B$, where $\mathbf{x}_S$ is outside volume $\mathbb{V}$ and $\mathbf{x}_B$ is inside this volume, reading

$$\hat{p}(\mathbf{x}_B, \mathbf{x}_S, \omega) = \hat{J}^{A}_{\text{dcp}}(\mathbf{x}_B, \mathbf{x}_S, \omega) + \hat{J}^{O}_{\text{dcp}}(\mathbf{x}_B, \mathbf{x}_S, \omega). \qquad (37)$$

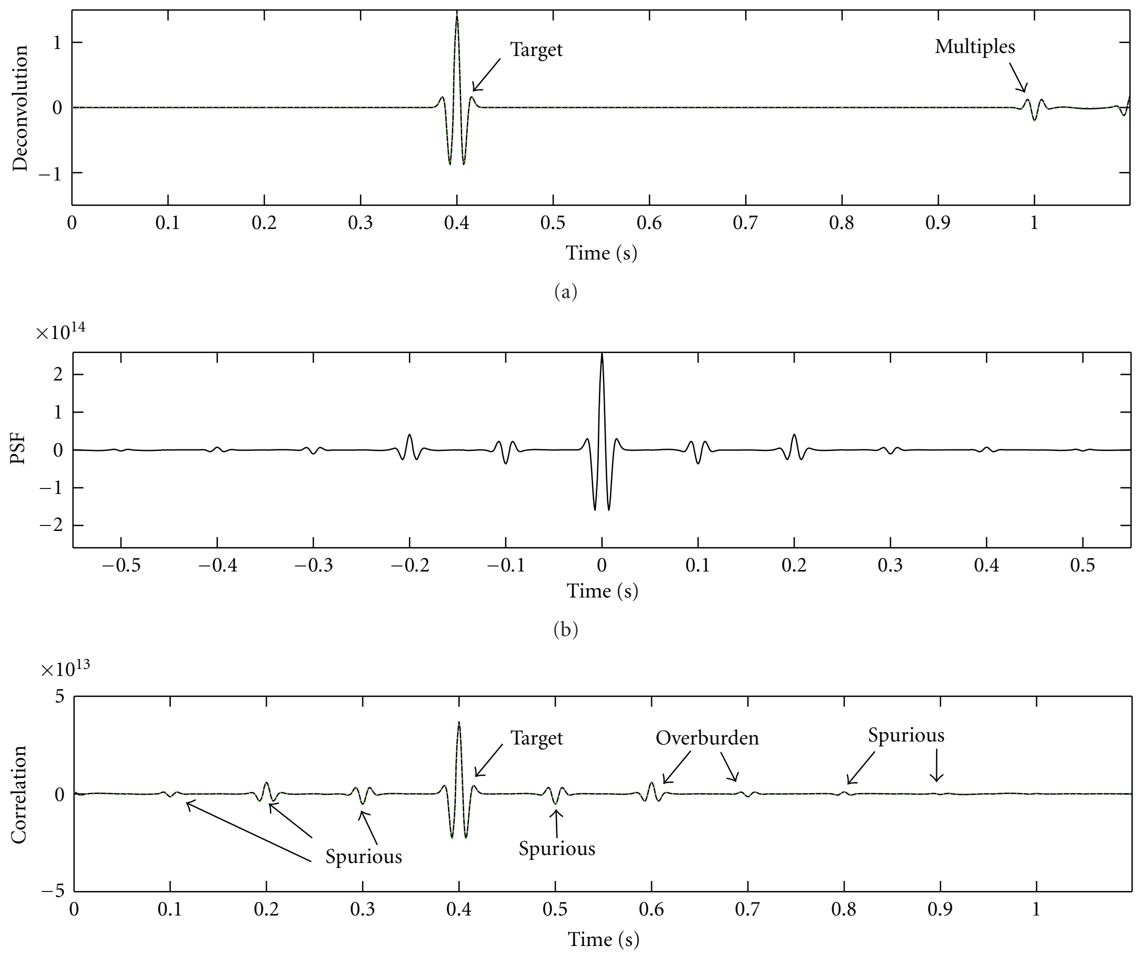

(c)

FIGURE 15: Deconvolution of perturbed fields for model D: (a) retrieved Green's function (black) and the reference response (dashed green); (b) point spread function Γ_{ptb}; (c) convolution of the reflection response with the PSF (black) and the correlation function C_{ptb} (dashed green).

On the right-hand side we find two integrals. $\hat{J}^{A}_{\text{dcp}}$ involves integration over the receiver array $\partial\mathbb{A}$:

$$\begin{aligned}
\hat{J}^{A}_{\text{dcp}}&(\mathbf{x}_B,\mathbf{x}_S,\omega)\\
&= -\int_{\partial A}\frac{1}{j\omega\rho(\mathbf{x}_A)}\\
&\quad\times\Big[\Big\{\mathbf{n}_A\cdot\nabla_A\hat{\hat{G}}(\mathbf{x}_B,\mathbf{x}_A,\omega)\Big\}\{\hat{p}(\mathbf{x}_A,\mathbf{x}_S,\omega)\}\\
&\qquad-\Big\{\hat{\hat{G}}(\mathbf{x}_B,\mathbf{x}_A,\omega)\Big\}\{\mathbf{n}_A\cdot\nabla_A\hat{p}(\mathbf{x}_A,\mathbf{x}_S,\omega)\}\Big]d\mathbf{x}_A.
\end{aligned}\tag{38}$$

Integral $\hat{J}^{O}_{\text{dcp}}$ is a similar integral over the interface $\partial\mathbb{O}$. Since this integral contains convolutions and its radius $r \to \infty$, it will vanish due to Sommerfeld's radiation conditions [41]. Since the reference state is homogeneous outside $\mathbb{V}$, $\hat{\hat{G}}(\mathbf{x}_B,\mathbf{x}_A,\omega)$ is purely ingoing at virtual source $\mathbf{x}_A$ ($\hat{\hat{G}} = \hat{\hat{G}}^{\text{in}}$ and $\hat{\hat{G}}^{\text{out}} = 0$). We substitute $\hat{p} = \hat{p}^{\text{in}} + \hat{p}^{\text{out}}$. It can be shown that the convolutions of ingoing fields at the virtual source $\mathbf{x}_A$ with outgoing fields $\hat{p}^{\text{out}}(\mathbf{x}_A,\mathbf{x}_S,\omega)$ cancel and that the remaining terms can be merged, yielding

$$\hat{p}(\mathbf{x}_B,\mathbf{x}_S,\omega) = \int_{\partial A}\hat{\hat{G}}_{\text{dcp}}(\mathbf{x}_B,\mathbf{x}_A,\omega)\hat{p}^{\text{in}}(\mathbf{x}_A,\mathbf{x}_S,\omega)d\mathbf{x}_A, \tag{39}$$

where we have introduced

$$\hat{\hat{G}}_{\text{dcp}}(\mathbf{x}_B,\mathbf{x}_A,\omega) = -\frac{2}{j\omega\rho(\mathbf{x}_A)}\mathbf{n}_A\cdot\nabla_A\hat{\hat{G}}(\mathbf{x}_B,\mathbf{x}_A,\omega). \tag{40}$$

In a similar way as for MDD of perturbed fields, a normal equation can be derived:

$$\hat{C}_{\text{dcp}}(\mathbf{x}_B,\mathbf{x}'_A,\omega) = \int_{\partial A}\hat{\hat{G}}_{\text{dcp}}(\mathbf{x}_B,\mathbf{x}_A,\omega)\hat{\Gamma}_{\text{dcp}}(\mathbf{x}_A,\mathbf{x}'_A,\omega)d\mathbf{x}_A, \tag{41}$$

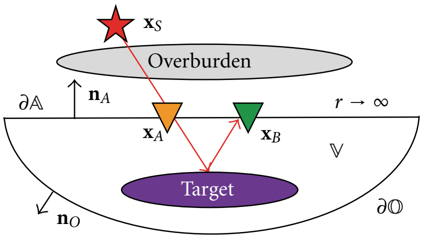

Figure 16: Configuration for controlled-source interferometry by multidimensional deconvolution of decomposed fields; integration volume $\mathbb{V}$ is enclosed by receiver array $\partial\mathbb{A}$ and an additional halfsphere $\partial\mathbb{O}$; $\mathbf{x}_S$ denotes a source location; $\mathbf{x}_A$ and $\mathbf{x}_B$ denote receiver locations at $\partial\mathbb{A}$ and $\mathbf{n}_A$ is the unit normal vector of the receiver array; $\mathbf{n}_O$ is the unit normal vector of $\partial\mathbb{O}$; heterogeneities between sources and receivers are referred to as "overburden," whereas heterogeneities below the receivers are referred to as "target."

where $\mathbf{x}'_A$ is at $\partial\mathbb{A}$. On the left-hand side we have the correlation function of the ingoing field at $\mathbf{x}'_A$ and the outgoing field at $\mathbf{x}_B$:

$$\hat{C}_{\mathrm{dcp}}(\mathbf{x}_B,\mathbf{x}'_A,\omega) = \sum_i W(\mathbf{x}_S)\hat{p}^{\mathrm{out}}\left(\mathbf{x}_B,\mathbf{x}_S^{(i)},\omega\right)\left\{\hat{p}^{\mathrm{in}}\left(\mathbf{x}'_A,\mathbf{x}_S^{(i)},\omega\right)\right\}^*. \qquad (42)$$

Note that (42) is similar to a discrete scaled version of (25), if "ingoing" and "outgoing" are interchanged with "downgoing" and "upgoing," medium parameters are constant at the source array and $\mathbf{x}'_A$ is replaced by $\mathbf{x}_A$. On the right-hand side we have the Point-Spread-Function (PSF) for decomposed fields, given by

$$\hat{\Gamma}_{\mathrm{dcp}}(\mathbf{x}_A,\mathbf{x}'_A,\omega) = \sum_i W(\mathbf{x}_S)\hat{p}^{\mathrm{in}}\left(\mathbf{x}_A,\mathbf{x}_S^{(i)},\omega\right)\left\{\hat{p}^{\mathrm{in}}\left(\mathbf{x}'_A,\mathbf{x}_S^{(i)},\omega\right)\right\}^*. \qquad (43)$$

If acquisition conditions allow, we can take a multidimensional inverse of the PSF $\hat{\Gamma}^{\mathrm{inv}}_{\mathrm{dcp}}$ and convolve it with the correlation function according to

$$\hat{\hat{G}}_{\mathrm{dcp}}(\mathbf{x}_B,\mathbf{x}''_A,\omega) = \int_{\partial A}\hat{C}_{\mathrm{dcp}}(\mathbf{x}_B,\mathbf{x}'_A,\omega)\hat{\Gamma}^{\mathrm{inv}}_{\mathrm{dcp}}(\mathbf{x}'_A,\mathbf{x}''_A,\omega)\,d\mathbf{x}'_A, \qquad (44)$$

where $\mathbf{x}''_A$ is at $\partial\mathbb{A}$ and

$$\int_{\partial A}\hat{\Gamma}_{\mathrm{dcp}}(\mathbf{x}_A,\mathbf{x}'_A,\omega)\hat{\Gamma}^{\mathrm{inv}}_{\mathrm{dcp}}(\mathbf{x}'_A,\mathbf{x}''_A,\omega)\,d\mathbf{x}'_A = \delta(\mathbf{x}_A-\mathbf{x}''_A). \qquad (45)$$

Implementation of (44) is referred to as MDD of decomposed fields. This method allows us to deghost and deblur the correlation function of decomposed fields. Moreover, we retrieve a response that lives in the reference medium, where all multiples from the overburden have been removed.

We return to model B (Figure 3(b)). In Figure 17(a) we show the result of MDD of decomposed fields (black) and the reference response (dashed green). The response does not contain any of the multiples that have been retrieved by MDD of perturbed fields (Figure 14(a)). Note that indeed the weak ghosts and multiples that we observed in the correlation function (Figure 11(c)) have been eliminated, as predicted by theory. The weakness of these events is reflected in the PSF, showing a scaled band-limited delta function with weak events at $t = \pm 0.2$ s and $t = \pm 0.5$ s. We convolve the reference response with the PSF to show that indeed the correlation function emerges, see Figure 17(c).

The effects of MDD of decomposed fields are more dramatically exposed by model D (Figure 3(d)). In Figure 18(a) we show that also for this model we can retrieve a response that is free of ghosts and multiples. Compared to MDD of perturbed fields (Figure 15(a)), we observe that the multiple at $t = 1.0$ s has been eliminated. The complex character of the PSF (Figure 18(b)) exposes the difference between the MDD response and the correlation function (Figure 12(c)). In Figure 18(c) we show that the correlation function can indeed be found by convolving the reference response with the PSF.

7. Spatial Aspects

So far we have mostly concentrated on temporal aspects (ghosts and multiples) of interferometry. There are spatial aspects as well. In the representations (32) and (41) we have shown that the correlation functions of perturbed and decomposed fields can be interpreted as the desired reflection response, blurred in time and space with the PSF. This means that we can only retrieve an accurate response by cross-correlation if the PSF is focused at the virtual source location. However, due to unbalanced source distributions, intrinsic losses, or heterogeneities in the overburden, the PSF can be spatially defocused. As a result, the retrieved data by cross-correlation will be blurred. We illustrate this with a salt flank example.

In Figure 19 we show a salt flank model, defined as a function of coordinates x_1 (horizontal distance) and x_3 (depth). Note the velocity gradient in the medium, producing diving waves that are useful for salt flank imaging. We place 201 receivers in a vertical well with 20 m vertical spacing along the interval $x_3 \in [1000\,\mathrm{m}, 5000\,\mathrm{m}]$ at $x_1 = 15000$ m. We place 401 sources at the surface with 30 m spacing along the interval $x_1 \in [0\,\mathrm{m}, 12000\,\mathrm{m}]$ at $x_3 = 0$ m. No free surface is incorporated. In the following we generate a virtual shot record as if there was a source at receiver $\mathbf{x}_A = (15000\,\mathrm{m}, 4000\,\mathrm{m})$ in the well using CC of perturbed fields. We generate a reference response by placing an active source at $\mathbf{x}_A$ and modeling the wavefield. In Figure 20 we show three snapshots of the emitted wavefield that was used for the reference response. We indicate three reflections by numbers 1, 2, and 3. These are the reflections we aim to retrieve.

We time-gate the incident fields of the observed data at the receiver array and subtract it from the full fields to extract the scattered fields. Next, we obtain the correlation function at virtual source $\mathbf{x}_A$ by stacking cross-correlations of incident and scattered fields over all 401 sources (see (33)). A Hanning taper is applied to the first 20 and last 20 sources.

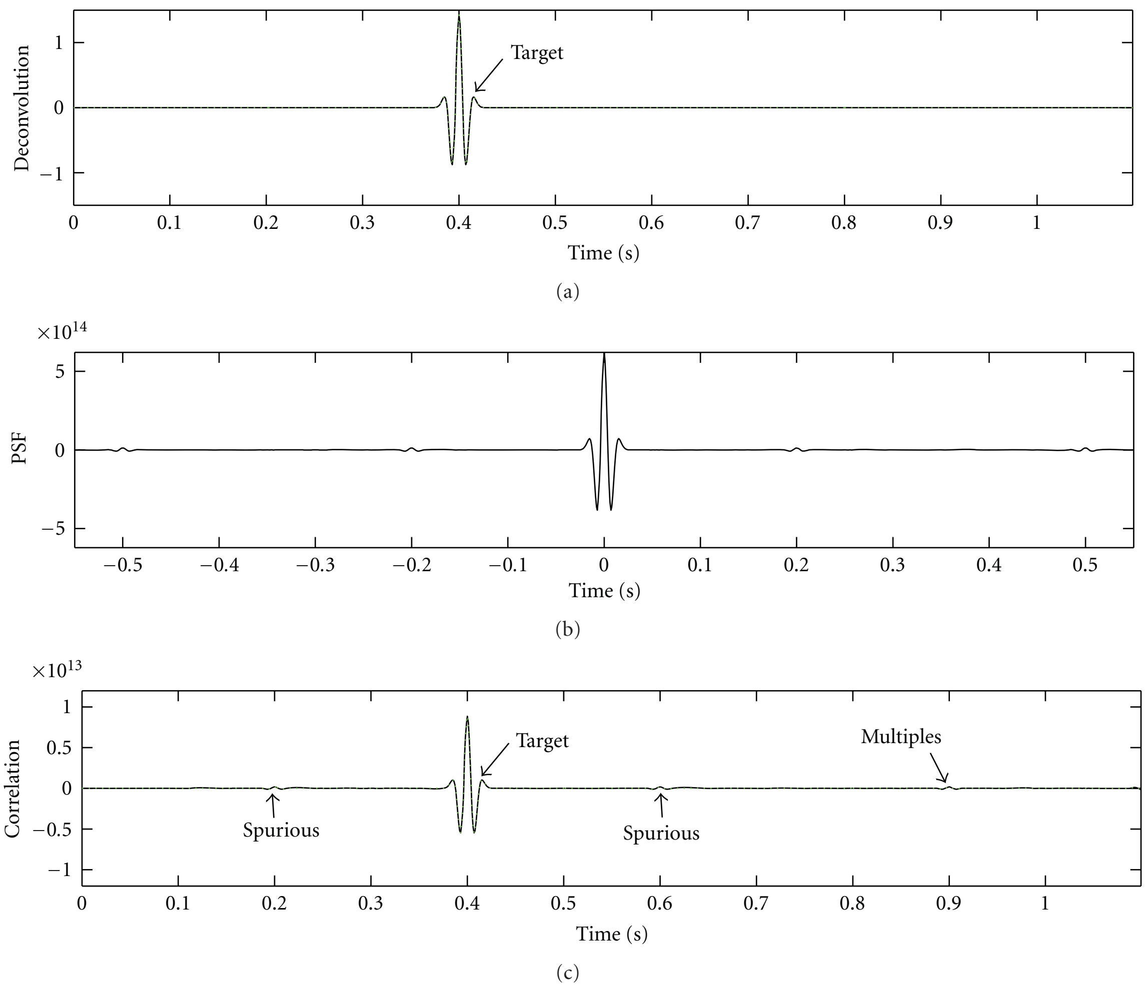

(a)

(b)

(c)

Figure 17: Deconvolution of decomposed fields for model B: (a) retrieved Green's function (black) and the reference response (dashed green); (b) point spread function Γ_{dcp}; (c) convolution of the reflection response with the PSF (black) and the correlation function C_{dcp} (dashed green).

In Figure 21 we show the retrieved response (red) and the reference response (black). For display purposes, only every 20th trace is shown. Note that the match is perfect and the reflections 1, 2, and 3 that were indicated in Figure 20 can easily be recognized.

In seismic interferometry, the retrieval of a reflection response is often explained by summations over correlation gathers. To briefly illustrate this concept, we cross-correlated the incident field at $\mathbf{x}_A = (15000\,\text{m}, 4000\,\text{m})$ with the scattered field at $\mathbf{x}_B = (15000\,\text{m}, 2000\,\text{m})$ for different source locations $\mathbf{x}_S$, see Figure 22. For display purposes, only every 20th trace is shown. To retrieve the trace at 2000 m of the virtual shot record (Figure 21), a stack over all traces in Figure 22 is required. It can be shown that constructive interference takes place at the stationary points, being the maxima in time of each reflector in Figure 22, obeying Fermat's principle. Destructive interference takes place outside these stationary points.

Alternatively, we could interpret interferometry as the process of focusing a virtual source, meaning that the PSF in (34) is converging towards a spatial and temporal delta function, indicating that the correlation function does indeed represent the desired reflection response, free of blurring. In Figure 23 we show the PSF for a virtual source at $\mathbf{x}_A = (15000\,\text{m}, 4000\,\text{m})$. As for a virtual shot gather, the traces of the PSF can be interpreted as summations over correlation gathers. In the so-called PSF correlation gathers, the incident field at $\mathbf{x}_A$ is correlated with the incident field at $\mathbf{x}'_A$ ("integrand" of (34)). If $\mathbf{x}_A = \mathbf{x}'_A$, this corresponds to auto-correlation, providing a significant contribution at $t = 0$, see Figure 24. These contributions will interfere constructively, to generate the desired spike in the PSF. If $\mathbf{x}_A \neq \mathbf{x}'_A$, cross-correlations of different source locations will map at different times; see Figure 25. If the virtual source is uniformly illuminated in each spatial direction, all such contributions will interfere destructively and the PSF will converge to the desired delta function. If this is the case, the virtual source will be perfectly focused, as in Figure 23. The two "legs" that can be observed in the PSF are caused by the finite source aperture. Finite source-aperture artifacts can be

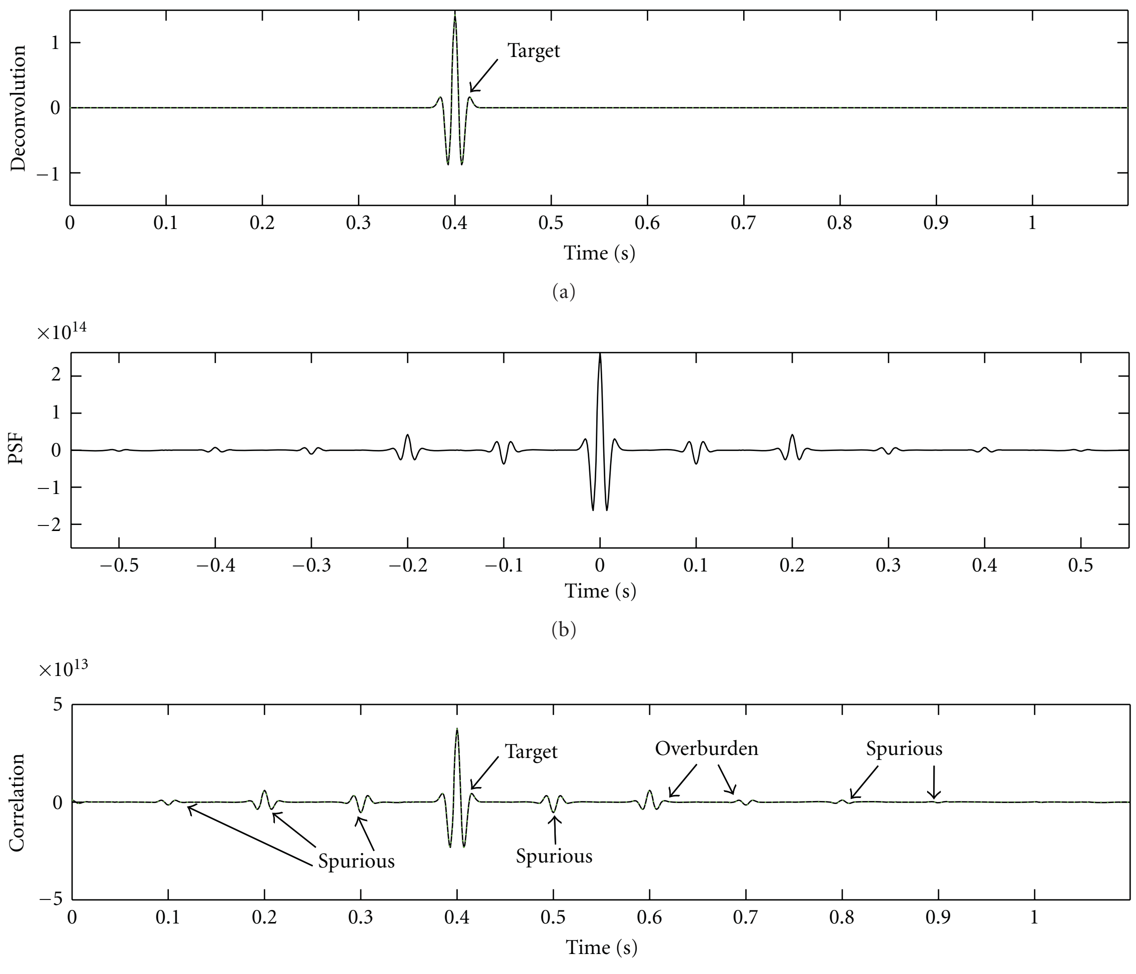

(a)

(b)

(c)

Figure 18: Deconvolution of decomposed fields for model D: (a) retrieved Green's function (black) and the reference response (dashed green); (b) point spread function Γ_{dcp}; (c) convolution of the reflection response with the PSF (black) and the correlation function C_{dcp} (dashed green).

reduced by tapering the edges of the source array [39], as has already been done in this example. It was shown by van der Neut and Thorbecke [47] that the legs of the PSF can be used to diagnose the need for and the effects of such tapering.

If illumination conditions vary with incidence angle, spatial blurring can occur. Illumination variations can be introduced at the source side, for instance if sources are nonuniformly distributed or source characteristics are spatially varying due to source coupling conditions. We mimic such a situation by assigning location- and frequency-dependent spectra to the sources, see Figure 26. In this particular example, the peak frequency and source strength vary randomly with the source location, superimposed by an additional trend in source strength along the array. Note that the low source numbers (corresponding to the left side of the array in Figure 19) are overilluminated with respect to the high source numbers (corresponding to the right side of the array in Figure 19). As a consequence of these variations, the PSF of the virtual source is no longer optimally focused, as shown in Figure 27. The events in the PSF that intersect the focus point ($\mathbf{x} = \mathbf{x}_A$ and $t = 0$) (apart from the legs), as seen in Figure 27, stem from incomplete destructive interference and are typical for spatial defocusing of the virtual source, leading to a distorted virtual source radiation pattern [10].

Virtual source defocusing can also be a consequence of velocity or density variations in the overburden. We illustrate this by introducing a gas cloud in the model, see Figure 28. In Figure 29 we show the PSF in the medium with gas cloud, where the variations in source spectra of Figure 26 have also been incorporated. Note that besides spatial defocusing, we also observe temporal defocusing stemming from gas cloud scattering. Events in the PSF that do not intersect the focus point ($\mathbf{x} = \mathbf{x}_A$ and $t = 0$), as seen in Figure 29, are typical indicators of temporal defocusing, which can be related to the ghosts and multiples that we discussed earlier in this paper.

In Figure 30 we show the correlation function for the model with varying source spectra and a gas cloud. Note that the correlation function is no longer perfectly matching the reference response, especially not in terms of amplitudes. This mismatch can be effectively removed from the retrieved data by MDD, meaning that the correlation function is filtered with the inverse of the PSF (see (36)). The retrieved gather after MDD is shown in Figure 31. Note that the match between retrieved and reference response has improved considerably. We do point out, however, that inversion artifacts can be created due to limited illumination conditions, as highlighted in the top of Figure 31.

In Figure 32 we show an image of the salt flank in the model with source spectra variations and a gas cloud. The image is obtained by one-way shot profile migration of the correlation functions at all possible virtual source locations. In dashed red we show the location of the salt flank, as taken from the velocity model. Note that interferometry has enabled us to image the top of the flank "from below" by smart utilization of the diving waves. Also note that artifacts can be observed, which might be interpreted as additional ghost reflectors or diffractors. As MDD allows us to refocus the virtual sources before migration, several of these artifacts can be removed by migrating data after MDD, as shown in Figure 33. We observe that several potential "ghost reflectors" have been eliminated throughout the gather. The continuity of the salt flank amplitude marked by "A" is improved. The strong artifact marked by "B" as well as various other artifacts in this part of the gather have been suppressed. Artifacts such as indicated by "C" have been eliminated, but new artifacts such as "D" have emerged. We point with special attention to events "E" and "F" that might well be mistakenly interpreted as the continuation of the lower part of the salt flank. Note that MDD has completely eliminated these spurious arrivals. Finally, we note that inversion artifacts have hardened the interpretation of the lowest part of the salt flank in "G." We conclude that MDD can indeed improve the image and remove defocusing effects, but care should be taken for potential inversion artifacts that can deteriorate parts of the image and mislead interpretation.

8. Discussion

An overview has been given of the ghosts that appear in correlation interferometry of full, perturbed and decomposed fields. Equations (12), (24), and (26) describe these ghosts in an additive way. Alternatively, the correlation functions of perturbed or decomposed fields can be interpreted as the desired reflection responses, convolved in space and time with the PSF, see (32) and (41). Analysis of the PSF's allows us to diagnose the quality of virtual source focusing in time and space. Along the temporal axis, the PSF gives information on possible ghosts and undesired multiples that may hamper the retrieved data. Along the spatial axis, the PSF gives information on focusing, that can be blurred due to unbalanced acquisition, intrinsic losses or complexities in the velocity model. The correlation function can be deblurred by filtering with the inverse of the PSF. This process is multidimensional deconvolution, allowing us to deghost, demultiple, and deblur the retrieved data.

The PSF can also provide insight in the effects of time-gating, which is often applied for separation of incident and scattered wavefields. In the Virtual Source method of Bakulin and Calvert [4], it is advocated to cross-correlate only the direct field instead of the full incident field. In Appendix B we use the PSF to show that narrow time-gates can improve the quality of virtual source focusing.

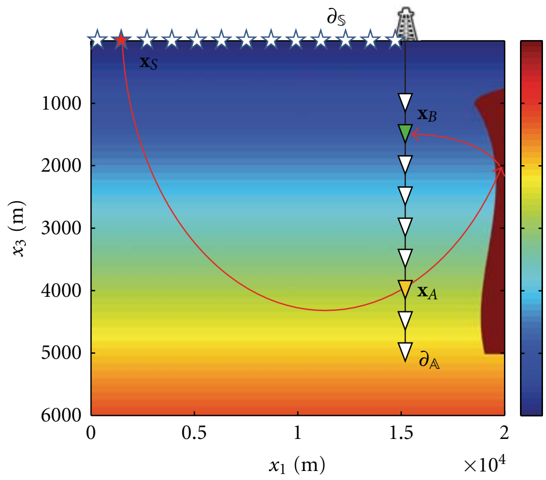

FIGURE 19: Velocity model for the salt flank imaging example. Sources are located at boundary $\partial\mathbb{S}$, covering $x_1 \in [0\,\text{m}, 12000\,\text{m}]$ at $x_3 = 0\,\text{m}$; receivers are located at boundary $\partial\mathbb{A}$, covering $x_3 \in [1000\,\text{m}, 5000\,\text{m}]$ at $x_1 = 15000\,\text{m}$; a reference virtual source is located at $\mathbf{x}_A = (15000\,\text{m}, 4000\,\text{m})$.

To compute the PSF for perturbed fields we require separation of the incident and scattered fields for each source. However, such time-gating can sometimes be problematic. Instead, an approximation of the PSF could also be obtained by time-gating the contributions around $t = 0$ in the correlation function of full fields. This PSF can provide valuable insights in spatial virtual source focusing in various types of applications. Wapenaar et al. [22], for instance, showed how an estimate of the PSF could be obtained from cross-correlations of ambient seismic noise records. These PSFs could then be used to correct Green's functions as retrieved by seismic interferometry for nonuniform passive source distributions.

Similarities exist between the derived methodology and model-driven redatuming [48]. Correlation-based interferometry can be related to correlation-based redatuming schemes such as those derived by Berryhill [49]. Multidimensional deconvolution of perturbed fields can be compared with rigorous redatuming [50]. Parallels can also be found with seismic migration and inversion [51]). The PSF that we defined for perturbed wavefields has close similarities with the resolution function in seismic inversion [52–54]. Similarly, inversion of the PSF can be compared with migration deconvolution [55] or refocusing migrated images [56]. However, in all these cases it is important to realize that having actual subsurface receivers allows us to redatum wavefields, including multiple scattered events, much more effectively than with any model-driven method.

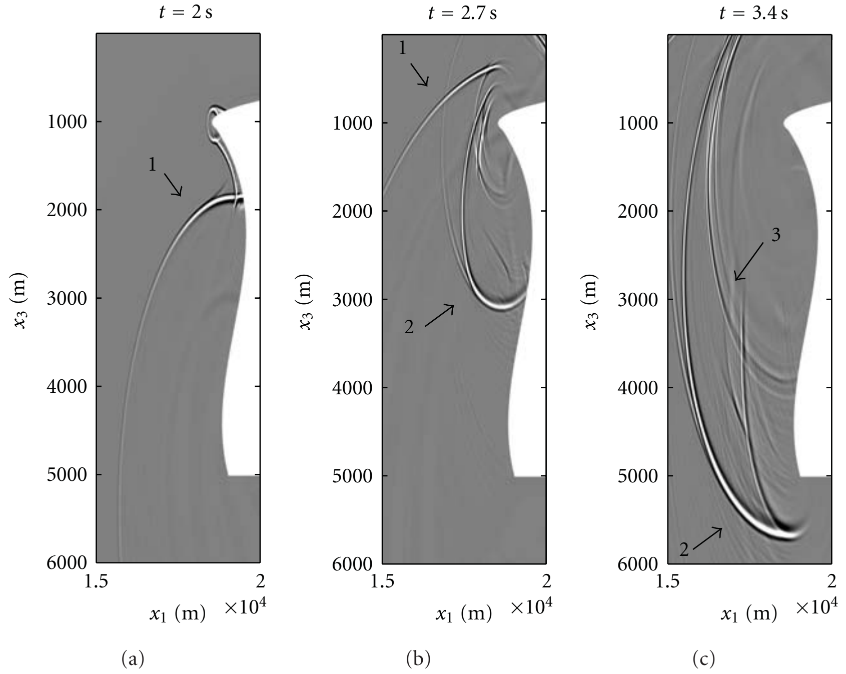

FIGURE 20: Snapshots at 2.0 s, 2.7 s and 3.4 s of the wavefield emitted by a source at $\mathbf{x}_A = (15000\,\mathrm{m}, 4000\,\mathrm{m})$; reflections 1, 2, and 3 are indicated.

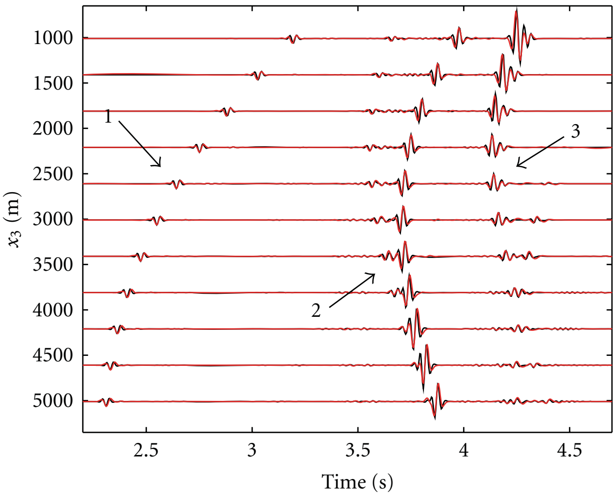

FIGURE 21: Reference response (black) and the correlation function (red) for a virtual source at $\mathbf{x}_A = (15000\,\mathrm{m}, 4000\,\mathrm{m})$; reflections 1, 2, and 3 are indicated.

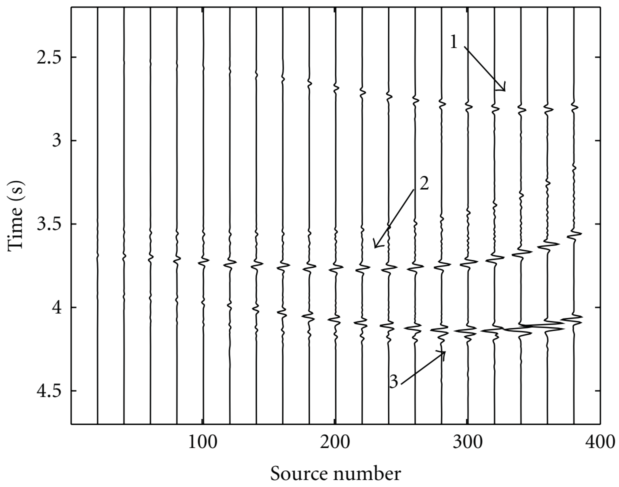

FIGURE 22: Correlation gather for a virtual source at $\mathbf{x}_A = (15000\,\mathrm{m}, 4000\,\mathrm{m})$ and a receiver at $\mathbf{x}_B = (15000\,\mathrm{m}, 2000\,\mathrm{m})$; reflections 1, 2, and 3 are indicated.

9. Conclusion

Controlled-source seismic interferometry is generally explained from cross-correlation based theory. Although this theory is exact, the required assumptions are often not fulfilled in practice. Because of one-sided illumination, complex subsurface structures, intrinsic losses, usage of single source types and free surface interactions, virtual sources can defocus and unphysical ghosts can enter the retrieved gathers. Even if all assumptions are fulfilled, particular undesired reflections from the overburden can still be retrieved by cross-correlation. Separation of incident and scattered fields or wavefield decomposition prior to cross-correlation can remove particular ghosts and multiples. Multidimensional deconvolution of perturbed (time-gated) fields allows us to refocus defocused virtual sources and remove additional ghosts and multiples. However, the method leaves particular multiples in place. To remove all multiples, multidimensional deconvolution should be applied to decomposed fields. It can be hard to

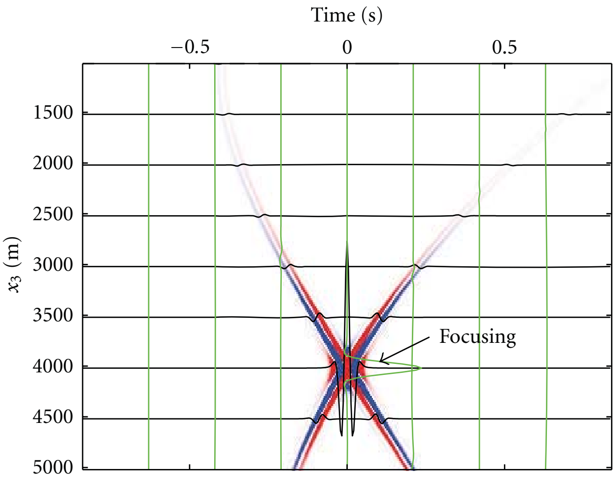

Figure 23: PSF for a virtual source at $\mathbf{x}_A = (15000\,\mathrm{m}, 4000\,\mathrm{m})$; the red-blue plot is clipped at 20% of the maximum amplitude; the black and green traces represent true-amplitude temporal and spatial traces, respectively.

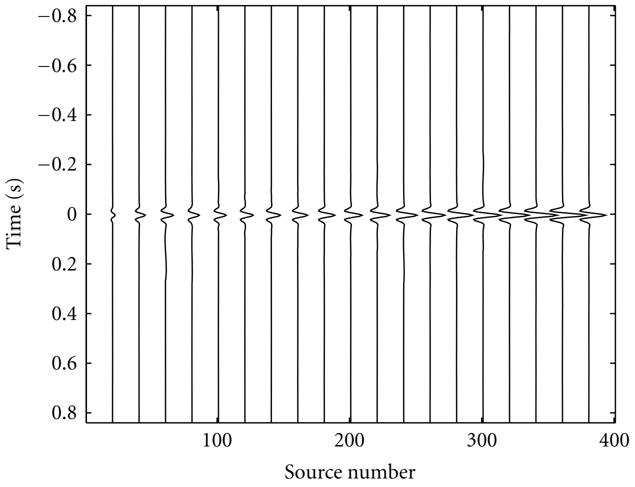

Figure 24: PSF correlation gather for receivers at $\mathbf{x}_A = (15000\,\mathrm{m}, 4000\,\mathrm{m})$ and $\mathbf{x}'_A = \mathbf{x}_A = (15000\,\mathrm{m}, 4000\,\mathrm{m})$.

stabilize the required inversion and artifacts can easily be introduced, especially if illumination conditions are limited. Through the interferometric Point Spread Function, we can diagnose illumination variations, ghosts and multiples. As this function can be obtained directly from the data, it can be a useful tool for analyzing virtual source focusing and, consequently, the quality of the retrieved data.

Appendices

A. Least-Squares Inversion

Since (30) does generally not have a unique solution, we aim to minimize a cost function instead. In least squares theory, this cost function is generally defined as [57]

$$\hat{E}(\mathbf{x}_B,\omega) = \sum_i W\left(\mathbf{x}_S^{(i)}\right)\hat{e}\left(\mathbf{x}_B,\mathbf{x}_S^{(i)},\omega\right)\hat{e}^*\left(\mathbf{x}_B,\mathbf{x}_S^{(i)},\omega\right), \quad \text{(A.1)}$$

where W is introduced as an additional weighting factor and $\hat{e}$ is the misfit between the left- and right-hand side of (30), that is

$$\hat{e}(\mathbf{x}_B,\mathbf{x}_S,\omega) = \hat{p}_{\mathrm{sc}}(\mathbf{x}_B,\mathbf{x}_S,\omega) - \int_{\partial A}\hat{G}_{\mathrm{ptb}}(\mathbf{x}_B,\mathbf{x}_A,\omega)\hat{p}_{\mathrm{inc}}(\mathbf{x}_A,\mathbf{x}_S,\omega)d\mathbf{x}_A. \quad \text{(A.2)}$$

In least-squares inversion, our goal is to minimize the cost function $\hat{E}$ at each receiver $\mathbf{x}_B$ and frequency-component ω. However, as such inversion is generally unstable, we pose an additional constraint on minimizing the solution length $\hat{L}$:

$$\hat{L}(\mathbf{x}_B,\omega) = \int_{\partial A}\hat{G}_{\mathrm{ptb}}(\mathbf{x}_B,\mathbf{x}_A,\omega)\left\{\hat{G}_{\mathrm{ptb}}(\mathbf{x}_B,\mathbf{x}_A,\omega)\right\}^* d\mathbf{x}_A. \quad \text{(A.3)}$$

Instead of minimizing $\hat{E}$, we minimize $\hat{E} + \varepsilon^2\hat{L}$, where ε determines the balance between minimizing the misfit and minimizing the solution length. Next we start to search for the solution $\hat{G}_{\mathrm{ptb}}$, obeying

$$\frac{\partial\left\{\hat{E}(\mathbf{x}_B,\omega)+\varepsilon^2\hat{L}(\mathbf{x}_B,\omega)\right\}}{\partial\hat{G}_{\mathrm{ptb}}(\mathbf{x}_B,\mathbf{x}_A,\omega)} = 0. \quad \text{(A.4)}$$

After some algebra, (A.4) can be rewritten as [57]

$$\hat{C}_{\mathrm{ptb}}(\mathbf{x}_B,\mathbf{x}'_A,\omega) = \int_{\partial A}\hat{G}_{\mathrm{ptb}}(\mathbf{x}_A,\mathbf{x}_B,\omega)\left[\hat{\Gamma}_{\mathrm{ptb}}(\mathbf{x}_A,\mathbf{x}'_A,\omega)+\varepsilon^2\delta(\mathbf{x}_A-\mathbf{x}'_A)\right]d\mathbf{x}_A, \quad \text{(A.5)}$$

where $\mathbf{x}'_A$ is at $\partial\mathbb{A}$. Quantities $\hat{C}_{\mathrm{ptb}}$ and $\hat{\Gamma}_{\mathrm{ptb}}$ are defined in (33) and (34). Inversion of (A.5) is equal to finding its least-squares inverse. By setting $\varepsilon = 0$, (A.5) is similar to (32). This result is often referred to as the normal equation. For more details, see Menke [57].

B. Time Gating

To separate incident and scattered fields, we generally rely on time-gating. Incident fields generally contain not only primaries but also multiples from the overburden. In the virtual source method of Bakulin and Calvert [4] it is advocated to cross-correlate only the direct field (instead of the full incident field) at the virtual source location with the scattered fields at the other receivers. In this appendix we study the advantage of such strategy, using the point spread function.

First, let us introduce the virtual source correlation function $\hat{C}_{\mathrm{vsm}}$ of the direct field at receiver $\mathbf{x}_A$ with the scattered field at receiver $\mathbf{x}_B$:

$$\hat{C}_{\mathrm{vsm}}(\mathbf{x}_B,\mathbf{x}_A,\omega) = \sum_i W\left(\mathbf{x}_S^{(i)}\right)\hat{p}_{\mathrm{sc}}\left(\mathbf{x}_B,\mathbf{x}_S^{(i)},\omega\right)\left\{\hat{p}_{\mathrm{dir}}\left(\mathbf{x}_A,\mathbf{x}_S^{(i)},\omega\right)\right\}^*, \quad \text{(B.1)}$$

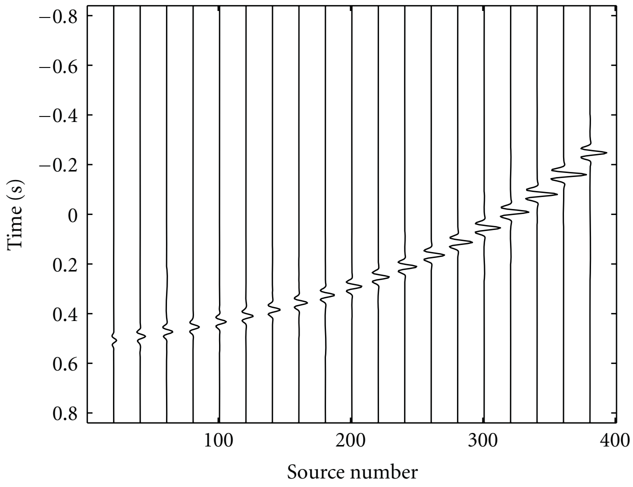

Figure 25: PSF correlation gather for receivers at $\mathbf{x}_A = (15000\,\text{m}, 4000\,\text{m})$ and $\mathbf{x}'_A = (15000\,\text{m}, 2000\,\text{m})$.

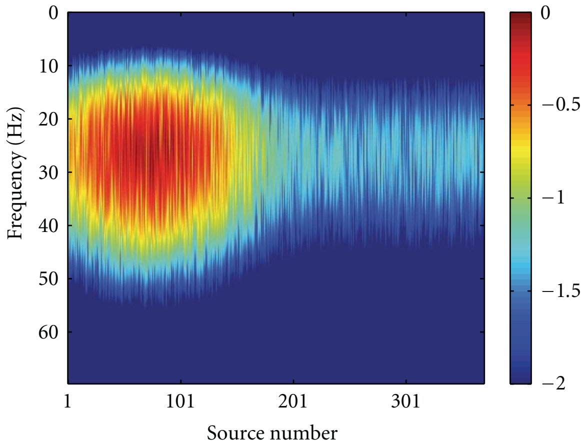

Figure 26: Source spectra to mimic varying source-side conditions (dB scale).

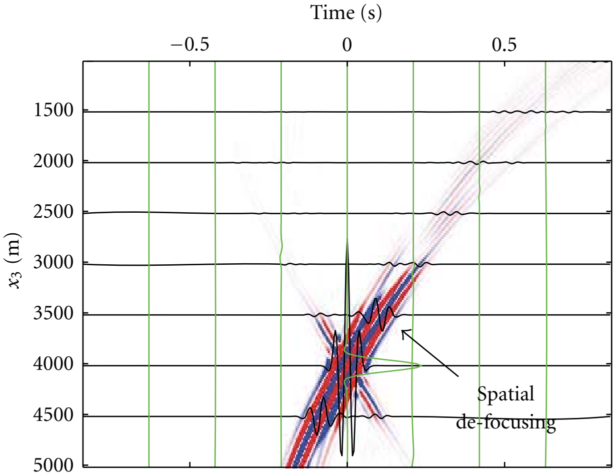

Figure 27: PSF for a virtual source at $\mathbf{x}_A = (15000\,\text{m}, 4000\,\text{m})$ for a model with varying source spectra; the red-blue plot is clipped at 20% of the maximum amplitude; the black and green traces represent true-amplitude temporal and spatial traces, respectively.

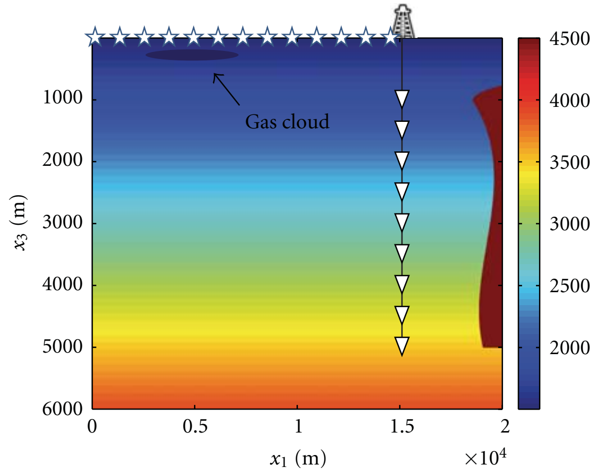

Figure 28: Velocity model for the salt flank imaging example with gas cloud.

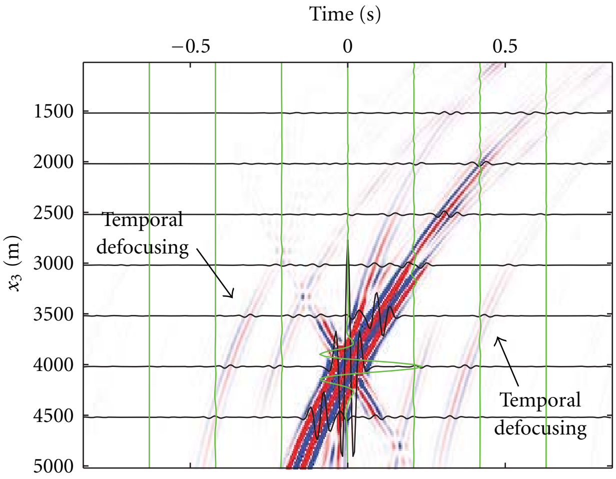

Figure 29: PSF for a virtual source at $\mathbf{x}_A = (15000\,\text{m}, 4000\,\text{m})$ for a model with varying source spectra and a gas cloud; the red-blue plot is clipped at 20% of the maximum amplitude; the black and green traces represent true-amplitude temporal and spatial traces, respectively.

where subscripts vsm and dir stand for "virtual source method" and "direct field," respectively. Obviously, the direct field does not contain the full incident field $\hat{p}_{\rm inc}$. A particular section $\Delta\hat{p}_{\rm inc}$ is not captured by the time-gate. We may substitute $\hat{p}_{\rm inc} = \hat{p}_{\rm dir} + \Delta\hat{p}_{\rm inc}$ into (30), to show that

$$\begin{aligned}&\hat{p}_{\rm sc}(\mathbf{x}_B,\mathbf{x}_S,\omega) - \Delta\hat{p}_{\rm sc}(\mathbf{x}_B,\mathbf{x}_S,\omega)\\&\quad = \int_{\partial A}\hat{G}_{\rm ptb}(\mathbf{x}_B,\mathbf{x}_A,\omega)\hat{p}_{\rm dir}(\mathbf{x}_A,\mathbf{x}_S,\omega)d\mathbf{x}_A,\end{aligned} \tag{B.2}$$

with

$$\Delta\hat{p}_{\rm sc}(\mathbf{x}_B,\mathbf{x}_S,\omega) = \int_{\partial A}\hat{G}_{\rm ptb}(\mathbf{x}_B,\mathbf{x}_A,\omega)\Delta\hat{p}_{\rm inc}(\mathbf{x}_A,\mathbf{x}_S,\omega)d\mathbf{x}_A. \tag{B.3}$$

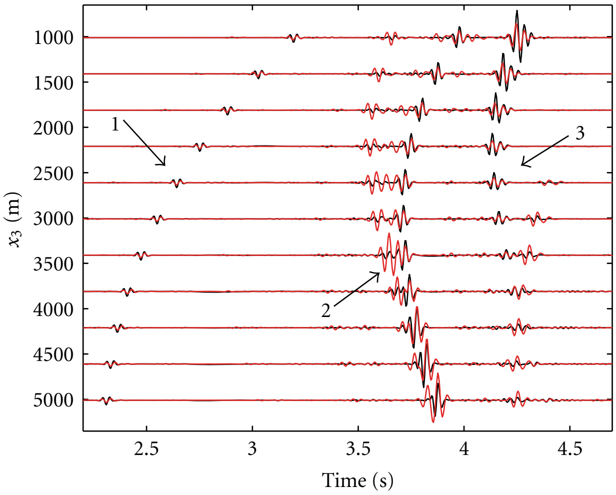

Figure 30: Reference response (black) and the correlation function (red) for a virtual source at $\mathbf{x}_A = (15000\,\text{m}, 4000\,\text{m})$ in a model with varying source spectra and a gas cloud; reflections 1, 2, and 3 are indicated.

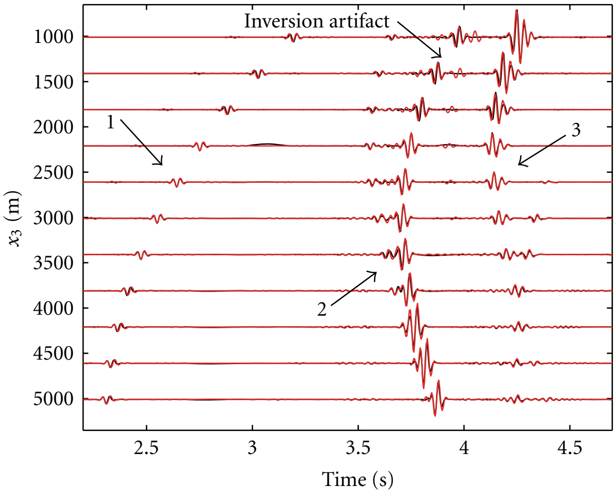

Figure 31: Reference response (black) and the retrieved response by MDD (red) for a virtual source at $\mathbf{x}_A = (15000\,\text{m}, 4000\,\text{m})$ in a model with varying source spectra and a gas cloud; reflections 1, 2, and 3 and an inversion artifact are indicated.

Equation (B.2) may be solved by MDD. With similar reasoning as expressed in Appendix A we can show that this yields the following normal equation:

$$\hat{C}_{\text{vsm}}(\mathbf{x}_B, \mathbf{x}'_A, \omega) = \int_{\partial A} \hat{G}_{\text{ptb}}(\mathbf{x}_B, \mathbf{x}_A, \omega) \hat{\Gamma}_{\text{vsm}}(\mathbf{x}_A, \mathbf{x}'_A, \omega)\, d\mathbf{x}_A + \hat{g}_{\text{vsm}}(\mathbf{x}_B, \mathbf{x}'_A, \omega), \tag{B.4}$$

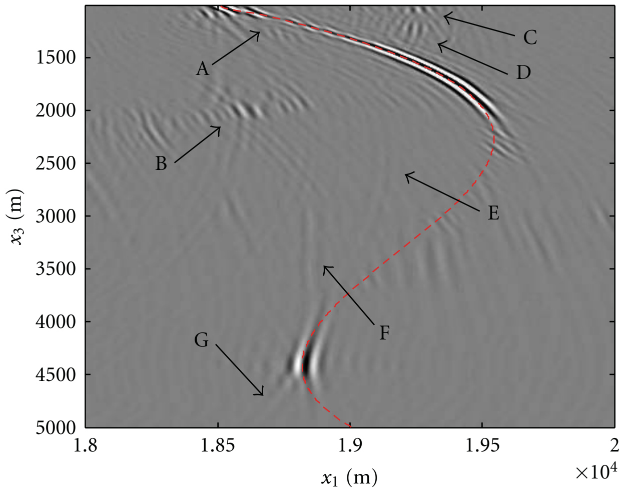

Figure 32: Migrated section of the salt flank from the CC data in a model with varying source spectra and a gas cloud; the location of the salt flank as taken from the velocity model is given by the red dashed line; markers A–G are discussed in the main text.

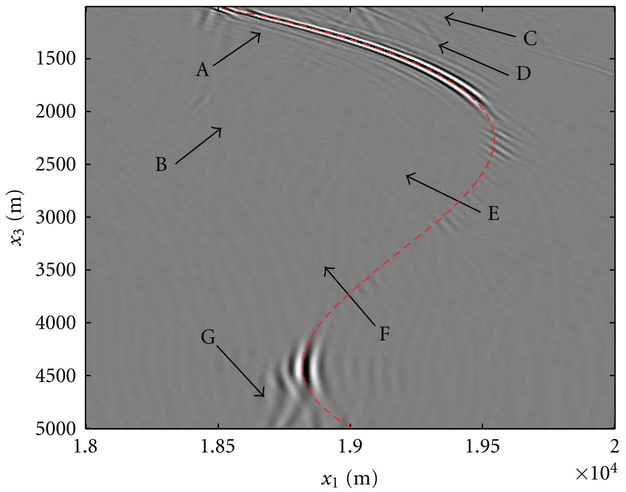

Figure 33: Migrated section of the salt flank from the MDD data in a model with varying source spectra and a gas cloud; the location of the salt flank as taken from the velocity model is given by the red dashed line; markers A–G are discussed in the main text.

where $\hat{C}_{\text{vsm}}$ is the correlation function of the virtual source method (B.1) evaluated at receiver $\mathbf{x}'_A$ instead of $\mathbf{x}_A$. $\hat{\Gamma}_{\text{vsm}}$ is the PSF of the virtual source method:

$$\hat{\Gamma}_{\text{vsm}}(\mathbf{x}'_A, \mathbf{x}_A, \omega) = \int_{\partial A} W(\mathbf{x}_S) \hat{p}_{\text{dir}}(\mathbf{x}'_A, \mathbf{x}_S, \omega) \{\hat{p}_{\text{dir}}(\mathbf{x}_A, \mathbf{x}_S, \omega)\}^* \, d\mathbf{x}_S. \tag{B.5}$$

$\hat{g}_{\mathrm{vsm}}$ is a ghost term associated with this strategy:

$$\hat{g}_{\mathrm{vsm}}(\mathbf{x}_B,\mathbf{x}_A,\omega) = -\int_{\partial A} W(\mathbf{x}_S)\Delta\hat{p}_{\mathrm{sc}}(\mathbf{x}_B,\mathbf{x}_S,\omega)\{\hat{p}_{\mathrm{dir}}(\mathbf{x}_A,\mathbf{x}_S,\omega)\}^{*} d\mathbf{x}_S. \tag{B.6}$$

With (B.4) we have shown that the response as retrieved by the virtual source method can be interpreted as the desired Green's function $\hat{G}_{\mathrm{ptb}}$ blurred by $\hat{\Gamma}_{\mathrm{vsm}}$ plus an additional ghost $\hat{g}_{\mathrm{vsm}}$. In (32) we derived that cross-correlation of the full incident field instead of the direct field yields the same Green's function blurred by $\hat{\Gamma}_{\mathrm{ptb}}$ without a ghost term. By setting the time-gate, we have thus introduced an additional ghost. However, since $\hat{\Gamma}_{\mathrm{vsm}}$ does only contain the cross-correlations of the direct field, this function behaves generally much more like the desired delta function than $\hat{\Gamma}_{\mathrm{ptb}}$. In other words: time-gating the direct field tends to focus the virtual source, which can also eliminate ghosts, multiples and blurring. A more detailed discussion on the aspects of time-gating is beyond the scope of this paper, but we refer to van der Neut and Bakulin [10] for an analysis in layered media.

Acknowledgments

This work was supported by the Dutch Technology Foundation STW, applied science division of NWO and the Technology Program of the Ministry of Economic Affairs. Part of this research was conducted at St Petersburg State University during a two-months stay of the first author. The authors thank Professor Boris Kashtan for hosting and for stimulating discussions at this university.

References

[1] A. Curtis, P. Gerstoft, H. Sato, R. Snieder, and K. Wapenaar, "Seismic interferometry—turning noise into signal," *Leading Edge*, vol. 25, no. 9, pp. 1082–1092, 2006.

[2] K. Wapenaar, E. Slob, R. Snieder, and A. Curtis, "Tutorial on seismic interferometry—part 2: underlying theory and new advances," *Geophysics*, vol. 75, no. 5, pp. 75A211–75A227, 2010.

[3] G. T. Schuster, *Seismic Interferometry*, Cambridge University Press, Cambridge, UK, 2009.

[4] A. Bakulin and R. Calvert, "The virtual source method: theory and case study," *Geophysics*, vol. 71, no. 4, pp. SI139–SI150, 2006.

[5] A. Derode, E. Larose, M. Tanter et al., "Recovering the Green's function from field-field correlations in an open scattering medium (L)," *Journal of the Acoustical Society of America*, vol. 113, no. 6, pp. 2973–2976, 2003.

[6] K. Wapenaar, J. Fokkema, and R. Snieder, "Retrieving the Green's function in an open system by cross correlation: a comparison of approaches (L)," *Journal of the Acoustical Society of America*, vol. 118, no. 5, pp. 2783–2786, 2005.

[7] E. C. Slob and K. Wapenaar, "Electromagnetic Green's functions retrieval by cross-correlation and cross-convolution in media with losses," *Geophysical Research Letters*, vol. 34, no. 5, Article ID L05307, 2007.

[8] F. Poletto and K. Wapenaar, "Virtual reflector representation theorem (acoustic medium)," *Journal of the Acoustical Society of America*, vol. 125, no. 4, pp. EL111–EL116, 2009.

[9] R. Snieder, K. Wapenaar, and K. Larner, "Spurious multiples in seismic interferometry of primaries," *Geophysics*, vol. 71, no. 4, pp. SI111–SI124, 2006.

[10] J. van der Neut and A. Bakulin, "Estimating and correcting the amplitude radiation pattern of a virtual source," *Geophysics*, vol. 74, no. 2, pp. SI27–SI36, 2009.

[11] I. Vasconcelos, R. Snieder, and H. Douma, "Representation theorems and Green's function retrieval for scattering in acoustic media," *Physical Review E*, vol. 80, no. 3, Article ID 036605, 2009.

[12] A. Bakulin, A. Mateeva, K. Mehta et al., "Virtual source applications to imaging and reservoir monitoring," *Leading Edge*, vol. 26, no. 6, pp. 732–740, 2007.

[13] K. Mehta, A. Bakulin, J. Sheiman, R. Calvert, and R. Snieder, "Improving the virtual source method by wavefield separation," *Geophysics*, vol. 72, no. 4, pp. V79–V86, 2007.

[14] I. Vasconcelos, R. Snieder, and B. Hornby, "Imaging internal multiples from subsalt VSP data—examples of target-oriented interferometry," *Geophysics*, vol. 73, no. 4, pp. S157–S168, 2008.

[15] R. Snieder, J. Sheiman, and R. Calvert, "Equivalence of the virtual-source method and wave-field deconvolution in seismic interferometry," *Physical Review E*, vol. 73, no. 6, Article ID 066620, 2006.

[16] D. C. Riley and J. F. Claerbout, "2-D multiple reflections," *Geophysics*, vol. 41, pp. 592–620, 1976.

[17] D. Loewenthal and E. A. Robinson, "On unified dual fields and Einstein deconvolution," *Geophysics*, vol. 65, no. 1, pp. 293–303, 2000.

[18] F. Poletto, M. Malusa, F. Miranda, and U. Tinivella, "Seismic-while-drilling by using dual sensors in drill strings," *Geophysics*, vol. 69, no. 5, pp. 1261–1271, 2004.

[19] F. Poletto and L. Petronio, "Seismic interferometry with a TBM source of transmitted and reflected waves," *Geophysics*, vol. 71, no. 4, pp. SI85–SI93, 2006.

[20] I. Vasconcelos and R. Snieder, "Interferometry by deconvolution—part 2: theory for elastic waves and application to drill-bit seismic imaging," *Geophysics*, vol. 73, no. 3, pp. S129–S141, 2008.

[21] I. Vasconcelos and R. Snieder, "Interferometry by deconvolution—part 1: theory for acoustic waves and numerical examples," *Geophysics*, vol. 73, no. 3, pp. S115–S128, 2008.

[22] K. Wapenaar, J. van der Neut, E. Ruigrok et al., "Seismic interferometry by crosscorrelation and by multi-dimensional deconvolution: a systematic comparison," *Geophysical Journal International*, vol. 185, pp. 1335–1364, 2001.

[23] L. Amundsen, L. T. Ikelle, and L. E. Berg, "Multidimensional signature deconvolution and free-surface multiple elimination of marine multicomponent ocean-bottom seismic data," *Geophysics*, vol. 66, no. 5, pp. 1594–1604, 2001.

[24] E. Holvik and L. Amundsen, "Elimination of the overburden response from multicomponent source and receiver seismic data, with source designature and decomposition into PP-, PS-, and SS-wave responses," *Geophysics*, vol. 70, no. 2, pp. S43–S59, 2005.

[25] J. van der Neut, K. Mehta, J. Thorbecke, E. Slob, and K. Wapenaar, "Controlled-source interferometric redatuming by cross-correlation and multi-dimensional deconvolution in elastic media," *Geophysics*, vol. 76, no. 4, pp. SA63–SA76, 2011.

[26] S. Minato, T. Matsuoka, T. Tsuji, D. Draganov, J. Hunziker, and K. Wapenaar, "Seismic interferometry using multidimensional deconvolution and crosscorrelation for crosswell seismic reflection data without borehole sources," *Geophysics*, vol. 76, no. 1, pp. SA19–SA34, 2011.

[27] E. Slob, "Interferometry by deconvolution of multicomponent multioffset GPR data," *IEEE Transactions on Geoscience and Remote Sensing*, vol. 47, no. 3, Article ID 4773210, pp. 828–838, 2009.

[28] J. Hunziker, E. C. Slob, and K. Wapenaar, "Controlled source electromagnetic interferometry by multidimensional deconvolution—spatial sampling aspects," in *Proceedings of the 71st Annual International Conference & Technical Exhibition*, vol. P074, EAGE, Extended Abstracts, 2009.

[29] Y. Fan, R. Snieder, and J. Singer, "3-D controlled source electromagnetic (CSEM) interferometry by multi-dimensional deconvolution," in *Proceedings of the 79th Annual International Meeting*, vol. 28, pp. 779–783, SEG Expanded Abstracts, 2009.

[30] E. Ruigrok, J. van der Neut, H. Djikpesse, C. Chen, and K. Wapenaar, "A feasibility study for the application of seismic interferometry by multi-dimensional deconvolution for lithosperic-scale imaging," *EGU General Assembly, Geophysical Research Abstracts*, vol. 12, p. EGU2010-9370, 2010.

[31] X. Xiao, M. Zhou, and G. T. Schuster, "Salt-flank delineation by interferometric imaging of transmitted P- to S-waves," *Geophysics*, vol. 71, no. 4, pp. SI197–SI207, 2006.

[32] B. E. Hornby and J. Yu, "Interferometric imaging of a salt flank using walkaway VSP data," *Leading Edge*, vol. 26, no. 6, pp. 760–763, 2007.

[33] R. Lu, M. Willis, X. Campman, J. Ajo-Franklin, and M. N. Toksöz, "Redatuming through a salt canopy and target-oriented salt-flank imaging," *Geophysics*, vol. 73, no. 3, pp. S63–S71, 2008.

[34] J. Ferrandis, A. Mateeva, P. Jorgensen, J. Lopez, and H. Dijkerman, "Application of virtual-source technology to the Zuidwending gas storage project," *The Leading Edge*, vol. 28, pp. 296–301, 2009.

[35] F. Poletto, L. Petronio, and F. Miranda, "Seismic interferometry in a crosshole-RVSP experiment," in *69th European Association of Geoscientists and Engineers Conference and Exhibition 2007 - "Securing The Future"*, pp. 169–173, gbr, June 2007.

[36] K. Mehta, D. Kiyashchenko, P. Jorgensen, J. Lopez, J. Ferrandis, and M. Costello, "Virtual source method applied to crosswell and horizontal well geometries," *Leading Edge*, vol. 29, no. 6, pp. 712–723, 2010.

[37] J. Byun, J. Yu, and S. J. Seol, "Crosswell monitoring using virtual sources and horizontal wells," *Geophysics*, vol. 75, no. 3, pp. SA37–SA43, 2010.

[38] K. Wapenaar and J. Fokkema, "Green's function representations for seismic interferometry," *Geophysics*, vol. 71, no. 4, pp. SI33–SI46, 2006.

[39] K. Mehta, R. Snieder, R. Calvert, and J. Sheiman, "Acquisition geometry requirements for generating virtual-source data," *Leading Edge*, vol. 27, no. 5, pp. 620–629, 2008.

[40] D. Draganov, K. Wapenaar, and J. Thorbecke, "Passive seismic imaging in the presence of white noise sources," *Leading Edge*, vol. 23, no. 9, pp. 889–892, 2004.

[41] J. T. Fokkema and P. M. van den Berg, *Seismic Applications of Acoustic Reciprocity*, Elsevier, Amsterdam, The Netherlands, 1993.

[42] K. Wapenaar, "Green's function retrieval by cross-correlation in case of one-sided illumination," *Geophysical Research Letters*, vol. 33, no. 19, Article ID L19304, 2006.

[43] C. P. A. Wapenaar, P. Herrmann, D. J. Verschuur, and A. J. Berkhout, "Decomposition of multicomponent seismic data into primary P- and S- wave responses," *Geophysical Prospecting*, vol. 38, no. 6, pp. 633–661, 1990.

[44] L. Amundsen and A. Reitan, "Decomposition of multicomponent sea-floor data into upgoing and downgoing P- and S-waves," *Geophysics*, vol. 60, no. 2, pp. 563–572, 1995.

[45] F. J. Barr, "Dual-sensor OBC technology," *Leading Edge*, vol. 16, no. 1, pp. 45–51, 1997.

[46] L. Petronio and F. Poletto, "Dual signals separation in shallow borehole hydrophone data," in *Proceedings of the 72nd EAGE Conference & Exhibition*, vol. F033, Extended Abstracts, 2010.

[47] J. van der Neut and J. Thorbecke, "Resolution function for controlled-source seismic interferometry: a data-driven diagnosis," in *Proceedings of the 79th International Meeting Society of Exploration Geophysicists*, vol. 28, pp. 4090–4094, Expanded Abstracts, 2009.

[48] G. T. Schuster and M. Zhou, "A theoretical overview of model-based and correlation-based redatuming methods," *Geophysics*, vol. 71, no. 4, pp. SI103–SI110, 2006.

[49] J. R. Berryhill, "Wave-equation datuming," *Geophysics*, vol. 44, no. 8, pp. 1329–1344, 1979.

[50] W. A. Mulder, "Rigorous redatuming," *Geophysical Journal International*, vol. 161, no. 2, pp. 401–415, 2005.

[51] J. Thorbecke and K. Wapenaar, "On the relation between seismic interferometry and the migration resolution function," *Geophysics*, vol. 72, no. 6, pp. T61–T66, 2007.

[52] G. T. Schuster and J. Hu, "Green's function for migration: continuous recording geometry," *Geophysics*, vol. 65, no. 1, pp. 167–175, 2000.

[53] G. Toxopeus, J. Thorbecke, K. Wapenaar, S. Petersen, E. Slob, and J. Fokkema, "Simulating migrated and inverted seismic data by filtering a geologic model," *Geophysics*, vol. 73, no. 2, pp. T1–T10, 2008.

[54] E. J. van Veldhuizen, G. Blacquière, and A. J. Berkhout, "Acquisition geometry analysis in complex 3D media," *Geophysics*, vol. 73, no. 5, pp. Q43–Q58, 2008.

[55] J. Yu, J. Hu, G. T. Schuster, and R. Estill, "Prestack migration deconvolution," *Geophysics*, vol. 71, no. 2, pp. S53–S62, 2006.

[56] C. Zhang and T. J. Ulrych, "Refocusing migrated seismic images in absorptive media," *Geophysics*, vol. 75, no. 3, pp. S103–S110, 2010.

[57] W. Menke, *Geophysical Data Analysis*, Academic Press, San Diego, Calif, USA, 1989.

Hindawi Publishing Corporation
International Journal of Geophysics
Volume 2011, Article ID 530728, 9 pages
doi:10.1155/2011/530728

Review Article

Measuring and Modeling of P- and S-Wave Velocities on Crustal Rocks: A Key for the Interpretation of Seismic Reflection and Refraction Data

Hartmut Kern

Institut für Geowissenschaften, Universität Kiel, 24098 Kiel, Germany

Correspondence should be addressed to Hartmut Kern, kern@min.uni-kiel.de

Received 7 January 2011; Accepted 20 February 2011

Academic Editor: Yu Zhang

Lithologic interpretations of the earth crust from seismic wave velocities are non-unique so that inferences about composition can not be drawn. In order to evaluate how elastic properties of rock materials are controlled by lithology at in situ pressures and temperatures, compressional (Vp), shear wave velocities (Vs) and velocity anisotropy of crustal rocks were measured at conditions of greater depth. The first part deals with the interdependence of elastic wave propagation and the physical and lithological parameters. In the second part data from laboratory seismic measurements and theoretical calculations are used to interpret (1) a shallow seismic reflection line (SE Finland) and (2) a refraction profile of a deep crust (Central China). The comparison of the calculated velocities with the experimentally-derived in situ velocities of the Finnish crustal rocks give hints that microcracks have an important bearing on the in situ seismic velocities, velocity anisotropy and the reflectivity observed at relative shallow depth. The coupling of the experimentally-derived in situ velocities of P- and S-wave and corresponding Poisson's ratios of relevant exhumed high-grade metamorphic crustal rocks from Central China with respective data from seismic refraction profiling provided a key for the lithologic interpretation of a deep seismic crustal structure.

1. Introduction

Investigation of the structure and composition of the earth's crust and upper mantle is a big challenge in Earth Sciences. Direct information about the structure and composition of the deep crust can be obtained either from crustal terrains exposed at the surface (e.g., [1, 2]) or from xenoliths brought to the surface by magmas (e.g., [3]). Deeply eroded Precambrian terrains (e.g., Srilanka), and upthrust tectonic slices in orogenic belts (e.g., Ivrea Zone, N. Italy; Serre Mountains, S. Calabria; Kapuskasing Zone, Canada) provide perhaps the best geologic guides to structural style and composition at depth. Such rocks are important in providing direct data although they contain a mixed message as they are no longer the in situ deep crust.

Indirect information about the structure and composition of the inaccessible deep crust (and upper mantle) is obtained by geophysical surveys. Most important is seismic reflection and refraction profiling, and both techniques have been successfully used (independently or in combination with data from electrical, gravity, and magnetic investigations) to probe the deep crust and upper mantle. Seismic reflection patterns provide a structural image of the crust, and seismic refraction profiles give us information about the velocity distribution within the crust. The measured seismic velocity structures are very helpful in providing a rough characterization of the earth's crust in different tectonic environments, but they are nonunique so that inferences about composition cannot be drawn from wave velocities (at least P-wave velocities). Even in case that we can directly correlate various lithologies with, for example, sonic log or VSP data (Kola superdeep borehole, Russia; KTB, Germany), a basic question to be answered remains: why are the in situ properties as they are, and which factors control the in situ rock properties? The basic reason for this ambiguity is that crustal and mantle rocks are very complex materials and that their seismic properties at depth are affected in a very complex manner by a number of lithologic and physical factors. P- and S-wave velocities are controlled by the matrix (intrinsic) properties of the rocks

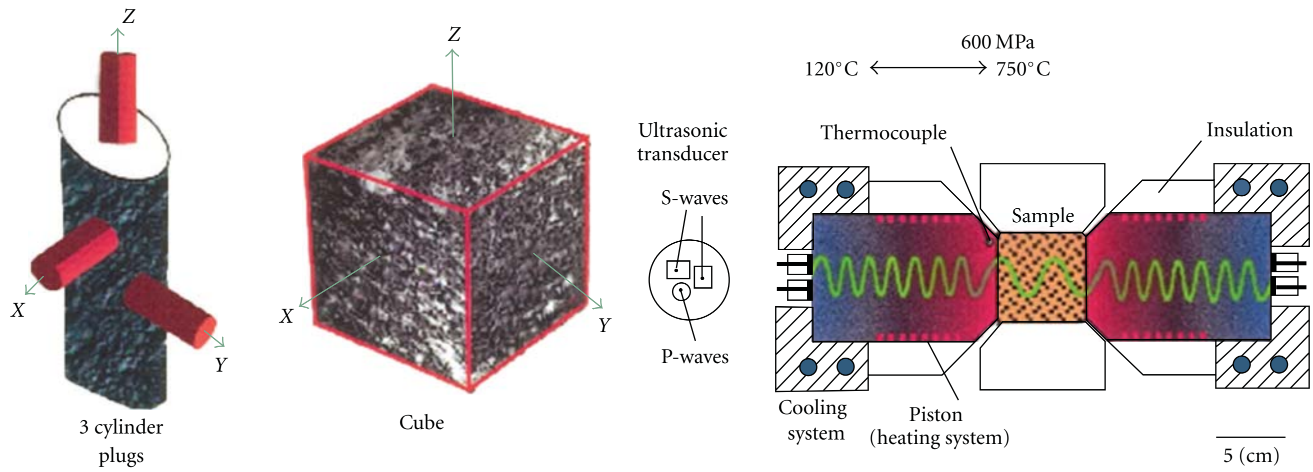

(a) (b)

Figure 1: Commonly used sample geometries for laboratory seismic measurements (a) and the piston-sample-transducer arrangement in a multianvil pressure apparatus (b).

(mineral mode, chemical composition, metamorphic grade, and crystallographic preferred orientation of constituent minerals) and by the physical environment of the crust (temperature, pressure, porosity, fluid content, etc.).

A unique ability to correlate the seismic data with the structure and composition of the in situ deep crust can be provided by coupling experimentally determined or calculated P- and S-wave velocities for relevant crustal rocks collected from surface outcrops or from xenoliths, simulating in situ conditions: (1) by laboratory seismic measurements at actual PT conditions (e.g., [4, 5]) and (2) by calculations from modal analyses and elastic properties of the rock-forming minerals and their pressure and temperature derivatives (e.g., [6]).

In the first part of this paper, we will show, as an example, how the seismic properties of a crustal rock are affected by pressure and temperature and analyze the relationship between velocities and structural and textural characteristics of the rock. We will focus on the directional dependence (anisotropy) of P- and S-wave velocities at PT conditions. In the second part, we will interpret seismic field data on the basis of measured and calculated velocities derived from relevant crustal rocks for two case studies: Firstly, we will investigate the nature of seismic reflections within the 2500 m crustal section penetrated by the Outokumpu scientific drill hole (SE Finland), and secondly, we will give a lithologic interpretation for a seismic refraction profile crossing the ultrahigh pressure (UHP) metamorphic belt of the Dabie mountains (China). (for details, see [7] and [5], resp.).

2. Laboratory Measurements of P- and S-Wave Velocities

Two sample geometries are commonly used for the experimental determination of elastic wave velocities and their directional dependence (anisotropy): (1) jacketed cylindrical samples in an internally heated fluid or gas apparatus (Figure 1(a), left) and (2) unjacketed cube-shaped specimens in an externally heated multianvil apparatus (Figure 1(a), right). On cylindrical samples, Vp and Vs measurements can be done only in one direction so that experiments on three sample cylinders taken in the three structural-related orthogonal directions are needed for the determination of velocity anisotropy. On cube-shaped samples, measurements of Vp and Vs can be done simultaneously in three orthogonal directions. In general, measurements are carried out in the *X, Y,* and *Z* directions of the foliation-related structural frame (*XY* is foliation, *X* is lineation and *Z* is foliation normal).

In our lab, measurements of P- and S-wave velocities are made on sample cubes (43 mm on edges) in a multianvil apparatus using the pulse transmission technique with transducers operating at 2 and 1 MHz for P- and S-waves, respectively. As illustrated in Figure 1(b), the piston-sample-transducer arrangement allows simultaneous measurements of Vp and Vs and their directional dependence (velocity anisotropy) in the *X, Y,* and *Z* directions of the sample cube as a function of pressure (up to 600 MPa) and temperature (up to 700°C) and direct determination of length changes (volume change) from the piston displacement. Shear wave splitting (Vs1-Vs2) is measured by two sets of orthogonally polarized transducers with perpendicular polarization directions. A complete set of measured data comprises three P-wave velocities and six S-wave velocities along with the length changes (volume change) of the sample. A full description of the apparatus is given in [8].

To illustrate the effect of pressure and temperature on elastic wave velocities, Figure 2 presents experimental data for a biotite gneiss (OKU 578) from the Outokumpu scientific deep drill hole (see Section 3). The biotite gneiss sample is recovered from 578 m depth and made up by 34.1 vol.-% quartz, 19.9 vol.-% plagioclase, 28.4 vol.-% biotite and 16.7 vol.-% muscovite. The modal compositions of all rock samples were calculated from bulk rock (X-ray fluorescence

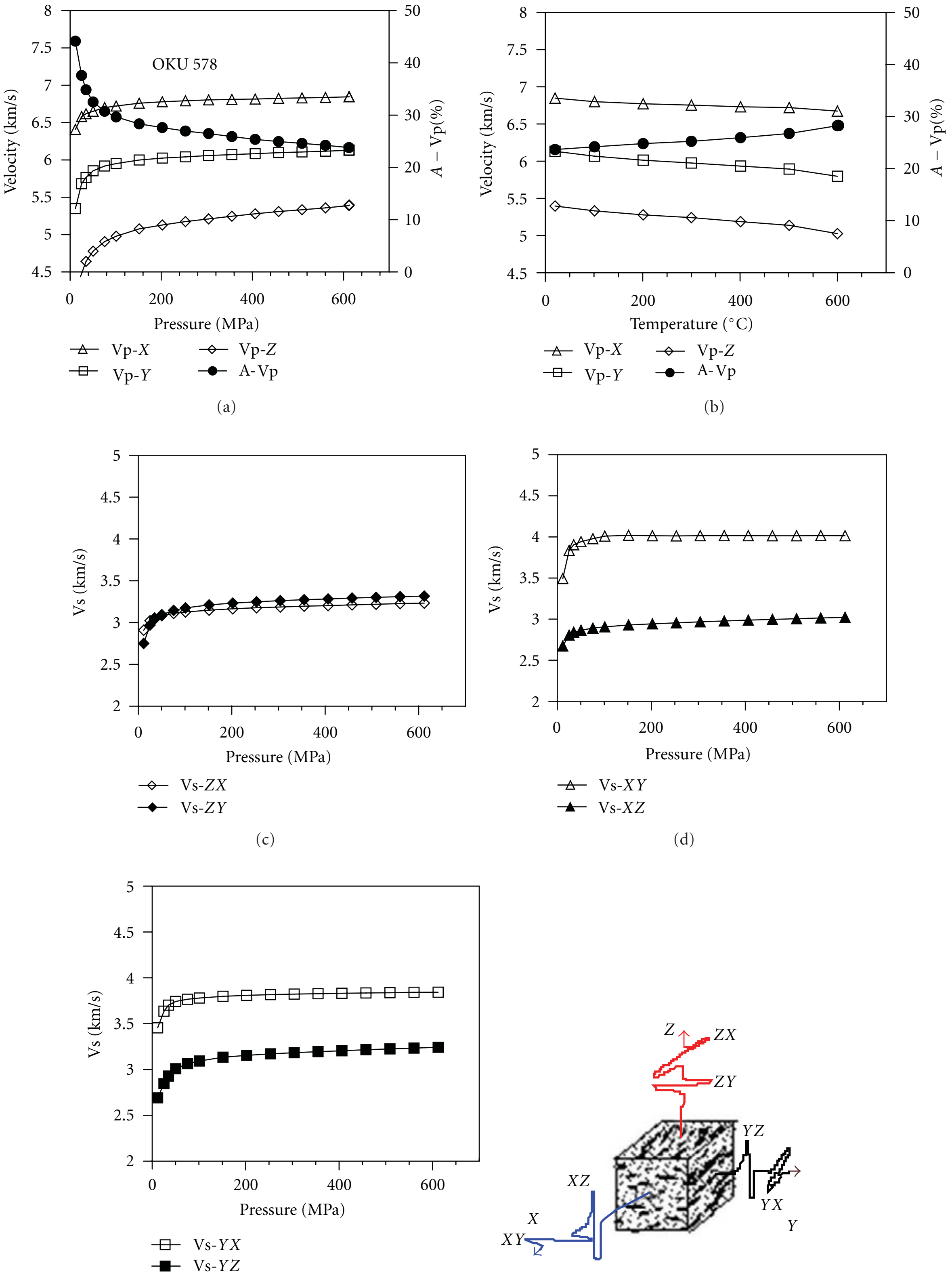

(a) (b)

(c) (d)

(e) (f)

Figure 2: P- and S-wave velocities as a function of pressure up to 600 MPa (room temperature) (Figure (a), (c)–(e), resp.) of a biotite gneiss (OKU 578) from Outokumpu, along with the temperature dependence of P-wave velocities measured at 600 MPa confining pressure (b). (f) illustrates the measuring directions of P- and S-wave velocities and shear wave polarization according the foliation-related structural frame *X*, *Y*, and *Z* (*XY* is foliation, *X* is lineation, and *Z* is foliation normal).

analysis, XRF) and mineral chemistry (microprobe), using least square fitting [7, 9].

Compressional and shear wave velocities measured in *X, Y,* and *Z* as a function of pressure (up to 600 MPa) at room temperature, along with the corresponding velocity anisotropy of P-waves (A-Vp) are plotted in Figure 2(a) and Figures 2(c)–2(e). P- and S-wave velocities are denoted by Vp_i and Vs_{ij}, respectively. The first subscript i of Vp and Vs indicates the propagation direction, and the second subscript j of Vs_i indicates the polarization direction of the shear wave (Figure 2(f)). Anisotropy is defined by the percent differences between maximum and minimum velocity with respect to mean velocity [10].

At increasing confining pressure, P- and S-wave velocities show a nonlinear increase approaching linear behaviour above about 200 MPa. The nonlinear rise on the curves is due to progressive closure of microcracks, typically illustrating the pressure sensitivity of P- and S-wave velocities. The velocities defining the nonlinear parts of the velocity versus. pressure curves (Figure 2(a)) can be used to interpret seismic data at shallow crustal depth (see Section 3). The linear lopes of the curves reflect the intrinsic rock properties. They are basically controlled by the volume percentage of major minerals, their single crystal elastic properties and their crystallographic preferred orientation (CPO). Increase of temperature at the high confining pressure of 600 MPa that prevents thermal cracking results in slight linear decrease in wave velocities (Figure 2(b)). From the regression of the linear parts of the pressure (200–600 MPa) and temperature curves (20°C–600°C) one can derive the intrinsic pressure and temperature derivatives of velocities and the reference velocity $\mathrm{V}_{0,}$which is the projected velocity of a nonporous or crack-free compacted rock at zero pressure. These data allow one to extrapolate seismic velocities to greater depth (where cracks are closed) for any P/T condition within the stability field of the constituent assemblage of rock-forming minerals (see Section 4).

The significant differences of P-wave velocities measured in the three structural directions *X, Y,* and *Z* of the Outokumpu biotite gneiss (OKU 578) indicate strong velocity anisotropy (Figure 2(a)). Anisotropy is typical for most of the rocks constituting the earth's crust (e.g., [11–13]). Highest velocities are generally measured parallel to foliation (*XY*-plane) and lineation [X] and lowest normal to foliation. Anisotropy (A-Vp) is almost highest at low pressure (Figure 2(a)) due to the effects resulting from oriented microcracks and crystallographic preferred orientation of the rock-forming minerals. Increasing pressure reduces the effect of cracks and the residual (intrinsic) anisotropy is mainly due to CPO (e.g., [14, 15]). Splitting of the two orthogonally polarized shear waves (S1 and S2) is an important diagnostic phenomenon for seismic anisotropy [16]. It is closely related to the structural frame (Figures 2(c)–2(e). Pronounced shear wave splitting is generally observed parallel to *X* and *Y* within the foliation plane with the fast split shear wave being polarized parallel to foliation. Normal to foliation, shear wave splitting is generally low. Note that in the Outokumpu biotite gneiss (OKU 578), there is practically no shear wave splitting observed normal to foliation (Figure 2(c)). This direction marks a singularity [16]; that is, S-waves propagate in this direction like in an isotropic medium.

Anisotropy of P- and S-wave velocities as well as shear wave splitting of the biotite gneiss (OKU 578) is mainly due to the high volume proportions of biotite and muscovite (about 28 vol.-% and 17 vol.-% resp.), their strong CPO and the very high anisotropy of both minerals (>40%). It should be noted that shape preferred orientation (SPO) of biotite and muscovite as well as oriented microcracks may also contribute to bulk anisotropy [17–19].

The experimentally derived relations between P- and S-wave wave propagation and shear wave polarization to the structural frame (foliation, lineation) are confirmed by 3D velocity calculations based on the preferred orientation (CPO) of the constituent minerals, their volume fraction, the crystal densities and their elastic stiffness coefficients [7, 17].

3. The Nature of Seismic Reflections Observed within a Crustal Section at Shallow Depth

Here, we use calculated and experimental velocity data of crustal rocks sampled by the Outokumpu deep drill hole (SE, Finland) for an interpretation of sonic log data and of crustal reflections observed on a high resolution reflection profile (OKU-1) close to the bore hole (Figures 3(a) and 3(b)).

The high-resolution seismic line (OKU-1) in SE, Finland, (Figure 3(c)) has revealed a high reflectivity zone between about 1300 m–1500 m depth [20]. The line is close to the Outokumpu scientific drill hole which has sampled a 2500 m crustal section within Paleoproterozoic metasedimentary and ophiolitic sequences [21]. The drilled Precambrian crustal section comprises a 1300 m thick biotite gneiss series at top, followed by a 200 m thick metaophiolite sequence, underlain again by a 500 m thick biotite gneiss sequence with intercalations of amphibolite and pegmatitic granite. From 2000 m downward the dominant rock types are pegmatitic granites (see Figure 4, left).

We selected 29 core samples covering the depth range 198 m–2491 m for petrophysical studies [7, 17], in order to interpret sonic log data and to provide constraints on the nature of the reflectivity zone revealed by the high resolution reflection line. For all samples, we calculated the average (isotropic) intrinsic P- and S-wave velocities by combining the modal composition of the rocks with the respective velocities of the isotropic monomineralic aggregates (VRH averages) of the constituent minerals [22]. On 13 oven-dried (80°C) cube-shaped samples representing main lithologies, we measured P- and S-wave velocities in 3 orthogonal directions at pressures up to 600 MPa in order to determine their cracks sensitivity and directional dependence. Velocity measurements as well as 3D velocity calculations, based on neutron diffraction CPO measurements [7, 17], show that velocity anisotropy and shear wave splitting are important properties of the biotite gneisses that dominate about 70% of the drilled crustal section. In Figure 4 (left), we compare the calculated velocities and the experimentally derived in situ velocities with sonic log data. It is clear from the diagram that the calculated intrinsic velocities (red symbols) are generally higher than those determined by the sonic

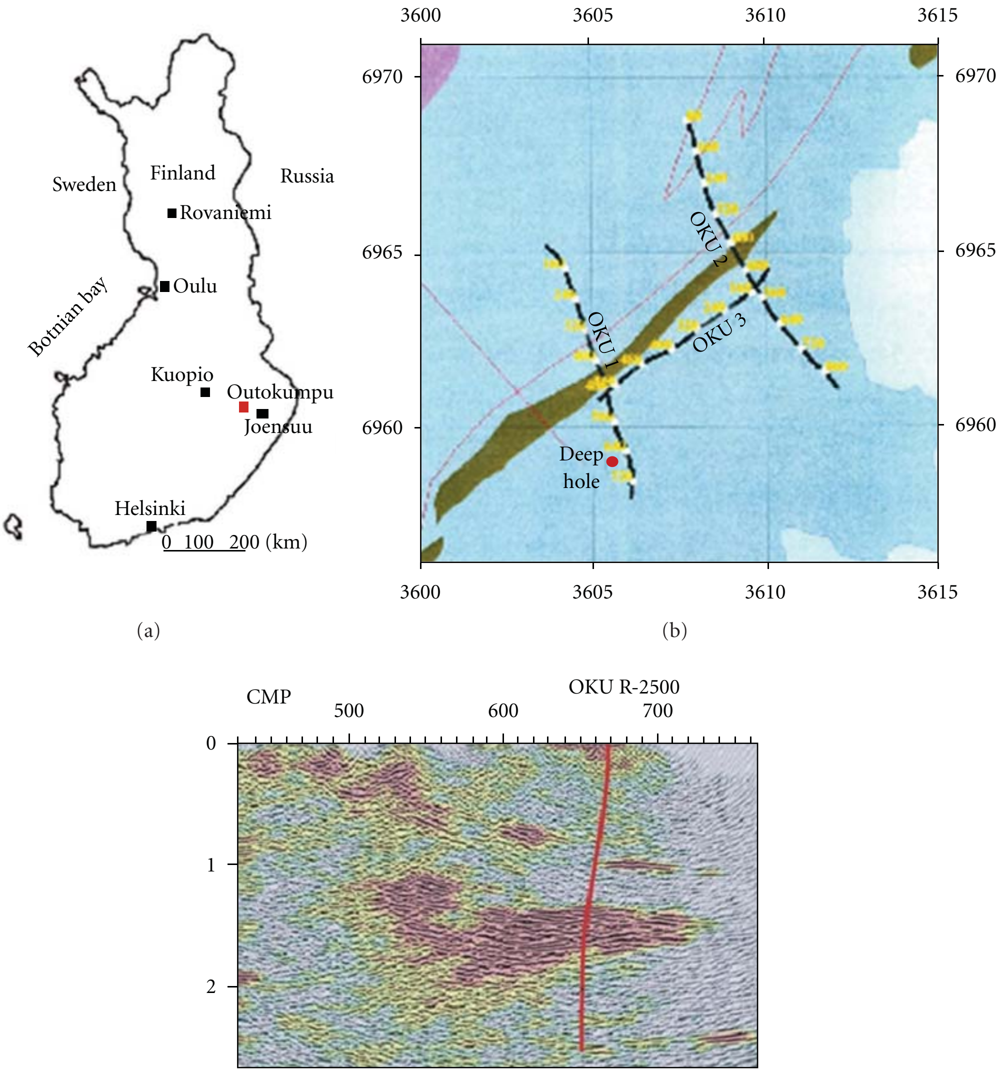

(a)

(b)

(c)

Figure 3: Location of the Outokumpu scientific drill hole (a), along with high-resolution reflection lines (b) and the end of the migrated OKU-1 section at Outokumpu (c) (after Heikkinen et al. [20] and Kukkonen et al. [21] resp.).

log, whereas the experimentally derived in situ data (green symbols) fit markedly better. Therefore, we conclude that microcracks that are not completely closed at the relatively shallow depth have an important bearing on the in situ velocities in addition to the lithologic control. Importantly, the experimentally derived velocities propagating in the Z direction (black symbols), that is, normal to subnormal to foliation (parallel to the bore hole), are closest to the sonic log data. It should be noted, however, that the possible effect of pore fluids has not been taken into account.

For assessing the potential importance of the various lithologic interfaces as seismic reflectors and the role of anisotropy, we calculated from the acoustic impedances I (velocity multiplied with density) the corresponding normal incidence reflection coefficients [$R_c = (I_1 - I_2)/(I_1 + I_2)$]. Figure 4 (right) compares the reflection coefficients derived from modal mineralogy and the isotropic aggregate velocities of the constituent minerals (left vertical line) with those derived from the average velocities obtained by the laboratory seismic measurements for the in situ pressure conditions (middle vertical line). Also included is a calculation based on velocities measured normal to foliation (parallel to Z), taking into account that the foliation of the rocks constituting the 2500 m crustal section is normal to subnormal to the borhole (right vertical line). The data refer to an average density of 2.57 g/cm^3. According to Warner [23], reflection coefficients close to +/− 0.1 are required for strong seismic reflections. From the reflection coefficients R_c derived from modeled as well as from experimental in situ velocities, we conclude that the multiple reflections within the metaophiolite series (Figure 4, right) are caused by the variation in lithology. This holds, in particular, for the contacts of the diopside skarn to serpentinites and serpentinites to pyr-hbl-gneiss and phlogopite-graph-gneiss.

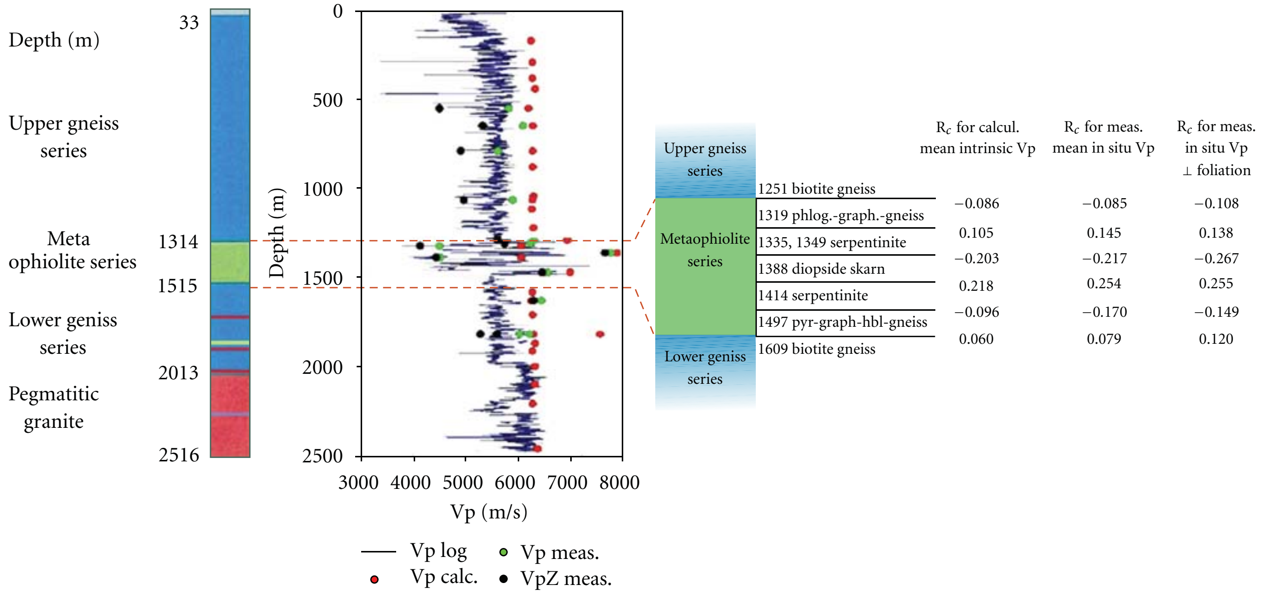

R_c for calcul. mean intrinsic Vp	R_c for meas. mean in situ Vp	R_c for meas. in situ Vp ⊥ foliation
−0.086	−0.085	−0.108
0.105	0.145	0.138
−0.203	−0.217	−0.267
0.218	0.254	0.255
−0.096	−0.170	−0.149
0.060	0.079	0.120

FIGURE 4: Comparison of sonic log data of the Outokumpu scientific drill hole with calculated intrinsic and measured in situ velocities of the investigated samples (left) along with calculated reflection coefficients (R_c) for the different lithologies (right).

From the strong directional dependence of wave propagation (slowest velocities normal to foliation; parallel to Z), we infer that reflectivity at the contacts of the upper and lower gneiss series with the metaophiolite series is significantly enhanced by effects from oriented microcracks that are not completely closed, in addition to the strong crystallographic preferred orientation (CPO) of the constituent phyllosilicates (biotite and muscovite) in the upper and lower gneiss series. From the experimental results, we infer that variations in lithology within the ophiolite-related assemblage are also responsible for the strong seismic reflections revealed by the high-resolution seismic reflection line (OKU-1) close to the borehole at the depth of 1300 m–1500 m (Figure 3(c)).

4. Lithologic Interpretation of a Crustal Seismic Velocity Structure Based on In Situ P- and S-Wave Velocities Derived from Experimental Data

We selected a seismic refraction profile crossing the Dabie Mountain (Central China) in order to document the potential of laboratory seismic measurements simulating in situ conditions for the lithologic interpretation of a seismic crustal velocity structure.

The Dabie-Sulu ultrahigh-pressure metamorphic belt (Figure 5(a)) represents a zone in which upper and lower continental crust has been subducted and then rapidly exhumed from the mantle back into the crust [24]. Seismic refraction profiles [25] reveal a four layer structure (upper, middle, upper-lower, and lowermost crust) with an average thickness of 34 km (Figure 5(b)). Experimental petrophysical investigations on about 30 UHP rock samples collected form surfaces exposures [5] provide the basis for a lithologic interpretation of the seismic velocity structure. The rock samples span compositions from felsic through intermediate to mafic, and metamorphic grades up to granulite and eclogite facies. They comprise tonalitic and trondhjemitic gneisses, metapelites, metagabbros, amphibolites, intermediate and mafic granulites, and eclogites. The experimental data include compressional (Vp) and shear wave velocities (Vs), velocity anisotropy, density, and intrinsic pressure and temperature derivatives of Vp and Vs derived from regression of the linear segments of the pressure (300–600 MPa) and temperature curves (20°C–500°C). Using a regional geotherm, velocity depth profiles were calculated for the different lithologies [5]. Because most of the cracks and fractures are closed at greater depth and the effects of cracks are thus largely eliminated, we used the intrinsic P-wave velocities together with the Poisson's ratios for a lithologic interpretation of the seismic model (Figure 5(b)) evaluated from seismic refraction data. The interpretation is based on the averages of velocities measured in the three directions X, Y, and Z, because no indications of seismic anisotropy are reflected by the seismic data. The combined measurements of P- and S-wave velocities on UHP rocks and the availability of seismic data on the P-wave velocity and the Poisson's ratio structure along a profile crossing the Dabie Mountains [25] provides valuable constraints on the composition of the crust. Figure 6 compares the ranges of experimentally derived in situ velocities and Poisson's ratios with the respective seismic refraction data (red circles). From the comparison, we infer that the seismic properties of the middle crust are in accordance with those measured on amphibolite-facies tonalitic-trondhjemitic and granitic gneisses. The upper-lower and lowermost crust may be interpreted by intermediate (or mixtures of felsic and mafic granulite) and mafic granulites, respectively. From the

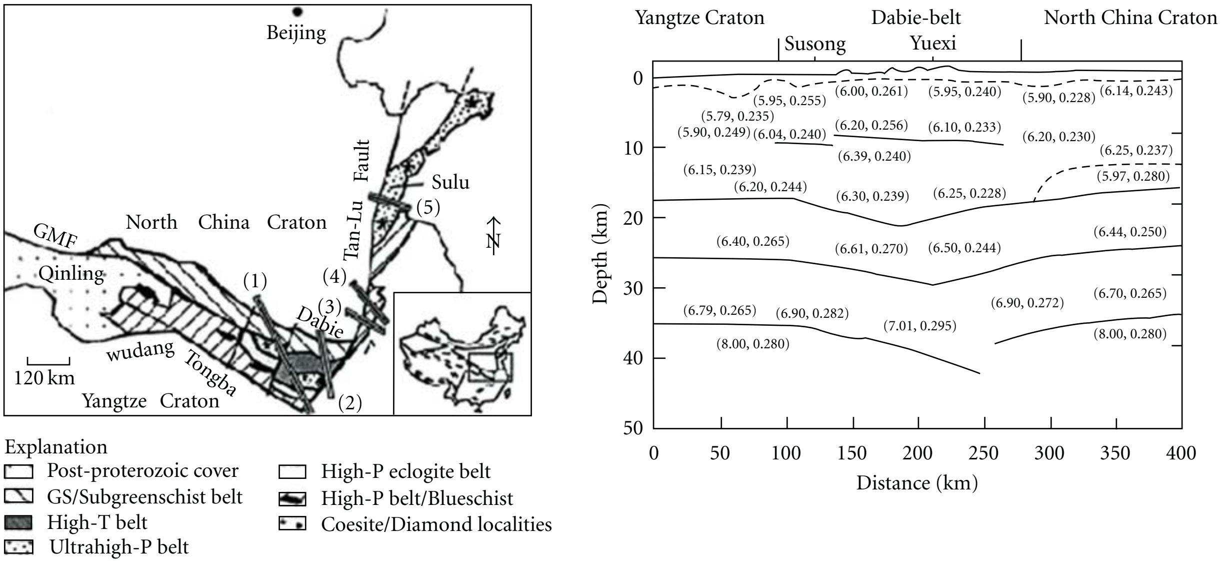

(a)

(b)

Figure 5: Regional map (a) of the Dabie-Sulu area [24] and a seismic model structure for P-wave velocities and Poisson's ratios (b) for the 34 km thick crust [25].

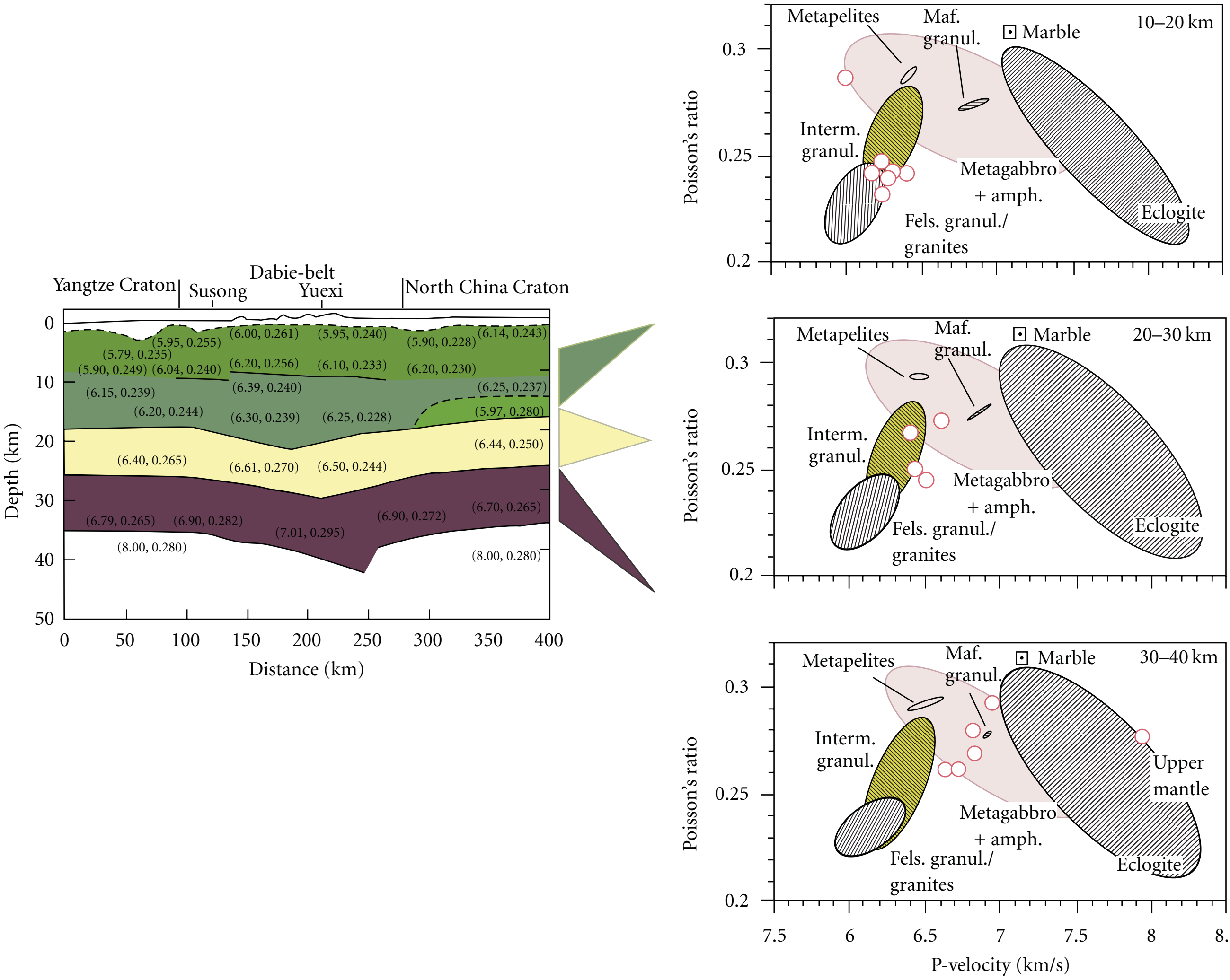

Figure 6: Comparison of ranges of experimentally derived in situ velocities and Poisson's ratios for UHP rocks for various depth of the four-layer crustal structure at Dabie [5] with respective seismic refraction data [26] (red circles).

combined Vp and Poisson's ratio data, we conclude that eclogite which is exposed in many outcrops is not a volumetrically important constituent of the deep crust in the Dabie mountains. The coupling of the laboratory-derived in situ seismic data (Vp and Poisson's ratio's) with refraction seismic data, along with evidence from geological and geochemical investigations [26], suggests that lower crustal delamination of high-density eclogitic rocks played an important role in the modification of the East China crust [5].

5. Summary

Coupling laboratory seismic measurements on crustal rocks from Outokumpu (SE, Finland) and the Dabie mountains (Central China) along with model calculations provided the basis for the following conclusions.

(1) Measured and calculated velocities of relevant rocks sampled by the Outokumpu scientific drill hole (SE Finland) show that variations of lithology within the ophiolite-related assemblage have the potential to generate the strong seismic reflections revealed by the nearby high-resolution seismic reflection line (OKU-1) at the depth of 1300 m–1500 m. Marked CPO- and crack-related seismic anisotropy of the biotite gneiss series hosting the ophiolite sequence may enhance the seismic reflections at their contacts.

(2) Correlation of in situ velocities and Poisson's ratios derived from P- and S-wave velocities measured on UHP metamorphic rocks collected from surface exposures in the Dabie mountains (Central China) with respective data of a refraction profile crossing the Dabie metamorphic belt allowed a lithologic interpretation of the velocity structure for the 34 km thick continental crust. Importantly, the comparison gives clear evidence that eclogite which is exposed in many outcrops is not a main constituent of the lowermost crust in the Dabie mountains.

Acknowledgment

The help in preparing the figures by Philip Kegler and Detlef Schulte-Kortnack is greatly appreciated.

References

[1] D. M. Fountain and M. H. Salisbury, "Exposed cross-sections through the continental crust: implications for crustal structure, petrology, and evolution," *Earth and Planetary Science Letters*, vol. 56, pp. 263–277, 1981.

[2] H. Kern and V. Schenk, "A model of velocity structure beneath Calabria, southern Italy, based on laboratory data," *Earth and Planetary Science Letters*, vol. 87, no. 3, pp. 325–337, 1988.

[3] H. Downes, C. Dupuy, and A. F. Leyreloup, "Crustal evolution of the Hercynian belt of Western Europe: evidence from lower-crustal granulitic xenoliths," *Chemical Geology*, vol. 83, no. 3-4, pp. 209–231, 1990.

[4] N. I. Christensen and W. W. Wepfer, "Laboratory techniques for determining seismic velocities and attenuations, with applications to the continental lithosphere," in *Geophysical Framework of the Continental United States*, L. C. Pakiser and W. D. Mooney, Eds., vol. 172, Geophysical Society of America Memoir, Boulder, Colo, USA, 1989.

[5] H. Kern, S. Gao, Z. Jin, T. Popp, and S. Jin, "Petrophysical studies on rocks from the Dabie ultrahigh-pressure (UHP) metamorphic belt, Central China: implications for the composition and delamination of the lower crust," *Tectonophysics*, vol. 301, no. 3-4, pp. 191–215, 1999.

[6] I. Jackson, R. L. Rudnick, S. Y. O'Reilly, and C. Bezant, "Measured and calculated elastic wave velocities for xenoliths from the lower crust and upper mantle," *Tectonophysics*, vol. 173, no. 1–4, pp. 207–210, 1990.

[7] H. Kern, K. Mengel, K. W. Strauss, T. I. Ivankina, A. N. Nikitin, and I. T. Kukkonen, "Elastic wave velocities, chemistry and modal mineralogy of crustal rocks sampled by the Outokumpu scientific drill hole: evidence from lab measurements and modeling," *Physics of the Earth and Planetary Interiors*, vol. 175, no. 3-4, pp. 151–166, 2009.

[8] H. Kern, B. Liu, and T. Popp, "Relationship between anisotropy of P and S wave velocities and anisotropy of attenuation in serpentinite and amphibolite," *Journal of Geophysical Research B: Solid Earth*, vol. 102, no. 2, pp. 3051–3065, 1997.

[9] K. Mengel and H. Kern, "Evolution of the petrological and seismic Moho—implications for the continental crust-mantle boundary," *Terra Nova*, vol. 4, no. 1, pp. 109–116, 1992.

[10] F. Birch, "The velocity of compressional wave velocities in rocks to 10 kbar, part 2," *Journal of Geophysical Research*, vol. 66, pp. 2199–2224, 1961.

[11] L. Burlini and D. M. Fountain, "Seismic anisotropy of metapelites from the Ivrea-Verbano zone and Serie dei Laghi (Northern Italy)," *Physics of the Earth and Planetary Interiors*, vol. 78, no. 3-4, pp. 301–317, 1993.

[12] G. Barruol and H. Kern, "Seismic anisotropy and shear-wave splitting in lower-crustal and upper-mantle rocks from the Ivrea Zone—experimental and calculated data," *Physics of the Earth and Planetary Interiors*, vol. 95, no. 3-4, pp. 175–194, 1996.

[13] H. Kern, T. Popp, F. Gorbatsevich, A. Zharikov, K. V. Lobanov, and Y. U. P. Smirnov, "Pressure and temperature dependence of Vp and Vs in rocks from the superdeep well and from surface analogues at Kola and the nature of velocity anisotrophy," *Tectonophysics*, vol. 338, no. 2, pp. 113–134, 2001.

[14] H. Kern and H. R. Wenk, "Fabric-related velocity anisotropy and shear wave splitting in rocks from the Santa Rosa mylonite zone, California," *Journal of Geophysical Research*, vol. 95, no. 7, pp. 11213–11223, 1990.

[15] S. Ji and M. H. Salisbury, "Shear-wave velocities, anisotropy and splitting in high-grade mylonites," *Tectonophysics*, vol. 221, no. 3-4, pp. 453–473, 1993.

[16] S. Crampin, "Geological and industrial implications of extensive-dilatancy anisotropy," *Nature*, vol. 328, no. 6130, pp. 491–496, 1987.

[17] T. I. Ivankina, H. Kern, and A. N. Nikitin, "Neutron texture measurements and 3D velocity calculations on strongly foliated biotite gneissses from the Outokumpu Deep Drill Hole," in *Proceedings of the 2nd International Workshop Outokumpu Deep Drilling Project*, I. T. Kukkonen, Ed., Program and Extended Abstracts. Geological Survey of Finland, Espoo, Finland, 2007.

[18] H. Kern, T. I. Ivankina, A. N. Nikitin, T. Lokajicek, and Z. Pros, "The effect of oriented microcracks and crystallographic and shape preferred orientation on bulk elastic anisotropy of a foliated biotite gneiss from Outokumpu," *Tectonophysics*, vol. 457, no. 3-4, pp. 143–149, 2008.

[19] E. M. Chesnokov, D. K. Tiwary, I. O. Bayuk, M. A. Sparkman, and R. L. Brown, “Mathematical modelling of anisotropy of illite-rich shale,” *Geophysical Journal International*, vol. 178, no. 3, pp. 1625–1648, 2009.

[20] P. J. Heikkinen, E. Koivisto, and I. T. Kukkonen, “FIRE high resolution seismic survey in Outokumpu,” in *Proceedings of the 2nd International Workshop Outokumpu Deep Drilling Project*, I. T. Kukkonen, Ed., pp. 47–50, Program and Extended Abstracts. Geological Survey of Finland, Espoo, Finland, 2007.

[21] I.T. Kukkonen, P. Heikkinen, E. Ekdahl et al., “Acquisition and geophysical characteristics of reflection seismic data on FIRE transects, Fennoscandian Shield,” in *Finnish Reflection Experiment 2001–2005*, I. T. Kukkonen and R. Lahtinen, Eds., pp. 241–246, Geological Survey of Finland, Espoo, Finland, 2006.

[22] H. Gebrande, “Elastic wave velocities and constants of elasticity of rock-forming minerals,” in *Physical Properties of Rocks*, G. Angenheister, Ed., vol. 1, pp. 1–96, Springer, New York, NY, USA, 1982.

[23] M. Warner, “Absolute reflection coefficients from deep seismic reflections,” *Tectonophysics*, vol. 173, no. 1–4, pp. 15–23, 1990.

[24] J. G. Liou, Q. Wang, M. Zhai, R. Y. Zhang, and B. Cong, “Ultrahigh-P metamorphic rocks and their associated lithologies from the Dabie Mountains, Central China,” in *Proceedings of the 3rd International Eclogite Field Symposium*, vol. 40, Chinese Science Bulletin, 1995.

[25] C. Y. Wang, Z. F. Ding, J. L. Song, Q. J. Wu, J. I. C. Zheng, and X. B. Zhang, “Shear wave velocity structure in Dabieshan orogenic belt,” *Acta Geophysica Sinica*, vol. 40, no. 3, pp. 344–346, 1997.

[26] S. Gao, B. R. Zhang, Z. M. Jin, H. Kern, T. C. Luo, and Z. I. D. Zhao, “How mafic is the lower continental crust?” *Earth and Planetary Science Letters*, vol. 161, no. 1–4, pp. 101–117, 1998.

Hindawi Publishing Corporation
International Journal of Geophysics
Volume 2011, Article ID 484653, 8 pages
doi:10.1155/2011/484653

Research Article

Azimuthally Anisotropic 3D Velocity Continuation

William Burnett and Sergey Fomel

The University of Texas at Austin, TX 78712, Austin, USA

Correspondence should be addressed to William Burnett, will.burnett@gmail.com

Received 28 October 2010; Accepted 5 March 2011

Academic Editor: Yu Zhang

We extend time-domain velocity continuation to the zero-offset 3D azimuthally anisotropic case. Velocity continuation describes how a seismic image changes given a change in migration velocity. This description turns out to be of a wave propagation process, in which images change along a velocity axis. In the anisotropic case, the velocity model is multiparameter. Therefore, anisotropic image propagation is multidimensional. We use a three-parameter slowness model, which is related to azimuthal variations in velocity, as well as their principal directions. This information is useful for fracture and reservoir characterization from seismic data. We provide synthetic diffraction imaging examples to illustrate the concept and potential applications of azimuthal velocity continuation and to analyze the impulse response of the 3D velocity continuation operator.

1. Introduction

Velocity continuation [1, 2] provides a framework for describing how a seismic image changes given a change in the migration velocity model. Similar in concept to residual migration [3], and cascaded migrations [4], velocity continuation is a continuous formulation of the same process. Velocity continuation has found applications in migration velocity analysis [5, 6] and diffraction imaging [7, 8].

Fomel [1] and Hubral et al. [9] point out that velocity continuation is a wave propagation process. Instead of wavefronts propagating as a function of time, images propagate as a function of migration velocity. Recent work has extended the concept to heterogeneous and anisotropic velocity models [10–15]. To account for anisotropy, the seismic velocity model must become multiparameter. Consequentially, velocity continuation generalizes to a process of implementing image transformations caused by changes in multiple parameters rather than the single isotropic velocity alone.

Accounting for azimuthal variations in seismic velocity results in better event focusing and improved imaging in such media [16]. Azimuthal variation in velocity has been shown to be an indicator of preferentially aligned vertical fractures [17], lateral heterogeneity [18], regional stress [19], or a combination of these factors. However, velocity analysis is commonly first performed on prestack common midpoint (CMP) gathers, where the geologic cause of any observed azimuthal velocity variation is ambiguous. Without the help of additional diagnostic gathers such as hybrid or cross-spread gathers [20], or an interpretive comparison between picked root mean square (RMS) and interval velocities [21], the cause of azimuthal variations in velocity can be identified only after migration.

Azimuthal seismic imaging commonly requires iterations between velocity analysis and imaging. Residual azimuthal variations in traveltime after migration can be measured by using migration binning schemes which preserve both offset and azimuth information [22, 23]. After the first pass of (isotropic) migration, azimuthal variations in velocity are detected from residual moveout, which then provides the velocity model for anisotropic migration. Iterative processing flows that use these strategies are popular not only because they are fairly efficient and intuitive, but also because they can be implemented with minimal modification to existing software. However, iterative imaging flows cannot guarantee convergence to the correct or optimal velocity model [24]. Velocity continuation has the underlying strategy of performing velocity analysis and imaging simultaneously and can thus be used to directly find an optimal velocity model without iteration. Sicking et al. [19] have demonstrated the success of a similar strategy of using imaging as a velocity analysis tool for 3D multiazimuth reflection seismic data. Azimuthal velocity continuation can provide a theoretical framework for this approach. With these benefits as motivation, we extend time-domain velocity continuation to 3D, accounting for the case of azimuthally variable migration velocity.

2. Theory

The theory of velocity continuation formulates the connection between the seismic velocity model and the seismic image as a wavefield evolution process. In doing so, the process can be implemented in the same variety of ways as seismic migration. Seismic migration in its many forms is commonly derived starting at the wave equation, which is approximated by its time and amplitude components by the eikonal and transport equations, and if necessary, a system of ray tracing equations. Velocity continuation is derived in the opposite order [2]. Starting with a geometrical description of the image, a corresponding kinematic equation for traveltime is derived to describe how the image moves according to changes in imaging parameters. Subsequently, the kinematic equation is used to derive a corresponding wave equation, which describes the dynamic behavior of the image as an evolution through imaging parameter coordinates. This section outlines the key steps of this derivation, starting with a traveltime equation that permits azimuthal variations in velocity.

Grechka and Tsvankin [25] truncate a two-dimensional Taylor series expansion for a generally inhomogeneous anisotropic media to derive the “NMO ellipse” moveout equation. Geometrically, the NMO ellipse model still assumes that events have hyperbolic moveout with offset, but it allows the velocity to change with azimuth. We start here by using the same truncated 2D Taylor series expansion to describe an azimuth-dependent traveltime equation for the summation surface of zero-offset time migration,

$$T^2(\mathbf{x},\mathbf{y},\mathbf{W}) = 4\left(\tau^2 + (\mathbf{x}-\mathbf{y})^T\mathbf{W}(\mathbf{x}-\mathbf{y})\right), \quad (1)$$

where τ is the one-way vertical traveltime after migration, $\mathbf{x}$ is the (x_1, x_2) surface position of the zero-offset receiver in survey coordinates, $\mathbf{y}$ is the surface position of the point source image, and superscript T denotes transpose. The three independent elements of the symmetric slowness matrix,

$$\mathbf{W} = \begin{pmatrix} W_{11} & W_{12} \\ W_{12} & W_{22} \end{pmatrix}, \quad (2)$$

have units of slowness squared, and the eigenvalues and eigenvectors of $\mathbf{W}$ determine the symmetry axes of the effective anisotropic medium [25]. In most common geologic situations, the eigenvalues of $\mathbf{W}$ are positive [26], and (1) describes an elliptical-hyperbolic traveltime surface in 3D—hyperbolic in cross-section view and elliptical in map view. The fast and slow moveout velocities are aligned with the major and minor axes of this ellipse. W_{11} and W_{22} are the squared moveout slownesses along their respective survey coordinates, x_1 and x_2. The third parameter, W_{12}, arises from observing the ellipse in the x_1-x_2 survey coordinates, which are generally rotated relative to its major and minor axes.

The three-parameter moveout model of (1) is analytically convenient and practical, but the parameters themselves are not intuitive to interpret in terms of more common geophysical or geological parameters. However, some simple geometric observations can help convert the three elements of $\mathbf{W}$ into more intuitive measurements. If the ellipse happens to be aligned with the survey coordinates, $W_{12} = 0$. Finding the rotation angle which properly diagonalizes $\mathbf{W}$ therefore allows one to predict the orientation of the symmetry axes. This amounts to an eigenvalue problem, where the fast and slow velocities can be found as the eigenvalues and eigenvectors of $\mathbf{W}$. The eigenvalues, W_{fast} and W_{slow}, of the slowness matrix can be found following [25],

$$W_{\text{slow, fast}} = \frac{1}{2}\left[W_{11} + W_{22} \pm \sqrt{(W_{11} - W_{22})^2 + 4W_{12}^2}\right]. \quad (3)$$

Since the eigenvalues have units of slowness squared, the smaller eigenvalue is $W_{\text{fast}} = 1/v_{\text{fast}}^2$. One can solve for the angle β between the acquisition coordinates and the symmetry axes by using the formula found by [25],

$$\beta = \tan^{-1}\left[\frac{W_{22} - W_{11} + \sqrt{(W_{22} - W_{11})^2 + 4W_{12}^2}}{2W_{12}}\right]. \quad (4)$$

The eigenvalues can then be used together with β to solve for the zero-offset migration slowness S as a function of source-receiver azimuth θ:

$$S^2(\theta) = W_{\text{slow}}\cos^2(\theta - \beta) + W_{\text{fast}}\sin^2(\theta - \beta). \quad (5)$$

Equations (3)–(5) allow one to convert the mathematically convenient parameters of $\mathbf{W}$ to more intuitive parameters, such as the fastest and slowest propagation velocities $(V_{\text{fast}}, V_{\text{slow}})$, the azimuth of the slowest velocity (β), and the percent anisotropy $(\sigma = 100 \times (1 - V_{\text{slow}}/V_{\text{fast}}))$. Alternatively, $\mathbf{W}$ can be converted into other common geophysical parameterizations. For example, Grechka and Tsvankin [25] show that once the effective parameters $\mathbf{W}$ have been converted to slowness as a function of azimuth by (5), they can be expressed in terms of horizontal transverse isotropy parameters as

$$S^2(\theta) = \frac{1}{V_{P0}^2}\frac{1 + 2\delta^{(v)}\sin^2(\theta)}{1 + 2\delta^{(v)}}, \quad (6)$$

where $\delta^{(v)}$ is the Thomsen-style parameter [27], introduced by Tsvankin [28], and V_{P0} is the vertical P-wave velocity.

Conventionally, one assumes that (1) characterizes a particular event defined in image coordinates $(\mathbf{x}, \tau)$, but one can also describe how that event would transform given a change in the image parameters $\mathbf{W}$. Regardless of the velocity model, the traveltime T must remain unchanged between different images. From this observation, we arrive at the following set of conditions:

$$\nabla_{\mathbf{x}} T^2 = \begin{pmatrix} \dfrac{\partial T^2}{\partial x_1} \\ \dfrac{\partial T^2}{\partial x_2} \end{pmatrix} = 8\tau \nabla_x \tau + 8\mathbf{W}(\mathbf{x}-\mathbf{y}) = 0,$$

$$\nabla_{\mathbf{W}} T^2 = \begin{pmatrix} \dfrac{\partial T^2}{\partial W_{11}} & \dfrac{\partial T^2}{\partial W_{12}} \\ \dfrac{\partial T^2}{\partial W_{12}} & \dfrac{\partial T^2}{\partial W_{22}} \end{pmatrix} = 8\tau \nabla_{\mathbf{W}} \tau + 4(\mathbf{x}-\mathbf{y})(\mathbf{x}-\mathbf{y})^T = 0. \tag{7}$$

Combining and reducing these conditions yields a system of equations that are defined only in the image parameter coordinates:

$$2\frac{\partial \tau}{\partial W_{11}} + \frac{\tau(W_{22}(\partial\tau/\partial x_1) - W_{12}(\partial\tau/\partial x_2))^2}{(W_{12}^2 - W_{11}W_{22})^2} = 0,$$
$$2\frac{\partial \tau}{\partial W_{22}} + \frac{\tau(W_{12}(\partial\tau/\partial x_1) - W_{11}(\partial\tau/\partial x_2))^2}{(W_{12}^2 - W_{11}W_{22})^2} = 0, \tag{8}$$

$$2\frac{\partial \tau}{\partial W_{12}} - \frac{2\tau(W_{12}(\partial\tau/\partial x_1) - W_{11}(\partial\tau/\partial x_2))(W_{22}(\partial\tau/\partial x_1) - W_{12}(\partial\tau/\partial x_2))}{(W_{12}^2 - W_{11}W_{22})^2} = 0. \tag{9}$$

The system of kinematic equations describing azimuthally anisotropic velocity continuation is then found by combining (8)–(9). In a vector notation, this becomes

$$\nabla_{\mathbf{W}} \tau + \frac{\tau}{2}\mathbf{W}^{-1}\nabla_{\mathbf{x}}\tau(\nabla_{\mathbf{x}}\tau)^T\mathbf{W}^{-1} = 0, \tag{10}$$

where $\nabla_{\mathbf{x}}$ and $\nabla_{\mathbf{W}}$ are in the form given by (7).

The method of characteristics [29] provides a link between a kinematic equation (such as (10)) and its corresponding wave-type equation. Fomel [2] demonstrates specifically how the method can be used to derive a velocity continuation wave equation from its kinematic counterpart. By first setting the characteristic surface condition,

$$\psi = t - \tau(\mathbf{x}, \mathbf{W}) = 0, \tag{11}$$

and replacing τ with ψ and t, we obtain an alternative form of (10):

$$\psi_t \nabla_{\mathbf{W}} \psi + \frac{t}{2}\mathbf{W}^{-1}\nabla_{\mathbf{x}}\psi(\nabla_{\mathbf{x}}\psi)^T\mathbf{W}^{-1} = 0. \tag{12}$$

Equation (11) guarantees that the wavefronts of time-domain image wavefield P exist only where the arrival time τ is equal to the recorded time t at a given location. Now take both ξ_i and ξ_j to represent each of t, W_{11}, W_{12}, W_{22}, x_1, and x_2. According to the method of characteristics, if Λ_{ij} is the coefficient in front of $(\partial\psi/\partial\xi_i)(\partial\psi/\partial\xi_j)$ from kinematic equation (12), then the corresponding wave equation will have the same coefficients Λ_{ij} in front of each $\partial^2 P/\partial\xi_i\partial\xi_j$ derivative. The time derivative ψ_t is equal to 1 given (11), and is included in the first term of (12) to facilitate the use of the method of characteristics. Then, by introducing $\mathbf{P}_{xx}$ as the spatial Hessian matrix of the wavefield,

$$\mathbf{P}_{xx} = \begin{pmatrix} \dfrac{\partial^2 P}{\partial x_1^2} & \dfrac{\partial^2 P}{\partial x_1 \partial x_2} \\ \dfrac{\partial^2 P}{\partial x_2 \partial x_1} & \dfrac{\partial^2 P}{\partial x_2^2} \end{pmatrix}, \tag{13}$$

we arrive at the azimuthally anisotropic post-stack velocity continuation wave equation,

$$\nabla_{\mathbf{W}} P_t = -\frac{t}{2}\mathbf{W}^{-1}\mathbf{P}_{xx}\mathbf{W}^{-1}. \tag{14}$$

In the isotropic case, $\mathbf{W}$ is diagonal and $W_{11} = W_{22}$. Equation (14) then reduces to the isotropic velocity continuation equation first derived by Claerbout [30].

3. Method

Since velocity continuation is described by a wave equation, it can be implemented in analogous ways to seismic migration. Here, we demonstrate a spectral implementation of (14). By first stretching the time coordinate of an input image from t to $\tilde{t} = t^2/2$, and then taking its 3D Fourier transform, (14) becomes the reduced partial differential equation:

$$i\Omega \nabla_{\mathbf{W}} \widehat{P} = \frac{1}{2}\mathbf{W}^{-1}\mathbf{k}\mathbf{k}^T\mathbf{W}^{-1}\widehat{P}, \tag{15}$$

where Ω is the Fourier dual of $\tilde{t}$ and $\mathbf{k}$ is the wavenumber vector (Fourier dual of $\mathbf{x}$). Equation (15) has the analytical solution,

$$\widehat{P}(\Omega, k_1, k_2, \mathbf{W}) = \widehat{P}(\Omega, k_1, k_2, \mathbf{W}_0)e^{-i/2\Omega\mathbf{k}^T(\mathbf{W}^{-1}-\mathbf{W}_0^{-1})\mathbf{k}}, \tag{16}$$

which shows that continuation of an image from an arbitrary $\mathbf{W}_0$ to $\mathbf{W}$ can be achieved by multiplication with a shifting exponential in the Fourier domain. One can also directly migrate an unmigrated image by using the 2 × 2 matrix $\mathbf{W}_0^{-1} = \mathbf{0}$ for the initial velocity. In practice, the coordinate stretch from t to $\tilde{t}$ should be carefully applied as data will be compressed along the time axis for early samples.

With a range of slowness matrices $\mathbf{W}$, equation (16) can be used to quickly generate the corresponding range of anisotropically migrated images. When the correct velocity

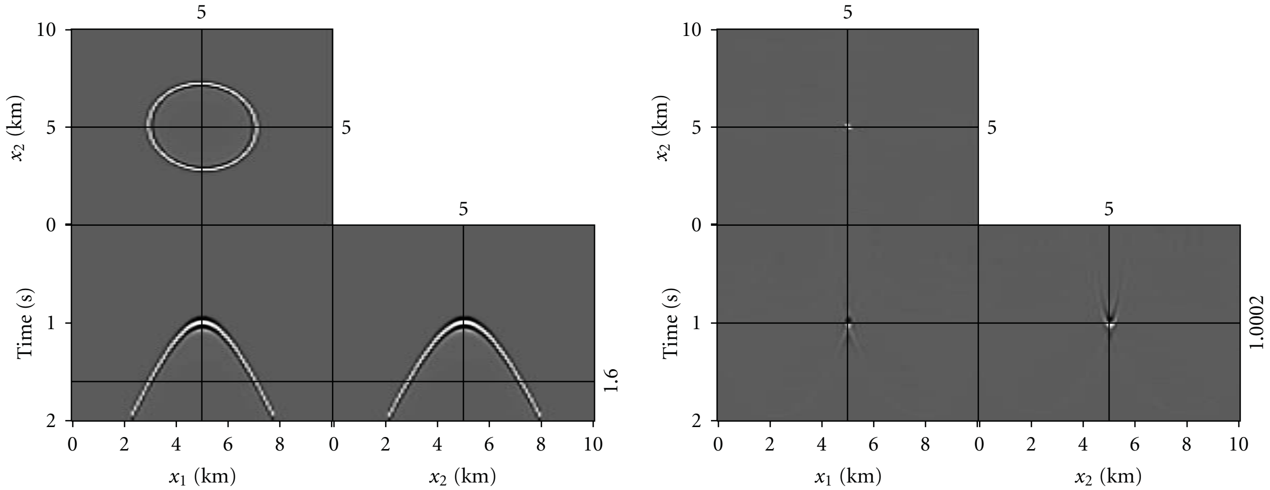

(a) Diffraction (b) Overmigrated

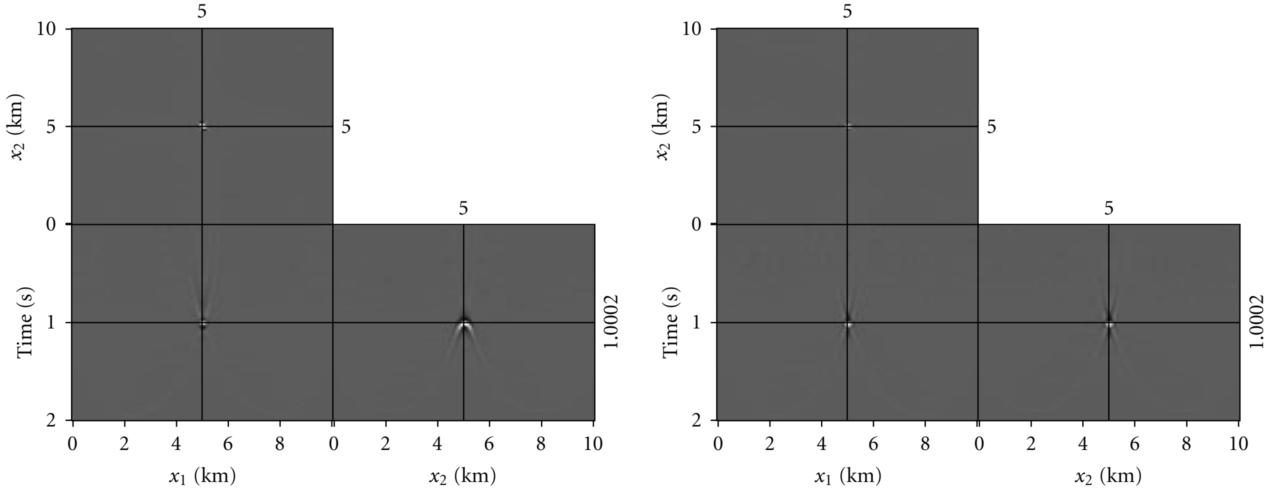

(c) Isotropic (d) Correct parameter

Figure 1: (a) A single azimuthally anisotropic diffraction. (b) The diffraction migrated by velocity continuation using correct parameters except $\sigma = 10$, resulting in overmigration along x_2. (c) Migration using the correct W_{11}, but assuming isotropy. The result is now undermigrated along x_2. (d) Migration using correct parameters. The image is well focused in both directions.

model is used, diffractions collapse to points, which we recognize as the image coming into focus. Although constant velocity models are used for each image, this type of spectral implementation can still be useful in the heterogeneous case, as different parts of the image will come into focus locally as the appropriate velocity is used [31, 32]. Once the range of images is generated, we search for the best focused image at each output location. We use the image attribute of kurtosis, defined as,

$$\phi(\mathbf{W}) = \frac{\iint P^4(\mathbf{x}, t, \mathbf{W}) d\mathbf{x} dt}{\left[\iint P^2(\mathbf{x}, t, \mathbf{W}) d\mathbf{x}\, dt\right]^2}, \tag{17}$$

to quantify how well a location is focused in a particular image [8, 33]. Including integration limits specifies a window size for locally measuring kurtosis in the image. In application, either the integration limits control the size of a "sliding window," or when viewing kurtosis as a local attribute, [34], they can be used to control the smoothness enforced by shaping regularization. In either case, the integration limits control a trade-off between the robustness of the focusing measurement and the resolution. From experience, typical limits for field data correspond to window sizes on the order of 10^1 samples in each dimension. It should be noted that the traveltime approximation of (1) loses accuracy in the presence of strong lateral heterogeneity, but is commonly used to estimate smooth effective parameter models. Following the maximum values through the resulting six-dimensional kurtosis hypercube, $\phi(t, \mathbf{x}, \mathbf{W})$, and then slicing corresponding pieces from the output images volume, $P(t, \mathbf{x}, \mathbf{W})$, reveals an effective medium-based heterogeneous velocity model and a well focused image. This spectral implementation and slicing procedure is similar to searching through a set of constant-velocity f–k migrations and can be completed without any prior knowledge of the velocity model [32, 35].

4. Examples

Two simple synthetic examples are provided below to illustrate 3D velocity continuation over a range of velocity models. In the first example, we apply velocity continuation to a point diffractor. In the second example, we apply the method to a synthetic post-stack image of a set of faults. The second example illustrates fracture characterization through diffraction imaging as a potential application for 3D azimuthal velocity continuation. The data in both examples are modeled using (1), which geometrically approximates a diffraction surface as an elliptical-hyperbolic surface. Field data and more accurately modeled data will generally also exhibit nonhyperbolic moveout, for which (1) does not account. The physical validity and limitations of (1) are thoroughly discussed by Grechka and Tsvankin [25], but we focus here on how well diffractions can be collapsed, and how well the velocity parameters can be measured, if the data are ideally described by (1).

Figure 1(a) shows a single diffraction event, modeled using (1). The fastest direction of propagation is at $\beta = 105^\circ$ counterclockwise from the x_1 axis, with $V_{\text{fast}} = 3.50\,\text{km/s}$. The data in Figure 1(a) were modeled with $\sigma = 7\%$ anisotropy, which may be quite high for most field cases, but it was chosen to allow the azimuthal variations in diffraction moveout to be visibly pronounced. As described above, we first stretch the time axis from t to $\tilde{t}$ and take the 3D Fourier transform of the data. Then we apply the phase-shift prescribed by (16) for a range of $\mathbf{W}$. We found it more intuitive to specify the parameter ranges in terms of V_{x_1}, β, and σ, and then convert them at each step into the three parameters of $\mathbf{W}$ for use in (16). The inverse of the in-line velocity squared $1/V_{x_1}^2$ is equivalent to W_{11}, which, along with a given fast azimuth β and percent anisotropy σ, can be used to calculate W_{12} and W_{22} using (3)–(5). Last, we apply the 3D inverse Fourier transform and unstretch from $\tilde{t}$ to t to obtain the 6D image volume. Examples from the image volume using incorrect parameters are shown in Figures 1(b) and 1(c). The correct parameters are used in Figure 1(d), where the image is well focused.

Since only a single diffraction is present in this example, we can measure kurtosis over a window spanning the entirety of each 3D image, reducing the kurtosis volume from 6D to 3D. Figure 2 is a 2D slice of the kurtosis volume at the correct $W_{11} = 1/V_{x_1}^2$ value of $0.0935 = 1/(3.27\,\text{km/s})^2$. The peak of the kurtosis map is near the correct values of $\sigma = 7$ and $\beta = 105^\circ$. Once the peak of the kurtosis map is identified, one could refine the increments around the peak to yield more accurate estimates. The physical limitations of resolving azimuthal velocity parameters are discussed by Al-Dajani and Alkhalifah [37].

In practice, a conventional in-line 2D velocity analysis directly yields W_{11} from $1/V_{x_1}^2$, so Figure 2 could illustrate a realistic scenario for using 3D velocity continuation to improve upon a previous isotropic velocity model. In such a case, one would use previous V_{x_1} picks to hold W_{11} constant and then effectively test a variety of W_{12} and W_{22} values. Since W_{11} and W_{22} are measured with respect to the survey coordinates, either (or both) can be measured independently via a single-azimuth semblance scan, along x_1 or x_2, respectively. The best isotropic velocity based on a fully multiazimuth semblance scan will generally not represent either W_{11} or W_{22}, but it can help limit the range of test parameters. Note that our method does not require prior knowledge of the velocity model, but without prior knowledge, the kurtosis measure remains a 6D volume. Although more difficult to visualize, the 6D kurtosis volume is computationally just as easily scanned for optimal imaging parameters as the 2D map in Figure 2.

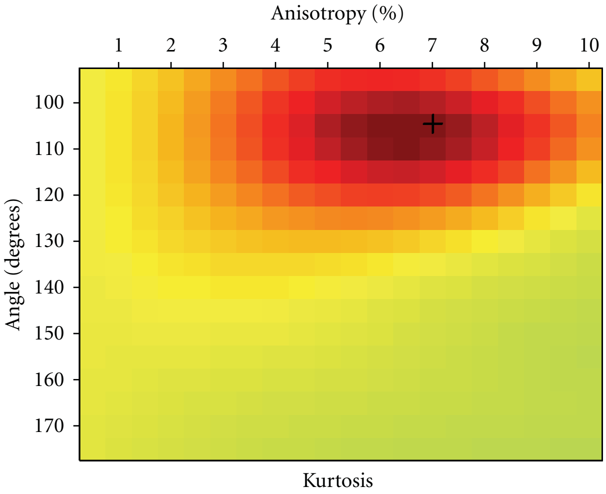

FIGURE 2: Kurtosis values for the velocity continuation of the diffraction in Figure 1(a). The map covers a range of anisotropy and angle values with an increment in β of 5° and an increment in σ of 0.5%. The correct values at 105° and 7% anisotropy (indicated by crosshairs) coincide with the peak of the kurtosis map.

In the next example, we illustrate the concept of applying 3D anisotropic velocity continuation to diffraction imaging and fracture characterization. Figure 3(a) shows a 3D synthetic post-stack diffraction data set, equivalent to the ideal separation of diffractions from specular reflections in post-stack data following Fomel et al. [8]. A fault map from Hargrove [36] (shown in Figure 3(a)) was digitized and used to create a 3D fracture model. Each fault location was used to generate a point diffraction in a homogeneous anisotropic background via (1). A timeslice of the modeled diffraction data is shown in Figure 3(b). The faults in the model typically have a strike of 112°, and in cases where faults and nearby fractures (which more likely influence the seismic velocity) are similarly aligned, the fast direction of seismic wave propagation tends to align with their strike. By assuming a typical tight sandstone velocity of $V_{\text{fast}} = 4.0\,\text{km/s}$ with 3% anisotropy, we choose the modeling $\mathbf{W}$ to be comprised of $W_{11} = 0.0659$, $W_{22} = 0.0631$, and $W_{12} = 0.0014$ (all in s^2/km^2). This results in a fast velocity direction along the strike of the faults. In Figure 3(d), we see that 3D velocity continuation using the correct parameters (again found by maximum kurtosis) allows the faults to be clearly imaged. If an intermediate isotropic velocity model is used, as in Figure 3(c), the diffractions are still imaged, but they are not as well focused compared to the anisotropically

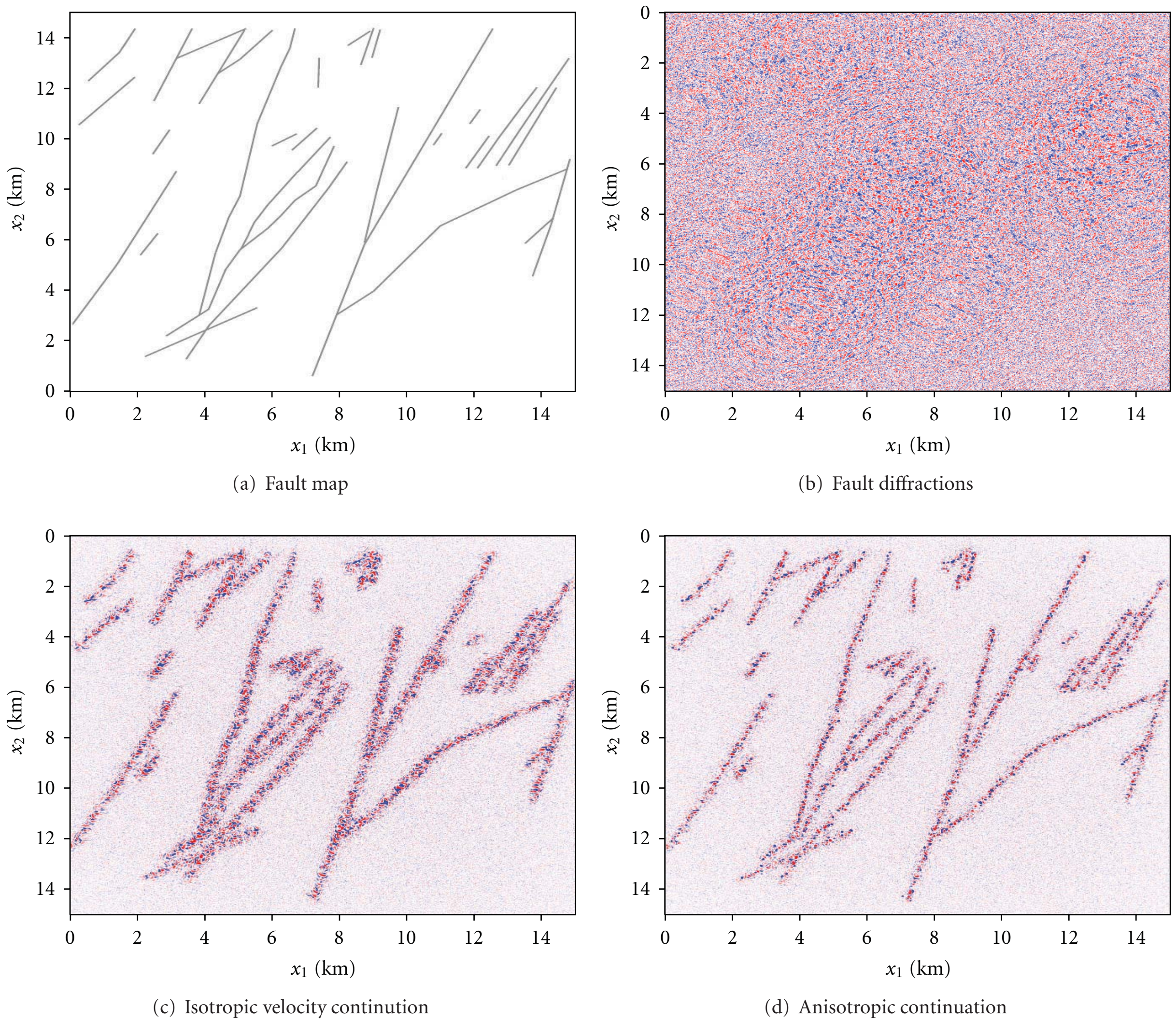

(a) Fault map

(b) Fault diffractions

(c) Isotropic velocity continution

(d) Anisotropic continuation

Figure 3: (a) Fault map from Northwest Scotland [36] used to model diffraction data. (b) Synthetic post-stack diffraction data modeled using (1) and a 3D model based on the fault map in (a). (c) Diffractions from (b) migrated using an isotropic velocity model. (d) Diffractions from (b) migrated by anisotropic 3D velocity continuation.

migrated diffractions in Figure 3(d). Conventionally, diffraction arrivals such as those in Figure 3(a) may be viewed as noise, but by separating them and treating them as signal, we can see here that imaging of steep and detailed features while simultaneously extracting anisotropy information may be possible.

5. Discussion and Conclusions

By extending time-domain velocity continuation to the azimuthally anisotropic 3D case, we have combined the concepts of azimuthal imaging and diffraction imaging. We assume a three-parameter migration slowness model that allows velocity to vary elliptically with azimuth. We have provided simple examples to illustrate the potential application of our method to fracture characterization through diffraction imaging. By treating diffractions as signal, our method performs azimuthal analysis on post-stack data, without the requirement for common-offset-vector or offset-vector-tile binning schemes. This is possible because, unlike reflections, diffractions can preserve azimuthal information post-stack. Post-stack data volumes have obvious advantages over prestack or vector-binned data for analysis, including smaller memory size and improved signal-to-noise ratio.

Allowing azimuthal variation in the migration velocity will result in improved imaging, which is clearly a benefit of 3D velocity continuation. However, the potential for fracture characterization may be even more useful. Our method has many of the same ideas as the azimuthal imaging and fracture characterization flow proposed by Sicking et al. [19] for reflection data. Under the velocity continuation framework, we can extend the azimuthal imaging idea to 3D diffraction imaging. Since diffraction-generating fractures and faults are often nearly vertical and preferentially aligned, they can be associated with azimuthal anisotropy. Fomel et al. [8] demonstrate that it is possible to separate diffractions from specular reflections and then image their associated discontinuities through the use of velocity continuation. Their method operates on post-stack data, as they show that diffractions are highly sensitive to migration velocity, even in the zero-offset case. Al-Dajani and Fomel [38] have successfully demonstrated zero-offset diffraction image focusing as a fracture detection attribute on azimuth-sectored 3D field data. Our proposed method uses multiazimuth image focusing primarily as a velocity analysis criterion, but kurtosis could also be used as an image attribute. In cases where subsurface fractures cause azimuthal anisotropy, kurtosis as an attribute may be indicative of fracture intensity [38]. By applying velocity continuation to 3D diffraction imaging, one may be able to estimate both the orientation and the intensity of fractures from the resulting anisotropic velocity model and maximum kurtosis volumes, respectively. This information can be useful in reservoir development, as it can provide insight to subsurface fluid flow behavior.

Although the spectral implementation of our method allows a range of possible images to be computed efficiently, it demands large amounts of memory to store a suite of images as well as the kurtosis volume. Modern computational hardware makes our approach feasible as is, especially for target-oriented imaging and analysis strategies. Future studies may lead to better optimization-based approaches to finding local kurtosis maxima, in which case, our method could be practical for dense parameter estimation throughout full 3D volumes.

The underlying strategy of velocity continuation is to simultaneously estimate the velocity model as the data are imaged. This is beneficial in the case of azimuthal anisotropy discussed here, as the ambiguity between structural heterogeneity and anisotropy is handled without the need for iteration. Other multiparameter seismic imaging problems, such as converted-wave imaging, which are also conventionally handled by iterative flows, could also benefit from prestack versions of the 3D velocity continuation strategy.

Acknowledgments

The authors would like to thank Vladimir Bashkardin, Hesam Kazemeini, Siwei Li, Yang Liu, and Xiaolei Song for helpful suggestions and Peter Eichhubl and Pete Hargrove for providing the example fracture map. The authors would also like to thank the three anonymous reviewers for comments helpful in improving this paper. Funding for this project is provided by RPSEA through the "Ultra-Deepwater and Unconventional Natural Gas and Other Petroleum Resource" program authorized by the US Energy Policy Act of 2005. RPSEA (www.rpsea.org) is a nonprofit corporation whose mission is to provide a stewardship role in ensuring the focused research, development and deployment of safe and environmentally responsible technology that can effectively deliver hydrocarbons from domestic resources to the citizens of the United States. RPSEA, operating as a consortium of premier US energy research universities, industry, and independent research organizations, manages the program under a contract with the US Department of Energy's National Energy Technology Laboratory.

References

[1] S. Fomel, "Method of velocity continuation in the problem of temporal seismic migration," *Russian Geology and Geophysics*, vol. 35, pp. 100–111, 1994.

[2] S. Fomel, "Velocity continuation and the anatomy of residual prestack time migration," *Geophysics*, vol. 68, no. 5, pp. 1650–1661, 2003.

[3] D. H. Rothman, S. A. Levin, and F. Rocca, "Residual migration: applications and limitations," *Geophysics*, vol. 50, no. 1, pp. 110–126, 1985.

[4] K. Larner and C. Beasley, "Cascaded migrations: improving the accuracy of finite-difference migration," *Geophysics*, vol. 52, no. 5, pp. 618–643, 1987, Errata in: *Geophysics*, vol. 52, no. 8, p. 1165.

[5] S. Fomel, "Time-migration velocity analysis by velocity continuation," *Geophysics*, vol. 68, no. 5, pp. 1662–1672, 2003.

[6] J. Schleicher, J. C. Costa, and A. Novais, "Time-migration velocity analysis by image-wave propagation of common-image gathers," *Geophysics*, vol. 73, no. 5, pp. VE161–VE171, 2008.

[7] A. Novais, J. Costa, and J. Schleicher, "Velocity determination by image-wave remigration," in *Proceedings of the 68th European Association of Geoscientists and Engineers International Conference*, pp. 157:1–157:4, Vienna, Austria, 2006.

[8] S. Fomel, E. Landa, and M. T. Taner, "Poststack velocity analysis by separation and imaging of seismic diffractions," *Geophysics*, vol. 72, no. 6, pp. U89–U94, 2007.

[9] P. Hubral, M. Tygel, and J. Schleicher, "Seismic image waves," *Geophysical Journal International*, vol. 125, no. 2, pp. 431–442, 1996.

[10] T. Alkhalifah and S. Fomel, "Residual migration in VTI media using anisotropy continuation," Tech. Rep. SEP-94, pp. 327–337, Stanford Exploration Project, 1997.

[11] F. Adler, "Kirchhoff image propagation," *Geophysics*, vol. 67, no. 1, pp. 126–134, 2002.

[12] E. Iversen, "Velocity rays for heterogeneous anisotropic media: theory and implementation," *Geophysics*, vol. 71, no. 5, pp. T117–T127, 2006.

[13] J. Schleicher and R. Aleixo, "Time and depth remigration in elliptically anisotropic media using image-wave propagation," *Geophysics*, vol. 72, no. 1, pp. S1–S9, 2007.

[14] J. Schleicher, A. Novais, and J. C. Costa, "Vertical image waves in elliptically anisotropic media," *Studia Geophysica et Geodaetica*, vol. 52, no. 1, pp. 101–122, 2008.

[15] A. A. Duchkov and M. V. de Hoop, "Velocity continuation in the downward continuation approach to seismic imaging," *Geophysical Journal International*, vol. 176, no. 3, pp. 909–924, 2009.

[16] C. Sicking and S. Nelan, "Azimuthal attribute methodologies: comparison of NMO super gathers, sectored isotropic migration, iterative azimuthal migration," in *Proceedings of the 78th Society of Exploration Geophysicists International Convention*, pp. 983–987, 2008.

[17] S. Crampin, "Effective anisotropic elastic constants for wave propagation through cracked solids," *Geophysical Journal of the Royal Astronomical Society*, vol. 76, no. 1, pp. 135–145, 1984.

[18] F. K. Levin, "Apparent velocity from dipping interface reflections," *Geophysics*, vol. 50, no. 11, pp. 2026–2032, 1985.

[19] C. Sicking, S. Nelan, and W. McLain, "3D azimuthal imaging," in *Proceedings of the 77th Society of Exploration Geophysicists International Convention*, pp. 2364–2364, 2007, Expanded Abstracts.

[20] J. W. Dunkin and F. K. Levin, "Isochrons for a three-dimensional seismic system," *Geophysics*, vol. 36, no. 6, pp. 1099–1137, 1971.

[21] E. Jenner, "Recognizing apparent P-wave azimuthal velocity anisotropy caused by lateral velocity variations," in *Proceedings of the 13th Annual International Workshop on Seismic Anisotropy*, pp. 71–72, 2008.

[22] P. W. Cary, "Common-offset-vector gathers: an alternative to cross-spreads for wide-azimuth 3-D surveys," in *Proceedings of the 69th Society of Exploration Geophysicists International Convention*, pp. 1496–1499, 1999.

[23] G. J. O. Vermeer, *Fundamentals of 3-D seismic survey design*, Ph.D. thesis, Delft University of Technology, Delft, The Netherlands, 1999.

[24] S. M. Deregowski, "Common-offset migrations and velocity analysis," *First Break*, vol. 8, no. 6, pp. 225–234, 1990.

[25] V. Grechka and I. Tsvankin, "3-D description of normal moveout in anisotropic inhomogeneous media," *Geophysics*, vol. 63, no. 3, pp. 1079–1092, 1998.

[26] I. Tsvankin, *Seismic Signatures and Analysis of Reflection Data in Anisotropic Media*, Elsevier, Berlin, Germany, 2005.

[27] L. Thomsen, "Weak elastic anisotropy," *Geophysics*, vol. 51, no. 10, pp. 1954–1966, 1986.

[28] I. Tsvankin, "Reflection moveout and parameter estimation for horizontal transverse isotropy," *Geophysics*, vol. 62, no. 2, pp. 614–629, 1997.

[29] R. Courant and D. Hilbert, *Methods of Mathematical Physics*, John Wiley & Sons, New York, NY, USA, 1989.

[30] J. F. Claerbout, "Velocity extrapolation by cascaded 15 degree migration," Tech. Rep. SEP-48, pp. 79–84, Stanford Exploration Project, 1986.

[31] W. S. Harlan, J. F. Claerbout, and F. Rocca, "Signal/ noise separation and velocity estimation," *Geophysics*, vol. 49, no. 11, pp. 1869–1880, 1984.

[32] P. Fowler, "Velocity independent imaging of seismic reflectors," in *Proceedings of the 54th Annual International Meeting Society of Exploration Geophysicists*, 1984.

[33] R. A. Wiggins, "Minimum entropy deconvolution," *Geoexploration*, vol. 16, no. 1-2, pp. 21–35, 1978.

[34] S. Fomel, "Local seismic attributes," *Geophysics*, vol. 72, no. 3, pp. A29–A33, 2007.

[35] W. Mikulich and D. Hale, "Steep-dip v(z) imaging from an ensemble of Stolt-like migrations," *Geophysics*, vol. 57, no. 1, pp. 51–59, 1992.

[36] P. Hargrove, *Fault-related fracture systems in the Cambrian Eriboll formation, Northwest Scotland: a field and petrographic study of a tight gas sandstone analog*, M.S. thesis, The University of Texas, Austin, Tex, USA, 2010.

[37] A. Al-Dajani and T. Alkhalifah, "Reflection moveout inversion for horizontal transverse isotropy: accuracy, limitation, and acquisition," *Geophysics*, vol. 65, no. 1, pp. 222–231, 2000.

[38] A. Al-Dajani and S. Fomel, "Fractures detection using multi-azimuth diffractions focusing measure: is it feasible?" in *Proceedings of the 80th Society of Exploration Geophysicists International Convention*, pp. 287–291, 2010.

Hindawi Publishing Corporation
International Journal of Geophysics
Volume 2011, Article ID 958483, 16 pages
doi:10.1155/2011/958483

Research Article

Advantages of Shear Wave Seismic in Morrow Sandstone Detection

Paritosh Singh and Thomas Davis

Colorado School of Mines, Golden, CO 80401-1843, USA

Correspondence should be addressed to Paritosh Singh, psingh@mymail.mines.edu

Received 25 December 2010; Accepted 7 March 2011

Academic Editor: Yu Zhang

The Upper Morrow sandstones in the western Anadarko Basin have been prolific oil producers for more than five decades. Detection of Morrow sandstones is a major problem in the exploration of new fields and the characterization of existing fields because they are often very thin and laterally discontinuous. Until recently compressional wave data have been the primary resource for mapping the lateral extent of Morrow sandstones. The success with compressional wave datasets is limited because the acoustic impedance contrast between the reservoir sandstones and the encasing shales is small. Here, we have performed full waveform modeling study to understand the Morrow sandstone signatures on compressional wave (P-wave), converted-wave (PS-wave) and pure shear wave (S-wave) gathers. The contrast in rigidity between the Morrow sandstone and surrounding shale causes a strong seismic expression on the S-wave data. Morrow sandstone shows a distinct high amplitude event in pure S-wave modeled gathers as compared to the weaker P- and PS-wave events. Modeling also helps in understanding the adverse effect of interbed multiples (due to shallow high velocity anhydrite layers) and side lobe interference effects at the Morrow level. Modeling tied with the field data demonstrates that S-waves are more robust than P-waves in detecting the Morrow sandstone reservoirs.

1. Introduction

The Anadarko Basin is one of the major hydrocarbon producing provinces in the USA. According to Sorenson [1], Panhandle-Hugoton field in Western Anadarko Basin is a giant oil field (estimated ultimate recovery (EUR) 1400 million bbl of oil) and the largest conventional gas field in North America (EUR > 75 tcf). Hydrocarbon production in the Anadarko basin is mainly from three geologic zones—the Upper Mississippian and Pennsylvanian sandstones, Permian carbonates, and Mississippian carbonates [2]. Permian Council Grove and Chase Group carbonate rock gas fields are by far the largest hydrocarbon producers in the basin. The Pennsylvanian Upper Morrow sandstone reservoir in western Anadarko Basin is a major oil-producing reservoir. It consists of multiple-stacked lenticular sandstone bodies formed within valley-fill complexes. These sandstones have confounded operators and investigators alike because of their irregular distribution. Compressional wave studies have been mostly done for characterizing the Morrow sandstones [3, 4]. It is difficult to detect these thin and discontinuous reservoir sandstones using P-wave datasets because of insufficient acoustic impedance contrast between Morrow sandstone and surrounding shales. The P-wave study is further limited since the interference effects due to side lobe of Morrow shale dominate the subtle P-wave AVO (amplitude versus offset) response [5]. Thus, P-wave seismic methods have not been successful in imaging Morrow sandstone accumulations within this valley-fill system.

Shear wave data can help improve structural imaging where P-impedance contrast is low, imaging through gas clouds, lithology and fluid estimation, fracture detection, and reservoir monitoring, which reduces risk and creates new exploration opportunities [6, 7]. Engelmark [8] showed modeling results where converted-wave imaging can be valuable when the acoustic-impedance contrast between seal and reservoir is weak. Alba Field is one of the field examples where converted-wave data has been successfully used to image low P-impedance reservoirs [9]. Margrave et al. [10] reported success interpreting channel sands with 3C data

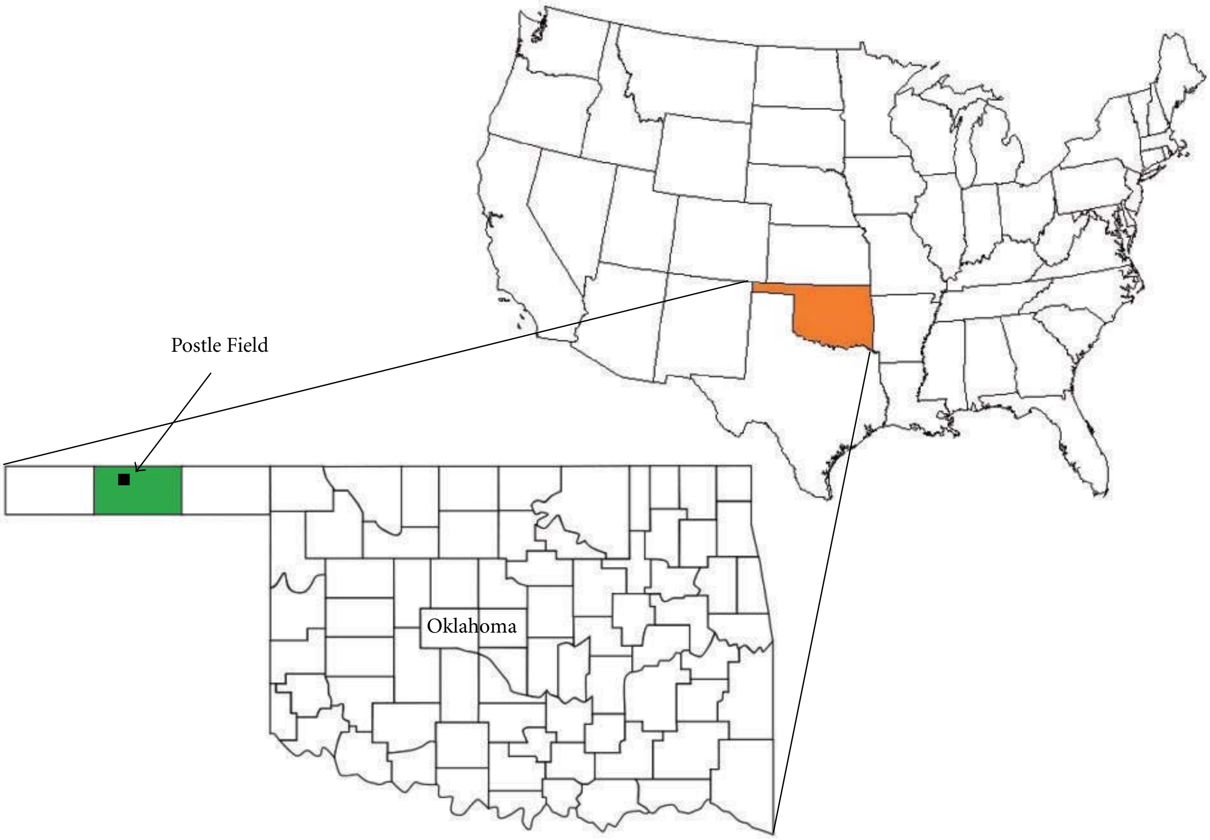

Figure 1: Location of Postle Field in Texas County, Oklahoma.

in Blackfoot Field by using V_p/V_s measurement. Knapp et al. [11] presented a case study in Gulf of Mexico to show the significance of converted-wave data in imaging through gas clouds. The importance of 4C data for lithology and fluid estimation has been showed by Engelmark [12]. Fractured reservoirs cause shear-wave birefringence as they propagate through them [13, 14]. The fast shear wave (S1) is polarized parallel to the fracture strike direction and the slow shear wave (S2) is polarized perpendicular to the dominant fracture strike direction in the symmetry axis plane. Crampin [15–18] stresses the importance of shear wave splitting phenomenon to exploration geophysics. Lynn and Thomsen [19] published one of the first field examples which demonstrate use of S-wave anisotropy in an exploration context. Mueller [20] has showed the use of S-wave splitting for Austin chalk fracture detection. Time lapse S-wave data has been used as a production-monitoring tool in unconventional reservoirs such as tight gas sandstone reservoir in Rulison Field [21] and carbonate reservoir in Weyburn Field [22].

Most of the above-mentioned studies have been done using converted-wave data. Importance of shear waves has been mostly demonstrated using PS-waves (Stewart et al. [23]) as compared to S-waves. The present study shows the value of S-wave data in imaging of Morrow sandstone reservoirs using full waveform modeling and real-data results. Study by Wilson [24] in Eva South field demonstrated that PS-waves can be successfully used for Morrow sandstone detection in an area where P-wave fails. He showed that V_p/V_s and PS1 amplitude maps improve the mapping of Morrow sandstone distribution. Blott [25] demonstrated the importance of 9C dataset in detecting the Morrow sandstones in Sorrento field by using V_p/V_s and S1 and S2 amplitude maps. Rampton [26] showed the usefulness of PS- and S-wave VSP (vertical seismic profile) data for detecting the reservoir sandstones, while verifying that compressional energy corresponds primarily to nonreservoir rock at the Morrow level. Wiley [5] indicates the presence of faults in such fields and there can be fractures associated with them in all the hydrocarbon producing geologic zones. Shear wave splitting can help in understanding these fractures and improve production.

This study is focused on Postle Field which was discovered in 1958. The production phases began with primary production, followed by water flooding in 1965 and CO_2 enhanced oil recovery from 1995. The field has produced nearly 120 million barrels or 40% of an estimated 300 million barrels of OOIP (original oil in-place) [27]. Thus, understanding the dynamics of the reservoir is very important in the design and success of the flood management in such mature fields. Multicomponent data can help in detecting the sandstone distribution and movement of CO_2 injection, since shear waves are sensitive to pressure changes and do not depend significantly on saturating fluids [28, 29].

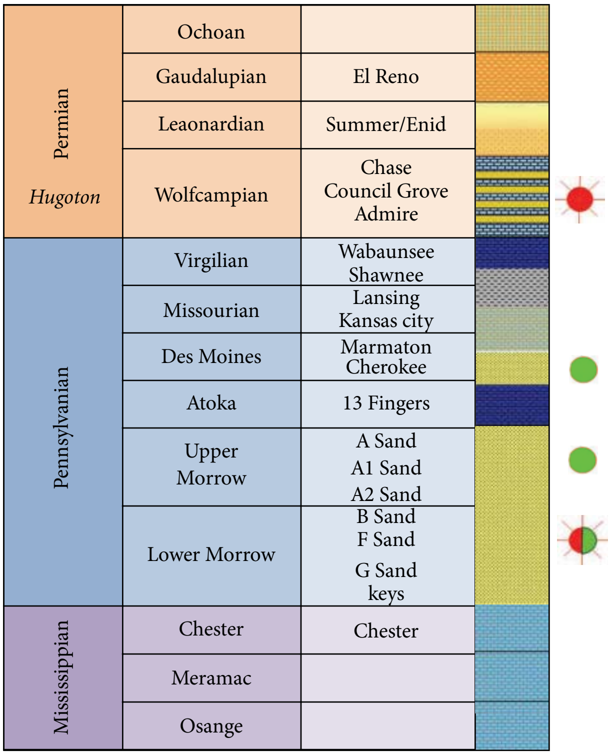

Figure 2: Stratigraphic column of Postle Field (courtesy Whiting Petroleum).

The main producing reservoir in the study area is the Morrow A sandstone. It is observed that the acoustic impedance percentage difference between Morrow shales and sandstones is ~10%, whereas the shear impedance percentage difference is ~40%. We perform full waveform modeling to understand the Morrow A sandstone AVO signatures on P-wave, PS-wave and S-wave [30]. Modeling demonstrates that Morrow sandstones can be better mapped using S-wave data, whereas P-wave and PS-wave data are insufficient in imaging these sandstones. Due to low acoustic impedance contrast and interference effects, P-wave AVO has not been used until now to characterize the Morrow sandstones. But elastic modeling suggests that S-wave AVO can be of great help in characterizing these sandstones. The modeling results in combination with the field data results show that pure S-wave data can help in finding new prospects and guide in future drilling locations. This is the first study to do full waveform modeling for understanding the Morrow A sandstone response on P-, PS- and S-waves and help in multicomponent data processing and interpretation. Modeling also helps in understanding the effect of shallow anhydrite layers on data quality and this study has never been done before for Morrow sandstone reservoirs. The importance of this study is the accumulation of strong evidence demonstrating the direct detection of reservoir sandstone using S-waves. This study encourages having more S-wave seismic studies in characterizing the Morrow sandstones in such mature fields.

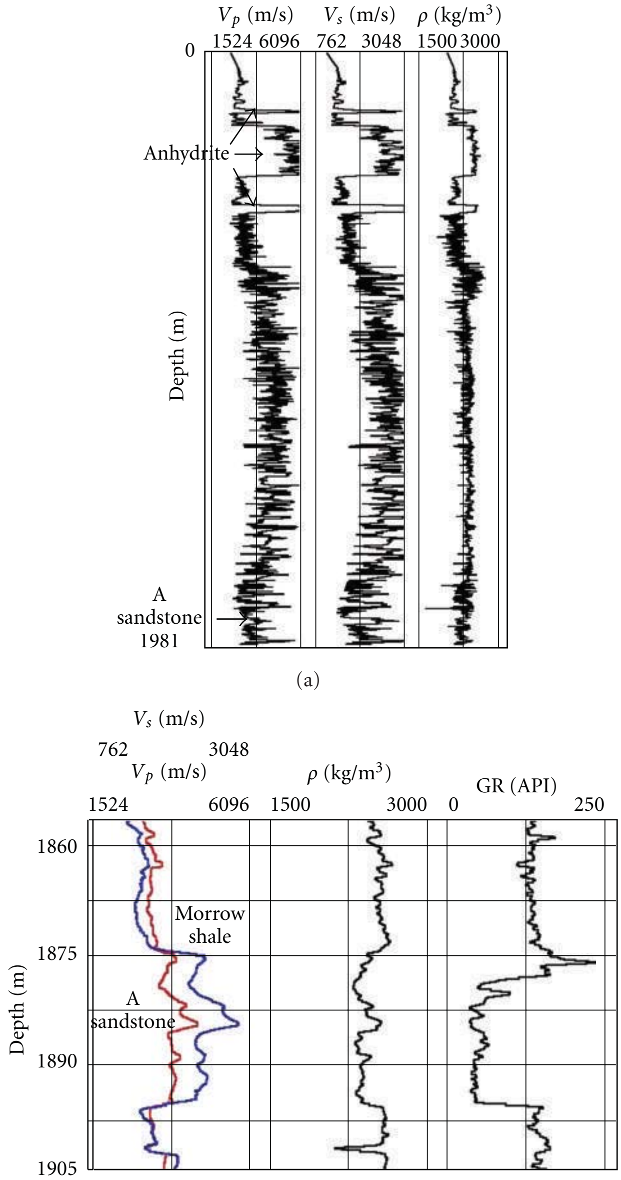

(a)

(b)

Figure 3: Well logs used for modeling show Morrow A sandstone at 1875 m and shallow anhydrite layers. Close-up of the Morrow interval (b) shows the strong S-wave velocity (blue curve) contrast as compared to P-wave velocity (red curve) contrast between Morrow shale and A sandstone.

2. Geologic Background

The study area is located in Postle Field, Anadarko Basin, Oklahoma (Figure 1). The area is flanked in the west by the Keys dome, in the south by the Amarillo uplift and in the north by the Hugoton embayment [31]. Figure 2 provides the generalized stratigraphic column of the Postle Field and the stratigraphy of this basin has been discussed in detail by Bowen and Weimer [32] and Henry and Hester [33]. Mississippian and older rocks are mainly carbonates, whereas Pennsylvanian and younger rocks are mainly shales with

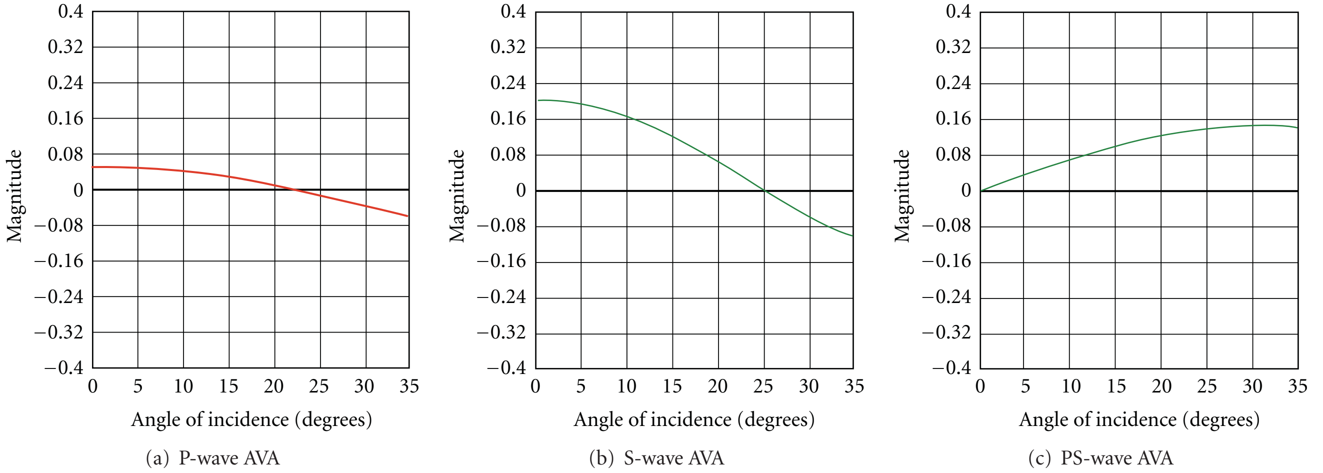

(a) P-wave AVA

(b) S-wave AVA

(c) PS-wave AVA

Figure 4: Amplitude versus angle (AVA) response for P-wave, S-wave, and PS-wave for the velocity contrast between Morrow shale and A sandstone shown in Figure 3.

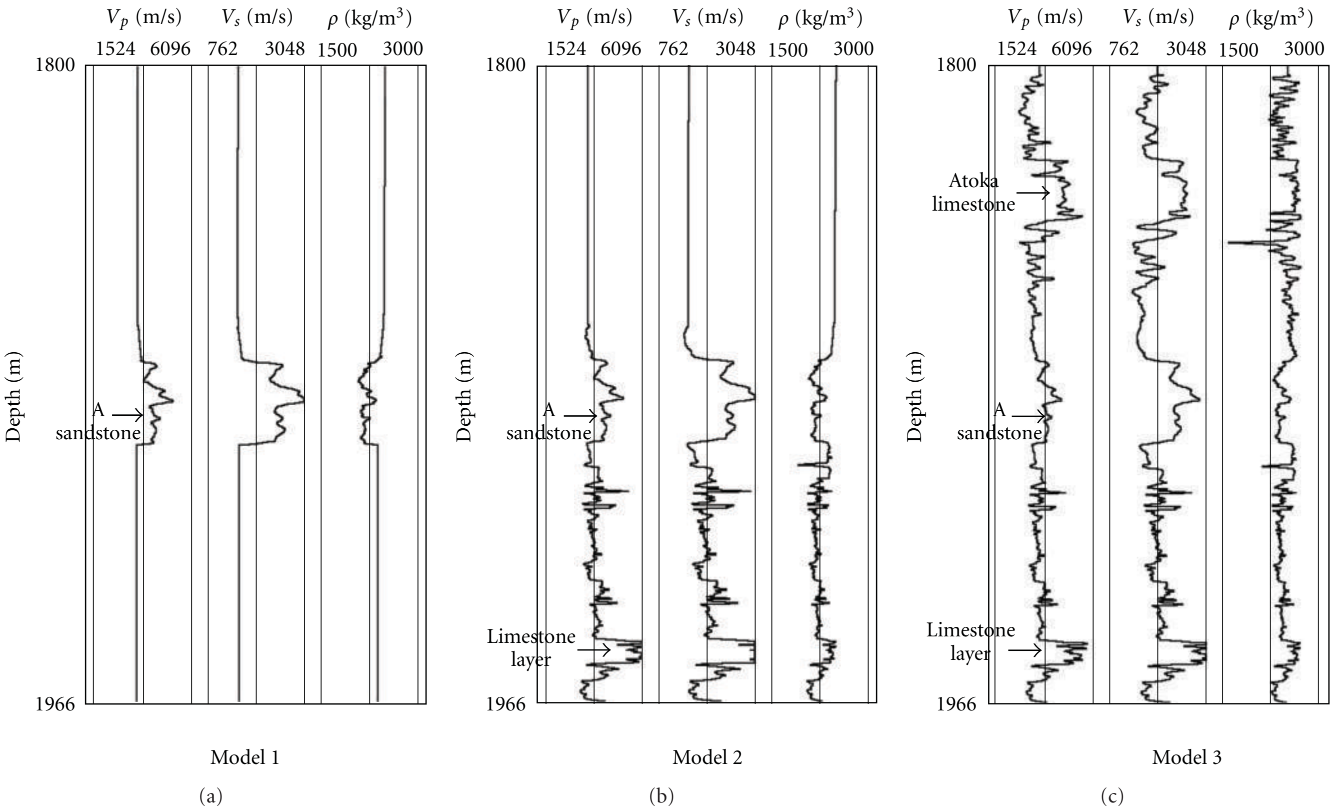

(a)

(b)

(c)

Figure 5: The three different 1D models used to understand the Morrow A sandstone response on synthetic gathers. Model 1—only Morrow A sandstone interval, Model 2—Morrow A sandstone with one limestone layer below, and Model 3—Morrow A sandstone with Atoka limestone above and one limestone layer below.

some sandstones. The Morrow formation lies uncoformably on top of Mississipian strata and conformably below the Thirteen Fingers limestone [34]. The Upper Morrow consists of multiple stacked lenticular sandstone bodies formed within valley fill complexes. The Morrow sandstones are major hydrocarbon producers in this basin along with the shallow Permian Council Grove and Chase Group carbonate rock gas reservoirs. The main reservoir in our study area is the Morrow A sandstone which are at a depth of around 1875 m and have an average thickness of 10 m (0–30 m).

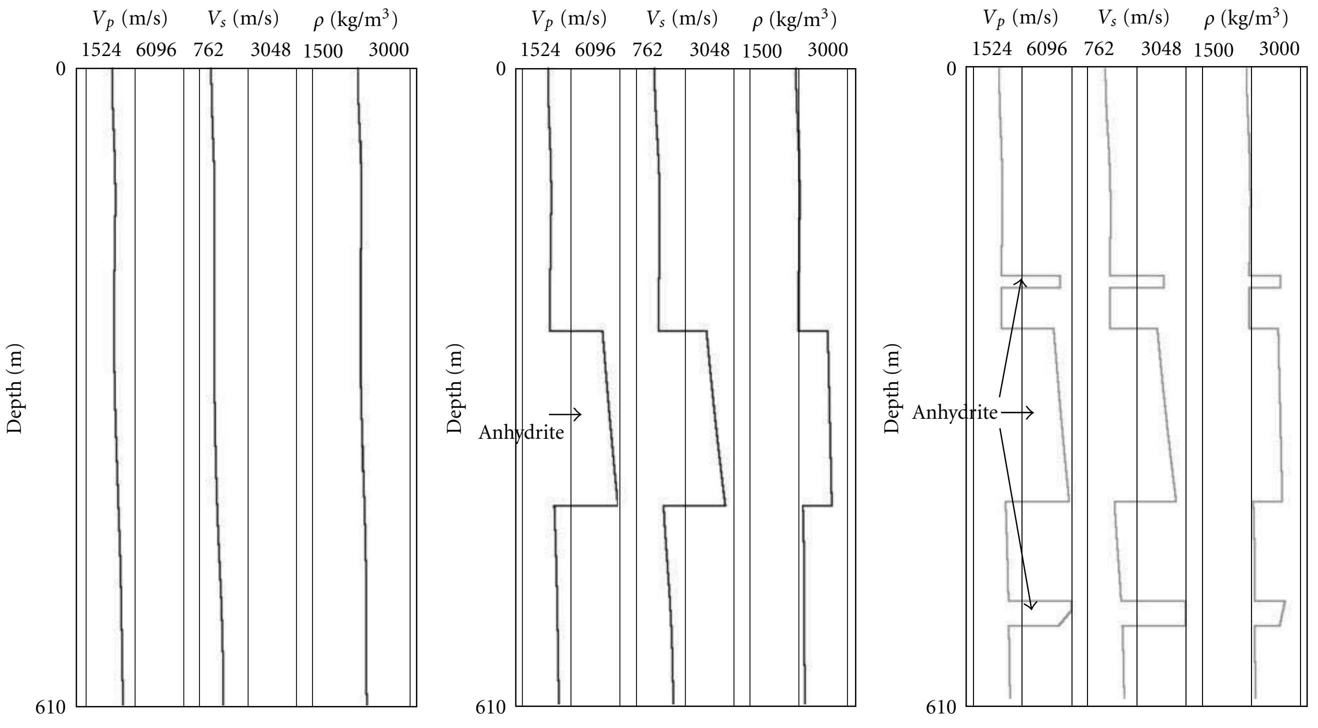

(a) Model a

(b) Model b

(c) Model b

Figure 6: The three different versions of the 1D models shown in Figure 5, used to understand the effect of shallow anhydrite layers. Model a—no anhydrite layer, Model b—one anhydrite layer, and Model c—three anhydrite layers.

The average porosity of this sand is 17% and the permeability is around 50 md.

3. Elastic Modeling

Seismic modeling is done to compute synthetic seismograms for a given geologic model. There are different methods for simulating seismic wave propagation including ray tracing, reflectivity, integral-equation, finite difference, finite element, and so forth, [36–38]. There are also hybrid approaches which combine two or more of the above methods [39]. In this study, we have used the finite difference technique for computing the elastic wave equation and generating the synthetic seismograms [40, 41]. It is necessary to compute synthetic gathers for horizontal and vertical source-receiver combinations in order to compare the seismic signatures of different wave modes (P-, PS-, and S-waves). Finite difference modeling simulates the full wavefield while preserving the amplitudes and phases. It helped in understanding the strong effect of multiples due to shallow high velocity anhydrite layers. Finite difference modeling is considered to be expensive in terms of computing time and memory, but since we are using a 1D model, this was not a problem. 2D multicomponent gathers are generated using this 1D model. The grid size is 4.572 m × 4.572 m and the model size is kept large enough to avoid interference between side reflections from the boundary and the main events. Finite difference modeling also allows us to look at the propagated wave field at certain time by taking snapshots.

4. Model Building

Well logs from a well with dipole sonic logging have been used for elastic parameters. Figure 3 shows the P-velocity (V_p), S-velocity (V_s), and density (ρ) logs from that well. There are three anhydrite layers between the surface and 550 m, and the reservoir Morrow A sandstone is at a depth of 1875 m. The close-up of Morrow level in Figure 3 shows the strong S-wave velocity contrast between Morrow shale and A sandstone as compared to P-wave velocity contrast. This leads to good amplitude versus angle (AVA) response for S-wave at the top of Morrow A sandstone as compared to P-wave and PS-wave (Figure 4). The well logs shown in Figure 3 are blocked, smoothed, and modified to have a detailed understanding of seismic response at the Morrow level. The three models (Figure 5) built to understand the Morrow A sandstone AVO response and interference effects are the following.

Model 1: only Morrow A sandstone interval,

Model 2: Morrow A sandstone with one limestone layer below,

Model 3: Morrow A sandstone with Atoka limestone above and one limestone layer below.

The presence of shallow high velocity anhydrite layers limits the incident angle and offset at the top of Morrow A sandstone. The rays are critically refracted at small angles of incidence at the top of the high velocity anhydrite layers,

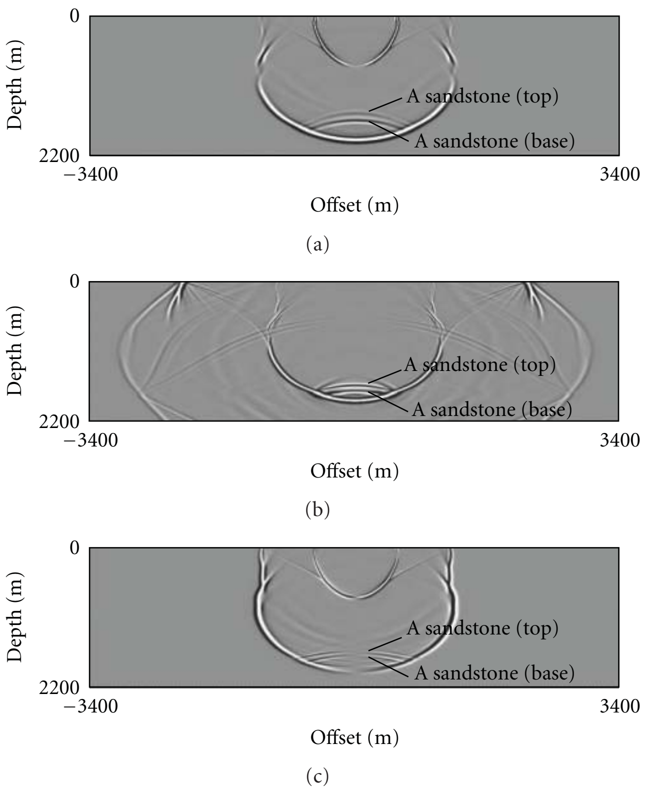

FIGURE 7: Wave propagation snapshots for (a) P-wave, (b) S-wave and (c) PS-wave using Model 1a. We observe that S-wave shows a stronger Morrow A sandstone response as compared to P- and PS-wave.

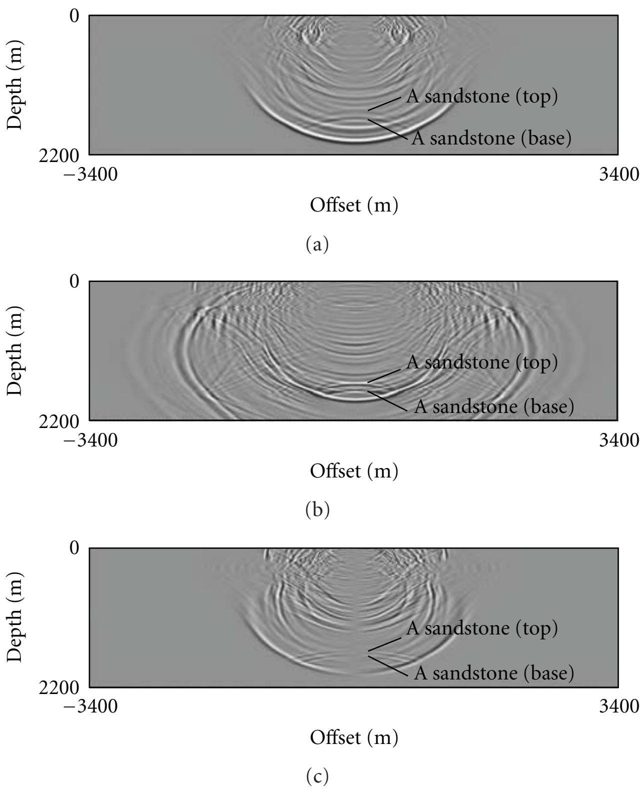

FIGURE 8: Wave propagation snapshots for (a) P-wave, (b) S-wave and (c) PS-wave using Model 1c. We observe that amplitude of multiples due to shallow anhydrite layers is stronger than the reflection from the top of Morrow A sandstone in P- and PS-wave snapshot. Whereas the Morrow A sandstone response is stronger than the amplitude of multiples in S-wave snapshot.

and hence, we do not get large angles and offsets for the target reservoir. The reverberations due to these high velocity anhydrite layers create strong multiples which have an adverse effect on data and are discussed in next section. These shallow layers vary in thickness and lithology laterally. To have a better understanding of the effect of these shallow anhydrite layers, Models 1, 2, and 3 are further divided into following three models (Figure 6).

Model a: No anhydrite layer,

Model b: One anhydrite layer,

Model c: Three anhydrite layers.

5. Morrow A Seismic Signature

Gathers are calculated for horizontal and vertical sources, and both the horizontal and vertical components are recorded. To have a close match with the field data, in this full waveform modeling study, all receiver components record different types of waves and none of the source-receiver combinations produce a pure P-, PS-, or S-wave records. But for simplicity, in this paper, we will refer to vertical source-vertical receiver recording as P-wave, vertical source-horizontal receiver recording as PS-wave, and horizontal source-horizontal receiver recording as S-wave recording, because these are the dominant waves in these source-receiver combinations. An 18 Hz Ricker wavelet is used for P-wave modeling and a 13 Hz Ricker wavelet is used for S- and PS- wave modeling. These wavelets are chosen based on the dominant frequency observed at Morrow level in real data.

5.1. Wave Propagation Snapshot. We know from well logs that the acoustic impedance contrast between Morrow sandstone and encasing shale is weak as compared to the shear impedance contrast. The wave propagation snapshots for P-wave, PS-wave, and S-wave confirm these observations. Figures 7(a) and 7(c) show the weak P-wave and PS-wave response at the top of Morrow A sandstone respectively, as compared to the strong S-wave response (Figure 7(b)), which is similar to the observation in Figure 5. This is for the case of Model 1a, that is, just the Morrow A sandstone with no anhydrite layer. Figures 8(a), 8(b), and 8(c) show the P-wave, S-wave and PS-wave propagation snapshot for Model 1c, that is, just the Morrow A sandstone with three anhydrite layers. The amplitude of multiples due to anhydrite layers is stronger than the reflection from the top of Morrow A sandstone in case of P- and PS-wave (Figures 8(a) and 8(c)), whereas for S-wave, the Morrow A sandstone response is stronger than the amplitude of multiples (Figure 8(b)).

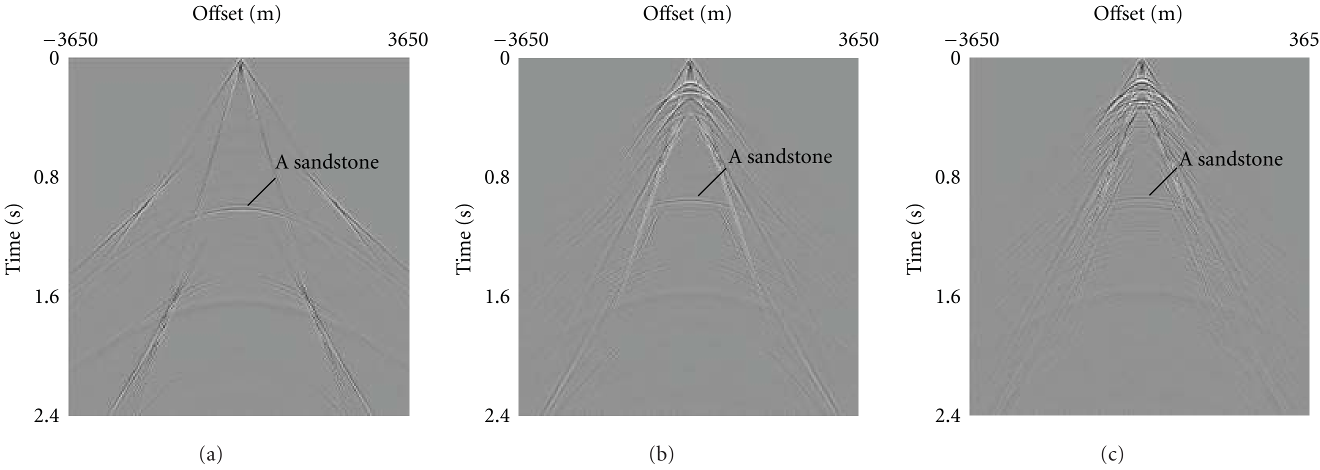

(a) (b) (c)

Figure 9: P-wave gather for the case of (a) Model 1a, (b) Model 1b, and (c) Model 1c, shows that the amplitude of multiples due to shallow anhydrite layers is comparable to the amplitude of primary reflections.

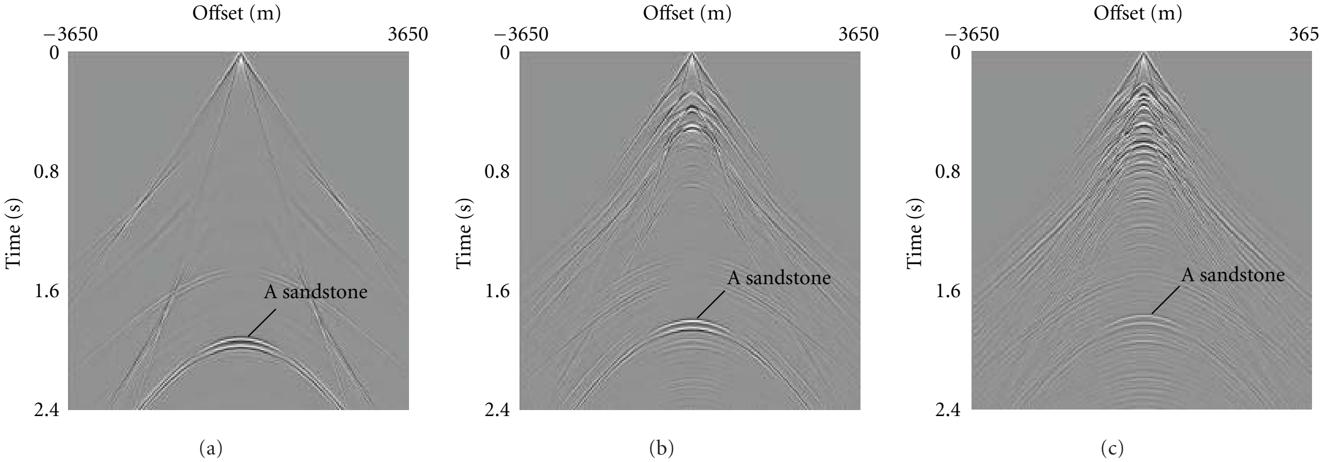

(a) (b) (c)

Figure 10: S-wave gather for the case of (a) Model 1a, (b) Model 1b, and (c) Model 1c, shows that the primary reflection amplitude is stronger than the amplitude of multiples.

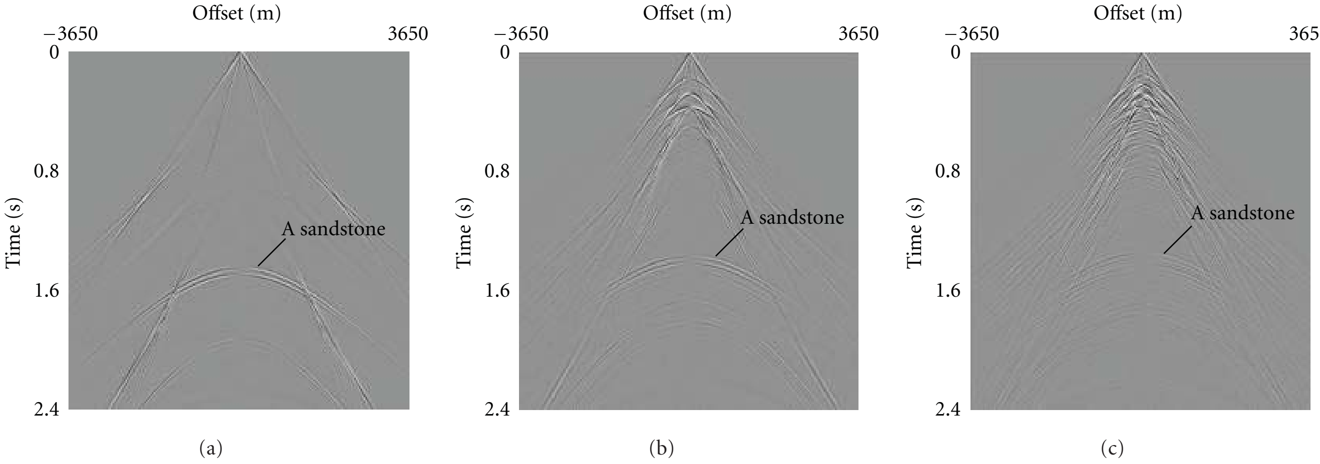

(a) (b) (c)

Figure 11: PS-wave gather for the case of (a) Model 1a, (b) Model 1b, and (c) Model 1c, shows that the amplitude of multiples due to shallow anhydrite layers is comparable to the amplitude of primary reflections.

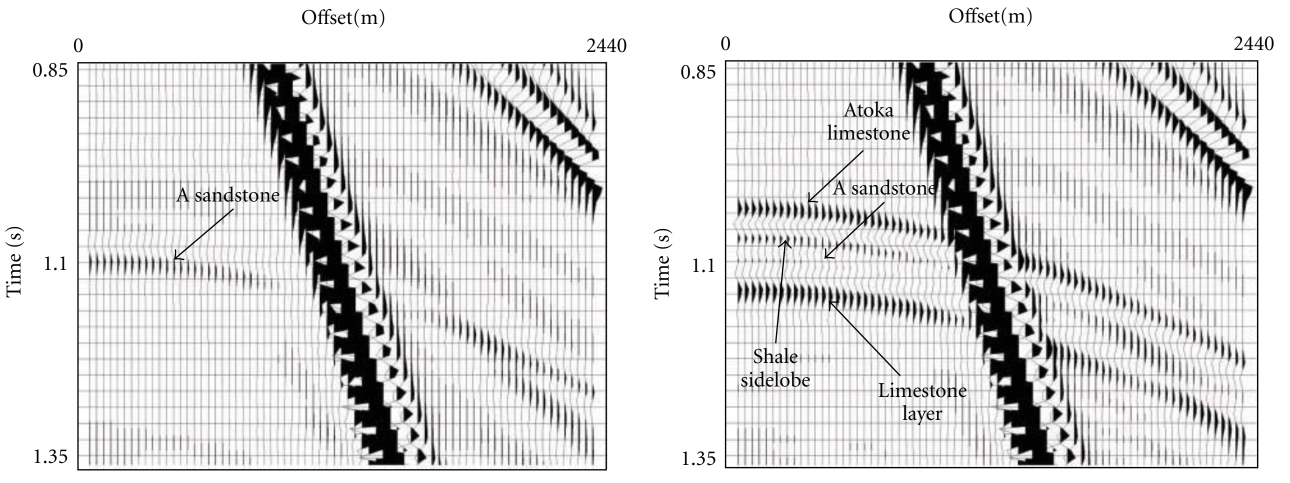

(a) (b)

Figure 12: (a) P-wave gather for Model 1a shows a Class II AVO anomaly at the top of Morrow A sandstone where a small peak changes into trough with offset. (b) The P-wave gather for Model 3a shows that the peak at the top of Morrow A sandstone is interfered with the side lobe of Morrow shale and bottom limestone layer. This gives a peak doublet at near offsets which changes to a single peak at far offsets.

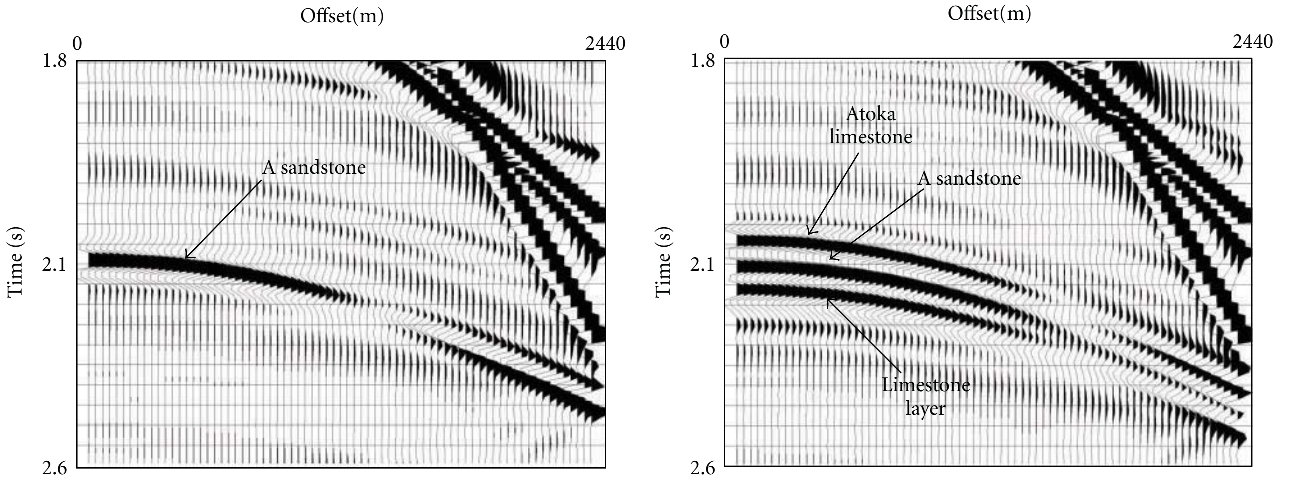

(a) (b)

Figure 13: (a) S-wave gather for Model 1a shows a strong peak response at the top of Morrow A sandstone which changes to trough with offset. (b) The S-wave gather for Model 3a shows that even in the presence of overlying shale and bottom limestone layer the Morrow A sandstone shows a distinct high amplitude AVO response.

5.2. Effect of Multiples. Internal multiples ringing in the shallow anhydrite layers have a significant effect on P-wave, PS-wave, and S-wave gathers. To have a better understanding of the effect of multiples on the three wave modes (Figures 9, 10, and 11), synthetic gathers are generated using Models 1a, 1b, and 1c. Since the acoustic impedance contrast between Morrow sandstone and shale is weak, the reverberations due to the anhydrite layers overshadow the Morrow A sandstone response in P-wave (Figure 9(c)). Melvin [42] describes the adverse effects of multiples in P-wave data at Postle Field and suggests ways to correct them. These multiples do not affect the S-wave gather significantly, since the Morrow A sandstones have a distinct high amplitude response compared to the weak reflectivity of multiples (Figure 10(c)). The PS-wave reflection from the Morrow A sandstone is also weak. Thus, the reverberations due to anhydrite layers overshadow the Morrow A sandstone response in PS-wave gather (Figure 11(c)). The data gets badly affected with increasing anhydrite layers.

5.3. Interference Effect. Figures 12, 13, and 14 show the zoomed sections from the P-wave, S-wave, and PS-wave gathers respectively. Models 1a and 3a with 19.5 m sandstone thickness have been used for understanding Morrow A sandstone AVO response and interference effects. For Model 1a, the P-wave gather shows a weak class II AVO response at the top of Morrow A sandstone (Figure 12(a)), where the peak changes to trough with offset. This is similar to

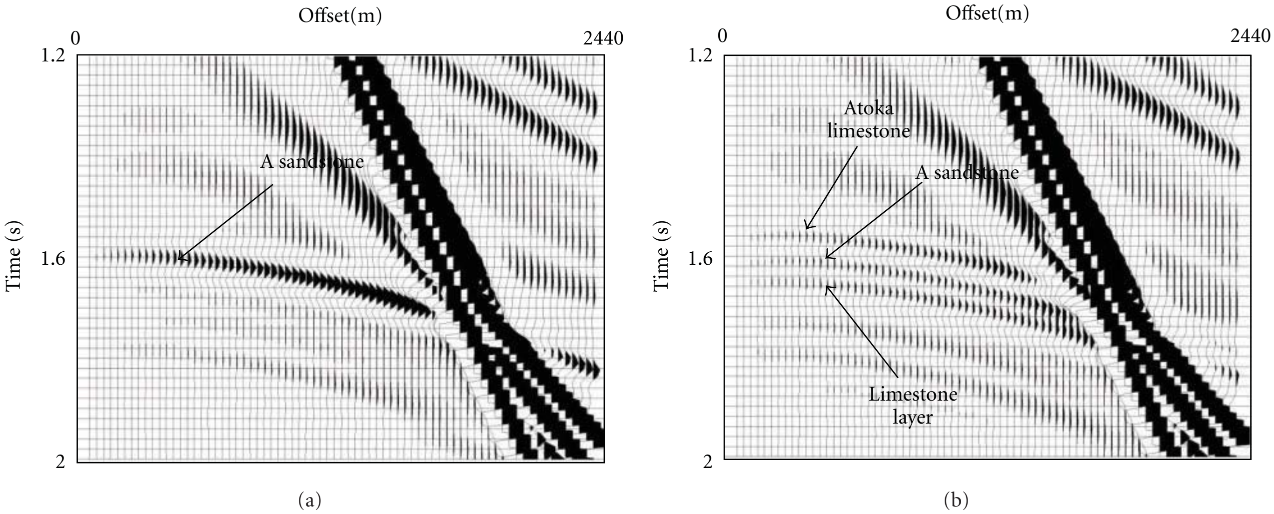

(a)

(b)

Figure 14: (a) PS-wave gather for Model 1a shows increasing peak amplitude with offset at the top of Morrow A sandstone. (b) The PS-wave gather for Model 3a shows that the peak response at the top of Morrow A sandstone is weakened due to the interference with Morrow shale and bottom limestone layer.

the P-wave AVA response shown in Figure 4. Figure 12(b) shows the interference effect of the Morrow shale and the underlying limestone layer on the Morrow A sandstone AVO response. It leads to a peak doublet with side lobe of Morrow shale showing stronger amplitude. With increasing offset the peak doublet changes into a single peak which makes P-wave AVO analysis difficult. Stacking will also give a peak doublet for Morrow A sandstone, having inseparable peaks (observed in real P-wave stack, Figure 18(a)). This makes horizon picking difficult and P-wave interpretation challenging.

The change in rigidity between the reservoir sandstone and surrounding shale causes a strong seismic expression on the S-wave data. For Model 1a, the response of Morrow A sandstone is a peak which turns to trough with increasing offsets (Figure 13(a)) and is similar to the S-wave AVA response shown in Figure 4. Even for Model 3a which has overlying shale and an underlying limestone layer, the S-wave gather shows a distinct high amplitude AVO response for Morrow A sandstone (Figure 13(b)). The synthetic gather shows that S-wave AVO can be very useful in characterizing the A sandstones. The real data S-wave stack (Figure 18(b)) shows a distinct high amplitude peak for Morrow A sandstone which makes interpretation simpler. For Model 1a, the PS-wave shows a weak peak response at the top of A sandstone and the amplitude increases with offset (Figure 14(a)). This is similar to the PS-wave AVA response shown in Figure 4. The peak response due to Morrow A sandstone is weakened due to the interference effect of Morrow shale and bottom limestone layer (Figure 14(b)).

The reservoir sandstone thickness varies from 0–30 m in the study area. Wedge modeling is done to understand the effect of changing sand thickness on different wave components. The sandstone thickness in the model is changed from 0 to 32.5 m at an increment of 6.5 m to understand the interference effect. P-wave, S-wave, and PS-wave gathers are displayed side by side in Figure 15 to compare the AVO responses for changing sand thicknesses. When the Morrow A sandstone is absent, the P-wave gather shows a weak peak response from the side lobe of Morrow shale. As the sand thickness increases, we observe a peak doublet after 13 m of sandstone thickness. The peak amplitude of this doublet increases with increasing sand thickness.

S-wave gather shows separate peak response even till 6.5 m of A sandstone. The peak amplitude for the S-wave event increases with increasing sandstone thickness. In the PS-gather, the peak at the top of A sandstone starts interfering with the peak of bottom limestone layer as the thickness drops down to 13 m sandstone, making interpretation difficult. For PS-waves also, the peak amplitude increases with increasing sandstone thickness. So, it is observed that with P-waves and PS-waves, it is difficult to detect A sandstones less than 13 m thick, whereas the S-wave gather shows a distinct high amplitude response even for 6.5 m sandstone thickness, which is very useful since the average thickness of A sandstone in the study is approximately 10 m.

6. Field Data Results

The Reservoir Characterization Project in Colorado School of Mines acquired and processed a 3D-9C survey in Postle field for reservoir characterization of Morrow A sandstones and for monitoring a CO2 flood. The study area is nearly 16.2 sq· km with 16 shot and receiver lines (Figure 16). The shot lines are in E-W direction with 268.2 m spacing and the receiver lines are in N-S direction with 268.2 m spacing. The shot point and receiver point interval is 33.5 m and the bin size is 33.5 m × 33.5 m. Data acquisition was done by keeping all the receivers active for each shot. While processing, the pre-stack shear wave data is rotated using Alford rotation [43], with fast shear (S1) in the direction of N105E. This fast

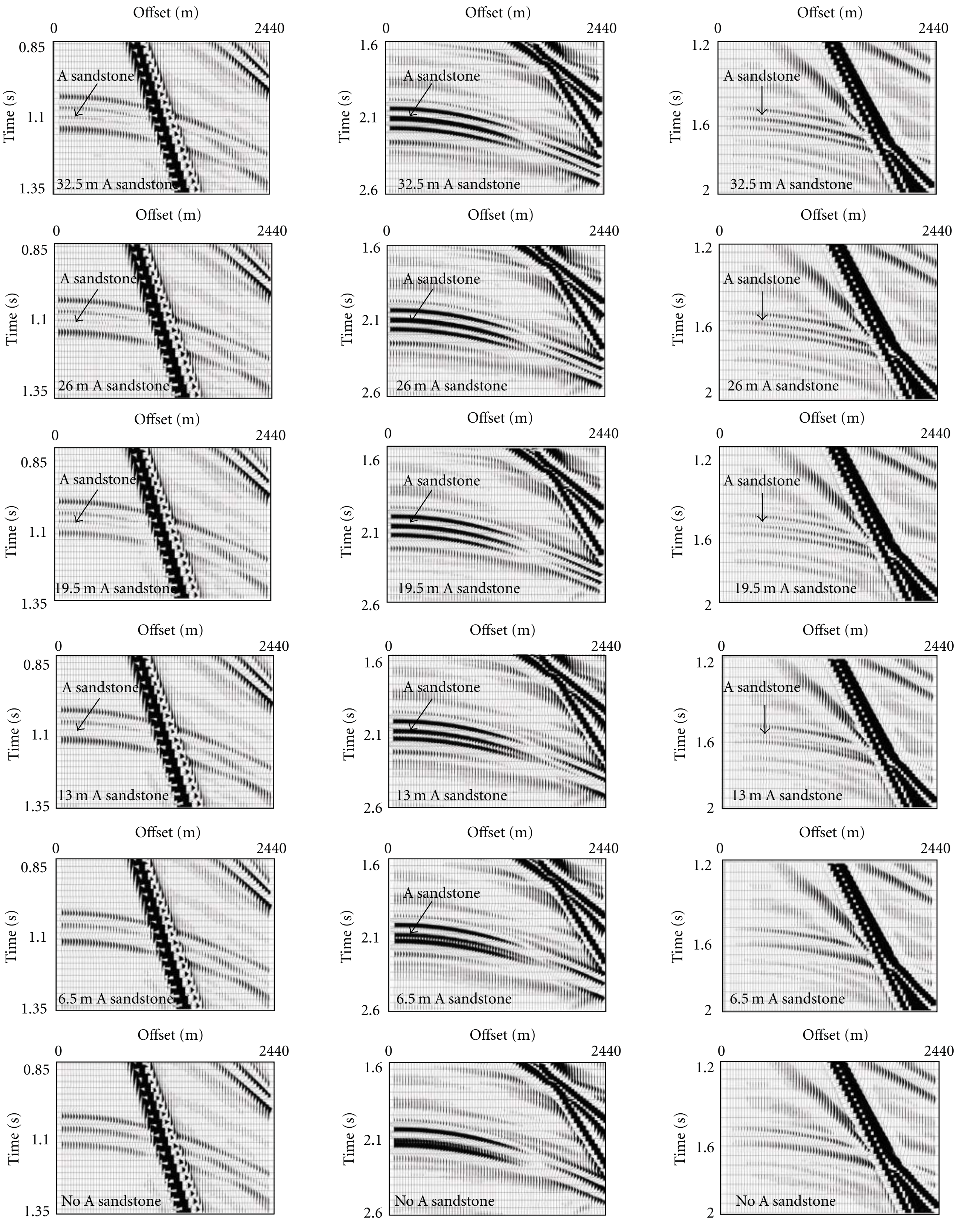

Figure 15: P-wave gathers (left), S-wave gathers (center) and PS-wave gathers (right) generated using Models 3a, with changing A sandstone thickness from 0 to 32.5 m. The synthetic gathers show that it is difficult to detect less than 13 m sandstone thickness using P-waves, since the peak doublet is absent. In PS-wave gather, the separate peak response is not present for 13 m of A sandstone thickness. The S-wave gather shows a distinct peak response even for 6.5 m of A sandstone thickness.

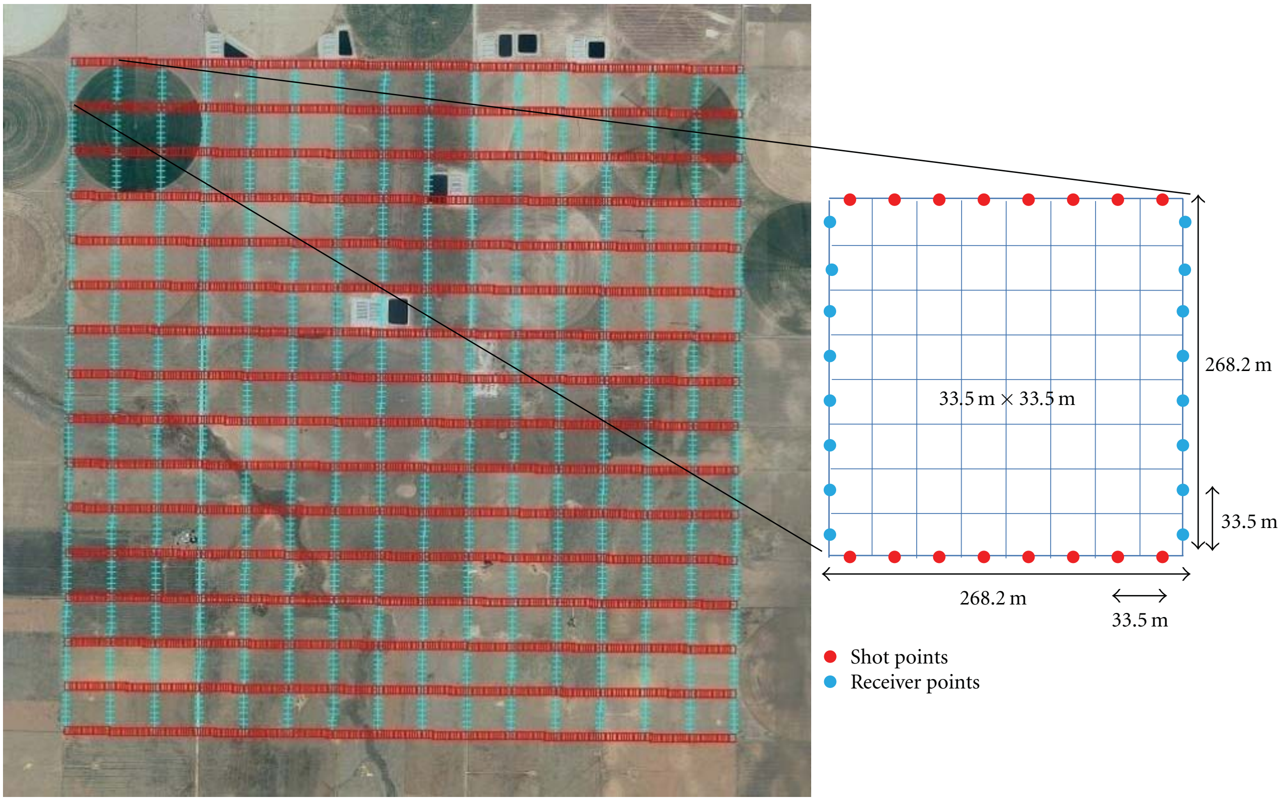

Figure 16: Acquisition parameters. Shot points are shown by red dots and receiver points are shown by blue dots. There are 16 shot lines in E-W direction and 16 receiver lines in N-S direction. Both shot and receivers point spacing is 33.5 m, and the data is binned at 33.5 m × 33.5 m.

shear wave direction or the direction of maximum horizontal stress has been obtained from well log information.

The P-wave gather in Figure 17(a) shows the AVO response similar to the synthetic gather (Figure 12(b)) around 1.07 s, where a peak doublet at near offset changes to single peak with increasing offset. The S1-wave gather in Figure 17(b) also shows an AVO response similar to the synthetic gather (Figure 13(b)) around 2.08 s, where a strong peak changes to trough with increasing offset. Figures 18(a) and 18(b) shows the P- and S1-wave stacks, respectively, along an inline passing through the well used for elastic modeling. Gamma Ray log from that well is shown by red curve in the stacks. The dip of the reflectors in P-wave stack and S1-wave stack is different, because the statics for each stack was computed independently. In the P-wave stack (Figure 18(a)), the horizon picked in blue is the Morrow shale, and the strong peak reflector above is Atoka limestone. Due to the interference with the side lobe of Morrow shale, Morrow A sandstone shows a peak doublet below Morrow shale trough. There are other Morrow sandstone layers below, but these cannot be seen clearly in the P-wave stack because of the weak acoustic impedance contrast. In the S1-wave stack (Figure 18(b)) the horizon picked in blue is the Morrow shale and the reflector above is Atoka limestone. In the S1-wave stack, the Morrow A sandstone has a strong peak amplitude below the Morrow shale trough. Due to the addition of static correction, the Morrow sandstone reflector in S1-wave stack appears around 2.25 s as compared to 2.08 s in gather. Owing to the good shear impedance contrast between Morrow sandstone and shale we can observe strong reflectors below Morrow A sandstone as well, indicating presence of other sandstone bodies below. This can help in future investigation of deeper reservoir possibilities.

P- and S1-amplitude maps were extracted along the Morrow A peak and are shown in Figures 19(a) and 19(b), respectively. Due to the adverse effect of multiples in the converted-wave data, PS-amplitude map has not been shown here. Those data need further processing to remove that noise. For the P-wave amplitude map, the sum of positive samples is computed in a 0.035 s window centered on Morrow A peak. For S1-wave the window is 0.05 sec. The window size for both P and S1-wave is chosen so that the complete Morrow A sandstone peak amplitude is considered. The well pattern is overlaid on top of the amplitude maps, since these are the places were A sandstone have been encountered. The wells drilled outside this pattern have not encountered Morrow A sandstone, hence we expect to see high amplitudes mainly in this well pattern area. The high amplitudes in S1-wave map lie mostly within the well pattern as compared to P-wave map. Thus, the well pattern matches better with the sandstone distribution map obtained from S1-wave stack as compared to P-wave stack. Figure 20 shows the gross sandstone thickness map constructed by picking the top and base of A and A1 sandstone in well

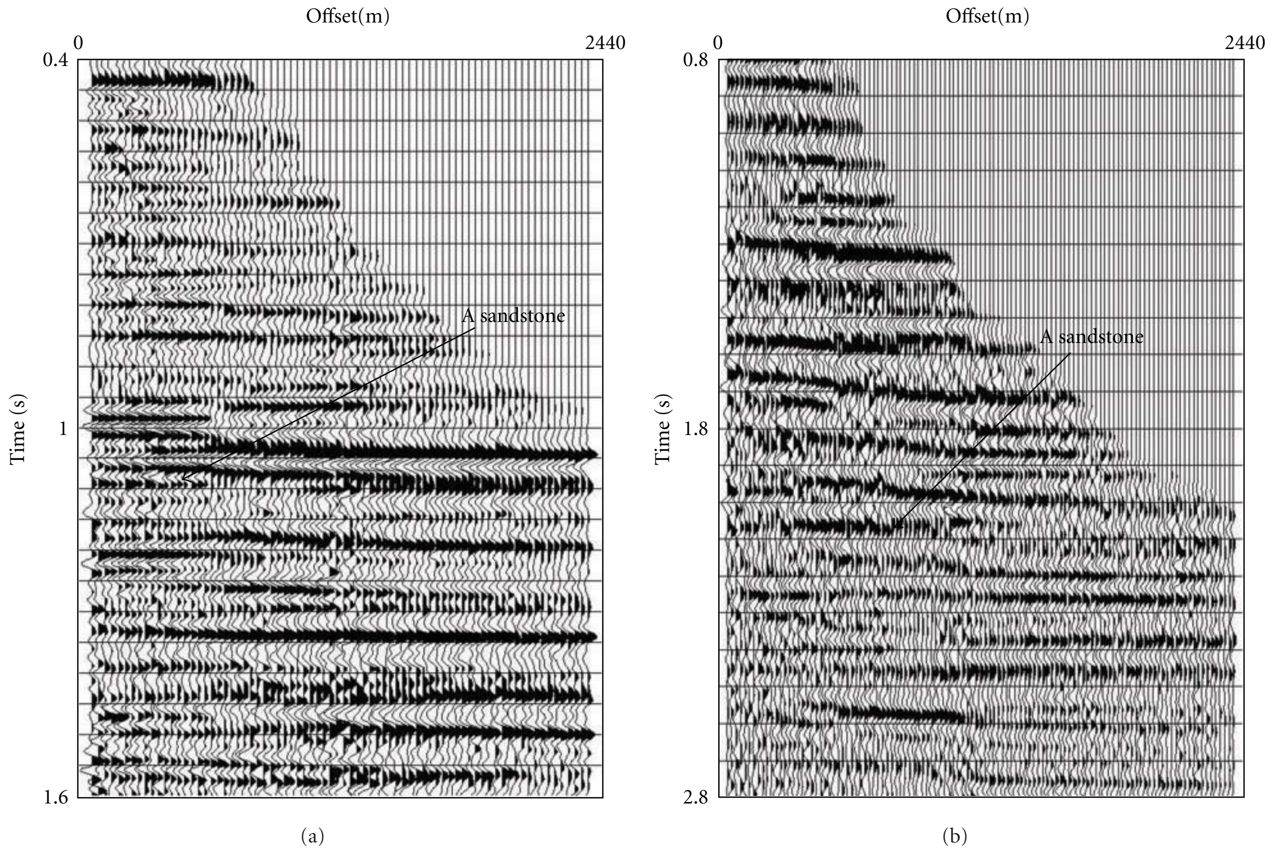

Figure 17: (a) P-wave gather shows a peak doublet at the top of Morrow A sandstone (1.07 s) which changes to single peak at far offsets. (b) S1-wave gather shows a peak response at the top of Morrow A sandstone (2.08 s) changing to trough with offset. The AVO response in real data P- and S1-wave gathers matches with the synthetic gather AVO response shown in Figures 12(b) and 13(b).

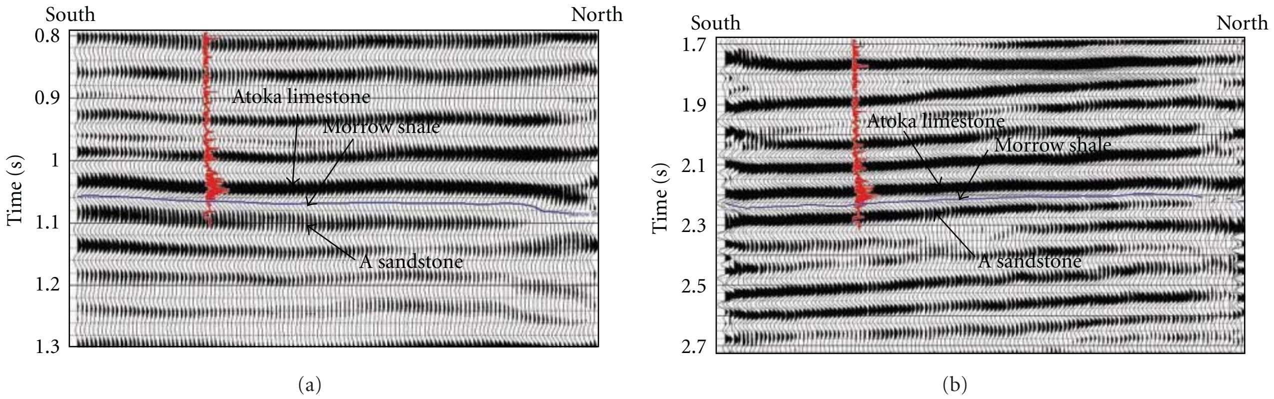

Figure 18: The above sections are (a) P-wave stack and (b) S1-wave stack along an inline passing through the well used for modeling study. The Morrow A sandstone peak interferes with the side lobe of shale to give a peak doublet in P-wave stack. The S1-wave stack has a distinct Morrow A sandstone peak response. The S1-wave stack also shows some high amplitude sand layers below Morrow A which are not clearly evident in P-wave stack.

logs and interpolating the calculated thickness between well locations (courtesy Whiting Petroleum). S1-amplitude map shows a trend similar to the gross A sandstone thickness map (Figure 20(a)), except for the high amplitude anomalies in the west (shown in black oval). The high amplitudes in the west may be due to Morrow A1 sandstone (Figure 20(b)), but further investigation is needed to confirm this. The Morrow A1 sandstone is another sandstone layer lying 3–15 meters below A sandstone and is prominent in western part of the study area. So, in the western part, where there is no Morrow A sandstone, we may get high amplitudes due to the presence of Morrow A1 sandstone.

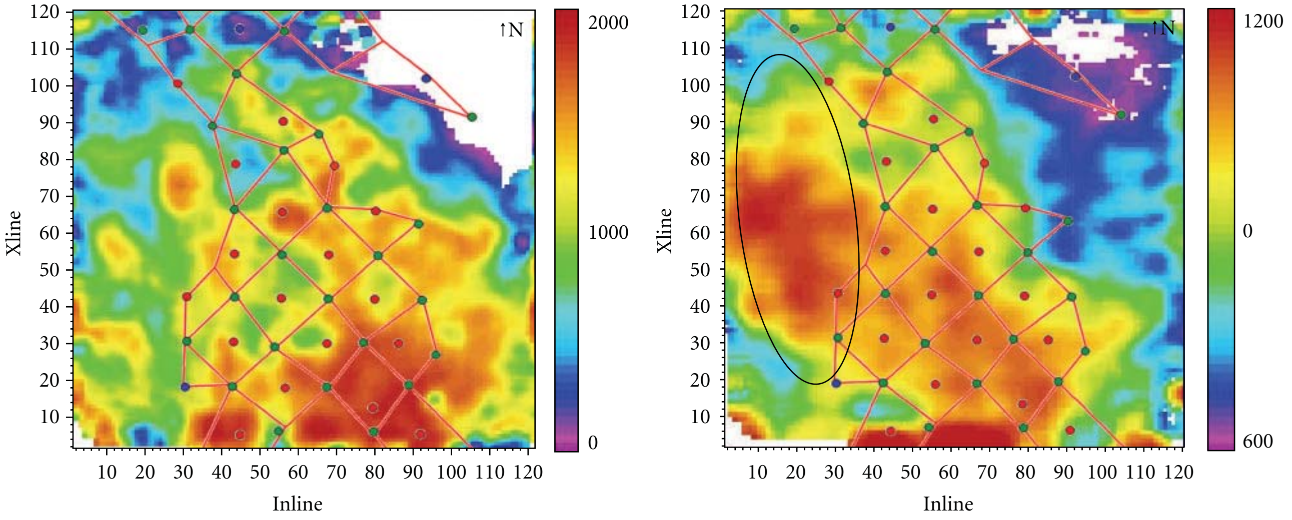

(a)

(b)

Figure 19: (a) P-wave amplitude map and (b) S1-wave amplitude map are shown with well pattern overlaid on them (green dots represent producer wells; red dots represent injector wells). The amplitude map is obtained by computing sum of positive samples in a 0.035 s window centered around peak doublet for P-wave and 0.05 s window centered around peak for S1-wave. The S1-wave amplitude shows better match with the well pattern, except in the western part of the study area (shown by black oval) where there is presence of Morrow A1 sandstone (Figure 20(b)).

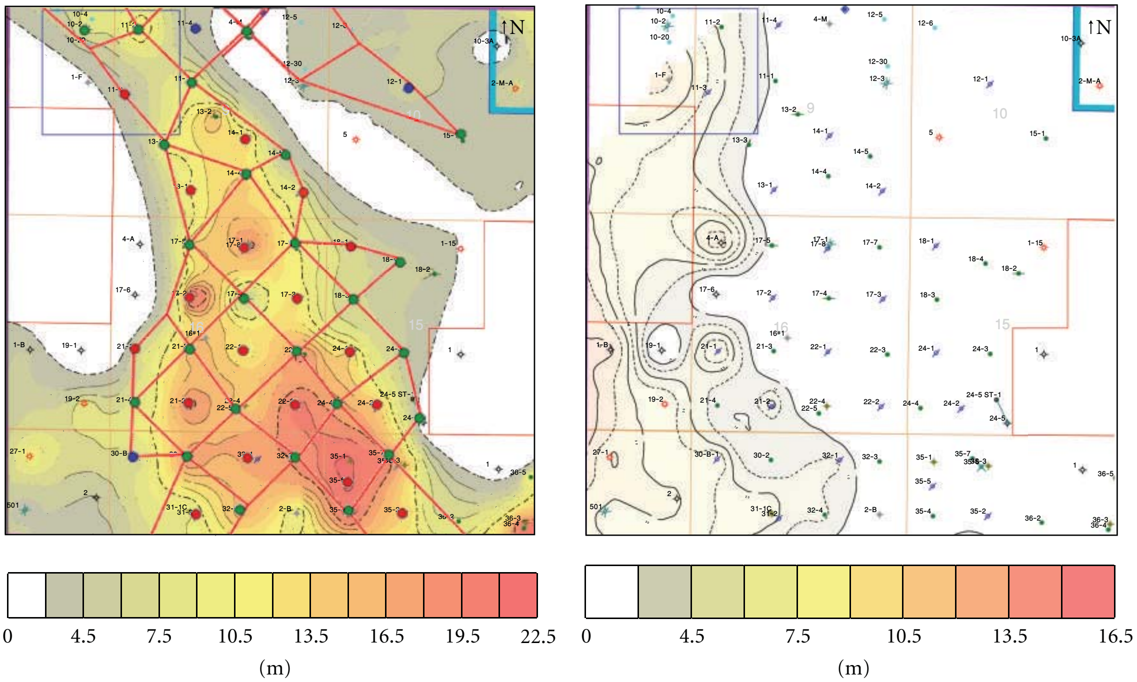

(a)

(b)

Figure 20: Gross sandstone thickness maps for (a) Morrow A sandstone and (b) Morrow A1 sandstone (courtesy Whiting Petroleum). The star in the map is the well used for elastic modeling.

The P- and S1-amplitude values are computed in a 4 × 4 (inline × xline) radius around the well locations in high fold area and compared with the gross A sandstone thickness value at each well location (Figure 21). Elastic modeling showed that for both P- and S-waves the peak amplitude increases with increasing A sandstone thickness. Figure 21 proves that the P- and S1-ampitude values increase with increasing A sandstone thickness. It also shows that S1-amplitude map has better correlation (correlation coefficient 0.60) with gross A sandstone thickness as compared

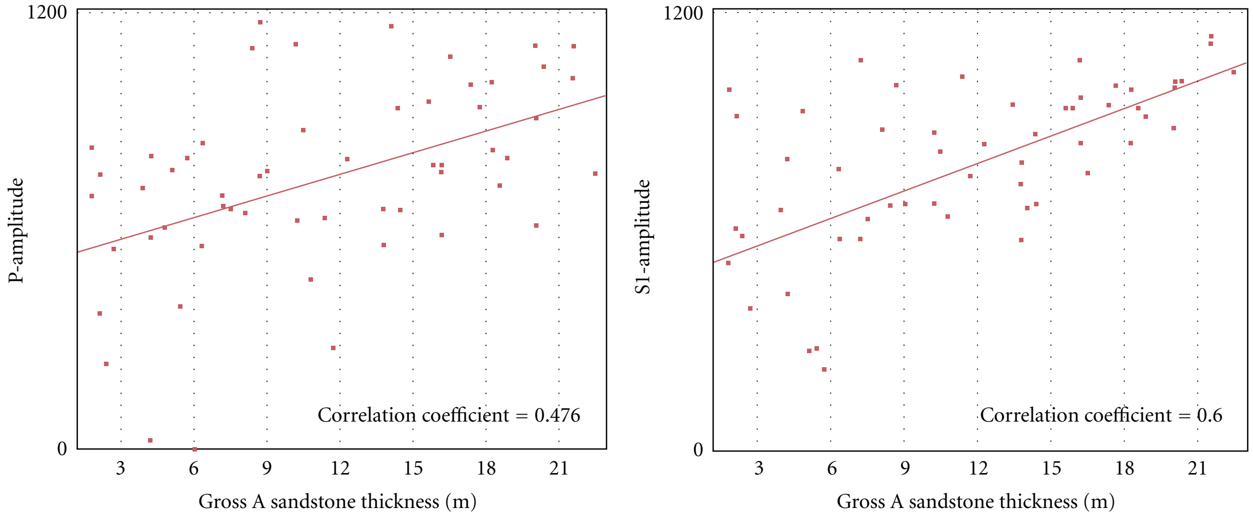

(a)

(b)

Figure 21: S1-wave amplitude map has a better correlation to gross A sandstone thickness than the P-wave amplitude map. For the S1-wave amplitude map, the correlation is not good when the sandstone thickness is less than 6.5 m, whereas the P-wave amplitude map does not show good correlation even for thicker sandstones.

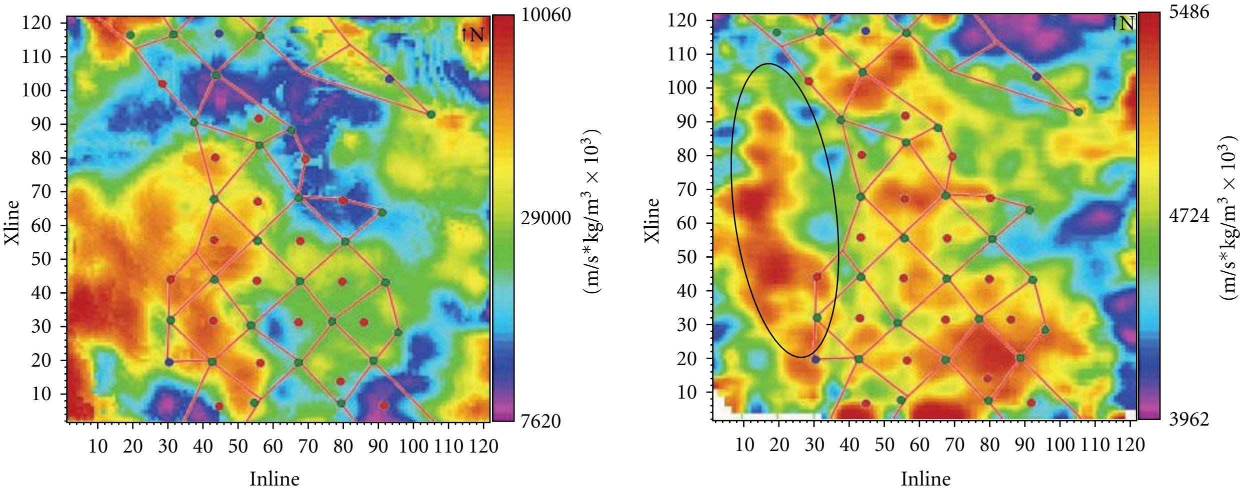

(a)

(b)

Figure 22: (a) P-wave impedance map and (b) S1-wave impedance map (right) are shown with well pattern overlaid on them (green dots represent producer wells; red dots represent injector wells). For P-waves, the impedance map is obtained by computing rms amplitude in a 0.009 s window centered on Morrow A sandstone. For S1-waves, the impedance map is obtained by computing rms amplitude in a 0.01 s window centered on Morrow A sandstone [35]. The S1-wave impedance shows better match with the well pattern. The high impedance in the west part of the study area (shown by black oval) ties with the presence of A1 sandstone (Figure 20(b)).

to P-amplitude map (correlation coefficient 0.476). The P-wave amplitude map does not show good correlation even for thicker sandstones and the correlation is almost same for all sandstone thicknesses. The S1-amplitudes map has good correlation for thicker sandstones and the correlation drops down mainly below 6.5 m of sandstone as predicted by the modeling. Thus, S1-amplitude map is a good indicator of Morrow A sandstone distribution and thickness.

Pinto [35] performed post stack impedance inversion on P- and S1-wave stacks and the results are shown in Figure 22. Comparing the P-impedance map (Figure 22(a)) with well pattern and gross A sandstone thickness map suggests that it is unable to map Morrow A noticeably. The failure of P-impedance map to detect the A sandstones is due to weak impedance contrast between Morrow shale and A sandstone, and also due to the interference between the A sandstone peak with the side lobe of Morrow shale and underlying limestone layer. Excluding the high impedance anomaly in the west, the S1-impedance map (Figure 22(b)) shows good sandstone distribution and ties well with the overlaid well pattern and the gross A sandstone distribution shown in Figure 20(a). The high impedance in the west part of the study area matches with the gross A1 sandstone distribution shown in Figure 20(b).

CO_2 flooding in the study area has proceeded towards the north part of the block and it is very important to find the sandstone distribution in the north. The S1-impedance map helps us in mapping sands in the north part of the block, where P-impedance map completely fails. This can be very useful in future well planning and increased production.

7. Conclusions

There are many examples like Postle Field in the world which have been producing for many decades but still have lot of reserves left to be exploited. These prolific reservoirs are important exploration plays, yet the reservoirs are difficult to detect using conventional P-wave seismic. New technologies and methods can help in exploiting these reserves. Shear wave data has the potential to revive and extend the life of mature fields like Postle. It helps in imaging the sandstones and also monitoring the enhanced oil recovery. This is because S-waves are more sensitive to pressure changes than are P-waves.

To date, mostly compressional wave studies have been done to characterize Morrow sandstones, with limited modeling studies. The full waveform modeling shows that S-waves are better than P- or PS-waves for Morrow sandstone detection. This study helped in understanding the Morrow A sandstone AVO response for different wave modes. The modeled gathers for P-, S-, and PS-wave show that stronger amplitudes correspond to thicker A sandstone accumulations. Modeling helped in understanding the interference effect due to the overlying shale and a limestone layer below. It also helped in understanding multiples caused by shallow anhydrite layers. S-wave data are commonly used for fracture mapping but this study shows their use in detecting thin reservoir sandstones. The present modeling study is tied to the results from field data showing how shear wave data have important implications for oil exploration and development in areas where P-wave data is unsatisfactory. The shear wave rotation analysis and data processing is still going on, and we hope to get better results from P-, PS-, and S-wave data interpretation in future.

Acknowledgments

The authors would like to thank BP America for providing the modeling software for this study and Mike O'Brien for helping us use the software. We would sincerely thank the Reservoir Characterization Project Sponsors and students for their support and encouragement. Special thanks to Whiting Petroleum for providing the multicomponent data and Fairfield Industries for processing it.

References

[1] R. P. Sorenson, "A dynamic model for the Permian Panhandle and Hugoton fields, western Anadarko basin," *American Association of Petroleum Geologists Bulletin*, vol. 89, no. 7, pp. 921–938, 2005.

[2] D. D. Rice, C. N. Threlkeld, and A. K. Vuletich, "Character, origin and occurrence of natural gases in the Anadarko basin, southwestern Kansas, western Oklahoma and Texas Panhandle, U.S.A," *Chemical Geology*, vol. 71, no. 1–3, pp. 149–157, 1988.

[3] J. R. Halverson, "Seismic expression of the upper Morrow sands, Western Anadarko Basin," *Geophysics*, vol. 53, no. 3, pp. 290–303, 1988.

[4] J. T. Noah, R. D. Teague, and G. Hofland, "Twin Morrow field: a case study," *The Leading Edge*, vol. 13, no. 1, pp. 25–30, 1994.

[5] M. Wiley, *Structural and stratigraphic controls on Morrow sandstone reservoir distribution from 3-D seismic data, Postle field, Texas county, Oklahoma*, M.S. thesis, Colorado School of Mines, Golden, Colo, USA, 2009, #T-6576.

[6] J. Gibson and S. Roche, "Multicomponent technology—reducing risk and creating opportunity," *Exploration and Production: The Oil and Gas Review*, pp. 1–7, 2005.

[7] J. Caldwell, P. Christie, F. Engelmark et al., "Shear waves shine brightly," *Oilfield Review*, vol. 11, no. 1, pp. 2–15, 1999.

[8] F. Engelmark, "Using converted shear waves to image reservoirs with low-impedance contrast," *The Leading Edge*, vol. 19, no. 6, pp. 600–603, 2000.

[9] M. K. MacLeod, R. A. Hanson, C. R. Bell, and S. McHugo, "The Alba field ocean bottom cable seismic survey: impact on field development," *The Leading Edge*, vol. 18, no. 11, pp. 1306–1312, 1999.

[10] G. F. Margrave, D. C. Lawton, and R. R. Stewart, "Interpreting channel sands with 3C-3D seismic data," *The Leading Edge*, vol. 17, no. 4, pp. 509–513, 1998.

[11] S. Knapp, N. Payne, and T. Johns, "Imaging through gas clouds: a case history in the Gulf of Mexico," in *Proceedings of the 71st Annual International Meeting*, pp. 776–779, SEG, 2002, Expanded Abstracts.

[12] F. Engelmark, "Using 4-C to characterize lithologies and fluids in clastic reservoirs," *The Leading Edge*, vol. 20, no. 9, pp. 1053–1055, 2001.

[13] S. Crampin, "Evaluation of anisotropy by shear-wave splitting," *Geophysics*, vol. 50, no. 1, pp. 142–152, 1985.

[14] M. A. Martin and T. L. Davis, "Shear-wave birefringence: a new tool for evaluating fractured reservoirs," *The Leading Edge*, vol. 8, no. 10, pp. 22–28, 1987.

[15] S. Crampin, "Anisotropy and transverse isotropy," *Geophysical Prospecting*, vol. 34, no. 1, pp. 94–99, 1986.

[16] S. Crampin, "Geological and industrial implications of extensive-dilatancy anisotropy," *Nature*, vol. 328, no. 6130, pp. 491–496, 1987.

[17] S. Crampin, "Nonparallel S-wave polarizations in sedimentary basins," in *Proceedings of the 58th Annual International Meeting*, pp. 1130–1132, SEG, 1988, Expanded Abstracts.

[18] S. Crampin, "The new geophysics: shear-wave splitting provides a window into the crack-critical rock mass," *The Leading Edge*, vol. 22, no. 6, pp. 536–549, 2003.

[19] H. B. Lynn and L. A. Thomsen, "Reflection shear-wave data collected near the principal axes of azimuthal anisotropy," *Geophysics*, vol. 55, no. 2, pp. 147–156, 1990.

[20] M. C. Mueller, "Using shear waves to predict lateral variability in vertical fracture intensity," *The Leading Edge*, vol. 11, no. 2, pp. 29–35, 1992.

[21] M. Rumon, *Shear wave time-lapse seismic monitoring of a tight gas sandstone reservoir, Rulison field, Colorado*, M.S. thesis, Colorado School of Mines, Golden, Colo, USA, 2006, #T-6187.

[22] M. Terrel, *Fracture permeability characterization at Weyburn field: from shear wave anisotropy through flow simulation*, Ph.D. thesis, Colorado School of Mines, Golden, Colo, USA, 2004, #T-5486.

[23] R. R. Stewart, J. E. Gaiser, R. J. Brown, and D. C. Lawton, "Converted-wave seismic exploration: applications," *Geophysics*, vol. 68, no. 1, pp. 40–57, 2003.

[24] T. Wilson, *Converted-Wave Morrow sandstone delineation, Eva South field, Texas County, Oklahoma*, M.S. thesis, Colorado School of Mines, Golden, Colo, USA, 2002, #T-5597.

[25] J. E. Blott, *Morrow valley fill sandstone reservoir characterization with 3D-3C seismology, Sorrento field, Colorado*, Ph.D. thesis, Colorado School of Mines, Golden, Colo, USA, 1997, #T-5006.

[26] D. C. Rampton, *The shear difference: improved characterization of a Morrow fluvial sandstone using the shear seismic response, Sorrento field, Southeast Colorado*, M.S. thesis, Colorado School of Mines, Golden, Colo, USA, 1995, #T-4759.

[27] T. L. Davis, "Dynamic reservoir characterization for high resolution connectivity mapping and conformance control. Morrow sandstone reservoir, Postle field, Oklahoma," Colorado School of Mines Proposal no. 8181, 2007.

[28] M. A. Zimmer, M. Prasad, G. Mavko, and A. Nur, "Seismic velocities of unconsolidated sands—part 1: pressure trends from 0.1 to 20 MPa," *Geophysics*, vol. 72, no. 1, pp. E1–E13, 2007.

[29] M. N. Toksöz, C. H. Cheng, and A. Timur, "Velocities of seismic waves in porous rocks," *Geophysics*, vol. 41, no. 4, pp. 621–645, 1976.

[30] P. Singh, T. Davis, and M. O'Brien, "Understanding Morrow A sands through elastic modeling," in *Proceedings of the 79th Annual International Meeting*, pp. 1252–1256, SEG, 2009, Expanded Abstracts.

[31] E. Arro, "Morrowan sandstones in the subsurface of the Hough area, Texas county, Oklahoma," *OCGS—The Shale Shaker Digest V*, vol. 15–17, pp. 16–30, 1965.

[32] D. W. Bowen and P. Weimer, "Regional sequence stratigraphic setting and reservoir geology of Morrow incised-valley sandstones (lower Pennsylvanian), eastern Colorado and western Kansas," *AAPG Bulletin*, vol. 87, no. 5, pp. 781–815, 2003.

[33] M. E. Henry and T. C. Hester, "Anadarko Basin Province (058)," 1995, http://certmapper.cr.usgs.gov/data/noga95/prov58/text/prov58.pdf .

[34] B. Rascoe Jr. and F. J. Adler, "Permo-Carboniferous hydrocarbon accumulations, Mid-Continent, U.S.A," *American Association of Petroleum Geologists Bulletin*, vol. 67, no. 6, pp. 979–1001, 1983.

[35] R. Pinto, "Vp/Vs: reservoir characterization project spring 2010 meeting presentation," Colorado School of Mines, 2010.

[36] J. M. Carcione, G. C. Herman, and A. P. E. ten Kroode, "Seismic modeling," *Geophysics*, vol. 67, no. 4, pp. 1304–1325, 2002.

[37] E. S. Krebes, "Seismic forward modeling," *CSEG Recorder*, pp. 28–39, 2004.

[38] G. F. Margrave and P. M. Manning, "Seismic modeling: an essential interpreter's tool," in *Proceedings of the CSEG National Convention*, 2004.

[39] I. Lecomte, H. Gjoystdal, A. Drottning, F. A. Maao, T. A. Johansen, and R. Bakke, "Efficient and flexible seismic modeling of reservoirs: a hybrid approach," *The Leading Edge*, vol. 23, no. 5, pp. 432–437, 2004.

[40] J. T. Etgen, "Finite-difference elastic anisotropic wave propagation," Stanford Exploration Project Report SEP-56, 1987.

[41] J. T. Etgen and M. J. O'Brien, "Computational methods for large-scale 3D acoustic finite-difference modeling: a tutorial," *Geophysics*, vol. 72, no. 5, pp. 223–230, 2007.

[42] C. E. Melvin, *The influence of P-wave multiple attenuation characterization of the Morrow A sandstone reservoir at Postle field, Texas county, Oklahoma*, M.S. thesis, Colorado School of Mines, Golden, Colo, USA, 2010.

[43] R. M. Alford, "Shear data in the presence of azimuthal anisotropy," in *Proceedings of the 56th Annual International Meeting*, pp. 476–479, SEG, 1986, Expanded Abstracts.

Hindawi Publishing Corporation
International Journal of Geophysics
Volume 2011, Article ID 316581, 8 pages
doi:10.1155/2011/316581

Research Article

Dynamically Focused Gaussian Beams for Seismic Imaging

Robert L. Nowack

Department of Earth and Atmospheric Sciences, Purdue University, West Lafayette, IN 47907, USA

Correspondence should be addressed to Robert L. Nowack, nowack@purdue.edu

Received 15 January 2011; Accepted 22 March 2011

Academic Editor: Yu Zhang

An initial study is performed in which dynamically focused Gaussian beams are investigated for seismic imaging. Focused Gaussian beams away from the source and receiver plane allow the narrowest and planar portions of the beams to occur at the depth of a specific target structure. To match the seismic data, quadratic phase corrections are required for the local slant stacks of the surface data. To provide additional control of the imaging process, dynamic focusing is investigated where all subsurface points are specified to have the same planar beam fronts. This gives the effect of using nondiffracting beams, but actually results from the use of multiple focusing depths for each Gaussian beam. However, now different local slant stacks must be performed depending on the position of the subsurface scattering point. To speed up the process, slant stacking of the local data windows is varied to match the focusing depths along individual beams when tracked back into the medium. The approach is tested with a simple model of 5-point scatterers which are then imaged with the data, and then to the imaging of a single dynamically focused beam for one shot gather computed from the Sigsbee2A model.

1. Introduction

Dynamically focused Gaussian beams are investigated for the seismic imaging of common-shot reflection data. This extends the work of Nowack [1] in which focusing of Gaussian beams propagated from the source, and receiver surface is used to allow the narrowest portions of the beams to occur at the depth of a specific target structure. The beam fronts at the beam waists are also planar leading to more stable beam summations for imaging. To match with the surface data, quadratic phase corrections are required for the local slant-stacks of the surface data. However, in the earlier approach only a single focusing depth can be specified. To provide additional control on the imaging process using focused Gaussian beams, a dynamic process is investigated where all subsurface points are specified to have planar beams of the same width. This gives the effect of using nondiffracting beams at the scatterers, but actually results from the use of multiple imaging depths for each Gaussian beam. As a result, there is a tradeoff in speed where now different slant stacks of the data are required for each subsurface point. In order to speed up the imaging process, the slant stacking of the data window is varied to match the focusing depths along individual beams when tracked back into the medium. These focused slant stacks are then matched to Gaussian beams with beam waists located at different subsurface locations. The approach is first tested using 5-point scatterers which are then imaged with the data, and then using a single dynamically focused beam for one shot gather computed from the Sigsbee2A model.

Summations of Gaussian beams have been applied for the computation of high-frequency seismic wavefields in smoothly varying inhomogeneous media (see e.g., Popov [2]; Cerveny et al. [3]; Nowack and Aki [4]). Reviews of Gaussian beam summation have been given by Cerveny [5, 6], Babich and Popov [7], and more recently by Popov [8], Nowack [9], Cerveny et al. [10], and Bleistein [11]. An advantage of summations using Gaussian beams to construct more general wavefields is that the individual Gaussian beams have no singularities along their paths, no two-point ray tracing is required, and triplicated arrivals are naturally incorporated into either forward or inverse modeling. More recently overcomplete frame-based Gaussian beam summations have been developed based on window and wavelet transforms to address some of the issues related to completeness of beam summations [12]. In an overcomplete frame-based approach, the wavefield is decomposed into beam fields that are localized both in position and direction. Although an orthonormal basis cannot be formed using a Gabor frame, an overcomplete frame expansion can be constructed which has the added benefit of providing redundancy in the expansion [13–17]. Here curved initial beams are used to decompose the data and these are then propagated into the subsurface using dynamically focused Gaussian beams. An alternative is to shoot beams from the scattering locations upwards to the source and receiver plane as was done by Popov et al. [18], but this will be computationally slower than shooting beams from the surface.

In order to test the dynamically focused Gaussian beam approach, a model is constructed with 5 small scatterers with depth in a vertically varying medium resulting in five diffracted arrivals each with different move-outs with distance. The partial image is then given for a single beam with different focusing depths such that the planar beam waists at the subsurface points are the same. However, when summed over all angles and data windows, the scatterers are properly imaged. This is then tested for a single dynamically focused beam for one-shot gather computed from the Sigsbee2a model. The advantage of using dynamically focused beams is the consistency of having the same focused beams for all subsurface points. A disadvantage is that now multiple slant stacks are required for different points of the subsurface which increases the computational burden compared to a standard Gaussian beam algorithm or a beam algorithm with a single focus depth. This can in part be offset by precomputing the beam stacks at a set number of focusing depths and then interpolating the results required at different subsurface points.

2. Gaussian Beam Imaging with Dynamically Focused Beams

In common-shot migration, each shot gather is migrated separately and the results are summed to give the final image $\delta m(\underline{x})$. Thus,

$$\delta m(\underline{x}) \sim \int d\underline{x}^s I^s(\underline{x}), \tag{1}$$

where the adjoint image for each shot point can be written as

$$\begin{gathered} I^s(\underline{x}) = \int \frac{d\omega}{2\pi} B(\omega) \int d\underline{x}^g \overline{g}(\underline{x},\underline{x}^s,\omega)\overline{g}(\underline{x},\underline{x}^g,\omega) u_s(\underline{x}^g,\underline{x}^s,\omega) \\ B(\omega) = \omega^2 \overline{S}(\omega), \end{gathered} \tag{2}$$

where ω is the radial frequency, $S(\omega)$ is the source time function, $\underline{x}^g$ is the geophone location, $\underline{x}^s$ is the source location, and $u_s(\underline{x}^g,\underline{x}^s,\omega)$ is the scattered field recorded at the geophones. $g(\underline{x},\underline{x}^g,\omega)$ and $g(\underline{x},\underline{x}^s,\omega)$ are the Green's functions, from the geophones and source to the subsurface scattering points $\underline{x}$. From reciprocity of the Green's function $g(\underline{x},\underline{x}',\omega) = g(\underline{x}',\underline{x},\omega)$ and $\overline{g}$ indicates the complex conjugate of g.

In the 2D case, the Green's function can be written in terms of a summation of Gaussian beams as

$$\begin{aligned} g(\underline{x},\underline{x}',\omega) &= \frac{-i}{4\pi}\left(\frac{\varepsilon}{v_0}\right)^{1/2} \int d\gamma\, u^{\mathrm{gb}}(\underline{x},\underline{x}',\omega) \\ &= \frac{-i}{4\pi}\left(\frac{\varepsilon}{v_0}\right)^{1/2} \int \frac{\mathrm{d}p_1^r}{p_3^r} u^{\mathrm{gb}}\left(\underline{x},\underline{x}',\underline{p}^r,\omega\right), \end{aligned} \tag{3}$$

where ε is the complex beam parameter [3] and

$$u^{\mathrm{gb}}(\underline{x},\underline{x}',\omega) = \left[\frac{v(s)}{q(s)}\right]^{1/2} \exp\left\{i\omega\tau(s) + \frac{i\omega}{2}M(s)n^2\right\}. \tag{4}$$

The coordinates (s,n) correspond to the subsurface position $\underline{x}$ in ray-centered coordinates, $\tau(s)$ is the travel time along the central ray, $v(s)$ is the velocity along the central ray, and the horizontal component of the ray parameter vector at the initial point is $p_1^r = \sin\gamma/v_0$, where γ is the take-off angle from the vertical.

The complex second derivative of the travel time field with respect to the transverse coordinate n can be written as

$$M(s) = M_R(s) + iM_I(s) = \frac{p(s)}{q(s)}, \tag{5}$$

where $M_R(s)$ is related to the wavefront curvature $K(s)$ of the beam by $M_R(s) = K(s)/v(s)$. To form a bounded Gaussian beam, then $M_I(s) > 0$. The variables $p(s)$ and $q(s)$ are solutions to the dynamic ray equations and for a beam solution are also complex [19]. The dynamic ray equations in 2D have two real fundamental solutions which can be written as

$$\pi(s,s_0) = \begin{bmatrix} q_1(s) & q_2(s) \\ p_1(s) & p_2(s) \end{bmatrix}, \tag{6}$$

where $\pi(s_0,s_0) = I$. $q_1(s)$, $p_1(s)$ are solutions for an initial plane wave and $q_2(s)$, and $p_2(s)$ are for an initial line source. The inverse of $\pi(s,s_0)$ is

$$\pi^{-1}(s,s_0) = \pi(s_0,s) = \begin{bmatrix} p_2(s) & -q_2(s) \\ -p_1(s) & q_1(s) \end{bmatrix}. \tag{7}$$

The two real solutions of the dynamic ray equations must then be combined to form a Gaussian beam. There are a number of ways to combine the solutions, but one way is [3]

$$\begin{aligned} q(s) &= \varepsilon q_1(s) + q_2(s), \\ p(s) &= \varepsilon p_1(s) + p_2(s), \end{aligned} \tag{8}$$

where ε is the beam parameter. The variable $q(s)$ is related to the complex geometrical spreading along the beam. Since for the fundamental solution matrix $\mathrm{Det}(\pi(s,s_0)) = 1$ for all points along the ray, the complex geometric spreading can never be zero at any point along the beam if it is nonzero at any one point. Since the Gaussian beam amplitude is related to the inverse square root of the geometric spreading, the beam amplitudes are always finite, even at caustics for the ray solution. This is one of the useful features of Gaussian beam solutions, in contrast to ray solutions.

The second derivative of the time field with respect to n can be written as

$$M(s) = M_R(s) + iM_I(s) = \frac{\varepsilon p_1(s) + p_2(s)}{\varepsilon q_1(s) + q_2(s)}. \tag{9}$$

Since at the source point $\pi(s_0, s_0) = I$ and $\varepsilon = \varepsilon_R - i\varepsilon_I$, then

$$M(s_0) = M_R(s_0) + iM_I(s_0) = \frac{1}{\varepsilon} = \frac{\varepsilon_R}{\varepsilon^*\varepsilon} + \frac{i\varepsilon_I}{\varepsilon^*\varepsilon}, \tag{10}$$

where $\varepsilon^*\varepsilon$ is the magnitude squared of ε. Alternatively, ε can be written in terms of $M(s_0)$ as

$$\varepsilon = \frac{M_R(s_0)}{M^*(s_0)M(s_0)} - \frac{iM_I(s_0)}{M^*(s_0)M(s_0)}, \tag{11}$$

where $M^*(s_0)M(s_0)$ is the magnitude squared of $M(s_0)$. Thus, the complex beam parameter can be specified either directly in terms of ε or in terms of $M(s_0)$.

The complex beam parameter can also be written

$$\varepsilon = \varepsilon_r - i\varepsilon_i = v_0 S_0 - iv_0 L_0^2, \tag{12}$$

where v_0 is an initial velocity. In a homogeneous medium, S_0 is the distance of the beam waist from the initial point of beam.

An alternate, and in some sense simpler way, to blend the solutions to the dynamic ray equations is

$$\begin{aligned} q(s) &= q_1(s) + M(s_0)q_2(s), \\ p(s) &= p_1(s) + M(s_0)p_2(s), \end{aligned} \tag{13}$$

where

$$M(s_0) = M_R(s_0) + iM_I(s_0) = \frac{1}{\varepsilon}. \tag{14}$$

In either case, we can obtain $M(s)$ at the scattering point, from the initial value of $M(s_0)$ along the source and receiver array by solving the dynamic ray equations for $p(s)$ and $q(s)$, and then forming $M(s) = p(s)/q(s)$. Alternatively, we can specify $M(s)$ at the scattering point and then use the solution matrix for the dynamic ray equation $\pi(s_0, s)$ from s to s_0 to obtain $p(s_0)$ and $q(s_0)$ at the initial point of the ray. From these, one can obtain the corresponding value of beam curvature $M(s_0)$ at the beginning point of the ray. At a point along the beam, $M(s)$ can be written as

$$M(s) = M_R(s) + iM_I(s) = \frac{K(s)}{v(s)} + iM_I(s), \tag{15}$$

where $K(s)$ is the wavefront curvature in ray coordinates, $v(s)$ is the velocity along the ray, and $M_I(s)$ is related to the transverse beam width, and these can be specified at the scattering point along the ray and used to determine the value at the beginning point of the ray.

The exponential term away from the central ray can be written as

$$\exp\left\{ \frac{-\omega}{2} M_I(s) n^2 \right\} = \exp\left\{ \frac{-n^2}{2L^2(s)} \right\}, \tag{16}$$

where $L(s) = (\omega M_I(s))^{-1/2}$ is the beam half-width transverse to the ray. At the initial point of the beam, $L(s_0) = (\omega M_I(s_0))^{-1/2} = (\varepsilon^*\varepsilon/\omega\varepsilon_I)^{1/2}$. For the case of the beam waist at the initial point of the beam $M_R(s_0) = 0$, and $L(s_0) = (v_0/\omega)^{1/2} L_0$ is the beam half-width at the beam waist. In a homogeneous medium, this is the narrowest point along the beam and is also the only point where the beam front is planar. For the case when $M_R(s_0) = 0$ where $s \neq s_0$, the beam front is planar at some point s along the ray and generally curved at the initial position $s = s_0$. Also, the beam waist is shifted along the beam away from the initial point of the beam.

Although the planar beam waist is often placed at the initial source point for forward modeling, it is also common to put the beam waist at the receiver location [5, 6]. This reduces the number of beams required for the summation at the receiver, and also planar beam fronts at the receiver provide more stable beam summations. Recent true amplitude migration formulations using Gaussian beams have used beams launched directly from the scattering points up to the surface with the beam waists specified at the scattering points [18, 20, 21]). However, it is more economical to launch beams from the source and receiver positions down into the subsurface since there are fewer source and receiver locations than subsurface scattering points, and this minimizes the amount of beam tracing required. In order to locate the beam waists in the subsurface when the beams are launched from the source and receiver aperture, then generally curved beam fronts are required along the source and receiver aperture.

For dynamic beam focusing in Gaussian beam imaging, the beams are launched from the initial source and receiver plane, but then are dynamically focused for each of the individual scattering points. Although the beams are generally nonplanar along the receiver plane, the initial beam parameters can be determined from the specified beam parameters at depth. However, now these curved beams on the initial surface must be matched to the local slant stacks of the data for beam parameters specified at each of the subsurface scattering points.

Assuming that the initial beam parameters have been determined from dynamic ray tracing for beam parameters specified at the scattering points, then the algorithm for imaging-focused Gaussian beams from Nowack [1] can be extended to dynamic focusing. For generally nonplanar initial beams at the source or receiver locations launched at some angle to the aperture plane, the quadratic part of the initial beam with respect to the horizontal x coordinate can be written as

$$\exp\left\{ \frac{i\omega}{2} \frac{K_x(s_0)}{v_0} (x - x_L)^2 \right\} \exp\left\{ \frac{-(x - x_L)^2}{2L_{x-\mathrm{ref}}^2(s)} \right\}, \tag{17}$$

where $K_x(s_0)$ is the initial real-valued horizontal beam curvature and $L_{x-\mathrm{ref}}(s_0)$ is the initial horizontal beam half-width at the reference frequency ω_{ref}. To match this with the initial parameters of the beam propagated into the medium, then the transverse coordinate of the beam $n = \cos\gamma(x - x_L)$ where γ is the angle of the beam with respect to the vertical. Given the initial values $K_x(s_0)$ and $L_{x-\mathrm{ref}}(s_0)$ along the source and receiver aperture, then the initial values for $M_R(s_0)$ and $M_I(s_0)$ for the beams are

$$M_R(s_0) = \frac{K_x(s_0)}{v_0 \cos^2(\gamma)}, \qquad M_I(s_0) = \left(\omega_{\text{ref}} \cos^2(\gamma) L^2_{x-\text{ref}}(s_0)\right)^{-1}, \tag{18}$$

and then the initial beam parameter $\varepsilon = \varepsilon_r - i\varepsilon_i$ can be obtained and used to construct the beam solution propagated into the medium.

The 2D resolution of unity by Gaussian functions in the aperture plane is

$$1 \sim \frac{1}{\sqrt{2\pi}} \frac{\Delta L}{\sigma} \sum_{m=-\infty}^{\infty} e^{-(x-m\Delta L)^2/2\sigma^2}, \tag{19}$$

where

$$\Delta L \ll 2\sigma. \tag{20}$$

Assuming a regularly spaced set of beam centers $x_L = m\Delta L$ along the receiver array, the initial locations of the Green's functions at the receivers can be phase shifted to these beam center locations with a phase adjustment of $p_1^g(x_1^g - m\Delta L) + K_x(s_0)(x_1^g - m\Delta L)^2/2v_0$. Then,

$$\begin{aligned} &g(\underline{x}, \underline{x}^g, \omega) \\ &\quad \sim C^g \int \frac{\mathrm{dp}_1^g}{p_3^g} u^{\text{gb}}\left(\underline{x}, \underline{x}^L, \underline{p}^g, \omega\right) e^{i\omega(p_1^g(x_1^g - m\Delta L) + K_x(s_0)(x_1^g - m\Delta L)^2/2v_0)}, \end{aligned} \tag{21}$$

where C^g represents the terms in front of the last integral in (3) for the receiver Green's functions and p_1^g is the horizontal component of the ray parameter vector along the receiver aperture. The imaging formula can then be written as

$$\begin{aligned} I_s(\underline{x}) = \sum_{m=-\infty}^{\infty} &\int \frac{d\omega}{2\pi} A_1(\omega) \int d\underline{x}^g \\ &\times \int \frac{\mathrm{dp}_1^g}{p_3^g} \overline{u}^{\text{gb}}\left(\underline{x}, \underline{x}^L, \underline{p}^g, \omega\right) \\ &\times e^{-i\omega(p_1^g(x_1^g - m\Delta L) + K_x(s_0)(x_1^g - m\Delta L)^2/2v_0)} \\ &\times \overline{g}(\underline{x}, \underline{x}^s, \omega) u_s(\underline{x}^r, \underline{x}^s, \omega) e^{-(x_1^g - m\Delta L)^2/2\sigma^2}, \end{aligned} \tag{22}$$

where

$$A_1(\omega) = \left(\frac{+i}{2\pi}\right)\left(\frac{\varepsilon}{v_0^g}\right)^{1/2} \omega^2 \overline{S}(\omega) \frac{1}{\sqrt{2\pi}} \frac{\Delta L}{\sigma}. \tag{23}$$

The source Green's function now needs to be decomposed into Gaussian beams, but for simplicity here will be just referred to as $\overline{g}(\underline{x}, \underline{x}^s, \omega)$, where the over-bar signifies the complex conjugate

The common-shot imaging formula for nonplanar, focused beams along the aperture plane can then be written as

$$\begin{aligned} I_s(\underline{x}) = \sum_{m=-\infty}^{\infty} \int \frac{d\omega}{2\pi} \int \frac{\mathrm{dp}_1^g}{p_3^g} A_1(\omega) \overline{g}(\underline{x}, \underline{x}^s, \omega) \\ \times \overline{u}^{\text{gb}}\left(\underline{x}, \underline{x}^L, \underline{p}^g, \omega\right) D_p\left(\underline{x}^L, \underline{x}^s, \underline{p}^g, \omega\right), \end{aligned} \tag{24}$$

where

$$\begin{aligned} D_p\left(\underline{x}^L, \underline{x}^s, \underline{p}^g, \omega\right) = \int \mathrm{dx}_1^g u_s(\underline{x}^g, \underline{x}^s, \omega) e^{-(x_1^g - m\Delta L)^2/2\sigma^2} \\ \times e^{-i\omega(p_1^g(x_1^g - m\Delta L) + K_x(s_0)(x_1^g - m\Delta L)^2/2v_0)}. \end{aligned} \tag{25}$$

This is a local slant-stack of the data with a quadratic phase correction term to match the data with the beams launched into the medium. The standard Gaussian beam migration formulas with the planar beam waists along the aperture plane do not include this quadratic phase correction term [14–17]. The beam centers are spaced along the receiver aperture plane at

$$x_1^L = m\Delta L, \quad \Delta L \ll 2\sigma, \tag{26}$$

and the initial horizontal beam widths are

$$\sigma = L_{x-\text{ref}}(s_0)\left(\frac{\omega_r}{\omega}\right)^{1/2}, \tag{27}$$

where $L_{x-\text{ref}}(s_0)$ is the horizontal half-width of an initial Gaussian function at the reference frequency ω_{ref}. The spacing of the beams in horizontal position and launch angle can then be determined based either on physical reasoning [14–17] or by arguments based on frames [13]. However, for curved beams along the initial plane, the data windows need to be broader to account for the wider beams at the surface.

3. Applications of Dynamically Focused Gaussian Beam Migration

In order to test the dynamically focused beam migration formulation, two examples are given. The first application has 5 compact sources located at depths of 8,000, 12,000, 16,000, 20,000, and 24,0000 ft at a distance of 40,000 ft from the left side of the model. The background velocity model has two layers. The first layer has a thickness of 6000 ft with a constant velocity of 5000 ft/sec. The second layer goes from 6000 ft to 30,000 ft in depth with a vertical velocity gradient of $v(z) = v_0 + k(z - z_b)$, where $v_0 = 5000$ ft/sec and $k = .15$. The shot position is located along the surface at a horizontal position of 40,000 ft from the left side of the model. The receiver array is from 25,000 ft to 55,000 ft on the surface. Figure 1 shows the computed wavefield from the 5 compact scatterers. The sampling rate is .008 sec, and the peak frequency of the data is 5 Hz.

Figure 2 shows the partial image of the data from a single vertically propagated Gaussian beam with the planar

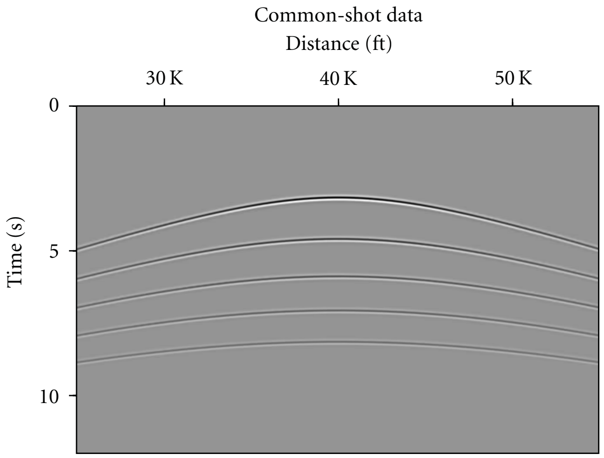

Figure 1: Computed common-shot data is shown for a shot point on the surface at a position of 40,000 ft. The receiver array is from 25,000 ft to 55,000 ft. Diffractions from 5 compact scatterers are shown each with a horizontal position of 40,000 ft and depths of 8,000, 12,000, 16,000, 20,000, and 24,000 ft.

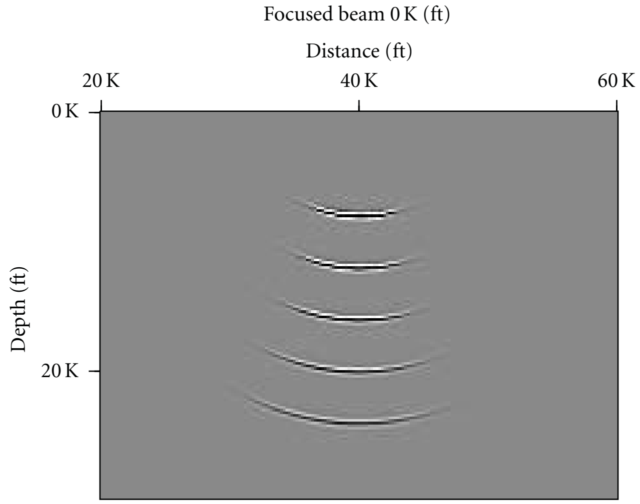

Figure 2: The partial image of the common shot data in Figure 1 using a single vertical Gaussian beam at a receiver position at 40,000 ft using a beam with a planar beam waist at the surface.

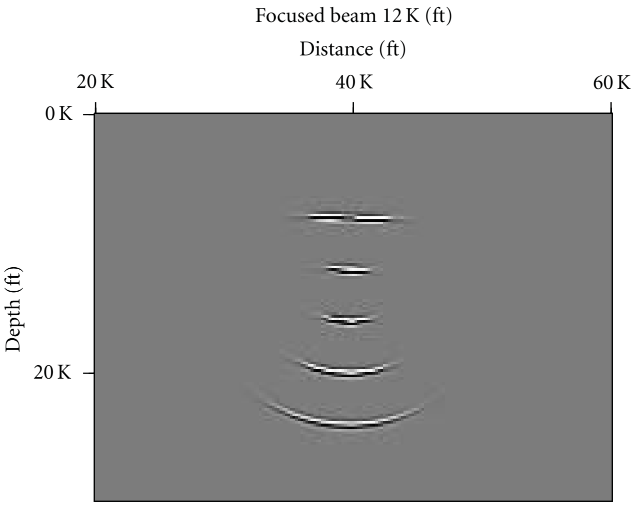

Figure 3: The partial image of the common-shot data in Figure 1 using a single vertical Gaussian beam at a receiver position at 40,000 ft using a focused beam with a beam waist at a depth of about 12,000 ft.

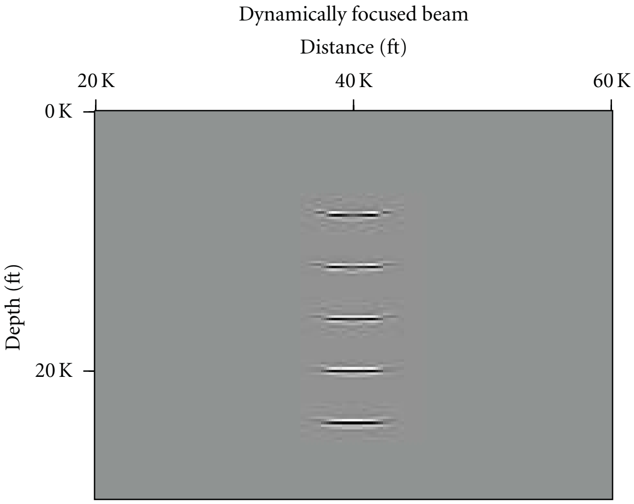

Figure 4: The partial image of the common shot data in Figure 1 using a vertical dynamically focused beam.

wavefront at the surface. For simplicity, the source side Green's function is constructed separately using Gaussian beams that are planar at the source location for all the examples given. Note on the figure that the images of the diffractors are curved and increase in width with depth. Figure 3 shows the partial image of the common shot data in Figure 1 using a single vertical Gaussian beam at a receiver position at 40,000 ft using a focused beam with the beam waist at a depth of 12,000 ft. Now the diffractor at a depth of 12,000 ft is the most focused using a single beam with the images of the other diffractors being broader and generally curved.

Figure 4 shows the partial image of the common shot data in Figure 1 using a single vertical Gaussian beam at a receiver position at 40,000 ft using dynamic focusing with the beam waist now specified at all depths. Now the partial image of the scatterers all have similar images with plane beam waists of the same beam widths for all scatterers. It would look as if we had been able to perform Gaussian beam migration with nondiffracting Gaussian beams. However, actually the image is formed with a number of different Gaussian beams for all scattering points in the medium such that in a dynamic fashion the beams have the same planar beam waists and beam widths at each scatterer.

Figure 5 shows the complete dynamically focused Gaussian beam image for the single-shot gather from Figure 1 using beams from all beam center locations launched at a range of angles. This results in focused images of all 5 scatterers and indicates that the imaging is being properly applied even with the shifted beam waists of the individual

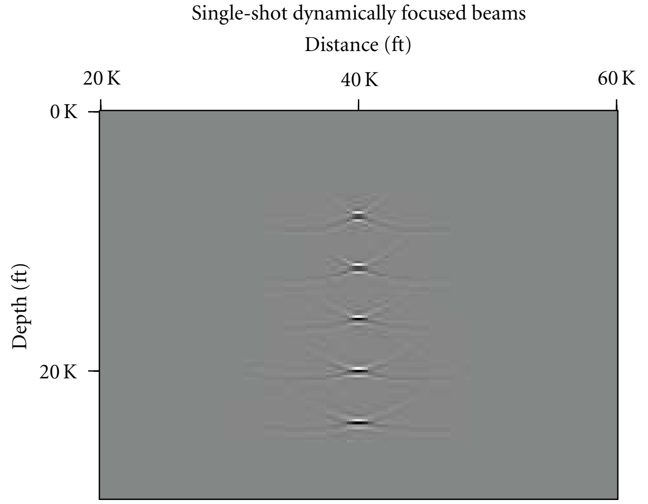

Figure 5: The Gaussian beam image is shown using the single-shot gather in Figure 1 with beams from all beam positions launched at a range of angles, each with dynamically focused beams. This results in focused images of all 5 scatterers and indicates that the imaging is being properly applied even with dynamically focused individual beam components.

beam components for all imaging points of the medium. The small tails result from the limited angle range for the summation of the beams for the one-shot gather.

The dynamically-focusing beam approach is now applied to a single-shot gather from the Sigsbee2A data set distributed by SMAART (Subsalt Multiples Attenuation and Reduction Team) and available at http://www.delphi.tudelft.nl/SMAART/. In order to test the focused beam approach, a single-shot gather with a shot location at 6,325 ft from the left edge of the model is used. The receiver array starts at the shot location and has a maximum offset of 26,025 ft with a spacing of 75 ft. The background velocity model has the first layer from the surface down to the seafloor with a velocity of 5000 ft/sec. The second layer goes from seafloor to 30,000 ft in depth with a background velocity of $v(z) = v_0 + k(z - z_{\text{seafloor}})$, where $v_0 = 5000$ ft/sec and $k = .30$. A salt dome exists with a velocity of 14,800 ft/sec in the middle and right parts of the model, but for the simple application here only one-shot gather away from the salt dome is used.

In Figure 6, the partial imaging for a single Gaussian beam is shown with the planar beam waist at the surface receiver depth. As in the earlier examples, the source side Green's function is constructed separately using Gaussian beams that are planar at the source location. The receiver Gaussian beam has an initial location near the source and the partial image for a beam with a slight angle from the vertical is shown. As in the earlier example, when the beam waist is at the surface receiver depth, then curved beam fronts result which broaden with depth over the depth range of the model shown between 15,000 and 30,000 ft. This is typical of standard implementations of Gaussian beam migration. However, in regions of a complicated background medium, the medium itself can cause additional focusing of the beams.

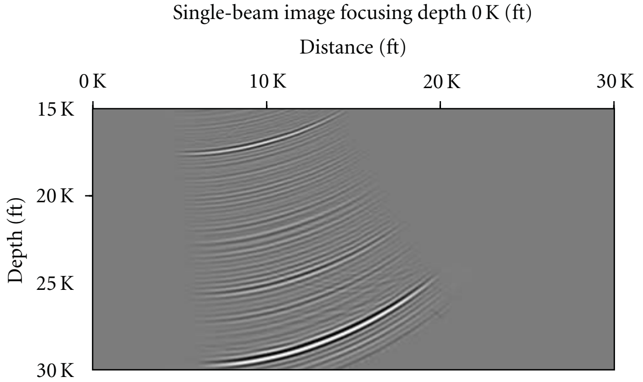

Figure 6: This shows the partial imaging result for a single Gaussian beam with the beam waist at the surface along the receiver array for one-shot gather from the Sigsbee2A dataset.

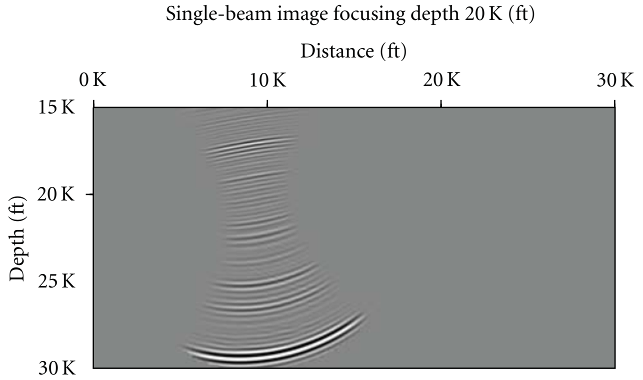

Figure 7: This shows the partial imaging result for a single Gaussian beam with the beam waist shifted to about 20,000 ft in depth for a single-shot gather from the Sigsbee2A dataset.

Figure 7 shows the partial imaging results for a single Gaussian beam with the beam waist shifted to about 20,000 ft in depth. At this depth, the narrowest part of the beam image occurs. If the target structure were located at this depth, then fewer beams would be required to form a complete image. Also, the beam images would have planar beam fronts at this depth leading to more stable images. However, as shown in Figure 7 at other depths, the partial image results in curved and broader beam fronts.

Figure 8 shows the imaging results using dynamic focusing where all subsurface points have planar beams with the same beam width. This has the appearance of an image from a single nondiffracting beam, but since Gaussian beams generally diffract this is really a composite image for Gaussian beams with multiple imaging depths for a single central beam. Nonetheless, this type of imaging can be important with certain true amplitude formulations where planar and localized beams are required at the imaging points in the subsurface [20, 21]. These formulations originally involved launching beams directly from the scattering points in the subsurface up to the surface [18]. In the faster alternative proposed here, dynamically focused Gaussian beams are launched from the surface down to the imaging points at

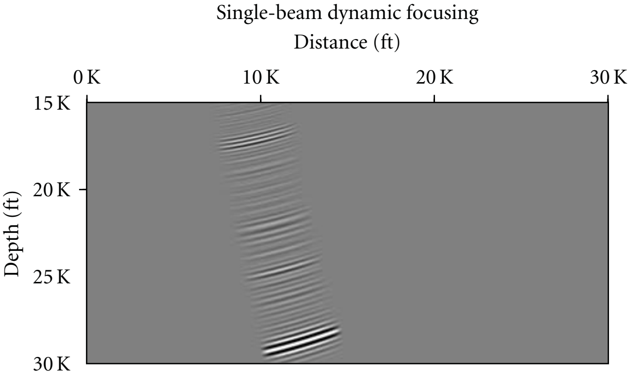

Figure 8: This shows the partial imaging result for a single dynamically focused beam for one-shot gather from the Sigsbee2A dataset.

depth instead. However, the use of dynamically focused Gaussian beams is still slower than traditional Gaussian beam imaging or imaging using focused Gaussian beams with a single focusing depth. Precomputing dynamically focused slant stacks of the data can be implemented to improve the speed of the algorithm, although this would shift some of the computational burden into precomputing and storage of the slant stacks.

An additional area of concern when specifying the beam-widths at the imaging points is that if narrow beam-widths are specified then, a finer ray sampling would be required for adequate subsurface coverage of the beams. This strategy was used by Albertin et al. [22] when using windowed, planar Maslov propagators. However, in contrast to windowed Maslov propagators, Gaussian beams asymptotically satisfy the wave equation without further windowing. For dynamic focusing with narrow beam-widths at the imaging points, a finer ray sampling would be feasible when imaging more localized subsurface targets. Planar beams with larger beam-widths could also be specified in the dynamic focusing approach, and this would still provide for stable imaging results.

4. Conclusions

The application of dynamically focused Gaussian beams has been initially investigated for seismic imaging and is an extension of the focused beam approach of Nowack [1]. The shifting of the beam waists away from the source and receiver aperture adds flexibility to Gaussian beam algorithms allowing for the narrowest portions of the beams to occur at the depth of a specific target structure. This minimizes the number of beams required to form an image at the target depth. Also, at the beam waists the beam fronts are planar leading to more stable beam summations for imaging. To match with the surface data, quadratic phase corrections are required for the local slant-stacks of the data. Using dynamically focused Gaussian beams allows for beams to have planar wavefronts and the same beam widths at all scattering points in the subsurface. It has the appearance of using non-diffracting Gaussian beams at the scatterers, but since all Gaussian beams diffract, this is really the result of using beams with multiple focusing depths. The use of planar and localized Gaussian beams at all the subsurface scattering points also has advantages with regard to certain true amplitude imaging formulations. However, using dynamically focused Gaussian beams from the surface down to the scattering points avoids having to launch beams from every scattering point in the medium up to the surface. Nonetheless, dynamically focused Gaussian beam imaging is still slower than using either traditional Gaussian beam imaging or using a single focusing depth for imaging. Dynamically focused imaging was initially tested using a single-shot gather for a model with 5 scatterers at different depths, and then for a dynamically focused Gaussian beam for one-shot gather computed from the Sigsbee2A model.

Acknowledgments

This work was supported in part by the National Science Foundation EAR06-35611 and the Air Force Geophysics Laboratory contract FA8718-08-C-002 and partly by the sponsors of the Geo-Mathematical Imaging Group (GMIG) at Purdue University.

References

[1] R. L. Nowack, “Focused Gaussian beams for seismic imaging,” in *Proceedings of the 78th Annual Meeting Society of Exploration Geophysicists, Expanded Abstracts (SEG ’08)*, pp. 2376–2380, 2008.

[2] M. M. Popov, “A new method of computation of wave fields using Gaussian beams,” *Wave Motion*, vol. 4, no. 1, pp. 85–97, 1982.

[3] V. Cerveny, M. M. Popov, and I. Psencík, “Computation of wavefields in inhomogeneous media—Gaussian beam approach,” *Geophysical Journal of the Royal Astronomical Society*, vol. 70, pp. 109–128, 1982.

[4] R. L. Nowack and K. Aki, “The two-dimensional Gaussian beam synthetic method: testing and application,” *Journal of Geophysical Research*, vol. 89, no. 9, pp. 7797–7819, 1984.

[5] V. Cerveny, “Gaussian beam synthetic seismograms.,” *Journal of Geophysics*, vol. 58, no. 1–3, pp. 44–72, 1985.

[6] V. Cerveny, “The applications of ray tracing to the numerical modeling of seismic wave fields in complex structures,” in *Seismic Shear Waves*, G. Dohr, Ed., pp. 1–124, Geophysical Press, London, UK, 1985.

[7] V. M. Babich and M. M. Popov, “Gaussian summation method (Review),” *Izvestiya Vysshikh Uchebnykh Zavedenii, Radiofizika*, vol. 32, pp. 1447–1466, 1989, translated in *Radiophysics and Quantum Electronics*, vol. 32, pp. 1063–1081, 1990.

[8] M. M. Popov, *Ray Theory and Gaussian Beam Method for Geophysicists*, Lecture Notes University of Bahia, Universidade Federal da Bahia, Salvador, Brazil, 2002.

[9] R. L. Nowack, “Calculation of synthetic seismograms with Gaussian beams,” *Pure and Applied Geophysics*, vol. 160, no. 3-4, pp. 487–507, 2003.

[10] V. Cerveny, L. Klimes, and I. Psencík, “Seismic ray method: recent developments,” *Advances in Geophysics*, vol. 48, pp. 1–128, 2007.

[11] N. Bleistein, "Mathematics of modeling, migration and inversion with Gaussian beams," Lecture Notes, 2007, http://www.cwp.mines.edu/~norm/ .

[12] D. Lugara, C. Letrou, A. Shlivinski, E. Heyman, and A. Boag, "Frame-based gaussian beam summation method: theory and applications," *Radio Science*, vol. 38, no. 2, p. 8026, 2003.

[13] H.G. Feichtinger and Strohmer T., Eds., *Gabor Analysis and Algorithms: Theory and Applications*, Birkhäuser, Boston, Mass, USA, 1998.

[14] N. R. Hill, "Gaussian beam migration," *Geophysics*, vol. 55, no. 11, pp. 1416–1428, 1990.

[15] N. Ross Hill, "Prestack Gaussian-beam depth migration," *Geophysics*, vol. 66, no. 4, pp. 1240–1250, 2001.

[16] D. Hale, "Migration by the Kirchhoff, slant stack and Gaussian beam methods," Tech. Rep. CWD-121, Center for Wave Phenomena, Colorado School of Mines, Golden, Colo, USA, 1992.

[17] R. L. Nowack, M. K. Sen, and P. L. Stoffa, "Gaussian beam migration of sparse common-shot data," in *Proceedings of the 73rd Annual Meeting Society of Exploration Geophysicists, Expanded Abstracts (SEG '03)*, pp. 1114–1117, Tulsa, Okla, USA, 2003.

[18] M. M. Popov, N. M. Semtchenok, P. M. Popov, and A. R. Verdel, "Depth migration by the Gaussian beam summation method," *Geophysics*, vol. 75, no. 2, pp. S81–S93, 2010.

[19] V. Cerveny, *Seismic Ray Theory*, Cambridge University Press, Cambridge, UK, 2000.

[20] M. I. Protasov and V. A. Cheverda, "True amplitude Gaussian beam imaging," in *Proceedings of the International Seminar Days on Diffraction (DD '05)*, pp. 225–234, St Petersburg, Russia, June-July 2005.

[21] M. I. Protasov and V. A. Cheverda, "True-amplitude seismic imaging," *Doklady Earth Sciences*, vol. 407, no. 3, pp. 441–445, 2006.

[22] U. Albertin, D. Yingst, and H. Jaramillo, "Comparing common-offset Maslov, Gaussian beam, and coherent state migrations," in *Proceedings of the 71st Annual Meeting Society of Exploration Geophysicists, Expanded Abstracts (SEG '01)*, pp. 913–916, San Antonio, Tex, USA, 2001.